

THESIS / THÈSE

DOCTOR OF SCIENCES

Multi-Scale Quantum Chemistry Investigation of Molecular Switches From Solution to Crystal

Quertinmont, Jean

Award date:
2020

Awarding institution:
University of Namur

[Link to publication](#)

General rights

Copyright and moral rights for the publications made accessible in the public portal are retained by the authors and/or other copyright owners and it is a condition of accessing publications that users recognise and abide by the legal requirements associated with these rights.

- Users may download and print one copy of any publication from the public portal for the purpose of private study or research.
- You may not further distribute the material or use it for any profit-making activity or commercial gain
- You may freely distribute the URL identifying the publication in the public portal ?

Take down policy

If you believe that this document breaches copyright please contact us providing details, and we will remove access to the work immediately and investigate your claim.

Université de Namur

**MULTI-SCALE QUANTUM CHEMISTRY
INVESTIGATION OF MOLECULAR SWITCHES:
FROM SOLUTION TO CRYSTAL**

October 8th, 2020

Jean Quertinmont

Supervised by Prof. B. Champagne

Abstract

This thesis aims at studying molecular switches in different media. In a first part, several chapters are dedicated to crystalline N-salicylideneaniline (anil) derivatives, which switch between an enol (E) and a keto (K) form. In a preliminary step, three exchange-correlation functionals (XCFs) and a atomic basis set have been selected, based on their performance compared to X-ray diffraction data to reproduce the molecular geometries, unit cell parameters, and relative $E \rightleftharpoons K$ energies of three anils. This has enabled the study of the effects of co-crystallization on the $E \rightleftharpoons K$ equilibrium of an anil, PYV3, and on its geometry, explaining the reduced thermochromism. Then, using an embedding scheme that reproduces the crystalline Colombic potential, the nuclear magnetic resonant (NMR) isotropic shielding values of PYV3 and of two of its co-crystals have been predicted, in view of enabling the interpretation of experimental data. Using this embedding scheme, the UV/Vis absorption spectra of PYV3 and its co-crystals have been modeled, allowing the interpretation of experimental spectra and a better understanding of the underlying geometrical and crystal field effects of co-crystallization. Then, anil-based covalent organic frameworks have been investigated, focusing on their relative energy, geometries, and linear and nonlinear optical (NLO) properties, giving a proof-of-concept of their potential as NLO-phores, as well as offering design guidelines. In a second part, molecular switches in solution are investigated. First, high-level methods [MP2 and CCSD(T)] are used to determine the equilibria of two anil ($E \rightleftharpoons K$) and three spiropyran (S)/merocyanine (M) ($S \rightleftharpoons M$) switches, reaching very close agreement with experiment. Then, multistate molecular switches have been studied. The NMR isotropic shielding values of a benzazoolooxazolidine (BOX) dithienylethene (DTE) hybrid have been modeled, which, combined with experiments, explains its gated-photochromism. Finally, a new family of switches, composed of two identical BOX units, and therefore three states, have been studied. It is demonstrated that their three states can be accessed in a controlled way and that they present large NLO contrasts. The role of the linker between the BOX units has been unraveled in view of improving their switching properties.

These different contributions show the central role of computational chemistry methods to interpret experimental data, to deduce structure-property relationships, and to contribute to the design of new intelligent molecules.

Acknowledgments

I am lucky to have many people to thank, so here are some of them.

First and foremost, my gratitude goes to Benoît who believed in me, gave the means and the mentorship to succeed and get the most out of this experience. One of the amazing aspect of science is the possibility, the chance, and in my opinion the need to collaborate. In that regard, I am very happy with my experiences during this Ph.D. Thanks to Johan Wouters and Tom Leyssens and all the members of the ARC CONTRAST, in particular Andrea and Nikolay, as well as Vanessa, and Gabriel. A big thank you goes to Lionel Sanguinet for the collaboration on the BOX systems whom shown not only respect but also interest in quantum chemistry. Thanks to Ayan Datta for the work on the COFs. Also on the topic of the COFs, a big thank you to Lorenzo Maschio for providing us with an in-house version of CRYSTAL17 but more importantly, advices and meaningful discussions. Thanks to Slim and Julien for their collaboration on the biphotochrome and DiBOX respectively, and to Freddy for his amazing expertise on UV/Vis absorption spectra and his work on the spiropyrans and anils. A big thank you to Vincent for DrawMol and adding many features to it, at my request.

I also owe thanks to the various fundings that allowed me to work on these various projects: the ARC CONTRAST for the work on the anils and their co-crystals ("Actions de Recherche Concertées" (ARC) de la Direction générale de l'Enseignement non obligatoire et de la Recherche scientifique - Direction de la Recherche scientifique - Communauté française de Belgique, under convention No. 15/20-068). The work on the COFs was supported by BELSPO for the Indo-Belgian Research and Technology Cooperation project BL/13/IN16 entitled "Optical Properties of MOFs/COFs". The collaboration with Lionel Sanguinet and Julien Stiennon, a part of the MORIARTY project, has benefited from financial support from Wallonie-Bruxelles International (WBI), from the Fund for Scientific Research (F.R.S.-FNRS), from the French Ministry of Foreign and European Affairs, and from the Ministry of Higher Education and Research in the frame of the Hubert Curien partnerships

All the calculations of this work were performed on the computers of the Consortium des Équipements de Calcul Intensif (CÉCI, <http://www.cec-hpc.be>) and particularly those of the Technological Platform of High-Performance Computing, for which the authors gratefully acknowledge the financial support of the FNRS-FRFC, of the Walloon Region, and of the University of Namur (Conventions No. 2.5020.11, GEQ U.G006.15, 1610468, and RW/GEQ2016), as well as on zenobe, the Tier-1 facility of the Walloon Region (Convention 1117545).

J'aimerais maintenant remercier tous les membres passés et présents du labo. Je pense en particulier à Audrey sans qui le labo n'a jamais été le même, et à Pierre et Orian, pour leur aide, patience avec mes innombrables questions, et leur amitié. Pour la bonne ambiance qu'ils ont apportée durant ces années, merci à Vincent, Marc, Kornelia, Julien, François, Jean, Maxime, Laurie, Damien, Idrice, Tarcus et Laura, ainsi que Jojo et Freddy. Un tout grand merci à Fred sans qui cette thèse contiendrait beaucoup moins de résultats et à Laurent. Je n'oublie pas non plus les collègues et amis des labos voisins : Marie-Ange, Marie et Loïc, ni les amis qui ont su rester proches malgré la "distance" : Lio, Gwenn et Gauthier.

Un tout grand merci à ma famille, mes parents, ma sœur et mon frère pour leur intérêt bienveillant et soutien malgré leur incompréhension devant ce travail.

Finalement, la meilleure pour la fin, mille merci à Charlotte. Merci de faire tant pour moi, de me soutenir. Tu es la plus précieuse des surprises de ces années de thèse. Merci !

Grâce à vous, ce travail a une valeur incroyable ! Je ne vous remercierai jamais assez.

CONTENTS

Abstract	ii
Acknowledgments	iii
Acronyms	x
1 Introduction and Objectives	1
1.1 Molecular Switches	1
1.2 NLO Molecular Switches	5
1.3 Engineering Molecular Switches	7
1.4 Solid State Switches	8
1.5 First Hyperpolarizability and Hyper-Rayleigh Scattering	9
1.6 Objectives and Sketch of the PhD Table of Contents	13
Bibliography	16
2 Methods	21
2.1 First Approximations and the Hartree-Fock Method	21
2.2 Density Functional Theory	26
2.3 Time-Dependent Density Functional Theory and Coupled-Perturbed Kohn-Sham	32
2.3.1 Excitation Energies and Oscillator Strengths	34
2.3.2 First Hyperpolarizability	34
2.3.3 Nuclear Magnetic Resonance	35
2.4 Møller-Plesset Perturbation Theory	37
2.5 Coupled Cluster & Coupled Cluster Linear Response	38
2.6 Solvent Effects	44
2.6.1 Polarizable Continuum Model	44
2.6.2 Conductor-like Screening Model	45
2.7 Generalization to Solids	46
2.7.1 Embedding	46
2.7.2 Periodic Boundary Conditions	48
Bibliography	52

Geometry Optimization of Crystalline Molecular Switches	61
3 Assessing Density Functional Theory Approaches for Predicting the Structure and Relative Energy of Salicylideneaniline Molecular Switches in the Solid State	62
3.1 Introduction	64
3.2 Methods and Computations	66
3.3 Results and Discussion	67
3.3.1 DFT vs XRD Structures for Anil Crystals	67
3.3.2 DFT vs XRD Structures for PYV3 Co-Crystals	71
3.3.3 Basis Set Effects	71
3.3.4 Switching from the Enol to the Keto Form	77
3.4 Conclusion	79
Bibliography	81
4 Effects of Empirical Dispersion Energy on the Geometrical Parameters and Relative Energy of a Salicylideneaniline Molecular Switch in the Solid State	87
4.1 Introduction	89
4.2 Computational Aspects	90
4.3 Results and Discussion	91
4.3.1 Crystal Structures and Molecular Geometries	91
4.3.2 Keto-Enol Energies	95
4.4 Conclusions	97
Bibliography	98
5 Periodic DFT Study of the Effects of Co-Crystallization on a N-Salicylideneaniline Molecular Switch	101
5.1 Introduction	103
5.2 Methods and Computations	103
5.3 Results and Discussion	105
5.3.1 Interaction Sites of PYV3	105
5.3.2 Relative Energy of the Enol and Keto Forms	107
5.3.3 Geometry Variations upon Enol-Keto Transformation	109
5.3.4 Mulliken Charges Analysis	115
5.4 Conclusions	119
Bibliography	120
6 Investigation of the Evolution of Isotropic Magnetic Shieldings along the Enol-Keto Tautomerism of a N-Salicylidene-3-Aminopyridine Derivative and two of its Co-Crystals in the Solid State	125
6.1 Introduction	127
6.2 Methods and Computations	129
6.3 Results and Discussion	130

6.3.1	Definition of the Embedding Schemes	130
6.3.2	Effect of the Embedding on the NMR Shieldings of PYV3	131
6.3.3	Effect of Co-Crystallization on the NMR Shieldings	135
6.4	Conclusions	137
	Bibliography	139
7	Unraveling the Effects of Co-Crystallization on the UV/Vis Absorption Spectra of a N-Salicylideneaniline. A Computational RI-CC2 Investigation	145
7.1	Introduction	147
7.2	Methods and Computational Aspects	149
7.2.1	Effects of the Basis Set	151
7.2.2	RI-CC2 vs. RI-CCSD	152
7.3	Results and Discussion	154
7.3.1	Effects of the Geometry	154
7.3.2	Effects of the Environment	156
7.3.3	Analysis of the NTOs	163
7.3.4	Looking for a Computationally more Efficient Method	167
7.4	Further Discussions, Conclusions, and Perspectives	168
	Bibliography	170
8	Salicylideneaniline-Based COFs: a New Family of Multi-State Second-Order Nonlinear Optical Switches	175
8.1	Introduction	177
8.2	Methods	178
8.3	Results and Discussion	181
8.3.1	Geometries and Relative Stability	181
8.3.2	Excitation Energies	183
8.3.3	Refractive Indices and Birefringence	185
8.3.4	Second-Order NLO Susceptibilities	185
8.4	Conclusions and Outlook	190
	Bibliography	191
9	Molecular Switches: Assessing their Thermodynamical Equilibria in Solution Using High-Level Quantum Chemistry Methods	197
9.1	Introduction	198
9.2	Theoretical and Computational Aspects	202
9.3	Results and Discussions	203
9.4	Conclusions and Outlook	206
	Bibliography	206
10	Assessing the Structure of Octastate Molecular Switches Using ^1H NMR Density Functional Theory Calculations	210
10.1	Introduction	212

10.2	Computational Methods	214
10.3	Results and Discussion	215
10.3.1	Geometrical Optimization of the Different Metastable States	215
10.3.2	¹ H NMR Chemical Shifts of Biphotochrome 1 in its Eight States	216
10.3.3	Conformational Effects on the NMR Signatures of the c-t-o (I) and o-t-o (II) States of Compounds 1 and 2 . .	222
10.4	Conclusions	225
	Bibliography	226
11	Multi-State Nonlinear Optical Switches: A Quantum Chemical Investigation of Compounds Bearing Two Identical Multi-Addressable Benzazolo-oxazolidine Units	231
11.1	Introduction	234
11.2	Theoretical and Computational Aspects	236
11.2.1	Synthesis	236
11.2.2	UV/vis Absorption and hyper-Rayleigh Scattering Measurements	238
11.2.3	Theoretical and Computational Aspects	239
11.3	Results and Discussion	241
11.3.1	Geometrical Structures	242
11.3.2	UV/Visible Absorption Spectra and Related Properties .	244
11.3.3	Nonlinear Optical Properties	250
11.4	Further Discussions, Conclusions, and Outlook	254
	Bibliography	257
12	Summary, Conclusions, and Perspectives	263
A	DFT Opt. Cryst. Anils. SI	267
B	Periodic DFT Study of the Effects of Co-Crystallization on a N-Salicylideneaniline Molecular Switch. Supporting Information.	272
C	Investigation of the Evolution of Isotropic Magnetic Shieldings along the Enol-Keto Tautomerism of a N-Salicylidene-3-Aminopyridine Derivative and two of its Co-Crystals in the Solid State. Supporting Information	278
D	Unraveling the Effects of Co-Crystallization on the UV/Vis Absorption Spectra of a N-Salicylideneaniline. A Computational RI-CC2 Investigation. Supporting Information	300
E	Salicylideneaniline-Based COFs: a New Family of Multi-State Second-Order Nonlinear Optical Switches. Supporting Information	316

F	Multi-State Multi-Addressable Nonlinear Optical Switches: A Quantum Chemical Investigation of Compounds Possessing Two Identical Benzazolooxazolidine Units. Supporting Information	324
F.1	Optimized Geometries and Maxwell-Boltzmann Distribution . . .	325
F.1.1	DiBOX-Bt	325
F.1.2	DiBOX-BtO	328
F.1.3	DiBOX-TtO	329
F.2	UV/vis Absorption Spectra and Related Quantities	331
F.2.1	DiBOX-Bt	331
F.2.2	DiBOX-BtO	336
F.2.3	DiBOX-TtO	336
F.3	Nonlinear Optical Properties	337
F.3.1	DiBOX-Bt	338
F.3.2	DiBOX-BtO	344
F.3.3	DiBOX-TtO	348
F.4	Redox Reactions	352
F.5	Synthesis	352
F.5.1	DiBOX-Bt	352
F.5.2	DiBOX-TtO	354
F.6	HRS Measurements	356
	Bibliography	358

ACRONYMS

AIE	aggregation-induced emission
AO	atomic orbital
App.	Appendix
BF	Bloch function
BLA	bond length alternation
BOX	benzazolo-oxazolidine
BZ	Brillouin zone
CC	coupled cluster
CC2	coupled cluster approximate doubles
CCLR	coupled cluster linear response
CCSD	coupled cluster singles and doubles
CCSD(T)	coupled cluster singles, doubles, and perturbative triples
CCSDT	coupled cluster singles, doubles, and triples
CO	crystalline orbital
COF	covalent organic framework
COSMO	conductor-like screening model
CP-KS	coupled-perturbed Kohn-Sham
DFT	density functional theory
DR	depolarization ratio
DTE	dithienylethene
ECP	effective core potential
E_{DFT}	DFT energy
EDG	electron donating group
E_{disp}	dispersion energy
Eq.	Equation
EWG	electron withdrawing group
Fig.	Figure
GGA	generalized gradient approximation
GIAO	gauge-including atomic orbital
GTO	Gaussian-type orbital
HC	2'-hydroxychalcone
HF	Hartree-Fock

HOMO	highest occupied molecular orbital
HRS	hyper-Rayleigh scattering
KS	Kohn-Sham
LCAO	linear combination of atomic orbitals
LDA	local density approximation
LMO	localized molecular orbital
LR	long range
LUMO	lowest unoccupied molecular orbital
m-GGA	meta general gradient approximation
MO	molecular orbital
MOF	metal organic framework
MP2	second-order Møller-Plesset
MR	middle range
NLA	nonlinear absorption
NLO	nonlinear optical
NMR	nuclear magnetic resonance
PBC	periodic boundary conditions
PCM	polarizable continuum model
PNO	pair of natural orbitals
Ref.	Reference
RI	resolution of the identity
SCF	self-consistent field
SFG	sum frequency generation
SHG	second harmonic generation
SR	short range
TD	time-dependent
TD-DFT	time-dependent density functional theory
TD-KS	time-dependent Kohn-Sham
TPA	two-photon absorption
UV	ultra-violet
Ψ	wave function
XC	exchange-correlation
XCF	exchange-correlation functional
XRD	X-ray diffraction

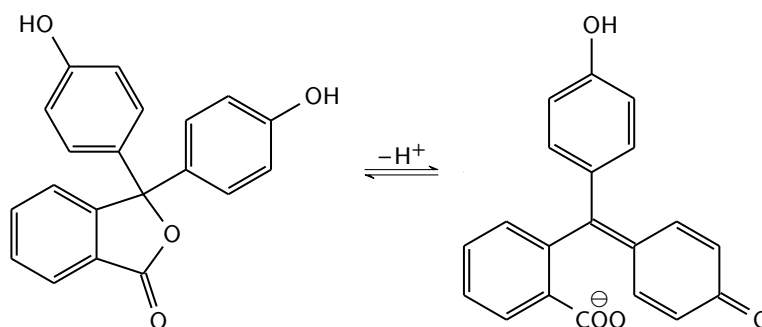
INTRODUCTION AND OBJECTIVES

Chemistry can simply be defined as the study of matter and its transformations. However it is far from simple! Matter is made of molecules which themselves are made of atoms. One part of the complexity of chemistry arises from the fact that atoms can be grouped together with virtually infinite possibilities, forming a quasi-infinite number of different molecules. Then, a further layer of complexity is added as multiple molecules can be mixed (using various methods) to form many more materials. An easy analogy can be done with LEGO blocks, where each block can be viewed as an atom. From this set of blocks, many different kinds of houses can be built, the molecules, and one ensemble of houses forms a village, a material. One way to classify molecules is to group them depending on their functions. Some have very straightforward roles, e.g. metals conduct electricity, proteins make life possible by transforming molecules into other essential molecules, etc. The general aim of this work is the study of a specific family of molecules: molecular switches. As their name suggests, they behave like switches, being either "on" or "off." While you flick your regular light switch with your finger, the stimulus to "flick" a molecular switch is not a mechanical force, but can be of different nature and is specific to the actual switch. The following pages will give examples of switches and for each of them, key features such as structural change(s) upon switching, stimulus, and targeted property are discussed. Then, the objectives of this work are laid out and the methods used are discussed in Chapter 2.

1.1 Molecular Switches

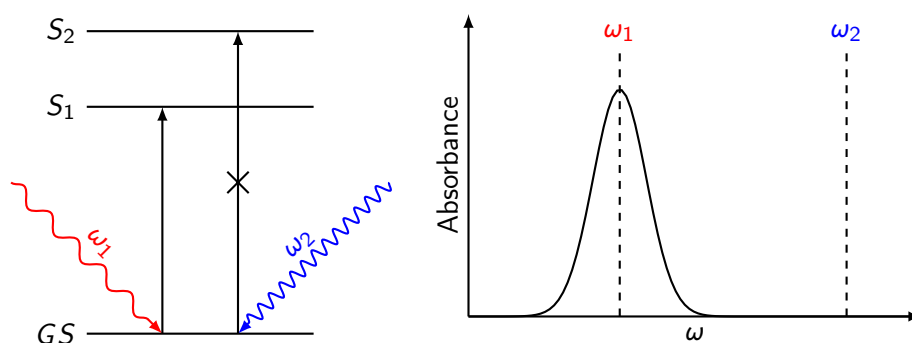
One of the most widely known molecular switch might very well be phenolphthaleine (Scheme 1.1),¹ as it is easy and safe to use and illustrates a very important concept in chemistry: acidity. Indeed, it is used as a pH indicator, being colorless in acidic conditions and bright pink in basic conditions ($\text{pH} \geq 8.2$). Because it lacks π -electron conjugation, the colorless form only absorbs in the ultra-violet (UV) range of light, thus being colorless. Upon deprotonation of one of the phenols, the central sp^3 carbon becomes sp^2 by breaking its C–O bond. This allows π -conjugation between the three carbon rings, decreasing the first excitation

energy. It now absorbs light in the visible region (between 400 and 760 nm),² with the maximum of absorption at ~ 550 nm. This switch is acidochromic: it changes color with pH. The color of an object depends on the light that it re-



Scheme 1.1: Phenolphthaleine, colorless form (l.h.s.) and pink form ($\text{pH} \geq 8.2$, r.h.s.)¹

flects/scatters, or by opposition, on the light that it absorbs. This means that a red shirt reflects/scatters red light and absorbs all others such as blue or green. Black is due to the absorption of all visible light, while white is the lack of absorption in the visible range. The absorption of light occurs when a photon energy matches the energy of a permitted electronic transition. The intensity of the absorption is determined by the oscillator strength, which is proportional to the product of the excitation energy by the square of the transition dipole moment. A UV/visible light absorption spectrum of a molecule thus explores its accessible excited states in addition to characterizing its color. Scheme 1.2 illustrates the absorption of UV/Vis light phenomenon and the resulting spectrum.

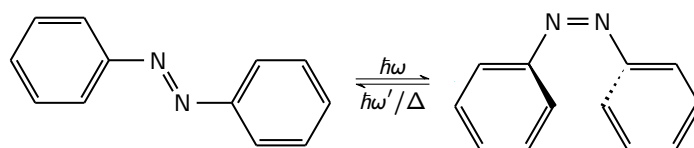


Scheme 1.2: Schematic representation of light absorption phenomena where GS is the electronic ground state S_n is the n^{th} electronic excited state of energy $\Delta E_n = \hbar\omega_n$ w.r.t. the GS energy. On the left-hand side, the diagram shows that the transition to S_1 is dipole allowed while the transition to S_2 is not. On the right-hand side, the resulting UV/Vis spectrum is shown.

Following up we target two heavily studied compounds: the azobenzene and

the dithienylethene (DTE) switches (see Schemes 1.3 and 1.4, respectively). DTEs belong to the family of the diarylethenes (DAEs). The number of publications featuring these compounds is quite large: 613 for azobenzene and 149 for DTE in 2019.* Azobenzene is the simplest molecule using the azo function ($-N=N-$) which can switch between a *trans* (*E*) (Scheme 1.3) and *cis* (*Z*) form. In the *E* conformation, the azo function and the phenyl rings are coplanar so that the molecule is fully π -conjugated. Upon switching to the *Z* conformation, the phenyl rings are tilted out of the "azo plane" thus breaking the phenyl-phenyl π -conjugation. The switching is triggered by light: UV light from *E* to *Z* and visible light or heat in the other direction. The change of color induced by light is called photochromism. For azobenzenes, the light usually used in photoswitching processes is in the UV region or the blue region of the visible. It means that the molecule absorbs the incident light and is promoted to an electronically excited state. While excited, the transformation occurs and then the molecule relaxes to the ground-state but in the other form of the switch, see Scheme 1.5. By opposition, processes such as acidochromism or thermochromism (a reversible change of color induced by a change of temperature) stay in the ground-state. The success of azobenzenes is due to their versatility and the efficiency of the isomerization.^{3–6} Aromatic chemistry allows for extensive functionalization of the phenyls in order to tune various properties of the switch (color,^{7,8} solubility,^{9,10} biocompatibility,^{11,12} etc).

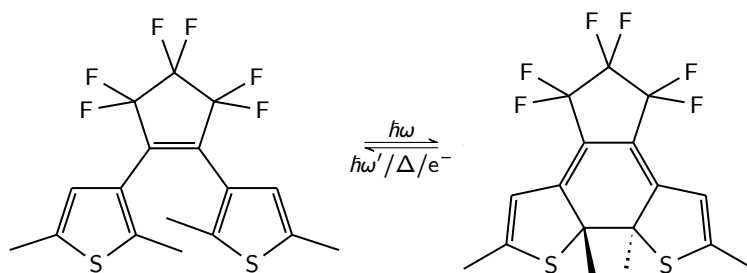
The DTE switch is also photochromic, although the switching mechanism is very different. In this case, the open form undergoes a photocyclization reaction, forming a new C–C bond, thus increasing the π -conjugation of the system (Scheme 1.4). Note that depending on how DTEs are functionalized, they can also be opened and/or closed by redox reactions.¹³ A change of color induced by a redox potential is called electrochromism. DTE-based switches have been extensively studied, especially in Japan, achieving amazing compounds such as crystals bending under light irradiation (photomechanical bending).¹⁴ The next



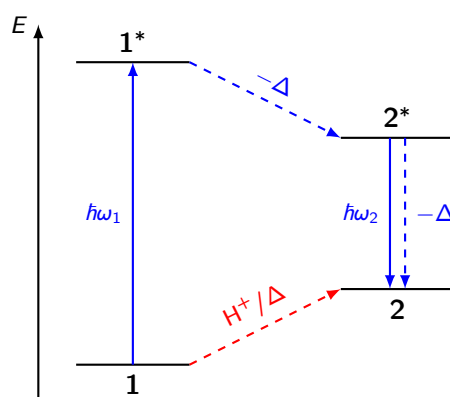
Scheme 1.3: Azobenzene switch, *trans* (*E*) isomer on the l.h.s. and *cis* (*Z*) one on the r.h.s.

family of compound is that of the benzazolo-oxazolidine (BOX), see Scheme 1.6. They switch similarly to phenolphthaleine: the sp^3 carbon of the closed form (Scheme 1.6) becomes sp^2 upon the breaking of the C–O bond. The open

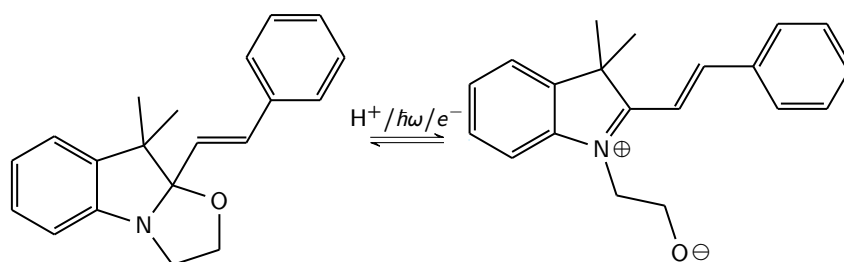
*According to www.scopus.com, consulted June 29th, 2020. Publications limited to the "Chemistry", "Material Science", "Chemical Engineering", "Biochemistry, Genetics, and Molecular Biology", and "Computer Science" subject areas.



Scheme 1.4: Dithienylethene switch, open form on the l.h.s. and closed one on the r.h.s.



Scheme 1.5: Schematic representation of a ground-state switching process (in red) and of a photoswitching process (in blue). 1 and 2 are ground-state forms of the switch and * refers to their excited states. Full (dashed) arrows refer to (non-)radiative transitions.



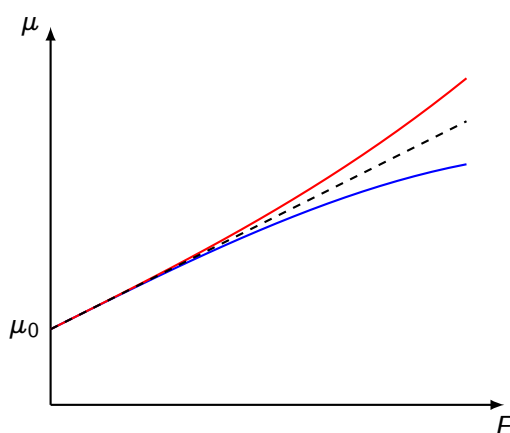
Scheme 1.6: Benzazolo-oxazolidine switch, closed form on the l.h.s. and open form on the r.h.s. (here as opened, by acid or oxidation, the open form would be positively charged, as the oxygen would be protonated).

form is more π -conjugated than the closed one. The nature of the stimuli is more versatile than for the previously discussed compounds as they are sensitive to light, pH, and in some cases to the redox potential.¹⁵ In addition to having a different color for each form, oxazolidines are well known for their nonlinear

optical (NLO) properties.^{16–19}

1.2 NLO Molecular Switches

NLO molecular switches are switches that in addition to displaying a change of color upon switching (linear optics), present a change of nonlinear response. NLO properties arise when the electric field, F , applied to a system is intense. Then, the dipole moment induced by the field can either be larger or smaller than the expected linear response value, see Scheme 1.7.²⁰ The induced dipole



Scheme 1.7: Schematic evolution of the amplitude of the dipole moment as a function of the amplitude of the irradiating electric field. The linear regime is represented by the dashed line while the nonlinear cases are in red and blue.

moment can be expressed as a Taylor expansion as a function of the electric field:

$$\mu = \mu_0 + \alpha F + \frac{1}{2}\beta F^2 + \dots \quad (1.1)$$

where μ_0 is the permanent dipole moment, α is the polarizability, and β is the first hyperpolarizability (the first nonlinear term). For crystals (and solids in general), the power expansion of the polarization P w.r.t. the electric field is preferred to the Taylor expansion of the dipole moment:

$$P = \epsilon_0 \left(\chi^{(1)} F + \chi^{(2)} F^2 + \dots \right) \quad (1.2)$$

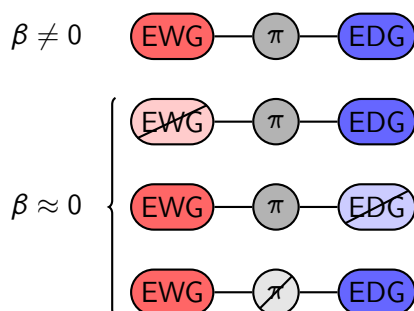
where ϵ_0 is the vacuum permittivity, $\chi^{(1)}$ is the first-order susceptibility, and $\chi^{(2)}$ the second-order one (the first nonlinear term). They are directly related to their molecular counterparts by the vacuum permittivity, ϵ_0 , and the volume

of the cell, V_{cell} :

$$\chi^{(1)} = \frac{\alpha}{\epsilon_0 V_{\text{cell}}} \quad (1.3)$$

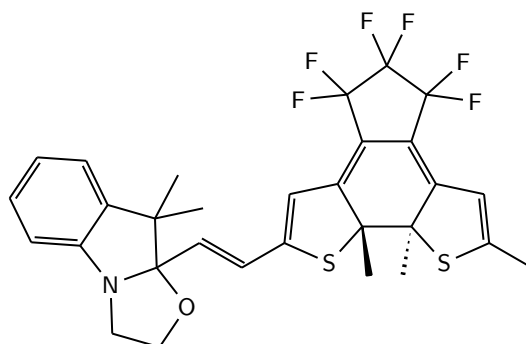
$$\chi^{(2)} = \frac{\beta}{2\epsilon_0 V_{\text{cell}}}. \quad (1.4)$$

The relationship between molecular structure and β has been extensively studied, highlighting a typical pattern to obtain nonlinear optical compounds.²¹ It consists of an electron withdrawing group (EWG) linked to an electron donating group (EDG) by a π -conjugated path. In the case of NLO molecular switches, one form of the switch presents this pattern while the alternative form breaks it, see Scheme 1.8. In Section 1.5, the first hyperpolarizability and one experimental method to evaluate it, hyper-Rayleigh scattering (HRS), are discussed in more details.



Scheme 1.8: Molecular patterns to get a nonlinear optical switch. The top line shows the pattern of the responsive form of the switch where EWG is an electron withdrawing group, π is a π -conjugated path, and EDG is an electron donating group. The three bottom lines represent three ways to break the NLO response.²²

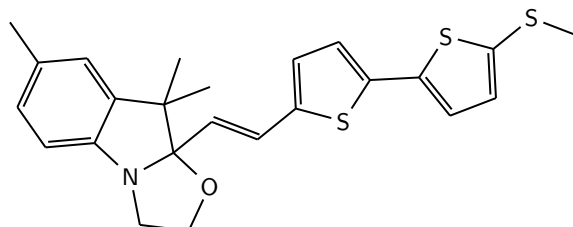
Not all molecular switches are limited to two forms. For instance, BOX switches are not limited to the two discussed forms as it features a double bond that can be isomerized, similarly to the azo switches. They can thus take 4 forms, combining open/closed BOX and *E/Z* double bond (2^2). Another way for increasing the number of states of a single molecule is to combine two or more switches together, such as a BOX-DTE hybrid,²³ see Scheme 1.9, featured later in Chapter 10. Considering the BOX, double bond, and DTE moieties, this switch has 8 states (2^3). With such a large number of states, their identification is a difficult task but it can be performed by using nuclear magnetic resonance (NMR).²⁴



Scheme 1.9: Fully closed form of a BOX-DTE hybrid switch.²³

1.3 Engineering Molecular Switches

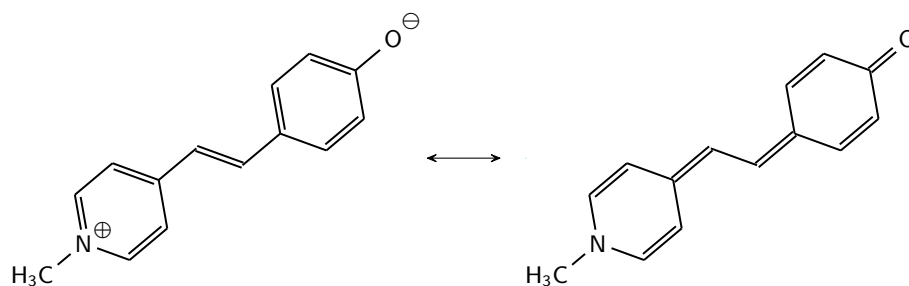
There are multiple strategies to modify and tune the properties of molecular switches. The most widely used one is to chemically functionalize a compound. For example, BOX switches can be made more sensitive to redox potential by combining them with a bithiophene group,²⁵ see Scheme 1.10. Thanks to a lower redox potential than the BOX, the bithiophene allows for the opening of the switch by transferring a radical from the bithiophene function to the nitrogen of the BOX, triggering the opening.²⁶ Another method is to change the media of



Scheme 1.10: BOX switch functionalized with a bithiophene function.²⁵

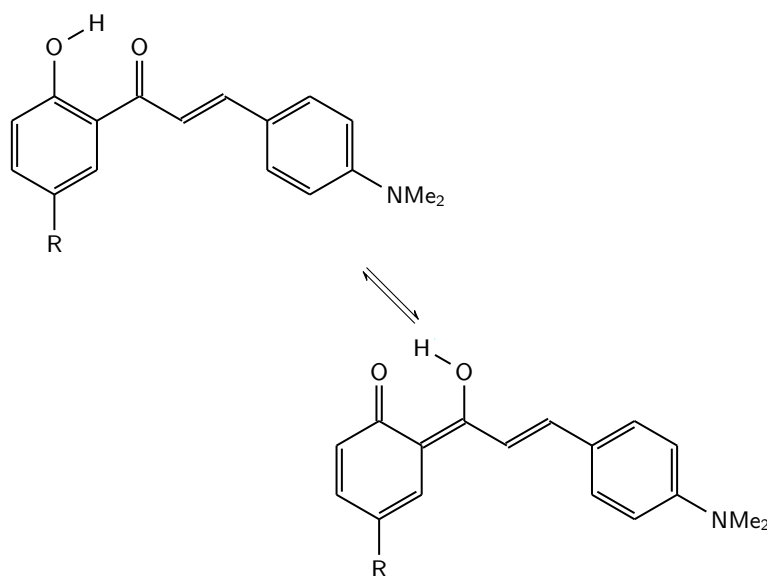
the switch, either by changing the solvent or by going to the solid state. Indeed, some compounds can display a wide range of colors depending on the solvent: solvatochromism.²⁷ A beautiful example is Brooker's dye (see Scheme 1.11)²⁸ which is yellow in water, red in ethanol, or blue in pyridine.²⁹ In that order, the dielectric constant of the solvent decreases so that the zwitterionic form becomes less stabilized, thus favoring the neutral form and red-shifting the maximum of absorption of the UV/Vis spectrum.

Other molecules can display aggregation-induced emission (AIE): while they do not show emissive properties (such as fluorescence) in solution, they do as they aggregate.^{30–32} Aggregation can happen in solution at high concentration, when molecules are deposited on surfaces, or by going to the solid state such as crystallization. There are molecular switches in the AIE family. Amongst them are the 2'-hydroxychalcones (HCs), see Scheme 1.12. In that example, HC1



Scheme 1.11: Brooker's dye (1-methyl-4-[(oxocyclohexadienylidene)ethylidene]-1,4-dihydropyridine).²⁸

presents AIE while HC2 does not.³³ Due to the different spatial arrangement within the unit cell, and thus intermolecular interactions, the pathways in the excited state are either enabled or blocked.³⁴



Scheme 1.12: 2'-Hydroxychalcone (HC) switch, for HC1, R = H and for HC2, R = OMe.

1.4 Solid State Switches

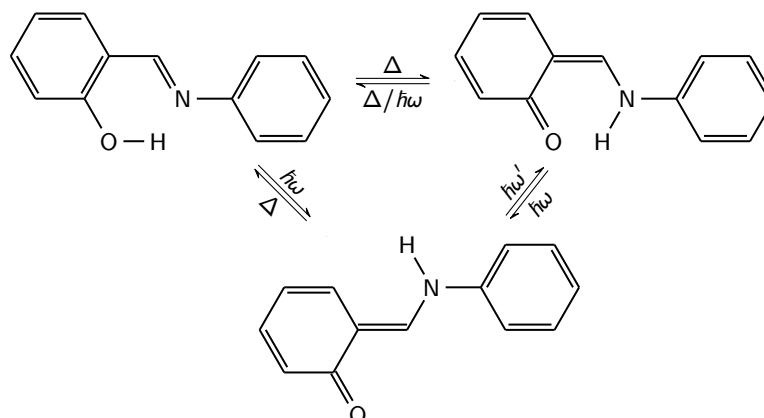
Crystallization is one of several method to bring a molecule from solution to the solid state. Crystals are periodic systems where the same unit cell is repeated in all three directions of space. The crystal is characterized by a space group that hold the symmetry information: how equivalent molecules relate to each others. For example, the crystal of a single molecule can have a unit cell containing one molecule, which is thus "copied-pasted" in space. Alternatively, the same

molecule could form a crystal in a different space group (a polymorph) with a unit cell containing two molecules related to each other by a center of inversion. Because two polymorphs contain different intermolecular interactions, they can also display different properties. In that last example, assuming that the crystallized molecule has a NLO response, the first crystal would also do, while the second one would not because of the center of inversion.

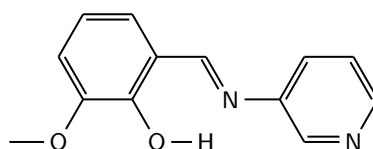
Expanding upon using crystallization to tune the properties of molecular switches, co-crystallization has been used to tune the properties of crystals. There are multiple applications of co-crystallization in both medicinal^{35–38} and material sciences.^{39–45} Although there is a debate as to the precise definition of co-crystallization, the general definition is the crystallization of at least two different compounds together. In the simplest case, a binary co-crystal, the secondary compound called coformer is chosen to interact with the target molecule without competing with its properties (e.g. the coformer does not absorb in the same zone as the main compound). Several chapters of this work (Chapters 3, 4, 6, and 7) are part of a broader research project: the ARC CONTRAST ("Actions de Recherche Concertées", "Concerted Research Actions") that gathers the efforts of three research groups from two Belgian universities: the groups of T. Leyssens from UCLouvain, J. Wouters from UNamur, and B. Champagne from UNamur. The objectives of CONTRAST are to study and develop the use of co-crystallization to enable thermo- and photo-chromism in crystals. One of the targeted family of compounds are the N-salicylideneanilines (or anils, see Scheme 1.13). They generally display three forms: the (generally) most stable one is the uncolored enol (E) form. From there, the orange *cis*-keto (cK or K) form can be obtained by heating (thermochromism). The red *trans*-keto (tK) form can only be accessed via photoswitching from either the E or cK form (photochromism). By using co-crystallization, an anil molecule can become photochromic, whereas the single crystal is only thermochromic.^{46–48} This was actually achieved for (E)-2-methoxy-6-(pyridine-3-yliminomethyl)phenol (PYV3, Scheme 1.14) using small molecules such as fumaric acid as coformer.⁴⁶

1.5 First Hyperpolarizability and Hyper-Rayleigh Scattering

We now complete this introductory chapter by presenting further notions of nonlinear optics. At the molecular level, the first hyperpolarizability, β , is responsible for multiple phenomena such as the Pockels effect, where a static and a dynamic electric fields generate a dynamic electric field of different polarization: $\beta(-\omega; \omega, 0)$ or the second harmonic generation (SHG), where an electric field generates a field of double frequency: $\beta(-2\omega; \omega, \omega)$. SHG, represented in Scheme 1.15, is also a particular case of sum frequency generation (SFG) where two electric fields of frequency ω_1 and ω_2 generate a third field of frequency $\omega_\sigma = \omega_1 + \omega_2$: $\beta(-\omega_\sigma; \omega_1, \omega_2)$. Hyper-Rayleigh scattering (HRS) is an incoherent SHG phenomenon used to experimentally determine the amplitude of β .



Scheme 1.13: N-salicylideneaniline (anil) switch, the top-left structure is the enol (E) form, the top-right one is the *cis*-keto (cK) form, and the bottom one the *trans*-keto (tK) form.



Scheme 1.14: (E)-2-methoxy-6-(pyridine-3-yliminomethyl)phenol (PYV3).

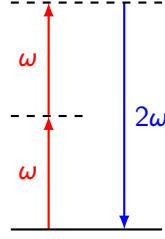
HRS experiments are versatile, as they allow for the characterization of both charged and neutral molecules. Its main limitations are solubility (experiments are performed in diluted condition to avoid the formation of aggregates) and the frequency of the laser used (the incident and scattered lights should not generate other phenomena such as absorption or fluorescence). The general principle of the experiment is that the intensity of the scattered light, $I_{2\omega}$, is proportional to the square of the intensity of the incident light, I_{ω} , and a quadratic average $\langle \beta_{\text{HRS}}^2 \rangle$:

$$I_{2\omega} \propto \langle \beta_{\text{HRS}}^2 \rangle I_{\omega}^2. \quad (1.5)$$

β_{HRS} can be defined as the sum of two polarization-dependent orientational averages of the elements of the β tensor:

$$\langle \beta_{\text{HRS}}^2 \rangle = \langle \beta_{\text{ZXX}}^2 \rangle + \langle \beta_{\text{ZZZ}}^2 \rangle. \quad (1.6)$$

$\langle \beta_{\text{ZXX}}^2 \rangle$ is associated with the situation where the incident light is polarized in the X direction and only the intensity of the Z-polarized scattered light is measured while for $\langle \beta_{\text{ZZZ}}^2 \rangle$ both incident and scattered lights are Z-polarized lights, see Scheme 1.16. Both $\langle \beta_{\text{ZXX}}^2 \rangle$ and $\langle \beta_{\text{ZZZ}}^2 \rangle$ are defined in terms of the

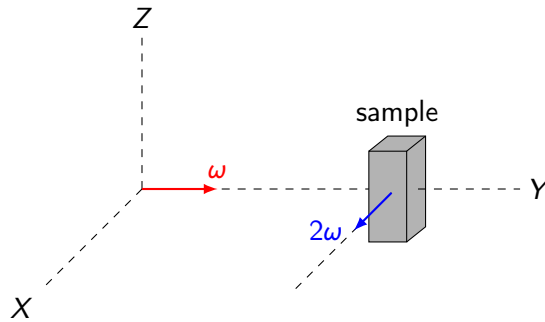


Scheme 1.15: Schematic representation of the second harmonic generation phenomenon. The full line refers to the electronic ground state, the dashed lines to virtual electronic states, and the arrows to the absorption or scattering of photons of energy equal to $\hbar\omega$ or $2\hbar\omega$, respectively.

elements of the molecular β tensor:

$$\begin{aligned} \langle \beta_{ZXX}^2 \rangle = & \frac{1}{35} \sum_i^{x,y,z} \beta_{iii}^2 + \frac{4}{105} \sum_{i \neq j}^{x,y,z} \beta_{iii} \beta_{ijj} - \frac{2}{35} \sum_{i \neq j}^{x,y,z} \beta_{iii} \beta_{jji} + \frac{8}{105} \sum_{i \neq j}^{x,y,z} \beta_{iij}^2 \\ & + \frac{3}{35} \sum_{i \neq j}^{x,y,z} \beta_{ijj}^2 - \frac{2}{35} \sum_{i \neq j}^{x,y,z} \beta_{iij} \beta_{jii} + \frac{1}{35} \sum_{i \neq j \neq k}^{x,y,z} \beta_{ijj} \beta_{ikk} - \frac{2}{105} \sum_{i \neq j \neq k}^{x,y,z} \beta_{iik} \beta_{jjk} \\ & - \frac{2}{105} \sum_{i \neq j \neq k}^{x,y,z} \beta_{iij} \beta_{jkk} + \frac{2}{35} \sum_{i \neq j \neq k}^{x,y,z} \beta_{ijk}^2 - \frac{2}{105} \sum_{i \neq j \neq k}^{x,y,z} \beta_{ijk} \beta_{jik} \quad (1.7) \end{aligned}$$

$$\begin{aligned} \langle \beta_{ZZZ}^2 \rangle = & \frac{1}{7} \sum_i^{x,y,z} \beta_{iii}^2 + \frac{4}{35} \sum_{i \neq j}^{x,y,z} \beta_{iij}^2 + \frac{2}{35} \sum_{i \neq j}^{x,y,z} \beta_{iii} \beta_{ijj} + \frac{4}{35} \sum_{i \neq j}^{x,y,z} \beta_{jii} \beta_{iij} \\ & + \frac{4}{35} \sum_{i \neq j}^{x,y,z} \beta_{iii} \beta_{jji} + \frac{1}{35} \sum_{i \neq j}^{x,y,z} \beta_{jii}^2 + \frac{4}{105} \sum_{i \neq j \neq k}^{x,y,z} \beta_{iij} \beta_{jkk} + \frac{1}{105} \sum_{i \neq j \neq k}^{x,y,z} \beta_{jii} \beta_{kkj} \\ & + \frac{4}{105} \sum_{i \neq j \neq k}^{x,y,z} \beta_{iij} \beta_{kkj} + \frac{2}{105} \sum_{i \neq j \neq k}^{x,y,z} \beta_{ijk}^2 + \frac{4}{105} \sum_{i \neq j \neq k}^{x,y,z} \beta_{ijk} \beta_{jik}. \quad (1.8) \end{aligned}$$



Scheme 1.16: Schematic representation of a hyper-Rayleigh scattering set-up.

A common convention is to use capital letters for the laboratory frame: X , Y , and Z while lower case letters refer to the molecular frame: x , y , and z . Using these two terms, the depolarization ratio (DR) is defined as:

$$\text{DR} = \frac{\langle \beta_{ZZZ}^2 \rangle}{\langle \beta_{ZXX}^2 \rangle} \quad (1.9)$$

$$\langle \beta_{\text{HRS}}^2 \rangle = \langle \beta_{ZZZ}^2 \rangle \left(1 + \frac{1}{\text{DR}} \right). \quad (1.10)$$

DR takes values between 1.5 and 9, as a function of the shape of the NLO-phore (the part of the molecule responsible for the NLO response). When Kleinman's conditions are satisfied, all lights involved in the process, their sums, and their differences are far from any electronic excitation.⁴⁹ In this frame, $\langle \beta_{ZXX}^2 \rangle$ and $\langle \beta_{ZZZ}^2 \rangle$ can be expressed using a mixed spherical-Cartesian formalism:⁵⁰

$$\langle \beta_{ZXX}^2 \rangle = \frac{1}{45} |\beta_{J=1}|^2 + \frac{4}{105} |\beta_{J=3}|^2 \quad (1.11)$$

$$\langle \beta_{ZZZ}^2 \rangle = \frac{9}{45} |\beta_{J=1}|^2 + \frac{6}{105} |\beta_{J=3}|^2 \quad (1.12)$$

$$\langle \beta_{\text{HRS}}^2 \rangle = \frac{10}{45} |\beta_{J=1}|^2 + \frac{10}{105} |\beta_{J=3}|^2 \quad (1.13)$$

where $|\beta_{J=1}|$ is the dipolar contribution and $|\beta_{J=3}|$ the octupolar one. They are defined as follows:^{51,52}

$$|\beta_{J=1}|^2 = \frac{3}{5} \sum_{i,j,k}^{x,y,z} \beta_{ijj} \beta_{ikk} \quad (1.14)$$

$$|\beta_{J=3}|^2 = \sum_{i,j,k}^{x,y,z} \beta_{ijk}^2 - |\beta_{J=1}|^2 \quad (1.15)$$

so that a new quantity can be defined, the nonlinear anisotropy parameter, ρ :⁵³

$$\rho = \frac{|\beta_{J=3}|}{|\beta_{J=1}|} \quad (1.16)$$

and relates to DR by:

$$\text{DR} = 9 \frac{1 + \frac{2}{7}\rho^2}{1 + \frac{12}{7}\rho^2}. \quad (1.17)$$

DR and ρ can take three typical values:

- for octupolar systems, $|\beta_{J=1}|$ is null so that $\rho = \infty$ and $\text{DR} = 1.5$ (as β_{ijk} , $i \neq j \neq k$, is the only remaining non-null term due to symmetry);
- for ideal unidimensional push-pull systems, only one β_{iii} term is not negligible so that $\text{DR} = 5$ and $\rho = 0.82$;
- for dipolar systems, $|\beta_{J=3}|$ is null so that $\rho = 0$ and $\text{DR} = 9$.

1.6 Objectives and Sketch of the PhD Table of Contents

As illustrated in the previous Sections, there is a broad variety of molecular switches focusing on various applications in material sciences. On the one hand, a phenomenon like thermochromism can be optimized in view of a specific sensing application. On the other hand, new multi-state multi-addressable molecular switches are targeted to broaden the panoply and efficiency of intelligent molecules. The design of these compounds requires adopting a multidisciplinary approach where, in addition to the synthesis or the preparation of the compounds as well as to their experimental characterizations, theoretical chemistry methods can play a role. This is the context of my PhD thesis.

Its main goal consists in using and developing quantum chemistry tools to study molecular switches, to better understand their structures and properties, and therefore to contribute to their design. Since molecular switches both in solution and in the crystal solid state are studied, these methods span different techniques and different scales, from the characterization of isolated molecules, to the description of solvation effects, and to the characterization of solid phase effects. Among these, multi-scale approaches have been optimized. While the objectives of each chapter are different, they are complementary and they show how quantum chemistry can assist experiments by predicting and explaining properties. In several cases, the performance of these methods is challenged in comparison to available experimental data before being applied to new compounds having a potential for the targeted application. In other cases, the use of quantum chemistry methods allows going deep into the details of the structure-property relationships, which is a strength in the molecular design. My PhD thesis is organized as follows.

Chapter 2 describes the theoretical background and the key methods that have been employed to achieve this PhD thesis.

Chapters 3 to 7 are contributions to the ARC project "CONTRAST" and focus on the study of crystalline anils. Chapters 3 and 4 deal with the optimization of their geometries, assessing the reliability of various exchange-correlation functionals (Chapter 3) and analyzing the effect of empirical London dispersion corrections (Chapter 4). This allows us to select efficient XC functionals. Indeed, a good geometry is a prerequisite to study any kind of properties and, at the start of my PhD, little was known about the performances of solid-state periodic boundary conditions (PBC) methods to predict of the geometries of molecular crystals. Then, co-crystallization effects are investigated, in particular, i) on the relative energy of the enol and keto forms of the reference PYV3 anil derivative and ii) their rationalization in terms of the change of geometry (Chapter 5). This E/K equilibrium is indeed central when optimizing thermochromic molecular switches or looking for the best coformer. One way to tackle this problem is by performing geometry optimization and studying the thermodynamical properties. These structural investigations have been performed in parallel to single-crystal

X-ray diffraction studies carried out by our collaborators. The next two chapters deal with molecular properties of the crystals and co-crystals of PYV3. Chapter 6 is devoted to the calculation of the NMR isotropic shielding constants of the enol and keto forms of PYV3 in different environments, which provide necessary complementary information to solid-state NMR in order to determine the relative amounts of the enol and keto forms as well as their evolutions with temperature, a key information for thermochromism. Then, Chapter 7 reports on the UV/visible absorption spectra of PYV3, their modifications upon enol-to-keto tautomerism and upon co-crystallization. Chapters 6 and 7 are both based on PBC methods to get the geometries and optimized embedding schemes to evaluate the properties of these molecules in various crystal environments.

Besides crystals and co-crystals, anil derivatives can constitute the active molecular units of covalent organic frameworks (COFs), leading to a new family of multi-state linear and nonlinear optical switches. This proof of concept has been addressed in the frame of an Indo-Belgium bilateral collaboration by investigating two-dimensional COFs built from the assembly of tris(N-salicylideneaniline) units (Chapter 8).

Some of these solid-state questions are directly backed up by studies in solution, where the description of the effects of the environment is generally simplified and allows for employing higher-level quantum chemistry methods. On the other hand, the molecules are more flexible and require taking into account their many conformers. So, Chapter 9 is the direct complement to Chapters 3 and 4. It challenges the use of high-level wavefunction methods to describe the switching equilibria of N-salicylideneaniline and spiropyran derivatives. The next two Chapters deal with multi-state molecular switches in solution. Chapter 10 shows how the calculation of NMR chemical shifts can assist in the interpretation of experimental data on the behavior of a biphotochromic switch composed of a BOX unit and a DTE unit. Finally, Chapter 11 investigates the properties of molecular switches built from two identical BOX units, which therefore present three states. This Chapter analyses whether it is possible to control the level of opening of these molecules while the different BOX's are chemically equivalent, how the chemical nature of the linker affects the selectivity of the successive openings, and how the level of opening of the switch modulates the linear and nonlinear optical properties of these systems.

Finally, general conclusions are drawn in Chapter 12 along with perspectives to the various aspects of my PhD thesis. Table 1.1 lists the compounds, properties, methods, and programs used in this work to guide the reader through the methods chapter.

Table 1.1: Summary of the compounds, properties, methods, and programs used per chapter.

Chapter	Compounds	Properties	Methods	Programs
3 4	Anil Crystals	Energy & Geometry	PBC DFT PBC DFT-D	CRYSTAL14
5 6 7	Anil Co-crystals	Energy & Geometry NMR Isotropic Shielding UV/Vis absorption spectra	PBC DFT Embedded CP-KS Embedded CCLR	CRYSTAL14 Ewald & Gaussian16 Ewald & TURBOMOLE
8	Covalent Organic Frameworks	Energy, Geometry, Linear & Nonlinear Optical Responses	PBC (TD-)DFT	CRYSTAL17
9 10	Anils & Spiropyranes/Merocyanines BOX-DTE Hybrid	Thermodynamic Functions State Thermodynamic Functions & NMR Isotropic Shielding	PCM, COSMO, DFT, MP2, & CCSD(T) PCM & (TD-)DFT	Gaussian16 & TURBOMOLE Gaussian16
11	DiBOXs	Thermodynamic Functions, Linear & Non-linear Optical Responses	PCM & (TD-)DFT	Gaussian16

Bibliography

- (1) Wittke, G. Reactions of Phenolphthalein at Various pH Values. *J. Chem. Educ.* **1983**, *60*, 239, DOI: 10.1021/ed060p239.
- (2) *IUPAC Compendium of Chemical Terminology*; Nič, M., Jirát, J., Košata, B., Jenkins, A., McNaught, A., Eds.; IUPAC: Research Triangle Park, NC, 2009, DOI: 10.1351/goldbook.
- (3) Yesodha, S. K.; Sadashiva Pillai, C. K.; Tsutsumi, N. Stable Polymeric Materials for Nonlinear Optics: A Review Based on Azobenzene Systems. *Prog. Polym. Sci.* **2004**, *29*, 45–74, DOI: 10.1016/j.progpolymsci.2003.07.002.
- (4) Barrett, C. J.; Mamiya, J.-i.; Yager, K. G.; Ikeda, T. Photo-Mechanical Effects in Azobenzene-Containing Soft Materials. *Soft Matter* **2007**, *3*, 1249, DOI: 10.1039/b705619b.
- (5) Beharry, A. A.; Woolley, G. A. Azobenzene Photoswitches for Biomolecules. *Chem. Soc. Rev.* **2011**, *40*, 4422, DOI: 10.1039/c1cs15023e.
- (6) Bandara, H. M. D.; Burdette, S. C. Photoisomerization in Different Classes of Azobenzene. *Chem. Soc. Rev.* **2012**, *41*, 1809–1825, DOI: 10.1039/C1CS15179G.
- (7) Han, M.; Norikane, Y.; Onda, K.; Matsuzawa, Y.; Yoshida, M.; Hara, M. Light-Driven Modulation of Fluorescence Color from Azobenzene Derivatives Containing Electron-Donating and Electron-Withdrawing Groups. *New J. Chem.* **2010**, *34*, 2892, DOI: 10.1039/c0nj00353k.
- (8) Yamada, S.; Bessho, J.; Nakasato, H.; Tsutsumi, O. Color Tuning Donor-Acceptor-Type Azobenzene Dyes by Controlling the Molecular Geometry of the Donor Moiety. *Dye. Pigment.* **2018**, *150*, 89–96, DOI: 10.1016/j.dyepig.2017.11.002.
- (9) Zhang, Z.; Burns, D. C.; Kumita, J. R.; Smart, O. S.; Woolley, G. A. A Water-Soluble Azobenzene Cross-Linker for Photocontrol of Peptide Conformation. *Bioconjug. Chem.* **2003**, *14*, 824–829, DOI: 10.1021/bc0340161.
- (10) Ravi, P.; Sin, S.; Gan, L.; Gan, Y.; Tam, K.; Xia, X.; Hu, X. New Water Soluble Azobenzene-Containing Diblock Copolymers: Synthesis and Aggregation Behavior. *Polymer (Guildf)*. **2005**, *46*, 137–146, DOI: 10.1016/j.polymer.2004.11.009.
- (11) Garcia-Amorós, J.; Díaz-Lobo, M.; Nonell, S.; Velasco, D. Fastest Thermal Isomerization of an Azobenzene for Nanosecond Photoswitching Applications under Physiological Conditions. *Angew. Chemie* **2012**, *124*, 12992–12995, DOI: 10.1002/ange.201207602.

- (12) Wen, H.; Zhang, W.; Weng, Y.; Hu, Z. Photomechanical Bending of Linear Azobenzene Polymer. *RSC Adv.* **2014**, *4*, 11776–11781, DOI: 10.1039/c3ra48035f.
- (13) Warford, C. C.; Lemieux, V.; Branda, N. R. In *Molecular Switches*, Feringa, B. L., Browne, W. R., Eds.; Wiley-VCH Verlag GmbH & Co. KGaA: Weinheim, Germany, 2011, pp 1–35, DOI: 10.1002/9783527634408.ch1.
- (14) *New Frontiers in Photochromism*; Irie, M., Yokoyama, Y., Seki, T., Eds.; Springer Japan: Tokyo, 2013, DOI: 10.1007/978-4-431-54291-9.
- (15) Szalóki, G.; Sanguinet, L. In *Photon-Working Switch*. Springer Japan: Tokyo, 2017, pp 69–91, DOI: 10.1007/978-4-431-56544-4_3.
- (16) Castet, F.; Ducasse, L.; Champagne, B.; Sanguinet, L.; Pozzo, J. L.; Adamietz, F.; Rodriguez, V. Experimental and theoretical determination of the first-order hyperpolarizability of photo- and acidochromic indolino[2,1-b]oxazolidines. *Synth. Met.* **2005**, *155*, 393–397, DOI: 10.1016/j.synthmet.2005.09.021.
- (17) Sanguinet, L.; Pozzo, J.-L.; Rodriguez, V.; Adamietz, F.; Castet, F.; Ducasse, L.; Champagne, B. Acido- and Phototriggered NLO Properties Enhancement. *J. Phys. Chem. B* **2005**, *109*, 11139–11150, DOI: 10.1021/jp0442450.
- (18) Sanguinet, L.; Pozzo, J. L.; Guillaume, M.; Champagne, B.; Castet, F.; Ducasse, L.; Maury, E.; Soulié, J.; Mançois, F.; Adamietz, F.; Rodriguez, V. Acidoswitchable NLO-phores; Benzimidazolo[2,3-b]oxazolidines. *J. Phys. Chem. B* **2006**, *110*, 10672–10682, DOI: 10.1021/jp060825g.
- (19) Mançois, F.; Sanguinet, L.; Pozzo, J. L.; Guillaume, M.; Champagne, B.; Rodriguez, V.; Adamietz, F.; Ducasse, L.; Castet, F. Acido-triggered nonlinear optical switches: Benzazolo-oxazolidines. *J. Phys. Chem. B* **2007**, *111*, 9795–9802, DOI: 10.1021/jp073386.
- (20) Verbiest, T.; Clays, K.; Rodriguez, V., *Second-order Nonlinear Optical Characterization Techniques*; CRC Press: 2009, DOI: 10.1201/9781420070736.
- (21) Kanis, D. R.; Ratner, M. A.; Marks, T. J. Design and Construction of Molecular Assemblies with Large Second-Order Optical Nonlinearities. Quantum Chemical Aspects. *Chem. Rev.* **1994**, *94*, 195–242, DOI: 10.1021/cr00025a007.
- (22) Coe, B. J. Molecular Materials Possessing Switchable Quadratic Nonlinear Optical Properties. *Chem. - A Eur. J.* **1999**, *5*, 2464–2471, DOI: 10.1002/(SICI)1521-3765(19990903)5:9<2464::AID-CHEM2464>3.0.CO;2-L.

- (23) Sevez, G.; Gan, J.; Delbaere, S.; Vermeersch, G.; Sanguinet, L.; Levillain, E.; Pozzo, J.-L. Photochromic Performance of a Dithienylethene-Indolinooxazolidine Hybrid. *Photochem. Photobiol. Sci.* **2010**, *9*, 131.
- (24) Szalóki, G.; Sevez, G.; Berthet, J.; Pozzo, J.-L.; Delbaere, S. A Simple Molecule-Based Octastate Switch. *J. Am. Chem. Soc.* **2014**, *136*, 13510–13513, DOI: 10.1021/ja506320j.
- (25) Szalóki, G.; Alévêque, O.; Pozzo, J.-L.; Hadji, R.; Levillain, E.; Sanguinet, L. Indolinooxazolidine: A Versatile Switchable Unit. *J. Phys. Chem. B* **2015**, *119*, 307–315, DOI: 10.1021/jp511825f.
- (26) Hadji, R.; Szalóki, G.; Alévêque, O.; Levillain, E.; Sanguinet, L. The Stepwise oxidation of Indolino[2,1-b]oxazolidine Derivatives. *J. Electroanal. Chem.* **2015**, *749*, 1–9, DOI: 10.1016/j.jelechem.2015.04.032.
- (27) Reichardt, C. Solvatochromic Dyes as Solvent Polarity Indicators. *Chem. Rev.* **1994**, *94*, 2319–2358, DOI: 10.1021/cr00032a005.
- (28) Brooker, L. G. S.; Keyes, G. H.; Sprague, R. H.; VanDyke, R. H.; VanLare, E.; VanZandt, G.; White, F. L. Studies in the Cyanine Dye Series. XI. 1 The Merocyanines. *J. Am. Chem. Soc.* **1951**, *73*, 5326–5332, DOI: 10.1021/ja01155a095.
- (29) Minch, M. J.; Shah, S. S. Merocyanin Dye Preparation for the Introductory Organic Laboratory. *J. Chem. Educ.* **1977**, *54*, 709, DOI: 10.1021/ed054p709.
- (30) Hong, Y.; Lam, J. W. Y.; Tang, B. Z. Aggregation-Induced Emission. *Chem. Soc. Rev.* **2011**, *40*, 5361, DOI: 10.1039/c1cs15113d.
- (31) Crespo-Otero, R.; Li, Q.; Blancafort, L. Exploring Potential Energy Surfaces for Aggregation-Induced Emission—From Solution to Crystal. *Chem. – An Asian J.* **2019**, *14*, 700–714, DOI: 10.1002/asia.201801649.
- (32) Zhao, Z.; Zhang, H.; Lam, J. W. Y.; Tang, B. Z. Aggregation-Induced Emission: New Vistas at the Aggregate Level. *Angew. Chemie Int. Ed.* **2020**, *59*, 9888–9907, DOI: 10.1002/anie.201916729.
- (33) Cheng, X.; Wang, K.; Huang, S.; Zhang, H.; Zhang, H.; Wang, Y. Organic Crystals with Near-Infrared Amplified Spontaneous Emissions Based on 2'-Hydroxychalcone Derivatives: Subtle Structure Modification but Great Property Change. *Angew. Chemie Int. Ed.* **2015**, *54*, 8369–8373, DOI: 10.1002/anie.201503914.
- (34) Dommett, M.; Rivera, M.; Crespo-Otero, R. How Inter- and Intramolecular Processes Dictate Aggregation-Induced Emission in Crystals Undergoing Excited-State Proton Transfer. *J. Phys. Chem. Lett.* **2017**, *8*, 6148–6153, DOI: 10.1021/acs.jpclett.7b02893.

- (35) Trask, A. V.; Motherwell, W. D. S.; Jones, W. Pharmaceutical Cocrystallization: Engineering a Remedy for Caffeine Hydration. *Cryst. Growth Des.* **2005**, *5*, 1013–1021, DOI: 10.1021/cg0496540.
- (36) Golob, S.; Perry, M.; Lusi, M.; Chierotti, M. R.; Grabnar, I.; Lassiani, L.; Voinovich, D.; Zaworotko, M. J. Improving Biopharmaceutical Properties of Vinpocetine Through Cocrystallization. *J. Pharm. Sci.* **2016**, *105*, 3626–3633, DOI: 10.1016/j.xphs.2016.09.017.
- (37) Machado, T. C.; Gelain, A. B.; Rosa, J.; Cardoso, S. G.; Caon, T. Cocrystallization as a Novel Approach to Enhance the Transdermal Administration of Meloxicam. *Eur. J. Pharm. Sci.* **2018**, *123*, 184–190, DOI: 10.1016/j.ejps.2018.07.038.
- (38) Harmsen, B.; Leyssens, T. Dual-Drug Chiral Resolution: Enantiospecific Cocrystallization of (*S*)-Ibuprofen Using Levetiracetam. *Cryst. Growth Des.* **2018**, *18*, 441–448, DOI: 10.1021/acs.cgd.7b01431.
- (39) Gao, H. Y.; Zhao, X. R.; Wang, H.; Pang, X.; Jin, W. J. Phosphorescent Cocrystals Assembled by 1,4-Diiodotetrafluorobenzene and Fluorene and Its Heterocyclic Analogues Based on C–I $\cdots\pi$ Halogen Bonding. *Cryst. Growth Des.* **2012**, *12*, 4377–4387, DOI: 10.1021/cg300515a.
- (40) Zhu, W.; Zhu, L.; Sun, L.; Zhen, Y.; Dong, H.; Wei, Z.; Hu, W. Uncovering the Intramolecular Emission and Tuning the Nonlinear Optical Properties of Organic Materials by Cocrystallization. *Angew. Chemie Int. Ed.* **2016**, *55*, 14023–14027, DOI: 10.1002/anie.201607712.
- (41) Sun, L.; Zhu, W.; Wang, W.; Yang, F.; Zhang, C.; Wang, S.; Zhang, X.; Li, R.; Dong, H.; Hu, W. Intermolecular Charge-Transfer Interactions Facilitate Two-Photon Absorption in Styrylpyridine-Tetracyanobenzene Cocrystals. *Angew. Chemie Int. Ed.* **2017**, *56*, 7831–7835, DOI: 10.1002/anie.201703439.
- (42) Babu, B.; Chandrasekaran, J.; Jayaramakrishnan, V.; Ho, M.-S.; Thirupugalmani, K.; Chandrasekar, S.; Thirumurugan, R. 2-Amino-6-Methylpyridinium Nitrophenolate Nitrophenol: An Organic Multiple Charge-Transfer Complex with Large Second Harmonic Generation for Optoelectronics Applications. *J. Therm. Anal. Calorim.* **2018**, *134*, 1059–1070, DOI: 10.1007/s10973-018-7386-5.
- (43) Gryl, M.; Seidler, T.; Wojnarska, J.; Stadnicka, K.; Matulková, I.; Němec, I.; Němec, P. Co-Crystals of 2-Amino-5-Nitropyridine Barbitol with Extreme Birefringence and Large Second Harmonic Generation Effect. *Chem. - A Eur. J.* **2018**, *24*, 8727–8731, DOI: 10.1002/chem.201802057.
- (44) Li, S.; Yan, D. Two-Component Aggregation-Induced Emission Materials: Tunable One/Two-Photon Luminescence and Stimuli-Responsive Switches by Co-Crystal Formation. *Adv. Opt. Mater.* **2018**, *6*, 1800445, DOI: 10.1002/adom.201800445.

- (45) D'Agostino, S.; Spinelli, F.; Taddei, P.; Ventura, B.; Grepioni, F. Ultra-long Organic Phosphorescence in the Solid State: The Case of Triphenylene Cocrystals with Halo- and Dihalo-penta/tetrafluorobenzene. *Cryst. Growth Des.* **2019**, *19*, 336–346, DOI: 10.1021/acs.cgd.8b01443.
- (46) Carletta, A.; Buol, X.; Leyssens, T.; Champagne, B.; Wouters, J. Polymorphic and Isomorphic Cocrystals of a N-Salicylidene-3-aminopyridine with Dicarboxylic Acids: Tuning of Solid-State Photo- and Thermochromism. *J. Phys. Chem. C* **2016**, *120*, 10001–10008.
- (47) Carletta, A.; Spinelli, F.; D'Agostino, S.; Ventura, B.; Chierotti, M. R.; Gobetto, R.; Wouters, J.; Grepioni, F. Halogen-Bond Effects on the Thermo- and Photochromic Behaviour of Anil-Based Molecular Co-crystals. *Chem. - A Eur. J.* **2017**, *23*, 5317–5329, DOI: 10.1002/chem.201605953.
- (48) Carletta, A.; Zbačnik, M.; Van Gysel, M.; Vitković, M.; Tumanov, N.; Stilinović, V.; Wouters Johan and Cinčić, D. Playing with Isomerism: Cocrystallization of Isomeric N-Salicylideneaminopyridines with Perfluorinated Compounds as Halogen Bond Donors and Its Impact on Photochromism. *Cryst. Growth Des.* **2018**, *18*, 6833–6842, DOI: 10.1021/acs.cgd.8b01064.
- (49) Kleinman, D. Nonlinear Dielectric Polarization in Optical Media. *Phys. Rev.* **1962**, *126*, 1977, DOI: 10.1103/PhysRev.126.1977.
- (50) Castet, F.; Bogdan, E.; Plaquet, A.; Ducasse, L.; Champagne, B.; Rodriguez, V. Reference Molecules for Nonlinear Optics: A Joint Experimental and Theoretical Investigation. *J. Chem. Phys.* **2012**, *136*, 024506, DOI: 10.1063/1.3675848.
- (51) Brasselet, S.; Zyss, J. Multipolar Molecules and Multipolar Fields: Probing and Controlling the Tensorial Nature of Nonlinear Molecular Media. *J. Opt. Soc. Am. B* **1998**, *15*, 257, DOI: 10.1364/JOSAB.15.000257.
- (52) Beaujean, P.; Champagne, B. Coupled cluster evaluation of the second and third harmonic scattering responses of small molecules. *Theor. Chem. Acc.* **2018**, *137*, 50, DOI: 10.1007/s00214-018-2219-y.
- (53) Zyss, J. Molecular Engineering Implications of Rotational Invariance in Quadratic Nonlinear Optics: From Dipolar to Octupolar Molecules and Materials. *J. Chem. Phys.* **1993**, *98*, 6583, DOI: 10.1063/1.464802.

METHODS

The goal of this chapter is to provide information on the methods used throughout this work. Because of the wide range of methods, first, the reference Hartree-Fock (HF) approximation is discussed in detail. Although there are no HF results presented in this work, it allows to introduce the most important approximations common to all the considered methods. Then the popular density functional theory (DFT) and time-dependent density functional theory (TD-DFT) are discussed, the latter specifically for the calculation of excitation energies and oscillator strengths, first hyperpolarizabilities, and nuclear magnetic resonance, which are all featured in this work. Post Hartree-Fock methods are introduced, starting with second-order Møller-Plesset (MP2) followed by coupled cluster (CC) and response-function theory, which allows for the calculation of the excitation energies and oscillator strengths at the coupled cluster approximate doubles (CC2) level of approximation. Finally, methods to model the environment in the calculation are developed, firstly, for solutions, and lastly for crystals.

2.1 First Approximations and the Hartree-Fock Method

Of all the approximations that are discussed in the following pages, the first and maybe most important one is the Born-Oppenheimer approximation.¹ It allows for the decomposition of the total wave function Ψ^{tot} into two intertwined parts: the nuclear one Ψ^{nuc} , describing the nuclei and the electronic one Ψ^{elec} , describing the electrons. This is of immense importance, as all the properties that we study depend on the electrons, allowing us to put aside the nuclear wave function and to consider the nuclear coordinates as parameters. The problem that has to be solved is the non-relativistic time-independent Schrödinger equation,² limited to the electronic wave function, $\Psi(\vec{r}_1, \vec{r}_2, \dots, \vec{r}_N) = \Psi$:

$$\hat{\mathcal{H}}\Psi = E\Psi \quad (2.1.1)$$

where $\hat{\mathcal{H}}$ is the electronic Hamiltonian operator, E is the energy of the system, \vec{r}_i is the position of the i^{th} electron, and N is the total number of electrons. In general, the electronic Hamiltonian is given as the sum of the kinetic operator,

\hat{T} , and the potential operator, \hat{V} :

$$\hat{\mathcal{H}} = \hat{T} + \hat{V} \quad (2.1.2)$$

$$\text{with } \hat{T} = - \sum_{i=1}^N \frac{1}{2} \nabla_i^2 \quad (2.1.3)$$

$$\text{and } \hat{V} = - \sum_{i=1}^N \sum_{A=1}^M \frac{Z_A}{r_{iA}} + \sum_{i=1}^N \sum_{i < j}^N \frac{1}{r_{ij}} \quad (2.1.4)$$

where the index i refers to electrons and N is their total number, the index A refers to the nuclei and M is their total number, Z_A is the atomic number of the atom A , r_{iA} is the distance between the i^{th} electron and the A^{th} atom ($r_{iA} = |\vec{r}_{iA}| = |\vec{r}_i - \vec{r}_A|$), and r_{ij} is the distance between the i^{th} and j^{th} electrons ($r_{ij} = |\vec{r}_{ij}| = |\vec{r}_i - \vec{r}_j|$).

In order to fulfill the antisymmetry principle,³ Slater proposed to approximate the wave function as the determinant of a matrix containing the occupied spinorbitals ($\Theta(\vec{x})$) of the system, the Slater determinant:⁴

$$\Psi(\vec{x}_1, \vec{x}_2, \dots, \vec{x}_N) = \frac{1}{\sqrt{N!}} \begin{vmatrix} \Theta_i(\vec{x}_1) & \Theta_j(\vec{x}_1) & \cdots & \Theta_k(\vec{x}_1) \\ \Theta_i(\vec{x}_2) & \Theta_j(\vec{x}_2) & \cdots & \Theta_k(\vec{x}_2) \\ \vdots & \vdots & \ddots & \vdots \\ \Theta_i(\vec{x}_N) & \Theta_j(\vec{x}_N) & \cdots & \Theta_k(\vec{x}_N) \end{vmatrix}. \quad (2.1.5)$$

This can be shortened using a notation that only shows the diagonal terms:

$$\begin{aligned} \Psi(\vec{x}_1, \vec{x}_2, \dots, \vec{x}_N) &= |\Theta_i(\vec{x}_1), \Theta_j(\vec{x}_2), \dots, \Theta_k(\vec{x}_N)\rangle \\ &= |i, j, \dots, k\rangle. \end{aligned} \quad (2.1.6)$$

Each spinorbital is the composition of a spatial orbital, noted $\phi(\vec{r})$, and of a spin function: $\alpha(\omega)$ or $\beta(\omega)$, for a spin up or down, respectively.⁵ Also, the combination of the spatial coordinate \vec{r} and of the spin coordinate ω gives the general electron coordinate \vec{x} .

The energy of the system described by the wave function Ψ is a functional of said wave function:

$$E[\Psi] = \langle \Psi | \hat{\mathcal{H}} | \Psi \rangle. \quad (2.1.7)$$

To derive the HF equation, we must establish the variational principle (which is a general principle).⁶ Starting from a trial wave function, Ψ , its energy $E[\Psi]$ is higher than that of the exact ground state wave function, $E_0[\Psi_0]$.

$$E_0 = \langle \Psi_0 | \hat{\mathcal{H}} | \Psi_0 \rangle \leq E = \langle \Psi | \hat{\mathcal{H}} | \Psi \rangle. \quad (2.1.8)$$

So, if Ψ was changed by a small amount ($\Psi \rightarrow \Psi + \delta\Psi$), then the energy

becomes:

$$E[\Psi + \delta\Psi] = \langle \Psi + \delta\Psi | \hat{\mathcal{H}} | \Psi + \delta\Psi \rangle \quad (2.1.9)$$

$$= E[\Psi] + \underbrace{\left(\langle \delta\Psi | \hat{\mathcal{H}} | \Psi \rangle + \langle \Psi | \hat{\mathcal{H}} | \delta\Psi \rangle \right)}_{\delta E} + \dots \quad (2.1.10)$$

Since our goal is to obtain the exact wave function of the electronic ground-state Ψ_0 , the first-order variation in E , δE , should be null. In other words, we want to minimize the energy.

Hartree and Fock proposed a method to minimize the energy of a wave function composed of a single Slater determinant.⁷⁻⁹ Starting from the expression for the ground state energy, Equation (Eq.) 2.1.7, the molecular spinorbitals are introduced through the Slater determinant:

$$E = \sum_i^{\text{occ}} \langle \Theta_i | \hat{\mathcal{H}} | \Theta_i \rangle \quad (2.1.11)$$

$$= \sum_i^{\text{occ}} \langle i | \hat{\mathcal{H}} | i \rangle. \quad (2.1.12)$$

Its minimization leads to the Hartree-Fock equation, which relies on the Fock operator, \hat{f} .^{8,9}

$$\hat{f}(\vec{x}_1)\Theta_i(\vec{x}_1) = \varepsilon_i\Theta_i(\vec{x}_1) \quad (2.1.13)$$

$$\text{with } \hat{f}(\vec{x}_1) = \hat{h}(\vec{r}_1) + \sum_{j=1}^N \left(\hat{J}_j(\vec{x}_1) - \hat{K}_j(\vec{x}_1) \right) \quad (2.1.14)$$

where ε_i is the energy of the i^{th} spinorbital, \hat{h} is the mono-electronic operator, \hat{J} is the Coulomb operator, and \hat{K} is the exchange one:

$$\hat{h}(\vec{r}_1) = -\frac{1}{2}\nabla_1^2 - \sum_A^M \frac{Z_A}{r_{1A}} \quad (2.1.15)$$

$$\text{and } h_{ii} = \langle \Theta_i | \hat{h} | \Theta_i \rangle; \quad (2.1.16)$$

$$\hat{J}_j(\vec{x}_1)\Theta_i(\vec{x}_1) = \left[\int d\vec{x}_2 \Theta_j^*(\vec{x}_2) \frac{1}{r_{12}} \Theta_j(\vec{x}_2) \right] \Theta_i(\vec{x}_1) \quad (2.1.17)$$

$$\begin{aligned} \text{and } J_{ij} &= \langle \Theta_i | \hat{J}_j | \Theta_i \rangle \\ &= \langle ij | ij \rangle = (ii|jj); \end{aligned} \quad (2.1.18)$$

$$\hat{K}_j(\vec{x}_1)\Theta_i(\vec{x}_1) = \left[\int d\vec{x}_2 \Theta_j^*(\vec{x}_2) \frac{1}{r_{12}} \Theta_i(\vec{x}_2) \right] \Theta_j(\vec{x}_1) \quad (2.1.19)$$

$$\begin{aligned} \text{and } K_{ij} &= \langle \Theta_i | \hat{K}_j | \Theta_i \rangle \\ &= \langle ij | ji \rangle = (ij | ij). \end{aligned} \quad (2.1.20)$$

By introducing the linear combination of atomic orbitals (LCAO) approximation, the molecular orbitals (MOs) are defined using a weighted sum of predefined set of atomic orbitals (AOs), $\{\varphi_\mu\}$:¹⁰

$$\Theta_i = \sum_{\mu=1}^K c_{\mu i} \varphi_\mu \quad (2.1.21)$$

where $c_{\mu i}$ are the LCAO coefficients and K is the total number of atomic orbitals. The elements of density matrix, \mathbf{D} , can be defined:

$$D_{\mu\nu} = \sum_{k=1}^N c_{\mu k}^* c_{\nu k} \quad (2.1.22)$$

and the HF equation in the MO frame (Eq. 2.1.13) can be rewritten in the AO one:

$$\hat{f}(\vec{x}_1) \sum_{\mu=1}^K c_{\mu i} \varphi_\mu(\vec{x}_1) = \epsilon_i \sum_{\mu=1}^K c_{\mu i} \varphi_\mu(\vec{x}_1). \quad (2.1.23)$$

In its matrix notation, the problem to solve is the Roothaan equations:⁵

$$\mathbf{FC} = \mathbf{SCE} \quad (2.1.24)$$

where \mathbf{F} is the Fock matrix, \mathbf{C} is the matrix of LCAO coefficients, \mathbf{S} is the overlap matrix:

$$S_{\mu\nu} = \langle \varphi_\mu | \varphi_\nu \rangle, \quad (2.1.25)$$

and \mathbf{E} is a diagonal matrix containing the energy of the molecular orbitals, ϵ . All these matrices have the dimensions of the set of atomic orbitals: (K, K) . The problem has to be solved iteratively (since the bi-electronic operators depend on the orbitals on which they are being applied, see Eq. 2.1.17 and 2.1.19), with the goal of obtaining the set of coefficients that minimizes the energy. This is a self-consistent field (SCF) method.

Due to the simplification of the bi-electronic integrals, the HF method lacks electron correlation. Indeed, the Coulomb term only yields the average repulsion energy that any electron feels due to all the others, while the exchange term accounts for the "exchange" of two electrons of the same spin. The Hartree-Fock exchange is also known as "exact" exchange since its mathematical form is

actually exact. The correlation energy E_{corr} is the difference between the exact energy and the one of HF.¹¹

The final step into using the HF approximation is to select a basis set of atomic orbitals. A practical solution is to use contractions of Gaussian type functions, or Gaussian-type orbitals (GTOs). They present a large advantage for the implementation of the equations: the product of Gaussians is a Gaussian. A full array of those basis sets were developed over the years. A popular family of basis sets was initially defined by Pople and coworkers^{12–19} and their naming follows a simple scheme. For instance, the 6-31+G(d) basis set (also written 6-31+G*) is characterized by:

- "6": 1 contraction of 6 Gaussians for the core electrons (except for the 1st row elements that have no core electrons)
- "31": 2 contractions for the electrons of valence: the first of 3 Gaussians and the second of 1 Gaussian
- "+": the addition of a set of diffuse s and p functions for the 2nd and 3rd row elements
- "G": stands for Gaussian
- "(d)": the addition of a set of polarization d functions for the 2nd and 3rd row elements. "(d,p)" (or "**") further adds a set of polarization p functions to the 1st row elements.

There are many more sets available online, from Pople and many others, thanks to the efforts of the "Basis Set Exchange" team (www.basissetexchange.org).^{20–22} This work features a variety of basis sets. Among those, several are of the Pople family: 6-21G, 6-31G, 6-31G(d), 6-31G(d,p), 6-311G, 6-311G(d), 6-311+G(d), 6-311G(d,p), and 6-311+G(2d,p). The second family of basis sets featured in this work is that of Ahlrichs and coworkers,^{23–26} which has been developed for the Turbomole package. They use the following naming scheme: "def2-": 2nd iteration of the default (Turbomole) basis set, followed by an acronym matching the description of the basis set:

- split-valence with polarization functions (except for H), SV(P) or with polarization functions for all atoms, SVP;
- triple- ζ valence with "small" sets of polarization functions, TZVP, or with "large" ones, TZVPP;
- quadruple- ζ valence with "small" sets of polarization functions, QZVP, or with "large" ones, QZVPP.

These basis sets can be further augmented by sets of diffuse functions adding "D" to the end of the naming scheme, e.g. def2-TZVPD. The complete family

has been used, except for the (very large) augmented quadruple basis sets (def2-QZVPD and def2-QZVPPD).

Finally, "large" or "heavy" atoms such as iodine pose a challenge as they have a lot of core electrons: either a single contraction of Gaussians (Pople basis sets) is a bad approximation, or it requires a very large amount of functions (Ahlichs basis sets) that heavily increase the computational cost. Effective core potentials (ECPs) offer a solution by substituting the core electrons by a pseudo-potential, while the valence electrons remain explicitly considered. They are fitted to reproduce potential energy curves and other electronic properties (such as electron affinity) of all-electron basis sets calculations (including full relativistic effects when required). This has the added benefit of partially including relativistic corrections, especially needed for atoms with heavy nucleus. The pseudo-potentials take the form of Gaussians, which is convenient as most quantum calculations rely on Gaussian-type orbitals. In this work, two different ECPs are used for iodine: LANL2DZ²⁷ in combination with Pople's 6-31G(d,p) basis set for the other atoms and def2-ECP in combination with the Ahlichs sets.²⁵

2.2 Density Functional Theory

Density functional theory (DFT) is featured in Chapters 3 to 11, except in Chapter 7. The strategy for DFT is similar to the one of Hartree-Fock, except that instead of the wave function being the key to all the properties of the system, it is the electron density, noted ρ . Despite this significant difference, the final equations of DFT have a lot of similarities with those of HF as they both are SCF methods.

The first theorem of Hohenberg and Kohn²⁸ shows that the ground state properties of a system are fully determined by the electron density. So while the energy was defined as a functional of the wave function within Hartree-Fock theory, $E[\Psi]$, it is now a functional of the electron density, $E[\rho]$. The electron density, $\rho(\vec{r})$, is obtained by integrating the squared wave function:²⁹

$$\rho(\vec{r}_1) = N \int \cdots \int |\Psi(\vec{x}_1, \vec{x}_2, \cdots, \vec{x}_N)|^2 d\vec{x}_1 d\vec{x}_2 \cdots d\vec{x}_N \quad (2.2.1)$$

where N is the total number of electrons:

$$N = \int \rho(\vec{r}) d\vec{r}. \quad (2.2.2)$$

Similarly to the variational principle used in the development of the Hartree-Fock approximation (Eq. 2.1.8), the second theorem of Hohenberg and Kohn²⁸ shows that for a trial electron density, ρ , the related energy is higher than that of the exact ground state electron density, ρ_0 :

$$E[\rho_0] \leq E[\rho] \quad (2.2.3)$$

where the energy is the sum of functionals of ρ :

$$E[\rho] = T[\rho] + V_{ee}[\rho] + V_{eN}[\rho]. \quad (2.2.4)$$

$T[\rho]$ is the kinetic energy functional, $V_{ee}[\rho]$ is the electron-electron (repulsion) potential energy functional, and $V_{eN}[\rho]$ is the electron-nucleus (attraction) potential energy functional. Of those terms, the attraction energy functional is easily defined:

$$V_{eN}[\rho] = \int d\vec{r} \rho(\vec{r}) V(\vec{r}) \quad (2.2.5)$$

where $V(\vec{r})$ is the electron-nuclei potential. As for the remaining terms, they are gathered into the Hohenberg and Kohn functional:^{29,30}

$$E[\rho] = V_{eN}[\rho] + F_{HK}[\rho] \quad (2.2.6)$$

$$\text{with } F_{HK}[\rho] = T[\rho] + J[\rho] + E_{ncl}[\rho] \quad (2.2.7)$$

where the repulsion term is split into two parts: the Coulomb functional, $J[\rho]$, and the non-classical functional, $E_{ncl}[\rho]$, which accounts for terms of self-interaction, correlation, and exchange.

Then, similarly to what was done in Hartree-Fock, Kohn and Sham proposed to express the wave function as a single Slater determinant.³¹ The density is thus given by:

$$\rho(\vec{r}) = \sum_i^N \int d\vec{\omega} |\Theta_i(\vec{x})|^2. \quad (2.2.8)$$

where Θ_i is the i^{th} Kohn-Sham (KS) spinorbital. By invoking a system of non-interacting electrons, F_{HK} , now the KS functional, F_{KS} , (Eq. 2.2.7) is written as:

$$F_{KS}[\rho] = T_s[\rho] + J[\rho] + E_{XC}[\rho] \quad (2.2.9)$$

where $T_s[\rho]$ is the kinetic energy functional of non-interacting electrons and $E_{XC}[\rho]$ is the exchange-correlation functional (XCF), which encompasses all the unknown and undefined terms of the electron interactions (from both the kinetic and potential energies):

$$E_{XC}[\rho] = T[\rho] - T_s[\rho] + E_{ncl}[\rho] \quad (2.2.10)$$

where E_{ncl} is the non-classical functional. The equation that has to be solved, the Kohn-Sham equation is thus:²⁹⁻³¹

$$\left[-\frac{1}{2} \nabla^2 + \hat{V}_{\text{eff}}(\vec{r}) \right] \Theta_i(\vec{x}) = \varepsilon_i \Theta_i(\vec{x}) \quad (2.2.11)$$

$$\text{with } \hat{V}_{\text{eff}}(\vec{r}) = \hat{J}(\vec{r}) + \hat{V}_{eN}(\vec{r}) + \hat{V}_{XC}(\vec{r}) \quad (2.2.12)$$

$$\text{and } \hat{V}_{XC}(\vec{r}) = \frac{\partial E_{XC}}{\partial \rho(\vec{r})} \quad (2.2.13)$$

where $\hat{V}_{\text{eff}}(\vec{r})$ is the effective potential and $\hat{V}_{\text{XC}}(\vec{r})$ the exchange-correlation (XC) potential. Since the spinorbitals have been introduced, the LCAO approximation can be used (thus defining the MOs in terms of the AOs) so that the matrix equation to solve has an identical form to the Hartree-Fock Equation (see Eq. 2.1.24):

$$\mathbf{F}_{\text{KS}}\mathbf{C} = \mathbf{S}\mathbf{C}\mathbf{E}. \quad (2.2.14)$$

It also needs to be solved iteratively, to obtain the set of coefficients that minimizes the energy.

In principle, DFT is exact but since the form of the XCF is unknown, the solutions are approximated. This led many people to develop various XCFs build with different strategies and objectives. The first design, the local density approximation (LDA) functionals, is rather simplistic as they only depend on the electron density: $E_{\text{XC}}[\rho]$. The second generation, the generalized gradient approximation (GGA) functionals, introduces a dependence on the gradient of ρ : $E_{\text{XC}}[\rho, \nabla\rho]$. Among this family, one of the best known GGA is the one developed for molecules by Perdew, Burke, and Ernzerhof: PBE.³² Later on, Perdew and coworkers adapted PBE to better suit solids and surfaces by changing the contribution of $\nabla\rho$ with the PBEsol variant³³ of PBE. The third generation, the meta-GGA (m-GGA) functionals, expands on the GGA by adding a dependence on the kinetic energy density ($\nabla^2\rho \sim \tau$): $E_{\text{XC}}[\rho, \nabla\rho, \tau]$. A well-known example of this family of functionals is the one developed by Tao, Perdew, Staroverov, and Scuseria: TPSS.³⁴ Further improvements can be made on both GGAs and m-GGAs by adding a percentage of exact exchange. Those functionals are called hybrids and can be of two kinds: global or range-separated. Global hybrids contain a fixed percentage of exact exchange, such as PBE0 or PBEsol0 which have 25 % of exact exchange. For example, the XC energy of PBE0, $E_{\text{XC}}^{\text{PBE0}}$, is:

$$E_{\text{XC}}^{\text{PBE0}} = E_{\text{XC}}^{\text{PBE}} + \frac{1}{4} (E_{\text{X}}^{\text{HF}} - E_{\text{X}}^{\text{PBE}}) \quad (2.2.15)$$

where $E_{\text{XC}}^{\text{PBE}}$ is the XC energy of PBE, E_{X}^{HF} is the HF exchange energy, and $E_{\text{X}}^{\text{PBE}}$ is the PBE one. By opposition, range-separated hybrids have a varying contribution of exact exchange: it depends on the distance between the interacting electrons. The latter is achieved by splitting the $1/r$ function into three parts:

$$\frac{1}{r} = \underbrace{\frac{\text{erfc}(\omega_{\text{SR}}r)}{r}}_{\text{short range}} + \underbrace{\frac{\text{erfc}(\omega_{\text{LR}}r) - \text{erfc}(\omega_{\text{SR}}r)}{r}}_{\text{middle range}} + \underbrace{\frac{\text{erf}(\omega_{\text{LR}}r)}{r}}_{\text{long range}} \quad (2.2.16)$$

where erf is the error function (which varies between 0 and 1 for r values going from 0 to $+\infty$), erfc is the complementary error function (which varies between 1 and 0 for r values going from 0 to $+\infty$), ω_{SR} and ω_{LR} are the short range (SR) and long range (LR) separation parameters, respectively, and r is the distance between the interacting electrons. The middle range (MR) contribution vanishes when the two range separation parameters are identical ($\omega_{\text{SR}} = \omega_{\text{LR}}$). All parts of

Eq. 2.2.16 are displayed in Scheme 2.1. There are many range-separated hybrids available such as HSE06,³⁵ a short range corrected variant of PBE with 25 % of SR exact exchange and $\omega_{\text{SR}} = 0.11 \text{ a}_0^{-1}$; HISS,³⁶ a middle range variant of PBE, has 60 % of MR exact exchange, $\omega_{\text{SR}} = 0.84 \text{ a}_0^{-1}$, and $\omega_{\text{LR}} = 0.20 \text{ a}_0^{-1}$; or LC- ω PBE,³⁷ a long range variant of PBE, with 100 % of LR exact exchange and $\omega_{\text{LR}} = 0.40 \text{ a}_0^{-1}$. For example, the XC energy of HSE06, $E_{\text{XC}}^{\text{HSE06}}$, is:

$$E_{\text{XC}}^{\text{HSE06}} = E_{\text{XC}}^{\text{PBE}} + \frac{1}{4} \left(E_{\text{X}}^{\text{SR,HF}} - E_{\text{X}}^{\text{SR,PBE}} \right) \quad (2.2.17)$$

where E_{X}^{SR} is the short range exchange energy. Other XCFs can have both SR and LR contributions such as ω B97X which has 16 % of SR exact exchange, 100 % of LR exact exchange, and $\omega_{\text{SR}} = \omega_{\text{LR}} = 0.30 \text{ a}_0^{-1}$. Expanding on hybrid XCFs, double-hybrid functionals include both exact exchange and a second-order Møller-Plesset (MP2) correlation correction calculated with the KS orbitals (discussed in Section 2.4).³⁸ An example is B2-PLYP, a double-hybrid variant of B3LYP.³⁹

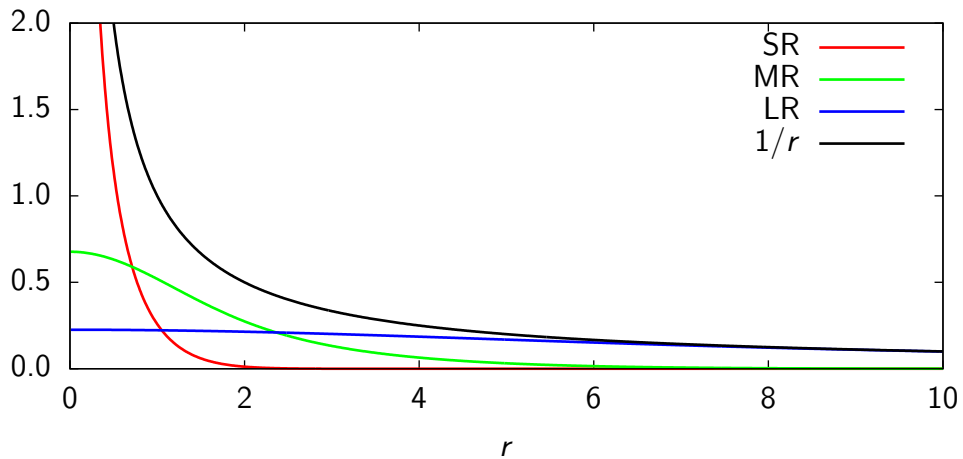
$$E_{\text{XC}}^{\text{B2-PLYP}} = (1 - a_{\text{X}})E_{\text{X}}^{\text{GGA}} + a_{\text{X}}E_{\text{X}}^{\text{HF}} + (1 - a_{\text{C}})E_{\text{C}}^{\text{GGA}} + a_{\text{C}}E_{\text{C}}^{\text{MP2}} \quad (2.2.18)$$

where $a_{\text{X}} = 0.53$ and $a_{\text{C}} = 0.27$ are the Hartree-Fock exchange energy contribution and the MP2 correlation contribution, respectively.

Finally, further improvements can be achieved by adding empirical dispersion energy (E_{disp}) correction to the DFT energy (E_{DFT}) in order to account for London dispersion interactions (as proposed by Grimme):⁴⁰

$$E_{\text{tot}} = E_{\text{DFT}} + E_{\text{disp}}. \quad (2.2.19)$$

In the second iteration of that scheme, DFT-D2, (which is the one used in this



Scheme 2.1: Representation of the $1/r$ function and its short (SR), middle (MR), and long range (LR) parts (see Eq. 2.2.16, with $\omega_{\text{SR}} = 0.8$ and $\omega_{\text{LR}} = 0.2$).

work), E_{disp} is given by:⁴¹

$$E_{\text{disp}} = -s_6 \sum_{A < B}^M \frac{C_6^{AB}}{R_{AB}^6} f_{\text{dmp}}(R_{AB}) \quad (2.2.20)$$

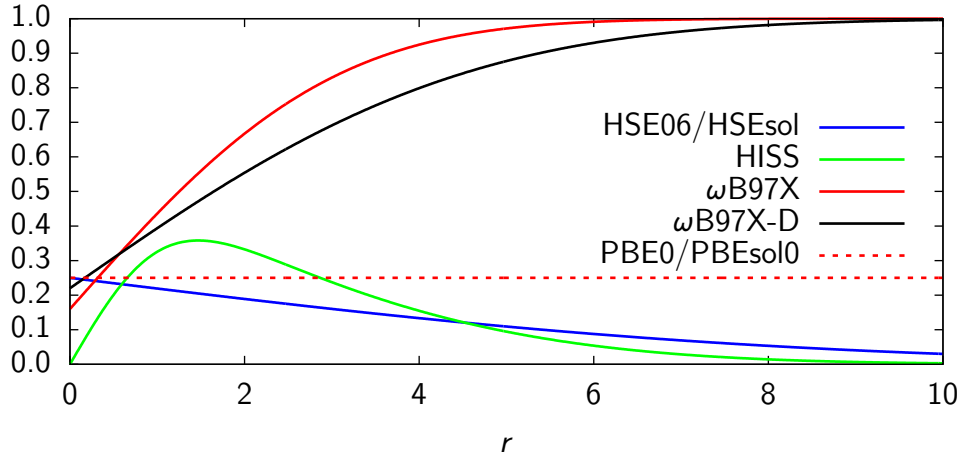
$$\text{with } f_{\text{dmp}}(R_{AB}) = \left[1 + \exp \left(-d \left\{ \frac{R_{AB}}{R_{vdW}} - 1 \right\} \right) \right]^{-1} \quad (2.2.21)$$

where s_6 is a scaling factor depending on the XCF (e.g. 0.75 for PBE or 1.05 for B3LYP), M is the number of atoms, C_6^{AB} is the dispersion coefficient associated with the pair of atoms AB ($C_6^{AB} = \sqrt{C_6^A C_6^B}$), R_{AB} is the interatomic distance of the pair AB , f_{dmp} is a damping function to avoid issues in the case of short R_{AB} values, R_{vdW} is the sum of atomic van der Waals radii, and finally, d defines the steepness of the function ($= 20$). The atomic dispersion coefficients, C_6^A , are derived from the London dispersion formula by computing the ionization potentials and static polarizabilities for each atom.

All the exchange-correlation functionals used in this work are listed in Table 2.1 along with their key features. Scheme 2.2 shows the exact exchange contribution of the hybrids. Overall, DFT can be very efficient but the accuracy of XCF is highly dependent on the targeted property and on the studied system.⁴² This means that for a new application or family of compounds, a comprehensive study is needed to find the best XCF for this particular calculation. Once the best XCF is identified, DFT is as fast as HF and can be as accurate as post HF methods like MP2 or CC theories.

Table 2.1: List and key features of the exchange-correlation functionals used (GH = Global Hybrid, RSH = Range-Separated Hybrid, disp = dispersion correction).

XCF	Type	Exact Exchange
B3LYP ⁴³	GH GGA	20 % of exact exchange
B3LYP-35	GH GGA	35 % of exact exchange
PBE ³²	GGA	—
HSE06 ³⁵	RSH GGA	25 % of SR exact exchange with $\omega = 0.11 a_0^{-1}$
HISS ³⁶	RSH GGA	60 % of MR exact exchange with $\omega_{SR} = 0.84 a_0^{-1}$ and $\omega_{LR} = 0.20 a_0^{-1}$
PBE0 ⁴⁴	GH GGA	25 %
PBEsol ³³	GGA	—
HSEsol ⁴⁵	RSH GGA	25 % of SR exact exchange with $\omega = 0.11 a_0^{-1}$
PBEsol0	RC GGA	25 % of exact exchange
ω B97X ⁴⁶	RSH GGA	16 % of SR exact exchange and 100 % of LR exact exchange with $\omega_{SR} = \omega_{LR} = 0.3 a_0^{-1}$
ω B97X-D ⁴⁶	RSH GGA + disp	22 % of SR exact exchange and 100 % of LR exact exchange with $\omega_{SR} = \omega_{LR} = 0.2 a_0^{-1}$
M06 ⁴⁷	GH m-GGA	27 % of exact exchange
M06-2X ⁴⁷	GH m-GGA	54 % of exact exchange



Scheme 2.2: Percentage of exact exchange as the function of the distance between the interacting electrons, r , for various hybrid exchange-correlation functionals: HSE06/HSEsol: 25 % at SR ($\omega = 0.11 a_0^{-1}$); HISS: 60 % at MR ($\omega_{SR} = 0.84 a_0^{-1}, \omega_{LR} = 0.20 a_0^{-1}$); ω B97X: 16 % at SR and 100 % at LR ($\omega = 0.3 a_0^{-1}$); ω B97X-D: 22 % at SR and 100 % at LR ($\omega = 0.2 a_0^{-1}$); and PBE0/PBESol0: 25 % of $1/r$.

2.3 Time-Dependent Density Functional Theory and Coupled-Perturbed Kohn-Sham

Time-dependent density functional theory (TD-DFT) is featured in Chapters 8 & 11 while coupled-perturbed Kohn-Sham (CP-KS) is in Chapters 6 & 10. All molecular properties discussed in this work can be derived from the wave function or, in the case of DFT, the electron density. To access them, a perturbation is added to the Hamiltonian and the new system has to be solved. Here, the calculation of properties within the DFT frame is discussed, starting with the most general case: a time-dependent (TD) perturbation, such as light. Then, the case of static perturbations is discussed for the calculation of NMR shielding constants. The time-dependent Schrödinger equation that needs to be solved reads:⁴⁸

$$i \frac{\partial \Psi(t)}{\partial t} = \hat{\mathcal{H}}(t) \Psi(t) \quad (2.3.1)$$

where, for compactness, $\Psi(t)$ stands for $\Psi(\vec{r}_1, \vec{r}_2, \dots, \vec{r}_N, t)$, and so on. Because time has been introduced, the founding theorems of DFT (Hohenberg & Kohn theorems) and the Kohn-Sham approximation are no longer valid (they are purely static). Thankfully, Runge and Gross⁴⁹ showed that similar rules and theorems can be established to develop time-dependent density functional theory (TD-DFT). They first assume that the TD external potential, $V_{\text{ext}}(\vec{r}, t)$ is Taylor expandable around $t = t_0$. On this basis, they showed that from an initial

wave function, two different external potentials, $V_{ext}(\vec{r}, t)$ and $V'_{ext}(\vec{r}, t)$, instantaneously lead to two different time-dependent densities, $\rho(\vec{r}, t)$ and $\rho'(\vec{r}, t)$, as soon as $t > t_0$. In other words, within the time-dependent scheme, the density is still uniquely defined by the external potential. They further demonstrated three theorems that are not discussed here but can be found in the Reference (Ref.) [49].

Secondly, thanks to van Leeuwen theorem,⁵⁰ the TD wave function of interacting electrons can be expressed in terms of non-interacting ones that reproduce the fully interacting electron density. For a TD electron density, $\rho(\vec{r}, t)$ obtained from the initial state Ψ_0 (characterized by a given interacting electron repulsion potential, V_{ee}) under the potential $V_{ext}(\vec{r}, t)$, there exists an alternative initial state Ψ'_0 (characterized by an alternative electron repulsion potential, V'_{ee}) and an alternative potential $V'_{ext}(\vec{r}, t)$ that also lead to $\rho(\vec{r}, t)$. The time-dependent Kohn-Sham (TD-KS) equation can now be written using the KS orbitals.⁵¹

$$i \frac{\partial \Theta_i(\vec{r}, t)}{\partial t} = [\hat{T}(\vec{r}) + \hat{V}_{eff}[\rho](\vec{r}, t)] \Theta_i(\vec{r}, t) \quad (2.3.2)$$

$$\text{with } \hat{V}_{eff}[\rho](\vec{r}, t) = \hat{V}_{ext}(\vec{r}, t) + \int d\vec{r}' \frac{\rho(\vec{r}', t)}{|\vec{r} - \vec{r}'|} + \hat{V}_{XC}(\vec{r}, t). \quad (2.3.3)$$

Just like for time-independent (stationary) DFT, the key to TD-DFT is the exchange-correlation potential, but in its time-dependent form. A very common approximation is to use the static exchange-correlation functional instead of working out the actual TD one, effectively using the TD density with the ground state, unperturbed, XC potential. This is the adiabatic approximation:⁵²

$$\hat{V}_{XC}[\rho](\vec{r}, t) = \hat{V}_{XC}[\rho_0](\vec{r}) \Big|_{\rho_0(\vec{r}) \rightarrow \rho(\vec{r}, t)}. \quad (2.3.4)$$

This approximation assumes that the electron density remains in its eigenstate upon being perturbed (the perturbation is slow compared to the electron density rearrangement). In the framework of these approximations, the linear electron density response, $\rho^{(1)}(\vec{r}, t)$ is given by:³⁰

$$\rho^{(1)}(\vec{r}, t) = \iint d\vec{r}' dt' \chi(\vec{r}, t, \vec{r}', t') V_{eff}^{(1)}(\vec{r}', t') \quad (2.3.5)$$

where $V_{eff}^{(1)}$ is the first-order perturbed effective potential and $\chi(\vec{r}, t, \vec{r}', t')$ is the first-order response function. $V_{eff}^{(1)}$ is given by:

$$V_{eff}^{(1)}(\vec{r}, t) = V_{ext}^{pert}(\vec{r}, t) + \int d\vec{r}' \frac{\rho^{(1)}(\vec{r}', t)}{|\vec{r} - \vec{r}'|} + \iint d\vec{r}' dt' f_{XC}(\vec{r}, t, \vec{r}', t') \rho^{(1)}(\vec{r}', t') \quad (2.3.6)$$

$$\text{with } f_{XC}(\vec{r}, t, \vec{r}', t') = \frac{\partial V_{XC}[\rho](\vec{r}, t)}{\partial \rho(\vec{r}', t')} \Big|_{\rho=\rho_0} \quad (2.3.7)$$

where f_{XC} is the exchange-correlation kernel. The self-consistency of the problem arises from the actual electron density response, $\rho^{(1)}$: it depends on $V_{eff}^{(1)}$ which itself depends on $\rho^{(1)}$. As for the response function, its Fourier transform with respect to $t - t'$ gives:³⁰

$$\chi(\vec{r}, \vec{r}', \omega) = \sum_i^{\text{occ}} \sum_a^{\text{unocc}} \left[\frac{\Theta_i^*(\vec{r}) \Theta_a(\vec{r}) \Theta_a^*(\vec{r}') \Theta_i(\vec{r}')}{\omega - (\epsilon_a - \epsilon_i) + i\Gamma} - \frac{\Theta_i(\vec{r}) \Theta_a^*(\vec{r}) \Theta_a(\vec{r}') \Theta_i^*(\vec{r}')}{\omega + (\epsilon_a - \epsilon_i) - i\Gamma} \right] \quad (2.3.8)$$

where ω (or $\hbar\omega$) is the energy of the perturbation, ϵ_j is the energy of the spinorbital j , and Γ is a damping factor.

2.3.1 Excitation Energies and Oscillator Strengths

The poles of the response function correspond to the excitation energies. To find them, the problem can be rewritten in a matrix form:^{53,54}

$$\begin{pmatrix} \mathbf{A} & \mathbf{B} \\ \mathbf{B}^* & \mathbf{A}^* \end{pmatrix} \begin{pmatrix} \mathbf{X} \\ \mathbf{Y} \end{pmatrix} = \omega \begin{pmatrix} \mathbf{1} & \mathbf{0} \\ \mathbf{0} & -\mathbf{1} \end{pmatrix} \begin{pmatrix} \mathbf{X} \\ \mathbf{Y} \end{pmatrix} \quad (2.3.9)$$

$$\text{with } A_{ia,jb} = \delta_{ij}\delta_{ab}(\epsilon_a - \epsilon_i) + (ia|jb) + (ia|f_{XC}|jb) \quad (2.3.10)$$

$$\text{and } B_{ia,jb} = (ia|bj) + (ia|f_{XC}|bj) \quad (2.3.11)$$

where ω are the excitation energies, X is associated with the excitation, and Y is associated with the de-excitation. Each excitation is characterized by an energy and one or multiple electronic transitions, e.g. 70 % highest occupied molecular orbital (HOMO) to lowest unoccupied molecular orbital (LUMO) ($H \rightarrow L$) transition and 30 % $H-1 \rightarrow L+1$ transition.

Then, by computing the transition dipole moment from the ground state g to the excited state e , $\vec{\mu}_{eg}$, the oscillator strength of the transition, f_{eg} , is available:

$$f_{eg} = \frac{2}{3} \|\vec{\mu}_{eg}\| \Delta E_{eg} \quad (2.3.12)$$

$$\text{with } \vec{\mu}_{eg} = \langle \Psi_e | \hat{\mu} | \Psi_g \rangle. \quad (2.3.13)$$

2.3.2 First Hyperpolarizability

The calculation of the first hyperpolarizability, β , requires the evaluation of the second-order derivative of the density matrix with respect to the electric field:

$$\beta_{pqr}(-\omega_\sigma; \omega_1, \omega_2) = \frac{\partial^2 \mu_p}{\partial F_r(\omega_2) \partial F_q(\omega_1)} \quad (2.3.14)$$

$$\beta_{pqr} = -2 \sum_{\mu, \nu}^K M_{\mu\nu, p} \frac{\partial D_{\mu\nu}}{\partial F_r(\omega_2) \partial F_q(\omega_1)} \Big|_{F=0} \quad (2.3.15)$$

$$= -2 \sum_{\mu, \nu}^K M_{\mu\nu, p} D_{\mu\nu}^{F_q, F_r}(\omega_1, \omega_2) \quad (2.3.16)$$

where $M_{\mu\nu,p}$ is an element of the dipole moment matrix (in the basis of the AOs) in the p^{th} direction, $\langle \varphi_\mu | \hat{\mu}_p | \varphi_\nu \rangle$. Thanks to the "2n+1" rule stating that the energy derivative to the order 2n+1 requires the perturbed orbitals to the order n,⁵⁵ the second-order derivative of the density matrix, $D_{\mu\nu}^{F_q, F_r}(\omega_1, \omega_2)$, is not needed to evaluate β . Only the first-order ones are: $D_{\mu\nu}^{F_q}(\omega_1)$ and $D_{\mu\nu}^{F_r}(\omega_2)$. The derivative of the density matrix is given by:⁵⁶

$$\mathbf{D}^{F_q}(\omega) = \mathbf{C}^{F_q}(\omega) \mathbf{n} \mathbf{C}^\dagger + \mathbf{C} \mathbf{n} \left(\mathbf{C}^{F_q}(\omega) \right)^\dagger \quad (2.3.17)$$

$$\text{with } \mathbf{C}^{F_q}(\omega) = \mathbf{C} \mathbf{U}^{F_q}(\omega) \quad (2.3.18)$$

where \mathbf{n} is a diagonal matrix ensuring that only the occupied spinorbitals are taken into account. Using Eq. 2.3.18 and plugging it into the perturbed SCF equation, we get:

$$\mathbf{C}^\dagger \mathbf{F}^{F_q}(\omega) \mathbf{C} + \mathbf{E} \mathbf{U}^{F_q}(\omega) + \omega \mathbf{U}^{F_q}(\omega) = \mathbf{U}^{F_q}(\omega) \mathbf{E} \quad (2.3.19)$$

$$\text{so that } U_{ij}^{F_q}(\omega) = \frac{G_{ij}^{F_q}(\omega)}{\varepsilon_j - \varepsilon_i - \omega} \quad (2.3.20)$$

$$\text{with } G_{ij}^{F_q}(\omega) = \sum_{\mu, \nu}^K c_{\mu i}^\dagger F_{\mu\nu}^{F_q}(\omega) c_{\nu j}. \quad (2.3.21)$$

The problem is solved iteratively as this last equation clearly shows the interdependence of \mathbf{F}^{F_q} and \mathbf{U}^{F_q} . Finally, the first hyperpolarizability is given by:⁵⁶

$$\begin{aligned} \beta_{pqr}(-\omega_\sigma; \omega_1, \omega_2) = & \\ & - tr \left[\mathbf{n} \left\{ \begin{aligned} & \mathbf{U}^{F_p}(-\omega_\sigma) \mathbf{G}^{F_q}(\omega_1) \mathbf{U}^{F_r}(\omega_2) + \mathbf{U}^{F_p}(-\omega_\sigma) \mathbf{G}^{F_r}(\omega_2) \mathbf{U}^{F_q}(\omega_1) + \\ & \mathbf{U}^{F_q}(\omega_1) \mathbf{G}^{F_p}(-\omega_\sigma) \mathbf{U}^{F_r}(\omega_2) + \mathbf{U}^{F_q}(\omega_1) \mathbf{G}^{F_r}(\omega_2) \mathbf{U}^{F_p}(-\omega_\sigma) + \\ & \mathbf{U}^{F_r}(\omega_2) \mathbf{G}^{F_p}(-\omega_\sigma) \mathbf{U}^{F_q}(\omega_1) + \mathbf{U}^{F_r}(\omega_2) \mathbf{G}^{F_q}(\omega_1) \mathbf{U}^{F_p}(-\omega_\sigma) \end{aligned} \right\} \right] \\ & - tr \left[\mathbf{n} \left\{ \begin{aligned} & \mathbf{U}^{F_p}(-\omega_\sigma) \mathbf{U}^{F_q}(\omega_1) \mathbf{E}^{F_r}(\omega_2) + \mathbf{U}^{F_p}(-\omega_\sigma) \mathbf{U}^{F_r}(\omega_2) \mathbf{E}^{F_q}(\omega_1) + \\ & \mathbf{U}^{F_q}(\omega_1) \mathbf{U}^{F_p}(-\omega_\sigma) \mathbf{E}^{F_r}(\omega_2) + \mathbf{U}^{F_q}(\omega_1) \mathbf{U}^{F_r}(\omega_2) \mathbf{E}^{F_p}(-\omega_\sigma) + \\ & \mathbf{U}^{F_r}(\omega_2) \mathbf{U}^{F_p}(-\omega_\sigma) \mathbf{E}^{F_q}(\omega_1) + \mathbf{U}^{F_r}(\omega_2) \mathbf{U}^{F_q}(\omega_1) \mathbf{E}^{F_p}(-\omega_\sigma) \end{aligned} \right\} \right] \\ & + tr \left(\mathbf{g}_{XC}(\omega_1, \omega_2) \mathbf{D}^{F_p}(-\omega_\sigma) \mathbf{D}^{F_q}(\omega_1) \mathbf{D}^{F_r}(\omega_2) \right) \end{aligned} \quad (2.3.22)$$

where tr stand for the trace (the sum of diagonal elements) and \mathbf{g}_{XC} is the second-order derivative of the XC potential with respect to the density.

2.3.3 Nuclear Magnetic Resonance

The shielding tensor of nucleus N , σ^N , is the second-order derivative of the energy with respect to the nucleus magnetic moment, m_N , and the (external) magnetic field, \vec{B} .^{57,58}

$$\sigma_{pq}^N = \frac{\partial^2 E}{\partial B_q \partial m_{Np}}. \quad (2.3.23)$$

Note that none of the perturbation are time-dependent. This corresponds to the time-dependent Kohn-Sham with $\omega = 0$, which is referred to as CP-KS. σ^N can be explicitly written as:

$$\sigma_{pq}^N = \sum_{\mu,\nu} D_{\mu\nu} \frac{\partial^2 h_{\mu\nu}}{\partial B_q \partial m_{Np}} \Big|_{B=0} + \sum_{\mu,\nu} \frac{\partial D_{\mu\nu}}{\partial B_q} \Big|_{B=0} \frac{\partial h_{\mu\nu}}{\partial m_{Np}} \quad (2.3.24)$$

where \mathbf{D} is the density matrix (see Eq. 2.1.22) and $h_{\mu\nu}$ is a mono-electronic integral. The derivatives of h are given by:^{57,58}

$$\frac{\partial h_{\mu\nu}}{\partial m_{Np}} = \left\langle \varphi_\mu \left| \frac{\partial \hat{h}}{\partial m_{Np}} \right| \varphi_\nu \right\rangle \quad (2.3.25)$$

$$\text{with } \frac{\partial \hat{h}}{\partial m_{Np}} = -\frac{i}{c} \frac{[(\vec{r} - \vec{R}_N) \times \vec{\nabla}]_p}{|\vec{r} - \vec{R}_N|^3} \quad (2.3.26)$$

$$\frac{\partial^2 h_{\mu\nu}}{\partial B_q \partial m_{Np}} = \left\langle \varphi_\mu \left| \frac{\partial^2 \hat{h}}{\partial B_q \partial m_{Np}} \right| \varphi_\nu \right\rangle \quad (2.3.27)$$

$$\text{with } \frac{\partial^2 \hat{h}}{\partial B_q \partial m_{Np}} = \frac{i}{2c^2} \frac{\vec{r} \cdot (\vec{r} - \vec{R}_N) \delta_{qp} - \vec{r}_q (\vec{r} - \vec{R}_N)_p}{|\vec{r} - \vec{R}_N|^3} \quad (2.3.28)$$

where \hat{h} is the mono-electronic operator (see Eq. 2.1.15), i is the imaginary number, c is the light velocity, \vec{r} is the position of the electron, \vec{R}_N is the position of the nucleus N , and δ is the Kronecker delta. As for the derivative of the density matrix, $D_{\mu\nu}^{B_q}$, it is given by:^{57,58}

$$D_{\mu\nu}^{B_q} = \sum_{\alpha,\beta} \left(U_{\alpha\beta}^{B_q \dagger} c_{\mu\alpha}^\dagger c_{\nu\beta} + c_{\mu\beta}^\dagger c_{\nu\alpha} U_{\alpha\beta}^{B_q} \right) \quad (2.3.29)$$

where the c are the LCAO coefficients and U is used to parametrize their derivatives. The magnetic field can be written as a function of the vector potential, \vec{A} , which is gauge dependent:^{57,58}

$$\vec{B} = \vec{\nabla} \times \vec{A}, \quad (2.3.30)$$

so that depending on the origin, \vec{B} is not the same, *i.e.* the effective external magnetic field is not the same on each nucleus. To deal with this issue, the gauge-including atomic orbitals (GIAOs) are introduced, $\varphi_p(\vec{B}, \vec{r})$:^{59,60}

$$\varphi_p(\vec{B}, \vec{r}) = \exp \left[-\frac{i}{2c} (\vec{B} \times \vec{R}_p) \cdot \vec{r} \right] \varphi_p(\vec{r}) \quad (2.3.31)$$

where \vec{R}_p is the center of the basis function.

2.4 Møller-Plesset Perturbation Theory

Second-order Møller-Plesset (MP2) is featured in Chapter 9. The largest flaw of Hartree-Fock theory is arguably the missing electron correlation. In their attempt to recover it, Møller and Plesset⁶¹ used the Rayleigh-Schrödinger perturbation theory.^{62,63} It states that the Hamiltonian can be partitioned in two parts:

$$\hat{H}\Psi = \left(\hat{H}^{(0)} + \lambda\hat{V}\right)\Psi = E\Psi \quad (2.4.1)$$

where $\hat{H}^{(0)}$ is the unperturbed Hamiltonian, λ is an ordering parameter, and \hat{V} is the (small) perturbation. The wave function and the energy can be written as a power series of terms of successive orders in the perturbation:

$$\Psi = \Psi^{(0)} + \lambda\Psi^{(1)} + \lambda^2\Psi^{(2)} + \dots \quad (2.4.2)$$

$$E = E^{(0)} + \lambda E^{(1)} + \lambda^2 E^{(2)} + \dots \quad (2.4.3)$$

By considering the perturbation \hat{V} as the electron correlation,⁶¹ *i.e.* the difference between the exact two-electron operator ($\propto 1/r$) and the HF one, the 0th to 2nd order perturbed energies are given by the following equations:

$$E^{(0)} = \sum_i^{\text{occ}} \varepsilon_i \quad (2.4.4)$$

$$E^{(1)} = -\frac{1}{2} \sum_{i,j}^{\text{occ}} (\langle ij|ij \rangle - \langle ij|ji \rangle) \quad (2.4.5)$$

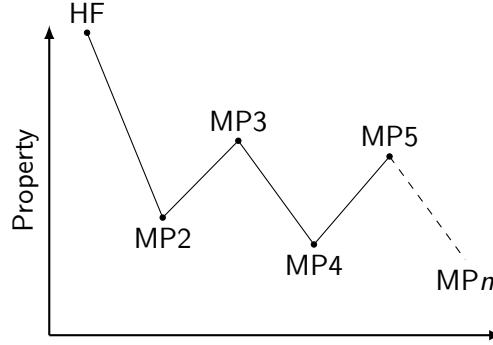
$$= -\frac{1}{2} \sum_{i,j}^{\text{occ}} \langle ij||ij \rangle$$

$$E^{(2)} = \sum_{i>j}^{\text{occ}} \sum_{a>b}^{\text{unocc}} \frac{|\langle ab||ij \rangle|^2}{\varepsilon_i + \varepsilon_j - \varepsilon_a - \varepsilon_b}. \quad (2.4.6)$$

The Hartree-Fock energy is the sum of the 0th and 1st order energies while adding the first correction to the HF energy, the 2nd order perturbed energy, gives the second-order Møller-Plesset (MP2) energy. It can be interpreted as the contribution of the doubly excited states ($\Theta_i(\vec{x}_1) \rightarrow \Theta_a(\vec{x}_1)$ and $\Theta_j(\vec{x}_2) \rightarrow \Theta_b(\vec{x}_2)$) to the energy. Note that these states are often used as the starting point for coupled cluster calculations.

The MP2 approximation is computationally more expensive than HF since it requires the evaluation of more integrals, but is also much more accurate thanks to the perturbative correlation correction. While MP2 is a straightforward improvement over HF, the improvements in accuracy of a property or of the molecular energy along the MP n series are not as simple to interpret as the series can show an oscillatory behavior (see Scheme 2.3).⁶⁴ As an added bonus

to the more accurate energy, the better description of the wave function means a better description of the dispersion energy (that previously had to be added explicitly, see Eq. 2.2.19).



Scheme 2.3: Schematic evolution of the MP_n series (reproduced from Ref.⁶⁴).

2.5 Coupled Cluster & Coupled Cluster Linear Response

Coupled cluster (CC) models are featured in Chapters 7 & 9 and coupled cluster linear response (CCLR) method in Chapter 7. Coupled cluster (CC) theory was first introduced to include correlation effects to the wave function of nuclei.⁶⁵ It was later applied to the electronic wave function, thus recovering the electron correlation missing in the Hartree-Fock theory. To do so, the CC wave function, $|CC\rangle$, is expressed as the exponential ansatz of a reference wave function, here a HF one, $|HF\rangle$:

$$|CC\rangle = \exp(\hat{T})|HF\rangle \quad (2.5.1)$$

where \hat{T} is the cluster operator. It can be written as the sum of one-orbital (\hat{T}_1), two-orbitals (\hat{T}_2), ..., n-orbitals (\hat{T}_n) cluster operators:⁶⁶

$$\hat{T} = \hat{T}_1 + \hat{T}_2 + \dots = \sum_{n=1} \hat{T}_n \quad (2.5.2)$$

$$\text{where } \hat{T}_1 = \sum_{i,a} t_i^a a_a^\dagger a_i \quad (2.5.3)$$

$$\hat{T}_2 = \sum_{i,j,a,b} t_{ij}^{ab} a_b^\dagger a_a^\dagger a_j a_i. \quad (2.5.4)$$

The t terms are the amplitudes and the i (a) index refers to occupied (un-occupied) HF orbitals. The cluster operators are expressed using the second quantization where the a operator allows for the *creation* of a spinorbital, a_i^\dagger , or its *annihilation*, a_i :

$$a_i^\dagger |vac\rangle = |i\rangle \quad (2.5.5)$$

$$a_i |i\rangle = |vac\rangle \quad (2.5.6)$$

where $|vac\rangle$ is the vacuum. The coupled cluster singles and doubles (CCSD) wave function is thus given by:⁶⁶

$$|CCSD\rangle = \exp(\hat{T}_1 + \hat{T}_2)|HF\rangle. \quad (2.5.7)$$

Once again, the problem to solve is the Schrödinger equation:⁶⁶

$$\hat{H}|CC\rangle = E|CC\rangle \quad (2.5.8)$$

$$\hat{H}e^{\hat{T}}|HF\rangle = Ee^{\hat{T}}|HF\rangle, \quad (2.5.9)$$

so that the CC energy is given by

$$\langle HF|e^{-\hat{T}}\hat{H}e^{\hat{T}}|HF\rangle = E. \quad (2.5.10)$$

In order to determine the t_i^a and t_{ij}^{ab} amplitudes (*i.e.* the wave function) and, subsequently the energy, Eq. 2.5.9 is projected on the whole list of μ configurations leading to a set of nonlinear equations:

$$\langle \mu|e^{-\hat{T}}\hat{H}e^{\hat{T}}|HF\rangle = 0 \quad (2.5.11)$$

where μ refers to $\Psi_{ij,\dots}^{ab,\dots}$, an excited determinant (*e.g.* μ_1 is a singly excited wave function). $e^{-\hat{T}}\hat{H}e^{\hat{T}}$ can be expanded in a Taylor series, giving the Baker-Campbell-Hausdorff (or Hausdorff) expansion:⁶⁶

$$e^{-\hat{T}}\hat{H}e^{\hat{T}} = \hat{H} + [\hat{H}, \hat{T}] + \frac{1}{2!} [[\hat{H}, \hat{T}], \hat{T}] + \frac{1}{3!} [[[\hat{H}, \hat{T}], \hat{T}], \hat{T}] + \dots \quad (2.5.12)$$

where the commutator is defined as:

$$[\hat{H}, \hat{T}] = \hat{H}\hat{T} - \hat{T}\hat{H}. \quad (2.5.13)$$

The naming scheme of the CC model might be misleading, as the CCSD model not only contains single and double excitations (*connected* singles and doubles) but also the so-called *disconnected* contributions:

T_1^2 the combination of single clusters, disconnected doubles;

T_1T_2 the combination of single and double clusters, disconnected triples;

etc.

Considering the fact that the Hamiltonian elements that differ by more than two spinorbitals are null (Brillouin's theorem), thus truncating the Hausdorff expansion, the CCSD energy expression can be obtained:

$$E_{CCSD} = E_{HF} + \langle HF | [\hat{H}, \hat{T}_2] | HF \rangle + \frac{1}{2} \langle HF | [[\hat{H}, \hat{T}_1], \hat{T}_1] | HF \rangle. \quad (2.5.14)$$

Note that only the connected singles and doubles, and the disconnected doubles are taken into account. This is also true for higher-level models such as CCSDT, but a higher level of accuracy is achieved as the t_1 and t_2 are relaxed by the coupling with higher terms. Indeed, the singles and doubles amplitudes of CCSD are given by:⁶⁶

$$\langle \mu_1 | \bar{\mathcal{H}} + [\bar{\mathcal{H}}, \hat{T}_2] | HF \rangle = 0 \quad (2.5.15)$$

$$\text{and } \langle \mu_2 | \bar{\mathcal{H}} + [\bar{\mathcal{H}}, \hat{T}_2] + \frac{1}{2} [[\bar{\mathcal{H}}, \hat{T}_2], \hat{T}_2] | HF \rangle = 0 \quad (2.5.16)$$

where t_1 and t_2 depend on each other, either explicitly for Eq. 2.5.15 or through the T_1 transformed Hamiltonian for Eq. 2.5.16:

$$\bar{\mathcal{H}} = e^{-\hat{T}_1} \hat{\mathcal{H}} e^{\hat{T}_1}. \quad (2.5.17)$$

To simplify the CCSD model and reduce its cost, the Hamiltonian can be partitioned into the Fock operator, \hat{F} , and the fluctuation operator, \hat{U} , which in the case of a HF reference wave function, represents the electronic correlation:^{67,68}

$$\hat{\mathcal{H}} = \hat{F} + \hat{U}. \quad (2.5.18)$$

In the coupled cluster approximate doubles (CC2) model,⁶⁷ the singles amplitudes are the same as in CCSD (Eq. 2.5.15) but the doubles are simplified and given by:

$$\langle \mu_2 | [\hat{F}, \hat{T}_2] + \bar{\mathcal{H}} | HF \rangle = 0. \quad (2.5.19)$$

This mainly achieves two goals: i) the CC2 energy is of MP2-like quality, which is a big improvement w.r.t. Hartree-Fock and ii) the inclusion of the singles allows the use of exact response function and the definition of excitation energies and transition moments. CC2 is exact to the second-order for the ground-state energy, *i.e.* the Hausdorff expansion is accurate up to the second-order while higher-order terms are incomplete. CCSD is exact to the third-order.

Alternatively, to improve upon CCSD without having to go to the extremely expensive coupled cluster singles, doubles, and triples (CCSDT), the contribution of the triples can be added perturbatively: the coupled cluster singles, doubles, and perturbative triples (CCSD(T)) model.⁶⁹ The perturbative contribution of the triples cluster \hat{T}_3 is added by way of disconnected triples using the optimized \hat{T}_1 and \hat{T}_2 amplitudes. This means that the triples cluster \hat{T}_3 has no impact on \hat{T}_1 or \hat{T}_2 , and that the CCSD(T) energy is given by:^{66,69}

$$E_{\text{CCSD(T)}} = E_{\text{CCSD}} + \Delta E_{\text{CCSD(T)}} \quad (2.5.20)$$

$$\text{with } \Delta E_{\text{CCSD(T)}} = E_T^{(4)} + E_{ST}^{(5)} \quad (2.5.21)$$

where $\Delta E_{\text{CCSD(T)}}$ is the perturbative correction from the triple excitations, $E_T^{(4)}$ is the fourth-order energy contribution of the triples, and $E_{ST}^{(5)}$ is the fifth-order energy contribution of the singles and triples.

Overall, there are plenty of CC wave functions available, here ordered by completeness w.r.t. the number of clusters used or when needed, w.r.t. the accuracy of the amplitudes (e.g. CC2 is less accurate than CCSD despite having the same number of clusters):

$$\text{CCS} < \text{CCD} < \text{CC2} < \text{CCSD} < \text{CCSD(T)} < \text{CC3} < \text{CCSDT} < \dots$$

This ordering also matches the accuracy on the ground-state energy. Note that due to Brillouin's theorem, the CCS model yields the HF energy (for the ground state). As for CCD, it only considers double excitations, which means that it lacks coupling with single excitations, as in CC2 or CCSD or with higher models such as in CC3⁶⁸ or CCSDT. The completeness of the models when considering the calculation of excitation energies is discussed later.

In general, one of the costlier parts of any quantum wave function calculation is the evaluation of the 4-center two-electron integrals. In order to reduce that cost, Feyereisen and coworkers proposed to use an auxiliary basis set, leading to the resolution of the identity (RI) approximation:^{70,71}

$$\langle \mu\nu | \tau\eta \rangle \simeq \langle \mu\nu | \underbrace{\sum_{PQ} |P\rangle V_{PQ}^{-1} \langle Q|}_{\simeq 1} | \tau\eta \rangle \quad (2.5.22)$$

$$\text{with } V_{PQ} = \langle P | Q \rangle \quad (2.5.23)$$

where P and Q refer to the basis function of the auxiliary basis set. This means that the expensive 4-center integrals are replaced by cheaper 3- and 2-center integrals. This approximation is used by default for CC calculations in TURBOMOLE where the auxiliary basis sets optimized for the Ahlrichs sets are available.^{24,72,73}

When computing integrals, the electronic space is explored. Indeed, the integrals are calculated for pairs of electrons, spanning both the occupied and virtual spaces. In order to reduce the computational cost, the pair of natural orbitals (PNO) approximation aims at condensing the information of the virtual space into a smaller number of orbitals.⁷⁴⁻⁷⁷ To do so, localized molecular orbitals (LMOs),^{78,79} also called natural orbitals, are used (instead of the "regular" MOs) to create pairs that describe the CC clusters. Due to their localized nature, the virtual space considered for each pair can be truncated based on the distance between the occupied and unoccupied LMOs. Using the PNO approximation, the correlation energy of schemes such as MP2 or CC can be recovered with errors of 1 to 2 %, while shortening the computation time: Ref. [76] reports a calculation time scaling of $10^{-10.8} K^{4.60}$ (K is the number of basis functions) for RI-MP2 down to $10^{-4.7} K^{2.67}$ for PNO-RI-MP2.⁸⁰

To obtain the excitation energies and the oscillator strengths, CCLR is discussed.^{66,81–84} Firstly, the time-dependent CC function needs to be established:

$$|CC(t)\rangle = \exp(-i\epsilon(t)) \exp(\hat{T}(t)) |HF\rangle \quad (2.5.24)$$

$$\text{with } \hat{T}(t) = t(t)\hat{\tau} \quad (2.5.25)$$

where $\exp(-i\epsilon(t))$ is a TD phase factor, $t(t)$ are the time-dependent amplitudes, and the $\hat{\tau}$ operators are the creation and annihilation operators (e.g. $\hat{\tau}_{\mu_1} = a_a^\dagger a_i$). Then, a time-dependent perturbation, \hat{V}^t , is added to the Hamiltonian, giving the TD Hamiltonian:

$$\hat{\mathcal{H}}(t) = \hat{F} + \hat{U} + \hat{V}^t(t) = \hat{\mathcal{H}}_0 + \hat{V}^t(t). \quad (2.5.26)$$

The CC2 TD amplitudes, $t_{\mu_1}(t)$ and $t_{\mu_2}(t)$, are given by:^{67,68,85}

$$\langle \mu_1 | \bar{\mathcal{H}}(t) + [\bar{\mathcal{H}}(t), \hat{T}_2(t)] | HF \rangle = i \frac{\partial t_{\mu_1}(t)}{\partial t} \quad (2.5.27)$$

$$\langle \mu_2 | [\hat{F} + \bar{V}(t), \hat{T}_2(t)] + \bar{\mathcal{H}}(t) | HF \rangle = i \frac{\partial t_{\mu_2}(t)}{\partial t}. \quad (2.5.28)$$

For CCSD, the $t_{\mu_1}(t)$ are the same as CC2 while the $t_{\mu_2}(t)$ are:

$$\langle \mu_2 | \bar{\mathcal{H}}(t) + [\bar{\mathcal{H}}(t), \hat{T}_2(t)] + \frac{1}{2} [[\bar{\mathcal{H}}(t), \hat{T}_2(t)], \hat{T}_2(t)] | HF \rangle = i \frac{\partial t_{\mu_2}(t)}{\partial t}. \quad (2.5.29)$$

The CC2 quasi energy can be expressed as a quasi energy Lagrangian where the constraints are the $t(t)$:^{67,68,85}

$$\begin{aligned} \mathcal{L} = & \langle HF | \hat{\mathcal{H}}(t) \exp(\hat{T}_1(t) + \hat{T}_2(t)) | HF \rangle \\ & + \sum_{\mu_1} \tilde{t}_{\mu_1} \left(\langle \mu_1 | \bar{\mathcal{H}}(t) + [\bar{\mathcal{H}}(t), \hat{T}_2(t)] | HF \rangle - i \frac{dt_{\mu_1}}{dt} \right) \\ & + \sum_{\mu_2} \tilde{t}_{\mu_2} \left(\langle \mu_2 | [\hat{F} + \hat{V}^t, \hat{T}_2(t)] + \bar{U}(t) | HF \rangle - i \frac{dt_{\mu_2}}{dt} \right). \end{aligned} \quad (2.5.30)$$

The linear response function is obtained from the derivative of the Lagrangian

w.r.t. the observable $A(-\omega)$ and the perturbation $B(\omega)$:⁶⁷

$$\langle\langle A; B \rangle\rangle_\omega = \frac{\partial^2 \mathcal{L}}{\partial A(-\omega) \partial B(\omega)} \quad (2.5.31)$$

$$\begin{aligned} &= \mathcal{P}_{A,B} \left\{ \left\langle HF \left| \left[\hat{A}(-\omega), \hat{T}_1^B(\omega) \right] + \frac{1}{2} \left[[\hat{\mathcal{H}}_0, \hat{T}_1^A(-\omega)], \hat{T}_1^B(\omega) \right] \right| HF \right\rangle \right. \\ &\quad + \sum_{\mu_1} \tilde{t}_{\mu_1}^{(0)} \left\langle \mu_1 \left| \left[\bar{A}(-\omega), \hat{T}^B(\omega) \right] + \frac{1}{2} \left[[\bar{\mathcal{H}}_0, \hat{T}^A(-\omega)], \hat{T}^B(\omega) \right] \right| HF \right\rangle \\ &\quad + \sum_{\mu_2} \tilde{t}_{\mu_2}^{(0)} \left\langle \mu_2 \left| \left[\bar{A}(-\omega), \hat{T}_2^B(\omega) \right] + \left[\left[\bar{A}(-\omega), \hat{T}_1^B(\omega) \right], \hat{T}_2^{(0)} \right] \right. \right. \\ &\quad \left. \left. + \frac{1}{2} \left[[\bar{\mathcal{H}}_0, \hat{T}_1^A(-\omega)], \hat{T}_1^B(\omega) \right] \right| HF \right\rangle \right\} \quad (2.5.32) \end{aligned}$$

where (0) refers to the unperturbed (or zeroth-order perturbed) operator and $\mathcal{P}_{A,B}$ is a permutation operator. The perturbed cluster amplitudes are then given by:⁶⁷

$$(\omega \mathbf{1} - \mathcal{A}) \mathbf{t}^A(\omega) = \boldsymbol{\xi}^A(\omega), \quad (2.5.33)$$

with the zeroth-order being:

$$\mathbf{t}^{(0)} \mathcal{A} = \boldsymbol{\eta}^{(0)}. \quad (2.5.34)$$

The coupled cluster Jacobian, \mathcal{A} is:⁶⁷

$$\mathcal{A} = \begin{pmatrix} \left\langle \mu_1 \left| [\bar{H}, \hat{\tau}_{\nu_1}] \exp(\hat{T}_2^{(0)}) \right| HF \right\rangle & \left\langle \mu_1 \left| [\bar{H}, \hat{\tau}_{\nu_2}] \right| HF \right\rangle \\ \left\langle \mu_2 \left| [\bar{H}, \hat{\tau}_{\nu_1}] \right| HF \right\rangle & \delta_{\mu\nu} \omega_{\mu_2} \end{pmatrix} \quad (2.5.35)$$

and the r.h.s. of the amplitude equations, $\boldsymbol{\xi}$ and $\boldsymbol{\eta}$, are:⁶⁷

$$\boldsymbol{\xi}^A = \begin{pmatrix} \left\langle \mu_1 \left| \bar{A} + [\bar{A}, \hat{T}_2^{(0)}] \right| HF \right\rangle \\ \left\langle \mu_2 \left| [\bar{A}, \hat{T}_2^{(0)}] \right| HF \right\rangle \end{pmatrix} \quad (2.5.36)$$

$$\eta_{\nu_i} = - \left\langle HF \left| [\bar{\mathcal{H}}_0, \hat{\tau}_{\nu_i}] \right| HF \right\rangle. \quad (2.5.37)$$

The excitation energies are the eigenvalues of the Jacobian:

$$\mathcal{A} \mathbf{S} = \omega \mathbf{S} \quad (2.5.38)$$

where \mathbf{S} describes the nature of the excitations in terms of singly, doubly, ... excited determinants. Overall, the problem is quite complex, especially when the resolution of the identity approximation is added to the mix.⁸⁶ Since the goal of this section is to give an understanding of the method, the final steps are summarized. It might not be obvious, but the Jacobian \mathcal{A} is not symmetric,

see Eq. 2.5.35. The eigenvalues problem can thus be solved to produce the said left-hand side, \mathbf{L} , or right-hand side solutions, \mathbf{R} :

$$\mathbf{L}\mathbf{A} = \mathbf{L}\omega \quad (2.5.39)$$

$$\mathbf{A}\mathbf{R} = \omega\mathbf{R}. \quad (2.5.40)$$

While this is not an issue to get the excitation energies: in principle, \mathbf{L} and \mathbf{R} give the same values; the evaluation of the transition dipole moments, which in turn gives the oscillator strengths, see Eq. 2.3.12, requires both solutions.

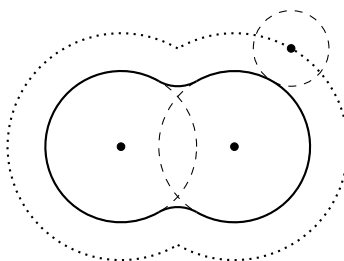
For the excitation energies of states with a determinant of singly-excited character, both CC2 and CCSD are exact to the second-order. As for states with an important doubly-excited character, they cannot be described by CC2 but are correct to the first-order with CCSD.^{67,68,84}

2.6 Solvent Effects

In the isolated phase, there are no intermolecular interactions, thus no extra step to the previously described methods (in 2.1 to 2.5) is needed. All calculations in this work have been performed either in solution or in the solid state. This section presents two models used to implicitly solvate molecules. They both represent the solvent as a polarizable continuum, taking advantage of the "quasi" isotropic nature of liquids.

2.6.1 Polarizable Continuum Model

The polarizable continuum model (PCM)^{87–89} belongs to the class of dielectric continuum models and is featured in Chapters 9, 10, & 11. They implicitly represent the solvent in calculations. By assuming that the only interaction between the solute and solvent is the Coulomb interaction, the solute is enclosed inside a charged cavity. Two surfaces can be defined, the solvent excluded surface (SES) and the solvent accessible surface (SAS), see Scheme 2.4. The charge density at the surface of the cavity, $\sigma(\vec{s})$, depends on the dielectric constant of



Scheme 2.4: Representation of the solvent excluded surface (SES) in full line and the solvent accessible surface (SAS) in dotted line.

the chosen solvent, ϵ :

$$\sigma(\vec{s}) = \frac{\epsilon - 1}{4\pi\epsilon} \left[\frac{\partial V(\vec{s})}{\partial \vec{n}} \right]_{S_{\text{in}}} \quad (2.6.1)$$

$$\text{with } V(\vec{s}) = V_{\text{slt}}(\vec{s}) + V_{\sigma}(\vec{s}) \quad (2.6.2)$$

where V is the total electric potential, V_{slt} is the potential due to the solute charge distribution, V_{σ} is the potential due to the charges at the surface of the cavity, \vec{n} is the normal to the surface (S), and S_{in} refers to the inside surface of the cavity. Using $\sigma(\vec{s})$, V_{σ} can be calculated and inserted in the Hamiltonian, thus effectively including the solvent polarization to the system:

$$\hat{\mathcal{H}} = \hat{T} + \hat{V}_{eN} + \hat{V}_{ee} + \hat{V}_{\sigma}. \quad (2.6.3)$$

Since a charge distribution is very impractical, S is split in small surfaces, ΔS , called tesserae. At the center of each tesserae is a charge which is obtained from integrating $\sigma(\vec{s})$ over ΔS . In the particular case of PCM, the problem is solved iteratively: V and σ depend on each other. This solvation model is the default one in the GAUSSIAN package⁹⁰ and can be combined with a wide range of calculations such as geometry optimization, calculation of NMR chemical shifts, excitation energies, hyperpolarizabilities, at different levels of approximation (HF, DFT, MP2, etc).

2.6.2 Conductor-like Screening Model

The conductor-like screening model (COSMO)⁹¹ is also a dielectric continuum model and is featured in Chapter 9. It was initially developed to correct some of the shortcomings of PCM: i) the added computational cost of having 2 iterative procedures and ii) the lack of analytical gradient (which has been developed since then). The proposed solution is to consider that the Green's function solution for conductors ($\epsilon = \infty$) can also be applied to dielectrics, hence the name of the model. For a spherical cavity, the screening energy (*i.e.* the solvation energy) is given by:

$$\Delta E = -\frac{1}{2} \mathbf{Q} \mathbf{D} \mathbf{Q} \quad (2.6.4)$$

$$\text{with } D_{ij} = \frac{R}{\sqrt{R^4 - 2R^2 r_i r_j + r_i^2 r_j^2}} \quad (2.6.5)$$

where \mathbf{Q} is the vector of N charges Q_i inside the sphere (at position r_i), \mathbf{D} is the Green's function of the sphere (the dielectric operator), and R is the radius of the sphere. When considering the tesserae setup, the screening energy becomes:

$$\Delta E = -\frac{1}{2} \mathbf{Q} \mathbf{B} \mathbf{A}^{-1} \mathbf{B} \mathbf{Q} \quad (2.6.6)$$

where $\mathbf{BA}^{-1}\mathbf{B}$ is the Green's function/dielectric operator with \mathbf{A} describing the self-interactions of the tesserae and \mathbf{B} the interaction between the charges and the tesserae. To account for the actual dielectric constant of a solvent, the screening energy is scaled by:

$$\frac{\epsilon - 1}{\epsilon + 1/2}. \quad (2.6.7)$$

The relative error for strong dielectrics is thus less than $\epsilon/2$ and up to 50 % for weak dielectrics ($\epsilon \approx 1$, which should be negligible since the screening energy is very small to begin with). Although this is a general solution, \mathbf{Q} and \mathbf{B} are obtained from the MOs. This solvation model is the default one in the TURBOMOLE package.⁸⁰

2.7 Generalization to Solids

While in solution, the solvent can be implicitly modeled due to its quasi isotropic nature, it is certainly not the case for solids. The solid state can be divided in two categories of systems which allow for or require different treatments. The first category is the amorphous systems, such as glasses. Since they are characterized by a random distribution of atoms or molecules, they can only be described by embedding methods, which share some similarities with the polarizable continuum methods. The second category of systems is made of crystals, which are characterized by spatial periodicity. This allows to consider the full size of the crystal by exploiting its translational symmetry. Embedding methods can also be used for crystal, which is what is discussed in the next section.

2.7.1 Embedding

Embedding methods are featured in Chapters 6 & 7. The general idea of the embedding model is to limit the quantum chemical calculations to a small part of the total system and to include the rest of it at a lower level of approximation. The simplest model represents the environment, the molecules surrounding the targeted molecule or cluster, as point-charges. Similarly to the solvation models presented in 2.6, the electric potential of the environment is added to the Hamiltonian so that only the Coulombic interactions are considered. Thanks to its simplicity, there are no restrictions on the system such as symmetry. Herein, we discuss the use of an embedding scheme for crystals.

When applied to crystals, a very large amount of point-charges needs to be considered, but the calculation of the Coulomb interactions is slowly and condi-

tionally converging:

$$E = \frac{1}{4\pi\epsilon_0} \frac{1}{2} \sum_{\vec{n}} \sum_{i=1}^N \sum_{j=1}^N \frac{q_i q_j}{|\vec{r}_i - \vec{r}_j + \vec{n} \cdot \mathbf{L}|} \quad (2.7.1)$$

$$\text{with } \vec{n} \cdot \mathbf{L} = n_1 \cdot \vec{a}_1 + n_2 \cdot \vec{a}_2 + n_3 \cdot \vec{a}_3 \quad (2.7.2)$$

where N is the number of charges in the unit cell, q_i is the charge of the i^{th} point-charge at position \vec{r}_i and \vec{n} is the position of the n^{th} unit cell of dimension $\mathbf{L} (= (\vec{a}_1, \vec{a}_2, \vec{a}_3)^T)$, where \vec{a} are the cell vectors. A convenient method to get the potential of a periodic system is the Ewald summation,⁹² which allows for a fast and unconditionally converging summation. The general idea is to split the single slowly-converging summation into two fast-converging ones. The first sum runs over the short interaction distances (E^{short}), in the direct space, while the second one deals with the long interaction distances (E^{long}), in the reciprocal space:

$$E^{\text{tot}} = E^{\text{short}} + E^{\text{long}} - E^{\text{self}} \quad (2.7.3)$$

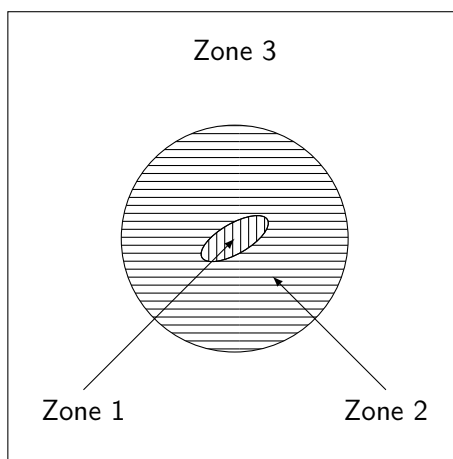
$$\text{with } E^{\text{short}} = \frac{1}{4\pi\epsilon_0} \frac{1}{2} \sum_{\vec{n}} \sum_{i=1}^N \sum_{j=1}^N \frac{q_i q_j}{|\vec{r}_i - \vec{r}_j + \vec{n} \cdot \mathbf{L}|} \text{erfc} \left(\frac{|\vec{r}_i - \vec{r}_j + \vec{n} \cdot \mathbf{L}|}{\sqrt{2}\sigma} \right) \quad (2.7.4)$$

$$E^{\text{long}} = \frac{1}{2V\epsilon_0} \sum_{\vec{k} \neq 0} \sum_{i=1}^N \sum_{j=1}^N \frac{q_i q_j}{k^2} e^{i\vec{k} \cdot (\vec{r}_i - \vec{r}_j)} e^{-\sigma^2 k^2 / 2} \quad (2.7.5)$$

$$E^{\text{self}} = \frac{1}{4\pi\epsilon_0} \frac{1}{\sqrt{2\pi}\sigma} \sum_{i=1}^N q_i^2 \quad (2.7.6)$$

where E^{self} is the self-interaction potential energy, σ is the parameter used to split the space in two (via the erfc function for the short range part and the exp one for the long range part), and \vec{k} is a reciprocal space vector, with k its norm. Unfortunately, this method is rarely available in quantum chemistry codes, which make the Ewald code extremely valuable.^{93,94} Its goal is to generate an array of point-charges that reproduces the actual Ewald potential. Effectively, this allows to replace an infinite number of charges by a finite amount. The total system is defined by the user as a supercell cell based on the unit cell, *e.g.* a $(2 \times 2 \times 2)$ supercell of a unit cell of 10 atoms would contain $2^3 \times 10 = 80$ atoms. Its dimensions are chosen to be cubic-like and large enough to properly surround the targeted system. In addition to defining the unit cell parameters and the point-charges coordinates and charges, the user defines three zones. The first one is simply the system on which a quantum calculation will later be run on; the second zone is composed of the X unchanged point-charges closest to the origin (where X is large enough to properly surround zone 1); and the last and third zone, in which charges will be fitted, is the difference between the total

system and the zones 1 and 2 (see Scheme 2.5). Then, the program computes the Ewald potential at the "atomic" positions of zone 1. Based on those values, a set of equations is solved, where the variables are the charges of zone 3. The program thus fits zone 3 so that zones 2 and 3 reproduce the Ewald potential. The positions, as well as the charges of zones 1 and 2, are not modified. In addition to reproducing the Ewald potential, the Ewald program ensures that the total charge and total dipole moment are null.



Scheme 2.5: Schematic representation of the 3 zones used by the Ewald program.

2.7.2 Periodic Boundary Conditions

Periodic boundary conditions (PBC) calculations are featured in Chapters 3 to 5 & 8. Crystals are characterized by their spatial periodicity. That very simple concept can be introduced into the SCF problem (thus usable by both Hartree-Fock and DFT). There are different approaches allowing periodicity within quantum calculations, *i.e.* PBC calculations. Here, the approach taken by the Crystal program is discussed,^{95–97} in particular the case of the Hartree-Fock approximation. The adaptation to DFT is straightforward. The key difference with molecular calculations is the use of crystalline orbitals (COs), $\chi(\vec{r}, \vec{k})$, instead of molecular orbitals. They are constructed using a linear combination of Bloch functions (BFs), ϕ , which themselves are built from the same kind of GTOs that compose classical MOs, $\{\varphi_\mu\}$.^{96–98}

$$\chi_i(\vec{r}, \vec{k}) = \sum_{\mu} c_{\mu i}(\vec{k}) \phi_{\mu}(\vec{r}, \vec{k}) \quad (2.7.7)$$

$$\phi_{\mu}(\vec{r}, \vec{k}) = \sum_{\vec{g}} \varphi_{\mu}(\vec{r} - \vec{A}_{\mu} - \vec{g}) e^{i\vec{k} \cdot \vec{g}} \quad (2.7.8)$$

where \vec{k} are reciprocal lattice vectors, c are the linear combination coefficients, \vec{g} is the unit cell position with respect to the reference unit cell (also known as the zero cell), the \vec{g} summation runs over all unit cells, \vec{A}_μ is the position of φ_μ within the zero cell. The SCF procedure previously established to obtain the MOs coefficients is still valid although now more complex because it has to be solved for multiple \vec{k} values:

$$\mathbf{F}(\vec{k})\mathbf{C}(\vec{k}) = \mathbf{S}(\vec{k})\mathbf{C}(\vec{k})\mathbf{E}(\vec{k}) \quad (2.7.9)$$

where just like the molecular case, \mathbf{S} is the overlap matrix, \mathbf{C} is the matrix of the c coefficients, \mathbf{E} is the diagonal energy matrix, and \mathbf{F} is the Fock matrix. To illustrate the expansion of \vec{k} -dependent matrices, the latter is expanded, showing its relationship with the cell dependent matrices ($\mathbf{F}^{\vec{g}}$):

$$\mathbf{F}(\vec{k}) = \sum_{\vec{g}} \mathbf{F}^{\vec{g}} e^{i\vec{k} \cdot \vec{g}}. \quad (2.7.10)$$

$\mathbf{F}^{\vec{g}}$ can be split in two parts: the one-electron part, $\mathcal{A}^{\vec{g}}$, and the two-electron one, $\mathcal{B}^{\vec{g}}$:

$$F_{\mu\nu}^{\vec{g}} = \mathcal{A}_{\mu\nu}^{\vec{g}} + \mathcal{B}_{\mu\nu}^{\vec{g}}. \quad (2.7.11)$$

$\mathcal{A}^{\vec{g}}$ contains the kinetic, $\mathcal{T}^{\vec{g}}$, and nuclear attraction terms, $\mathcal{Z}^{\vec{g}}$:

$$\mathcal{A}_{\mu\nu}^{\vec{g}} = \mathcal{T}_{\mu\nu}^{\vec{g}} + \mathcal{Z}_{\mu\nu}^{\vec{g}} \quad (2.7.12)$$

$$\text{with } \mathcal{T}_{\mu\nu}^{\vec{g}} = \langle \varphi_\mu^0 | \hat{T} | \varphi_\nu^{\vec{g}} \rangle \quad (2.7.13)$$

$$\text{and } \mathcal{Z}_{\mu\nu}^{\vec{g}} = \langle \varphi_\mu^0 | \hat{Z} | \varphi_\nu^{\vec{g}} \rangle \quad (2.7.14)$$

where φ_μ^0 is the μ^{th} AO in the zero cell, $\varphi_\nu^{\vec{g}}$ is the ν^{th} AO in the g^{th} cell, and \hat{T} and \hat{Z} are the kinetic and nuclear attraction operators, respectively. Then, the two-electron terms include the Coulomb, $\mathcal{J}^{\vec{g}}$, and exchange, $\mathcal{K}^{\vec{g}}$, terms:

$$\mathcal{B}_{\mu\nu}^{\vec{g}} = \mathcal{J}_{\mu\nu}^{\vec{g}} + \mathcal{K}_{\mu\nu}^{\vec{g}} \quad (2.7.15)$$

$$\text{with } \mathcal{J}_{\mu\nu}^{\vec{g}} = \sum_{\tau,\eta}^K \sum_{\vec{n}} D_{\tau\eta}^{\vec{n}} \sum_{\vec{h}} \left\langle \varphi_\mu^0 \varphi_\nu^{\vec{g}} \left| \frac{1}{r} \right| \varphi_\tau^{\vec{h}} \varphi_\eta^{\vec{h}+\vec{n}} \right\rangle \quad (2.7.16)$$

$$\text{and } \mathcal{K}_{\mu\nu}^{\vec{g}} = -\frac{1}{2} \sum_{\tau,\eta}^K \sum_{\vec{n}} D_{\tau\eta}^{\vec{n}} \sum_{\vec{h}} \left\langle \varphi_\mu^0 \varphi_\tau^{\vec{h}} \left| \frac{1}{r} \right| \varphi_\nu^{\vec{g}} \varphi_\eta^{\vec{h}+\vec{n}} \right\rangle \quad (2.7.17)$$

where the \vec{n} and \vec{h} summations run over all unit cells and \mathbf{D} is the density matrix. The latter is given by:

$$D_{\tau\eta}^{\vec{n}} = 2 \int_{\text{BZ}} d\vec{k} e^{i\vec{k} \cdot \vec{n}} \sum_{\nu}^K c_{\tau\nu}^*(\vec{k}) c_{\eta\nu}(\vec{k}) \theta(\epsilon_F - \epsilon_\nu(\vec{k})) \quad (2.7.18)$$

where the integration is performed over the irreducible Brillouin zone (BZ) (the equivalent of the primitive cell but in the reciprocal space) and θ is a step function ensuring that only the occupied bands (of energy $\epsilon_\nu(\vec{k})$ lower than the Fermi energy ϵ_F) are considered. Because of the infinite nature of the system, both the Coulomb and the nuclear attraction summations go to infinite values (positively and negatively, respectively) but together, they are conditionally convergent. To alleviate this issue, the Mulliken shell net charge, ρ_λ , is introduced which allows to treat together the J and Z terms into one converging summation over the unit cells:^{97–99}

$$J_{\mu\nu}^{\vec{g}} + Z_{\mu\nu}^{\vec{g}} = \sum_{\lambda}^K \sum_{\vec{h}} \int d\vec{r} d\vec{r}' \varphi_{\mu}^{\vec{0}}(\vec{r}) \varphi_{\nu}^{\vec{g}}(\vec{r}) \frac{\rho_{\lambda}(\vec{r}' - \vec{h})}{|\vec{r} - \vec{r}' - \vec{h}|} \quad (2.7.19)$$

$$\text{with } \rho_{\lambda}(\vec{r}' - \vec{h}) = \sum_{\tau \in \lambda}^K \sum_{\eta} \sum_{\vec{n}} D_{\tau\eta}^{\vec{n}} \varphi_{\tau}^{\vec{h}}(\vec{r}') \varphi_{\eta}^{\vec{h}+\vec{n}}(\vec{r}') - Z_{\lambda} \quad (2.7.20)$$

where the shell λ groups multiple AOs belonging to the same atom and Z_{λ} is the fraction of the nuclear charge associated with the shell. Each shell is either composed of the AOs with the same quantum numbers n and l (e.g. the 2p shell contains the 3 2p AOs: 2p_x, 2p_y, and 2p_z) or composed of AOs with the same exponents, i.e. the sp shells. A single s-type GTO is assigned to each shell. Its exponent is set as the smallest exponent of the GTOs in the shell, i.e. the largest AO. This allows for the fast determination of the space in which shells i) directly overlap so that Eq. 2.7.19 is treated exactly (two-electron zone) or ii) do not overlap and the Mulliken shell net charge is evaluated using a multipolar expansion (one-electron zone).

Because of the multiple summations over all unit cells and the integration over the Brillouin zone, PBC calculations require more parameters than for non-periodic calculations. Those are addressed in the methodology part of Chapter 3.

Dispersion energy correction can also be used in the solid state.⁹⁷ While the general equations still hold (Eq. 2.2.19, 2.2.20, and 2.2.21), a summation over the unit cell is added to the dispersion energy (Eq. 2.2.20) and the expression of the damping function is adapted:

$$E_{\text{disp}} = -s_6 \sum_{A < B}^M \sum_{\vec{g}} \frac{C_{AB}^{\vec{g}}}{R_{AB,\vec{g}}^6} f_{\text{dmp}}(R_{AB,\vec{g}}) \quad (2.7.21)$$

$$\text{with } f_{\text{dmp}}(R_{AB,\vec{g}}) = \left[1 + \exp \left(-d \left\{ \frac{R_{AB,\vec{g}}}{R_{\text{vdW}}} - 1 \right\} \right) \right]^{-1} \quad (2.7.22)$$

where $R_{AB,\vec{g}}$ is the distance between atom A of the zero cell and atom B of the \vec{g} cell.

Moving on to the calculation of optical properties ($\chi^{(1)}$ and $\chi^{(2)}$) raises a significant issue: the first-order perturbation operator is not periodic.^{97,100} A solution can be found for an insulator: the perturbation operator in the basis of the BFs, $\hat{\Omega}(\vec{k})$, is given by:

$$\hat{\Omega}(\vec{k}, \omega) = i\vec{F}(\omega) \cdot e^{i\vec{k} \cdot \vec{r}} \nabla_{\vec{k}} e^{-i\vec{k} \cdot \vec{r}} \quad (2.7.23)$$

where periodicity has been introduced. It allows the calculation of the first-order susceptibility:⁹⁷

$$\chi_{pq}^{(1)}(-\omega; \omega) = -\frac{2}{\epsilon_0 V_{\text{cell}} N_k} \sum_{\vec{k}}^{\text{BZ}} \mathcal{P}_{p,q} \left\{ \sum_i^{\text{occ}} \sum_a^{\text{unocc}} \sum_{\mu, \nu}^K c_{i\mu}^*(\vec{k}) \Omega_{\mu\nu}^p(\vec{k}, -\omega) c_{\nu a}(\vec{k}) U_{ai}^{F_q}(\vec{k}, \omega) \right\} \quad (2.7.24)$$

where \mathcal{P} is a permutation operator and $\Omega_{\mu\nu}^p$ are the elements of the perturbation matrix in the p direction. Similarly to the molecular case, the matrix \mathbf{U} is used to parametrize the derivative¹⁰¹ of the LCAO coefficients (Eq. 2.3.18 and 2.3.20). Then, the SHG second-order susceptibility follows:^{102,103}

$$\chi_{pqr}^{(2)}(-2\omega; \omega, \omega) = -\frac{1}{2\epsilon_0 V_{\text{cell}} N_k} \sum_{\vec{k}}^{\text{BZ}} \mathcal{P}_{p,q,r} \left\{ \sum_{i,j}^{\text{occ}} \sum_{a,b}^{\text{unocc}} U_{ai}^{F_p*}(\vec{k}, -2\omega) \left[G_{ab}^{F_q}(\vec{k}, \omega) U_{bi}^{F_r}(\vec{k}, \omega) - U_{aj}^{F_r}(\vec{k}, \omega) G_{ji}^{F_q}(\vec{k}, \omega) + i \frac{\partial U_{ai}^{F_r}(\vec{k}, \omega)}{\partial k_q} \right] \right\}. \quad (2.7.25)$$

Again, the matrix \mathbf{G}^{F_q} is similar to that of the molecular case (Eq. 2.3.21). As for the derivative of \mathbf{U}^{F_r} w.r.t. \vec{k} , it depends on the derivative of the LCAO coefficients w.r.t. \vec{k} :

$$\frac{\partial c_{\mu i}(\vec{k})}{\partial k_p} = c_{\mu i}^{k_p}(\vec{k}) = \sum_j^N c_{\mu j}(\vec{k}) Q_{ji}^{k_p}(\vec{k}). \quad (2.7.26)$$

The off-diagonal terms of \mathbf{Q}^{k_p} depend on the derivatives of the Fock matrix and of the overlap one w.r.t. to \vec{k} : \mathbf{F}^{k_p} and \mathbf{S}^{k_p} , respectively:

$$\text{with } Q_{ij}^{k_p}(\vec{k}) = \sum_{\mu, \nu}^K \frac{c_{i\mu}^*(\vec{k}) F_{\mu\nu}^{k_p}(\vec{k}) c_{\nu j}(\vec{k}) - c_{i\mu}^*(\vec{k}) S_{\mu\nu}^{k_p}(\vec{k}) c_{\nu j}(\vec{k}) \epsilon_j(\vec{k})}{\epsilon_j(\vec{k}) - \epsilon_i(\vec{k})}. \quad (2.7.27)$$

Bibliography

- (1) Born, M.; Oppenheimer, R. Zur Quantentheorie der Molekeln. *Ann. Phys.* **1927**, *389*, 457–484, DOI: 10.1002/andp.19273892002.
- (2) Schrödinger, E. Quantisierung als Eigenwertproblem. *Ann. Phys.* **1926**, *384*, 361–376, DOI: 10.1002/andp.19263840404.
- (3) Pauli, W. Über den Zusammenhang des Abschlusses der Elektronengruppen im Atom mit der Komplexstruktur der Spektren. *Zeitschrift für Phys.* **1925**, *31*, 765–783, DOI: 10.1007/BF02980631.
- (4) Slater, J. C. The Theory of Complex Spectra. *Phys. Rev.* **1929**, *34*, 1293–1322, DOI: 10.1103/PhysRev.34.1293.
- (5) Szabo, A.; Ostlund, N. S., *Modern Quantum Chemistry: Introduction to Advanced Electronic Structure Theory*; Dover Publications, Inc.: Mineola, New York, 1996.
- (6) Ritz, W. Über eine neue Methode zur Lösung gewisser Variationsprobleme der mathematischen Physik. *J. für die Reine und Angew. Math.* **1909**, *1909*, 1–61, DOI: 10.1515/crll.1909.135.1.
- (7) Hartree, D. R. The Wave Mechanics of an Atom with a Non-Coulomb Central Field Part I Theory and Methods. *Math. Proc. Cambridge Philos. Soc.* **1928**, *24*, 89–110, DOI: 10.1017/S0305004100011919.
- (8) Fock, V. "Selfconsistent field" mit Austausch für Natrium. *Zeitschrift für Phys.* **1930**, *62*, 795–805, DOI: 10.1007/BF01330439.
- (9) Fock, V. Näherungsmethode zur Lösung des quantenmechanischen Mehrkörperproblems. *Zeitschrift für Phys.* **1930**, *61*, 126–148, DOI: 10.1007/BF01340294.
- (10) Lennard-Jones, J. E. The Determination of Molecular Orbitals. *Proc. R. Soc. London. Ser. A. Math. Phys. Sci.* **1949**, *198*, 1–13, DOI: 10.1098/rspa.1949.0083.
- (11) Löwdin, P.-O. In *Adv. Chem. Phys.* Prigogine, I., Ed.; John Wiley & Sons, Inc.: 1958; Vol. 2, pp 207–322, DOI: 10.1002/9780470143483.ch7.
- (12) Binkley, J. S.; Pople, J. A. Self-Consistent Molecular Orbital Methods. XIX. Split-Valence Gaussian-Type Basis Sets for Beryllium. *J. Chem. Phys.* **1977**, *66*, 879–880, DOI: 10.1063/1.433929.
- (13) Binkley, J. S.; Pople, J. A.; Hehre, W. J. Self-Consistent Molecular Orbital Methods. 21. Small Split-Valence Basis Sets for First-Row Elements. *J. Am. Chem. Soc.* **1980**, *102*, 939–947, DOI: 10.1021/ja00523a008.

- (14) Blaudeau, J.-P.; McGrath, M. P.; Curtiss, L. A.; Radom, L. Extension of Gaussian-2 (G2) Theory to Molecules Containing Third-Row Atoms K and Ca. *J. Chem. Phys.* **1997**, *107*, 5016–5021, DOI: 10.1063/1.474865.
- (15) Dill, J. D.; Pople, J. A. Self-Consistent Molecular Orbital Methods. XV. Extended Gaussian-Type Basis Sets for Lithium, Beryllium, and Boron. *J. Chem. Phys.* **1975**, *62*, 2921–2923, DOI: 10.1063/1.430801.
- (16) Francl, M. M.; Pietro, W. J.; Hehre, W. J.; Binkley, J. S.; Gordon, M. S.; DeFrees, D. J.; Pople, J. A. Self-Consistent Molecular Orbital Methods. XXIII. A Polarization-Type Basis Set for Second-Row Elements. *J. Chem. Phys.* **1982**, *77*, 3654–3665, DOI: 10.1063/1.444267.
- (17) Gordon, M. S.; Binkley, J. S.; Pople, J. A.; Pietro, W. J.; Hehre, W. J. Self-Consistent Molecular-Orbital Methods. 22. Small Split-Valence Basis Sets for Second-Row Elements. *J. Am. Chem. Soc.* **1982**, *104*, 2797–2803, DOI: 10.1021/ja00374a017.
- (18) Rassolov, V. A.; Pople, J. A.; Ratner, M. A.; Windus, T. L. 6-31G* Basis Set for Atoms K Through Zn. *J. Chem. Phys.* **1998**, *109*, 1223–1229, DOI: 10.1063/1.476673.
- (19) Rassolov, V. A.; Ratner, M. A.; Pople, J. A.; Redfern, P. C.; Curtiss, L. A. 6-31G* Basis Set for Third-Row Atoms. *J. Comput. Chem.* **2001**, *22*, 976–984, DOI: 10.1002/jcc.1058.abs.
- (20) Feller, D. The Role of Databases in Support of Computational Chemistry Calculations. *J. Comput. Chem.* **1996**, *17*, 1571–1586.
- (21) Schuchardt, K. L.; Didier, B. T.; Elsethagen, T.; Sun, L.; Gurumoorthi, V.; Chase, J.; Li, J.; Windus, T. L. Basis Set Exchange: A Community Database for Computational Sciences. *J. Chem. Inf. Model.* **2007**, *47*, 1045–1052.
- (22) Pritchard, B. P.; Altarawy, D.; Didier, B.; Gibson, T. D.; Windus, T. L. New Basis Set Exchange: An Open, Up-to-Date Resource for the Molecular Sciences Community. *J. Chem. Inf. Model.* **2019**, *59*, 4814–4820, DOI: 10.1021/acs.jcim.9b00725.
- (23) Schäfer, A.; Horn, H.; Ahlrichs, R. Fully Optimized Contracted Gaussian Basis Sets for Atoms Li to Kr. *J. Chem. Phys.* **1992**, *97*, 2571–2577, DOI: 10.1063/1.463096.
- (24) Weigend, F.; Häser, M.; Patzelt, H.; Ahlrichs, R. RI-MP2: Optimized Auxiliary Basis Sets and Demonstration of Efficiency. *Chem. Phys. Lett.* **1998**, *294*, 143–152, DOI: 10.1016/S0009-2614(98)00862-8.
- (25) Weigend, F.; Ahlrichs, R. Balanced Basis Sets of Split Valence, Triple Zeta Valence and Quadruple Zeta Valence Quality for H to Rn: Design and Assessment of Accuracy. *Phys. Chem. Chem. Phys.* **2005**, *7*, 3297, DOI: 10.1039/b508541a.

- (26) Rappoport, D.; Furche, F. Property-Optimized Gaussian Basis Sets for Molecular Response Calculations. *J. Chem. Phys.* **2010**, *133*, 134105, DOI: 10.1063/1.3484283.
- (27) Wadt, W. R.; Hay, P. J. Ab Initio Effective Core Potentials for Molecular Calculations. Potentials for Main Group Elements Na to Bi. *J. Chem. Phys.* **1985**, *82*, 284–298, DOI: 10.1063/1.448800.
- (28) Hohenberg, P.; Kohn, W. Inhomogeneous Electron Gas. *Phys. Rev.* **1964**, *136*, 864, DOI: 10.1103/PhysRev.136.B864.
- (29) Parr, R. G.; Yang, W., *Density-Functional Theory of Atoms and Molecules*; Oxford University Press: New York, 1989.
- (30) Tsuneda, T., *Density Functional Theory in Quantum Chemistry*; Springer Japan: Tokyo, 2014, DOI: 10.1007/978-4-431-54825-6.
- (31) Kohn, W.; Sham, L. J. Self-Consistent Equations Including Exchange and Correlation Effects. *Phys. Rev.* **1965**, *140*, 1133, DOI: 10.1103/PhysRev.140.A1133.
- (32) Perdew, J. P.; Burke, K.; Ernzerhof, M. Generalized Gradient Approximation Made Simple. *Phys. Rev. Lett.* **1996**, *77*, 3865–3868.
- (33) Perdew, J. P.; Ruzsinszky, A.; Csonka, G. I.; Vydrov, O. A.; Scuseria, G. E.; Constantin, L. A.; Zhou, X.; Burke, K. Restoring the Density-Gradient Expansion for Exchange in Solids and Surfaces. *Phys. Rev. Lett.* **2008**, *100*, 136406.
- (34) Tao, J.; Perdew, J. P.; Staroverov, V. N.; Scuseria, G. E. Climbing the Density Functional Ladder: Nonempirical Meta-Generalized Gradient Approximation Designed for Molecules and Solids. *Phys. Rev. Lett.* **2003**, *91*, 146401, DOI: 10.1103/PhysRevLett.91.146401.
- (35) Krukau, A. V.; Vydrov, O. A.; Izmaylov, A. F.; Scuseria, G. E. Influence of the Exchange Screening Parameter on the Performance of Screened Hybrid Functionals. *J. Chem. Phys.* **2006**, *125*, 224106.
- (36) Henderson, T. M.; Izmaylov, A. F.; Scuseria, G. E.; Savin, A. The Importance of Middle-Range Hartree-Fock-Type Exchange for Hybrid Density Functionals. *J. Chem. Phys.* **2007**, *127*, 221103.
- (37) Vydrov, O. A.; Scuseria, G. E. Assessment of a Long-Range Corrected Hybrid Functional. *J. Chem. Phys.* **2006**, *125*, DOI: 10.1063/1.2409292.
- (38) Zhao, Y.; Lynch, B. J.; Truhlar, D. G. Doubly Hybrid Meta DFT: New Multi-Coefficient Correlation and Density Functional Methods for Thermochemistry and Thermochemical Kinetics. *J. Phys. Chem. A* **2004**, *108*, 4786–4791, DOI: 10.1021/jp049253v.

- (39) Grimme, S. Semiempirical hybrid density functional with perturbative second-order correlation. *J. Chem. Phys.* **2006**, *124*, 034108, DOI: 10.1063/1.2148954.
- (40) Grimme, S. Accurate Description of van der Waals Complexes by Density Functional Theory Including Empirical Corrections. *J. Comput. Chem.* **2004**, *25*, 1463–1473, DOI: 10.1002/jcc.20078.
- (41) Grimme, S. Semiempirical GGA-type Density Functional Constructed with a Long-Range Dispersion Correction. *J. Comput. Chem.* **2006**, *27*, 1787–1799, DOI: 10.1002/jcc.20495.
- (42) Peverati, R.; Truhlar, D. G. Quest for a Universal Density Functional: The Accuracy of Density Functionals Across a Broad Spectrum of Databases in Chemistry and Physics. *Philos. Trans. R. Soc. A Math. Phys. Eng. Sci.* **2014**, *372*, 20120476, DOI: 10.1098/rsta.2012.0476.
- (43) Stephens, P. J.; Devlin, F. J.; Chabalowski, C. F.; Frisch, M. J. Ab Initio Calculation of Vibrational Absorption and Circular Dichroism Spectra using Density Functional Force Fields. *J. Phys. Chem.* **1994**, *98*, 11623–11627.
- (44) Adamo, C.; Barone, V. Toward Chemical Accuracy in the Computation of NMR Shieldings: the PBE0 Model. *Chem. Phys. Lett.* **1998**, *298*, 113–119.
- (45) Schimka, L.; Harl, J.; Kresse, G. Improved Hybrid Functional for Solids: The HSEsol Functional. *J. Chem. Phys.* **2011**, *134*, 024116.
- (46) Chai, J.-D.; Head-Gordon, M. Systematic Optimization of Long-Range Corrected Hybrid Density Functionals. *J. Chem. Phys.* **2008**, *128*, 084106, DOI: 10.1063/1.2834918.
- (47) Zhao, Y.; Truhlar, D. G. The M06 Suite of Density Functionals for Main Group Thermochemistry, Thermochemical Kinetics, Noncovalent Interactions, Excited States, and Transition Elements: Two New Functionals and Systematic Testing of Four M06-Class Functionals and 12 Other Function. *Theor. Chem. Acc.* **2008**, *120*, 215, DOI: 10.1007/s00214-007-0310-x.
- (48) Ullrich, C. A., *Time-Dependent Density-Functional Theory: Concepts and Applications*; Oxford University Press: 2011.
- (49) Runge, E.; Gross, E. K. Density-Functional Theory for Time-Dependent Systems. *Phys. Rev. Lett.* **1984**, *52*, 997–1000, DOI: 10.1103/PhysRevLett.52.997.
- (50) Van Leeuwen, R. Mapping from Densities to Potentials in Time-Dependent Density-Functional Theory. *Phys. Rev. Lett.* **1999**, *82*, 3863–3866, DOI: 10.1103/PhysRevLett.82.3863.

- (51) Gross, E.; Kohn, W. In *Adv. Quantum Chem.* 1990; Vol. 21, pp 255–291, DOI: 10.1016/S0065–3276(08)60600–0.
- (52) Ullrich, C. A.; Gossmann, U. J.; Gross, E. K. U. Time-Dependent Optimized Effective Potential. *Phys. Rev. Lett.* **1995**, *74*, 872–875, DOI: 10.1103/PhysRevLett.74.872.
- (53) Casida, M. E. In *Recent Advances in Density Functional Methods. Part I*, Chong, D. P., Ed.; World Scientific Publishing Co. Pte. Ltd.: Singapore, 1995; Chapter 5, pp 155–192, DOI: 10.1142/9789812830586_0005.
- (54) Bauernschmitt, R.; Ahlrichs, R. Treatment of Electronic Excitations within the Adiabatic Approximation of Time Dependent Density Functional Theory. *Chem. Phys. Lett.* **1996**, *256*, 454–464, DOI: 10.1016/0009–2614(96)00440–X.
- (55) Nee, T.-S.; Parr, R. G.; Bartlett, R. J. Direct Determination of the Rotational Barrier in Ethane Using Perturbation Theory. *J. Chem. Phys.* **1976**, *64*, 2216–2225, DOI: 10.1063/1.432448.
- (56) Van Gisbergen, S. J. A.; Snijders, J. G.; Baerends, E. J. Calculating Frequency-Dependent Hyperpolarizabilities using Time-Dependent Density Functional Theory. *J. Chem. Phys.* **1998**, *109*, 10644–10656, DOI: 10.1063/1.477762.
- (57) Gauss, J. Effects of Electron Correlation in the Calculation of Nuclear Magnetic Resonance Chemical Shifts. *J. Chem. Phys.* **1993**, *99*, 3629–3643, DOI: 10.1063/1.466161.
- (58) Cheeseman, J. R.; Trucks, G. W.; Keith, T. A.; Frisch, M. J. A Comparison of Models for Calculating Nuclear Magnetic Resonance Shielding Tensors. *J. Chem. Phys.* **1996**, *104*, 5497–5509, DOI: 10.1063/1.471789.
- (59) London, F. Théorie Quantique des Courants Interatomiques dans les Combinaisons Aromatiques. *J. Phys. le Radium* **1937**, *8*, 397–409, DOI: 10.1051/jphysrad:01937008010039700.
- (60) Ditchfield, R. Self-Consistent Perturbation Theory of Diamagnetism. *Mol. Phys.* **1974**, *27*, 789–807, DOI: 10.1080/00268977400100711.
- (61) Møller, C.; Plesset, M. S. Note on an Approximation Treatment for Many-Electron Systems. *Phys. Rev.* **1934**, *46*, 618–622, DOI: 10.1103/PhysRev.46.618.
- (62) Strutt, J. W., *The Theory of Sound*; McMillan & Co: Cambridge, 1877, DOI: 10.1017/CB09781139058087.
- (63) Schrödinger, E. Quantisierung als Eigenwertproblem. *Ann. Phys.* **1926**, *385*, 437–490, DOI: 10.1002/andp.19263851302.

- (64) Cremer, D. Møller-Plesset Perturbation Theory: from Small Molecule Methods to Methods for Thousands of Atoms. *Wiley Interdiscip. Rev. Comput. Mol. Sci.* **2011**, *1*, 509–530, DOI: 10.1002/wcms.58.
- (65) Coester, F.; Kümmel, H. Short-Range Correlations in Nuclear Wave Functions. *Nucl. Phys.* **1960**, *17*, 477–485, DOI: 10.1016/0029-5582(60)90140-1.
- (66) Crawford, T. D.; Schaefer, H. F. In *Reviews in Computational Chemistry, Volume 14*, Lipkowitz, K. B., Boyd, D. B., Eds., 2007, pp 33–136, DOI: 10.1002/9780470125915.ch2.
- (67) Christiansen, O.; Koch, H.; Jørgensen, P. The Second-Order Approximate Coupled Cluster Singles and Doubles Model CC2. *Chem. Phys. Lett.* **1995**, *243*, 409–418, DOI: 10.1016/0009-2614(95)00841-Q.
- (68) Christiansen, O.; Koch, H.; Jørgensen, P. Response Functions in the CC3 Iterative Triple Excitation Model. *J. Chem. Phys.* **1995**, *103*, 7429–7441, DOI: 10.1063/1.470315.
- (69) Raghavachari, K.; Trucks, G. W.; Pople, J. A.; Head-Gordon, M. A Fifth-Order Perturbation Comparison of Electron Correlation Theories. *Chem. Phys. Lett.* **1989**, *157*, 479–483, DOI: 10.1016/S0009-2614(89)87395-6.
- (70) Vahtras, O.; Almlöf, J.; Feyereisen, M. Integral Approximations for LCAO-SCF Calculations. *Chem. Phys. Lett.* **1993**, *213*, 514–518, DOI: 10.1016/0009-2614(93)89151-7.
- (71) Feyereisen, M.; Fitzgerald, G.; Komornicki, A. Use of Approximate Integrals in Ab Initio Theory. An Application in MP2 Energy Calculations. *Chem. Phys. Lett.* **1993**, *208*, 359–363, DOI: 10.1016/0009-2614(93)87156-W.
- (72) Hellweg, A.; Hättig, C.; Höfener, S.; Klopper, W. Optimized Accurate Auxiliary Basis Sets for RI-MP2 and RI-CC2 Calculations for the Atoms Rb to Rn. *Theor. Chem. Acc.* **2007**, *117*, 587–597, DOI: 10.1007/s00214-007-0250-5.
- (73) Hellweg, A.; Rappoport, D. Development of New Auxiliary Basis Functions of the Karlsruhe Segmented Contracted Basis Sets Including Diffuse Basis Functions (def2-SVPD, def2-TZVPPD, and def2-QVPPD) for RI-MP2 and RI-CC Calculations. *Phys. Chem. Chem. Phys.* **2015**, *17*, 1010–1017, DOI: 10.1039/C4CP04286G.
- (74) Meyer, W. Ionization Energies of Water from PNO-CI Calculations. *Int. J. Quantum Chem.* **1971**, *5*, 341–348, DOI: 10.1002/qua.560050839.
- (75) Meyer, W. PNO-CI Studies of Electron Correlation Effects. I. Configuration Expansion by Means of Nonorthogonal Orbitals, and Application to the Ground State and Ionized States of Methane. *J. Chem. Phys.* **1973**, *58*, 1017–1035, DOI: 10.1063/1.1679283.

- (76) Schmitz, G.; Helmich, B.; Hättig, C. A $O(N^3)$ Scaling PNO-MP2 Method using a Hybrid OSV-PNO Approach with an Iterative Direct Generation of OSVs. *Mol. Phys.* **2013**, *111*, 2463–2476, DOI: 10.1080/00268976.2013.794314.
- (77) Schmitz, G.; Hättig, C.; Tew, D. P. Explicitly Correlated PNO-MP2 and PNO-CCSD and their Application to the S66 Set and Large Molecular Systems. *Phys. Chem. Chem. Phys.* **2014**, *16*, 22167–22178, DOI: 10.1039/c4cp03502j.
- (78) Lennard-Jones, J. E. The Molecular Orbital Theory of Chemical Valency. II. Equivalent Orbitals in Molecules of Known Symmetry. *Proc. R. Soc. London. Ser. A. Math. Phys. Sci.* **1949**, *198*, 14–26, DOI: 10.1098/rspa.1949.0084.
- (79) Lennard-Jones, J. E.; Pople, J. A. The Molecular Orbital Theory of Chemical Valency. IV. The Significance of Equivalent Orbitals. *Proc. R. Soc. London. Ser. A. Math. Phys. Sci.* **1950**, *202*, 166–180, DOI: 10.1098/rspa.1950.0092.
- (80) TURBOMOLE V7.4 2019, a development of University of Karlsruhe and Forschungszentrum Karlsruhe GmbH, 1989-2007 TURBOMOLE GmbH, since 2007; available from <http://www.turbomole.org>.
- (81) Koch, H.; Jørgensen, P. Coupled Cluster Response Functions. *J. Chem. Phys.* **1990**, *93*, 3333–3344, DOI: 10.1063/1.458814.
- (82) Koch, H.; Kobayashi, R.; Sanchez de Merás, A.; Jørgensen, P. Calculation of Size-Intensive Transition Moments from the Coupled Cluster Singles and Doubles Linear Response Function. *J. Chem. Phys.* **1994**, *100*, 4393–4400, DOI: 10.1063/1.466321.
- (83) Pedersen, T. B.; Koch, H. Coupled Cluster Response Functions Revisited. *J. Chem. Phys.* **1997**, *106*, 8059–8072, DOI: 10.1063/1.473814.
- (84) Sneskov, K.; Christiansen, O. Excited State Coupled Cluster Methods. *Wiley Interdiscip. Rev. Comput. Mol. Sci.* **2012**, *2*, 566–584, DOI: 10.1002/wcms.99.
- (85) Hättig, C.; Köhn, A. Transition Moments and Excited-State First-Order Properties in the Coupled-Cluster Model CC2 using the Resolution-of-the-Identity Approximation. *J. Chem. Phys.* **2002**, *117*, 6939–6951, DOI: 10.1063/1.1506918.
- (86) Hättig, C.; Weigend, F. CC2 Excitation Energy Calculations on Large Molecules using the Resolution of the Identity Approximation. *J. Chem. Phys.* **2000**, *113*, 5154, DOI: 10.1063/1.1290013.
- (87) Miertuš, S.; Scrocco, E.; Tomasi, J. Electrostatic Interaction of a Solute with a Continuum. A Direct Utilization of Ab Initio Molecular Potentials for the Prevision of Solvent Effects. *Chem. Phys.* **1981**, *55*, 117, DOI: 10.1016/0301-0104(81)85090-2.

- (88) Cancès, E.; Mennucci, B.; Tomasi, J. A New Integral Equation Formalism for the Polarizable Continuum Model: Theoretical Background and Applications to Isotropic and Anisotropic Dielectrics. *J. Chem. Phys.* **1997**, *107*, 3032, DOI: 10.1063/1.474659.
- (89) Tomasi, J.; Mennucci, B.; Cammi, R. Quantum Mechanical Continuum Solvation Models. *Chem. Rev.* **2005**, *105*, 2999–3094, DOI: 10.1021/cr9904009.
- (90) Frisch, M. J. et al. Gaussian~16 Revision B.01, Gaussian Inc. Wallingford CT, 2016.
- (91) Klamt, A.; Schüürmann, G. COSMO: A New Approach to Dielectric Screening in Solvents with Explicit Expressions for the Screening Energy and its Gradient. *J. Chem. Soc. Perkin Trans. 2* **1993**, 799–805, DOI: 10.1039/P29930000799.
- (92) Ewald, P. P. Die Berechnung optischer und elektrostatischer Gitterpotentiale. *Ann. Phys.* **1921**, *369*, 253–287, DOI: 10.1002/andp.19213690304.
- (93) Derenzo, S. E.; Klintenberg, M. K.; Weber, M. J. Determining Point Charge Arrays that Produce Accurate Ionic Crystal Fields for Atomic Cluster Calculations. *J. Chem. Phys.* **2000**, *112*, 2074–2081, DOI: 10.1063/1.480776.
- (94) Klintenberg, M.; Derenzo, S.; Weber, M. Accurate Crystal Fields for Embedded Cluster Calculations. *Comput. Phys. Commun.* **2000**, *131*, 120–128, DOI: 10.1016/S0010-4655(00)00071-0.
- (95) Dovesi, R.; Orlando, R.; Erba, A.; Zicovich-Wilson, C. M.; Civalleri, B.; Casassa, S.; Maschio, L.; Ferrabone, M.; De La Pierre, M.; D’Arco, P.; Noël, Y.; Causà, M.; Rérat, M.; Kirtman, B. CRYSTAL14: A Program For the Ab Initio Investigation of Crystalline Solids. *Int. J. Quantum Chem.* **2014**, *114*, 1287–1317, DOI: 10.1002/qua.24658.
- (96) Dovesi, R.; Erba, A.; Orlando, R.; Zicovich-Wilson, C. M.; Civalleri, B.; Maschio, L.; Rérat, M.; Casassa, S.; Baima, J.; Salustro, S.; Kirtman, B. Quantum-Mechanical Condensed Matter Simulations with CRYSTAL. *Wiley Interdiscip. Rev. Comput. Mol. Sci.* **2018**, *8*, e1360, DOI: 10.1002/wcms.1360.
- (97) Dovesi, R. et al., *CRYSTAL17 User’s Manual*; University of Torino: Torino, 2017.
- (98) Saunders, V.; Freyria-Fava, C.; Dovesi, R.; Salasco, L.; Roetti, C. On the Electrostatic Potential in Crystalline Systems where the Charge Density is Expanded in Gaussian Functions. *Mol. Phys.* **1992**, *77*, 629–665, DOI: 10.1080/00268979200102671.

- (99) Dovesi, R.; Pisani, C.; Roetti, C.; Saunders, V. R. Treatment of Coulomb Interactions in Hartree-Fock Calculations of Periodic Systems. *Phys. Rev. B* **1983**, *28*, 5781–5792, DOI: 10.1103/PhysRevB.28.5781.
- (100) Ferrero, M.; Rérat, M.; Orlando, R.; Dovesi, R.; Bush, I. J. Coupled Perturbed Kohn-Sham Calculation of Static Polarizabilities of Periodic Compounds. *J. Phys. Conf. Ser.* **2008**, *117*, 1–8, DOI: 10.1088/1742-6596/117/1/012016.
- (101) Bernasconi, L.; Tomić, S.; Ferrero, M.; Rérat, M.; Orlando, R.; Dovesi, R.; Harrison, N. M. First-Principles Optical Response of Semiconductors and Oxide Materials. *Phys. Rev. B - Condens. Matter Mater. Phys.* **2011**, *83*, 1–7, DOI: 10.1103/PhysRevB.83.195325.
- (102) Maschio, L.; Rérat, M.; Kirtman, B.; Dovesi, R. Calculation of the Dynamic First Electronic Hyperpolarizability $\beta(-\omega_\sigma; \omega_1, \omega_2)$ of Periodic Systems. Theory, Validation, and Application to Multi-Layer MoS₂. *J. Chem. Phys.* **2015**, *143*, 244102, DOI: 10.1063/1.4937770.
- (103) Rérat, M.; Maschio, L.; Kirtman, B.; Civalleri, B.; Dovesi, R. Computation of Second Harmonic Generation for Crystalline Urea and KDP. An ab Initio Approach through the Coupled Perturbed Hartree-Fock/Kohn-Sham Scheme. *J. Chem. Theory Comput.* **2016**, *12*, 107–113, DOI: 10.1021/acs.jctc.5b00791.

GEOMETRY OPTIMIZATION OF CRYSTALLINE MOLECULAR SWITCHES

The following two chapters deal with the optimization of the geometry of crystalline anils. Although there are a lot of publications of the subject of crystalline molecular switches, none discussed the choice of the exchange-correlation functional and of the basis set. The common solution was to use B3LYP with dispersion energy correction and some Pople basis set, within periodic boundary conditions, or not.

ASSESSING DENSITY FUNCTIONAL THEORY APPROACHES FOR PREDICTING THE STRUCTURE AND RELATIVE ENERGY OF SALICYLIDENEANILINE MOLECULAR SWITCHES IN THE SOLID STATE

JOURNAL OF PHYSICAL CHEMISTRY C, 2017, 121, 6898–6908

Jean Quertinmont[†], Andrea Carletta[†], Nikolay A. Tumanov[†], Tom Leyssens[‡],
Johan Wouters[†], & Benoît Champagne[†]

[†] *Unité de Chimie Physique Théorique et Structurale, Chemistry Department, University of Namur, 61 rue de Bruxelles, B-5000 Namur, Belgium*

[‡] *Institute of Condensed Matter and Nanosciences, Université Catholique de Louvain, 1 Place Louis Pasteur, B-1348 Louvain-La-Neuve, Belgium*

All calculations, their analysis, and the writing of the first draft were performed by J.Q.

Abstract

The geometrical structures of salicylideneaniline (anil) molecular switches in the solid state have been determined using periodic structure calculations and a variety of DFT XC functionals, of which several have been tuned for the solid state. The first target was on predicting the unit cell and intramolecular geometrical parameters for three anil derivatives, i.e. the PYV3 and HC crystals, where the enol (E) form is dominant in the crystalline state at low temperature (~ 100 K) and the POC crystal, which is mostly composed of the keto (K) form. The best performance for the unit cell parameters, in comparison with single crystal XRD data, is achieved with XC functionals developed for the solid state (PBEsol and PBEsol0) as well as with ω B97X. On the other hand, the differences between the functionals are much smaller when considering the bond lengths and the valence angles so that the deviations with respect to XRD data in the bond length alternations of the key $\text{O}-\text{C}=\text{C}-\text{C}=\text{N}-\text{C}$ (or $\text{O}=\text{C}-\text{C}=\text{C}-\text{N}-\text{C}$) π -conjugated segment are smaller than 0.02 \AA for PBEsol0 and ω B97X. Similar trends are observed for the two polymorphic co-crystals of PYV3 with fumaric or succinic acid. The second target was the characterization of the variations of energy and structural parameters when switching between the enol and keto forms. All XC functionals predict that PYV3 present a larger ΔE_{KE} value than HC and, as expected, both are larger than for POC. Still, only hybrid functionals correctly predict which form is the most stable in the crystalline state. Then, the bond length changes in the $\text{O}-\text{C}=\text{C}-\text{C}=\text{N}-\text{C}$ (or $\text{O}=\text{C}-\text{C}=\text{C}-\text{N}-\text{C}$) π -conjugated segment that occur upon enol to keto transformation are similarly predicted by all functionals and are consistent with the reversal of the single/double bonds pattern.

3.1 Introduction

Molecular switches, such as photochromic and thermochromic compounds, are widely studied because of their potential applications in sensing devices.^{1–8} To understand and optimize these dynamical properties, over the last decades, a broad variety of multiaddressable and multifunctional compounds have been designed and/or synthesized figuring out optimized linear as well as non-linear optical properties and devices.^{9–18} Still, so far the focus (design and characterizations) was mainly on the liquid state, both in experimental and theoretical studies. However, in order to move towards real applications, the liquid phase is replaced by the more practical solid phase. This can be achieved either by grafting the switch on a surface^{19–22} or by crystallization of the switch.^{10,12,15,23–31}

When studying molecular switches, the two first key information are the relative energies of their two (or multiple) forms and their structural differences. In the case of crystals not only the individual molecular geometries (intramolecular parameters) but also the crystal packing, which defines the spacing between the molecules and thus their intermolecular interactions, determine their switching properties. The challenge for theoreticians is therefore to find simulation methods that are sufficiently accurate for relative energy and structure determination purpose within reasonable computational costs. There are two categories of methods³² to describe the (organic) solid state, (i) the crystalline orbital methods for periodic systems^{33–36} and (ii) localized orbital/fragment embedding field approaches for both periodic and non-periodic systems.^{37–39} Here, the focus is on the first category of methods. Owing to its reliability to describe the structure of gases, liquids, and inorganic crystals, density functional theory (DFT) is a good candidate for optimizing the structure of molecular crystals. Still, its performance depends on the content of the exchange-correlation (XC) functional. Moreover, as shown recently by Ruggiero and coworkers,⁴⁰ the choice of a XC functional for the study of molecular crystals is still an open question since a balanced treatment is needed to describe the intra- and intermolecular interactions. In their work on three ionic crystals of pyridine carboxylic acid containing a variety of interactions such as hydrogen bonding, ion-ion, π -stacking, and London dispersion forces, they identify ω B97X as a good candidate since it contains both short- and long-range exact exchange, enabling the description of the whole range of interactions. The present contribution extends their investigation and aims at assessing and then selecting reliable XC functionals for describing the structure of three molecular crystals composed of salicylideneaniline (anil) switches (Figure 3.1). This is achieved by comparison with single-crystal X-ray diffraction (XRD) data. Anils commute between an enol (E) and a keto (K) form (Figure 3.1), of which the relative stability depends on the substituents as well as on the surrounding medium. Three anils have been selected due to their thermochromic and/or photochromic properties in the solid state:^{23,29} anil (a), (E)-2-methoxy-6-(pyridine-3-yliminomethyl)phenol (PYV3) displays thermochromism whereas

it becomes photochromic when co-crystallized with fumaric or succinic acids²⁹ ; anils (b), N-(5-chloro-2-hydroxybenzylidene)-aniline (HC), and (c), N-(5-chloro-2-hydroxybenzylidene)-hydroxyaniline (POC). The choice of these two last crystals originates from the fact that their dominant forms are different (E for (b) while K for (c)) whereas their structure only differs by a hydroxyl group. Besides addressing anils that present different (E or K) ground state equilibrium structures, this paper describes the structure of co-crystals made of PYV3 with acid co-formers. Among the XC functionals, this paper concentrates on functionals developed for the solid state⁴¹ and makes comparison to more traditional functionals. The paper is organized as follows: next Section summarizes the theoretical and computational approaches, Section 3.3 presents and analyzes the results before conclusions are drawn in Section 3.4.

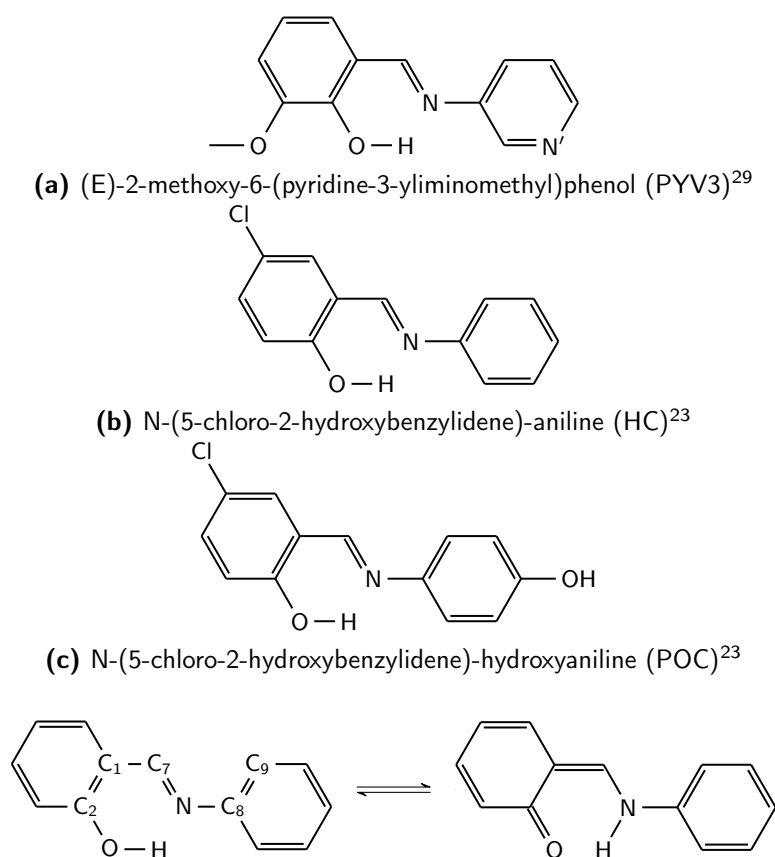


Figure 3.1: Structures, names, and acronyms of anils (a)-(c) in their enol form as well as the general keto-enol tautomeric equilibrium. Key bonds and atoms for characterizing the geometries are highlighted on the general enol structure.

3.2 Methods and Computations

All computations were performed with the CRYSTAL14 program.⁴² Among the available XC functionals, B3LYP,⁴³ PBE,⁴⁴ HSE06,⁴⁵ HISS,⁴⁶ PBE0,⁴⁷ PBEsol,⁴¹ HSEsol,⁴⁸ and PBEsol0 functionals were selected. Taking into account the conclusions of Ref [40], ω B97X was also considered. B3LYP, build from Becke's B88 exchange⁴⁹ and the Lee-Yang-Parr (LYP) correlation,⁵⁰ is the most commonly used functional for gas and liquid phase calculations and its performances for geometry optimization in those media are recognized. It is therefore interesting to assess how it performs for the crystalline state. Hybrids based on the PBE generalized gradient approximation (GGA) were also considered. First PBE0 was chosen. It is a global hybrid with 25 % of Hartree-Fock (HF) exchange whereas B3LYP contains 20 % of HF exchange. On the other hand, HSE06 and HISS are short-range and medium-range corrected hybrid functionals [$(c_{SR} = 0.25, c_{LR} = 0, \omega = 0.11 a_0^{-1} = (4.81 \text{ \AA})^{-1})$ and $(c_{SR} = 0, c_{MR} = 0.60, c_{LR} = 0, \omega_{SR} = 0.84 a_0^{-1} = (0.63 \text{ \AA})^{-1}, \omega_{LR} = 0.20 a_0^{-1} = (2.65 \text{ \AA})^{-1})$, respectively], also based on PBE. Then, XC functionals tuned for the solid state were adopted. Indeed, the PBEsol functional was developed by fine tuning the gradient contributions of both the exchange and correlation terms.⁴¹ In PBE, the exchange energy parameter μ is set to about two times the electron gas value $2\mu_{GE} \approx 0.2195$ while for solids the electron density is closer to an electron gas and therefore $\mu_{GE} = 0.1235$ is more adequate and it defines PBEsol. As for the correlation energy parameter β , the PBE value is $\beta_{GE} = 0.0667$ so that PBE recovers the response of local density approximation (LDA) functionals in a weak potential. On the other hand, in PBEsol, β is set to 0.046 to recover the Tao-Perdew-Staroverov-Scuseria (TPSS) meta-GGA⁵¹ XC energy at the surface of a jellium. Alike PBE0, the global hybrid functional PBEsol0 follows naturally, as well as the short-range corrected hybrid functional HSEsol. Besides their HF exchange component, both have the same parameters as their PBE variant. Finally, ω B97X has exact exchange in both its short and long range limits ($c_{SR} = 0.16, c_{LR} = 1, \omega = 0.3 a_0^{-1} = (1.76 \text{ \AA})^{-1}$) while the DFT contribution comes from Becke's B97 XC functional.⁵²

In the CRYSTAL14 calculations, the default integration grid, a pruned grid with 75 radial points and 974 angular points, was used while the truncation criteria for the bielectronic integrals (TOLINTEG keyword) were set to 8 8 8 8 16 (ITOL1 to ITOL5), unless stated otherwise. 10^{-ITOL1} is the threshold for the Coulomb overlap [if smaller than the criterion, the related integral is not taken into account and the lattice summation is truncated], 10^{-ITOL2} is the Coulomb penetration threshold [if larger than the criterion, the related integral is treated exactly (four-center integral) or else, is approximated (three-center integral)], 10^{-ITOL3} , 10^{-ITOL4} , and 10^{-ITOL5} are the criteria for the truncation of the summations for the exchange energy [on the point symmetry and two lattice vectors, respectively]. The default value of 4 for the maximum order of the

shell multipoles was used to describe the long-range part of the electron-electron Coulomb interactions. Contrary to many solid state programs, in CRYSTAL14, the basis set functions are Gaussian functions. The basis set choice was Pople's double zeta plus polarization basis, 6-31G(d,p), though the impact of selecting smaller or larger basis sets was also studied. Moreover the effect of the basis set superposition error (BSSE) on the relative energy of the E and K forms was investigated. The BSSE on their energies was calculated with the counterpoise method for atoms within a distance of 3.0 Å, as implemented in CRYSTAL14. The Pack-Monkhorst shrinking factor was set to 6 for the three lattice vectors, yielding 64 integration points in the irreducible part of the Brillouin zone (IBZ) for PYV3 and HC and 80 points for POC.

Starting from the single-crystal X-ray diffraction structures, the crystal structures were either fully optimized (F-OPT) or only the fractional coordinates of the asymmetric unit (restrained optimization, R-OPT) were optimized while freezing the unit cell parameters to the experimental values. In both cases, the default convergence criteria were used. The criterion for SCF convergence on the total energy and on the total energy variation between two optimization steps were 10^{-7} a.u.. The criteria for the RMS deviations of the gradients and the displacements were set to 3×10^{-4} a.u. and 12×10^{-4} a.u., respectively while the maximum values of the gradients and displacements were fixed to 4.5×10^{-4} a.u. and 18×10^{-4} a.u., respectively.

3.3 Results and Discussion

3.3.1 DFT vs XRD Structures for Anil Crystals

The geometries obtained with F-OPT are compared to XRD data. Table 3.1 gives the average mean absolute (MAE) and mean signed errors (MSE) for the unit cell parameters, bond lengths, valence angles, and torsion angles. Since the XRD experiment underestimates the bond lengths involving hydrogen atoms, the mean errors are also calculated by ignoring the bonds or angles involving these atoms.

The single-crystal XRD data, used for the comparisons with the calculations, have been gathered at 105 K for PYV3 and 90 K for HC and POC and are included in Figures 3.2 and 3.3 (see Ref. [23] and [29] for more details). The crystallographic data are available on the Cambridge Structural Database⁵³ with the CCDC numbers 1456341 (PYV3), 119131 (HC), and 119133 (POC). While PYV3 and HC crystallized in the pure enol form (no evidence of the K form was found), in the case of POC, both enol and keto forms are present. Ogawa and coworker estimated their populations at different temperatures by means of electronic spectra measurements and analysis of XRD data (based on bond lengths). At 90 K, both methods estimate the population of the keto form to be 90 %. In view of comparisons between the calculations and XRD geometries this aspect is very important because calculations give structural information at

0 K for truly pure E or K forms.

Based on the averaged errors, all the XC functionals, except ω B97X, overestimate the XRD unit cell parameters, highlighting an underestimation of the strength of the intermolecular interactions and, subsequently, of the stabilization energies. The largest errors are obtained with B3LYP, then with the PBE-based functionals whereas a good agreement with experiment is achieved with the PBEsol-based functionals, and in particular with PBEsol and PBEsol0. Still, the best performance is achieved with the ω B97X XC functional for which the average MAE on the unit cell parameters is as low as 0.07 Å. However, as shown in Figure 3.2, for the best functionals, there are differences between the unit cell parameters and typically one can be underestimated, while the other ones are overestimated. This is well illustrated for HC where a is systematically underestimated whereas b and c are overestimated. Owing to these compensating errors, ω B97X and PBEsol-based XC functionals perform very well for predicting the unit cell volume whereas errors obtained with the PBE-based functionals attain typically 10 % or more.

For the bond lengths, all the average errors are of the order of 0.01 Å (when ignoring the H atoms) and 0.5° for the valence angles, which is satisfactory. These errors raise to 2° for the torsion angles, provided one considers the absolute values. As expected, for all functionals, the errors made on the bonds involving hydrogen atoms are large. Therefore, from now on, only the errors calculated without H atoms are commented. Among the PBE-based functionals, the smallest bond length discrepancies (obtained with HSE06 and PBE0) are smaller than those of B3LYP. For the PBEsol-based functionals, HSEsol and PBEsol0 perform the best and quasi similarly to B3LYP. There are no large discrepancies between the PBE- and PBEsol-based functionals, which are all equally reliable. Note that an even better agreement with experimental values (MSE of -8×10^{-5} Å) is obtained with ω B97X. Figure 3.3 shows the bond lengths variations of key bonds (highlighted in Figure 3.1) with respect to experiment. In addition, two ratios are considered, the N- and C-ratios, which describe the π -conjugation and are defined as:

$$\text{N-ratio} = \frac{d(\text{N}-\text{C}_8)}{d(\text{C}_7=\text{N})} \quad (3.1)$$

$$\text{C-ratio} = \frac{d(\text{C}_1-\text{C}_7)}{d(\text{C}_2=\text{C}_1)} \quad (3.2)$$

Systematic and general trends are observed (i) for the enol species (PYV3 and HC), the single bond lengths in the O₂-to-C₈ conjugated path are slightly underestimated (~ 0.02 Å) while the double bond ones are slightly overestimated, in particular with the GGA functionals. The errors on the ratios are twice larger (~ 0.02) with the GGA functionals (PBE and PBEsol) than with the hybrids. In particular, for PYV3, the $d(\text{N}-\text{C}_8) - d(\text{C}_7=\text{N})$ and $d(\text{C}_1-\text{C}_7) - d(\text{C}_2=\text{C}_1)$ bond length alternations (BLA) calculated with PBEsol0 attain 0.102 Å and 0.033 Å in

comparison with the 0.120(4) Å and 0.051(5) Å experimental values, respectively whereas the values are 0.084 Å and 0.013 Å for PBEsol ; (ii) this leads to an underestimation of the N- and C-ratios by up to 3 % for the GGA's and up to 1.5 % for the global hybrids ; (iii) globally these differences with respect to XRD data corresponds to an underestimation of the enol character or an overestimation of the keto character ; (iv) ω B97X differs from the other hybrid functionals since the C₁–C₇ bond length is overestimated and the C₇=N₁ one is underestimated, thus leading to slightly overestimated BLA values of 0.128 Å and 0.059 Å and overestimated ratios by up to 1 %. In the case of the keto species (POC): (v) for each bond, the deviations have the same signs as for the enol forms but this corresponds to an underestimation of the double bond lengths and an overestimation of the single ones ; (vi) this also corresponds to an overestimation of the keto character but this is a simplification because the POC crystal also contains a small amount ($\sim 10\%$) of enol form²³ ; and (vii) the performance of GGA functionals are also different while ω B97X gives contrasted results with respect to the global hybrids.

The prediction of accurate valence and torsion angles is as important as for the bond lengths because they are closely intertwined with the unit cell parameters and intermolecular interactions. All XC functionals yield very small MAEs (inferior to 1°) on the valence angles with negligible MSEs (maximum 0.1°). Figure S1 highlights these deviations with respect to experiment for the two valence angles linking the phenyl rings (C₁–C₇–N and C₇–N–C₈). The variations are small ($\leq 2^\circ$) and there is no systematic trend among the XC functionals. Averaged errors on the torsion angles are small ($\text{MAE} \leq 2^\circ$) and negative. This includes the estimates of the C₂–C₁–C₇–N and C₁–C₇–N–C₈ torsions but not the C₇–N–C₈–C₉ torsion angle for which the deviations w.r.t. experiment are one order of magnitude larger, especially for POC (Figure S1). The torsion angle describing the intramolecular H-bond C₂–O \cdots N–C₇ deviates by less than 2° from the experimental values (which are close to 0°). Additionally, the errors for the angle between the planes of the phenyl rings C₂–C₁ \cdots C₈–C₉ are as large as those on the C₇–N–C₈–C₉, which is consistent since they are interrelated and since the other torsion angles are accurately determined. Among the functionals, no fully consistent trends are observed but generally (i) B3LYP has the largest errors, (ii) the GGA's provide more accurate data, (iii) for PYV3 and HC the PBEsol-based XC functionals perform better than the PBE-based ones, and (iv) the best agreement with the experimental values is achieved with ω B97X since it gives a better description of the overall torsion of the molecules (C₂–C₁ \cdots C₈–C₉ torsion angle).

Table 3.1: Statistics on the differences between the DFT-optimized geometrical parameters and XRD data as a function of the XC functional. The 6-31G(d,p) basis set was employed for all calculations. The reported values are the Mean Absolute Errors (MAE) and Mean Signed Errors (MSE) averaged over the three anil crystals.

		B3LYP	PBE	HSE06	HISS	PBE0	PBEsol	HSEsol	PBEsol0	ω B97X [†]
Unit cell parameters	MSE {a,b,c} [Å]	0.798	0.509	0.497	0.384	0.514	0.111	0.131	0.118	-0.009
	MAE {a,b,c} [Å]	0.798	0.509	0.551	0.384	0.586	0.223	0.226	0.197	0.069
	MSE { β } [°]	3.2	2.1	2.6	2.5	2.9	1.4	1.7	1.9	1.5
	MAE { β } [°]	3.2	2.1	2.6	2.5	2.9	1.4	1.7	1.9	1.5
	MSE {V} [Å ³]	258.2	154.9	141.5	102.2	145.3	16.9	22.8	22.4	-8.3
	MAE {V} [Å ³]	258.2	154.9	141.5	102.2	145.3	20.3	26.5	27.0	8.3
Bond lengths [Å]	MSE	0.050	0.058	0.047	0.040	0.047	0.058	0.047	0.047	0.048
	MAE	0.052	0.059	0.051	0.051	0.051	0.061	0.054	0.053	0.051
	MSE ignoring H	0.005	0.010	-0.001	-0.009	-0.001	0.006	-0.004	-0.004	0.000
	MAE ignoring H	0.007	0.012	0.006	0.009	0.006	0.011	0.007	0.006	0.005
Valence angles [°]	MSE	0.0	0.0	0.0	0.0	0.0	0.0	0.0	0.0	0.0
	MAE	0.8	0.8	0.7	0.8	0.8	0.9	0.8	0.8	0.7
	MSE ignoring H	0.1	0.1	0.1	0.1	0.1	0.0	0.0	0.0	0.1
	MAE ignoring H	0.4	0.5	0.4	0.5	0.5	0.6	0.5	0.5	0.3
Torsion angles [°]	MSE	-0.8	-0.5	-0.6	-0.5	-0.7	-0.4	-0.4	-0.4	-0.2
	MAE	2.1	1.7	1.9	1.8	2.0	1.8	1.8	1.8	1.5
	MSE ignoring H	-1.3	-0.7	-0.9	-0.8	-1.0	-0.6	-0.6	-0.7	-0.2
	MAE ignoring H	2.0	1.3	1.7	1.6	1.9	1.4	1.4	1.5	0.9

[†] TOLINTEG = 7 7 7 16

3.3.2 DFT vs XRD Structures for PYV3 Co-Crystals

Some of us have recently shown that PYV3 can co-crystallize with one co-former, either fumaric (FA) or succinic (SA) acid.²⁹ In each case two polymorphic co-crystals have been observed (PYV3 FA1, PYV3 FA2, PYV3 SA1, and PYV3 SA2 ; Figure 3.4). Crystallographic data is available on the Cambridge Structural Database⁵³ with the CCDC numbers 1060634 (PYV3 FA1), 1060636 (PYV3 FA2), 1400289 (PYV3 SA1), and 1456340 (PYV3 SA2) ; all in the E form at room temperature (~ 293 K). On this basis, we expanded the assessment of DFT to those four co-crystals at least for the three better performing XC functionals: HSEsol, PBEsol0, and ω B97X (Table 3.2). It appears that the behavior of each XC functional is similar for PYV3 and its co-crystals, in particular for the N- and C-ratios as well as for the torsion angles. Discrepancies on the unit cell volumes are larger than for PYV3. Overall, HSEsol and PBEsol0 perform almost identically, except for PYV3 SA1 for which the error on the volume is twice larger for PBEsol0 (from -1.5 to -2.8 %). ω B97X gives slightly worse unit cell volumes but it better describes the ratios (especially the N one, by a factor 3) as well as the intermolecular H-bond lengths (between the nitrogen of the pyridine moiety of PYV3, N_{py} and one of the acidic oxygen of the co-former, O_{FA} or O_{SA}).

3.3.3 Basis Set Effects

Using the PBEsol0 XC functional, the effects of the basis set were assessed on the geometrical structure of PYV3 crystal. The following Pople's sets were employed (as taken from Basis Set Exchange^{54,55}): 6-21G, 6-31G, 6-31G(d), 6-31G(d,p), 6-311G, 6-311G(d), and 6-311G(d,p) (Table 3.3). With 6-21G, all starting points of the optimization (including enol-like forms) end up with the K form and therefore no further results are provided. Starting from the 6-31G(d) basis set, the comparisons with single crystal XRD data shows that i) the addition of a third set of valence functions improves the N-/C-ratios and volume estimates but not the torsion angles, ii) the inclusion of p polarization functions on the H atoms has a small impact except on the volume where it is detrimental, and iii) the 6-31G basis set gives very accurate volume and torsion angles but less accurate ratios.

Now comparing the keto form to the enol one, the energy variation, $\Delta E_{KE} = E(K) - E(E)$, is expected to be positive because experimentally the E form is observed. Based on the fact that the switching corresponds to an intramolecular hydrogen transfer, no substantial effects are expected on the unit cell parameters and volume while the N- and C-ratios have to decrease. Three basis sets, 6-31G, 6-311G, and 6-311G(d), yield negative energy variations. Concerning the structural parameters, ΔV is always negative and does not exceed 20 \AA^3 (1.8 %). This variation of cell volume is in line with the variations of cell parameters that can experimentally be observed in XRD structures based on data measured at different temperatures (classically low temperature (100 K) versus room temper-

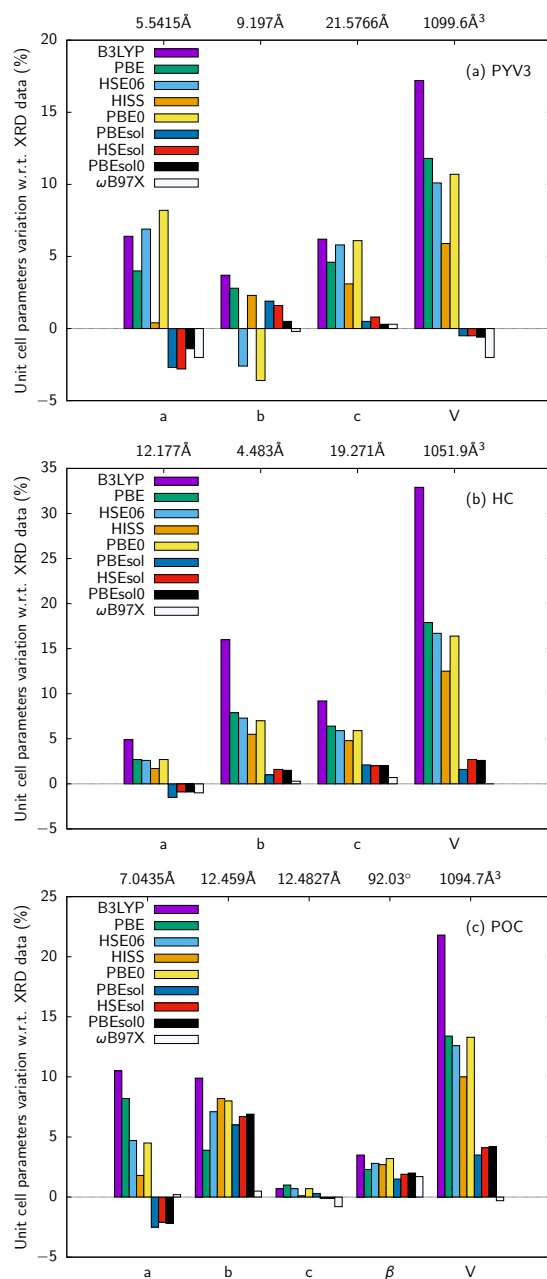


Figure 3.2: Differences (in %) between the optimized unit cell parameters and the XRD values as a function of the XC functional, $\Delta = [d(\text{DFT}) - d(\text{XRD})]/d(\text{XRD})$. The XRD values are given on the top of each figure. The 6-31G(d,p) basis set and full optimization scheme (F-OPT) were employed for all calculations.

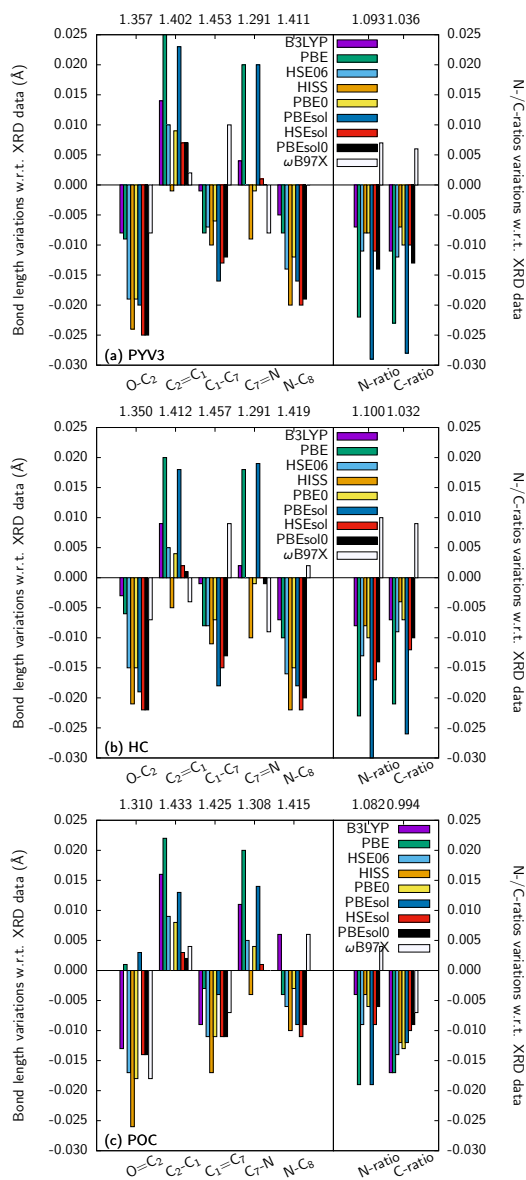


Figure 3.3: Deviations of key bond lengths optimized with different XC functionals with respect to XRD data. The XRD values are given on the top of each figure, $\Delta = d(\text{DFT}) - d(\text{XRD})$. The 6-31G(d,p) basis set and full optimization scheme (F-OPT) were employed for all calculations.

Table 3.2: Differences between the optimized unit cell parameters and key geometrical parameters and the XRD values as a function of the XC functional for PYV3 and its polymorphic co-crystals with fumaric (FA) or succinic (SA) acid. The 6-31G(d,p) basis set was employed for all calculations.

XRD		HSEsol				PBEsol0	ω B97X [†]
PYV3							
V [Å ³]	1099.6(3)	ΔV [Å ³]	-5.6	-7.0	-21.9		
N-ratio	1.093(4)	ΔN-ratio	-0.016	-0.014	0.007		
C-ratio	1.036(5)	ΔC-ratio	-0.015	-0.013	0.006		
torsion [‡] [°]	148.4(2)	Δtorsion [‡] [°]	-2.9	-3.1	-1.0		
PYV3 FA1							
V [Å ³]	1395.18(6)	ΔV [Å ³]	-30.8	-30.9			
N-ratio	1.099(6)	ΔN-ratio	-0.023	-0.020			
C-ratio	1.031(7)	ΔC-ratio	-0.011	-0.009			
torsion [‡] [°]	149.7(2)	Δtorsion [‡] [°]	-1.8	-2.1			
N _{py} –O _{FA} [Å]	2.640(3)	ΔN _{py} –O _{FA} [Å]	-0.082	-0.081			
PYV3 FA2							
V [Å ³]	1421.93(9)	ΔV [Å ³]	-57.5	-57.0	-75.9		
N-ratio	1.104(6)	ΔN-ratio	-0.031	-0.029	-0.008		
C-ratio	1.030(6)	ΔC-ratio	-0.012	-0.011	0.008		
torsion [‡] [°]	-145.7(2)	Δtorsion [‡] [°]	3.3	3.4	1.1		
N _{py} –O _{FA} [Å]	2.623(3)	ΔN _{py} –O _{FA} [Å]	-0.063	-0.063	0.037		
PYV3 SA1							
V [Å ³]	1403.98(10)	ΔV [Å ³]	-21.4	-39.7	-81.8		
N-ratio	1.105(4)	ΔN-ratio	-0.028	-0.026	-0.008		
C-ratio	1.031(4)	ΔC-ratio	-0.011	-0.010	0.007		
torsion [‡] [°]	148.7(1)	Δtorsion [‡] [°]	-2.3	-2.5	-0.5		
N _{py} –O _{FA} [Å]	2.656(2)	ΔN _{py} –O _{SA} [Å]	-0.091	-0.090	-0.016		
PYV3 SA2							
V [Å ³]	2758.3(7)	ΔV [Å ³]	-100.2	-100.2	-134.1		
N-ratio	1.115(4)	ΔN-ratio	-0.034	-0.032	-0.010		
C-ratio	1.046(4)	ΔC-ratio	-0.013	-0.012	0.007		
torsion [‡] [°]	19.9(2)	Δtorsion [‡] [°]	4.6	4.6	2.7		
N _{py} –O _{FA} [Å]	2.651(2)	ΔN _{py} –O _{SA} [Å]	-0.116	-0.114	0.006		

[†] TOLINTEG = 7 7 7 16

[‡] torsion = C₂-C₁...C₈-C₉

ature). About the bond lengths, the inclusion of d polarization functions on the second period atoms increases the ratio differences by about 40 %. The BLAs display the same behavior as the ratios. The further addition of p polarization functions on the H atoms has little effect on the ratios while it significantly increases ΔE_{KE} . In the case of 6-311G(d), it helps going from a dominant keto structure ($\Delta E_{KE} = -1.3 \text{ kJ mol}^{-1}$) to a structure dominated by the enol form ($\Delta E_{KE} = 7.6 \text{ kJ mol}^{-1}$). The effects of BSSE on ΔE_{KE} were investigated by using the counterpoise method and the corrected ΔE_{KE} values are given Table 3.3. This correction is slightly larger for the K form than the E form, which results in a stabilization of the E form by up to 2.0 kJ mol^{-1} . These small corrections are consistent with the work of Spackman and Mitchell.⁵⁶ The overall small differences between the 6-31G(d,p) and 6-311G(d,p) basis sets justify the use of the computationally less costly 6-31G(d,p) basis set.

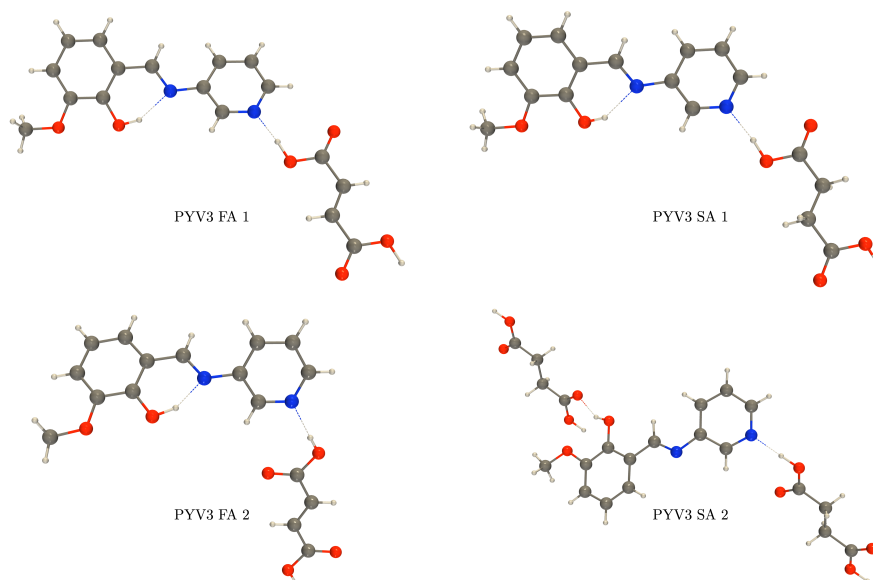


Figure 3.4: Supramolecular synthons of the PYV3 based co-crystals and their acronyms.²⁹

Table 3.3: Basis set effects on the geometrical structure of PYV3 crystal as determined with the PBEsol0 XC functional and full geometry optimization. The top part reports, for the enol form, the differences with respect to XRD data whereas the bottom part gives the variations between the K and E forms [$\Delta X = X(K) - X(E)$, where X is a property]. Values in parentheses account for BSSE corrections.

		6-31G	6-31G(d)	6-31G(d,p)	6-311G	6-311G(d) [†]	6-311G(d,p) [†]
$\Delta = E - \text{XRD}$	ΔV [\AA^3]	0.5	4.3	-7.0	-6.2	2.9	6.2
	ΔN -ratio	-0.021	-0.013	-0.014	-0.016	-0.009	-0.009
	ΔC -ratio	-0.021	-0.012	-0.013	-0.016	-0.010	-0.011
	$\Delta \text{torsion}^\ddagger$ [$^\circ$]	-2.2	-3.3	-3.1	-3.5	-4.5	-4.9
		ΔE_{KE} [kJ mol^{-1}]	-14.4 (-15.9)	2.2 (0.2)	7.1 (5.4)	-12.8 (-14.2)	-1.3 (-2.0)
$\Delta = K - E$	ΔV [\AA^3]	-13.3	-15.5	-12.3	-14.3	-16.9	-19.8
	ΔN -ratio	-0.015	-0.022	-0.020	-0.016	-0.024	-0.023
	ΔC -ratio	-0.039	-0.056	-0.051	-0.042	-0.057	-0.054
	$\Delta \text{torsion}^\ddagger$ [$^\circ$]	0.5	2.6	2.6	2.2	4.0	4.5

[†] TOLINTEG = 7 7 7 7 16

[‡] torsion = $C_2 - C_1 \cdots C_8 - C_9$

3.3.4 Switching from the Enol to the Keto Form

In a next step, we checked whether the different calculation methods are able to reproduce which form (enol or keto) is the most stable and how they describe the changes of geometry between the two forms.

Relative Energy of the Enol and Keto Forms

The PYV3 and HC crystalline structures are consistent with quasi-pure enol (E) form while POC crystal is composed in majority of the keto (K) form, from 90 to 375 K. Thus, the $\Delta E_{KE} = E(K) - E(E)$ energy differences for PYV3 and HC are expected to be positive but negative for POC. Rigorously, the populations should be determined by the Gibbs free energies. Still, the ΔPV contribution is very small at ambient pressure and the entropy difference between the two forms is assumed to be negligible. In addition to comparing the various XC functionals, the R-OPT and F-OPT optimization schemes are compared. Calculated values are given in Table 3.4. The discussion starts with the F-OPT results. Two calculations fail to recover the expected relative energy: HC/PBE and HC/PBEsol, while PBEsol fails to optimize the E form of POC. It appears that the ordering of the ΔE_{KE} values is the same with all XC functionals: $PYV3 > HC > POC$. So, all methods predict that for the PYV3 the enol/keto difference is larger than for the HC and, as expected, even larger than for POC. Despite most values being qualitatively accurate and consistent between the different anils, they vary broadly: from 1.0 to 12.9 kJ mol⁻¹ for PYV3, from 0.7 to 4.0 kJ mol⁻¹ for HC,

Table 3.4: Energy difference ($\Delta E_{KE} = E(K) - E(E)$) per molecule in kJ mol⁻¹ as calculated with different XC functionals and optimization schemes. The 6-31G(d,p) basis set was applied in all calculations.

Method	F-OPT			R-OPT		
	PYV3	HC	POC	PYV3	HC	POC
B3LYP	8.3	4.0	-7.2	1.7	-1.0	-11.4
PBE	2.6	-2.4	-11.8	0.3	-4.9	— [‡]
HSE06	8.5	2.6	-7.8	2.0	0.2	-10.1
HISS	8.8	3.4	-7.2	2.7	2.1	-8.5
PBE0	11.0	3.2	-7.3	2.1	0.9	-9.3
PBEsol	1.0	-3.3	— [‡]	0.6	-2.4	— [‡]
HSEsol	6.9	0.7	-10.5	2.0	1.7	-9.7
PBEsol0	7.1	1.2	-10.0	2.1	2.3	-9.1
ω B97X [†]	12.9	3.8	-3.5	3.6	5.3	-4.4

[†] TOLINTEG = 7 7 7 7 16

[‡] No stable enol form was found

and from -11.8 to -3.5 kJ mol^{-1} for POC. Noticeably, HSEsol and PBEsol0 yield very similar values for each of the three crystals.

The calculations carried out using the restricted geometry optimization provide qualitatively the same results with respect to the ΔE_{KE} energy ordering ($\text{PYV3} > \text{HC} > \text{POC}$), except for PBEsol0 and ωB97X . Quantitatively there are differences. For POC, the ΔE_{KE} values increase in absolute values by as much as 4.2 kJ mol^{-1} when using B3LYP or the PBE-based functionals whereas the differences are smaller than 1 kJ mol^{-1} with the "solid state" evolution of PBE or with ωB97X . For PYV3, a restricted optimization disfavors the enol form in all cases and by as much as 9 kJ mol^{-1} using PBE0. Finally, in the case of HC the results are more contrasted with increased (B3LYP, PBE, HSE06, HISS, PBE0) or decreased (PBEsol, HSEsol, PBEsol0, ωB97X) stability of the keto form. Overall, B3LYP and the PBE-based functionals stabilize more the enol form than the keto one when going from the restrained system to the fully relaxed one, for all three crystals (see Figure S2). On the other hand, the PBEsol-based functionals present the opposite behavior: stronger stabilization of K versus E. ωB97X displays no systematic trend. Owing to these non-systematic variations, the full optimization procedure appears as the most reliable method.

Geometry Variations upon Enol-Keto Switching

Since for each anil, only one form was (dominantly) observed, these results cannot be compared to experiment. On the other hand, they can be used to determine *a priori* the structure of the other anil form, which could be obtained upon triggering by external stimuli or by co-crystallization. Results presented in Figure S3 show consistently that all the unit cell parameters do not vary in the same way. Consequently, since one or two optimized parameters increase (decrease) the resulting effect on the volume is a small variation, bounded to -4% (with the exception of HC with B3LYP). Some trends are observed among the XC functionals: (i) the B3LYP results are the most different ; (ii) the "sol" functionals provide smaller variations than other ones for PYV3 and HC while it is the opposite for POC ; and (iii) ωB97X has again a contrasted behavior, with values similar to the "sol" functionals (PYV3), similar to the PBE-based ones (HC), and different (POC).

The variations of the bond lengths (Figure 3.5) display the alternating behavior characteristic of the enol to keto transformation with shortening of $d_{\text{O}-\text{C}_2}$ and $d_{\text{C}_1-\text{C}_7}$ but lengthening of $d_{\text{C}_2-\text{C}_1}$ and $d_{\text{C}_7-\text{N}}$, leading to negative variations of the N- and C-ratios (Eqs. 3.1-3.2). Though the amplitudes of the E to K geometrical variations are not exactly the same for the three compounds and the different XC functionals, there are clear and consistent trends: $d_{\text{O}-\text{C}_2}$ decreases by ~ 0.06 Å while the C_1-C_7 bond is less shortened (~ 0.04 Å) ; similarly the C_2-C_1 bond is lengthened by ~ 0.03 Å and $d_{\text{C}_7-\text{N}}$ almost equally increases. On the other hand, the $\text{N}-\text{C}_8$ bond length increases by 0.01 Å only in POC, which is attributed to the presence of an electron donating group in para position of

the N–C₈ bond.

All functionals display the same tendencies for the valence angles (Figure S4): a small increase for C₁–C₇–N (maximum 2.5°) and about the double for C₇–N–C₈ (maximum 6°). Then, the C₂–O...N–C₇ torsion angle changes little, which is attributed to the locking action of the intramolecular H-bond. Accordingly, the variation for PYV3 is barely larger than 2° and it is smaller for the other crystals. Similarly, the C₂–C₁–C₇–N and C₁–C₇–N–C₈ torsion angles do not vary much with changes generally smaller than 2°. For the last two angles describing either the torsion of the pyridine/phenyl ring with respect to the anil part (C₇–N–C₈–C₉) or the torsion between the two rings (C₂–C₁...C₈–C₉), their variations are more difficult to describe since the rotation around the N–C₈ bond is rather free (the only constraint being the π -conjugaison). For PYV3 and HC, those angles increase from E to K but they decrease for POC. In the three cases, the amplitude of this variation is smaller than 5° for HC and POC whereas smaller than 10° for PYV3. Finally, the variations of these torsion angles depend not negligibly on the XC functional and the best consistency between the whole set of functionals is observed for PYV3.

3.4 Conclusion

Periodic structure calculations have been performed using the CRYSTAL14 program together with a variety of DFT XC functionals to describe the structure of salicylideneaniline (anil) molecular switches in the solid state. The first focus was on predicting the unit cell and intramolecular geometrical parameters for three anil derivatives, i.e. the PYV3 and HC crystals, where the enol form is dominant in the crystalline state at low temperature and the POC crystal, which is mostly composed of the keto form. The best performance for the unit cell parameters, in comparison with single crystal XRD data, is achieved with XC functionals developed for the solid state (PBEsol and PBEsol0) as well as with ω B97X, which includes both short- and long-range Hartree-Fock exchange. On the other hand, the differences between the functionals are much smaller when considering the bond lengths and the valence angles so that the deviations with respect to XRD data in the bond length alternations of the key O=C=C–C=N–C (or O=C–C=C–N–C) π -conjugated segment are smaller than 0.02 Å for PBEsol0 and ω B97X. Moreover, the accuracy on the torsion angles attains 2° or better, with the exception of the torsion angle determining the position of the phenyl/pyridine ring. Similar trends are observed for the two polymorphic co-crystals of PYV3 with fumaric or succinic acid. The second focus was the characterization of the changes of energy and structural parameters when switching between the enol and keto forms. Only hybrid functionals correctly predict which form is the most stable in the crystalline state and, for such a comparison, full geometry optimizations are shown preferable with respect to restricted optimizations where the unit cell parameters are frozen. Still, all XC

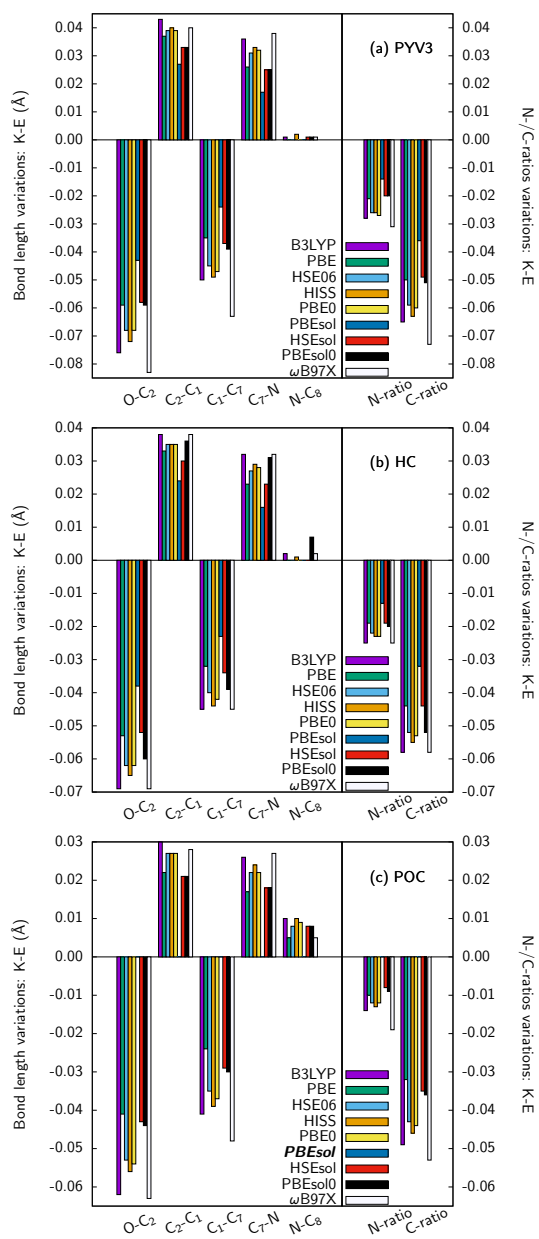


Figure 3.5: Variation of the bond lengths for the E→K reaction, $\Delta = d(K) - d(E)$, as optimized with different XC functionals after full geometry optimization with the 6-31G(d,p) basis set.

functionals consistently predict that PYV3 present a larger ΔE_{KE} value than HC and, as expected, both are larger than for POC. Then, the bond length changes in the O=C=C-C=N-C (or O=C-C=C-N-C) π -conjugated segment that occur upon enol to keto transformation are similarly predicted by all functionals and are consistent with the reversal of the single/double bonds pattern. Finally, the 6-31G(d,p) basis set has been shown to be adequate to describe these variations of energy and geometrical structures.

Supplementary Information

Figures with the deviations of key angles optimized with different XC functionals with respect to XRD data, the energy differences between the restricted (R-OPT) and full (F-OPT) optimization schemes, and the variations of the unit cell parameters and angles along the E→K reaction as optimized with different XC functionals, see Appendix (App.) A.

Acknowledgement

This work was carried out thanks to funding of "Actions de Recherche Concertées" (ARC) de la Direction générale de l'Enseignement non obligatoire et de la Recherche scientifique – Direction de la Recherche scientifique – Communauté française de Belgique, under convention No. 15/20-068. This research used resources of the "Plateforme Technologique de Calcul Intensif (PTCI)" (<http://www.ptci.unamur.be>) located at the University of Namur, Belgium, which is supported by the F.R.S.-FNRS under the convention No. 2.5020.11. The PTCI is member of the "Consortium des Équipements de Calcul Intensif (CÉCI)" (<http://www.cec-hpc.be>).

Bibliography

- (1) *Organic Photochromic and Thermochromic Compounds*; Crano, J. C., Guglielmetti, R. J., Eds.; Plenum: New York, NY, 1998.
- (2) Kawata, S.; Kawata, Y. Three-Dimensional Optical Data Storage Using Photochromic Materials. *Chem. Rev.* **2000**, *100*, 1777–1788.
- (3) Hadjoudis, E.; Mavridis, I. M. Photochromism and Thermochromism of Schiff Bases in the Solid State: Structural Aspects. *Chem. Soc. Rev.* **2004**, *33*, 579–588.
- (4) Amimoto, K.; Kawato, T. Photochromism of Organic Compounds in the Crystal State. *J. Photochem. Photobiol. C Photochem. Rev.* **2005**, *6*, 207–226.

- (5) *Molecular Switches*; Feringa, B. L., Browne, W. R., Eds.; Wiley-VCH Verlag GmbH & Co. KGaA: Weinheim, Germany, 2011, DOI: 10.1002/9783527634408.
- (6) *Tautomerism: Methods and Theories*; Antonov, L., Ed.; Wiley-VCH: 2013.
- (7) *Tautomerism: Concepts and Applications in Science and Technology*; Antonov, L., Ed.; WILEY-VCH: 2016.
- (8) Padalkar, V. S.; Seki, S. Excited-State Intramolecular Proton-Transfer (ESIPT)-Inspired Solid State Emitters. *Chem. Soc. Rev.* **2016**, *45*, 169–202.
- (9) Coe, B. J. Molecular Materials Possessing Switchable Quadratic Non-linear Optical Properties. *Chem. - A Eur. J.* **1999**, *5*, 2464–2471, DOI: 10.1002/(SICI)1521-3765(19990903)5:9<2464::AID-CHEM2464>3.0.CO;2-L.
- (10) Morimoto, M.; Irie, M. Photochromism of Diarylethene Single Crystals: Crystal Structures and Photochromic Performance. *Chem. Commun.* **2005**, 3895.
- (11) Raymo, F. M.; Tomasulo, M. Electron and Energy Transfer Modulation with Photochromic Switches. *Chem. Soc. Rev.* **2005**, *34*, 327.
- (12) Robert, F.; Naik, A. D.; Tinant, B.; Robiette, R.; Garcia, Y. Insights into the Origin of Solid-State Photochromism and Thermochromism of N-Salicylideneanils: the Intriguing Case of Aminopyridines. *Chem. - A Eur. J.* **2009**, *15*, 4327–4342.
- (13) Sevez, G.; Gan, J.; Delbaere, S.; Vermeersch, G.; Sanguinet, L.; Levillain, E.; Pozzo, J.-L. Photochromic Performance of a Dithienylethene-Indolinooxazolidine Hybrid. *Photochem. Photobiol. Sci.* **2010**, *9*, 131.
- (14) Natali, M.; Giordani, S. Molecular Switches as Photocontrollable “Smart” Receptors. *Chem. Soc. Rev.* **2012**, *41*, 4010.
- (15) Hutchins, K. M.; Dutta, S.; Loren, B. P.; MacGillivray, L. R. Co-Crystals of a Salicylideneaniline: Photochromism Involving Planar Dihedral Angles. *Chem. Mater.* **2014**, *26*, 3042–3044.
- (16) Jiménez-Sánchez, A.; Rodríguez, M.; Métivier, R.; Ramos-Ortíz, G.; Maldonado, J. L.; Réboles, N.; Farfán, N.; Nakatani, K.; Santillan, R. Synthesis and Crystal Structures of a Series of Schiff Bases: a Photo-, Solvato- and Acidochromic Compound. *New J. Chem.* **2014**, *38*, 730–738.
- (17) Bondu, F.; Quertinmont, J.; Rodriguez, V.; Pozzo, J.-L.; Plaquet, A.; Champagne, B.; Castet, F. Second-Order Nonlinear Optical Properties of a Dithienylethene-Indolinooxazolidine Hybrid: a Joint Experimental and Theoretical Investigation. *Chem. Eur. J.* **2015**, *21*, 18749–18757.

- (18) Beaujean, P.; Bondu, F.; Plaquet, A.; Garcia-Amorós, J.; Cusido, J.; Raymo, F. M.; Castet, F.; Rodriguez, V.; Champagne, B. Oxazines: a New Class of Second-Order Nonlinear Optical Switches. *J. Am. Chem. Soc.* **2016**, *138*, 5052–5062.
- (19) Wen, Y.; Yi, W.; Meng, L.; Feng, M.; Jiang, G.; Yuan, W.; Zhang, Y.; Gao, H.; Jiang, L.; Song, Y. Photochemical-Controlled Switching Based on Azobenzene Monolayer Modified Silicon (111) Surface. *J. Phys. Chem. B* **2005**, *109*, 14465–14468.
- (20) Nénon, S.; Champagne, B. SCC-DFTB Calculation of the Static First Hyperpolarizability: From Gas Phase Molecules to Functionalized Surfaces. *J. Chem. Phys.* **2013**, *138*, 204107.
- (21) Heinke, L.; Cakici, M.; Dommaschk, M.; Grosjean, S.; Herges, R.; Bräse, S.; Wöll, C. Photoswitching in Two-Component Surface-Mounted Metal–Organic Frameworks: Optically Triggered Release from a Molecular Container. *ACS Nano* **2014**, *8*, 1463–1467.
- (22) Schulze, M.; Utecht, M.; Moldt, T.; Przyrembel, D.; Gahl, C.; Weinelt, M.; Saalfrank, P.; Tegeder, P. Nonlinear Optical Response of Photochromic Azobenzene-Functionalized Self-Assembled Monolayers. *Phys. Chem. Chem. Phys.* **2015**, *17*, 18079–18086.
- (23) Ogawa, K.; Kasahara, Y.; Ohtani, Y.; Harada, J. Crystal Structure Change for the Thermochromy of N-Salicylideneanilines. The First Observation by X-ray Diffraction. *J. Am. Chem. Soc.* **1998**, *120*, 7107–7108.
- (24) Gilli, P.; Bertolasi, V.; Pretto, L.; Antonov, L.; Gilli, G. Variable-Temperature X-ray Crystallographic and DFT Computational Study of the NH···O/N···HO Tautomeric Competition in 1-(Arylazo)-2-naphthols. Outline of a Transition-State Hydrogen-Bond Theory. *J. Am. Chem. Soc.* **2005**, *127*, 4943–4953.
- (25) Sliwa, M.; Létard, S.; Malfant, I.; Nierlich, M.; Lacroix, P. G.; Asahi, T.; Masuhara, H.; Yu, P.; Nakatani, K. Design, Synthesis, Structural and Nonlinear Optical Properties of Photochromic Crystals: Toward Reversible Molecular Switches. *Chem. Mater.* **2005**, *17*, 4727–4735.
- (26) Sliwa, M.; Spangenberg, A.; Malfant, I.; Lacroix, P. G.; Métivier, R.; Pansu, R. B.; Nakatani, K. Structural, Optical, and Theoretical Studies of a Thermochromic Organic Crystal with Reversibly Variable Second Harmonic Generation. *Chem. Mater.* **2008**, *20*, 4062–4068.
- (27) Baroncini, M.; d’Agostino, S.; Bergamini, G.; Ceroni, P.; Comotti, A.; Sozzani, P.; Bassanetti, I.; Grepioni, F.; Hernandez, T. M.; Silvi, S.; Venturi, M.; Credi, A. Photoinduced Reversible Switching of Porosity in Molecular Crystals Based on Star-Shaped Azobenzene Tetramers. *Nat. Chem.* **2015**, *7*, 634–640.

- (28) Jacquemin, P.-L.; Robeyns, K.; Devillers, M.; Garcia, Y. Photochromism Emergence in N-Salicylidene p-Aminobenzenesulfonate Diallylammonium Salts. *Chem. - A Eur. J.* **2015**, *21*, 6832–6845.
- (29) Carletta, A.; Buol, X.; Leyssens, T.; Champagne, B.; Wouters, J. Polymorphic and Isomorphic Cocrystals of a N-Salicylidene-3-aminopyridine with Dicarboxylic Acids: Tuning of Solid-State Photo- and Thermochromism. *J. Phys. Chem. C* **2016**, *120*, 10001–10008.
- (30) Mercier, G. M.; Robeyns, K.; Leyssens, T. Altering the Photochromic Properties of N-Salicylideneanilines Using a Co-Crystal Engineering Approach. *Cryst. Growth Des.* **2016**, *16*, 3198–3205.
- (31) Safin, D. A.; Robeyns, K.; Babashkina, M. G.; Filinchuk, Y.; Rotaru, A.; Jureschi, C.; Mitoraj, M. P.; Hooper, J.; Brela, M.; Garcia, Y. Polymorphism Driven Optical Properties of an Anil Dye. *CrystEngComm* **2016**, *18*, 7249–7259.
- (32) Hirata, S. Quantum Chemistry of Macromolecules and Solids. *Phys. Chem. Chem. Phys.* **2009**, *11*, 8397.
- (33) Maschio, L.; Usvyat, D.; Schütz, M.; Civalieri, B. Periodic Local Møller–Plesset Second Order Perturbation Theory Method Applied to Molecular Crystals: Study of Solid NH₃ and CO₂ Using Extended Basis Sets. *J. Chem. Phys.* **2010**, *132*, 134706.
- (34) Macher, M.; Klimeš, J.; Franchini, C.; Kresse, G. The Random Phase Approximation Applied to Ice. *J. Chem. Phys.* **2014**, *140*, 084502.
- (35) Skelton, J. M.; Lora da Silva, E.; Crespo-Otero, R.; Hatcher, L. E.; Raithby, P. R.; Parker, S. C.; Walsh, A. Electronic Excitations in Molecular Solids: Bridging Theory and Experiment. *Faraday Discuss.* **2015**, *177*, 181–202.
- (36) Rychkov, D. A.; Hunter, S.; Kovalskii, V. Y.; Lomzov, A. A.; Pulham, C. R.; Boldyreva, E. V. Towards an Understanding of Crystallization from Solution. DFT Studies of Multi-component Serotonin Crystals. *Comput. Theor. Chem.* **2016**, *1088*, 52–61.
- (37) Manby, F. R.; Stella, M.; Goodpaster, J. D.; Miller, T. F. A Simple, Exact Density-Functional-Theory Embedding Scheme. *J. Chem. Theory Comput.* **2012**, *8*, 2564–2568.
- (38) Seidler, T.; Stadnicka, K.; Champagne, B. Evaluation of the Linear and Second-Order NLO Properties of Molecular Crystals within the Local Field Theory: Electron Correlation Effects, Choice of XC Functional, ZPVA Contributions, and Impact of the Geometry in the Case of 2-Methyl-4-nitroaniline. *J. Chem. Theory Comput.* **2014**, *10*, 2114–2124.
- (39) Beran, G. J. O.; Hartman, J. D.; Heit, Y. N. Predicting Molecular Crystal Properties from First Principles: Finite-Temperature Thermochemistry to NMR Crystallography. *Acc. Chem. Res.* **2016**, *49*, 2501–2508.

- (40) Ruggiero, M. T.; Gooch, J.; Zubieta, J.; Korter, T. M. Evaluation of Range-Corrected Density Functionals for the Simulation of Pyridinium-Containing Molecular Crystals. *J. Phys. Chem. A* **2016**, *120*, 939–947.
- (41) Perdew, J. P.; Ruzsinszky, A.; Csonka, G. I.; Vydrov, O. A.; Scuseria, G. E.; Constantin, L. A.; Zhou, X.; Burke, K. Restoring the Density-Gradient Expansion for Exchange in Solids and Surfaces. *Phys. Rev. Lett.* **2008**, *100*, 136406.
- (42) Dovesi, R.; Orlando, R.; Erba, A.; Zicovich-Wilson, C. M.; Civalleri, B.; Casassa, S.; Maschio, L.; Ferrabone, M.; De La Pierre, M.; D'Arco, P.; Noël, Y.; Causà, M.; Rérat, M.; Kirtman, B. CRYSTAL14: a Program for the Ab Initio Investigation of Crystalline Solids. *Int. J. Quantum Chem.* **2014**, *114*, 1287–1317.
- (43) Stephens, P. J.; Devlin, F. J.; Chabalowski, C. F.; Frisch, M. J. Ab Initio Calculation of Vibrational Absorption and Circular Dichroism Spectra using Density Functional Force Fields. *J. Phys. Chem.* **1994**, *98*, 11623–11627.
- (44) Perdew, J. P.; Burke, K.; Ernzerhof, M. Generalized Gradient Approximation Made Simple. *Phys. Rev. Lett.* **1996**, *77*, 3865–3868.
- (45) Krukau, A. V.; Vydrov, O. A.; Izmaylov, A. F.; Scuseria, G. E. Influence of the Exchange Screening Parameter on the Performance of Screened Hybrid Functionals. *J. Chem. Phys.* **2006**, *125*, 224106.
- (46) Henderson, T. M.; Izmaylov, A. F.; Scuseria, G. E.; Savin, A. The Importance of Middle-Range Hartree-Fock-Type Exchange for Hybrid Density Functionals. *J. Chem. Phys.* **2007**, *127*, 221103.
- (47) Adamo, C.; Barone, V. Toward Chemical Accuracy in the Computation of NMR Shieldings: the PBE0 Model. *Chem. Phys. Lett.* **1998**, *298*, 113–119.
- (48) Schimka, L.; Harl, J.; Kresse, G. Improved Hybrid Functional for Solids: The HSEsol Functional. *J. Chem. Phys.* **2011**, *134*, 024116.
- (49) Becke, A. D. Density-Functional Thermochemistry. III. The Role of Exact Exchange. *J. Chem. Phys.* **1993**, *98*, 5648.
- (50) Lee, C.; Yang, W.; Parr, R. G. Development of the Colle-Salvetti Correlation-Energy Formula into a Functional of the Electron Density. *Phys. Rev. B* **1988**, *37*, 785.
- (51) Tao, J.; Perdew, J. P.; Staroverov, V. N.; Scuseria, G. E. Climbing the Density Functional Ladder: Nonempirical Meta-Generalized Gradient Approximation Designed for Molecules and Solids. *Phys. Rev. Lett.* **2003**, *91*, 146401.

- (52) Becke, A. D. Density-Functional Thermochemistry. V. Systematic Optimization of Exchange-Correlation functionals. *J. Chem. Phys.* **1997**, *107*, 8554.
- (53) Groom, C. R.; Bruno, I. J.; Lightfoot, M. P.; Ward, S. C. The Cambridge Structural Database. *Acta Crystallogr. Sect. B Struct. Sci. Cryst. Eng. Mater.* **2016**, *72*, 171–179.
- (54) Feller, D. The Role of Databases in Support of Computational Chemistry Calculations. *J. Comput. Chem.* **1996**, *17*, 1571–1586.
- (55) Schuchardt, K. L.; Didier, B. T.; Elsethagen, T.; Sun, L.; Gurumoorthi, V.; Chase, J.; Li, J.; Windus, T. L. Basis Set Exchange: A Community Database for Computational Sciences. *J. Chem. Inf. Model.* **2007**, *47*, 1045–1052.
- (56) Spackman, M. A.; Mitchell, A. S. Basis Set Choice and Basis Set Superposition Error (BSSE) in Periodic Hartree–Fock Calculations on Molecular Crystals. *Phys. Chem. Chem. Phys.* **2001**, *3*, 1518–1523.

EFFECTS OF EMPIRICAL DISPERSION ENERGY ON THE GEOMETRICAL PARAMETERS AND RELATIVE ENERGY OF A SALICYLIDENEANILINE MOLECULAR SWITCH IN THE SOLID STATE

CRYSTALS, 2018, 8, 125

Jean Quertinmont[†], Tom Leyssens[‡], Johan Wouters[†], & Benoît Champagne[†]

[†] *Unité de Chimie Physique Théorique et Structurale, Chemistry Department, University of Namur, 61 rue de Bruxelles, B-5000 Namur, Belgium*

[‡] *Institute of Condensed Matter and Nanosciences, Université Catholique de Louvain, 1 Place Louis Pasteur, B-1348 Louvain-La-Neuve, Belgium*

All calculations, their analysis, and the writing of the first draft were performed by J.Q.

Abstract

The geometries of the enol (E) and keto (K) forms of a crystalline salicylideneaniline molecular switch, (E)-2-methoxy-6-(pyridine-3-yliminomethyl)phenol (PYV3), have been determined using periodic DFT calculations with a variety of XCFS. They are compared to X-ray diffraction (XRD) data as well as to geometries obtained using empirical dispersion energy in the form of the second iteration of Grimme's scheme either with its original parameters (DFT-D2) or with parameters revised for the solid state (DFT-D*). Using DFT, a good agreement with experiment on the unit cell parameters is achieved with the PBEsol, PBEsol0, and ω B97X XCFS. DFT-D2 overcontracts the unit cell with all considered XCFS, whereas DFT-D* lessens this effect thus allowing B3LYP, PBE, and PBE0 to achieve reasonable agreement with respect to XRD data. When considering molecular geometries both DFT and DFT-D* are in agreement on bond lengths, both systematically underestimating (overestimating) the length of the single (double) bonds (within 0.003 Å), and on valence angles attaining differences of 2° with respect to XRD data. The error on torsion angles are less spread out with DFT-D* (averaging 1°) than DFT for which only PBEsol, PBEsol0, and ω B97X perform well. Finally, the relative keto-enol energies, ΔE_{KE} , have been calculated, showing that the inclusion of dispersion energy stabilizes more the keto form than the enol one. This results in the PBE and PBEsol XCFS wrongly predicting the keto form as the most stable form.

4.1 Introduction

Thermochromic and photochromic compounds have been extensively studied and still attract a lot of attention as they have many potential applications.¹⁻⁸ With the focus moving from the liquid phase to the more practical solid one, computational methods well set for quantum calculations of inorganic solids are now being challenged by the molecular crystalline state. In particular, accurate description of the intramolecular parameters (defined by the fractional coordinates of the asymmetric unit) and the intermolecular ones (defined by the unit cell parameters) is required as a starting point for the prediction and study of their properties. Density functional theory (DFT) was recently shown to be an efficient tool granted that the appropriate exchange-correlation functional (XCF) is used.^{9,10} In Ref. [9], Ruggiero and co-workers have assessed the reliability of a range of XCFs for the optimization of three pyridine carboxylic acid crystals and they have highlighted the performances of ω B97X.¹¹ Then in Ref. [10], we have shown the effectiveness of three XCFs (HSEsol,¹² PBEsol0, and ω B97X¹¹) to optimize the molecular and crystal structures of three salicylideneanilines. Still, with respect to the XCFs used so far, for a precise description of the solid state, modifications can be made to DFT by adding London dispersion interactions to the DFT energy (Equation (Eq.) 4.1) in the form of empirical terms as proposed by Grimme.¹³

$$E_{\text{DFT-D}} = E_{\text{DFT}} + E_{\text{disp}} \quad (4.1)$$

where E_{disp} is the empirical dispersion energy. We consider the second iteration of that scheme, containing less empirical parameters than the first one, and known as DFT-D2. General expression for E_{disp} reads:

$$E_{\text{disp}} = -s_6 \sum_{\mathbf{g}} \sum_{ij} f_{\text{dmp}}(R_{ij}, \mathbf{g}) \frac{C_6^{ij}}{R_{ij,\mathbf{g}}^6}, \quad (4.2)$$

with the first summation running over all lattice vectors, \mathbf{g} , and the second one running over all atom pairs (excluding the self-interaction case, when $i = j$ for $\mathbf{g} = 0$), s_6 is a scaling factor depending on the functional, $C_6^{ij} = \sqrt{C_6^{ii} C_6^{jj}}$ is the dispersion coefficient for the ij pair, $R_{ij,\mathbf{g}}$ is the distance between atom i in the reference cell ($\mathbf{g} = 0$) and atom j in the cell \mathbf{g} , and $f_{\text{dmp}}(R_{ij,\mathbf{g}})$ is a damping function:

$$f_{\text{dmp}}(R_{ij,\mathbf{g}}) = \left[1 + e^{-d \left(\frac{R_{ij,\mathbf{g}}}{R_{vdw}} - 1 \right)} \right]^{-1}. \quad (4.3)$$

In the latter expression, R_{vdw} is the sum of the van der Waals radii of the i and j atoms and d defines the steepness of the function. Since this scheme was parameterized for clusters, Ugliengo and coworkers proposed to scale the coefficients published by Grimme in order to better describe the dispersion energy in molecular crystals, leading to DFT-D* (these modifications include a decrease of the scaling factor by a factor 0.95 and a scale up of the atomic van der

Waals radii by 1.05 and 1.30 for heavy and hydrogen atoms, respectively).¹⁴ This modification results in smaller dispersion energies.

In this paper, we aim at evaluating the effects of adding these empirical dispersion energy terms (DFT-D2 and DFT-D*) on the optimized geometrical parameters of a molecular crystal from the salicylideneanilines family, (E)-2-methoxy-6-(pyridine-3-yliminomethyl)phenol (PYV3, Figure (Fig.) 4.1). This compound is in fact a molecular switch that can commute between an enol (E) and a keto (K) form, so that our second focus is on the relative energies between these two forms. These theoretical predictions performed with DFT-D2 and DFT-D* XCFs are compared to X-ray diffraction (XRD) data as well as to those predictions obtained with more traditional DFT functionals.¹⁰ The Paper is organized as follows: next Section summarizes the key computational aspects (additional details can be found in Ref. [10]); Section 4.3 presents and discusses the results before conclusions are drawn in Section 4.4.

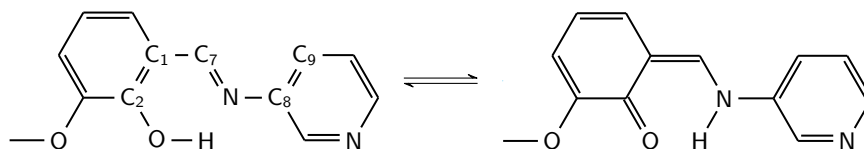


Figure 4.1: Structure and keto-enol equilibrium of the studied salicylideneaniline: (E)-2-methoxy-6-(pyridine-3-yliminomethyl)phenol (PYV3). Key bonds and atoms for characterizing the geometries are highlighted on the enol structure.

4.2 Computational Aspects

Calculations were performed with the Crystal14 package¹⁵ using various XCFs: B3LYP,¹⁶ PBE,¹⁷ PBE0,¹⁸ PBEsol,¹⁹ PBEsol0, and ω B97X¹¹ with and without including London dispersion interactions. This is achieved by using the empirical dispersion corrections due to Grimme.¹³ First, the original parameters were employed (DFT-D2), then those revised for the crystalline state (DFT-D*).¹⁴ The steepness d of the damping function was set to 20 and a cutoff distance of 25 Å was set for the lattice summations. The default integration grid was used; the truncation criteria for the bielectronic integrals (TOLINTEG keyword) were set to 8 8 8 8 16 for all XCFs, except for ω B97X: 7 7 7 7 16; the maximum order of the shell multipole is kept to the default, as well as all convergence criteria for both the SCF cycles and the optimization. A Pack-Monkhorst shrinking factor of 6 was used, yielding 64 integration points in the irreducible Brillouin zone. Pople's 6-31G(d,p) basis set was used as taken from Basis Set Exchange.^{20,21}

4.3 Results and Discussion

4.3.1 Crystal Structures and Molecular Geometries

First the optimized structures of PYV3 obtained using the three "levels" of DFT, *i.e.* DFT, DFT-D2, and DFT-D*, and a selection of XCFs are compared to X-ray diffraction (XRD) data obtained at 105 K, corresponding to the enol form.²² The focus is set first on the unit cell volumes (Table 4.1) and the unit cell parameters (Fig. 4.2), then on key bond lengths and angles (Fig. 4.3 and 4.4).

On the unit cell volume, using the reference DFT XCFs yield either large errors with respect to XRD data (B3LYP 17 %, PBE 12 %, and PBE0 11 %) or volumes within a satisfying range (≤ 2 %): PBEsol < -1 %, PBEsol0 < -1 %, ω B97X < -2 %. Then, the addition of empirical dispersion energy leads overall to smaller unit cell volumes. In the case of DFT-D2, the unit cells are over-contracted, meaning relative errors ranging from -15 to -8 %, while the DFT-D* results tone down this effect to provide volumes either in closer agreement with the experimental values for those XCFs performing poorly with DFT (B3LYP -5 %, PBE -3 %, and PBE0 -6 %), or still over-contracting the unit cell volume for PBEsol, PBEsol0, and ω B97X (errors between -11.6 and -11.2 %).

Table 4.1: Differences of unit cell volume [$\Delta V = V(E) - V(\text{XRD})$, in \AA^3 , and $\Delta V/V = \Delta V/V(\text{XRD})$, in %] as calculated with different XCFs and models for PYV3. The 6-31G(d,p) basis set was applied for all calculations.

Method	DFT	DFT-D2	DFT-D*
B3LYP	189.0 (17.2 %)	-112.9 (-10.3 %)	-52.3 (-4.8 %)
PBE	129.4 (11.8 %)	-89.3 (-8.1 %)	-36.2 (-3.3 %)
PBE0	117.3 (10.7 %)	-112.3 (-10.5 %)	-61.1 (-5.6 %)
PBEsol	-5.2 (-0.5 %)	-169.3 (-15.4 %)	-122.9 (-11.2 %)
PBEsol0	-7.0 (-0.6 %)	-170.5 (-15.5 %)	-127.2 (-11.6 %)
ω B97X ¹	-21.9 (-2.0 %)	-163.4 (-14.9 %)	-124.9 (-11.4 %)

¹ TOLINTEG = 7 7 7 7 16

Figure 4.2 shows the unit cell parameters (a , b , and c) variations with respect to XRD data. When using conventional DFT XCFs (B3LYP, PBE, and PBE0) variations on the unit cell parameters, Fig. 4.2a, all are positive (except for PBE) and larger than 3 %. On the other hand, when using XCFs optimized for the solid state (PBEsol and PBEsol0) as well as ω B97X the differences with respect to XRD data are smaller than 3 % and not systematically positive (leading to error cancellation on the estimated unit cell volume, *e.g.* for PBEsol: the error on a , -2.7 %, is partially cancelled by the one of b , 1.9 %, while c is fairly accurate, 0.5 %).

In the case of DFT-D*, Fig. 4.2b, the a parameter is strongly underestimated (errors between -6 and -10 %) for all XCFs while the errors on b are positive

(except for ω B97X) allowing for error compensations on the volume when c is accurate (between -0.8 and 0.4 %): B3LYP, PBE, and PBE0. This explains why the volume is closer to experiment with these three functionals (-5.6 to -3.3 %) than with PBEsol, PBEsol0, and ω B97X (-11.6 to -11.2 %). Indeed, for the latter XCFs, the errors on the a and c parameters are both negative (-2.3 to -3.1 %) and are not compensated by the errors on b . Finally, the DFT-D2 model, Fig. 4.2c, results in strong and systematic underestimations of all parameters, ranging from -2.5 to -7.7 %. A distinction can be made for the a parameter as determined with B3LYP, PBE, and PBE0 for which the error is smaller, ~ 3 %, than with the other XCFs, ~ 7 %, while the errors for b and c are similar among the XCFs. This results in B3LYP, PBE, and PBE0 volumes that are slightly better than the PBEsol, PBEsol0, and ω B97X ones.

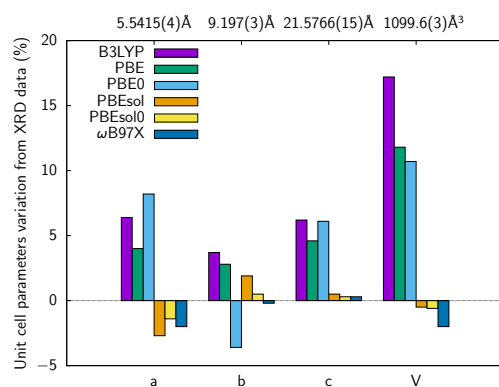
Accurate unit cell parameters constitute a good starting point for further investigations of thermodynamical or optical properties, at least, as long as the bond lengths and angles are also accurately modelled. Fig. 4.3 shows the variations with respect to XRD data for key bond lengths along the O–C₂–C₁–C₇–N–C₈ path (Fig. 4.1). Moreover, two bond length ratios are considered, the N- and C-ratios, which describe the π -conjugation and are defined as follows:

$$\text{C-ratio} = \frac{d(\text{C}_1\text{--C}_7)}{d(\text{C}_2\text{--C}_1)}, \quad (4.1)$$

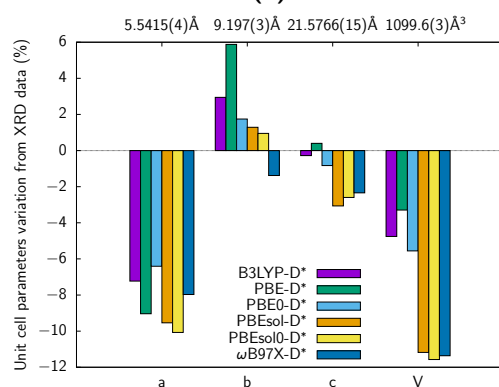
$$\text{N-ratio} = \frac{d(\text{N--C}_8)}{d(\text{C}_7\text{--N})}. \quad (4.2)$$

The comparison to experiment is not presented for DFT-D2 since we have shown above its poor reliability for the unit cell parameters. Fig. 4.3a, for DFT, and 4.3b, for DFT-D*, highlight the systematic underestimation (overestimation) of the single (double) bond lengths, with the exception of C₁–C₇ and C₇=N with ω B97X. Still, in the worst cases, these errors are smaller than 0.025 Å and generally of the order of 0.01 Å. This results in slightly too small N-/C-ratios, especially in the case of the two GGA XCFs, PBE and PBEsol, whereas the ω B97X's ratios are slightly positive. The DFT-D* results are extremely similar to the DFT ones since the differences do not exceed 0.003 Å. This affects the ratios by about the same amount.

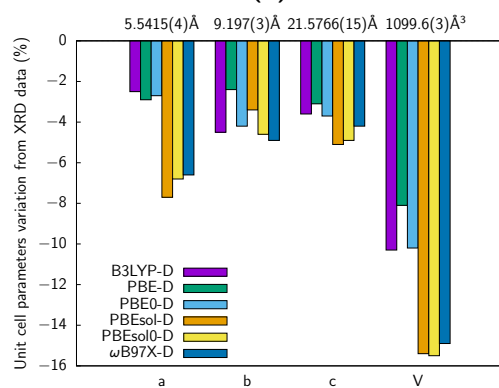
As for the valence and torsion angles, the variations with respect to XRD data are presented in Fig. 4.4 for two valence angles (C₁–C₇–N and C₇–N–C₈), the three torsion angles involving the C₇=N bond (C₂–C₁–C₇–N, C₁–C₇–N–C₈, and C₇–N–C₈–C₉), one torsion angle associated with the H-bond (C₂–O–N–C₇), and one torsion angle describing the global torsion of the molecule (C₂–C₁–C₈–C₉). Like previously, only DFT and DFT-D* results are discussed (Fig. 4.4a and 4.4b, respectively). The absolute errors on the valence angles are within the $[-2^\circ; 2^\circ]$ range for all XCFs and both types of DFT levels ($\sim 2^\circ$ of relative error). Then, for the torsion angles, in the case of DFT without dispersion, they are systematically underestimated, except for ω B97X. Furthermore, the error on



(a)



(b)



(c)

Figure 4.2: Differences (in %) between the optimized unit cell parameters and the XRD values as a function of the XCF, $\Delta = [X(\text{Calc.}) - X(\text{XRD})]/X(\text{XRD})$: (a) with DFT; (b) with DFT-D*; and (c) with DFT-D2. The XRD values are given on the top of each figure. The 6-31G(d,p) basis set was employed for all calculations.

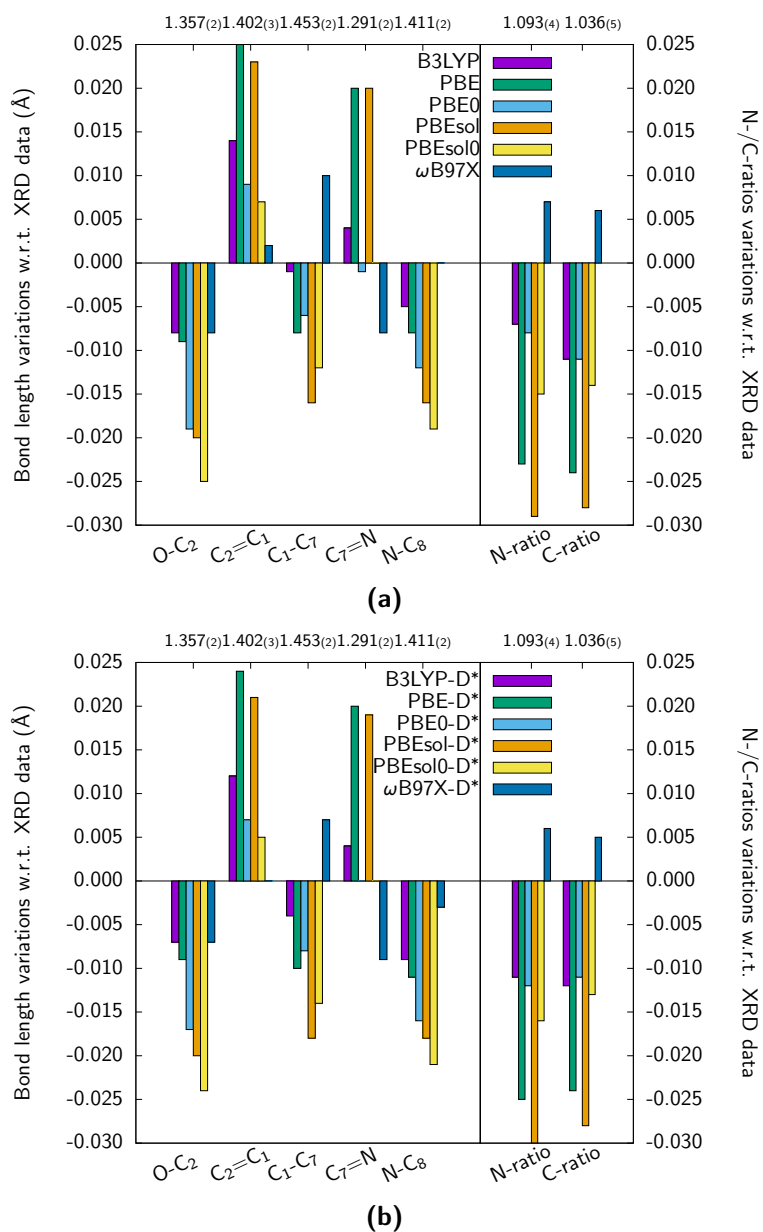


Figure 4.3: Differences between the bond lengths of the optimized structure and of the XRD data as a function of the XRD, $\Delta = [d(\text{DFT}) - d(\text{XRD})]$: (a) with DFT and (b) with DFT-D*. The XRD values are given on the top of each figure. The 6-31G(d,p) basis set was employed for all calculations.

the molecular torsion (angle $C_2-C_1-C_8-C_9$) and, to a smaller extent on the angle $C_7-N-C_8-C_9$, is quite large for those XCFs that poorly perform for the unit cell parameters (with errors ranging between -5.7° and -10.5° for B3LYP, PBE, and PBE0) whereas for the other XCFs (PBEsol, PBEsol0, and ω B97X), the deviations are much smaller: -3.1° , -3.1° , and -1.0° , respectively. This highlights the key role of the torsion angles on the unit cell parameters or, in other words, their interdependence. It is however difficult to tell which one is the driving force and creates a bias on the other quantity.

When using the DFT-D* model, the amplitude of the errors is greatly reduced compared to standard DFT, in particular for B3LYP, PBE, and PBE0. Note that the scale of Fig. 4.4a for DFT goes from -12 to 4° while that of Fig. 4.4b for DFT-D*, from -2 to 4° . For DFT-D*, the errors on the torsion angles are mainly positive, except for the $C_1-C_7-N-C_8$ angle. For the important molecular torsion ($C_2-C_1-C_8-C_9$), the error is around 1° for all XCFs, except for PBE0 ($<1^\circ$) and ω B97X (2°), which is on par with the errors of PBEsol, PBEsol0, and ω B97X with DFT for the same angle. Accurate molecular torsions are obtained in parallel with accurate unit cell parameters but the molecular torsion is not the only criterion to satisfy.

4.3.2 Keto-Enol Energies

After investigating the geometrical structures, the effect of these methods on the relative energy of the keto and enol forms is analyzed (Table 4.2). Experimentally, only the enol form of PYV3 is observed both at low and room temperatures by XRD, *i.e.* the enol form (E) is more stable than the keto one (K). The relative energy, $\Delta E_{KE} = E(K) - E(E)$, is thus expected to be positive. Table 4.2 shows the relative energies computed with the selected XCFs. Although ΔE_{KE} varies significantly depending on the XCF, all DFT values are positive, ranging from 3 to 13 kJ/(mol of asymmetric unit), in agreement with experiment. When adding dispersion energy, the keto form is more stabilized than the enol one so that the relative ΔE_{KE} energy gets less positive, if not negative like in the case of PBE and PBEsol [-2.5 and -2.7 kJ/(mol asym. unit) for DFT-D2 and -1.3 and -1.9 kJ/(mol asym. unit) for DFT-D*, respectively]. Since we know from experiment that ΔE_{KE} is positive, these two XCFs are not considered any further. DFT-D2 values, ranging from 2.7 to 10.2 kJ/(mol asym. unit), vary little from the DFT-D* ones (ranging from 3.4 to 9.9 kJ/(mol asym. unit)). Still, as expected, the dispersion energies obtained with DFT-D2 are larger than with DFT-D*, which favors the keto form thus decreasing the relative energy ΔE_{KE} (with the exception of ω B97X). The K/E Boltzmann distributions at 298.15 K are then analyzed to further quantify the effects of the dispersion energy. In the case of ω B97X, barely no change is observed, with keto population increasing from 1 % with DFT to 2 % with DFT-D2/D*. The effects are much larger for the other functionals, and they correspond to at least a 10 % increase of the keto form upon adding dispersion, *i.e.* from 1 % to 14 % for PBE0, from 3 % to

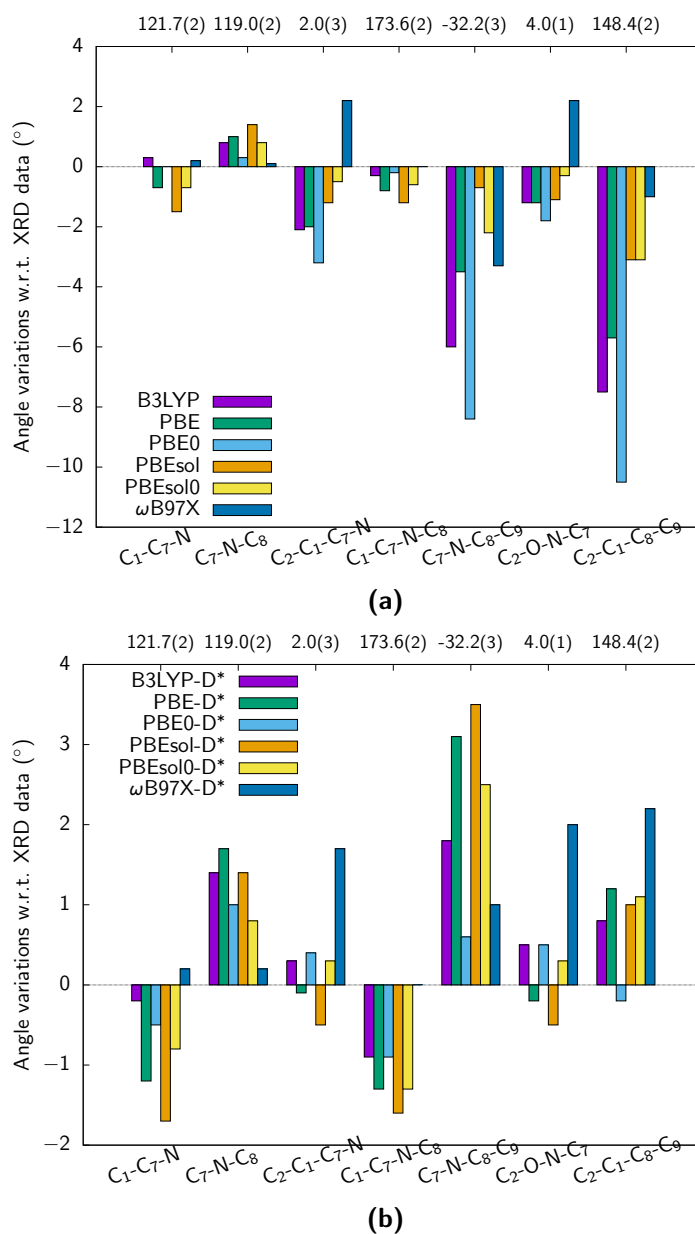


Figure 4.4: Differences between the angles of the optimized structure and of the XRD data as a function of the XCF, $\Delta = [a(\text{DFT}) - a(\text{XRD})]$: (a) with DFT and (b) with DFT-D*. The XRD values are given on the top of each figure. The 6-31G(d,p) basis set was employed for all calculations.

25 % for B3LYP, and from 5 % to 20 % for PBEsol0.

Table 4.2: Keto-enol energy differences [$\Delta E_{KE} = E(K) - E(E)$, in kJ/(mol asym. unit)] as calculated with different XCFs for PYV3. The percentage of keto calculated using Boltzmann's distribution at 298.15 K is given in parentheses. The 6-31G(d,p) basis set was employed in all calculations.

Method	DFT	DFT-D2	DFT-D*
B3LYP	8.3 (3 %)	2.7 (25 %)	3.4 (20 %)
PBE	2.6 (26 %)	-2.5 (73 %)	-1.3 (63 %)
PBE0	11.0 (1 %)	4.5 (14 %)	5.3 (11 %)
PBEsol	1.0 (40 %)	-2.7 (75 %)	-1.9 (68 %)
PBEsol0	7.1 (5 %)	3.4 (20 %)	4.0 (17 %)
ω B97X ¹	12.9 (1 %)	10.2 (2 %)	9.9 (2 %)

¹ TOLINTEG = 7 7 7 7 16

4.4 Conclusions

Density functional theory has been challenged for the geometry optimization of molecular switches in their solid crystalline state. By performing comparisons with X-ray diffraction (XRD) data, a recent contribution¹⁰ has demonstrated that HSEsol,¹² PBEsol0, and ω B97X¹¹ can already be effective but, in this work, one has questioned whether the addition of empirical dispersion energy, as proposed by Grimme,¹³ could not further improve these results. First, we have shown that the use of the original dispersion parameters (DFT-D2) overcontracts the unit cell for the selected XCFs (B3LYP,¹⁶ PBE,¹⁷ PBE0,¹⁸ PBEsol,¹⁹ PBEsol0, and ω B97X). On the other hand, the down-scaled parameters proposed for the solid state (DFT-D*)¹⁴ decrease this effect so that the B3LYP, PBE, and PBE0 XCFs achieve, for the unit cell volume, a rather good agreement with XRD data, though, mostly due to error compensations. Looking at the molecular geometries, the main conclusions are i) the inclusion of dispersion energy has almost no effect on the bond lengths, though systematically underestimating (overestimating) the length of the single (double) bonds, with the maximum difference between DFT and DFT-D* attaining 0.003 Å; ii) the valence angles are also barely affected when using DFT-D* compared to DFT with relative errors with respect to XRD data of 2 % or less in both cases; and iii) in the case of the torsion angles, the use of DFT-D* XCFs improves the results since the variations with respect to XRD data are less spread out. The average errors with DFT-D* are of the order of 1° whereas with the DFT ones, only the PBEsol, PBEsol0, and ω B97X XCFs perform well. This means that an accurate description of the unit cell parameters leads to accurate molecular torsions but that accurate molecular torsions do not constitute a sufficient condition to fully describe the

intermolecular interactions, and to reproduce the XRD unit cell. Finally, for all XCFs, the relative keto-enol energies ΔE_{KE} have been calculated, showing that the inclusion of dispersion stabilizes more the keto form than the enol one. As a consequence, the PBE and PBEsol XCFs incorrectly predict that the keto form is the most stable. On the other hand, with the exception of ω B97X, the other functionals predict a decrease of ΔE_{KE} but it remains positive. All these results and conclusions tend to argue that the PBEsol0 and ω B97X XCFs are reliable to predict molecular crystal structures and that there is no clear advantage of using empirical energy dispersion corrections as they were originally proposed¹³ or later reparameterized for solids.¹⁴

Acknowledgments

This work was carried out thanks to funding of "Actions de Recherche Concertées" (ARC) de la Direction générale de l'Enseignement non obligatoire et de la Recherche scientifique - Direction de la Recherche scientifique - Communauté française de Belgique, under convention No.15/20-068. This research used resources of the "Plateforme Technologique de Calcul Intensif (PTCI)" (<http://www.ptci.unamur.be>) located at the University of Namur, Belgium, which is supported by the F.R.S.-FNRS under the convention No. 2.5020.11. The PTCI is a member of the "Consortium des Équipements de Calcul Intensif (CÉCI)" (<http://www.ceci-hpc.be>). The authors thank Andrea Carletta for our discussions.

Bibliography

- (1) *Organic Photochromic and Thermochromic Compounds*; Crano, J. C., Guglielmetti, R. J., Eds.; Plenum: New York, NY, 1998.
- (2) Kawata, S.; Kawata, Y. Three-Dimensional Optical Data Storage Using Photochromic Materials. *Chem. Rev.* **2000**, *100*, 1777–1788.
- (3) Hadjoudis, E.; Mavridis, I. M. Photochromism and Thermochromism of Schiff Bases in the Solid State: Structural Aspects. *Chem. Soc. Rev.* **2004**, *33*, 579–588.
- (4) Amimoto, K.; Kawato, T. Photochromism of Organic Compounds in the Crystal State. *J. Photochem. Photobiol. C Photochem. Rev.* **2005**, *6*, 207–226.
- (5) *Molecular Switches*; Feringa, B. L., Browne, W. R., Eds.; Wiley-VCH Verlag GmbH & Co. KGaA: Weinheim, Germany, 2011, DOI: 10.1002/9783527634408.
- (6) *Tautomerism: Methods and Theories*; Antonov, L., Ed.; Wiley-VCH: 2013.

- (7) *Tautomerism: Concepts and Applications in Science and Technology*; Antonov, L., Ed.; WILEY-VCH: 2016.
- (8) Padalkar, V. S.; Seki, S. Excited-State Intramolecular Proton-Transfer (ESIPT)-Inspired Solid State Emitters. *Chem. Soc. Rev.* **2016**, *45*, 169–202.
- (9) Ruggiero, M. T.; Gooch, J.; Zubietta, J.; Korter, T. M. Evaluation of Range-Corrected Density Functionals for the Simulation of Pyridinium-Containing Molecular Crystals. *J. Phys. Chem. A* **2016**, *120*, 939–947.
- (10) Quertinmont, J.; Carletta, A.; Tumanov, N. A.; Leyssens, T.; Wouters, J.; Champagne, B. Assessing density functional theory approaches for predicting the structure and relative energy of salicylideneaniline molecular switches in the solid state. *J. Phys. Chem. C* **2017**, *121*, 6898–6908, DOI: 10.1021/acs.jpcc.7b00580.
- (11) Chai, J.-D.; Head-Gordon, M. Systematic Optimization of Long-Range Corrected Hybrid Density Functionals. *J. Chem. Phys.* **2008**, *128*, 084106, DOI: 10.1063/1.2834918.
- (12) Schimka, L.; Harl, J.; Kresse, G. Improved Hybrid Functional for Solids: The HSEsol Functional. *J. Chem. Phys.* **2011**, *134*, 024116.
- (13) Grimme, S. Semiempirical GGA-type Density Functional Constructed with a Long-Range Dispersion Correction. *J. Comput. Chem.* **2006**, *27*, 1787–1799, DOI: 10.1002/jcc.20495.
- (14) Civalieri, B.; Zicovich-Wilson, C. M.; Valenzano, L.; Ugliengo, P. B3LYP augmented with an empirical dispersion term (B3LYP-D*) as applied to molecular crystals. *CrystEngComm* **2008**, *10*, 405–410, DOI: 10.1039/B715018K.
- (15) Dovesi, R.; Orlando, R.; Erba, A.; Zicovich-Wilson, C. M.; Civalieri, B.; Casassa, S.; Maschio, L.; Ferrabone, M.; De La Pierre, M.; D'Arco, P.; Noël, Y.; Causà, M.; Rérat, M.; Kirtman, B. CRYSTAL14: a Program for the Ab Initio Investigation of Crystalline Solids. *Int. J. Quantum Chem.* **2014**, *114*, 1287–1317.
- (16) Stephens, P. J.; Devlin, F. J.; Chabalowski, C. F.; Frisch, M. J. Ab Initio Calculation of Vibrational Absorption and Circular Dichroism Spectra using Density Functional Force Fields. *J. Phys. Chem.* **1994**, *98*, 11623–11627.
- (17) Perdew, J. P.; Burke, K.; Ernzerhof, M. Generalized Gradient Approximation Made Simple. *Phys. Rev. Lett.* **1996**, *77*, 3865–3868.
- (18) Adamo, C.; Barone, V. Toward Chemical Accuracy in the Computation of NMR Shieldings: the PBE0 Model. *Chem. Phys. Lett.* **1998**, *298*, 113–119.

- (19) Perdew, J. P.; Ruzsinszky, A.; Csonka, G. I.; Vydrov, O. A.; Scuseria, G. E.; Constantin, L. A.; Zhou, X.; Burke, K. Restoring the Density-Gradient Expansion for Exchange in Solids and Surfaces. *Phys. Rev. Lett.* **2008**, *100*, 136406.
- (20) Feller, D. The Role of Databases in Support of Computational Chemistry Calculations. *J. Comput. Chem.* **1996**, *17*, 1571–1586.
- (21) Schuchardt, K. L.; Didier, B. T.; Elsethagen, T.; Sun, L.; Gurumoorthi, V.; Chase, J.; Li, J.; Windus, T. L. Basis Set Exchange: A Community Database for Computational Sciences. *J. Chem. Inf. Model.* **2007**, *47*, 1045–1052.
- (22) Carletta, A.; Buol, X.; Leyssens, T.; Champagne, B.; Wouters, J. Polymorphic and Isomorphic Cocrystals of a N-Salicylidene-3-aminopyridine with Dicarboxylic Acids: Tuning of Solid-State Photo- and Thermochromism. *J. Phys. Chem. C* **2016**, *120*, 10001–10008.

PERIODIC DFT STUDY OF THE EFFECTS OF CO-CRYSTALLIZATION ON A N-SALICYLIDENEANILINE MOLECULAR SWITCH

CHEMPHYSCHEM 2019, 20, 2434-2442

Jean Quertinmont[†], Tom Leyssens[‡], Johan Wouters[†], & Benoît Champagne[†]

[†] *Unité de Chimie Physique Théorique et Structurale, Chemistry Department, University of Namur, 61 rue de Bruxelles, B-5000 Namur, Belgium*

[‡] *Institute of Condensed Matter and Nanosciences, Université Catholique de Louvain, 1 Place Louis Pasteur, B-1348 Louvain-La-Neuve, Belgium*

All calculations, their analysis, and the writing of the first draft were performed by J.Q. The discussion on the torsion of the anil was added post publication and the scheme 5.2 was edited in consequence.

Abstract

This work aims at better understanding the complex effects of co-crystallization on a single salicylideneaniline molecular switch, (E)-2-methoxy-6-(pyridine-3-yliminomethyl)phenol (PYV3), which can tautomerize between an enol and a keto form. A combination of periodic boundary conditions DFT and molecular wavefunction calculations has been adopted for examining a selection of PYV3 co-crystals, presenting hydrogen bonds (H-bonds) or halogen bonds (X-bonds), for which X-ray diffraction data are available. Three aspects are targeted: i) the energy (H-bond strength, enol to keto relative energy, and geometry relaxation energies), ii) the geometrical structure (PYV3 to co-crystal and enol to keto geometrical variations), and iii) the electron distribution (PYV3 to co-crystal and enol to keto Mulliken charge variations). These allow i) explaining the preference for forming H-bonds with the nitrogen of the pyridine of PYV3 with respect to the oxygens and the importance of the crystal field, ii) distinguishing the peculiar behavior of the SulfonylDiPhenol (SDP) coformer, which stabilizes the keto form of PYV3, iii) describing the relative stabilization of the enol form upon co-crystallization (with the exception of SDP) and therefore iv) substantiating the co-crystallization-induced reduction of thermochromism observed for several PYV3 co-crystals.

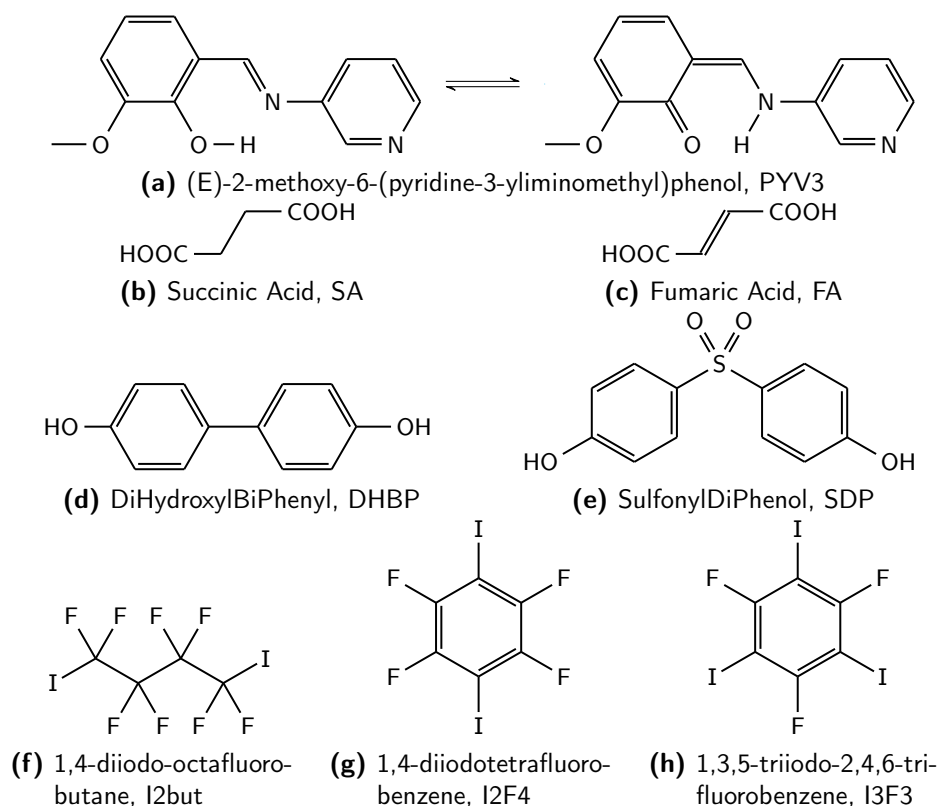
5.1 Introduction

In order to tune solid state properties of organic and inorganic compounds, many methods have been developed, such as doping^{1–4} or substitution.^{5–9} Among them, co-crystallization, *i.e.* the crystallization of at least two different compounds together, is studied in both medicinal^{10–13} and materials science.^{14–20} For the latter, it has been used to optimize optical properties such as absorption,¹⁶ fluorescence,¹⁹ phosphorescence,^{14,20} and second harmonic generation.^{15,17,18} Although any non-bonded interaction can be used to generate co-crystals (e.g. π - π stacking, Coulombic interactions, etc), directional interactions —hydrogen and halogen bonds (denoted H-bonds and X-bonds, respectively)— allow for a better control over the interactions found in the resulting co-crystals. Previously, some of us have shown experimentally that co-crystallization affects the thermo- and photochromic behaviors of N-salicylideneanilines (or anils), depending on the coformer (the secondary compound).^{21–23} Anils are dynamical compounds, whose color changes when triggered by external stimuli.^{24–26} They are able to switch between an enol (E) and a keto (K) form and each ought to be affected differently by the coformer. This work aims at evaluating and understanding the influence of the two classes of coformers, those forming H-bonds and those making X-bonds by employing quantum chemistry methods and by focusing on the relative energies, the geometries, and the Mulliken charges of a selected anil, (E)-2-methoxy-6-(pyridine-3-yliminomethyl)phenol (PYV3, see Scheme 5.1a). The H-bond coformers, succinic acid (SA), fumaric acid (FA), dihydroxybiphenyl (DHBP), and sulfonyldiphenol (SDP), are shown Schemes 5.1b, c, d, and e, respectively. The X-bond coformers are 1,4-diiodo-octafluorobutane (I2but), 1,4-diiodotetrafluorobenzene (I2F4), and 1,3,5-triiodo-2,4,6-trifluorobenzene (I3F3), and are given in Schemes 5.1f, g, and h, respectively.

This paper is organized as follows. In the next Section, the computational details are described. Section 5.3 first analyzes the two H-bond interaction sites of PYV3. Then, the effect of co-crystallization on the energies is broken down, followed by its geometrical changes and the analysis of the Mulliken charges, before ending with the conclusions.

5.2 Methods and Computations

Full geometry optimizations (including of the unit cell parameters) and total energy calculations were performed with the CRYSTAL14 package²⁷ using periodic boundary conditions (PBC) with density functional theory (DFT). Charge distribution calculations were carried out with the latest CRYSTAL17 package.²⁸ As we have shown in previous works (see Ref. [29] and [30]), the PBEsol0 exchange-correlation functional (XCF) (based on PBEsol³¹ with 25 % of exact exchange) in combination with Pople's 6-31G(d,p) basis set (as taken from Basis Set Exchange^{32,33}) is an efficient method to reproduce the unit cell parameters

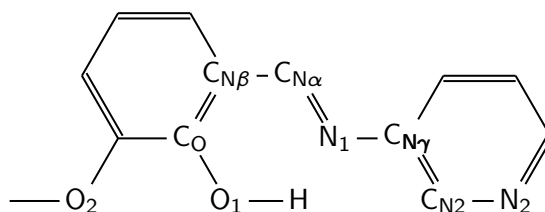


Scheme 5.1: Structures of the compound and coformers under investigation, (a) anil and its enol-keto equilibrium; coformers interacting by H-bonding (b)-(e) or X-bonding (f)-(h).

and molecular geometry of salicylideneanilines as obtained by single crystal X-ray diffraction. The PBEsol0 XCF does not require adding empirical dispersion corrections to perform well since it has been tailored to crystals (see Ref. [30] for more details on that particular issue and Ref. [31] for the details on the elaboration of the PBEsol0 XCF). Iodine atoms were described with the LANL2DZ effective core potential and basis set, as taken from Basis Set Exchange.^{32,33} The default convergence parameters were used with a shrinking factor of the irreducible Brillouin zone of 6 (yielding between 64 and 112 k-points of integration) and tolerance criteria for the exchange and correlation integrals (TOLINTEG keyword) of "8 8 8 8 16". More details on the CRYSTAL14 calculations are given in Ref. [29]. Note that these calculations deal with the limiting or pure forms of the anils, where 100 % of the molecules adopt the enol or the keto form. So, these PBC calculations do not account for disorder or for any dynamical effects. Gas phase potential energy scans were generated and analyzed with the DRAW-MOL suite³⁴ and performed at the MP2/aug-cc-pVDZ level of approximation using the GAUSSIAN16 package.³⁵

5.3 Results and Discussion

The combination of PYV3 with the 7 selected coformers (see Scheme 5.1) has yielded 8 co-crystals, for which Figure 5.1 shows the main intermolecular interaction(s) between PYV3 and each coformer. The asymmetric units are composed of one molecule of PYV3 and one coformer, except I3F3. In the later case, it contains two molecules of PYV3 and one molecule of coformer: one PYV3 interacts through both the N₂ and the O₁ and O₂ atoms (I3F3-O), while the second PYV3 interacts only through N₂ (I3F3-N) (see Scheme 5.2 for the atom numbering and Figure 5.1h for the representation of I3F3-N/-O). In all cases, the nitrogen of the pyridine moiety (N₂) interacts with the coformer either by H-bonding or by X-bonding. Fumaric acid yielded two polymorphic co-crystals, noted FA1 and FA2, the former being isostructural to the SA co-crystal. The second and last stand-out co-crystal is SDP as it interacts through both the N₂ nitrogen and the O₁ and O₂ oxygen atoms. Comparing the optimized structures with the single crystal X-ray diffraction (XRD) data (taken from the Cambridge Structural Database,³⁶ CSD refcodes EDEQAG01 (PYV3), IRALUK (PYV3·FA 1), IRALUK01 (PYV3·FA 2), IRAMEV (PYV3·SA), JOBROK (PYV3·DHBP), JOBRUQ (PYV3·SDP), NINMAB (PYV3·I2but), SEDFIT (PYV3·I2F4), and NINPIM (PYV3·I3F3)), the root mean square deviation averaged over all crystals amounts to 0.398 Å (2.7 %) for the unit cell lengths, 1.90° (2.0 %) for the unit cell angles, and 29.0 Å³ (1.9 %) for the unit cell volumes. The averaged RMSD on the bond lengths that do not contain hydrogen atom amounts to 0.013 Å. Overall, the optimized structures are in good agreement with experiment and the performance of the method is consistent with our recent investigations.^{29,30}



Scheme 5.2: Atom numbering of PYV3.

5.3.1 Interaction Sites of PYV3

All coformers interact with the N₂ atom of PYV3 while only two interact with its oxygens. To elucidate the situation observed for H-bonding systems, a molecule of hydrofluoric acid, H–F (bond length sets to 0.917 Å), was used as a rigid probe to compare both interaction sites (Figure 5.2a). The geometry of PYV3 was kept fixed to the one obtained from its crystal optimization geometry. Figure

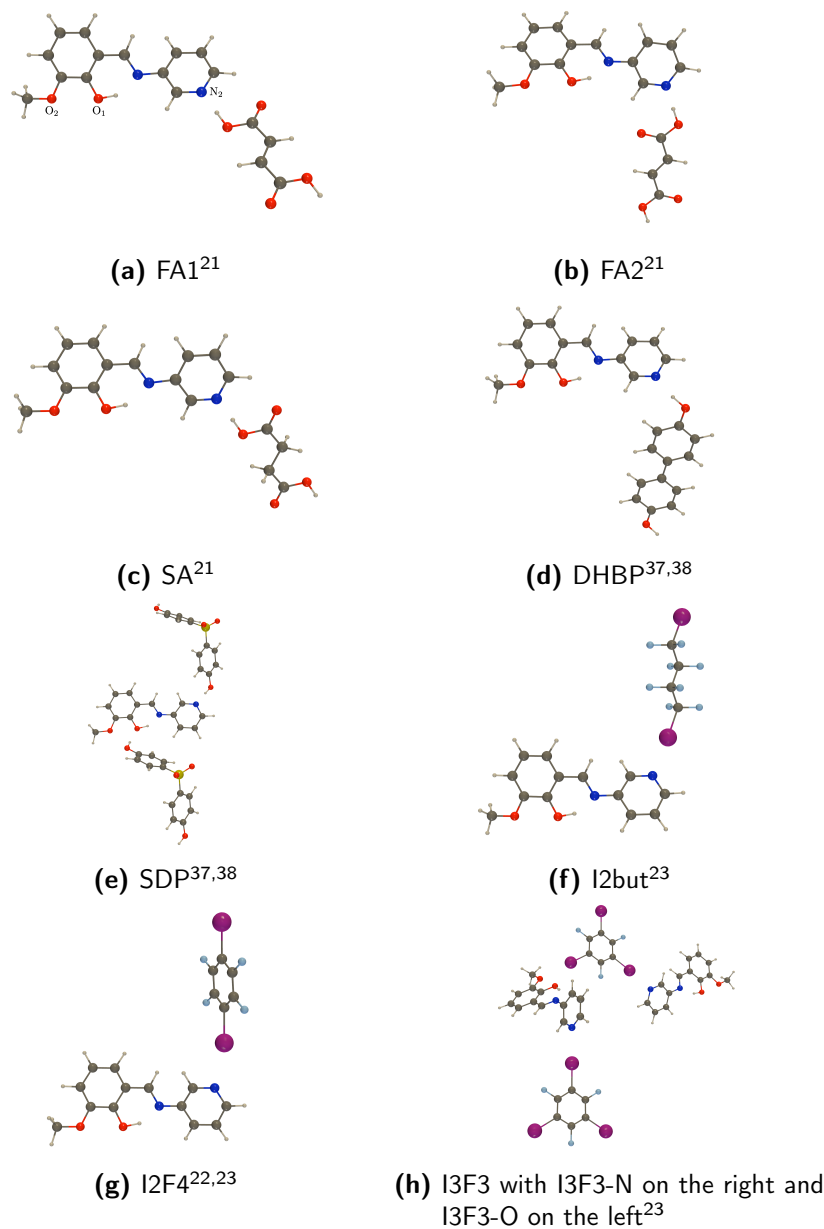


Figure 5.1: Representation of the PYV3-coformer synthons as extracted from the co-crystal structure optimized at the PBC/PBEsol0/6-31G(d,p)/I(LANL2DZ) level of approximation. The enol form was considered for all co-crystals. The corresponding references to the X-ray diffraction structures are also provided.

5.2b shows the $N_2 \cdots HF$ scans for both the enol and keto forms while Figures 5.2c and 5.2d show the corresponding 2D scans for the oxygens, respectively. On the N_2 scans, both the enol and keto forms have their minimum at 1.74 Å. The stabilization energy for the enol amounts to 52 kJ mol^{-1} while for the keto form, it is slightly smaller, by 3 kJ mol^{-1} . For both the enol and keto forms, the probe molecule interacts more strongly with the oxygen involved in the intramolecular H-bond, O_1 , than the one from the methoxy group, O_2 . Consequently, for the enol form, the minimum on the potential energy surface is characterized by a O_1-H distance of 1.81 Å, in comparison to 2.60 Å for O_2-H . For the keto form, the first distance gets even smaller with a d_{O_1-H} value of 1.72 Å while $d_{O_2-H} = 2.63$ Å. Thus, for the keto, the HF probe gets closer to O_1 (by 0.09 Å) and further to O_2 (by 0.03 Å), and subsequently, its stabilization energy gets larger than for the enol, -54 kJ mol^{-1} vs. -42 kJ mol^{-1} . Comparing both acceptor sites, for the enol form, the interaction with the probe is stronger with the nitrogen than with the oxygen pair, by 10 kJ mol^{-1} . By opposition, in the case of the keto, the H-bonding with the oxygens leads to more stable situations than with the nitrogen, by 15 kJ mol^{-1} . The same conclusions can be drawn for the X-bond interactions (probed with CF_3I , see Figure B.1 in the Supporting Information): the enol form favors the interaction on N_2 with respect to the oxygens (by 5 kJ mol^{-1}) while it is the opposite for the keto form (by 7 kJ mol^{-1}).

5.3.2 Relative Energy of the Enol and Keto Forms

The accurate determination of the correct enol/keto proportion remains an important challenge as shown by some of us in a study focusing on the evaluation of the enol/keto ratio in solution by combining TDDFT simulations of absorption spectra with experiment (Ref [39]). Table 5.1 shows the enol to keto relative energies per asymmetric unit, $\Delta E_{EK}^{as.u.} = [E_K^{cell} - E_E^{cell}]/[\text{number of as.u. per cell}]$, for PYV3 and its co-crystals (as obtained after crystal geometry optimization). With the exception of PYV3-SDP, the enol crystals are more stable than the keto ones: $\Delta E_{EK}^{as.u.} > 0$. Then, the switching process requires more energy for the co-crystals than for the PYV3 crystal (ignoring the kinetics): $\Delta E_{EK}^{as.u.}[\text{co-crystals}] > \Delta E_{EK}^{as.u.}[\text{PYV3}]$, highlighting the role of the cofomer to stabilize the enol form and/or destabilize the keto one. These results are in agreement with the experimental evidence that the thermochromism is reduced in FA1, FA2, and SA.²¹ For SDP, the keto co-crystal is more stable than the enol one, by 15 kJ mol^{-1} , in agreement with XRD data where the major observed form is the keto at both low (105(2) K) and room (293(2) K) temperatures.³⁷ $\Delta E_{EK}^{as.u.}$ of FA2 is smaller by a marginal amount, 0.5 kJ mol^{-1} , with respect to FA1. Another noticeable value is that of I3F3 with the largest $\Delta E_{EK}^{as.u.}$ (31.1 kJ mol^{-1}), which also corresponds to the asymmetric unit containing not one but two PYV3 (so two PYV3 enols are switching to the keto form). In this particular case, the average switching energy per chromophore is 15.5 kJ mol^{-1} which is well within the trend of the other co-crystals.

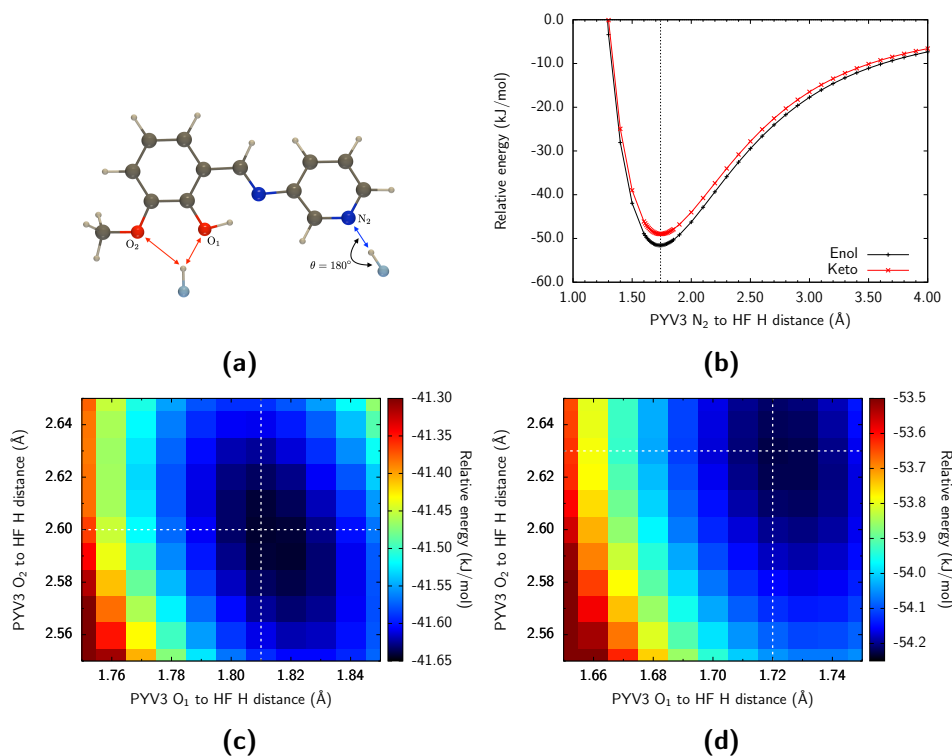


Figure 5.2: Potential energy scans for the PYV3[PYV3]...H-F complex using a H-F molecule as a probe, computed at MP2/aug-cc-pVDZ level of approximation. (a) sketch of the molecules and interactions with H-F for the N₂ (along the blue arrow) and O₁ and O₂ (along the red arrows); (b) N₂...HF potential energy scans, for the enol, the minimum is at (1.74 Å, -51.6 kJ mol⁻¹) while for the keto, at (1.74 Å, -49.0 kJ mol⁻¹); (c) O₁...HF and O₂...HF 2D potential energy scans for the enol form, minimum at (1.81 Å, 2.60 Å, -41.6 kJ mol⁻¹) and (d) for the keto form, minimum at (1.72 Å, 2.63 Å, -54.2 kJ mol⁻¹).

In order to understand the effect of the coformer on the PYV3 E/K equilibrium, additional single point calculations were performed on the isolated PYV3 species using its geometries in the crystals. First, the gas phase enol to keto relative energy, $\Delta E_{EK}^{\text{isolated}} = E_K^{\text{isolated}} - E_E^{\text{isolated}}$, was computed at the PBEsol0/6-31G(d,p) level of approximation. For PYV3, the $\Delta E_{EK}^{\text{isolated}}$ is much larger than $\Delta E_{EK}^{\text{as.u.}}$, showing the role of the crystal field and of the interactions in better stabilizing the keto form than the enol one. The same trend is observed for the co-crystals with a noticeable difference for PYV3-SDP for which $\Delta E_{EK}^{\text{isolated}}$ is smaller, by about 10 kJ mol^{-1} , but favoring the enol form, contrary to what is observed in the co-crystal.

In addition to the effect on the E/K equilibrium, co-crystallization also impacts the geometry of PYV3, either because the crystal packing is different from the pure PYV3 crystal or because of the PYV3-coformer interactions. Thus, the energy of geometrical relaxation, ΔE^{relax} , when PYV3 (in its E or K form) goes from its geometry in the PYV3 crystal (PYV3[PYV3]) to its geometry in the different co-crystals (PYV3[co-crystal]) was calculated. It reads:

$$\Delta E_E^{\text{relax}} = E_E^{\text{isolated}}(\text{PYV3[co-crystal]}) - E_E^{\text{isolated}}(\text{PYV3[PYV3]}) \quad (5.1)$$

$$\Delta E_K^{\text{relax}} = E_K^{\text{isolated}}(\text{PYV3[co-crystal]}) - E_K^{\text{isolated}}(\text{PYV3[PYV3]}). \quad (5.2)$$

$\Delta\Delta E_{EK}^{\text{relax}}$ is then defined as their differences:

$$\Delta\Delta E_{EK}^{\text{relax}} = \Delta E_K^{\text{relax}} - \Delta E_E^{\text{relax}}. \quad (5.3)$$

All these values are given in Table 5.1 and summarized in Figure B.2 (see the supporting information). The $\Delta E_E^{\text{relax}}$ values highlight the systematic stabilization of the enol form when it switches from its geometry in the crystal to its geometry in the co-crystal, except for the SDP co-crystal. For the keto form, this modification of geometry can be accompanied either by a destabilization or a stabilization but in the latter case, always by a smaller amount than for the enol. This leads to positive $\Delta\Delta E_{EK}^{\text{relax}}$ values, again, except for SDP, for which the enol is destabilized and the keto stabilized. Thus, taking the PYV3 crystal as reference, its $\Delta E_{EK}^{\text{isolated}}$ value of 37 kJ mol^{-1} slightly increases when it adopts its co-crystal geometry (except with SDP). This appears to be related to the stronger geometry relaxation of the E vs. K forms. This foresees, qualitatively, the increase of $\Delta E_{EK}^{\text{as.u.}}$ from PYV3 to its co-crystals. On the other hand, for SDP, there is a clear stabilization of the keto vs. the enol form and the results show that it originates from an increase of the enol form energy when PYV3 adopts its co-crystal geometry.

5.3.3 Geometry Variations upon Enol-Keto Transformation

Table 5.2 lists the PYV3 bond lengths and intramolecular H-bond angle as well as their variations upon co-crystallization for both the enol and keto forms. Our

Table 5.1: Crystal enol to keto relative energies per asymmetric unit (as.u.), $\Delta E_{EK}^{\text{as.u.}} = (E_K^{\text{cell}} - E_E^{\text{cell}})/(\text{number of as.u. per cell})$. Isolated enol to keto relative energies, $\Delta E_{EK}^{\text{isolated}} = E_K^{\text{isolated}} - E_E^{\text{isolated}}$, geometry relaxation energies from PYV3[PYV3] to PYV3[co-crystal] for the enol and keto forms, $\Delta E_E^{\text{relax}} = E_E^{\text{isolated}}(\text{PYV3[co-crystal]}) - E_E^{\text{isolated}}(\text{PYV3[PYV3]})$ and $\Delta E_K^{\text{relax}} = E_K^{\text{isolated}}(\text{PYV3[co-crystal]}) - E_K^{\text{isolated}}(\text{PYV3[PYV3]})$, and their differences, $\Delta\Delta E_{EK}^{\text{relax}} = \Delta E_K^{\text{relax}} - \Delta E_E^{\text{relax}}$. All values were obtained at the PBC/PBEsol0/6-31G(d,p)/I(LANL2DZ) level of approximation and are given in kJ mol^{-1} .

		$\Delta E_{EK}^{\text{as.u.}}$	$\Delta E_{EK}^{\text{isolated}}$	$\Delta E_E^{\text{relax}}$	$\Delta E_K^{\text{relax}}$	$\Delta\Delta E_{EK}^{\text{relax}}$
Crystal	PYV3	7.1	36.8	0.0	0.0	0.0
Co-crystals	SA	18.2	41.4	-6.2	-1.5	4.7
	FA1	18.2	41.2	-6.5	-2.1	4.4
	FA2	17.7	39.5	-0.1	2.7	2.8
	DHBP	12.7	41.0	-4.2	0.1	4.2
	SDP	-15.3	29.0	7.2	-0.6	-7.8
	I2but	12.5	43.6	-4.4	2.4	6.9
	I2F4	12.2	41.4	-1.2	3.5	4.6
	I3F3	31.1	—	—	—	—
	I3F3-N	—	37.2	-4.7	-4.3	0.5
	I3F3-O	—	40.7	-11.3	-7.3	3.9

aim consists in highlighting the key geometrical changes that could explain the ΔE^{relax} values discussed in the previous paragraph.

Starting from the enol forms, SA and FA1 are identically affected, *e.g.* the $\text{O}_1\text{--H}$ and the H-bond angle ($\text{O}_1\text{--H}\cdots\text{N}_1$) get smaller (-0.02 \AA and -2.2° , respectively) while $\text{N}_1\cdots\text{H}$ and $\text{O}_1\cdots\text{N}_1$ are larger by 0.09 \AA and 0.06 \AA , respectively. Variations of similar amplitude are obtained for I3F3-O, despite the supplementary interaction on O_1 and O_2 . A stronger covalent $\text{O}_1\text{--H}$ bond stabilizes the enol form, consistently with the negative $\Delta E_E^{\text{relax}}$ values obtained for these crystals (SA and FA1: -6 kJ mol^{-1} , I3F3-O: -11 kJ mol^{-1}). In FA2, the $\text{N}_1\cdots\text{H}$ and $\text{O}_1\cdots\text{N}_1$ distances also get shorter but the variations are smaller (-0.02 \AA) with negligible change of the $\text{O}_1\text{--H}$ bond length. In addition, $\text{O}_1\text{--C}_\text{O}$ is shorter by less than 0.01 \AA and $\text{C}_\text{O}\text{--C}_\text{N}\beta$ is larger by about the same amount. These latter changes are consistent with an increased keto character with respect to PYV3, balanced by a strong H-bond, leading to almost negligible stabilization (-0.1 kJ mol^{-1}). SDP co-crystal displays an even shorter $\text{N}_1\cdots\text{H}$ bond length than FA2, characterized by variations of -0.03 \AA with respect to -0.02 \AA and the $\text{O}_1\cdots\text{N}_1$ distance further decreases (-0.02 \AA), in addition to a longer $\text{O}_1\text{--H}$ bond (0.02 \AA) and a shorter H-bond angle (-1.2°). The $\text{O}_1\text{--H}$ elongation and $\text{N}_1\cdots\text{H}$ shortening correspond to a displacement of the hydrogen towards the

N_1 atom and to the destabilization of the enol form ($\Delta E_E^{\text{relax}} = 7 \text{ kJ mol}^{-1}$). Upon co-crystallization with DHBP, the $N_1 \cdots H$ and $O_1 \cdots N_1$ distances become larger by 0.03 \AA and 0.02 \AA , respectively, with a small shortening of the O_1-H bond length (-0.01 \AA). This again corresponds to a stronger enol character and a higher stability, as previously computed ($\Delta E_E^{\text{relax}} = -4 \text{ kJ mol}^{-1}$). I3F3-N is similarly modified to DHBP ($\Delta E_E^{\text{relax}} = -5 \text{ kJ mol}^{-1}$) but the elongation of the bonds is smaller (-0.02 \AA vs. -0.03 \AA for $N_1 \cdots H$ and -0.01 \AA vs. -0.02 \AA for $O_1 \cdots N_1$), as well as a slight shortening of the O_1-C_O bond (-0.01 \AA). I2but is also similar to DHBP, explaining the similar $\Delta E_E^{\text{relax}}$ value (-4 kJ mol^{-1}). Finally, I2F4 is barely affected, in agreement with the very small $\Delta E_E^{\text{relax}}$ value (-1 kJ mol^{-1}).

Concerning the geometrical variations of the keto form, in general, the carbon-carbon bonds of the enol/keto ring are more affected than in the case of the enol form. Again, SA and FA1 present similar variations upon co-crystallization: the $O_1 \cdots H$ H-bond gets longer by 0.06 \AA and, in parallel, the $O_1 \cdots N_1$ distance increases by 0.03 \AA while the angle is smaller by 3° . In addition, the $O_1=C_O$ and $C_{N\beta}=C_{N\alpha}$ bonds are shorter by 0.01 \AA and $C_{N\alpha}-N_1$ is longer by 0.01 \AA , which is consistent with a stronger keto character — although the $C_O=C_{N\beta}$ is barely increased (by less than 0.01 \AA). This corroborates the negative $\Delta E_K^{\text{relax}}$ value (-2 kJ mol^{-1}). FA2 is affected in the opposite way: the $O_1 \cdots H$ and $O_1 \cdots N_1$ distances get shorter by 0.10 \AA and 0.05 \AA , respectively, while the N_1-H bond length and the $O_1 \cdots H-N_1$ bond angle increase by 0.02 \AA and 3.0° . Unlike FA1, the FA2 non-hydrogen containing bonds are merely affected. These geometrical variations are consistent with the destabilization of the keto form of FA2 with respect to pure PYV3 ($\Delta E_K^{\text{relax}} = 3 \text{ kJ mol}^{-1}$). For DHBP, the co-crystallization has a small impact on the keto geometry since the largest bond length variation, for the $O_1 \cdots H$ bond, attains only -0.01 \AA , in agreement with the calculated relative energies (small destabilization of 0.1 kJ mol^{-1}). In the case of SDP, the geometrical changes are much larger, though $\Delta E_K^{\text{relax}}$ only amounts to -0.6 kJ mol^{-1} . Indeed, the $O_1 \cdots H$ distance increases by 0.12 \AA and the $O_1 \cdots N_1$ one by 0.05 \AA , which favors the K form. On the other hand the $C_O-C_{N\beta}$ bond is shortened by 0.01 \AA , stabilizing the enol form. This explains the small $\Delta E_K^{\text{relax}}$ value. Concerning the X-bond co-crystals, I2but and I2F4 are similarly affected: a decrease of the $O_1 \cdots H$ and $O_1 \cdots N_1$ bond lengths by 0.06 \AA and 0.03 \AA , respectively, and an increase of the N_1-H bond and $O_1 \cdots H-N_1$ angle by 0.01 \AA and 3° . I2F4 differs itself from I2but by a slightly longer $C_{N\alpha}-N_1$ bond length variation: 0.007 \AA vs. 0.004 \AA , meaning a slightly larger keto character and destabilization, as previously shown (2 kJ mol^{-1} for I2but and 3 kJ mol^{-1} for I2F4). For I3F3-N, the H-bond distances are less impacted by the co-crystallization ($O_1 \cdots H$ and $N_1-H \sim 0.02 \text{ \AA}$ or less). On the other hand, the $O_1=C_O$ bond length decreases (-0.01 \AA), which corresponds to a stabilization of the K form. Finally, I3F3-O's $O_1 \cdots H$ bond is larger by 0.02 \AA while $O_1 \cdots H-N_1$, $O_1=C_O$, and $C_{N\beta}=C_{N\alpha}$ are all smaller by 2.1° , 0.01 \AA , and 0.01 \AA , respectively. The latter changes are typical of an increased keto contribution and thus, stabilization with respect to the pure

keto PYV3, in agreement with the $\Delta E_K^{\text{relax}}$ calculation (-7 kJ mol^{-1}).

For the enol to keto bond lengths variations, all co-crystals follow the same trends as PYV3 (Figure 5.3). In particular, in the keto/enol delocalization ring ($\text{H}-\text{O}_1-\text{C}_\text{O}=\text{C}_\text{N}\beta-\text{C}_\text{N}\alpha=\text{N}_1$) single bonds shorten and double bonds lengthen. Note that the $\text{O}_1\cdots\text{N}_1$ distance decreases when going from the enol to keto form, except for SDP where it increases by 0.07 \AA (which is also consistent with the Mulliken charges, see next section). Furthermore, the amplitudes of the $\text{O}_1\cdots\text{N}_1$ shortening are much larger for the co-crystals, ranging between -0.03 \AA and -0.06 \AA , than for PYV3 with -0.01 \AA . Finally, for all crystal/co-crystals, the $\text{N}_1-\text{C}_\text{N}\gamma$ bond is very weakly impacted by the proton transfer, despite the fact that N_2 interacts with the coformer.

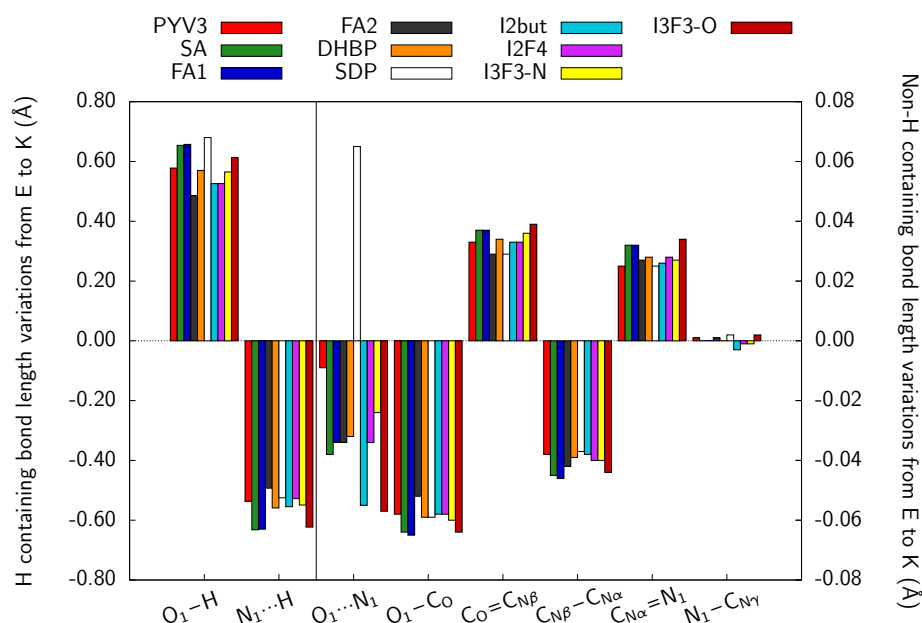


Figure 5.3: Selected bond length variations (in \AA) in PYV3 when switching from the enol to keto forms, as a function of the nature of the coformer. The geometries were obtained at the PBC/PBEsol0/6-31G(d,p)/I(LANL2DZ) level of approximation.

Table 5.2: Key bond lengths and H-bond angle for PYV3 crystal and their variations [$\Delta\alpha = \alpha(\text{co-crystal}) - \alpha(\text{PYV3})$ with α a distance or an angle] when forming co-crystals (bond lengths and bond length variations in Å; angle and angle variations in °). Large values are highlighted in bold. The geometries were obtained at the PBC/PBEsol0/6-31G(d,p)/I(LANL2DZ) level of approximation.

Enol

	PYV3	SA	FA1	FA2	DHBP	SDP	I2but	I2F4	I3F3-N	I3F3-O
O ₁ -H	1.020	-0.016	-0.015	-0.003	-0.006	0.016	-0.009	-0.005	-0.005	-0.016
N ₁ ...H	1.597	0.090	0.088	-0.023	0.026	-0.030	0.030	0.003	0.015	0.086
O ₁ ...N ₁	2.536	0.061	0.059	-0.027	0.017	-0.021	0.018	-0.002	0.007	0.052
O ₁ -H...N ₁	150.7	-2.2	-2.2	-0.4	-0.4	-1.2	-0.5	-0.1	-0.4	-2.9
O ₁ -C _O	1.332	-0.003	-0.003	-0.006	-0.001	0.004	-0.002	-0.002	-0.005	-0.006
C _O =C _{Nβ}	1.409	-0.001	-0.001	0.005	-0.001	-0.004	-0.001	-0.002	0.000	-0.001
C _{Nβ} -C _{Nα}	1.441	-0.003	-0.002	0.001	-0.003	0.000	-0.003	-0.003	-0.001	-0.002
C _{Nα} =N ₁	1.291	0.001	0.001	0.002	0.001	0.000	0.003	0.004	-0.002	-0.004
N ₁ -C _{Nγ}	1.393	0.001	0.001	-0.003	-0.001	0.000	-0.001	-0.003	0.000	0.000

Continued on next page

Table 5.2 – continued from previous page

	Keto									
	PYV3	SA	FA1	FA2	DHBP	SDP	I2but	I2F4	I3F3-N	I3F3-O
O ₁ ...H	1.598	0.060	0.064	−0.095	−0.014	0.118	−0.061	−0.057	−0.018	0.019
N ₁ −H	1.060	−0.005	−0.005	0.021	0.004	−0.018	0.012	0.012	0.003	0.000
O ₁ ...N ₁	2.527	0.032	0.034	−0.052	−0.006	0.053	−0.028	−0.027	−0.008	0.004
O ₁ ...H−N ₁	143.1	−3.0	−3.2	3.0	0.6	−5.8	3.0	2.6	1.1	−2.1
O ₁ =C _O	1.274	−0.009	−0.010	0.000	−0.002	0.003	−0.002	−0.002	−0.007	−0.012
C _O −C _{Nβ}	1.442	0.003	0.003	0.001	0.000	−0.008	−0.001	−0.002	0.003	0.005
C _{Nβ} =C _{Nα}	1.403	−0.010	−0.010	−0.003	−0.004	0.001	−0.003	−0.005	−0.003	−0.008
C _{Nα} −N ₁	1.316	0.008	0.008	0.004	0.004	0.000	0.004	0.007	0.000	0.005
N ₁ −C _{Nγ}	1.394	0.000	0.000	−0.003	−0.002	0.001	−0.005	−0.005	−0.002	0.001

The torsion angle between the linker and the pyridine, $C_{N\alpha}-N_1-C_{N\gamma}-C_{N2}$, ϕ , is given Table 5.3. It shows that PYV3 and its H-bond co-crystals are *trans*-like with torsions of about 150° , except for SDP which actual *cis* ($\phi \approx 0^\circ$). The X-bond co-crystals are *cis*-like with torsions ranging from 19° to 45° . To account for the π -conjugation between the pyridine and the rest of the molecule, the smallest torsion angle between the linker and the pyridine, θ , and the variation upon co-crystallization, $\Delta\theta$, are given in Table 5.3. Considering θ , all crystal have about the same off-plane torsion, except for SDP, which is planar. For the enols, the variations for the co-crystals are small, of the order of 1° , except for FA2 (5°) and I3F3-O (13°) that have larger angles than PYV3 (decreased π -conjugation) and DHBP (-2°) and SDP (-30°) that have smaller angles (increased π -conjugation). On average, the variations for the keto forms are larger with only FA2 and DHBP being of the order of 1° : 1.1° and 0.1° , respectively. SA, FA1, and I3F3-O displays lower π -conjugation with $\Delta\theta$ values of 3° , 3° , and 7° , respectively while the remaining co-crystals, SDP, I2but, I2F4, I3F3-N, show greater π -conjugation: -25° , -9° , -8° , and -8° , respectively.

Table 5.3: Torsion angle ($C_{N\alpha}-N_1-C_{N\gamma}-C_{N2}$, ϕ) and smallest torsion angle (θ) between the linker and the pyridine moiety (in $^\circ$) in the reference PYV3 crystal and the variations of θ (in $^\circ$) upon co-crystallization. The geometries were obtained at the PBC/PBEsol0/6-31G(d,p)/I(LANL2DZ) level of approximation.

Crystal	Enol			Keto		
	ϕ	θ	$\Delta\theta$	ϕ	θ	$\Delta\theta$
PYV3	147.8	32.2	0.0	151.9	28.1	0.0
SA	147.4	32.6	0.4	149.1	30.9	2.8
FA1	147.9	32.1	-0.1	149.3	30.7	2.6
FA2	142.7	37.4	5.2	150.8	29.2	1.1
DHBP	149.7	30.3	-1.9	152.0	28.0	-0.1
SDP	1.8	1.8	-30.4	2.7	2.7	-25.4
I2but	32.8	32.8	0.7	18.7	18.7	-9.4
I2F4	31.4	31.4	-0.8	20.3	20.3	-7.8
I3F3-N	33.2	33.2	1.1	20.0	20.0	-8.1
I3F3-O	45.1	45.1	12.9	34.9	34.9	6.8

5.3.4 Mulliken Charges Analysis

Table 5.4 shows the relevant Mulliken atomic charges of PYV3 and their variations with respect to the PYV3 crystal, for all co-crystals, as determined at the PBC/PBEsol0/6-31G(d,p)/I(LANL2DZ) level of approximation. Table B.2 in the Supporting Information compares the Mulliken and Hirshfeld charges of

PYV3 in its E and K forms and shows that the E to K differences follow the same trends. These Hirshfeld charges were obtained using the iterative Hirshfeld method^{40,41} with CRYSTAL17²⁸ at the PBC/PBEsol0/6-31G(d,p) level of approximation with the XXL integration grid. Considering the Mulliken values in Table 5.4, the variations with respect to PYV3 are small for both the enol and keto forms, with a few exceptions: firstly, for the N₂ atom and secondly, on SDP.

Concerning N₂, the negative Mulliken charges are significantly larger for all enol and keto co-crystals. H-bonded co-crystals are the most affected with an increase of 0.11 e to 0.16 e (26 % to 39 %) while for the X-bonded co-crystals, the increase varies between 0.05 e and 0.06 e (12 % and 15 %). The charges of all the other atoms barely change except for SDP H and O₁ in its enol form [variations of 0.11 e (27 %) and −0.15 e (25 %), respectively] and H and N₁ for the keto form [variations of 0.09 e (24 %) and −0.12 e (20 %), respectively]. The very large charge variation of the hydrogen might explain SDP's O₁⋯N₁ different behavior compared to all other crystals, *i.e.* a large increase instead of the opposite (see previous section).

Table 5.4: Mulliken charges and variations with respect to PYV3 calculated at the PBC/PBEsol0/6-31G(d,p)/I(LANL2DZ) level of approximation (in e). Large values are highlighted in bold.

Enol										
	PYV3	SA	FA1	FA2	DHBP	SDP	I2but	I2F4	I3F3-N	I3F3-O
H	0.40	−0.00	−0.00	0.00	0.00	0.11	0.00	0.01	−0.01	0.01
O ₁	−0.59	0.02	0.03	0.02	0.01	−0.15	0.02	0.01	0.03	0.02
N ₁	−0.60	0.00	0.01	−0.01	−0.00	−0.03	−0.01	−0.01	0.03	0.00
N ₂	−0.41	−0.16	−0.16	−0.14	−0.12	−0.13	−0.06	−0.06	−0.06	−0.05
Keto										
	PYV3	SA	FA1	FA2	DHBP	SDP	I2but	I2F4	I3F3-N	I3F3-O
H	0.38	0.00	0.00	0.02	0.01	0.09	0.01	0.01	0.01	0.01
O ₁	−0.63	0.03	0.03	0.01	0.01	−0.05	0.01	0.01	0.01	0.04
N ₁	−0.59	−0.02	−0.02	−0.04	−0.02	−0.12	−0.03	−0.03	−0.01	−0.01
N ₂	−0.42	−0.15	−0.15	−0.14	−0.12	−0.11	−0.05	−0.05	−0.05	−0.05

About the enol to keto charge distribution differences, represented in Figure 5.4, only some of the atoms follow the same trend amongst all crystals: H, for which the charge decreases by about 0.02 e (as it becomes bonded to a less electronegative atom); C_O , where the charge is more positive by about 0.07 e (since it is no longer aromatic and the charge on O_1 is usually more negative); the charge on $\text{C}_\text{N}\beta$ becomes more negative by about 0.05 e (because it is bonded to the positive C_O atom and loses its aromaticity); $\text{C}_\text{N}\gamma$ charge becomes more positive by about 0.03 e , except for I3F3-N with a much larger increase of 0.09 a.u. ; and for O_2 , the charge increases only by 0.01 e even for the co-crystals where it is involved in intermolecular interactions (SDP and I3F3-O). O_1 charge decreases as one would have expected when going from an enol to a keto by about 0.03 e , except for two co-crystals: I3F3-O, which is less affected with a decrease of only 0.01 e and SDP, for which the charge increases by 0.06 e . This highlights that the interaction between the coformer and PYV3 O_1 is much stronger for SDP than for I3F3. About $\text{C}_\text{N}\alpha$, the charge becomes less positive by about 0.02 e except for FA2 for which it increases slightly (0.01 e). The charge of PYV3 N_1 increases by 0.01 e while it decreases weakly/strongly depending on the co-crystal (except for I3F3-O with a slight increase of 0.003 e): -0.005 e for DHBP and I2F4 and up to -0.08 e for SDP. This is the largest qualitative difference between PYV3 and its co-crystals regarding the Mulliken charges.

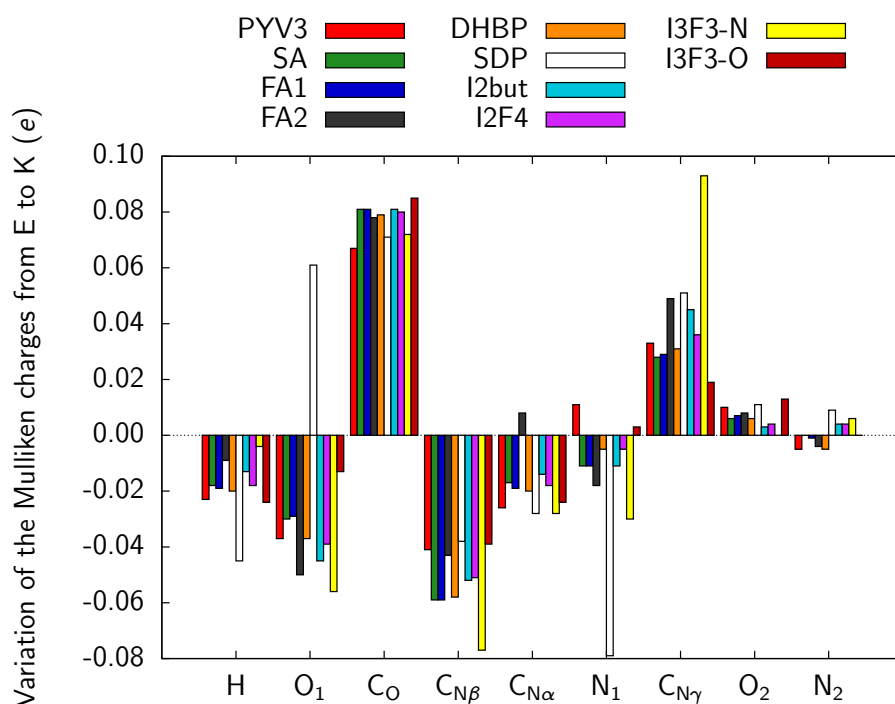


Figure 5.4: Enol to keto Mulliken charges differences calculated at the PBC/PBEsol0/6-31G(d,p)/I(LANL2DZ) level of approximation (in e).

Finally, the charge differences for N_2 are not systematic and vary between -0.005 for DHBP and 0.009 e for SDP.

5.4 Conclusions

Co-crystallization has extremely complex effects on the structures and properties of organic chromophores, as illustrated in this investigation on the PYV3 salicylideneaniline, which switches between an enol and a keto form. In our attempt to decipher them, using theoretical chemistry methods, we broke them down in three categories associated with the energy (H-bond strength, enol to keto relative energy, and geometry relaxation energies), the geometrical structure (PYV3 to co-crystal and enol to keto geometrical variations), and the electron distribution (PYV3 to co-crystal and enol to keto Mulliken charge variations).

First, potential energy scans of a HF probe molecule with the nitrogen and oxygen interaction sites shows that the enol form favors the interaction on the nitrogen (N_2) by about 6 kJ mol^{-1} with respect to the oxygens while the opposite is obtained for the keto form by an even larger amount (12 kJ mol^{-1}). This correlates with the fact that among the studied co-crystals, only two show interactions between the coformer and the oxygens of the anil while the interaction with the nitrogen of the pyridine ring (N_2) is always present. Subsequently, since the enol form of PYV3 is mostly present in solution, the interaction on the nitrogen is thus the most probable in both liquid and crystalline states. This suggests that co-crystallization under the keto form could be favored by increasing its population in solution with careful control of the conditions impacting the enol/keto equilibrium (specific intermolecular interactions with the solvent, substituents, temperature, and light exposure).

Looking at the relative keto/enol energy, the enol crystals are more stable than the keto ones, except for the SDP co-crystal, in agreement with experiment. Furthermore, the switching requires more energy for the co-crystals than for the pure PYV3 crystal (ignoring the kinetics), which is also in agreement with the experimental data. Indeed for the co-crystals with FA1, FA2, and SA, the thermochromism was found to be reduced with respect to the pure PYV3 crystal.²¹ Calculations on isolated PYV3 molecules have then highlighted the role of the crystal field and of the geometry relaxations on the enol/keto relative energies. In particular, with the exception of the SDP co-crystal, where the keto form is dominant, the geometry relaxation induced by co-crystallization better stabilizes the enol form than the keto one. These geometry relaxation energies are associated to geometrical variations within the keto/enol delocalization ring ($H-O_1-CO=C_{N\beta}-C_{N\alpha}=N_1$), which follow the same trends for all crystals, again, with the exception of PYV3-SDP. These have been analyzed in parallel with the Mulliken charge distribution, showing that the interaction with the coformer makes the N_2 charge more negative.

Overall, we have showed that the effect of co-crystallization can not be singu-

larly characterized but is a collective effect. The change of packing (short-range intermolecular interactions and long-range crystal field interactions) affects the geometry, the electronic distribution, and the energy of a target molecule in different ways, despite the key compound-coformer interaction being the same. e.g. the SA, FA, and DHBP cofomers, forming a single H-bond on N₂, yield three "types" of co-crystals, PYV3-SA/FA1, PYV3-FA2, and PYV3-DHBP. Moreover, the study of the PYV3-SDP co-crystal shows how the interaction with the co-former modifies the structure and electron distribution, stabilizing the ever so elusive crystalline keto form.

Acknowledgements

The authors would like to thank Andrea Carletta and Nikolay N. Tumanov who provided the experimental crystal structures. This work was carried out thanks to funding of "Actions de Recherche Concertées" (ARC) de la Direction générale de l'Enseignement non obligatoire et de la Recherche scientifique - Direction de la Recherche scientifique - Communauté française de Belgique, under convention No. 15/20-068. This research used resources of the "Plateforme Technologique de Calcul Intensif (PTCI)" (<http://www.ptci.unamur.be>) located at the University of Namur, Belgium, which is supported by the FNRS-FRFC, the Walloon Region, and the University of Namur (Conventions No. 2.5020.11, GEQ U.G006.15, 1610468, and RW/GEQ2016). The PTCI is member of the "Consortium des Équipements de Calcul Intensif (CÉCI)" (<http://www.cec-hpc.be>).

Bibliography

- (1) Wang, J. et al. Influence of Nitrogen Doping on Device Operation for TiO₂-Based Solid-State Dye-Sensitized Solar Cells: Photo-Physics from Materials to Devices. *Nanomaterials* **2016**, 6, 35, DOI: 10.3390/nano6030035.
- (2) Konsolakis, M.; Carabineiro, S.; Marnellos, G.; Asad, M.; Soares, O.; Pereira, M.; Órfão, J.; Figueiredo, J. Effect of Cobalt Loading on the Solid State Properties and Ethyl Acetate Oxidation Performance of Cobalt-Cerium Mixed Oxides. *J. Colloid Interface Sci.* **2017**, 496, 141–149, DOI: 10.1016/J.JCIS.2017.02.014.
- (3) Weng, Q.; Kvashnin, D. G.; Wang, X.; Cretu, O.; Yang, Y.; Zhou, M.; Zhang, C.; Tang, D.-M.; Sorokin, P. B.; Bando, Y.; Golberg, D. Tuning of the Optical, Electronic, and Magnetic Properties of Boron Nitride Nanosheets with Oxygen Doping and Functionalization. *Adv. Mater.* **2017**, 29, 1700695, DOI: 10.1002/adma.201700695.

- (4) Yu, M.; Wang, Z.; Hou, C.; Wang, Z.; Liang, C.; Zhao, C.; Tong, Y.; Lu, X.; Yang, S. Nitrogen-Doped Co_3O_4 Mesoporous Nanowire Arrays as an Additive-Free Air-Cathode for Flexible Solid-State Zinc-Air Batteries. *Adv. Mater.* **2017**, *29*, 1602868, DOI: 10.1002/adma.201602868.
- (5) Buannic, L.; Orayech, B.; López Del Amo, J.-M.; Carrasco, J.; Katcho, N. A.; Aguesse, F.; Manalastas, W.; Zhang, W.; Kilner, J.; Llordés, A. Dual Substitution Strategy to Enhance Li^+ Ionic Conductivity in $\text{Li}_7\text{La}_3\text{Z}_2\text{O}_{12}$ Solid Electrolyte. *Chem. Mater.* **2017**, *29*, 1769–1778, DOI: 10.1021/acs.chemmater.6b05369.
- (6) Henwood, A. F.; Zysman-Colman, E. Lessons Learned in Tuning the Optoelectronic Properties of Phosphorescent Iridium(iii) Complexes. *Chem. Commun.* **2017**, *53*, 807–826, DOI: 10.1039/C6CC06729H.
- (7) Kotobuki, M.; Song, S.; Takahashi, R.; Yanagiya, S.; Lu, L. Improvement of Li Ion Conductivity of $\text{Li}_5\text{La}_3\text{Ta}_2\text{O}_{12}$ Solid Electrolyte by Substitution of Ge for Ta. *J. Power Sources* **2017**, *349*, 105–110, DOI: 10.1016/J.JPOWSOUR.2017.03.032.
- (8) Naito, H.; Nishino, K.; Morisaki, Y.; Tanaka, K.; Chujo, Y. Luminescence Color Tuning from Blue to Near Infrared of Stable Luminescent Solid Materials Based on Bis-*o*-Carborane-Substituted Oligoacenes. *Chem. - An Asian J.* **2017**, *12*, 2134–2138, DOI: 10.1002/asia.201700815.
- (9) Jouhara, A.; Dupré, N.; Gaillot, A.-C.; Guyomard, D.; Dolhem, F.; Poizot, P. Raising the Redox Potential in Carboxyphenolate-Based Positive Organic Materials via Cation Substitution. *Nat. Commun.* **2018**, *9*, 4401, DOI: 10.1038/s41467-018-06708-x.
- (10) Trask, A. V.; Motherwell, W. D. S.; Jones, W. Pharmaceutical Cocrystallization: Engineering a Remedy for Caffeine Hydration. *Cryst. Growth Des.* **2005**, *5*, 1013–1021, DOI: 10.1021/cg0496540.
- (11) Golob, S.; Perry, M.; Lusi, M.; Chierotti, M. R.; Grabnar, I.; Lassiani, L.; Voinovich, D.; Zaworotko, M. J. Improving Biopharmaceutical Properties of Vinpocetine Through Cocrystallization. *J. Pharm. Sci.* **2016**, *105*, 3626–3633, DOI: 10.1016/j.xphs.2016.09.017.
- (12) Machado, T. C.; Gelain, A. B.; Rosa, J.; Cardoso, S. G.; Caon, T. Cocrystallization as a Novel Approach to Enhance the Transdermal Administration of Meloxicam. *Eur. J. Pharm. Sci.* **2018**, *123*, 184–190, DOI: 10.1016/j.ejps.2018.07.038.
- (13) Harmsen, B.; Leyssens, T. Dual-Drug Chiral Resolution: Enantiospecific Cocrystallization of (*S*)-Ibuprofen Using Levetiracetam. *Cryst. Growth Des.* **2018**, *18*, 441–448, DOI: 10.1021/acs.cgd.7b01431.

- (14) Gao, H. Y.; Zhao, X. R.; Wang, H.; Pang, X.; Jin, W. J. Phosphorescent Cocrystals Assembled by 1,4-Diiodotetrafluorobenzene and Fluorene and Its Heterocyclic Analogues Based on C-I $\cdots\pi$ Halogen Bonding. *Cryst. Growth Des.* **2012**, *12*, 4377–4387, DOI: 10.1021/cg300515a.
- (15) Zhu, W.; Zhu, L.; Sun, L.; Zhen, Y.; Dong, H.; Wei, Z.; Hu, W. Uncovering the Intramolecular Emission and Tuning the Nonlinear Optical Properties of Organic Materials by Cocrystallization. *Angew. Chemie Int. Ed.* **2016**, *55*, 14023–14027, DOI: 10.1002/anie.201607712.
- (16) Sun, L.; Zhu, W.; Wang, W.; Yang, F.; Zhang, C.; Wang, S.; Zhang, X.; Li, R.; Dong, H.; Hu, W. Intermolecular Charge-Transfer Interactions Facilitate Two-Photon Absorption in Styrylpyridine-Tetracyanobenzene Cocrystals. *Angew. Chemie Int. Ed.* **2017**, *56*, 7831–7835, DOI: 10.1002/anie.201703439.
- (17) Babu, B.; Chandrasekaran, J.; Jayaramakrishnan, V.; Ho, M.-S.; Thirupugalmani, K.; Chandrasekar, S.; Thirumurugan, R. 2-Amino-6-Methylpyridinium Nitrophenolate Nitrophenol: An Organic Multiple Charge-Transfer Complex with Large Second Harmonic Generation for Optoelectronics Applications. *J. Therm. Anal. Calorim.* **2018**, *134*, 1059–1070, DOI: 10.1007/s10973-018-7386-5.
- (18) Gryl, M.; Seidler, T.; Wojnarska, J.; Stadnicka, K.; Matulková, I.; Němec, I.; Němec, P. Co-Crystals of 2-Amino-5-Nitropyridine Barbitol with Extreme Birefringence and Large Second Harmonic Generation Effect. *Chem. - A Eur. J.* **2018**, *24*, 8727–8731, DOI: 10.1002/chem.201802057.
- (19) Li, S.; Yan, D. Two-Component Aggregation-Induced Emission Materials: Tunable One/Two-Photon Luminescence and Stimuli-Responsive Switches by Co-Crystal Formation. *Adv. Opt. Mater.* **2018**, *6*, 1800445, DOI: 10.1002/adom.201800445.
- (20) D'Agostino, S.; Spinelli, F.; Taddei, P.; Ventura, B.; Grepioni, F. Ultra-long Organic Phosphorescence in the Solid State: The Case of Triphenylene Cocrystals with Halo- and Dihalo-penta/tetrafluorobenzene. *Cryst. Growth Des.* **2019**, *19*, 336–346, DOI: 10.1021/acs.cgd.8b01443.
- (21) Carletta, A.; Buol, X.; Leyssens, T.; Champagne, B.; Wouters, J. Polymorphic and Isomorphic Cocrystals of a N-Salicylidene-3-aminopyridine with Dicarboxylic Acids: Tuning of Solid-State Photo- and Thermochromism. *J. Phys. Chem. C* **2016**, *120*, 10001–10008.
- (22) Carletta, A.; Spinelli, F.; D'Agostino, S.; Ventura, B.; Chierotti, M. R.; Gobetto, R.; Wouters, J.; Grepioni, F. Halogen-Bond Effects on the Thermo- and Photochromic Behaviour of Anil-Based Molecular Co-crystals. *Chem. - A Eur. J.* **2017**, *23*, 5317–5329, DOI: 10.1002/chem.201605953.

- (23) Carletta, A.; Zbačnik, M.; Van Gysel, M.; Vitković, M.; Tumanov, N.; Stilinović, V.; Wouters Johan and Cinčić, D. Playing with Isomerism: Cocrystallization of Isomeric N-Salicylideneaminopyridines with Perfluorinated Compounds as Halogen Bond Donors and Its Impact on Photochromism. *Cryst. Growth Des.* **2018**, *18*, 6833–6842, DOI: 10.1021/acs.cgd.8b01064.
- (24) Hutchins, K. M.; Dutta, S.; Loren, B. P.; MacGillivray, L. R. Co-Crystals of a Salicylideneaniline: Photochromism Involving Planar Dihedral Angles. *Chem. Mater.* **2014**, *26*, 3042–3044.
- (25) Mercier, G. M.; Robeyns, K.; Leyssens, T. Altering the Photochromic Properties of N-Salicylideneanilines Using a Co-Crystal Engineering Approach. *Cryst. Growth Des.* **2016**, *16*, 3198–3205.
- (26) Gryl, M.; Rydz, A.; Wojnarska, J.; Krawczuk, A.; Koziel, M.; Seidler, T.; Ostrowska, K.; Marzec, M.; Stadnicka, K. M. Origin of chromic effects and crystal-to-crystal phase transition in the polymorphs of tyraminium violurate. *IUCrJ* **2019**, *6*, 226–237, DOI: 10.1107/S2052252518017037.
- (27) Dovesi, R.; Orlando, R.; Erba, A.; Zicovich-Wilson, C. M.; Civalleri, B.; Casassa, S.; Maschio, L.; Ferrabone, M.; De La Pierre, M.; D’Arco, P.; Noël, Y.; Causà, M.; Rérat, M.; Kirtman, B. CRYSTAL14: a Program for the Ab Initio Investigation of Crystalline Solids. *Int. J. Quantum Chem.* **2014**, *114*, 1287–1317.
- (28) Dovesi, R.; Erba, A.; Orlando, R.; Zicovich-Wilson, C. M.; Civalleri, B.; Maschio, L.; Rérat, M.; Casassa, S.; Baima, J.; Salustro, S.; Kirtman, B. CRYSTAL17. *Wiley Interdiscip. Rev. Comput. Mol. Sci.* **2018**, *8*, e1360.
- (29) Quertinmont, J.; Carletta, A.; Tumanov, N. A.; Leyssens, T.; Wouters, J.; Champagne, B. Assessing density functional theory approaches for predicting the structure and relative energy of salicylideneaniline molecular switches in the solid state. *J. Phys. Chem. C* **2017**, *121*, 6898–6908, DOI: 10.1021/acs.jpcc.7b00580.
- (30) Quertinmont, J.; Leyssens, T.; Wouters, J.; Champagne, B. Effects of Empirical Dispersion Energy on the Geometrical Parameters and Relative Energy of a Salicylideneaniline Molecular Switch in the Solid State. *Crystals* **2018**, *8*, 125, DOI: 10.3390/cryst8030125.
- (31) Perdew, J. P.; Ruzsinszky, A.; Csonka, G. I.; Vydrov, O. A.; Scuseria, G. E.; Constantin, L. A.; Zhou, X.; Burke, K. Restoring the Density-Gradient Expansion for Exchange in Solids and Surfaces. *Phys. Rev. Lett.* **2008**, *100*, 136406.
- (32) Feller, D. The Role of Databases in Support of Computational Chemistry Calculations. *J. Comput. Chem.* **1996**, *17*, 1571–1586.

- (33) Schuchardt, K. L.; Didier, B. T.; Elsethagen, T.; Sun, L.; Gurumoorthi, V.; Chase, J.; Li, J.; Windus, T. L. Basis Set Exchange: A Community Database for Computational Sciences. *J. Chem. Inf. Model.* **2007**, *47*, 1045–1052.
- (34) Liégeois, V.; UNamur DrawMol, 2018.
- (35) Frisch, M. J. et al. Gaussian~16 Revision B.01, Gaussian Inc. Wallingford CT, 2016.
- (36) Groom, C. R.; Bruno, I. J.; Lightfoot, M. P.; Ward, S. C. The Cambridge Structural Database. *Acta Crystallogr. Sect. B Struct. Sci. Cryst. Eng. Mater.* **2016**, *72*, 171–179.
- (37) Smulders, C.; Carletta, A.; Wouters, J. Ingénierie cristalline du thermo- et photochromisme des N-salicylidèneaminopyridines par cocrystallisation, 2017.
- (38) Carletta, A. Photochromic multicomponent crystalline materials based on N-salicylideneanilines, Ph.D. Thesis, Université de Namur, 2019.
- (39) Zutterman, F.; Louant, O.; Mercier, G.; Leyssens, T.; Champagne, B. Predicting Keto–Enol Equilibrium from Combining UV/Visible Absorption Spectroscopy with Quantum Chemical Calculations of Vibronic Structures for Many Excited States. A Case Study on Salicylideneanilines. *J. Phys. Chem. A* **2018**, *122*, 5370–5374, DOI: 10.1021/acs.jpca.8b03389.
- (40) Hirshfeld, F. L. Hirshfeld charges. *Theor. Chim. Acta* **1977**, *44*, 129–138.
- (41) Bultinck, P.; Van Alsenoy, C.; Ayers, P. W.; Carbo-Dorca, R. Hirshfeld charges II. *J. Chem. Phys.* **2007**, *126*, 144111.

INVESTIGATION OF THE
EVOLUTION OF ISOTROPIC
MAGNETIC SHIELDINGS ALONG
THE ENOL-KETO TAUTOMERISM
OF A *N*-SALICYLIDENE-3-AMINO-
PYRIDINE DERIVATIVE AND TWO
OF ITS CO-CRYSTALS IN THE
SOLID STATE

To Be Published

This chapter contains all the computational and theoretical aspects of a paper that is currently under rewriting to combine these with experimental data. All calculations, their analysis, and the writing of this Chapter were performed by J.Q.

Abstract

This work addresses the effects of co-crystallization of the PYV3 *N*-salicylidene-aniline derivative with dihydroxybiphenyl (DHBP) and sulfonyldiphenol (SDP) on its NMR signatures by employing a two-step approach where i) the crystal structure is optimized by taking advantage of the translational symmetry of the crystal using band structure calculations and ii) the NMR shielding constants are calculated using a fragment-based method where the quantum chemistry (QC) fragment is embedded in the polarization field created by point charges. These point charges have been determined in such a way to reproduce the crystalline Coulombic potential in the QC region and, in particular, using a self-consistent reaction field approach. The application of this method has focused on the differences of NMR signatures between the enol and keto forms of PYV3, $\Delta\sigma_{EK}$, with the aim that, in a future step, these data could be used in parallel with variable-temperature NMR experiments on this crystalline molecular switch to determine its keto/enol ratio as a function of co-crystallization. The calculations have revealed the importance of the $\Delta\sigma_{EK}$ values of nuclei to target experimentally and their modifications induced by co-crystallization by relating these to the topology of the intermolecular H-bonds between PYV3 and its coformers.

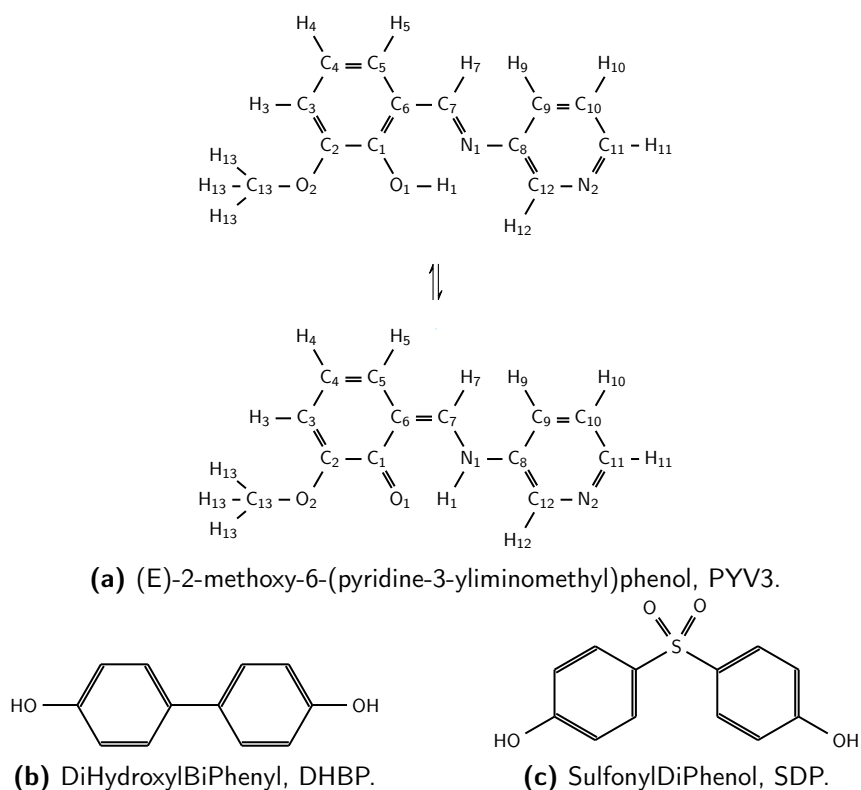
6.1 Introduction

Molecular switches have a wide range of applications, from sensor devices to optoelectronics.^{1–4} Besides the selective control of their transformation, one of the challenges accompanying their development is the characterization of the equilibrium constants between the different forms of the compound, *i.e.* the quantification of the amount of its two (or more) forms. In solution, nuclear magnetic resonance (NMR) is a powerful method because it allows the quantitative identification of each state of the switch as a function of the temperature,^{5,6} of the pH,^{7,8} of the redox potential,⁹ or of the solvent conditions.^{5,6} Since the interpretation of the experimental NMR spectra can be non straightforward, it is useful to combine it with quantum chemistry simulations. The reliability of this combined experiment/simulation approach has been illustrated by our group and others^{10–17} for assigning the structures, the stereostructures, and the conformations of complex molecules, including molecular switches. A lot of insights can be gained (based on bond lengths, atomic charges, or directly from the isotropic magnetic shieldings). Variable-temperature NMR was also used to trace the change of anionic ordering and the fast ion motions in an organic salt displaying tunable nonlinear optical switching properties.¹⁸ Though, like for switches in solution, quantum chemical calculations could also be used to help interpreting the experimental data about solid state switches, to our knowledge, this has not yet been done.

An alternative method for the determination of the forms of a molecular switch is Fourier transform infrared (FTIR) spectroscopy. It can be performed for solutions as well as for solids (*e.g.* film casted onto KBr plate) and it also provides a quantitative tool of identification.¹⁹ Moreover, in the crystalline state, variable temperature single crystal X-ray diffraction (XRD) is another relevant *method*. It was used on salicylideneanilines to follow a C–O bond length and therefore to address the keto/enol ratio.²⁰

In this work, quantum chemical calculations of NMR shielding constants provide insights to *future* variable-temperature NMR experiments on a crystalline molecular switch, a *N*-salicylideneaniline or anil derivative [(E)-2-methoxy-6-(pyridine-3-yliminomethyl)phenol, PYV3, Scheme 6.1a] and on two of its co-crystals (with dihydroxylbiphenyl, DHBP and sulfonyldiphenol, SDP, Schemes 6.1b and c). Anils commute between enol (E) and keto (K) forms (Scheme 6.1a). Since both forms could present a fast exchange rate during Magic Angle Spinning NMR (MAS-NMR) experiments (rendering any quantification impossible), calculations yield the magnetic isotropic shieldings of the pure limit forms, thus facilitating the experimental quantification of the E/K ratio possible.

Since a few decades, different methods have been developed and employed for calculating and interpreting NMR shielding constants in the solid state. Density functional theory (DFT) based gauge-including projector augmented wave (GIPAW) is commonly used to compute the chemical shift of molecular crys-



Scheme 6.1: Structures of the compound and coformers, (a) anil and its enol-keto equilibrium and the two coformers (b) and (c).

tals, despite some of its limitations, such as the high calculation cost when using global hybrid exchange-correlation functionals (XCFs).^{21–27} To work around this, fragment and cluster methods have been successfully used with global hybrids XCFs (such as PBE0 and B3LYP) and Gaussian-type basis sets (with the gauge-independent atomic orbitals, GIAO, method).^{28–32} With these methods, the molecular crystal is broken down into fragments/clusters: a small cluster is typically treated using DFT within the electric field created by point-charges describing the remaining part of the crystal. This methodology has shown its efficiency for NMR properties^{28–32} but not only since it has also been applied to describe linear and non-linear optical properties of molecular crystals.^{33–38}

In this work, the fragment method is employed and the point-charge embedding is defined to reproduce the Ewald potential of the crystal within a micro-Volt (μV) scale, thanks to a modified version of the Ewald program.^{39,40} The approach consists, first, in the optimization of the crystal structure (the molecular geometry as well as the intermolecular distances) by taking advantage of the translation symmetry of the crystal and, secondly, in the modeling of the NMR properties at an acceptable computational cost while conserving the key surrounding effects of the crystal and good accuracy. The underlying methodological aspects and the

computational details are described in Section 6.2. Several embedding/modeling schemes are used and, therefore, they are discussed first in Section 6.3. Then, this Section presents the calculated NMR shieldings of the two forms of the title compound and highlights the most sensitive nuclei to the switching as well as the effects of co-crystallization. Lastly, conclusions are drawn.

6.2 Methods and Computational Details

The crystal structures were fully optimized using periodic boundary conditions (PBC) density functional theory (DFT) as implemented within the CRYSTAL14 package.⁴¹ We have previously shown that the global hybrid exchange-correlation functional PBEsol0 (based on PBEsol⁴² with 25 % of Hartree-Fock exchange) in combination with Pople's 6-31G(d,p) basis set (as taken from Basis Set Exchange^{43,44}) yields accurate crystal geometries, including the unit cell parameters.^{45,46} The default convergence parameters were used with a shrinking factor of the irreducible Brillouin zone of 6 (yielding between 64 and 112 points of integration) and tolerance criteria for the exchange and correlation integrals (TOLINTEG keyword) of "8 8 8 8 16". More details are given in Ref. [45].

The NMR isotropic shielding values ($\sigma_{\text{iso}} = \sigma$) were calculated at the B3LYP/6-311+G(2d,p) level of theory with the gauge-independent atomic orbital method,⁴⁷ as implemented in the Gaussian16 package,⁴⁸ and using different point-charge embedding schemes (see next paragraph and Subsection 6.3.1). The performance of the B3LYP XCF for evaluating NMR chemical shifts was substantiated in several of our recent works.^{12,15,16}

The Ewald program,⁴⁰ modified to support partial charges, was used to generate arrays of point charges reproducing the crystalline Coulombic potential in the quantum chemistry (QC) region. It is based on the following algorithm:³⁹ i) the unit cell charges are used to generate a neutral array containing typically a few 10 000 point charges at their crystallographic positions (as obtained here from PBC calculations); ii) the array is divided into three zones: zone 1 (a volume defined by the cluster of interest that will subsequently be described at the QC level), zone 2 (several hundred additional point charges that together with zone 1 fill a *spherical volume*), and zone 3 (all other point charges); iii) the Ewald formula is used to compute the site potentials at all point charges in zones 1 and 2; iv) a system of simultaneous linear equations is solved to find the zone 3 point charge values that reproduce the Ewald potential values for the sites in zones 1 and 2 site while constraining the total charge and dipole moments to zero; and v) the solution is checked at 1000 additional points randomly chosen in zone 1. The parameters used to reproduce the Ewald potential with an accuracy of the order of 1 μV are listed for each system in Table C.1 of the supporting information. Two charge definitions are employed: i) Mulliken charges and ii) electrostatic potential dipole (ESPD) charges. The ESPD charges are evaluated such as to best reproduce the electrostatic potential,⁴⁹ together with the exact

dipole moment as a constraint.

6.3 Results and Discussion

6.3.1 Definition of the Embedding Schemes

The most trivial and quite logical choice for embedding charges in cluster calculations of crystal properties are those obtained from PBC calculations. Still, this raises questions because the results that will be obtained for the embedded QC system will depend on the size and shape of the embedding region. Alternatives exist and can solve this problem, including the method proposed by Derenzo *et al.*³⁹ that consists in determining an array of point charges by solving a system of simultaneous linear equations to reproduce the Ewald potential in an extended part of the cluster including the QC region.

Following the method of Derenzo *et al.*,³⁹ several embedding schemes have been designed. In the first one, the Mulliken charges evaluated along the crystal structure optimization [PBC/PBEsol0/6-31G(d,p)] are used. It means that, at the end of the Ewald procedure, the charges in zones 1 and 2 are those of the PBC/PBEsol0/6-31G(d,p) calculations while those in zone 3 have been optimized. This first and simplest embedding scheme is denoted Ewald-PBC-Mulliken or, more simply, *Mulliken*. This embedding aims at polarizing the QC electron density. As a matter of fact, this embedding is obtained from a different level of approximation [PBC/PBEsol0/6-31G(d,p)] to that used for performing the QC NMR calculations [B3LYP/6-311+G(2d,p)], which could create some under- or over-polarization bias. Alternatively, i) these Mulliken embedding charges can be used to compute the wavefunction of the embedded system at the B3LYP/6-311+G(2d,p) level of approximation, ii) from this embedded wavefunction the ESPd charges can be evaluated, and iii) the latter can be used as input of the Ewald program to obtain a second type of embedding, denoted Ewald-ESPd or *ESPd*. Still, though some polarization effects between the atoms of the different zones are taken into account, this is not done self-consistently. Finally, by pursuing the ESPd scheme, successive relaxed ESPd charges can be calculated for the QC region and used as input for the Ewald calculation until the charges are converged, like in a self-consistent reaction field method (*scrf*). The corresponding embedding was therefore named *scrf-ESPd*. In our calculations, the threshold on the convergence was set at 0.001 e for their root mean square deviations. For each crystal, the embedded (QC) cluster was selected to contain one PYV3 molecule and the surrounding coformers forming intermolecular hydrogen bonds with it (Figure 6.1a for DHBP and 6.1b for SDP, see also Table C.1).

The charges for all the atoms of PYV3 enol and keto forms in all three embedding schemes are given in Tables C.2 and C.3 in the Supporting Information. In general, the ESPd and *scrf-ESPd* charges are quite similar (MAE of 0.02-0.03 a.u. for the PYV3 crystal in its enol and keto forms as well as for their co-

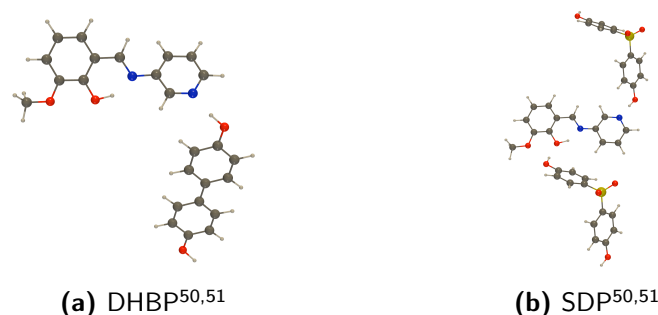


Figure 6.1: Representation of the PYV3-coformer synthons as extracted from the co-crystal structure optimized at the PBC/PBEsol0/6-31G(d,p) level of approximation. The enol form was considered.

crystals with DHBP but slightly larger for their co-crystals with SDP) and much different from the so-called Mulliken charges (MAE with respect to scrf-ESPd of 0.15-0.16 a.u. for the PYV3 crystal in its enol and keto forms but slightly less for their co-crystals, in particular with DHBP). Moreover, the ESPd charges of the isolated PYV3 molecule, as calculated at the B3LYP/6-311+G(2d,p) level, are also given in Tables C.2 and C.3 and are denoted *i*-ESPd for isolated-ESPd. By comparison with the ESPd values, these *i*-ESPd charges allow highlighting the polarization nature of the embedding, which induces electron transfer from the C₇H₇=N₁ (C₇H₇-N₁H₁) bridge to the O₁-H₁ (O₁) group.

6.3.2 Effect of the Embedding on the NMR Shieldings of PYV3

The embedding has a clear impact on the isotropic shielding constants (σ) of all nuclei and it is particularly large for the N and O heteroatoms (Figures 6.2 and 6.3). The largest effects are associated with the O₁, N₂, and O₂ atoms with $\Delta\sigma = \sigma(\text{embedded}) - \sigma(\text{isolated})$ values as large as 60 ppm for O₁ for the enol form of PYV3. For the C atoms, the amplitudes of the $\Delta\sigma$ values are smaller than 10 ppm. Going into more details, for both tautomers, the embedding leads to a deshielding of the C₃, C₅, C₇, C₉, and C₁₀ nuclei whereas the opposite occurs for C₁, C₂, C₁₁, C₁₂, and C₁₃. Then, the $\Delta\sigma$ amplitudes for the H atoms attain at most 1.1 ppm with systematic deshielding of 0.5 ppm to 1.0 ppm for H₃, H₅, H₇, H₉, H₁₀, and H₁₃ (considering their average). H₁₁ and H₁₂ are shielded but by a smaller amount (0.1 ppm to 0.2 ppm). The whole list of σ values for both tautomers and in their different environments is given Table C.6 (Supporting Informations). To a good approximation, these results give the impression that the molecule is cut into two parts, the top part that is mostly characterized by deshieldings and the bottom part by shieldings.

The different embedding schemes provide qualitatively similar shielding and deshielding values. Still, like for the charges, the MAE values are larger when comparing the Mulliken charge embedding scheme to the reference scrf-ESPd

method than ESPd with scrf-ESPd. In all the cases, these differences are smaller than the embedding effects themselves.

We can now look at our main target, the variations of shielding between the enol and keto forms, the $\Delta\sigma_{EK} = \sigma(K) - \sigma(E)$ values. First, the $\Delta\sigma_{EK}$ values keep generally their main characteristics (in sign and in amplitude) when considering the crystal embedding (Figure 6.4 and Table C.7 in the Supporting Information). This results from the fact that the embedding effects have the same shielding or deshielding effects on the atoms of both E and K forms. The exceptions are N₁, C₄, C₆, and H₁ but in these cases, the embedding effects are smaller than the isolated $\Delta\sigma_{EK}$ values. Then, for each type of nucleus, at least one atom exhibits a large variation of shielding when PYV3 switches from its enol to its keto form. For the isolated PYV3 molecule, these atoms are N₁ (from -40 to 90 ppm so that $\Delta\sigma_{EK} = 130$ ppm), O₁ (from 170 to -74 ppm with $\Delta\sigma_{EK} = -244$ ppm), C₁ (from 21 to 2 ppm, $\Delta\sigma_{EK} = -19$ ppm), and H₁ (from -16.1 to 14.1 ppm, $\Delta\sigma_{EK} = -2.1$ ppm) while ii) for the embedded molecule (scrf-ESPd results), the differences get smaller and amount, in the same order, to 119, -199, -19, and -1.8 ppm.

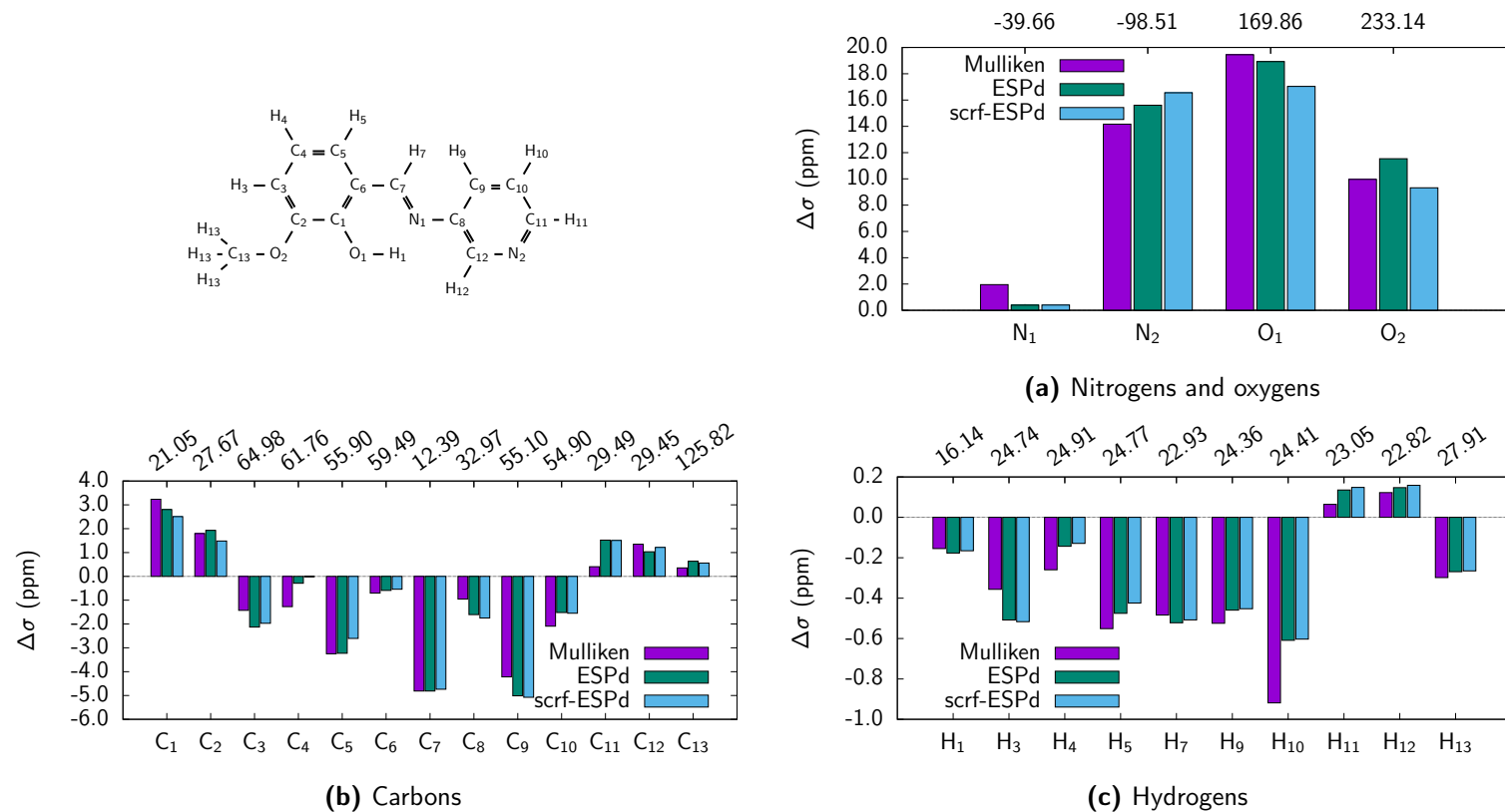


Figure 6.2: PYV3 enol isotropic NMR shielding variations with respect to the isolated molecule, $\Delta\sigma = \sigma(\text{embedding}) - \sigma(\text{isolated})$ (ppm) as a function of the embedding scheme (obtained at the B3LYP/6-311+G(2d,p)//PBC/PBEsol0/6-31G(d,p) level of approximation). The isolated molecule values are given on top of each figure.

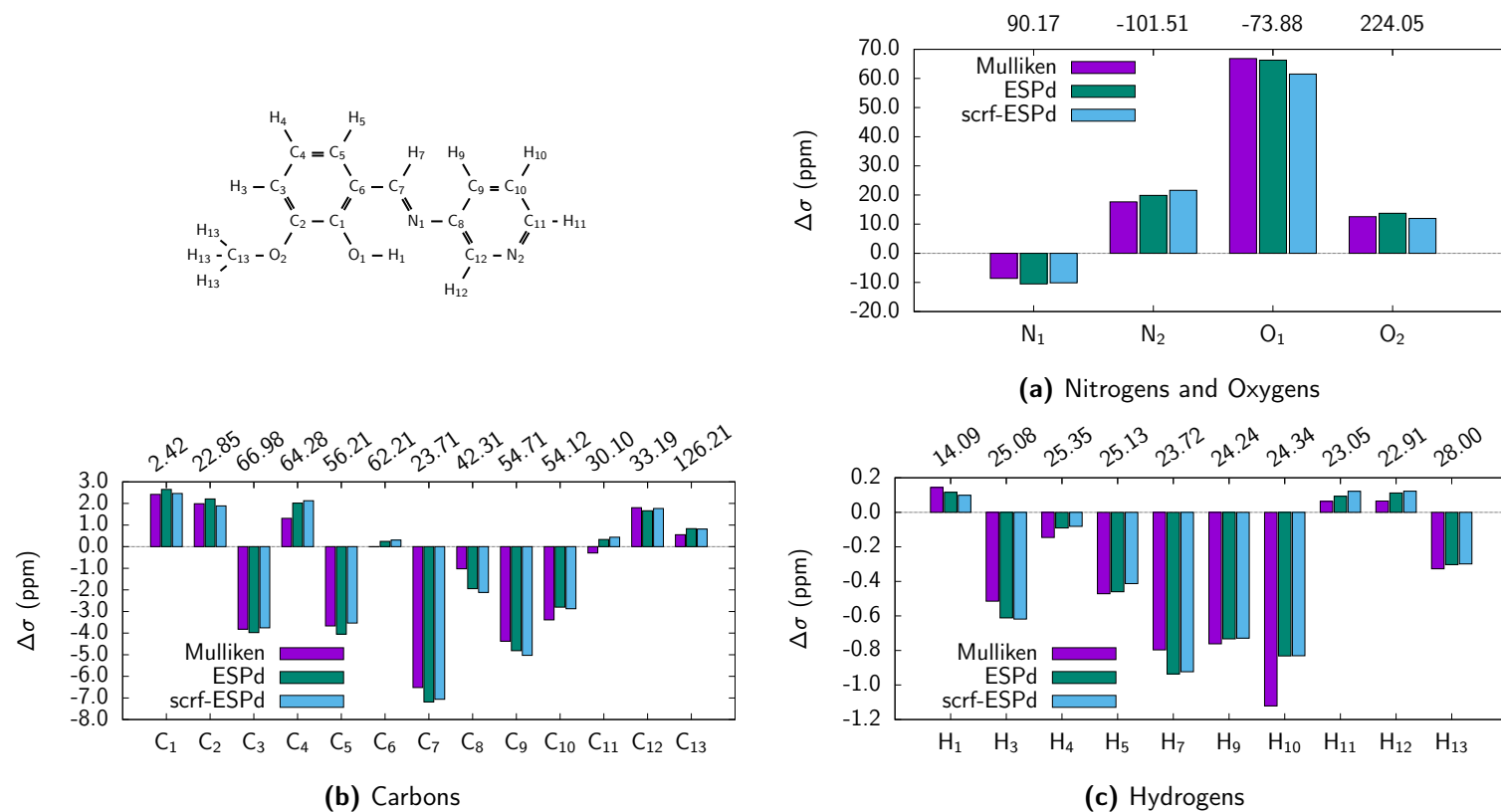


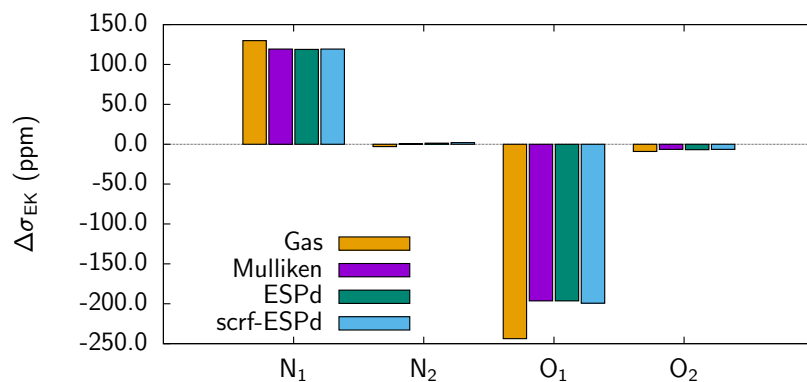
Figure 6.3: PYV3 keto isotropic NMR shielding variations with respect to the isolated molecule, $\Delta\sigma = \sigma(\text{embedding}) - \sigma(\text{isolated})$ (ppm) as a function of the embedding scheme (obtained at the B3LYP/6-311+G(2d,p)//PBC/PBEsol0/6-31G(d,p) level of approximation). The isolated molecule values are given on top of each figure.

6.3.3 Effect of Co-Crystallization on the NMR Shieldings

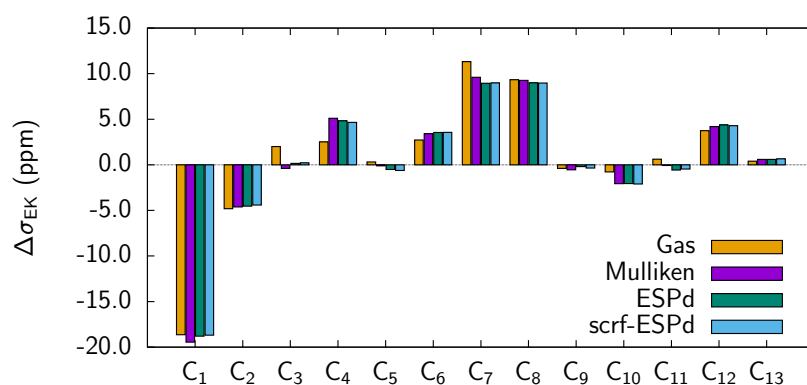
The effects of co-crystallization on the shielding constants are now investigated by focusing on the values calculated using the scrf-ESPd embedding scheme since it is the most evolved method. Figure 6.5 shows i) the difference of isotropic NMR shielding from the pure PYV3 crystal to its co-crystals for the different nuclei, $\Delta\sigma_{\text{co-crystal}} = \sigma_{\text{co-crystal}} - \sigma_{\text{PYV3}}$ (6.5a-6.5d) and ii) the corresponding $\Delta\sigma_{\text{EK,co-crystal}}$ values (Figures 6.5e-6.5f). These can be viewed either as a difference of co-crystallization effects on the K and E forms, $\Delta\sigma_{\text{EK,co-crystal}} = \Delta\sigma_{\text{co-crystal,K}} - \Delta\sigma_{\text{co-crystal,E}}$ or as a difference of enol-to-keto variations between the co-crystals and the PYV3 crystal, $\Delta\sigma_{\text{EK,co-crystal}} = \Delta\sigma_{\text{EK,co-crystal}} - \Delta\sigma_{\text{EK,PYV3}}$. Additional information on the co-crystals are given in Tables C.4 and C.5 (charges of the enol and keto PYV3 forms in the DHBP and SDP co-crystals as a function of the method to describe the embeddings) as well as in Tables C.8 and C.9 (σ and $\Delta\sigma_{\text{EK}}$ values of the DHBP co-crystal for different embedding schemes) and in Tables C.10 and C.11 (σ and $\Delta\sigma_{\text{EK}}$ values of the SDP co-crystal for different embedding schemes). Finally, Tables C.12 and C.13 summarize the σ and $\Delta\sigma_{\text{EK}}$ values together with their variations upon co-crystallization, respectively.

Globally, the co-crystallization effects on the shielding constants are stronger in the case of SDP (or more atoms are impacted), which forms H-bonds with N_2 as well as with O_1 and, to a lower extent, with O_2 , than of DHBP, which only forms a H-bond with N_2 . Note also that the orientation of the pyridyl group is different in the co-crystal with SDP in comparison with the PYV3 crystal and the co-crystal with DHBP since the N_2 atom points in the opposite direction (Figure 6.1). In the case of the co-crystal with DHBP, as expected, the largest variation induced by co-crystallization is observed for the N_2 atom, which is shielded 25 ppm and 21 ppm for the E and K forms, respectively. Moreover, modifications of the shielding constants occur for other atoms as well: in its enol form, 4.5 ppm, -0.7 ppm, 0.7 ppm, and 0.6 ppm for N_1 , O_1 , C_1 , and H_1 , while, for the keto form, 6.6 ppm, -7.2 ppm, -0.5 ppm, and -0.3 ppm, respectively.

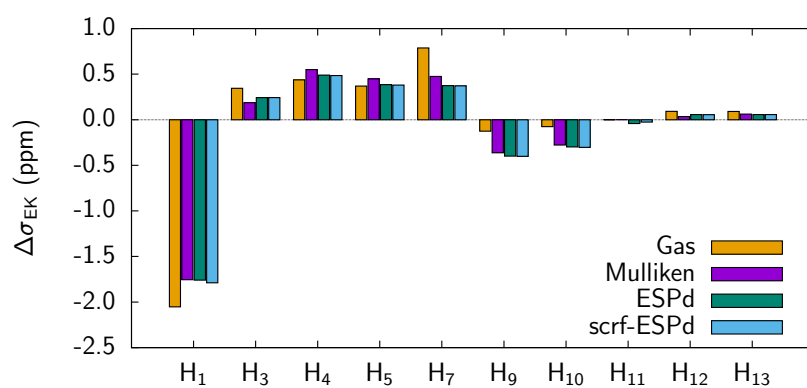
For the co-crystal with SDP, the largest σ variation is also associated with N_2 atom, which is shielded by 27 ppm and 21 ppm for the E and K forms, respectively. In addition, the N_1 atom of the enol form is shielded by 9.4 ppm with respect to the PYV3 crystal, the O_2 atom is deshielded by 6.5 ppm, whereas the impact on the shielding of O_1 is negligible. Then, for other atoms involved in the intramolecular H-bonds, we note that C_1 is shielded by 2.5 ppm, C_7 is shielded by 9.0 ppm, and H_1 is deshielded by 1.9 ppm. The effects on the keto forms are quite different with a small effect on N_1 (+0.5 ppm), a huge shielding of O_1 (25.6 ppm), a deshielding of O_2 (-7.8 ppm), a 2.1 ppm shielding of C_1 , a 7.1 ppm shielding of C_7 , and a 2.6 ppm shielding of H_1 . Finally, the difference of orientation of the pyridyl group leads to large effects on the C_9 (deshielding) and C_{12} (shielding) atoms, for both E and K forms, though their amplitudes are different. This demonstrates that co-crystallization of PYV3 with SDP results



(a) Nitrogens and Oxygens



(b) Carbons



(c) Hydrogens

Figure 6.4: PYV3 enol to keto isotropic NMR shielding variations, $\Delta\sigma_{EK} = \sigma(K) - \sigma(E)$ (ppm), as a function of the environment (obtained at the B3LYP/6-311+G(2d,p)//PBC/PBEsol0/6-31G(d,p) level of approximation).

in substantial modifications of the NMR signatures, extending over the whole structure.

The analysis of co-crystallization effects on the $\Delta\sigma_{EK}$ results from the corresponding effects on the enol and keto forms, discussed above. In the case of the SDP co-crystal, the $\Delta\sigma_{EK}$ variation is the largest for O_1 (26.3 ppm) and the variations are also important for N_1 (−8.8 ppm), N_2 (−5.9 ppm), C_7 (6.8 ppm), C_{12} (−4.0 ppm), and H_1 (4.2 ppm). Turning now to the PYV3 DHBP co-crystal, the differences do not exceed 10 ppm with values of −6.5 ppm (O_1), 4.9 ppm (O_2), 2.4 ppm (N_1), −4.1 ppm (N_2), and −0.9 ppm (H_1).

6.4 Further discussions, Conclusions, and Outlook

The effects of co-crystallization of the PYV3 *N*-salicylideneaniline derivative with dihydroxybiphenyl (DHBP) and sulfonyldiphenol (SDP) on its NMR signatures have been revealed by employing a two-step approach where i) the crystal structure is optimized by taking advantage of the translational symmetry of the crystal using band structure periodic boundary conditions calculations and ii) the NMR shielding constants are calculated using a fragment-based method where the quantum chemistry (QC) fragment is embedded in the polarization field created by point charges. These point charges are defined in such a way to reproduce the crystalline Coulombic potential in the QC region. Part of the work has dealt with the elaboration of a self-consistent reaction field approach where the charges in the QC zone are consistent with those of the polarizing surrounding as well as with the comparison of this embedding method with simpler ones, highlighting the approximations of the latter.

Then, the method was employed to PYV3 and its co-crystals by focusing on the differences of NMR signatures between their enol and keto forms with the goal that, in a future step, these data could be used in parallel with variable-temperature NMR experiments on this crystalline molecular switch to determine its keto/enol ratio as a function of co-crystallization. As expected, when switching from the enol to the keto form, the major chemical shift variations are associated with the six atoms involved in the intramolecular H-bonds ($H_1-O_1-C_1=C_6-C_7=N_1$ for the enol form and $O_1=C_1-C_6=C_7-N_1-H_1$ for the keto form). Indeed, for PYV3, the N_1 atom is shielded by about 120 ppm, the O_1 atom is deshielded by about 200 ppm, C_1 is deshielded by about 19 ppm, and H_1 by about 1.8 ppm. When PYV3 is co-crystallized with DHBP, H-bonds are formed with the N_2 atom of the pyridyl group, leading to its deshielding by about 4.0 ppm as well as to other small to medium (de)shieldings of the other nuclei. On the other hand, the effects of co-crystallization with SDP are much larger. Like DHBP, SDP forms H-bonds with the N_2 atom of the pyridyl group but also with the O_1 and O_2 atoms, which leads to (de)shieldings of many nuclei: the O_1 atom is shielded by 26.3 ppm, the H_1 atom by 4.2 ppm while N_1 and N_2 are deshielded by 8.8 ppm and 5.8 ppm, respectively. Note that additional

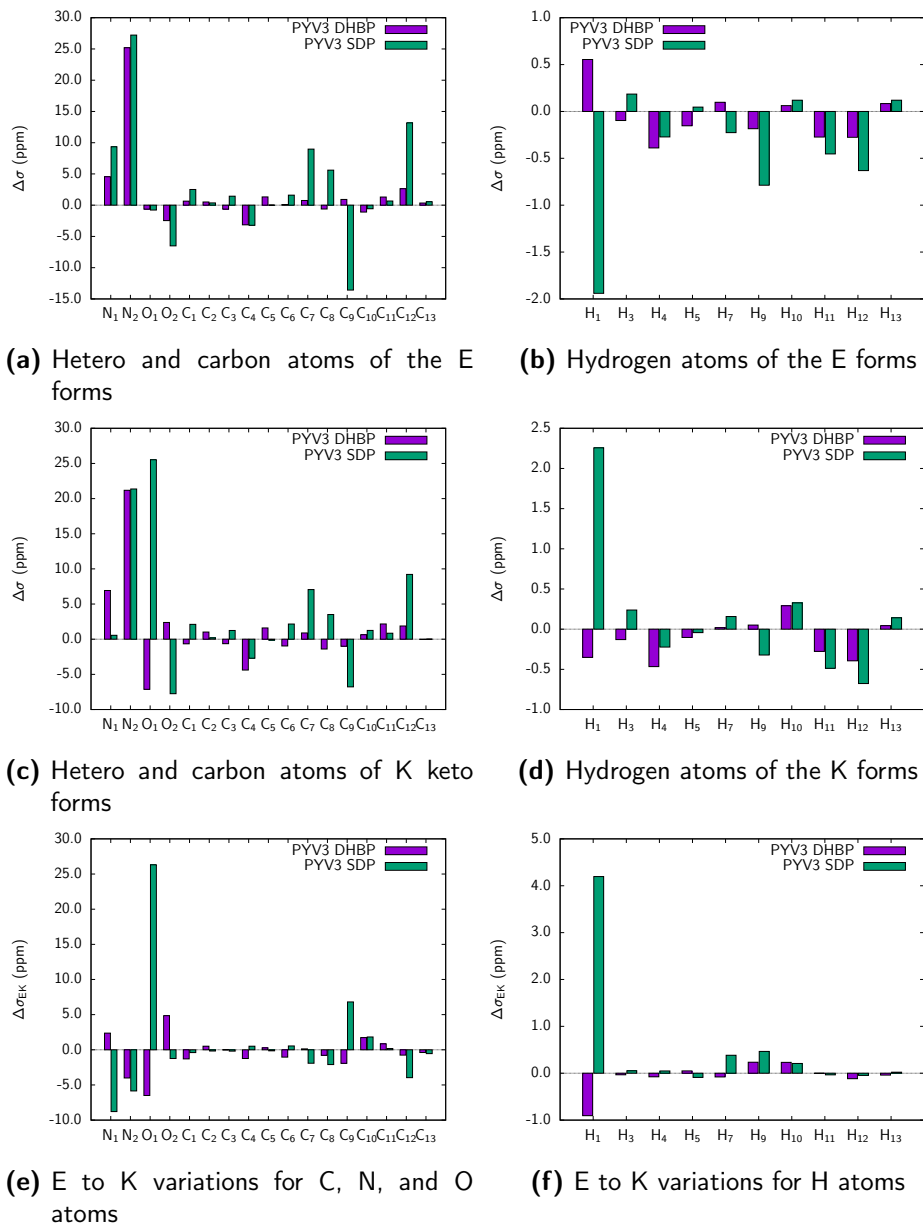


Figure 6.5: Variations of isotropic NMR shielding constants from PYV3 to the co-crystals, $\Delta\sigma_{\text{co-crystal}} = \sigma_{\text{co-crystal}} - \sigma_{\text{PYV3}}$ (in ppm) and of their corresponding enol to keto switching, $\Delta\sigma_{\text{EK,co-crystal}} = \Delta\sigma_{\text{co-crystal,K}} - \Delta\sigma_{\text{co-crystal,E}} = \Delta\sigma_{\text{EK,co-crystal}} - \Delta\sigma_{\text{EK,PYV3}}$ (in ppm) as calculated at the B3LYP/6-311+G(2d,p)//PBC/PBEsol0/6-31G(d,p) level of approximation using the scrf-ESPd embedding scheme.

variations of the shielding constants originate from the different orientation of the pyridyl group. As a complement in view of rationalizing the results, a certain relationship between the shielding constants and the scrf-ESPd atomic charges of the aromatic C atoms has been unraveled, as shown in Figure C.1 with a R^2 value of 0.64.

This method being quite general, it can be applied to other molecular crystals and co-crystals. More importantly, the above results are now expected to be compared to experiment with a double aim: i) for crystals where the enol or the keto form is largely dominant, experiment will enable to assess the accuracy of the method, as it was done successfully in many occasions for molecules in solutions while ii) for crystals where the keto/enol ratio is undefined, this method could help rationalizing the results of variable-temperature NMR experiments.

Acknowledgements

This work was carried out thanks to funding of "Actions de Recherche Concertées" (ARC) de la Direction générale de l'Enseignement non obligatoire et de la Recherche scientifique - Direction de la Recherche scientifique - Communauté française de Belgique, under convention No. 15/20-068. This research used resources of the "Plateforme Technologique de Calcul Intensif (PTCI)" (<http://www.ptci.unamur.be>) located at the University of Namur, Belgium, which is supported by the FNRS-FRFC, the Walloon Region, and the University of Namur (Conventions No. 2.5020.11, GEQ U.G006.15, 1610468, and RW/GEQ2016). The PTCI is member of the "Consortium des Équipements de Calcul Intensif (CÉCI)" (<http://www.ceci-hpc.be>).

Bibliography

- (1) *Organic Photochromic and Thermochromic Compounds*; Crano, J. C., Guglielmetti, R. J., Eds.; Plenum: New York, NY, 1998.
- (2) *Molecular Switches*; Feringa, B. L., Browne, W. R., Eds.; Wiley-VCH Verlag GmbH & Co. KGaA: Weinheim, Germany, 2011, DOI: 10.1002/9783527634408.
- (3) *Tautomerism: Methods and Theories*; Antonov, L., Ed.; Wiley-VCH: 2013.
- (4) *Tautomerism: Concepts and Applications in Science and Technology*; Antonov, L., Ed.; WILEY-VCH: 2016.
- (5) Anelli, P.-L. et al. Toward Controllable Molecular Shuttles. *Chem. - A Eur. J.* **1997**, *3*, 1113–1135, DOI: 10.1002/chem.19970030719.
- (6) Chong, Y. S.; Dial, B. E.; Burns, W. G.; Shimizu, K. D. Covalent Locking and Unlocking of an Atropisomeric Molecular Switch. *Chem. Commun.* **2012**, *48*, 1296–1298, DOI: 10.1039/c2cc16511b.

- (7) Im Jun, S.; Wook Lee, J.; Sakamoto, S.; Yamaguchi, K.; Kim, K. Rotaxane-Based Molecular Switch with Fluorescence Signaling. *Tetrahedron Lett.* **2000**, *41*, 471–475, DOI: 10.1016/S0040-4039(99)02094-8.
- (8) Cao, Z.-q.; Miao, Q.; Zhang, Q.; Li, H.; Qu, D.-h.; Tian, H. A fluorescent bistable [2]rotaxane molecular switch on SiO₂ nanoparticles. *Chem. Commun.* **2015**, *51*, 4973–4976, DOI: 10.1039/C4CC09976A.
- (9) Aidibi, Y.; Guerrin, C.; Alévêque, O.; Leriche, P.; Delbaere, S.; Sanguinet, L. BT-2-BOX: An Assembly toward Multimodal and Multilevel Molecular System Simple as a Breeze. *J. Phys. Chem. C* **2019**, *123*, 11823–11832, DOI: 10.1021/acs.jpcc.9b00546.
- (10) *Calculation of NMR and EPR Parameters*; Kaupp, M., Bühl, M., Malkin, V., Eds.; Wiley-VCH: 2004.
- (11) Smith, S.; Goodman, J. Assigning the Stereochemistry of Pairs of Diastereoisomers Using GIAO NMR Shift Calculation. *J. Org. Chem.* **2009**, *74*, 4597–4607.
- (12) Diliën, H.; Marin, L.; Botek, E.; Champagne, B.; Lemaure, V.; Beljonne, D.; Lazzaroni, R.; Cleij, T. J.; Maes, W.; Lutsen, L.; Vanderzande, D.; Adriaenssens, P. J. Fingerprints for Structural Defects in Poly(thienylene vinylene) (PTV): A Joint Theoretical–Experimental NMR Study on Model Molecules. *J. Phys. Chem. B* **2011**, *115*, 12040–12050, DOI: 10.1021/jp206663v.
- (13) Szalóki, G.; Sevez, G.; Berthet, J.; Pozzo, J.-L.; Delbaere, S. A Simple Molecule-Based Octastate Switch. *J. Am. Chem. Soc.* **2014**, *136*, 13510–13513, DOI: 10.1021/ja506320j.
- (14) Flaig, D.; Maurer, M.; Hanni, M.; Braunger, K.; Kick, L.; Thubauville, M.; Ochsenfeld, C. Benchmarking Hydrogen and Carbon NMR Chemical Shifts at HF, DFT, and MP2 Levels. *J. Chem. Theor. Comput.* **2014**, *10*, 572–578.
- (15) Hadj Mohamed, S.; Trabelsi, M.; Champagne, B. Assigning the Stereochemistry of Syn and Anti β -trimethylsiloxy- α -trimethylsilyl Alkanoic Acid Silyl Esters Using GIAO ¹H NMR Chemical Shift Calculations. *J. Molec. Struct.* **2017**, *1141*, 436–440.
- (16) Hadj Mohamed, S.; Quertinmont, J.; Delbaere, S.; Sanguinet, L.; Champagne, B. Assessing the Structure of Octastate Molecular Switches Using ¹H NMR Density Functional Theory Calculations. *J. Phys. Chem. C* **2018**, *122*, 1800–1808, DOI: 10.1021/acs.jpcc.7b11221.
- (17) Berthet, J.; Agouridas, L.; Chen, S.; Allouchi, H.; Melnyk, P.; Champagne, B.; Delbaere, S. Synthesis and Switching Properties of New Derivatives of Azoresveratrol. *Dye. Pigment.* **2019**, *171*, 107666, DOI: 10.1016/j.dyepig.2019.107666.

- (18) Sun, Z.; Luo, J.; Zhang, S.; Ji, C.; Zhou, L.; Li, S.; Deng, F.; Hong, M. Solid-State Reversible Quadratic Nonlinear Optical Molecular Switch with an Exceptionally Large Contrast. *Adv. Mater.* **2013**, *25*, 4159–4163, DOI: 10.1002/adma.201301685.
- (19) Campos, R.; Reuther, J. F.; Mammoottil, N. R.; Novak, B. M. Solid State Sensing of Nonpolar VOCs Using the Bistable Expansion and Contraction of Helical Polycarbodiimides. *Macromolecules* **2017**, *50*, 4927–4934, DOI: 10.1021/acs.macromol.7b01095.
- (20) Ogawa, K.; Kasahara, Y.; Ohtani, Y.; Harada, J. Crystal Structure Change for the Thermochromy of N-Salicylideneanilines. The First Observation by X-ray Diffraction. *J. Am. Chem. Soc.* **1998**, *120*, 7107–7108.
- (21) Pickard, C. J.; Mauri, F. All-Electron Magnetic Response with Pseudopotentials: NMR Chemical Shifts. *Phys. Rev. B* **2001**, *63*, 245101, DOI: 10.1103/PhysRevB.63.245101.
- (22) Yates, J. R.; Pickard, C. J.; Mauri, F. Calculation of NMR Chemical Shifts for Extended Systems Using Ultrasoft Pseudopotentials. *Phys. Rev. B* **2007**, *76*, 024401, DOI: 10.1103/PhysRevB.76.024401.
- (23) Truflandier, L.; Paris, M.; Boucher, F. Density Functional Theory Investigation of 3D Transition Metal NMR Shielding Tensors in Diamagnetic Systems Using the Gauge-Including Projector Augmented-Wave Method. *Phys. Rev. B* **2007**, *76*, 035102.
- (24) Bonhomme, C.; Gervais, C.; Babonneau, F.; Coelho, C.; Pourpoint, F.; Azaïs, T.; Ashbrook, S. E.; Griffin, J. M.; Yates, J. R.; Mauri, F.; Pickard, C. J. First-Principles Calculation of NMR Parameters Using the Gauge Including Projector Augmented Wave Method: A Chemist's Point of View. *Chem. Rev.* **2012**, *112*, 5733–5779, DOI: 10.1021/cr300108a.
- (25) Reddy, G. N. M.; Cook, D. S.; Iuga, D.; Walton, R. I.; Marsh, A.; Brown, S. P. An NMR Crystallography Study of the Hemihydrate of 2', 3'-O-Isopropylidineguanosine. *Solid State Nucl. Magn. Reson.* **2015**, *65*, 41–48, DOI: 10.1016/j.ssnmr.2015.01.001.
- (26) Szeleszczuk, Ł.; Pisklak, D. M.; Zielińska-Pisklak, M.; Wawer, I. Effects of Structural Differences on the NMR Chemical Shifts in Cinnamic Acid Derivatives: Comparison of GIAO and GIPAW Calculations. *Chem. Phys. Lett.* **2016**, *653*, 35–41, DOI: 10.1016/j.cpllett.2016.04.075.
- (27) Marín-Luna, M.; Alkorta, I.; Elguero, J. A Theoretical NMR Study of Selected Benzazoles: Comparison of GIPAW and GIAO-PCM (DMSO) Calculations. *Magn. Reson. Chem.* **2018**, *56*, 164–171, DOI: 10.1002/mrc.4674.

- (28) Özcan, N.; Kortelainen, T.; Golovanov, V.; Rantala, T. T.; Vaara, J. Electron Spin Resonance Parameters of Bulk Oxygen Vacancy in Semi-conducting Tin Dioxide. *Phys. Rev. B* **2010**, *81*, 235202, DOI: 10.1103/PhysRevB.81.235202.
- (29) Beran, G. J. O.; Hartman, J. D.; Heit, Y. N. Predicting Molecular Crystal Properties from First Principles: Finite-Temperature Thermochemistry to NMR Crystallography. *Acc. Chem. Res.* **2016**, *49*, 2501–2508.
- (30) Hartman, J. D.; Kudla, R. A.; Day, G. M.; Mueller, L. J.; Beran, G. J. O. Benchmark Fragment-Based ^1H , ^{13}C , ^{15}N and ^{17}O Chemical Shift Predictions in Molecular Crystals. *Phys. Chem. Chem. Phys.* **2016**, *18*, 21686–21709, DOI: 10.1039/C6CP01831A.
- (31) Hartman, J. D.; Balaji, A.; Beran, G. J. O. Improved Electrostatic Embedding for Fragment-Based Chemical Shift Calculations in Molecular Crystals. *J. Chem. Theory Comput.* **2017**, *13*, 6043–6051, DOI: 10.1021/acs.jctc.7b00677.
- (32) Hartman, J. D.; Beran, G. J. Accurate ^{13}C and ^{15}N Molecular Crystal Chemical Shielding Tensors from Fragment-Based Electronic Structure Theory. *Solid State Nucl. Magn. Reson.* **2018**, *96*, 10–18, DOI: 10.1016/j.ssnmr.2018.09.003.
- (33) Seidler, T.; Stadnicka, K.; Champagne, B. Evaluation of the Linear and Second-Order NLO Properties of Molecular Crystals within the Local Field Theory: Electron Correlation Effects, Choice of XC Functional, ZPVA Contributions, and Impact of the Geometry in the Case of 2-Methyl-4-nitroaniline. *J. Chem. Theory Comput.* **2014**, *10*, 2114–2124, DOI: 10.1021/ct5001654.
- (34) Seidler, T.; Stadnicka, K.; Champagne, B. Second-order Nonlinear Optical Susceptibilities and Refractive Indices of Organic Crystals from a Multiscale Numerical Simulation Approach. *Adv. Opt. Mater.* **2014**, *2*, 1000–1006, DOI: 10.1002/adom.201400245.
- (35) Seidler, T.; Champagne, B. Which Charge Definition for Describing the Crystal Polarizing Field and the $\chi^{(1)}$ and $\chi^{(2)}$ of Organic Crystals? *Phys. Chem. Chem. Phys.* **2015**, *17*, 19546–19556, DOI: 10.1039/C5CP03248B.
- (36) Wilbraham, L.; Adamo, C.; Labat, F.; Ciofini, I. Electrostatic Embedding to Model the Impact of Environment on Photophysical Properties of Molecular Crystals: A Self-Consistent Charge Adjustment Procedure. *J. Chem. Theory Comput.* **2016**, *12*, 3316–3324, DOI: 10.1021/acs.jctc.6b00263.

- (37) Dommett, M.; Rivera, M.; Crespo-Otero, R. How Inter- and Intramolecular Processes Dictate Aggregation-Induced Emission in Crystals Undergoing Excited-State Proton Transfer. *J. Phys. Chem. Lett.* **2017**, *8*, 6148–6153, DOI: 10.1021/acs.jpclett.7b02893.
- (38) Rivera, M.; Dommett, M.; Crespo-Otero, R. ONIOM(QM:QM') Electrostatic Embedding Schemes for Photochemistry in Molecular Crystals. *J. Chem. Theory Comput.* **2019**, *15*, 2504–2516, DOI: 10.1021/acs.jctc.8b01180.
- (39) Derenzo, S. E.; Klintonberg, M. K.; Weber, M. J. Determining Point Charge Arrays that Produce Accurate Ionic Crystal Fields for Atomic Cluster Calculations. *J. Chem. Phys.* **2000**, *112*, 2074–2081, DOI: 10.1063/1.480776.
- (40) Klintonberg, M.; Derenzo, S.; Weber, M. Accurate Crystal Fields for Embedded Cluster Calculations. *Comput. Phys. Commun.* **2000**, *131*, 120–128, DOI: 10.1016/S0010-4655(00)00071-0.
- (41) Dovesi, R.; Orlando, R.; Erba, A.; Zicovich-Wilson, C. M.; Civalieri, B.; Casassa, S.; Maschio, L.; Ferrabone, M.; De La Pierre, M.; D'Arco, P.; Noël, Y.; Causà, M.; Rérat, M.; Kirtman, B. CRYSTAL14: a Program for the Ab Initio Investigation of Crystalline Solids. *Int. J. Quantum Chem.* **2014**, *114*, 1287–1317.
- (42) Perdew, J. P.; Ruzsinszky, A.; Csonka, G. I.; Vydrov, O. A.; Scuseria, G. E.; Constantin, L. A.; Zhou, X.; Burke, K. Restoring the Density-Gradient Expansion for Exchange in Solids and Surfaces. *Phys. Rev. Lett.* **2008**, *100*, 136406.
- (43) Feller, D. The Role of Databases in Support of Computational Chemistry Calculations. *J. Comput. Chem.* **1996**, *17*, 1571–1586.
- (44) Schuchardt, K. L.; Didier, B. T.; Elsethagen, T.; Sun, L.; Gurumoorthi, V.; Chase, J.; Li, J.; Windus, T. L. Basis Set Exchange: A Community Database for Computational Sciences. *J. Chem. Inf. Model.* **2007**, *47*, 1045–1052.
- (45) Quertinmont, J.; Carletta, A.; Tumanov, N. A.; Leyssens, T.; Wouters, J.; Champagne, B. Assessing density functional theory approaches for predicting the structure and relative energy of salicylideneaniline molecular switches in the solid state. *J. Phys. Chem. C* **2017**, *121*, 6898–6908, DOI: 10.1021/acs.jpcc.7b00580.
- (46) Quertinmont, J.; Leyssens, T.; Wouters, J.; Champagne, B. Effects of Empirical Dispersion Energy on the Geometrical Parameters and Relative Energy of a Salicylideneaniline Molecular Switch in the Solid State. *Crystals* **2018**, *8*, 125, DOI: 10.3390/cryst8030125.

- (47) Cheeseman, J. R.; Trucks, G. W.; Keith, T. A.; Frisch, M. J. A Comparison of Models for Calculating Nuclear Magnetic Resonance Shielding Tensors. *J. Chem. Phys.* **1996**, *104*, 5497–5509, DOI: 10.1063/1.471789.
- (48) Frisch, M. J. et al. Gaussian~16 Revision B.01, Gaussian Inc. Wallingford CT, 2016.
- (49) Breneman, C. M.; Wiberg, K. B. Determining Atom-Centered Monopoles from Molecular Electrostatic Potentials. The Need for High Sampling Density in Formamide Conformational Analysis. *J. Comput. Chem.* **1990**, *11*, 361–373, DOI: 10.1002/jcc.540110311.
- (50) Smulders, C.; Carletta, A.; Wouters, J. Ingénierie cristalline du thermo- et photochromisme des N-salicylidèneaminopyridines par cocrystallisation, 2017.
- (51) Carletta, A. Photochromic multicomponent crystalline materials based on N-salicylideneanilines, Ph.D. Thesis, Université de Namur, 2019.

UNRAVELING THE EFFECTS OF CO-CRYSTALLIZATION ON THE UV/VIS ABSORPTION SPECTRA OF A N-SALICYLIDENEANILINE. A COMPUTATIONAL RI-CC2 INVESTIGATION

Just Accepted in MOLECULES

Jean Quertinmont[†], Tom Leyssens[‡], Johan Wouters[†], & Benoît Champagne[†]

[†] *Unité de Chimie Physique Théorique et Structurale, Chemistry Department, University of Namur, 61 rue de Bruxelles, B-5000 Namur, Belgium*

[‡] *Institute of Condensed Matter and Nanosciences, Université Catholique de Louvain, 1 Place Louis Pasteur, B-1348 Louvain-La-Neuve, Belgium*

This chapter focuses on modeling the UV/Vis absorption spectra of co-crystals of an anil at the coupled cluster (CC) level of approximation. It will be submitted in the near future. All calculations, their analysis, and writing of the first draft were performed by J.Q.

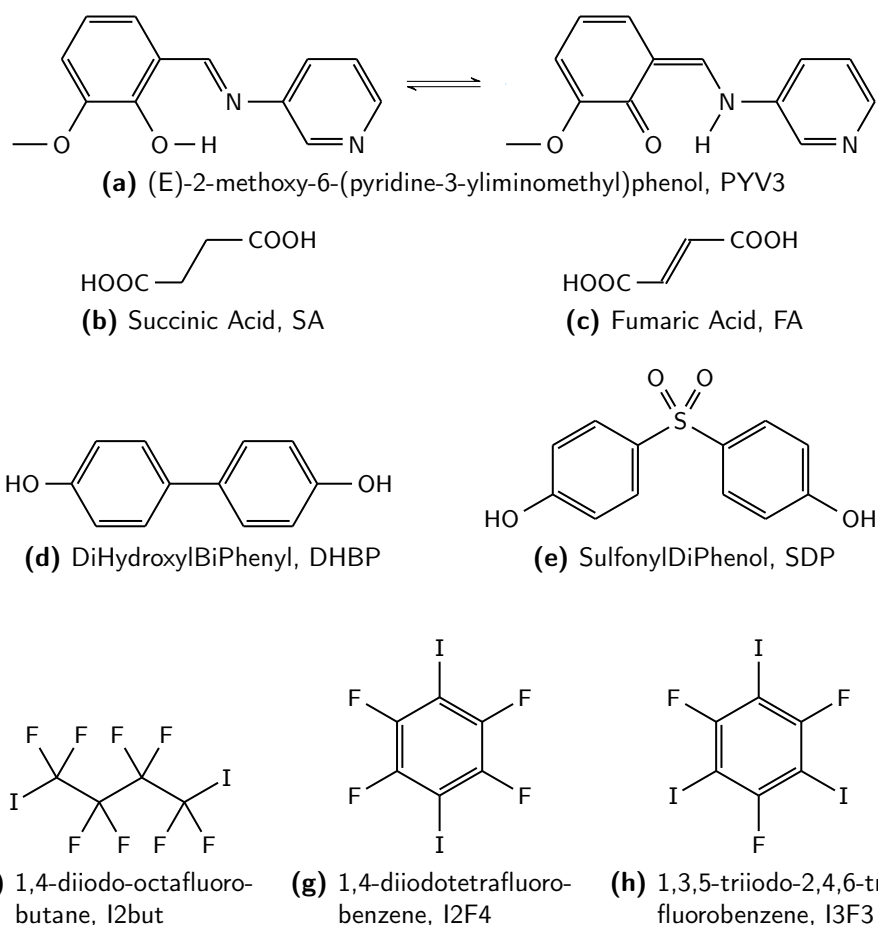
Abstract

This work aims at unraveling the effects of co-crystallization on the optical properties of a N-salicylideneaniline-derived molecular switch transforming between an enol and a keto form. This is achieved by way of a two step multi-scale method where i) the molecular geometry and unit cell parameters are optimized using a periodic boundary conditions density functional theory method and ii) the optical properties are computed for a selection of clusters embedded in an array of point-charges that reproduce the crystal field electronic potential. The optical properties (vertical excitation energies and oscillator strengths) are obtained at the RI-CC2/def2-TZVPD level of approximation. This method allows to decompose the effects of co-crystallization into i) indirect effects, the geometry changes of the chromophore due to crystal packing with the coformer, and ii) direct ones, the polarization due to the interacting coformer and to the crystal field. For the former effects, variations of a crucial torsion angle lead to modification of the π -conjugation and therefore to the decrease or increase of the excitation energies. About the latter, they are antagonistic: i) the coformer is not directly involved in the excitations but its polarization decreases the excitation energies while ii) the crystal field has the opposite effect. For the co-crystals with succinic and fumaric acids, combining these direct and indirect effects leads to a hypsochromic shift of the first absorption band with respect to the reference crystal, in agreement with experimental data.

7.1 Introduction

Co-crystallization can be used to tune the properties of molecular switches: for example, a N-salicylideneaniline (anil), which equilibrates between an enol (E) and a keto (K) form becomes photochromic upon co-crystallization with two different coformers: succinic acid (SA) or fumaric acid (FA).¹ The coformer can have effects at multiple levels: changing the thermodynamics and/or the kinetics of the tautomeric equilibrium and modifying its electronic properties such as the UV/Vis absorption or the excited states dynamics. These are generally related to a change of the geometry as well as to steric hindrance and confinement effects. The effects on the relative energy and on the geometry have already been addressed in Ref. [2]. Focusing now on the effects on the UV/Vis absorption spectra, a series of hydrogen bond and halogen bond co-crystals of (E)-2-methoxy-6-(pyridine-3-yliminomethyl)phenol, PYV3, are studied (Scheme 7.1 for its structure, the enol/keto equilibrium, and the coformers). The synthons of the enol forms of the co-crystals are given in Figure 7.1. Note that in the case of the fumaric acid (FA) coformer, there are two polymorphic co-crystals named PYV3-FA1 and PYV3-FA2, where the former is isostructural to PYV3-SA. Based on those, we define the "monomer" of the co-crystal as a single anil molecule (either in its enol or keto form) and the "heteromers" as the anil and its directly interacting coformer(s). In our nomenclature, PYV3[PYV3-SA] stands for the monomer of the co-crystal of PYV3 with succinic acid, *i.e.* the PYV3 molecule in the geometry of its co-crystal with SA. Similarly, PYV3+SA[PYV3-SA] is the heteromer of the same co-crystal, *i.e.* one PYV3 and one SA molecule as in the PYV3-SA co-crystal (synthon c of Figure 7.1). The objective of this work is to study the effects of co-crystallization on the optical properties: the excitation energies, the oscillator strengths, the electronic transitions, and the UV/Vis absorption spectra.

The proposed methodology consists in combining firstly periodic boundary conditions (PBC) density functional theory (DFT) method to optimize both the molecular geometry and unit cell parameters of the crystal and secondly an embedding method to compute the optical properties. This methodology allows to decompose the effects of the (co-)crystal surrounding into direct and indirect effects. The latter originates from the fact that upon (co-)crystallization, the geometry of the chromophore is modified, which leads to variations of the optical properties. On the other hand, the former originates from the effect of the surrounding polarization on the ground and excited state wavefunctions, and therefore influences the absorption spectra. The calculation of the optical properties is achieved by extracting a monomer or heteromer from the crystal structure and then embedding it in an array of point-charges fitted to reproduce the full Coulombic potential of the crystal. The array is computed by the Ewald program.^{3,4} It uses three zones: the first one contains the molecule(s) on which a quantum treatment is performed on, zone 2 is made of unmod-



Scheme 7.1: Structures of PYV3 and its coformers, (a) anil and its enol-keto equilibrium; coformers interacting by H-bond (b)-(e) or X-bond (f)-(h).

ified point-charges, while the point-charges of zone 3 are fitted to reproduce the Ewald potential. The three zones are user-defined. The calculations of the optical properties are done at the coupled cluster approximate doubles (CC2) level of approximation⁵ in combination with the resolution of the identity (RI) approximation:^{6,7} RI-CC2. This method presents the advantage of being less computationally demanding than the more accurate coupled cluster singles and doubles (CCSD) model. While time-dependent DFT (TD-DFT) could have been used, it poses significant additional questions: which exchange correlation functional (XCF) to use? Can a single functional be accurate for both excitation energies and oscillator strengths? Or for both the anil and its coformers? Thus, to get away from those potential issues, RI-CC2 was selected. Yet, this is not a perfect solution, as it comes with its own issues, namely how approximate are the doubles compared to CCSD? This particular topic, as well as the choice of the basis set are therefore tackled in the next Section. Despite that, it was

already shown that CC2 performs well for both the excitation energies and the oscillator strengths.^{8–13} One of the tools used to analyze the excited states are the NTOs, which describe the electronic transitions in a more "natural" fashion than with MOs.^{14,15} Their properties and methods of calculations are described in the following section. This three-step scheme has already been successfully applied to the evaluation of different types of properties in the solid state,^{16–19} including in the case of anil derivatives.^{17,18}

7.2 Methods and Computational Aspects

Crystal geometries were taken from Ref. [2]. They have been obtained from full geometry optimizations (geometry of the molecules and unit cell parameters) performed using periodic boundary conditions (PBC) density functional theory (DFT) calculations, as implemented in the CRYSTAL14 package.²⁴ Previously, we have shown that the PBEsol0 exchange correlation functional (the global hybrid variant of PBEsol²⁵) used with Pople's 6-31G(d,p) (as taken from the Basis Set Exchange website^{26–28}) is appropriate for the optimization of crystalline anils.^{29,30} For iodine, the LANL2DZ effective core potential (ECP) was used. Default convergence parameters were used while the shrinking factor of the irreducible Brillouin zone was set to 6 (yielding between 64 and 112 points of integration) and the tolerance criteria for the Coulomb and exchange integrals (keyword TOLINTEG) was set to "8 8 8 8 16".

The Mulliken charges were evaluated with the same method as for the crystal geometry optimizations. Using those charges, the Ewald program^{3,4} (modified to handle partial charges) was used to generate arrays of point-charges that reproduce the full Coulombic potential of the crystal. The parameters used for each crystal are given in the Supporting Information, Table D.1.

Vertical excitation energies and oscillator strengths were computed using the coupled cluster approximate doubles (CC2)⁵ and coupled cluster singles and doubles (CCSD) models in combination with the resolution of the identity (RI) approximation^{6,7} (RI-CC2 and RI-CCSD) with Ahlrichs and coworkers' basis sets^{31–34} as implemented in the TURBOMOLE package.³⁵ The DrawSpectrum program from the DrawMol suite³⁶ was then used to transform the excited state data into UV/Vis absorption spectra using Gaussian functions with full width at half maximum value of 0.3 eV.

To analyze the excitations, the natural transition orbitals (NTOs) were computed by TURBOMOLE³⁵ and then represented using DrawMol.³⁶ An excited state can be described by a huge combination of simple determinant-based electronic transitions, which are given in terms of the MOs. The transition density matrix of single excitations, \mathbf{T} , thus takes the dimensions (N_o, N_u) , where N_o is the number of occupied MOs and N_u the number of unoccupied MOs. By applying unitary transformations to \mathbf{T} , it can be reduced to a square matrix of dimension (N_o, N_o) . This effectively condenses the information of the transitions into a

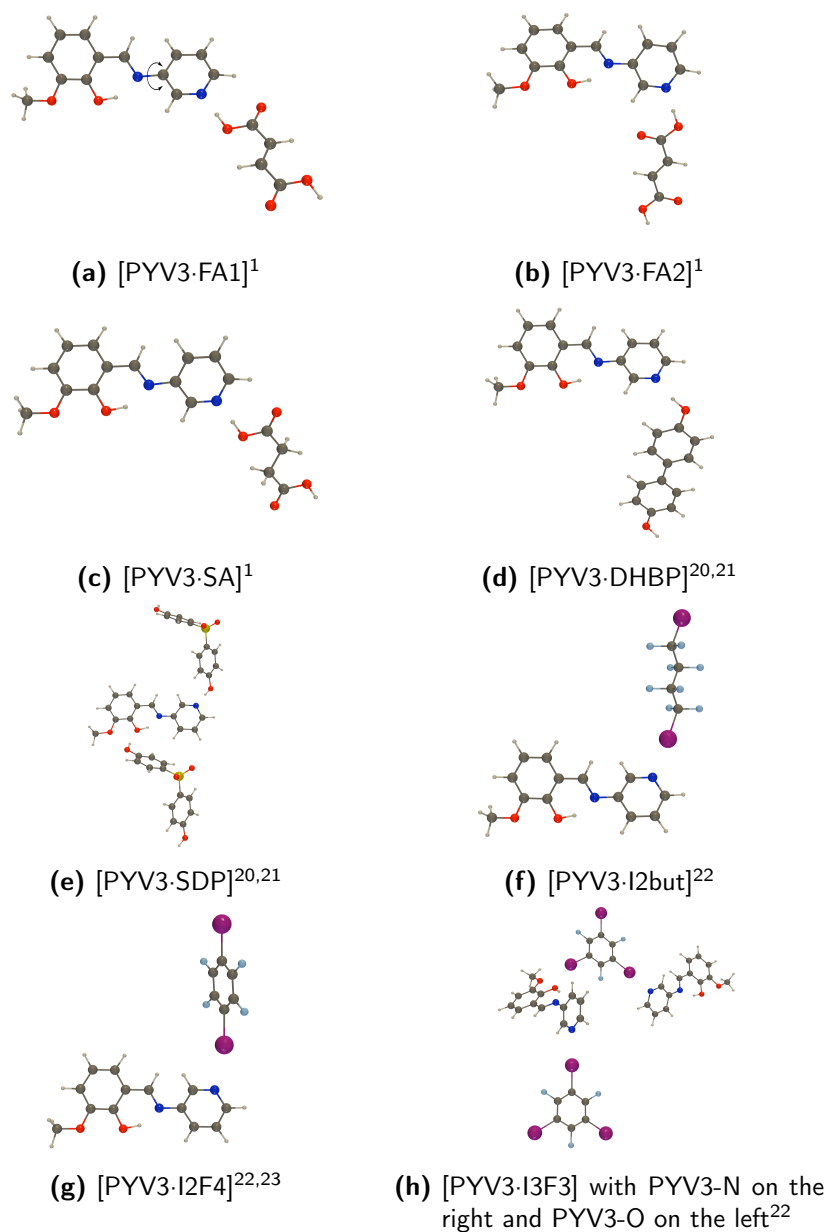


Figure 7.1: Representation of the PYV3-coformer synthons as extracted from the co-crystal structure optimized at the PBC/PBEsol0/6-31G(d,p)/I(LANL2DZ) level of approximation. Here, the enol form was considered for all co-crystals. The corresponding references to the X-ray diffraction structures are also provided. In the case of a, an arrow has been added to define the pyridine torsion angle.

smaller set of orbitals, the NTOs, that describe the hole created by the electronic promotion (in the occupied space) and the corresponding created particle (in the unoccupied space).^{14,15}

7.2.1 Effects of the Basis Set

In order to select a basis set, the UV/Vis absorption spectrum of both forms of the PYV3-I2but heteromer (PYV3+I2but[PYV3-I2but]) were simulated for a broad selection of Ahlrichs basis sets (from a split valence set, def2-SVP, to a quadruple- ζ one, def2-QZVP), see Figure 7.2. The composition of the considered basis sets are given in Table D.2. For iodine, the def-ECP effective core potential was used. Both enol and keto spectra present two absorption bands, at about 365 nm and 290 nm for the enol and 450 nm and 310 nm for the keto forms. As the basis set becomes larger (and thus more complete), the excitation energies decrease and the bands are red-shifted. Since the def2-TZVPD, def2-TZVPPD, and def2-QZVP spectra overlap perfectly, the smallest of three equally performing sets, def2-TZVPD, is therefore a suitable basis set for further calculations on the co-crystals. In order to confirm the selection of def2-TZVPD,

Table 7.1: RI-CC2 first wavelength of excitation (λ , in nm), excitation energy (E_{eg} , in eV), and oscillator strength (f), and their variations ($\Delta\lambda$ and Δf) w.r.t. def2-QZVP for the isolated PYV3-I2but heteromer as a function of the basis set. All calculations were performed at the RI-CC2 level of approximation.

Basis Set	Enol					
	λ	$\Delta\lambda$	E_{eg}	ΔE_{eg}	f	Δf
def2-SVP	355.7	−12.8	3.486	0.121	0.167	0.034
def2-SVPD	364.7	−3.7	3.400	0.034	0.138	0.005
def2-TZVP	367.0	−1.5	3.378	0.013	0.138	0.005
def2-TZVPP	367.2	−1.3	3.377	0.012	0.138	0.004
def2-TZVPD	368.3	−0.2	3.367	0.002	0.133	0.000
def2-TZVPPD	368.5	0.1	3.365	0.000	0.133	0.000
def2-QZVP	368.4	0.0	3.365	0.000	0.133	0.000
Basis Set	Keto					
	λ	$\Delta\lambda$	E_{eg}	ΔE_{eg}	f	Δf
def2-SVP	424.7	−24.9	2.920	0.162	0.323	0.065
def2-SVPD	442.6	−6.9	2.801	0.043	0.269	0.012
def2-TZVP	446.0	−3.6	2.780	0.022	0.265	0.007
def2-TZVPP	446.3	−3.2	2.778	0.020	0.265	0.007
def2-TZVPD	449.4	−0.1	2.759	0.001	0.256	−0.001
def2-TZVPPD	449.6	0.1	2.757	−0.001	0.256	−0.001
def2-QZVP	449.5	0.0	2.758	0.000	0.257	0.000

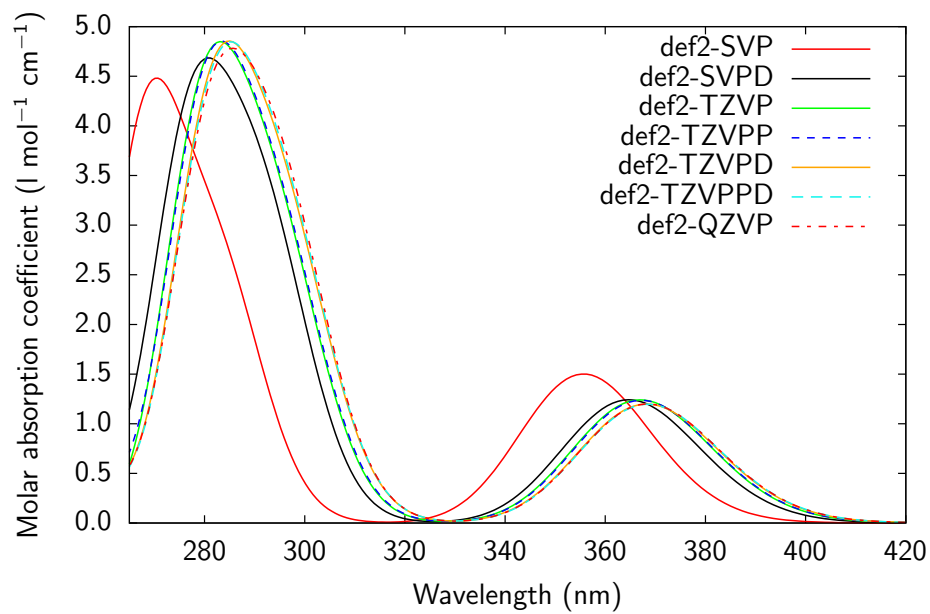
the 1st excitation energies, oscillator strengths, and their variations with respect to the largest considered set for both forms of the l2but heteromer are given in Table 7.1. With errors of the order of 0.1 nm for the wavelengths (corresponding to 0.001 eV on the excitation energies) and 0.001 for the oscillator strengths, def-TZVPD yields converged results with respect to def2-QZVP. Unless stated otherwise, all the following calculations were performed with the def2-TZVPD basis set.

7.2.2 RI-CC2 vs. RI-CCSD

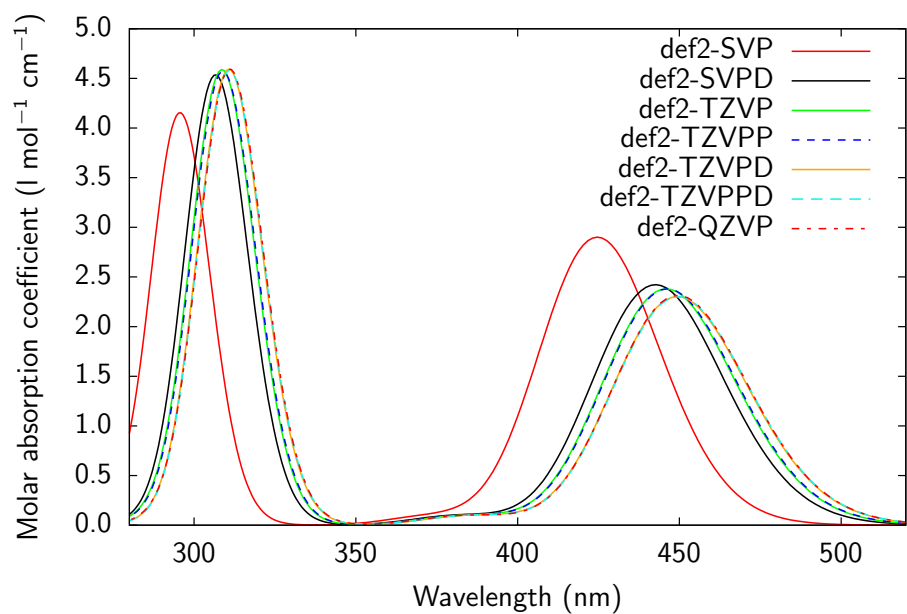
In order to evaluate the error made by using RI-CC2, isolated phase RI-CCSD excitation energy calculations on the monomers of PYV3 (PYV3[PYV3]) have been performed, see Table 7.2. Note that RI-CCSD oscillator strengths are not available in TURBOMOLE³⁵ and thus can not be compared to the RI-CC2 ones. For the first 5 excited states, RI-CC2 systematically underestimates the excitation energy. The error made is state dependent, e.g. the error for excited state 1 of

Table 7.2: Wavelengths and energies of excitation of the first 5 excited states (in nm and eV) and error ($\Delta\lambda$ and ΔE_{eg} , respectively) and the average error and standard deviations (Std. Dev.) w.r.t. CCSD for the isolated forms of PYV3[PYV3]. All calculations employ the RI approximation and the def2-TZVPD basis set.

State	Enol					
	CC2		CCSD		$\Delta\lambda$	ΔE_{eg}
	λ	E_{eg}	λ	E_{eg}		
1	360	3.44	324	3.83	37	−0.39
2	293	4.23	276	4.49	17	−0.25
3	273	4.55	252	4.92	20	−0.37
4	260	4.76	248	5.01	13	−0.25
5	253	4.90	242	5.12	11	−0.22
Average					19	−0.30
Std. Dev.					10	0.08
	Keto					
	CC2		CCSD		$\Delta\lambda$	ΔE_{eg}
	λ	E_{eg}	λ	E_{eg}		
1	440	2.82	404	3.07	36	−0.25
2	386	3.21	325	3.82	61	−0.60
3	304	4.08	283	4.38	21	−0.31
4	276	4.49	258	4.80	17	−0.30
5	258	4.81	247	5.03	11	−0.21
Average					29	−0.34
Std. Dev.					20	0.16



(a) Enol



(b) Keto

Figure 7.2: RI-CC2 UV/Vis absorption spectra of the isolated enol and keto heteromers of PYV3·I2but, PYV3+I2but[PYV3·I2but], as a function of the basis set.

the enol form amounts to 37 nm (0.39 eV), while for state 2, the error is 17 nm (0.25 eV). This leads to the following average errors and standard deviations: (19 ± 10) nm for the enol and (29 ± 20) nm for the keto forms. In other words, to recover the RI-CCSD spectra, the RI-CC2 cannot simply be shifted. The difference between the two methods is due to the different contributions of the singles and doubles clusters, T_1 and T_2 , to the excited states between the RI-CC2 and RI-CCSD results, see Table D.3. Indeed, the contribution of T_1 to an excited state relates to the character of the excitation. For RI-CC2 calculations, T_1 strongly contributes to all 5 calculated excited states, $\sim 88\%$, meaning that they have a single excitation character. When going to RI-CCSD, the T_1 contributions further increase to $\sim 92\%$, thus confirming the singles character.^{37,38} Had one of the excitations actually be of double character, the T_1 contribution would have decreased when going from RI-CC2 (which does not explicitly allow for double excitations⁵) to RI-CCSD.

The RI-CC2 NTOs of the enol form perfectly match the RI-CCSD ones, see Figure D.1. All particles are purely of π nature while from states 1 to 3, purely π holes become increasingly mixed with some σ character: for state 2, a σ part is on the double bond and for state 3 on the pyridine part (right hand side). The largest difference between the two methods is for the 3rd excited state: the hole NTO for RI-CCSD is less localized on the pyridine part than for RI-CC2, see Figures D.1e and D.1f. On the other hand, the corresponding particles are identical. For the keto form, the NTOs of the RI-CC2 and RI-CCSD excited states are the same, where both holes and particles are of π nature, see Figure D.2. Overall, RI-CC2 recovers the features of the excitations calculated with RI-CCSD, the main difference being energy shifts that are excited state dependent.

7.3 Results and Discussion

7.3.1 Effects of the Geometry

The effects of co-crystallization are multifold. Ref. [2] analyses some of those: the changes in the relative energy of the tautomers, in the geometries, and in the atomic charges distributions. This work used the crystal geometries that have been optimized in Ref. [2]. The root mean square deviation for the atomic positions of the PYV3 co-crystals compared to PYV3 range from 0.131 Å to 1.637 Å for the enol forms and from 0.037 Å to 1.630 Å for the keto ones. These large values are associated with the significant variations of the torsion angle of the pyridine. More details can be found in Ref. [2]. The characteristics of first excitation of the isolated monomers of PYV3 (PYV3[PYV3]) and of its co-crystals (PYV3[PYV3.XXX]) are given Table 7.3. For the enol forms, the PYV3·FA2, PYV3·DHBP, and PYV3·l2F4 co-crystals are barely affected, with variations of up to 2 nm for the first excitation wavelengths. The corresponding oscillator strength variations do not exceed 6%. Figure 7.3a shows those simulated spectra, highlighting the overlap of the first bands (fully characterized

by the first excitation). The second bands feature two excitations. They are more affected by the co-crystallization than the first ones. Indeed, changes in both excitation energies and oscillator strengths result in i) similarly positioned but less (PYV3·FA2) or more (PYV3·DHBP) intense bands or ii) blue-shifted bands (PYV3·I2but and PYV3·I2F4), see also Table D.4. Compared to PYV3, both are red-shifted by ~ 8 nm but because the 2nd excitation is much less intense in favor of the 3rd one, the actual band maximum is blue-shifted by about 10 nm. The second set of co-crystals (Figure 7.3b), co-crystals PYV3·SA, ·FA1, and ·I3F3, display larger first excitation energies with blue shifts ranging from 7 nm to 27 nm. As expected from Ref. [2] that highlights the isostructurality of the PYV3·SA and PYV3·FA1 co-crystals, their spectra almost perfectly overlap. Both of their bands are slightly blue-shifted (2 nm) with respect to PYV3 and thanks to a larger oscillator of the 2nd excitation, the second band is more intense. The largest variations are obtained for the PYV3·3F3 monomers: the first excitation of PYV3·N[PYV3·I3F3] is shifted by -18 nm and is less intense by 13 % while that of PYV3·O[PYV3·I3F3] by -27 nm and 25 %. Similarly to PYV3·I2but and PYV3·I2F4, the 2nd bands of PYV3·N[PYV3·I3F3] and PYV3·O[PYV3·I3F3] are strongly blue-shifted and more intense than PYV3. In these cases, the 2nd and 3rd excitations are both blue-shifted in addition to a strong decrease of oscillator strength of the 2nd excitation and an even stronger increase of the 3rd one (Table D.4). Lastly, SDP is the only example of a strong decrease of the excitation energy, *i.e.* a red-shift of the first excitation wavelength by 15 nm. Like for its second band, it is uniquely defined by the second excitation of similar energy, but stronger oscillator strength, than PYV3.

Table 7.3: RI-CC2/def2-TZVPD first wavelength and energy of excitation (λ , in nm and E_{eg} , in eV) and oscillator strength (f) for the isolated monomers of PYV3 (PYV3[PYV3]) and their variations upon co-crystallization (PYV3[PYV3·XXX]).

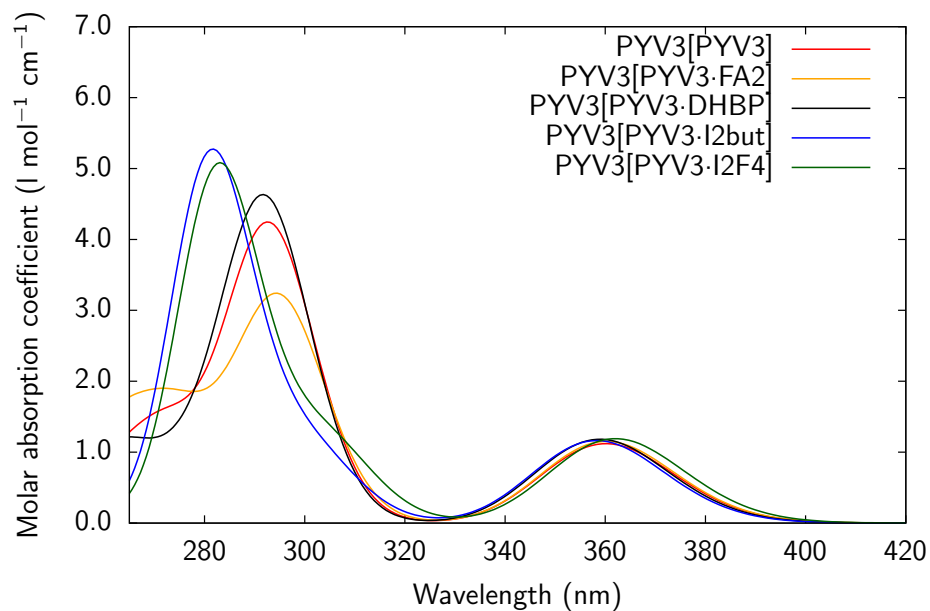
Crystal	Enol			Keto		
	λ	E_{eg}	f	λ	E_{eg}	f
PYV3[PYV3]	360	3.44	0.125	440	2.82	0.240
PYV3[PYV3·SA]	-7	$+0.07$	$+5\%$	-8	$+0.06$	$+6\%$
PYV3[PYV3·FA1]	-7	$+0.07$	$+5\%$	-8	$+0.06$	$+7\%$
PYV3[PYV3·FA2]	0	0.00	$+3\%$	-7	$+0.04$	0%
PYV3[PYV3·DHBP]	-1	$+0.01$	$+6\%$	-3	$+0.02$	0%
PYV3[PYV3·SDP]	$+15$	-0.14	$+14\%$	$+14$	-0.09	$+8\%$
PYV3[PYV3·I2but]	-2	$+0.02$	$+4\%$	$+2$	-0.01	$+2\%$
PYV3[PYV3·I2F4]	$+2$	-0.02	$+6\%$	0	0.00	$+2\%$
PYV3·N[PYV3·I3F3]	-18	$+0.18$	-13%	-12	$+0.08$	$+17\%$
PYV3·O[PYV3·I3F3]	-27	$+0.28$	-25%	-29	$+0.20$	$+11\%$

For the keto forms, the first excitations of the PYV3 molecule are barely affected by co-crystallization in the case of the PYV3·DHBP, PYV3·I2but, and PYV3·I2F4 co-crystals (Figure 7.4a, with shifts ranging from -3 nm to 2 nm and oscillator strengths variations of 0% to 2%). Similarly, the third excitations, *i.e.* the second bands, are barely affected: shifts ranging from 0 nm to 4 nm and oscillator strengths variations of 0% to 1% (Table D.5). These UV/Vis absorption spectra are given in Figure 7.4a. The remaining co-crystals, PYV3·SA, ·FA1, ·FA2, ·I3F3, and SDP, are shown in Figure 7.4b. Again, PYV3·SA and PYV3·FA1 have identical spectra where the first band is blue-shifted by 8 nm but the second one is barely changed (~ 2 nm shift and $\sim 2\%$ less intense). PYV3·FA2 differs from PYV3 only by the position of the first band, shifted by -7 nm. The PYV3 chromophore sees the largest increase of the first excitation energy corresponding to $\Delta\lambda$ of 12 nm for PYV3·N[PYV3·I3F3] and 29 nm for PYV3·O[PYV3·I3F3]. They also display stronger absorptions (17% for PYV3·N and 11% for PYV3·O). Their second bands are less affected. Indeed, PYV3·N[PYV3·I3F3] is not shifted while IPYV3·O[PYV3·I3F3] is shifted by -11 nm (less than half of the 1st band). Their intensities are on par with that of PYV3 (-3% to 1%). Like for the enols, PYV3·SDP is the only case with a significant decrease of the 1st excitation energy, or $\Delta\lambda = 14$ nm, also accompanied by a stronger absorption with respect to PYV3 (by 8%). The 2nd band (3rd excitation) is also red-shifted, but by a smaller amount, 6 nm.

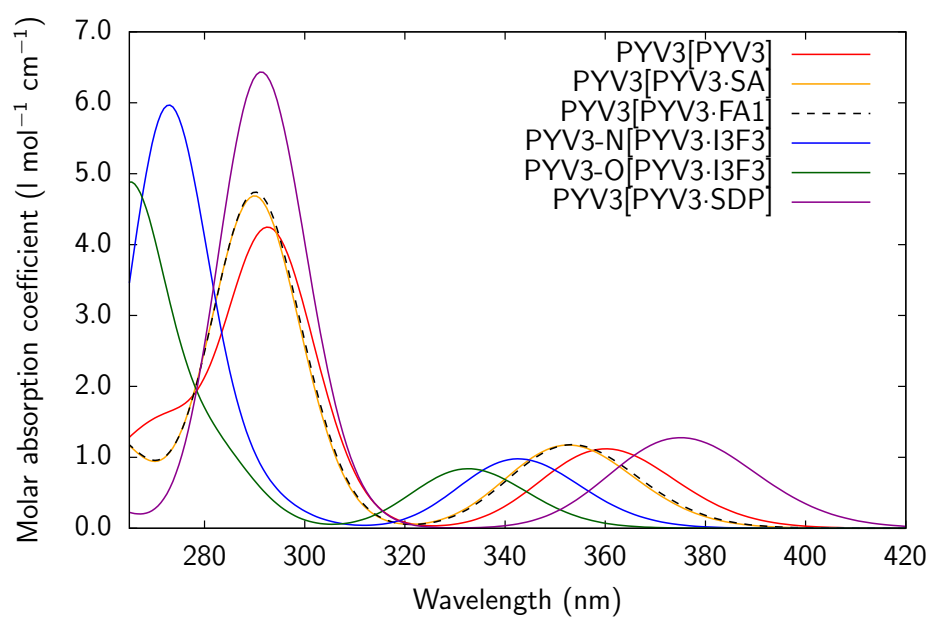
The first excitation shifts of PYV3·O[PYV3·I3F3] (-28 nm) and PYV3[PYV3·SDP] (15 nm) are related to the torsion angle between the linker and the pyridine. Indeed, it directly relates to the π -conjugation between both rings of PYV3. For PYV3·SDP, the torsion angles of the enol and keto forms are close to 0° (2° and 3° , respectively) which, compared to the PYV3 crystal values of $\sim 30^\circ$, means a greater π -conjugation and thus lower excitation energies. The opposite is true for PYV3·O[PYV3·I3F3] where its torsion angles are larger than for PYV3: 45° and 35° for the enol and keto forms, respectively. For the other co-crystals, there is no direct relationship between the variations of the torsion angles compared to PYV3[PYV3] and those, smaller, of the wavelengths of excitation.

7.3.2 Effects of the Environment

The effects of the environment are added in two steps: firstly, by considering the heteromers instead of the monomers in order to account for specific intermolecular interactions, then by further adding a point-charge embedding that reproduces the Ewald potential of the crystal, in order to include the crystal field polarization. These calculations allow for the study of the direct effects of co-crystallization on the optical properties. For illustrative purpose, this section limits itself to two co-crystals, PYV3·SA and PYV3·FA1, which are isostructural. This will allow assessing whether the explicit and implicit crystal field effects display differences or not, despite their isostructurality.

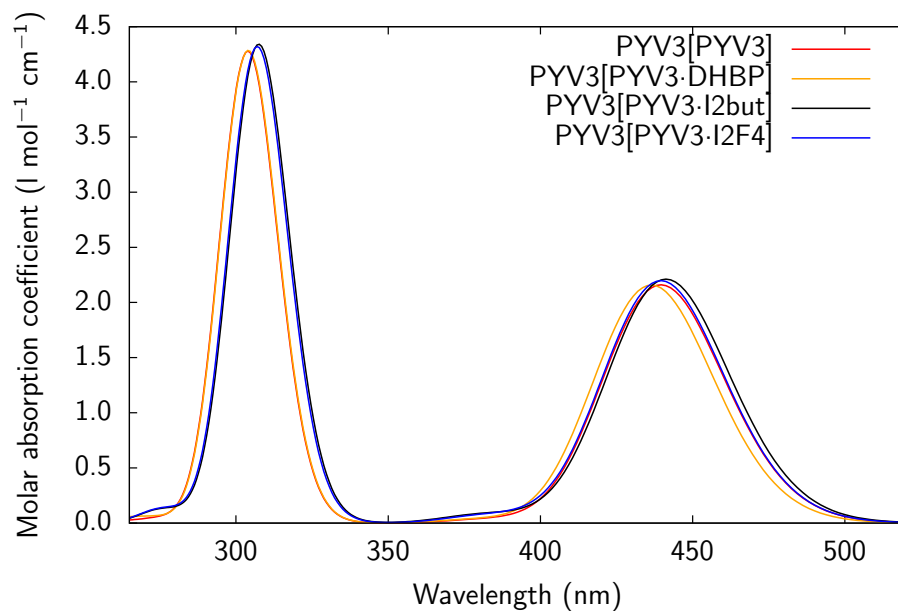


(a)

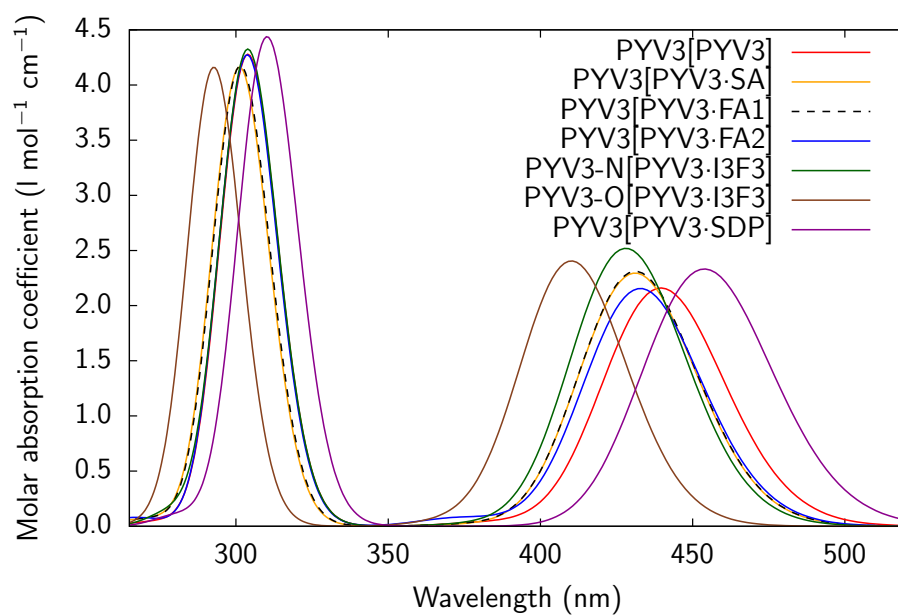


(b)

Figure 7.3: RI-CC2/def2-TZVPD UV/Vis absorption spectra of isolated monomers of all-enol crystals (PYV3[PYV3.XXX]).



(a)



(b)

Figure 7.4: RI-CC2/def2-TZVPD UV/Vis absorption spectra of isolated monomers of all-keto crystals (PYV3[PYV3·XXX]).

Table 7.4: RI-CC2/def2-TZVPD first excitation wavelength and energy (λ in nm and E_{eg} , in eV, respectively) and oscillator strength (f) for the isolated monomer of PYV3 (PYV3[PYV3]) and the variations for the heteromers of co-crystals (PYV3+XXX[PYV3·XXX]).

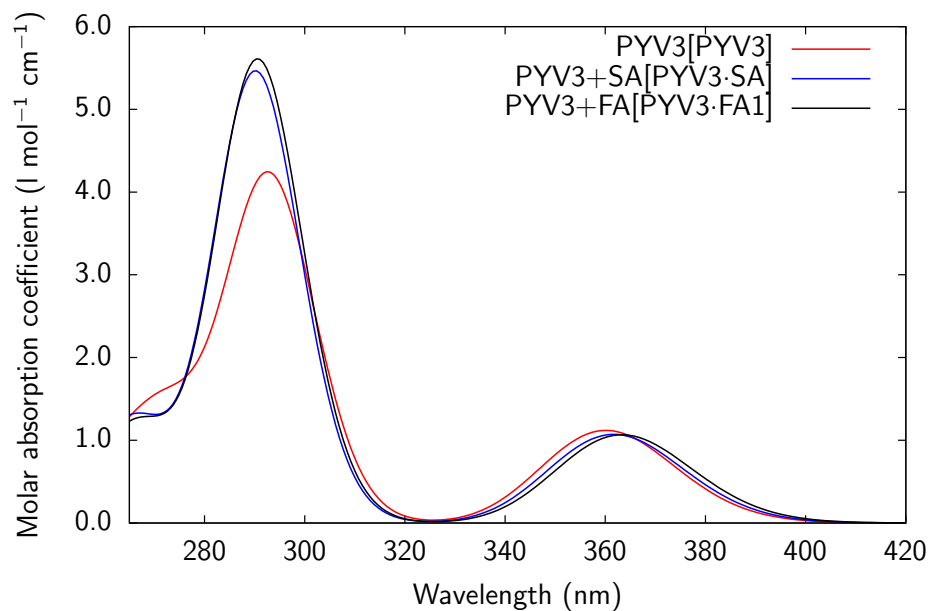
	Enol			Keto		
	λ	E_{eg}	f	λ	E_{eg}	f
PYV3[PYV3]	360	3.44	0.125	440	2.82	0.240
PYV3+SA[PYV3·SA]	+2	-0.02	-4 %	-2	+0.02	+2 %
PYV3+FA[PYV3·FA1]	+3	-0.03	-5 %	-1	+0.01	+3 %

Inclusion of the Coformers

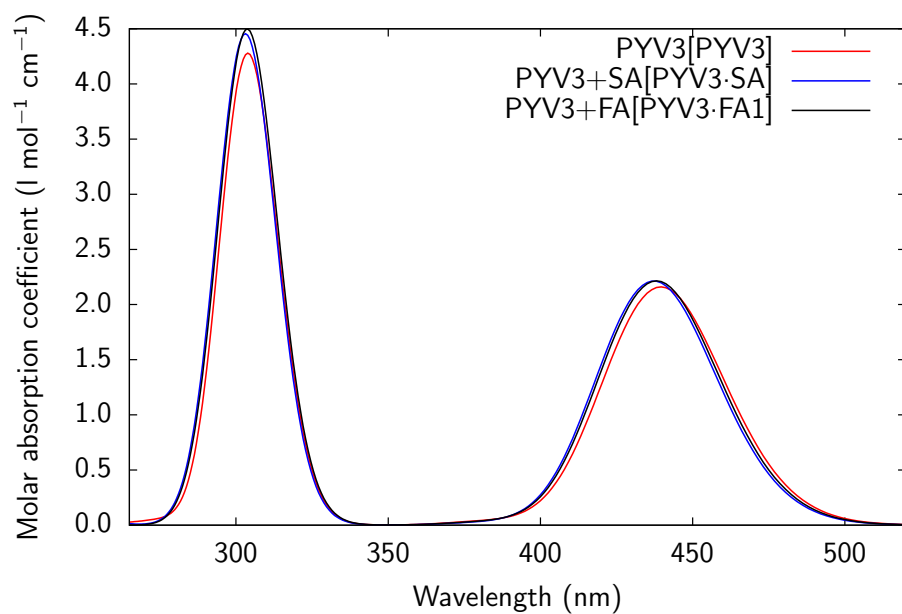
By studying heteromers instead of monomers, *i.e.* PYV3+SA[PYV3·SA] and PYV3+FA[PYV3·FA1], both the geometry effects previously discussed and the electronic effects of the coformer are considered simultaneously. Table 7.4 gives the 1st excitation data for the heteromers of PYV3·SA and PYV3·FA1 in comparison to PYV3. By adding the coformers, the first absorption band is slightly red-shifted for the enol forms (by ~ 2 nm) and blue-shifted for the keto (by ~ 1 nm) compared to PYV3[PYV3]. The effect on the oscillator strength is small with variations of just a few percents with respect to PYV3: from -5 % to 3 %. Looking at the simulated spectra, Figure 7.5a, the enol heteromers of both PYV3·SA and PYV3·FA1 show more intense 2nd bands due to larger oscillator strengths for the second excited state (by 30 %, Table D.6). The said bands are also slightly blue-shifted (by 2 nm) as the 2nd excitations of PYV3·SA and PYV3·FA1 are blue-shifted. In the case of PYV3·FA1, the 3rd excitation is forbidden in favor of the 4th one that presents the same character as the corresponding excitation for PYV3·SA (see later the discussion on the NTOs). For the keto forms, the effects of the geometry and of the inclusion of the coformer cancel each others for the 2nd bands (3rd excited states), so that they appear as unaffected (Figure 7.5b, Tables 7.4 and D.7).

Inclusion of the Crystal Field

The final step in this stepwise procedure for including the effects of the environment is to add an embedding of point-charges fitted to reproduce the crystalline Coulombic potential. Table 7.5 gives the 1st excitation data for the isolated and embedded forms of PYV3 and the variations for the embedded heteromers of the PYV3·SA and ·FA1 co-crystals. Starting with the effect of the embedding on PYV3, the first excitation energy of both forms increases, blue-shifting the 1st absorption band by 23 nm for the enol and 17 nm for the keto. On the other hand, the oscillator strengths decrease, by 18 % for the enol and 14 % for the



(a) Enol.



(b) Keto.

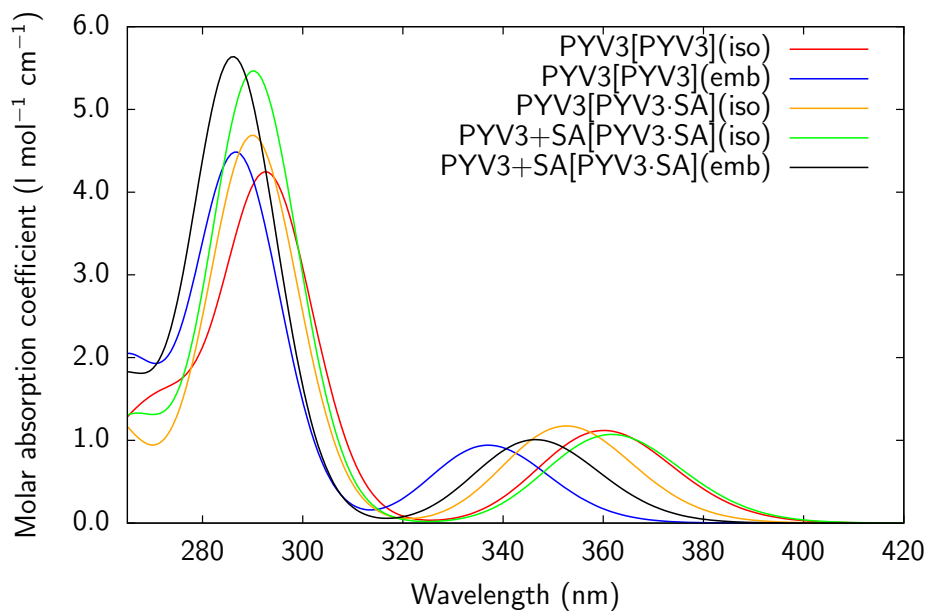
Figure 7.5: RI-CC2/def2-TZVPD UV/Vis absorption spectra of the isolated PYV3[PYV3] and of the isolated heteromers of PYV3·SA and PYV3·FA1 co-crystals (PYV3+SA[PYV3·SA] and PYV3+FA[PYV3·FA1]).

keto forms. The spectra, Figure 7.6, show that the second bands are also blue-shifted but more intensively. This is due to the increase of both the excitation energies and the intensities of the excited states contributing to the 2nd bands, see Tables D.8 and D.9.

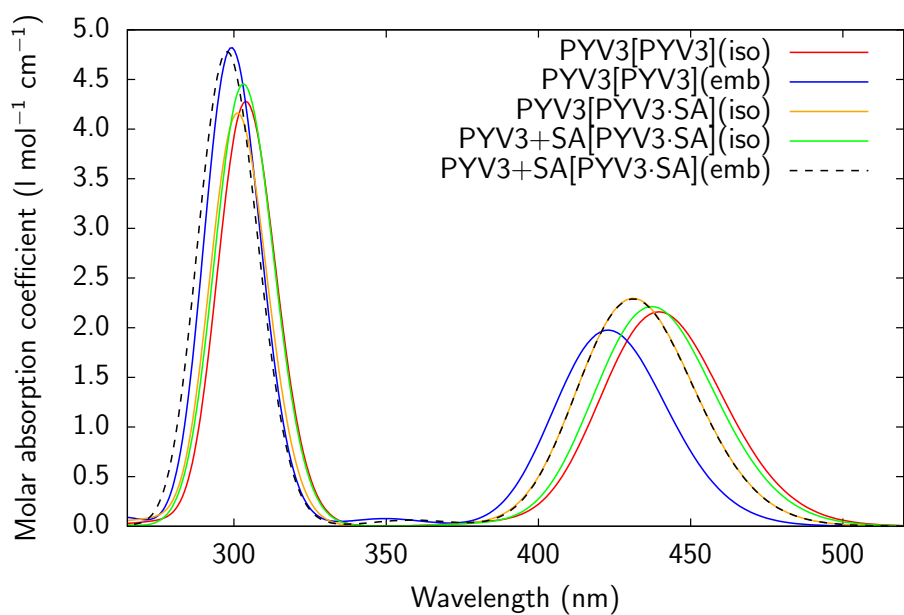
Table 7.5: RI-CC2/def2-TZVPD first wavelength of excitation (λ , in nm) and oscillator strength (f) for the isolated and embedded monomer of PYV3 (PYV3[PYV3]) and the variations for the embedded heteromers of co-crystals (PYV3+XXX[PYV3·XXX], w.r.t. the embedded PYV3).

	Enol			Keto		
	λ	E_{eg}	f	λ	E_{eg}	f
PYV3[PYV3] (iso)	360	3.44	0.125	440	2.82	0.240
PYV3[PYV3] (emb)	337	3.68	0.105	423	2.93	0.220
PYV3+SA[PYV3·SA] (emb)	+9	−0.10	+7 %	+8	−0.06	+16 %
PYV3+FA[PYV3·FA1] (emb)	+11	−0.11	+7 %	+10	−0.07	+16 %

Figure 7.6 shows the UV/Vis absorption spectra of the various models of simulation for PYV3 and its co-crystal with SA. As just discussed for PYV3, the inclusion of the crystal field increases the excitation energies. This is also the case for PYV3+SA[PYV3·SA] when going from the isolated model to the embedded one for the two absorption bands of both enol and keto forms. For the enol, the 1st excitation is shifted by −16 nm (0.15 eV), the 2nd by −4 nm (0.06 eV), and the 3rd by −2 nm (0.03 eV) with respect to the isolated molecule, *i.e.* PYV3[PYV3] (Tables 7.5 and D.8). For the keto form, the variation on the first excitation is smaller than for the enol: −6 nm (0.04 eV). Its 2nd band, previously described by one excitation, is now defined by two almost degenerated excitations, the 3rd and 4th ones, at −4 nm (0.05 eV) and −11 nm (0.15 eV) with respect to the 3rd excitation of the isolated heteromer, respectively (Table D.9). The nature of these particular excitations is discussed in the next Section. Compared to the embedded PYV3, the first absorption band of the co-crystal is red-shifted while the second one is unshifted. For the enol, the first band is of similar intensity while the second one is more intense. This is due to the larger oscillator strength of the 2nd excitation, despite a smaller value for the 3rd one. By opposition, the first band of the keto gets more intense than in PYV3[PYV3] while the second one is similar (despite the dual excitation in the band). After embedding, the excitation energies of PYV3·SA and PYV3·FA1 remain very similar, with maximum differences of −2 nm, showing the extent of the effects of isostructurality (Figure D.3).



(a) Enol.



(b) Keto.

Figure 7.6: RI-CC2/def2-TZVPD UV/Vis absorption spectra of all models considered for PYV3 and PYV3-SA.

7.3.3 Analysis of the NTOs

Concerning the NTOs, which characterize the nature of the electronic transitions, there are not affected by the changes of geometry. Figure 7.7 shows the NTOs of the enol and keto forms of the 1st excited states for the isolated PYV3[PYV3], PYV3[PYV3·SA], PYV3[PYV3·SDP], and PYV3·O[PYV3·I3F3]. All holes have the same π topology localized on the salicylidene part while all particles are the same, being of π character, fully delocalized over the molecule. As previously mentioned, the 3rd excited state for the enol form of the isolated PYV3+FA[PYV3·FA1] is actually forbidden in favor of the 4th one. Despite this change, the NTOs of that excitation are almost identical to those of the 3rd excited state of PYV3[PYV3] (Figure D.4). They differ by a smaller contribution of the pyridine to the hole. The same goes for the embedded PYV3+FA[PYV3·FA1] 4th excited state. When adding the effect of the crystal field to PYV3[PYV3], the NTOs are unaffected for both the enol and keto forms, as seen in Figures D.5 and D.6, respectively.

For all the models considered for the SA and FA1 co-crystals, the NTOs are almost not affected (Figure 7.8) except for the 3rd excitation of the embedded keto forms. Despite those few changes, all natural transition orbitals are localized on PYV3, *i.e.* the coformer polarizes PYV3 but does not directly contribute to the actual excitation. As previously mentioned, upon inclusion of crystal field, the 3rd excited state of the keto form of PYV3+SA[PYV3·SA] becomes degenerated into two excited states (the same goes for PYV3+FA[PYV3·FA1]). Each excitation is described by two pairs of NTOs, where the first one contributes to about 2/3 of the excitation and the second one to the remaining third (Figure 7.9). The holes of the first pair of NTOs have almost the same π topology as the isolated ones. For the second pairs, the holes are localized on the salicylidene part of the molecule and are of π nature. All the particles are similar to that of the isolated system. They differ by smaller contributions of the salicylidene part of the molecule for the first pair and increased σ character for the second pair.

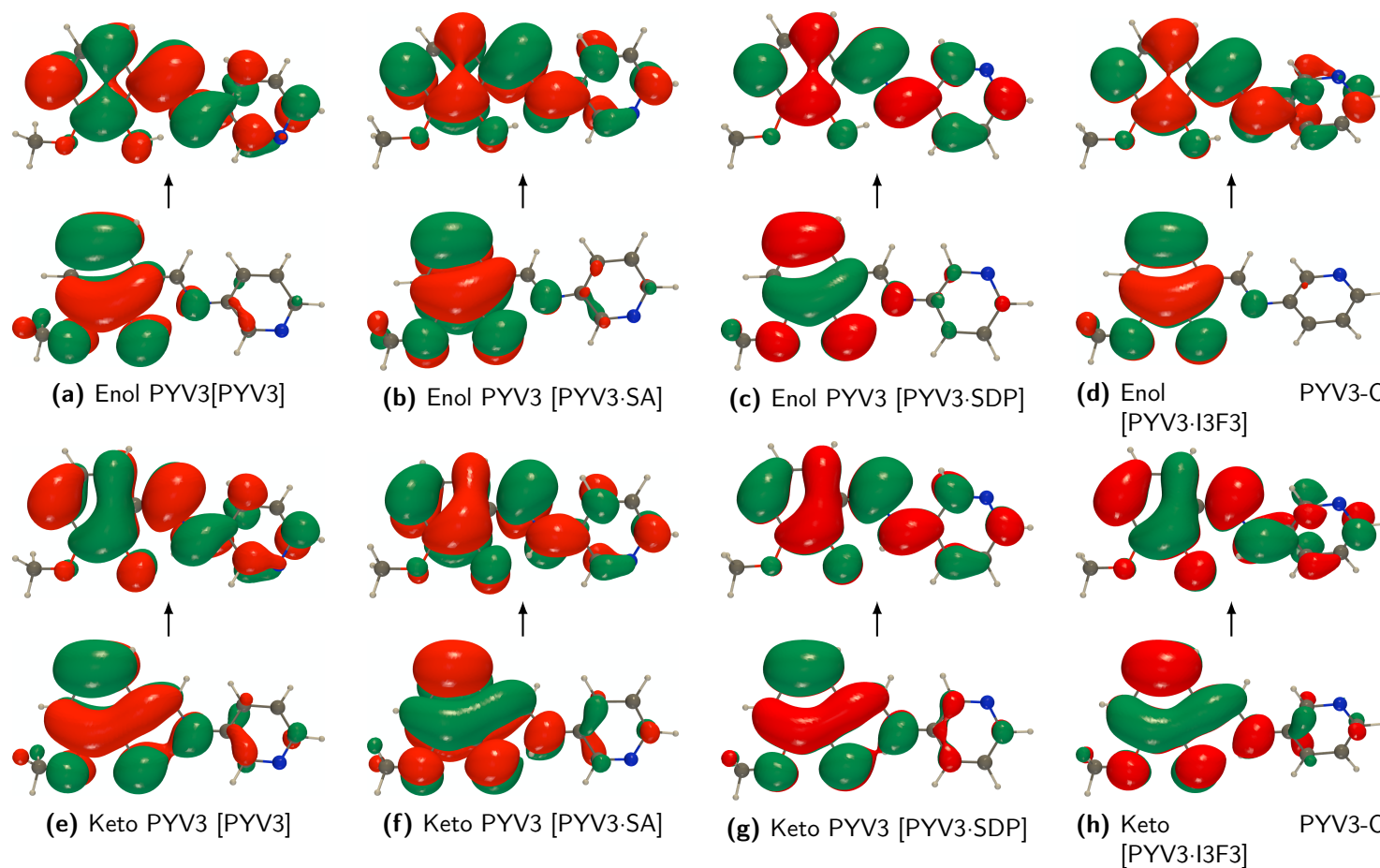


Figure 7.7: RI-CC2/def2-TZVPD NTOs (holes below the arrows and particles above them) of the first excited state of isolated monomers of PYV3, PYV3-SA, PYV3-SDP, and PYV3-I3F3 (isovalue of 0.02 a.u.).

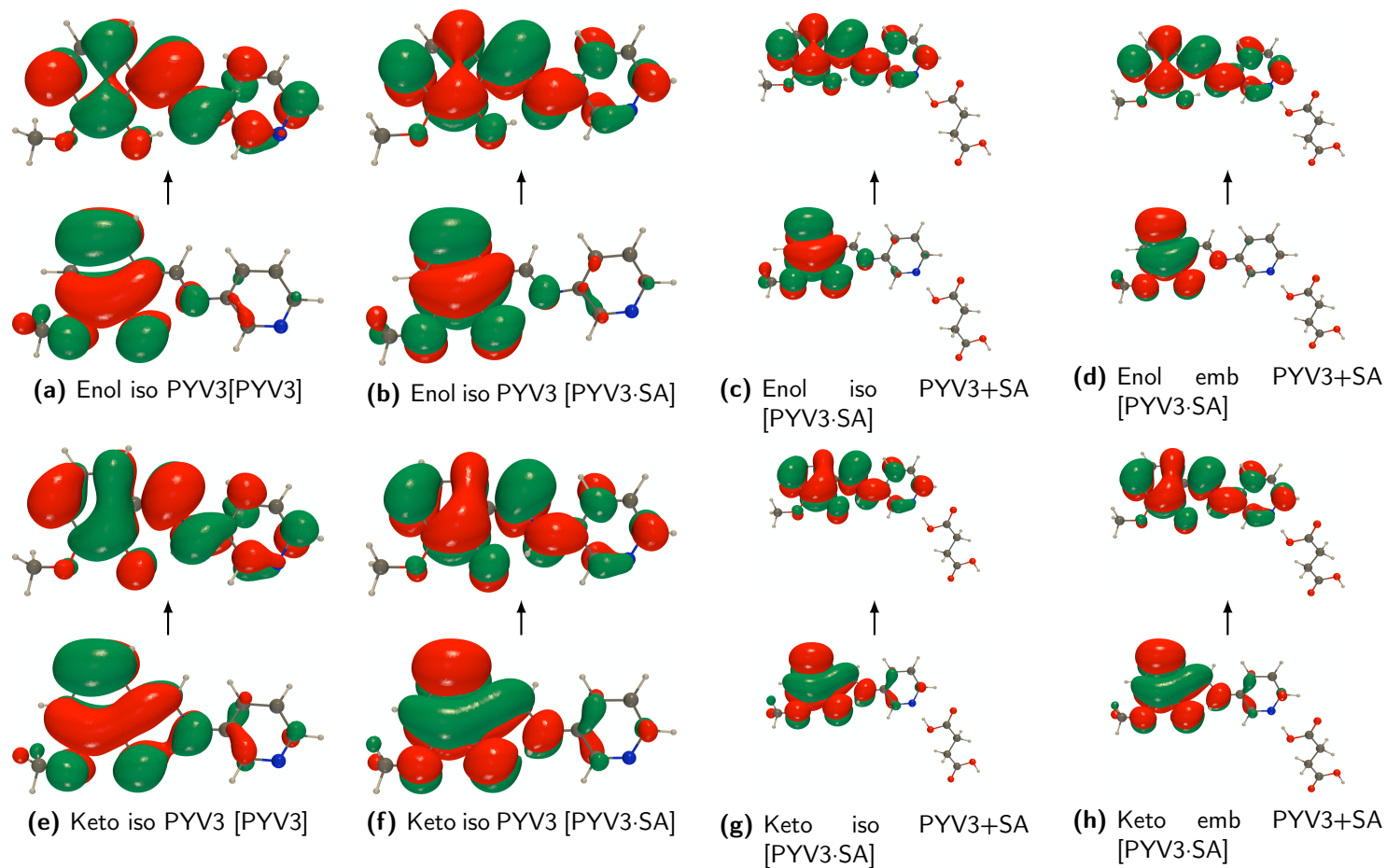


Figure 7.8: RI-CC2/def2-TZVPD NTOs (holes below the arrows and particles above them) of the first excited state of isolated PYV3 [PYV3] and the various models of PYV3-SA (isovalue of 0.02 a.u.). "Iso" stands for isolated while "emb" for embedded in crystal field point-charges.

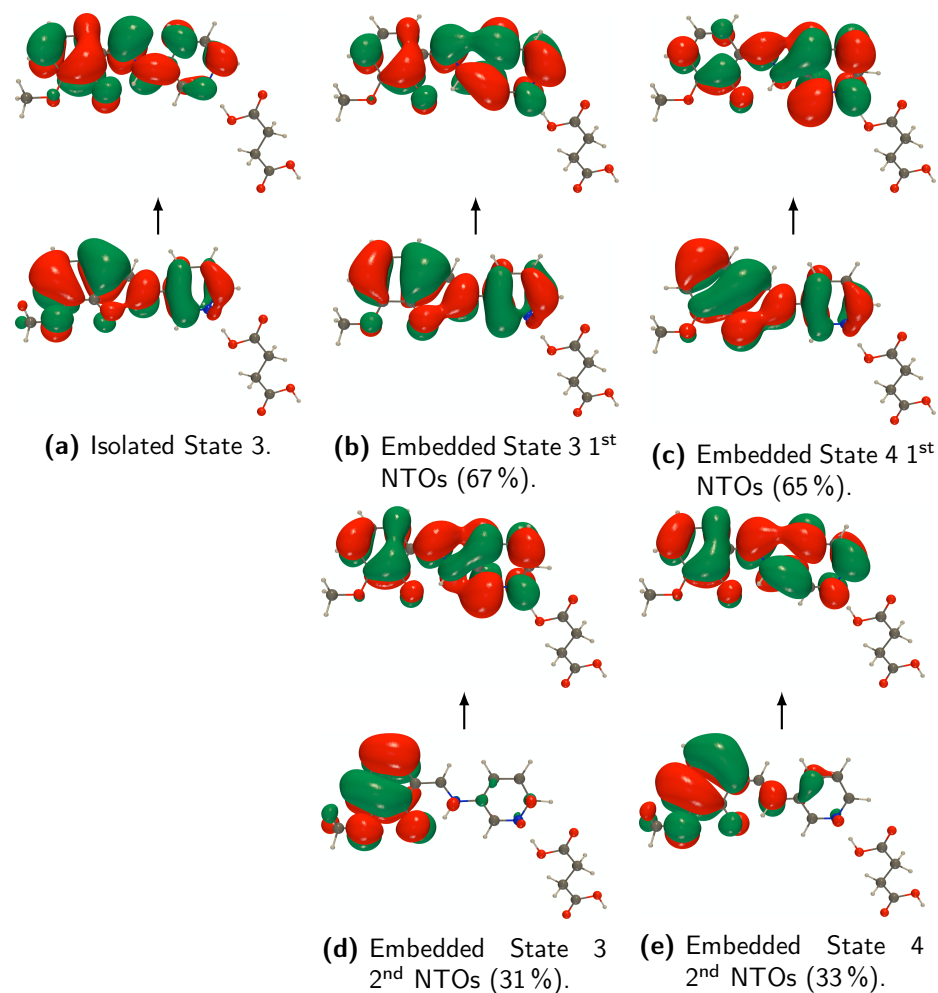


Figure 7.9: RI-CC2/def2-TZVPD NTOs (holes below the arrows and particles above them) of the 3rd isolated keto form of PYV3+SA[PYV3·SA] and of the 3rd and 4th excited states of the embedded one (isovalue of 0.02 a.u.).

7.3.4 Looking for a Computationally more Efficient Method

Table 7.6: RI-CC2 wavelengths of excitation with the def2-TZVPD (TZ) and composite (SV-TZ) methods (λ , in nm) and def2-TZVPD (TZ) and def2-SVPD (SV) oscillator strengths, f , and absolute errors (AE) for the embedded heteromers of SA and FA1 (PYV3+SA[PYV3·SA] and PYV3+FA[PYV3·FA1]).

Co-Crystal	State	Enol						
		λ^{TZ}	$\lambda^{\text{SV-TZ}}$	AE(nm)	AE(eV)	f^{TZ}	f^{SV}	AE
PYV3+SA [PYV3·SA] (emb)	1	346.5	346.7	0.2	−0.002	0.112	0.116	0.003
	2	286.2	286.4	0.1	−0.002	0.624	0.616	−0.009
	3	264.2	264.4	0.2	−0.004	0.167	0.178	0.011
PYV3+FA [PYV3·FA1] (emb)	1	347.6	347.8	0.2	−0.002	0.113	0.116	0.003
	2	286.7	286.8	0.1	−0.002	0.632	0.622	−0.009
	4	265.0	265.2	0.3	−0.005	0.167	0.178	0.012
Keto								
PYV3+SA [PYV3·SA] (emb)	1	431.1	431.2	0.1	−0.001	0.255	0.267	0.012
	3	300.2	300.3	0.0	−0.001	0.360	0.373	0.012
	4	293.2	293.3	0.1	−0.002	0.210	0.193	−0.017
PYV3+FA [PYV3·FA1] (emb)	1	432.9	433.0	0.1	−0.001	0.256	0.268	0.012
	3	301.3	301.4	0.0	−0.000	0.333	0.345	0.012
	4	294.4	294.5	0.2	−0.002	0.244	0.227	−0.017

One limitation of this computational scheme is its cost for large heteromers, *e.g.* PYV3+2×SDP[PYV3·SDP] or PYV3-N+PYV3-O+2×I3F3[PYV3·I3F3], when employing the extended def2-TZVPD basis set.

To circumvent this issue, we propose a composite technique where the effects of the cofomer on the wavelengths of excitation are computed with the def2-SVPD basis set and added to the def2-TZVPD wavelengths of the monomer (Eq. 7.1). Alternatively, the same quantities can be seen as the def2-SVPD heteromer wavelength with a basis set correction on the molecule contributing most to the spectra (Eq. 7.2).

$$\lambda^{\text{TZ}}(\text{hetero}) \approx \lambda^{\text{SV-TZ}}(\text{hetero}) = \lambda^{\text{TZ}}(\text{mono}) + \left[\lambda^{\text{SV}}(\text{hetero}) - \lambda^{\text{SV}}(\text{mono}) \right] \quad (7.1)$$

$$= \lambda^{\text{SV}}(\text{hetero}) + \left[\lambda^{\text{TZ}}(\text{mono}) - \lambda^{\text{SV}}(\text{mono}) \right] \quad (7.2)$$

where TZ refers to a def2-TZVPD calculation and SV to a def2-SVPD one. In Table 7.6, the def2-TZVPD data for the excitations with non-negligible oscillator

strengths are given for the embedded heteromers of PYV3-SA and PYV3-FA1 alongside the composite scheme values and its absolute errors. Overall, the composite scheme underestimates the excitation energies, but with errors that do not exceed 0.2 nm (0.005 eV) and as low as 0.02 nm (0.0003 eV). It is therefore safe to say that the composite scheme is accurate. Note that the errors on the keto excited state energies are smaller by about a factor two than the enol ones. The oscillator strengths obtained with def2-SVPD are comparable to the def2-TZVPD ones (Table 7.6), with errors that do not exceed ± 0.02 . The composite spectra and the real def2-TZVPD ones are shown in Figure 7.10. As expected by the errors previously discussed, the spectra almost perfectly overlap. Furthermore, the def2-SVPD NTOs are identical to the def2-TZVPD ones (Figures D.7 and D.8). A further step would be to use the embedded monomer RI-CCSD/def2-TZVPD excitation energies as a reference instead of the RI-CC2 ones.

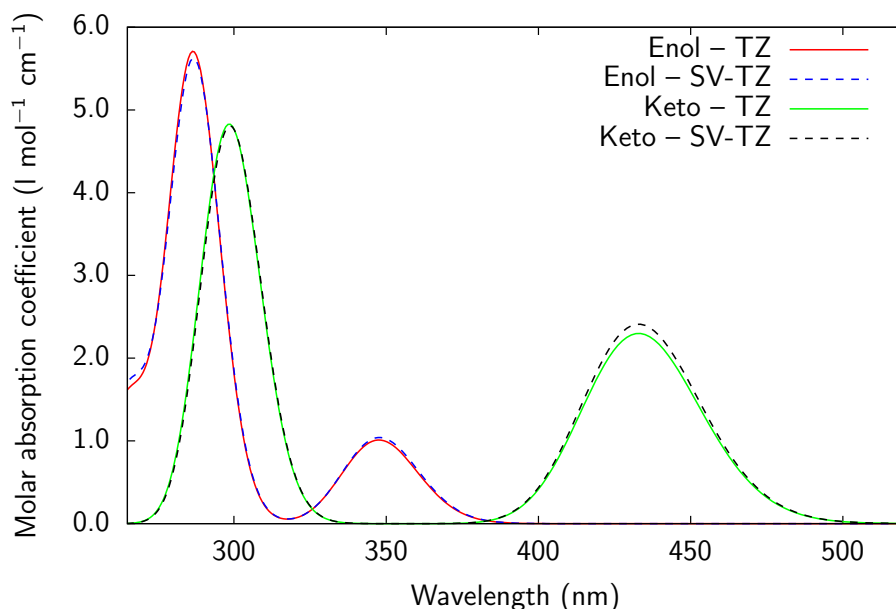


Figure 7.10: RI-CC2 composite (SV-TZ, dashed lines) and def2-TZVPD (TZ, full lines) spectra for the embedded heteromers of SA and FA1.

7.4 Further Discussions, Conclusions, and Perspectives

This work aims at deciphering the effects of co-crystallization on the optical properties of PYV3, a N-salicylideneaniline derivative. To do so, a two step multi-scale method has been established. First the molecular geometry and the unit cell parameters are optimized using periodic boundary conditions density functional theory. Then, an embedding method is used to compute the RI-CC2

excitation energies and oscillator strengths. As a first step to compute the RI-CC2 optical properties, a basis set amongst the Ahlrichs family was selected: def2-TZVPD. It reproduces the results of the larger def2-QZVP basis set. Then, the accuracy of RI-CC2 is confirmed by comparing its excitation energies with RI-CCSD results. Indeed, despite small differences on the excitation energies with respect to RI-CCSD, RI-CC2 recovers the nature of the excitations. Then, in order to decipher the various effects of co-crystallization on the optical properties, the excitation properties and UV/Vis absorption spectra of isolated anil molecules as extracted from the co-crystals are computed. The changes of geometry of the chromophore in the co-crystals leads to various effects on the excited states contributing to the UV/Vis absorption spectra. While for most cofomers this results in negligible effect or in an increase of the excitation energies (occasionally accompanied by variations of the absorption intensities), PYV3·SDP is the only one showing a significant decrease of the 1st excitation energy. This has been attributed to the planarization of PYV3 in the PYV3·SDP co-crystal. Then, the effects of the environment are included in two steps: i) considering heteromers, *i.e.* the anil and its directly interacting cofomer and ii) including the crystal field thanks to an embedding of point-charges that reproduce the full Coulombic potential of the crystal. Combining both aspects of the environment shows that the PYV3·SA co-crystal has lower first excitation energies compared to the pure crystal of PYV3. Analyzing these variations in details, we have shown that the presence of the succinic acid cofomer counteracts the hypsochromic shift due to the geometry and that crystal field effects leads to hypsochromic shifts of about 10 nm. Similar results have then been obtained for the isostructural PYV3·FA1 co-crystal, showing that the geometry and the crystal field effects are negligibly modified by the difference in chemical nature of the cofomer, succinic versus fumaric acid.

Based on these calculations of the vertical excitation energies of PYV3 and its co-crystals with SA and FA, comparisons have been drawn with experiment, where the onsets of absorption for the enol and keto forms have been determined from the spectra of Ref. [1]. For the enol form, this onset of absorption goes from 460 nm in the case of PYV3 to 465 nm and 475 nm for PYV3·SA and PYV3·FA1 in comparison to 337 nm, 346 nm, and 348 nm, respectively, demonstrating the good qualitative agreement. In addition, for the keto form, the calculated values amount to 423 nm, 431 nm, and 433 nm in comparison to experimental values of 560 nm, 565 nm, and 575 nm, for PYV3, PYV3·SA, and PYV3·FA1, respectively. Though the small co-crystallization-induced hypsochromic shifts are predicted for PYV3·SA and PYV3·FA1 by the two step multi-scale method, the absorption spectra remain similar and the nature of the transitions, as revealed by a NTO analysis, is not affected by co-crystallization. Thus, at this level of investigation, there is no evidence to explain the difference in the photochromic behavior of the PYV3 crystal compared to the PYV3·SA and PYV3·FA1 co-crystals. Studying the excited state dynamics appears necessary to address this effect, which goes beyond the aim of the present work.

Finally, a composite scheme to obtain accurate but computationally more accessible UV/Vis absorption spectra has been established, and proven to be successful in recovering the key features of the excitations. In view of future investigations, we note that other approaches can be explored such as other charge definitions (electrostatic potential, ESP, charges or natural bond orbital, NBO, charges), self-consistent embeddings, or extracting the excitation energies from frequency dispersion fits of the polarizability (available for selected DFT functionals in CRYSTAL17³⁹). Still, improvements can be achieved by including vibronic and excitonic couplings, which goes beyond the scope of this study.

Acknowledgements

The authors would like to thank Andrea Carletta and Nikolay N. Tumanov who provided the experimental crystal structures. This work was carried out thanks to funding of "Actions de Recherche Concertées" (ARC) de la Direction générale de l'Enseignement non obligatoire et de la Recherche scientifique - Direction de la Recherche scientifique - Communauté française de Belgique, under convention No. 15/20-068. This research used resources of the "Plateforme Technologique de Calcul Intensif (PTCI)" (<http://www.ptci.unamur.be>) located at the University of Namur, Belgium, which is supported by the FNRS-FRFC, the Walloon Region, and the University of Namur (Conventions No. 2.5020.11, GEQ U.G006.15, 1610468, and RW/GEQ2016). The PTCI is member of the "Consortium des Équipements de Calcul Intensif (CÉCI)" (<http://www.ceci-hpc.be>).

Bibliography

- (1) Carletta, A.; Buol, X.; Leyssens, T.; Champagne, B.; Wouters, J. Polymorphic and Isomorphic Cocrystals of a N-Salicylidene-3-aminopyridine with Dicarboxylic Acids: Tuning of Solid-State Photo- and Thermochromism. *J. Phys. Chem. C* **2016**, *120*, 10001–10008.
- (2) Quertinmont, J.; Leyssens, T.; Wouters, J.; Champagne, B. Periodic DFT Study of the Effects of Co-Crystallization on a N-Salicylideneaniline Molecular Switch. *ChemPhysChem* **2019**, *20*, 2434–2442, DOI: 10.1002/cphc.201900463.
- (3) Klintonberg, M.; Derenzo, S.; Weber, M. Accurate Crystal Fields for Embedded Cluster Calculations. *Comput. Phys. Commun.* **2000**, *131*, 120–128, DOI: 10.1016/S0010-4655(00)00071-0.
- (4) Derenzo, S. E.; Klintonberg, M. K.; Weber, M. J. Determining Point Charge Arrays that Produce Accurate Ionic Crystal Fields for Atomic Cluster Calculations. *J. Chem. Phys.* **2000**, *112*, 2074–2081, DOI: 10.1063/1.480776.

- (5) Christiansen, O.; Koch, H.; Jørgensen, P. The Second-Order Approximate Coupled Cluster Singles and Doubles Model CC2. *Chem. Phys. Lett.* **1995**, *243*, 409–418, DOI: 10.1016/0009-2614(95)00841-Q.
- (6) Vahtras, O.; Almlöf, J.; Feyereisen, M. Integral Approximations for LCAO-SCF Calculations. *Chem. Phys. Lett.* **1993**, *213*, 514–518, DOI: 10.1016/0009-2614(93)89151-7.
- (7) Feyereisen, M.; Fitzgerald, G.; Komornicki, A. Use of Approximate Integrals in Ab Initio Theory. An Application in MP2 Energy Calculations. *Chem. Phys. Lett.* **1993**, *208*, 359–363, DOI: 10.1016/0009-2614(93)87156-W.
- (8) Christiansen, O.; Koch, H.; Jørgensen, P. The second-order approximate coupled cluster singles and doubles model CC2. *Chem. Phys. Lett.* **1995**, *243*, 409–418, DOI: 10.1016/0009-2614(95)00841-Q.
- (9) Hättig, C.; Weigend, F. CC2 Excitation Energy Calculations on Large Molecules using the Resolution of the Identity Approximation. *J. Chem. Phys.* **2000**, *113*, 5154, DOI: 10.1063/1.1290013.
- (10) Schreiber, M.; Silva-Junior, M. R.; Sauer, S. P. A.; Thiel, W. Benchmarks for electronically excited states: CASPT2, CC2, CCSD, and CC3. *J. Chem. Phys.* **2008**, *128*, 134110, DOI: 10.1063/1.2889385.
- (11) Kánnár, D.; Szalay, P. G. Benchmarking Coupled Cluster Methods on Valence Singlet Excited States. *J. Chem. Theory Comput.* **2014**, *10*, 3757–3765, DOI: 10.1021/ct500495n.
- (12) Louant, O.; Champagne, B.; Liégeois, V. Investigation of the Electronic Excited-State Equilibrium Geometries of Three Molecules Undergoing ESIP: A RI-CC2 and TDDFT Study. *J. Phys. Chem. A* **2018**, *122*, 972–984, DOI: 10.1021/acs.jpca.7b10881.
- (13) Zutterman, F.; Louant, O.; Mercier, G.; Leyssens, T.; Champagne, B. Predicting Keto–Enol Equilibrium from Combining UV/Visible Absorption Spectroscopy with Quantum Chemical Calculations of Vibronic Structures for Many Excited States. A Case Study on Salicylideneanilines. *J. Phys. Chem. A* **2018**, *122*, 5370–5374, DOI: 10.1021/acs.jpca.8b03389.
- (14) Luzanov, A. V.; Sukhorukov, A. A.; Umanskii, V. E. Application of transition density matrix for analysis of excited states. *Theor. Exp. Chem.* **1976**, *10*, 354–361, DOI: 10.1007/BF00526670.
- (15) Martin, R. L. Natural transition orbitals. *J. Chem. Phys.* **2003**, *118*, 4775–4777, DOI: 10.1063/1.1558471.
- (16) Orendt, A.; Facelli, J. In 2007, pp 115–178, DOI: 10.1016/S0066-4103(07)62003-1.

- (17) Presti, D.; Labat, F.; Pedone, A.; Frisch, M. J.; Hratchian, H. P.; Ciofini, I.; Menziani, M. C.; Adamo, C. Computational Protocol for Modeling Thermochromic Molecular Crystals: Salicylidene Aniline As a Case Study. *J. Chem. Theory Comput.* **2014**, *10*, 5577–5585, DOI: 10.1021/ct500868s.
- (18) Presti, D.; Labat, F.; Pedone, A.; Frisch, M. J.; Hratchian, H. P.; Ciofini, I.; Cristina Menziani, M.; Adamo, C. Modeling emission features of salicylidene aniline molecular crystals: A QM/QM' approach. *J. Comput. Chem.* **2016**, *37*, 861–870, DOI: 10.1002/jcc.24282.
- (19) Dommett, M.; Rivera, M.; Crespo-Otero, R. How Inter- and Intramolecular Processes Dictate Aggregation-Induced Emission in Crystals Undergoing Excited-State Proton Transfer. *J. Phys. Chem. Lett.* **2017**, *8*, 6148–6153, DOI: 10.1021/acs.jpcllett.7b02893.
- (20) Smulders, C.; Carletta, A.; Wouters, J. Ingénierie cristalline du thermo- et photochromisme des N-salicylidèneaminopyridines par cocrystallisation, 2017.
- (21) Carletta, A. Photochromic multicomponent crystalline materials based on N-salicylideneanilines, Ph.D. Thesis, Université de Namur, 2019.
- (22) Carletta, A.; Zbačnik, M.; Van Gysel, M.; Vitković, M.; Tumanov, N.; Stilinović, V.; Wouters Johan and Cinčić, D. Playing with Isomerism: Cocrystallization of Isomeric N-Salicylideneaminopyridines with Perfluorinated Compounds as Halogen Bond Donors and Its Impact on Photochromism. *Cryst. Growth Des.* **2018**, *18*, 6833–6842, DOI: 10.1021/acs.cgd.8b01064.
- (23) Carletta, A.; Spinelli, F.; D'Agostino, S.; Ventura, B.; Chierotti, M. R.; Gobetto, R.; Wouters, J.; Grepioni, F. Halogen-Bond Effects on the Thermo- and Photochromic Behaviour of Anil-Based Molecular Co-crystals. *Chem. - A Eur. J.* **2017**, *23*, 5317–5329, DOI: 10.1002/chem.201605953.
- (24) Dovesi, R.; Orlando, R.; Erba, A.; Zicovich-Wilson, C. M.; Civalleri, B.; Casassa, S.; Maschio, L.; Ferrabone, M.; De La Pierre, M.; D'Arco, P.; Noël, Y.; Causà, M.; Rérat, M.; Kirtman, B. CRYSTAL14: a Program for the Ab Initio Investigation of Crystalline Solids. *Int. J. Quantum Chem.* **2014**, *114*, 1287–1317.
- (25) Perdew, J. P.; Ruzsinszky, A.; Csonka, G. I.; Vydrov, O. A.; Scuseria, G. E.; Constantin, L. A.; Zhou, X.; Burke, K. Restoring the Density-Gradient Expansion for Exchange in Solids and Surfaces. *Phys. Rev. Lett.* **2008**, *100*, 136406.
- (26) Feller, D. The Role of Databases in Support of Computational Chemistry Calculations. *J. Comput. Chem.* **1996**, *17*, 1571–1586.

- (27) Schuchardt, K. L.; Didier, B. T.; Elsethagen, T.; Sun, L.; Gurumoorthi, V.; Chase, J.; Li, J.; Windus, T. L. Basis Set Exchange: A Community Database for Computational Sciences. *J. Chem. Inf. Model.* **2007**, *47*, 1045–1052.
- (28) Pritchard, B. P.; Altarawy, D.; Didier, B.; Gibson, T. D.; Windus, T. L. New Basis Set Exchange: An Open, Up-to-Date Resource for the Molecular Sciences Community. *J. Chem. Inf. Model.* **2019**, *59*, 4814–4820, DOI: 10.1021/acs.jcim.9b00725.
- (29) Quertinmont, J.; Carletta, A.; Tumanov, N. A.; Leyssens, T.; Wouters, J.; Champagne, B. Assessing density functional theory approaches for predicting the structure and relative energy of salicylideneaniline molecular switches in the solid state. *J. Phys. Chem. C* **2017**, *121*, 6898–6908, DOI: 10.1021/acs.jpcc.7b00580.
- (30) Quertinmont, J.; Leyssens, T.; Wouters, J.; Champagne, B. Effects of Empirical Dispersion Energy on the Geometrical Parameters and Relative Energy of a Salicylideneaniline Molecular Switch in the Solid State. *Crystals* **2018**, *8*, 125, DOI: 10.3390/cryst8030125.
- (31) Schäfer, A.; Horn, H.; Ahlrichs, R. Fully Optimized Contracted Gaussian Basis Sets for Atoms Li to Kr. *J. Chem. Phys.* **1992**, *97*, 2571–2577, DOI: 10.1063/1.463096.
- (32) Weigend, F.; Häser, M.; Patzelt, H.; Ahlrichs, R. RI-MP2: Optimized Auxiliary Basis Sets and Demonstration of Efficiency. *Chem. Phys. Lett.* **1998**, *294*, 143–152, DOI: 10.1016/S0009-2614(98)00862-8.
- (33) Weigend, F.; Ahlrichs, R. Balanced Basis Sets of Split Valence, Triple Zeta Valence and Quadruple Zeta Valence Quality for H to Rn: Design and Assessment of Accuracy. *Phys. Chem. Chem. Phys.* **2005**, *7*, 3297, DOI: 10.1039/b508541a.
- (34) Rappoport, D.; Furche, F. Property-Optimized Gaussian Basis Sets for Molecular Response Calculations. *J. Chem. Phys.* **2010**, *133*, 134105, DOI: 10.1063/1.3484283.
- (35) TURBOMOLE V7.4 2019, a development of University of Karlsruhe and Forschungszentrum Karlsruhe GmbH, 1989-2007 TURBOMOLE GmbH, since 2007; available from <http://www.turbomole.org>.
- (36) Liégeois, V.; UNamur DrawMol, 2018.
- (37) Koch, H.; Christiansen, O.; Jørgensen, P.; Olsen, J. Excitation Energies of BH, CH₂ and Ne in Full Configuration Interaction and the Hierarchy CCS, CC2, CCSD and CC3 of Coupled Cluster Models. *Chem. Phys. Lett.* **1995**, *244*, 75–82, DOI: 10.1016/0009-2614(95)00914-P.

- (38) Christiansen, O.; Koch, H.; Jørgensen, P.; Olsen, J. Excitation Energies of H₂O, N₂ and C₂ in Full Configuration Interaction and Coupled Cluster Theory. *Chem. Phys. Lett.* **1996**, *256*, 185–194, DOI: 10.1016/0009-2614(96)00394-6.
- (39) Dovesi, R.; Erba, A.; Orlando, R.; Zicovich-Wilson, C. M.; Civalleri, B.; Maschio, L.; Rérat, M.; Casassa, S.; Baima, J.; Salustro, S.; Kirtman, B. CRYSTAL17. *Wiley Interdiscip. Rev. Comput. Mol. Sci.* **2018**, *8*, e1360.

SALICYLIDENEANILINE-BASED COFs: A NEW FAMILY OF MULTI-STATE SECOND-ORDER NONLINEAR OPTICAL SWITCHES

Submitted to J. PHYS. CHEM. C

Jean Quertinmont[†], Lorenzo Maschio[‡], Ayan Datta[§], & Benoît Champagne[†]

[†] *Theoretical Chemistry Laboratory, Unit of Theoretical and Structural Physical Chemistry, Namur Institute of Structured Matter, University of Namur, B-5000 Namur, Belgium*

[‡] *Dipartimento di Chimica, Università di Torino, Via P. Giuria 5, 10125 Torino, Italy*

[§] *School of Chemical Sciences, Indian Association for the Cultivation of Science, Jadavpur, Kolkata – 700032, India.*

All calculations and their analysis were performed by J.Q.

Abstract

This work demonstrates that covalent organic frameworks (COFs) can exhibit large second-order nonlinear (NLO) responses and that these NLO responses can be modulated as a function of the successive enol-imine/keto-enamine tautomerisms, leading to efficient solid-state second-order NLO switches. The proof of concept is given by evidencing, by means of periodic boundary conditions (time-dependent) density functional theory calculations, the large amplitudes of the second-order NLO susceptibility, $\chi^{(2)}$, of two-dimensional COFs built from the assembly of tris(N-salicylideneaniline) units as well as their variations when switching between keto and enol forms. Calculations further demonstrate the key role of symmetry, *i.e.* on the distribution of enol and keto functions in the unit cell, on the $\chi^{(2)}$ values as well as on their dipolar/octupolar character.

8.1 Introduction

Covalent organic frameworks (COFs) are porous crystalline materials built from strong covalent bonds between light elements.¹ The high accessible surface area and the mechanical robustness of these crystalline polymer networks make them ideal candidates as gas storage media, catalytic supports, sensing platforms, and energy storage devices, to cite a few applications.^{2–4} These structural, electronic, thermodynamic, and kinetic properties can further be combined with linear and nonlinear optical properties to elaborate multifunctional materials, in particular when the COFs switch between several forms. Very little is known about the nonlinear optical (NLO) properties of COFs whereas several studies have tackled those of the closely-related metal organic frameworks (MOFs).⁵ Among the few works on the NLO responses of COFs, in a recent paper Biswal et al.⁶ have reported the large nonlinear absorption (NLA) coefficient of regioregular porphyrin COFs. Moreover, by taking advantage of their precise spatial orientation in COFs, Deng and co-workers have revealed the two-photon absorption (TPA) potential of chromophores, which exhibit up to a 110-fold enhancement of their TPA cross section with respect to their molecular responses.⁷ There is a continuing interest for materials exhibiting NLO responses because they are active components in applications such as laser modulation, data storage and processing, bioimaging, and optical transmission technologies,^{8,9} and much has yet to be done to assess the potential of COFs. Note that both NLA and TPA are third-order NLO phenomena whereas, to our knowledge, the second-order NLO responses of COFs (like the second harmonic generation (SHG)) have not yet been studied. Among these NLO materials, when triggered by an external stimulus (change of pH or redox potential, irradiation by light, complexation of an analyte) some present the ability to switch between two or several forms that display differences in their second- or third-order NLO responses. These systems are known as NLO switches,^{10–13} and many examples have been reported, from molecules in solutions to functionalized surfaces and molecular crystals.^{14–27} Still, in the crystal state, owing to compactness and the associated steric hindrance to structural switching, fewer NLO switches are known.^{17,18} On the other hand, owing to the cavities in their structures, which can facilitate the motions of molecular fragments, COFs — as well as MOFs — are ideal candidates to exhibit NLO switching behavior.

As a matter of fact, the present contribution aims at assessing second-order NLO responses of a family of COFs built from the assembly of tris(*N*-salicylideneaniline) units by means of quantum chemical calculations, and also their linear optical responses. The targeted linear responses are the linear optical (at pulsation ω) susceptibility, $\chi^{(1)}(-\omega; \omega) = \chi^{(1)}$, as well as the refractive indices and birefringence while the second-order NLO responses are the second-order nonlinear optical susceptibility associated with the SHG phenomenon, $\chi^{(2)}(-2\omega; \omega, \omega) = \chi^{(2)}$. As first purpose, this paper gives the proof of con-

cept that COFs can exhibit second-order NLO switching properties. On the basis of their recent experimental investigations^{28,29} as well as of studies on the second-order NLO switching behavior of N-salicylideneaniline derivatives,³⁰ five two-dimensional (2D) COFs featuring enol-imine/keto-enamine tautomerism have been selected (Scheme 8.1). COFs **1** to **4** have been synthesized by Banerjee and co-workers²⁸ using Schiff base reaction of 1,3,5-triformylphloroglucinol with p-phenylenediamine (**1**), 2,5-dimethyl-p-phenylenediamine (**2**), 4,4'-azodianiline (**3**), and 4,4'-diaminostilbene (**4**), respectively. COFs **1** and **2** only differ by the presence of two methyl groups on the phenyl linker while COFs **3** and **4** possess more extended linkers namely azobenzene and stilbene, respectively. Finally, COF **5** presents an anthraquinone linker and was originally designed for its charge storage ability.²⁹ From the viewpoint of modulating the second-order NLO responses, taking COF **1** as reference, the donor character of the linker increases in the case of **2** and more substantially in the case of **3** and **4** with their azobenzene and stilbene donors while the anthraquinone linker of COF **5** is an acceptor unit.

These COFs structures can be viewed as 3D materials composed of 2D sheets forming honeycomb-like structures (Scheme 8.1). The size of the hexagonal channels depends on the nature of the π -conjugated linker between the tris(N-salicylideneaniline) units, which are the nodes of the network (vertices of the hexagons). The inner part of each hexagon presents a total of six keto or enol functions. They are numbered according to Scheme E.1. For each COF, this leads to a total of 14 tautomers (Table E.1). Still, in this investigation, only periodic structures are considered in the sense that all the hexagons are identical. This prevents from studying highly disordered systems but varying the enol and keto content of the unit cell already ensures chemical diversity. The corresponding structures representations are sketched in Table E.1, together with the COFs space groups.

Besides the proof-of-concept of COFs as second-order NLO switches, this paper addresses the following questions: i) how large is the second-order NLO responses of N-salicylideneaniline-based COFs in comparison to reference molecular crystals?, ii) what is the amplitude of the variations of $\chi^{(2)}$ upon keto-to-enol switching?, and iii) how to rationalize these linear and nonlinear responses in view of optimizing them?

8.2 Methods

All computations were carried out using periodic boundary conditions (PBC) density functional theory (DFT) as implemented in the CRYSTAL17 package.^{31–33} The range-separated ω B97X exchange-correlation (XC) functional³⁴ was used with Pople's 6-31G(d,p) basis set (taken from Basis Set Exchange).³⁵ Starting from the single crystal X-ray diffraction structures, full geometry optimizations were performed. In recent contributions, some of us demonstrated the perfor-

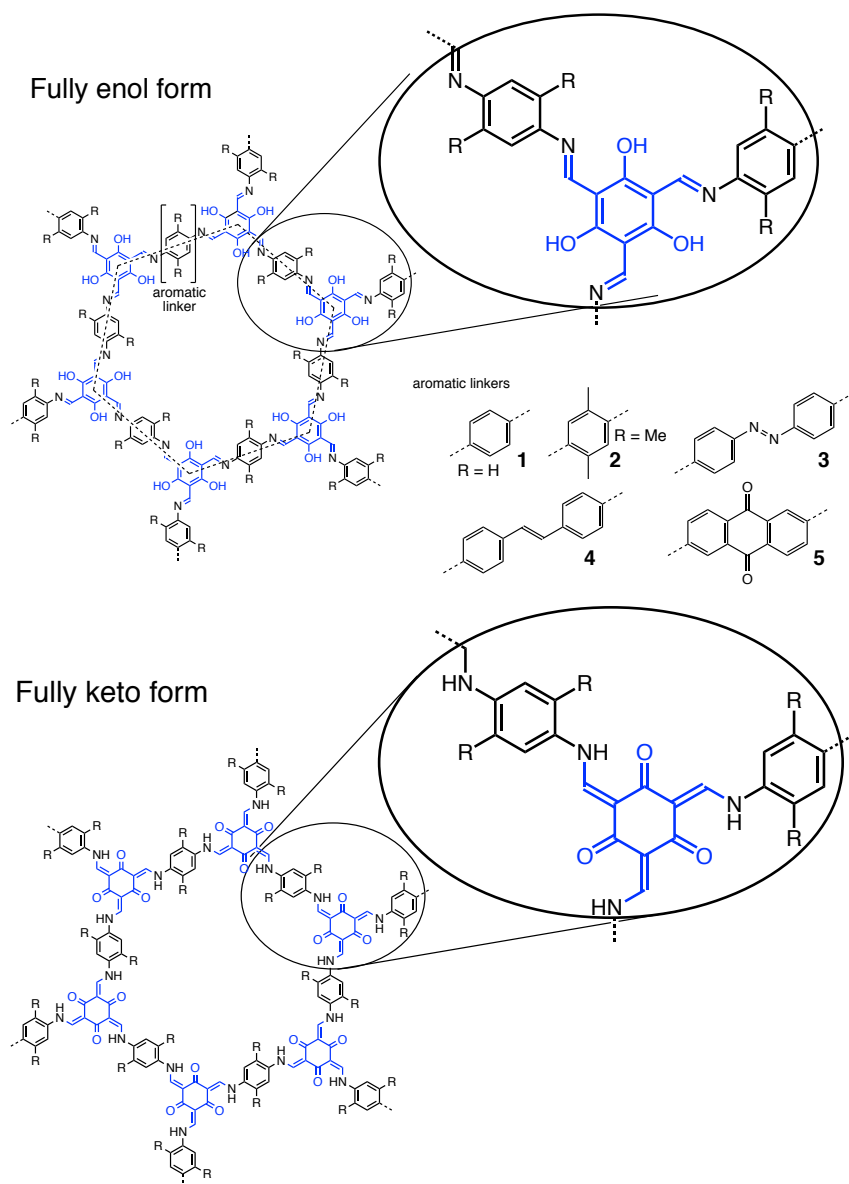


Figure 8.1: Structure of COFs 1-5 in their fully enol (top) and fully keto (bottom) forms. In the top figure the hexagon containing six (enol) functions is represented.

mance of the ω B97X XC functional to get geometries of molecular crystals in good agreement with single-crystal X-ray diffraction geometries, even without adding corrections for London dispersion interactions.^{36,37} Then, linear $[\chi^{(1)}]$ and second-order nonlinear $[\chi^{(2)}]$ optical properties were enacted at the DFT level using the linear and quadratic response function methods implemented in a local version of CRYSTAL17.^{38–42} This scheme i) is based on the substitution of the unbound electric dipole moment operator (\vec{r}) by another perturbation operator ($\vec{\Omega}_{\vec{k}} = \vec{r} + i\vec{\nabla}_{\vec{k}}$) that is block-diagonal in the same reciprocal \vec{k} -space as the unperturbed Fock matrix, ii) takes advantage of the $2n + 1$ rule, and iii) enables calculating both the static and dynamic responses. This approach presents some advantages to calculate the $\chi^{(1)}$ and $\chi^{(2)}$ responses because it provides in a single step these responses. In this way, contrary to other methods that have been employed to calculate the optical responses of molecular crystals and MOFs it does not suffer from various limitations: i) in the cluster approach, the optical responses depend on the cluster size and shape as well as on the way the dangling bonds are saturated,⁴³ ii) it does not involve a two-step procedure where molecular responses need to be computed first before evaluating the macroscopic ones,^{44,45} and iii) with respect to other PBC-based perturbative approaches it does not require the use of a scissor operator to correct the underestimated band gaps.^{46,47}

The number of non-equivalent non-zero $\chi^{(1)}$ components depends on the space group (in particular, in centro-symmetric crystals all $\chi^{(2)}$ tensor components vanish). These components are listed in Table E.1. In addition to the tensor components, which are listed in Supporting Information (besides the negligible $\chi_{XZZ}^{(2)}$ and $\chi_{YZZ}^{(2)}$), we have provided three invariants, their dipolar $|\chi_{J=1}^{(2)}|$ and octupolar $|\chi_{J=3}^{(2)}|$ components as well as their ratio, the nonlinear anisotropy, $\rho = |\chi_{J=3}^{(2)}| / |\chi_{J=1}^{(2)}|$. These quantities, of which the full expressions can be found in Ref. [48] are generally considered for molecules and clusters but can also be generalized to COFs.^{49,50} To visualize the $\chi^{(2)}$ tensor, the unit sphere representation (USR), initially proposed for the first hyperpolarizability tensor,⁵¹ was adopted. It consists i) in computing the induced polarization:

$$\vec{P}_{ind} = \vec{\chi}^{(2)} : \vec{E}^2(\theta, \phi) \quad (8.1)$$

where the tensor nature of $\chi^{(2)}$ has been evidenced and $\vec{E}(\theta, \phi)$ is a unit vector of electric field, of which the polarization direction is defined in spherical coordinates by the θ and ϕ angles and ii) by representing all the induced polarization vectors on a sphere centered on the center of mass of the primitive unit cell. This enables highlighting the directions where the second-order polarization is the strongest (it corresponds to the largest induced dipoles), its orientation (the acceptor-donor direction), and subsequently showing how much the $\chi^{(2)}$ response is dipolar/octupolar. These USR were plotted using the Drawmol package.⁵²

The excitation energies to the lowest dipole-allowed excited states were evaluated from the frequency dispersion of the dynamic $\chi^{(1)}(-\omega; \omega)$ response, with $\hbar\omega$ the incident photon energy. Indeed, within time-dependent perturbation theory $\chi^{(1)}(-\omega; \omega)$ can be written under the form of a summation over the excited states and close to resonance the contribution of each excited state (e) to frequency dispersion, $\mathcal{F}(\omega)$, reads

$$\frac{\chi^{(1)}(-\omega; \omega)}{\chi^{(1)}(0; 0)} = \mathcal{F}(\omega) = \Re(\omega) + i\Im(\omega) \quad (8.2)$$

$$= \frac{\omega_{eg}^4 - \omega_{eg}^2 \omega^2}{(\omega_{eg}^2 - \omega^2)^2 + \omega^2 \Gamma_{eg}^2} + i \frac{\omega_{eg}^2 \omega \Gamma_{eg}}{(\omega_{eg}^2 - \omega^2)^2 + \omega^2 \Gamma_{eg}^2} \quad (8.3)$$

with $\Re(\omega)$ and $\Im(\omega)$ their real and imaginary parts, respectively. $\hbar\omega_{eg}$ is the corresponding excitation energy and Γ_{eg} is the damping factor. So, at resonance, *i.e.* when $\hbar\omega$ matches a vertical excitation energy, the real part amounts to zero while its imaginary counterpart attains a maximum. The dynamic $\chi^{(1)}(-\omega; \omega)$ responses were calculated for a range of incident photon energies with $\Gamma_{eg} = \Gamma = 10^{-3}$ a.u.. Using the above $\mathcal{F}(\omega)$ form for each transition we evaluated by least-squares regression the $\hbar\omega_{eg}$ that give the best fit to the calculated data. Both the real and imaginary components of the $\chi^{(1)}$ response were employed and they gave very similar excitation energies. Illustrative results are given in Figures E.1 and E.2 to show the frequency dispersions, the fitting curves, and the corresponding excitation energies of COF 1 (4K2E/1-2 and 5K1E). For these slab materials, the in-plane diagonal components of the $\chi^{(1)}$ response present resonances between 2 and 4 eV demonstrating that for these low-energy excitations the dipole transition moments are in-plane polarized. On the other hand, optical transitions polarized along Z , *i.e.* perpendicular to the COF slabs, are associated with $\chi_{ZZ}^{(1)}$, appear above 6 eV, and are not discussed in this work.

To enact CRYSTAL17 calculations, default convergence criteria were used while the irreducible Brillouin zone was sampled on a 4 4 6 grid (SHRINK keyword). The truncation criteria for the Coulomb and exchange integrals were set to 7 7 7 7 16 (TOLINTEG keyword) for the geometry optimization calculations while for the calculation of the linear and nonlinear optical properties, TOLINTEG was set to tighter criteria: 10 10 10 30 100.

8.3 Results and Discussion

8.3.1 Geometries and Relative Stability

After full geometry optimization at the ω B97X/6-31G(d,p) level, the relative energies (Table 8.1) demonstrate that the fully keto form is the most stable and that the first keto-to-enol transformation costs between 32 and 36 kJ mol⁻¹. Then, for the second keto-to-enol transformation the energy cost depends on

which pair of keto sites. If the transformation occurs on a different tris(N-salicylideneaniline) node, about the same amount of energy (sites 1 and 2) is required or a bit more (sites 1 and 4). On the other hand, if it occurs on the same node the needed energy is much smaller (25–28 kJ mol⁻¹). The third transformation is again less demanding if it occurs on the same node (sites 1, 3, and 5) with energy between 4 and 9 kJ mol⁻¹. This lower cost results from the fact that the combination of three enol functions on the same node restores the aromaticity of the ring (see also below for the discussion on the geometry). Finally, the energy cost to go from 6K0E to 0K6E is about twice larger than to switch between 6K0E and 3K3E/1-3-5, demonstrating to a good extent the additive character and the weak impact of the adjacent nodes.

The aromaticity driving force was substantiated here by geometrical criteria, the CC bond lengths and the bond length alternation (BLA) in the ring. So, considering the node with the sites 1, 3, and 5, the average CC bond length in the ring ranges from 1.465 Å in 6K0E, to 1.449 Å in 5K1E, 1.431 Å in 4K2E/1-3, and 1.414 Å in 3K3E/1-3-5 for COF **1** (similar results are obtained for the other rings but the nomenclature is different). Then, BLA was evaluated as the average bond length differences between adjacent CC bonds of the ring of the same node. Considering 6K0E, 5K1E, 4K2E/1-3, and 3K3E/1-3-5, the ring BLA of **1** amounts to 0.010, 0.018, 0.018, and 0.003 Å, respectively. As expected, 3K3E/1-3-5 is the most aromatic with a negligible BLA. Then, comes 6K0E where there are three keto functions on each ring (BLA = 0.010 Å). Finally, 5K1E and 4K2E/1-3 combines one enol and two keto functions or *vice versa*, which increases the BLA by a factor of two with respect to 6KE0. Looking at the bond lengths of the molecular segments that are mostly affected by the keto-to-enol switching ($\text{O}=\text{C}-\text{C}=\text{C}-\text{NH} \rightarrow \text{HO}-\text{C}=\text{C}-\text{C}=\text{N}$), the variations as determined at the same PBC/ ω B97X/6-31G(d,p) level, are typically 0.01–0.02 Å larger in the present tris(N-salicylideneaniline) units than in more simple N-salicylideneaniline, like (E)-2-methoxy-6-(pyridine-3-yliminomethyl)phenol (PYV3), highlighting cooperative effects in the former ones.³⁶ Similar geometrical effects are observed for the four other COFs as well.

The Mulliken charge distributions have been analyzed to highlight which sub-units are electron donors or acceptors. For all COFs and no matter what is the K/E ratio, the aromatic linkers (Scheme 8.1) are donors, with charges between 1.2 e and 1.6 e. The charges on the two tris(N-salicylideneaniline) nodes, the electron acceptors, are very similar, with amplitudes generally smaller by 0.1 e. This demonstrates a small or negligible charge transfer between them and therefore the second-order NLO responses are not expected to have a charge-transfer origin like in push-pull π -conjugated systems. When the K/E ratio decreases, the charge transfer decreases by up to 0.20–0.25 e. Finally, the amount of charge transfer increases from COF **5** (1.40/1.19 e), to **3** (1.50/1.28 e), to **4** (1.53/1.33 e), to **1** (1.55/1.31 e), and to **2** (1.62/1.37 e), where the first value corresponds to the charge on the aromatic linker for the all-keto form while the second for the all-enol form. Again, as analyzed subsequently, there is no evident

Table 8.1: Relative energies (kJ mol^{-1} per primitive cell) of the different tautomers of COFs 1-5 as evaluated at the PBC/ ω B97X/6-31G(d,p) level of approximation.

Tautomer	1	2	3	4	5
6K0E	0.0	0.0	0.0	0.0	0.0
5K1E	32.5	33.4	36.0	34.9	36.0
4K2E	1-2	63.6	65.6	71.2	69.2
	1-3	57.2	59.0	64.3	62.0
	1-4	68.4	69.4	72.8	70.8
3K3E	1-2-3	86.6	89.7	98.4	95.5
	1-3-4	92.5	94.5	100.8	97.7
	1-3-5	61.5	67.9	71.4	68.1
	1-4-5	92.0	94.4	100.6	97.5
2K4E	1-2-3-4	114.0	117.5	127.3	123.2
	1-2-4-5	120.5	123.0	130.1	125.7
	1-3-4-5	95.2	101.6	107.2	103.0
1K5E	121.6	128.0	135.4	130.0	136.9
0K6E	127.6	135.7	142.5	136.0	144.3

correlation between these charge transfer amplitudes and the $\chi^{(2)}$ responses of the different tautomers.

8.3.2 Excitation Energies

Using the optimized structures, the two lowest-energy dipole-allowed excitation energies ($\hbar\omega_{eg}$) and band gaps ($\Delta E_{\text{HL}} = \epsilon_{\text{LUCO}} - \epsilon_{\text{HOCO}}$, with the LUCO and HOCO, the lowest-unoccupied crystalline orbital and the highest-occupied crystalline orbital) were evaluated. The excitation energies were calculated by least-squares fitting the few-state approximation $\chi^{(1)}(-\omega; \omega)$ expression to a set of complex $\chi^{(1)}(-\omega; \omega)$ values calculated for incident photon energies between 1.63 and 5.99 eV (0.06 and 0.22 a.u.) and a damping factor of 0.03 eV (10^{-3} a.u.) (Figures E.1 and E.2). These electronic transitions are polarized in the plane (XY) of the COF slabs. For COF 1 they present a complex dependence on the tautomer form (Table 8.2).

For hexagonal symmetry (6KE0, 3K3E/1-3-5, and 0K6E), these transitions are degenerate and respectively polarized along the X and Y axis. For the other space symmetries, the energy splitting ranges from 0.15 to 0.35 eV. The first excitation energy of the all-keto form (3.40 eV) is slightly smaller than for its corresponding all-enol form (3.53 eV) while mixing enol and keto tautomers results

Table 8.2: Band gap (ΔE_{HL}) and excitation energies ($\hbar\omega_n$, eV) of the tautomers of COF **1** as evaluated at the PBC/ ω B97X/6-31G(d,p) level of approximation. In parentheses are given the differences with respect to the 6KE0 tautomer.

Tautomer	ΔE_{HL}	$\hbar\omega_1$	$\hbar\omega_2$	
6K0E	5.85	3.40 ^a		
5K1E	5.68 (−0.17)	3.28 (−0.12)	3.43 (0.03)	
4K2E	1-2	5.65 (−0.20)	3.23 (−0.17) ^b	3.41 (0.01) ^c
	1-3	5.63 (−0.22)	3.27 (−0.13) ^b	3.41 (0.01) ^c
	1-4	5.50 (−0.35)	3.15 (−0.25)	3.49 (0.09)
3K3E	1-2-3	5.67 (−0.18)	3.18 (−0.22)	3.40 (0.00)
	1-3-4	5.47 (−0.38)	3.24 (−0.16)	3.34 (−0.06)
	1-3-5	6.02 (0.17)	3.44 (0.04) ^a	
	1-4-5	5.50 (−0.35)	3.18 (−0.22)	3.43 (0.03)
2K4E	1-2-3-4	5.58 (−0.27)	3.17 (−0.23)	3.32 (−0.08)
	1-2-4-5	5.32 (−0.52)	3.15 (−0.25) ^b	3.43 (0.03) ^c
	1-3-4-5	5.82 (−0.03)	3.31 (−0.09)	3.49 (0.09)
1K5E	5.72 (−0.13)	3.30 (−0.10)	3.45 (0.05)	
0K6E	6.27 (0.42)	3.53 (0.13) ^a		

^a This transition is degenerated. One is polarized along *X* while the other along *Y* ;

^b This transition is polarized along *X* ;

^c This transition is polarized along *Y* ;

Otherwise, the transitions are polarized in the *XY* plane.

generally in smaller first excitation energies (the smallest value is achieved for 4K2E/1-4 and 2K4E/1-2-4-5 with a value of 3.15 eV). The exception is 3K3E/1-3-5 where one center bears only enol forms (1, 3, and 5 sites, Scheme E.1) while the other only keto forms (2, 4, and 6 sites, Scheme E.1). In that case, the degenerate first excitation energies are slightly larger than in 6K0E (but slightly smaller than in 0K6E) and also larger than for the other 3K3E tautomers. This is attributed to aromaticity, which opens slightly the gap. A similar effect is observed in the case of 2K4E/1-3-4-5, for the same reason. To a good extent, the variations of $\hbar\omega_{eg}$ follow those of the band gap, though the latter are systematically larger by about 2 eV. The variations of the second excitation energy are smaller. This rather small E-to-K shift (less than 0.4 eV) contrasts with the large enol-to-keto bathochromic shift observed for simple salicylideneaniline,⁵³ as well as for tris(salicylideneaniline)⁵⁴ derivatives in solution. Therefore, the variations of the linear and nonlinear optical susceptibilities are not expected to

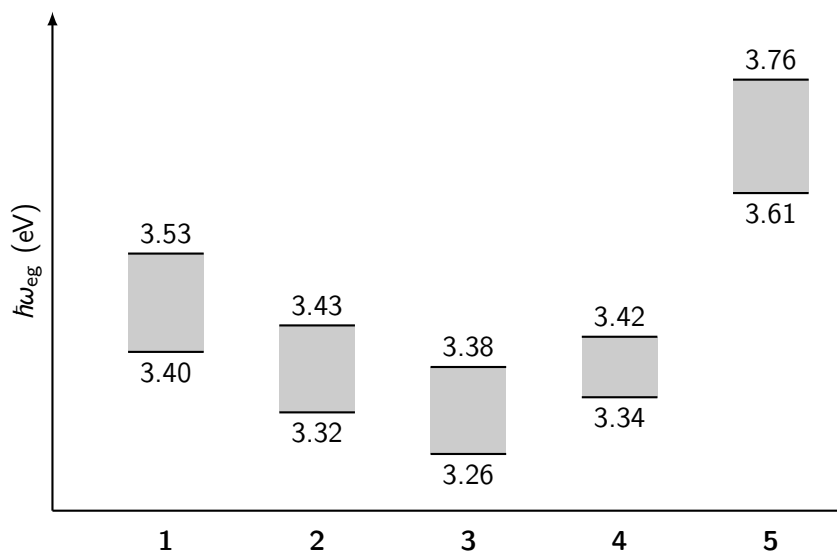


Figure 8.2: Excitation energies ($\hbar\omega_{eg}$, eV) of the 6K0E (bottom) and 0K6E (top) tautomers of COFs 1-5.

be driven by changes in the excitation energies.

The lowest excitation energies were then evaluated for the full-keto and full-enol tautomers of the other COFs (Figure 8.2) highlighting i) the systematic smaller values by 0.08–0.15 eV of the full keto form, ii) the relatively minor modifications when increasing the size of the π -conjugated linker, and iii) the largest values obtained in the case of an anthraquinone linker.

8.3.3 Refractive Indices and Birefringence

Consistently with the small variations of the optical gap and excitation energies as a function of tautomer, for a given COF, the refractive indices and birefringence also depend hardly on the E/K distribution (Table E.2). On the other hand, the variations are much larger among the different COFs, which can be explained by their different porosity (empty space) as a function of the size of the linker (Table 8.3). This is evidenced by the differences between the larger $n_{XY} = (n_X + n_Y)/2$ values of COFs 1 and 2 having smaller aromatic linkers — and therefore smaller cavities — and the smaller n_{XY} values of COFs 3 and 4 having larger cavities while COF 5 presents intermediate values. Similarly, the birefringence is larger for COFs 1 and 2 than for COFs 3, 4, and 5.

8.3.4 Second-Order NLO Susceptibilities

With respect to the linear responses, the $\chi^{(2)}$ tensor components and invariants (Tables 8.4, E.3-E.6) present a stronger dependence on the tautomer, as

Table 8.3: Linear optical properties of the 6K0E (0K6E) tautomers of the different COFs: average refractive index in the XY plane, $n_{XY} = (n_X + n_Y)/2$, refractive index along Z , n_Z , and birefringence, $\delta = (n_{XY} - n_Z)$. All values were evaluated at the PBC/ ω B97X/6-31G(d,p) level of approximation for $\omega = 0$.

COFs	n_{XY}	n_Z	δ
1	1.479 (1.481)	1.110 (1.114)	0.369 (0.367)
2	1.505 (1.508)	1.146 (1.150)	0.359 (0.358)
3	1.352 (1.347)	1.077 (1.079)	0.275 (0.269)
4	1.338 (1.338)	1.074 (1.076)	0.264 (0.262)
5	1.370 (1.367)	1.095 (1.097)	0.276 (0.270)

expected for an odd-order property. COFs appear therefore as potential second-order solid state NLO switches. When comparing to reference compounds like urea, the amplitude of the COFs $\chi^{(2)}$ tensor components is large but still smaller than in 2-methyl-4-nitroaniline (MNA). Indeed, for the former $\chi_{XYZ}^{(2)}$ amounts to 2.4 pm V^{-1} at 1064 nm ,⁵⁵ while for the latter $\chi_{111}^{(2)}$ gets as large as 300 pm V^{-1} at the same wavelength.⁵⁶

Results in Tables E.3-E.6 show that the largest component is usually $\chi_{XXX}^{(2)}$, then $\chi_{YYY}^{(2)}$, and finally the off-diagonal ones. For all COFs and all tautomer forms except 3K3E/1-3-5, the dipolar contribution is larger than the octupolar one, and typically twice larger (Table 8.4). In the case of 3K3E/1-3-5, which presents a hexagonal structure, the response is fully octupolar. The difference between the dipolar and octupolar responses of the COF 1 is further evidenced by their unit sphere representations (Figure 8.3).

No matter which π -linker is considered, the largest responses are generally obtained for the 3K3E and 2K4E tautomer forms, followed by 4K2E, 1K5E, and 5K1E. Considering the successive switching of the keto functions into enol ones, $\chi_{XXX}^{(2)}$ takes the following values (in pm V^{-1}): 0 (6K0E), 3.5 (5K1E), 7.3 (4K2E/1-3, as the most stable form), 0.8 (3K3E), -2.8 (2K4E), 3.9 (1K5E), and 0 (0K6E). These values demonstrate that switching the keto functions has a clear impact on the second-order NLO responses. How large it will be in practice remains to be seen since the keto-to-enol transformation will most probably not occur in the same way in all the unit cells.

Comparing their largest $\chi^{(2)}$ tensor components ($\chi_{YYY}^{(2)}$) 1K5E and 5K1E demonstrates that the keto form has a stronger potential than the enol form to achieve large $\chi^{(2)}$ responses. At first sight this appears contradictory because in 1K5E there are more enol than keto units. However, 1K5E differs with respect to the centrosymmetric 0K6E by only one keto function and therefore one can attribute the $\chi^{(2)}$ response to the unique keto site that breaks the centrosymmetry. As discussed above the keto forms are associated with slightly smaller band gaps and excitation energies but also with smaller unit cell polarization

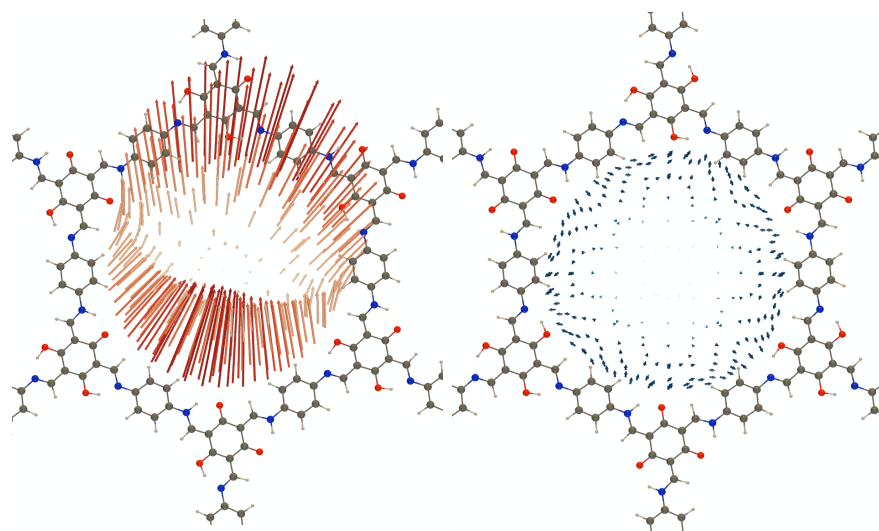


Figure 8.3: Unit sphere representation of the static $\chi^{(2)}$ tensor of COF **1** in its 3K3E/1-2-3 (left, dipolar character) and 3K3E/1-3-5 (right, octupolar character) as calculated at the PBC/ ω B97X/6-31G(d,p) level of approximation (USR factor of 1.0).

(cfr Mulliken charges). Large second-order NLO responses were also observed for the keto form of a 2-hydroxy-1-naphthaldehyde derivative,⁵⁷ but this is not a general conclusion since the keto/enol relative values depend strongly on the nature and position of the donor and acceptor groups on the anil core.⁵⁸

The $\chi^{(2)}$ response depends also on the nature of the π -linker, with a clear trend: $2 > 1 > 3 > 4 > 5$. To a good extent, these variations and ordering originate from the length of the π -linker: the longer the π -linker, the larger the primitive unit cell volume (Table E.7) and, therefore, for a given "molecular" β response, the macroscopic response gets smaller [$\chi^{(2)} = \beta/(2\epsilon_0 V)$]. This explains the differences between COFs **1** and **2** on the one hand and COFs **3** and **4** on the other hand. The larger response of **2** with respect to **1** is attributed to the better donor character of its π -linker, bearing two methyl groups. When putting aside the effects of the volume, the largest value is achieved with COF **3** but it is diluted in the larger volume. The smallest responses are observed for COF **5**, owing to its π -linker with the smallest donor effect.

Figure 8.4 displays the typical frequency dispersion of $\chi^{(2)}$ of these COFs derivatives, which deviates from the linear dependence in ω_L^2 , though the first electronic resonance is still far away. The last points in the graph correspond a photon energy $\hbar\omega$ of 1.16 eV ($\lambda = 1064$ nm) or a SHG energy of 2.32 eV whereas the first resonance is at 3.3 eV or higher.

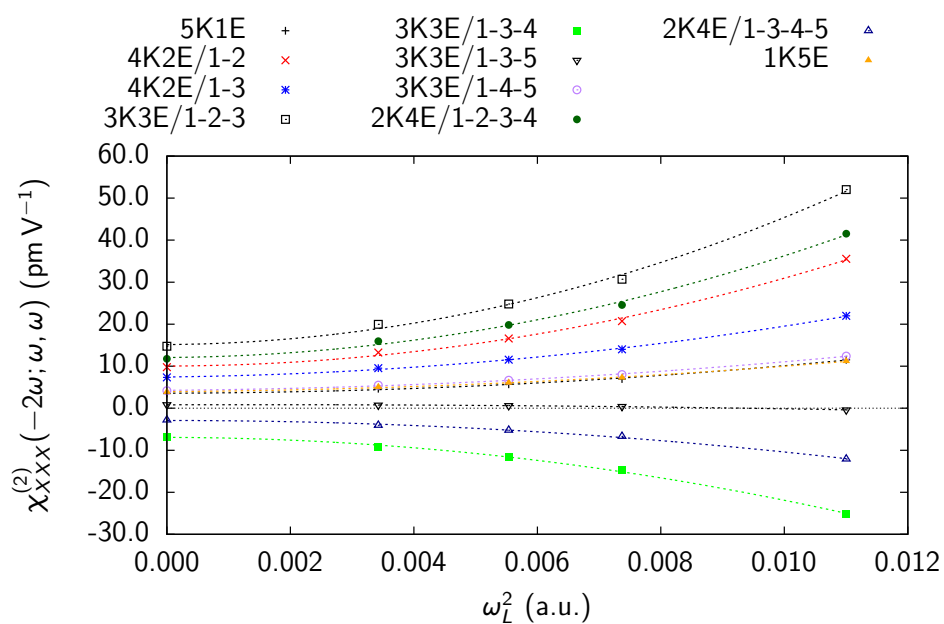


Figure 8.4: Frequency dispersion of the $\chi_{XXX}^{(2)}$ tensor component of COF 1 for its different non-centrosymmetric tautomer forms as calculated at the PBC/ ω B97X/6-31G(d,p) level of approximation. The lines are the quadratic fits in $\omega_L^2 = 6\omega^2$.

Table 8.4: Dipolar and octupolar components to the static $\chi^{(2)}$ (pm V⁻¹) and their ratio (ρ) for the tautomers of COF 1-5 as evaluated at the PBC/ ω B97X/6-31G(d,p) level of approximation. Centrosymmetric tautomers (6K0E, 4K2E/1-4, 2K4E/1-2-4-5, and 0K6E) have zero values and these are not reported.

Tautomer		1	2	3	4	5
		$ \chi_{J=1}^{(2)} , \chi_{J=3}^{(2)} \left(\rho = \chi_{J=3}^{(2)} / \chi_{J=1}^{(2)} \right)$				
5K1E		5.4, 2.7 (0.51)	5.6, 2.9, 0.51	3.3, 1.7 (0.51)	2.9, 1.5 (0.50)	2.3, 1.4 (0.59)
4K2E	1-2	10.2, 5.2 (0.51)	10.7, 5.4 (0.51)	5.9, 3.0 (0.50)	5.3, 2.7 (0.50)	4.2, 2.1 (0.50)
	1-3	7.9, 4.0 (0.51)	8.1, 4.1 (0.51)	4.8, 2.4 (0.50)	4.4, 2.2 (0.50)	3.0, 2.0 (0.67)
3K3E	1-2-3	15.6, 7.9 (0.51)	15.9, 8.1 (0.51)	8.7, 4.4 (0.50)	7.9, 4.0 (0.50)	5.7, 3.0 (0.52)
	1-3-4	7.4, 3.8 (0.52)	7.7, 3.9 (0.51)	4.2, 2.1 (0.51)	3.8, 1.9 (0.50)	2.7, 1.6 (0.58)
	1-3-5 ^a	0, 2.2 (∞)	0, 2.4 (∞)	0, 1.1 (∞)	0, 1.3 (∞)	0, 1.0 (∞)
	1-4-5	7.0, 3.6 (0.51)	7.1, 3.7 (0.52)	4.4, 2.2 (0.51)	3.9, 2.0 (0.51)	2.8, 1.5 (0.54)
2K4E	1-2-4-5	15.8, 8.0 (0.51)	16.0, 8.1 (0.50)	8.8, 4.5 (0.50)	8.1, 4.0 (0.50)	5.6, 2.8 (0.50)
	1-3-4-5	5.9, 4.0 (0.68)	6.1, 4.2 (0.68)	3.3, 2.1 (0.65)	3.0, 2.0 (0.68)	2.4, 1.4 (0.59)
1K5E		8.4, 5.0 (0.59)	8.6, 5.0 (0.59)	4.8, 2.7 (0.58)	4.4, 2.5 (0.57)	3.1, 1.8 (0.57)

^a The anisotropy factors of the 3K3E/1-3-5 tautomers were set to infinity, due to numerical precision, their $|\chi_{J=1}^{(2)}|$ values were not exactly zero.

8.4 Conclusions and Outlook

Periodic boundary conditions density functional theory calculations have been performed to characterize the second-order nonlinear optical responses, $\chi^{(2)}$, of covalent organic frameworks built from the assembly of tris(N-salicylideneaniline) units displaying tautomerisms between enol-imine and keto-enamine forms. At a typical laser wavelength of 1064 nm, the $\chi^{(2)}$ amplitudes are one order of magnitude larger than for the reference urea crystal but still about one order of magnitude smaller than in the crystal of MNA, a push-pull π -conjugated compound. These results are the first demonstrating that covalent organic frameworks can exhibit large second-order nonlinear responses. The symmetry as well as the unit cell size have been found to be the key parameters in order to design COFs with improved $\chi^{(2)}$ responses. Indeed, larger π -linkers between the tris(N-salicylideneaniline) nodes of the COFs lead to a reduction of the $\chi^{(2)}$ responses, which can be interpreted as a kind of dilution since the porosity of the COFs increases. The symmetry was shown to have an impact on the $\chi^{(2)}$ amplitudes as well as on their dipolar versus octupolar character. Moreover, these calculations demonstrate that the NLO responses of these COFs can be modulated as a function of the successive enol-imine/keto-enamine tautomerisms, leading to efficient solid-state second-order NLO switches. On the other hand, for the investigated COFs, the linear optical responses (excitation energies, refractive indices, and birefringence) exhibit smaller variations as a function of the nature of the π -linker or as a function of keto-enol switching.

We hope that this computational solid-state chemistry proof-of-concept will stimulate experimental investigations on the measurement of the NLO responses of COFs, on their variations as a function of the successive switching operations between the enol-imine and keto-enamine forms, as well as on the design of multifunctional materials, owing to their already-recognized catalytic and sensing properties. Moreover, modulating the π -linker by adding strong donor/acceptor deserves also to be investigated since it turned out to be a rewarding strategy to optimize molecular NLO switches.¹³

Acknowledgments

J.Q. thanks the "Actions de Recherche Concertées" (ARC) de la Direction générale de l'Enseignement non obligatoire et de la Recherche scientifique - Direction de la Recherche scientifique - Communauté française de Belgique, under convention No. 15/20-068 for his PhD grant. J.Q., A.D., and B.C. thank BELSPO for fundings through the Indo-Belgian Research and Technology Cooperation project BL/13/IN16 entitled "Optical Properties of MOFs/COFs". The authors thank N. Mandal for preliminary investigations on this topic. The calculations were performed on the computers of the Consortium des Équipements de Calcul Intensif (CÉCI, <http://www.cec-ihpc.be>) and particularly those of the

Technological Platform of High-Performance Computing, for which the authors gratefully acknowledge the financial support of the FNRS-FRFC, of the Walloon Region, and of the University of Namur (Conventions No. 2.5020.11, GEQ U.G006.15, 1610468, and RW/GEQ2016), as well as on zenobe, the Tier-1 facility of the Walloon Region (Convention 1117545).

Bibliography

- (1) Diercks, C. S.; Yaghi, O. M. The Atom, the Molecule, and the Covalent Organic Framework. *Science* **2017**, *355*, eaal1585, DOI: 10.1126/science.aal1585.
- (2) Waller, P. J.; Gándara, F.; Yaghi, O. M. Chemistry of Covalent Organic Frameworks. *Acc. Chem. Res.* **2015**, *48*, 3053–3063, DOI: 10.1021/acs.accounts.5b00369.
- (3) Kandambeth, S.; Dey, K.; Banerjee, R. Covalent Organic Frameworks: Chemistry beyond the Structure. *J. Am. Chem. Soc.* **2019**, *141*, 1807–1822, DOI: 10.1021/jacs.8b10334.
- (4) Geng, K.; He, T.; Liu, R.; Dalapati, S.; Tan, K. T.; Li, Z.; Tao, S.; Gong, Y.; Jiang, Q.; Jiang, D. Covalent Organic Frameworks: Design, Synthesis, and Functions. *Chem. Rev.* **2020**, acs.chemrev.9b00550, DOI: 10.1021/acs.chemrev.9b00550.
- (5) Wang, C.; Zhang, T.; Lin, W. Rational Synthesis of Noncentrosymmetric Metal–Organic Frameworks for Second-Order Nonlinear Optics. *Chem. Rev.* **2012**, *112*, 1084–1104, DOI: 10.1021/cr200252n.
- (6) Biswal, B. P.; Valligatla, S.; Wang, M.; Banerjee, T.; Saad, N. A.; Mariserla, B. M. K.; Chandrasekhar, N.; Becker, D.; Addicoat, M.; Senkovska, I.; Berger, R.; Rao, D. N.; Kaskel, S.; Feng, X. Nonlinear Optical Switching in Regioregular Porphyrin Covalent Organic Frameworks. *Angew. Chemie Int. Ed.* **2019**, *58*, 6896–6900, DOI: 10.1002/anie.201814412.
- (7) Zhang, L. et al. Covalent Organic Framework for Efficient Two-Photon Absorption. *Matter* **2020**, *2*, 1049–1063, DOI: 10.1016/j.matt.2020.01.019.
- (8) Verbiest, T.; Clays, K.; Rodriguez, V., *Second-order Nonlinear Optical Characterization Techniques*; CRC Press: 2009, DOI: 10.1201/9781420070736.
- (9) Reeve, J. E.; Anderson, H. L.; Clays, K. Dyes for Biological Second Harmonic Generation Imaging. *Phys. Chem. Chem. Phys.* **2010**, *12*, 13484, DOI: 10.1039/c003720f.

- (10) Coe, B. J. Molecular Materials Possessing Switchable Quadratic Non-linear Optical Properties. *Chem. - A Eur. J.* **1999**, *5*, 2464–2471, DOI: 10.1002/(SICI)1521-3765(19990903)5:9<2464::AID-CHEM2464>3.0.CO;2-L.
- (11) Delaire, J. A.; Nakatani, K. Linear and Nonlinear Optical Properties of Photochromic Molecules and Materials. *Chem. Rev.* **2000**, *100*, 1817–1846, DOI: 10.1021/cr980078m.
- (12) Asselberghs, I.; Clays, K.; Persoons, A.; Ward, M. D.; McCleverty, J. Switching of Molecular Second-Order Polarisability in Solution. *J. Mater. Chem.* **2004**, *14*, 2831, DOI: 10.1039/b401434k.
- (13) Castet, F.; Rodriguez, V.; Pozzo, J.-L.; Ducasse, L.; Plaquet, A.; Champagne, B. Design and Characterization of Molecular Nonlinear Optical Switches. *Acc. Chem. Res.* **2013**, *46*, 2656–2665, DOI: 10.1021/ar4000955.
- (14) Sliwa, M.; Létard, S.; Malfant, I.; Nierlich, M.; Lacroix, P. G.; Asahi, T.; Masuhara, H.; Yu, P.; Nakatani, K. Design, Synthesis, Structural and Nonlinear Optical Properties of Photochromic Crystals: Toward Reversible Molecular Switches. *Chem. Mater.* **2005**, *17*, 4727–4735.
- (15) Boubekeur-Lecaque, L.; Coe, B. J.; Harris, J. A.; Helliwell, M.; Asselberghs, I.; Clays, K.; Foerier, S.; Verbiest, T. Incorporation of Amphiphilic Ruthenium(II) Ammine Complexes into Langmuir–Blodgett Thin Films with Switchable Quadratic Nonlinear Optical Behavior. *Inorg. Chem.* **2011**, *50*, 12886–12899, DOI: 10.1021/ic202145b.
- (16) Green, K. A.; Cifuentes, M. P.; Samoc, M.; Humphrey, M. G. Metal Alkynyl Complexes as Switchable NLO Systems. *Coord. Chem. Rev.* **2011**, *255*, 2530–2541, DOI: 10.1016/j.ccr.2011.02.021.
- (17) Ségerie, A.; Castet, F.; Kanoun, M. B.; Plaquet, A.; Liégeois, V.; Champagne, B. Nonlinear Optical Switching Behavior in the Solid State: A Theoretical Investigation on Anils. *Chem. Mater.* **2011**, *23*, 3993–4001, DOI: 10.1021/cm2015516.
- (18) Serra-Crespo, P.; van der Veen, M. A.; Gobechiya, E.; Houthoofd, K.; Filinchuk, Y.; Kirschhock, C. E. A.; Martens, J. A.; Sels, B. F.; De Vos, D. E.; Kapteijn, F.; Gascon, J. NH₂-MIL-53(Al): A High-Contrast Reversible Solid-State Nonlinear Optical Switch. *J. Am. Chem. Soc.* **2012**, *134*, 8314–8317, DOI: 10.1021/ja300655f.
- (19) De, S.; Ray, M.; Pati, A. Y.; Das, P. K. Base Triggered Enhancement of First Hyperpolarizability of a Keto–Enol Tautomer. *J. Phys. Chem. B* **2013**, *117*, 15086–15092, DOI: 10.1021/jp410368z.

- (20) Li, P.-X.; Wang, M.-S.; Zhang, M.-J.; Lin, C.-S.; Cai, L.-Z.; Guo, S.-P.; Guo, G.-C. Electron-Transfer Photochromism To Switch Bulk Second-Order Nonlinear Optical Properties with High Contrast. *Angew. Chemie Int. Ed.* **2014**, *53*, 11529–11531, DOI: 10.1002/anie.201406554.
- (21) Matczyszyn, K.; Olesiak-Banska, J.; Nakatani, K.; Yu, P.; Murugan, N. A.; Zaleśny, R.; Roztoczyńska, A.; Bednarska, J.; Bartkowiak, W.; Kongsted, J.; Ågren, H.; Samoć, M. One- and Two-Photon Absorption of a Spiropyran–Merocyanine System: Experimental and Theoretical Studies. *J. Phys. Chem. B* **2015**, *119*, 1515–1522, DOI: 10.1021/jp5071715.
- (22) Van Bezouw, S.; Campo, J.; Lee, S.-H.; Kwon, O.-P.; Wenseleers, W. Organic Compounds with Large and High-Contrast pH-Switchable Nonlinear Optical Response. *J. Phys. Chem. C* **2015**, *119*, 21658–21663, DOI: 10.1021/acs.jpcc.5b06968.
- (23) Boixel, J.; Guerchais, V.; Le Bozec, H.; Chantzis, A.; Jacquemin, D.; Colombo, A.; Dragonetti, C.; Marinotto, D.; Roberto, D. Sequential Double Second-Order Nonlinear Optical Switch by an Acido-Triggered Photochromic Cyclometallated Platinum(II) Complex. *Chem. Commun.* **2015**, *51*, 7805–7808, DOI: 10.1039/C5CC01893E.
- (24) Schulze, M.; Utecht, M.; Moldt, T.; Przyrembel, D.; Gahl, C.; Weinelt, M.; Saalfrank, P.; Tegeder, P. Nonlinear Optical Response of Photochromic Azobenzene-Functionalized Self-Assembled Monolayers. *Phys. Chem. Chem. Phys.* **2015**, *17*, 18079–18086.
- (25) Tonnelé, C.; Champagne, B.; Muccioli, L.; Castet, F. Second-Order Nonlinear Optical Properties of Stenhouse Photoswitches: Insights from Density Functional Theory. *Phys. Chem. Chem. Phys.* **2018**, *20*, 27658–27667, DOI: 10.1039/C8CP05843A.
- (26) Tonnelé, C.; Champagne, B.; Muccioli, L.; Castet, F. Nonlinear Optical Contrast in Azobenzene-Based Self-Assembled Monolayers. *Chem. Mater.* **2019**, *31*, 6759–6769, DOI: 10.1021/acs.chemmater.9b01241.
- (27) Avramopoulos, A.; Zaleśny, R.; Reis, H.; Papadopoulos, M. G. A Computational Strategy for the Design of Photochromic Derivatives Based on Diarylethene and Nickel Dithiolene with Large Contrast in Nonlinear Optical Properties. *J. Phys. Chem. C* **2020**, *124*, 4221–4241, DOI: 10.1021/acs.jpcc.9b10563.
- (28) Kandambeth, S.; Mallick, A.; Lukose, B.; Mane, M. V.; Heine, T.; Banerjee, R. Construction of Crystalline 2D Covalent Organic Frameworks with Remarkable Chemical (Acid/Base) Stability via a Combined Reversible and Irreversible Route. *J. Am. Chem. Soc.* **2012**, *134*, 19524–19527, DOI: 10.1021/ja308278w.

- (29) Chandra, S.; Kundu, T.; Kandambeth, S.; BabaRao, R.; Marathe, Y.; Kunjir, S. M.; Banerjee, R. Phosphoric Acid Loaded Azo (-N=N-) Based Covalent Organic Framework for Proton Conduction. *J. Am. Chem. Soc.* **2014**, *136*, 6570–6573, DOI: 10.1021/ja502212v.
- (30) Castet, F.; Champagne, B. In *Tautomerism*; Wiley-VCH Verlag GmbH & Co. KGaA: Weinheim, Germany, 2016, pp 175–202, DOI: 10.1002/9783527695713.ch8.
- (31) Dovesi, R.; Orlando, R.; Erba, A.; Zicovich-Wilson, C. M.; Civalleri, B.; Casassa, S.; Maschio, L.; Ferrabone, M.; De La Pierre, M.; D'Arco, P.; Noël, Y.; Causà, M.; Rérat, M.; Kirtman, B. CRYSTAL14: a Program for the Ab Initio Investigation of Crystalline Solids. *Int. J. Quantum Chem.* **2014**, *114*, 1287–1317.
- (32) Dovesi, R.; Erba, A.; Orlando, R.; Zicovich-Wilson, C. M.; Civalleri, B.; Maschio, L.; Rérat, M.; Casassa, S.; Baima, J.; Salustro, S.; Kirtman, B. CRYSTAL17. *Wiley Interdiscip. Rev. Comput. Mol. Sci.* **2018**, *8*, e1360.
- (33) Dovesi, R. et al. The CRYSTAL Code, 1976–2020 and Beyond, a Long Story. *J. Chem. Phys.* **2020**, *152*, 204111, DOI: 10.1063/5.0004892.
- (34) Chai, J.-D.; Head-Gordon, M. Systematic Optimization of Long-Range Corrected Hybrid Density Functionals. *J. Chem. Phys.* **2008**, *128*, 084106, DOI: 10.1063/1.2834918.
- (35) Pritchard, B. P.; Altarawy, D.; Didier, B.; Gibson, T. D.; Windus, T. L. New Basis Set Exchange: An Open, Up-to-Date Resource for the Molecular Sciences Community. *J. Chem. Inf. Model.* **2019**, *59*, 4814–4820, DOI: 10.1021/acs.jcim.9b00725.
- (36) Quertinmont, J.; Carletta, A.; Tumanov, N. A.; Leyssens, T.; Wouters, J.; Champagne, B. Assessing density functional theory approaches for predicting the structure and relative energy of salicylideneaniline molecular switches in the solid state. *J. Phys. Chem. C* **2017**, *121*, 6898–6908, DOI: 10.1021/acs.jpcc.7b00580.
- (37) Quertinmont, J.; Leyssens, T.; Wouters, J.; Champagne, B. Effects of Empirical Dispersion Energy on the Geometrical Parameters and Relative Energy of a Salicylideneaniline Molecular Switch in the Solid State. *Crystals* **2018**, *8*, 125, DOI: 10.3390/cryst8030125.
- (38) Ferrero, M.; Rérat, M.; Orlando, R.; Dovesi, R.; Bush, I. J. Coupled Perturbed Kohn-Sham Calculation of Static Polarizabilities of Periodic Compounds. *J. Phys. Conf. Ser.* **2008**, *117*, 1–8, DOI: 10.1088/1742-6596/117/1/012016.

- (39) Lacivita, V.; Rérat, M.; Kirtman, B.; Ferrero, M.; Orlando, R.; Dovesi, R. Calculation of the Dielectric Constant ϵ and First Nonlinear Susceptibility $\chi^{(2)}$ of Crystalline Potassium Dihydrogen Phosphate by the Coupled Perturbed Hartree–Fock and Coupled Perturbed Kohn–Sham Schemes as Implemented in the CRYSTAL code. *J. Chem. Phys.* **2009**, *131*, 204509, DOI: 10.1063/1.3267048.
- (40) Orlando, R.; Lacivita, V.; Bast, R.; Ruud, K. Calculation of the First Static Hyperpolarizability Tensor of Three-Dimensional Periodic Compounds with a Local Basis Set: A Comparison of LDA, PBE, PBE0, B3LYP, and HF Results. *J. Chem. Phys.* **2010**, *132*, 244106, DOI: 10.1063/1.3447387.
- (41) Maschio, L.; Rérat, M.; Kirtman, B.; Dovesi, R. Calculation of the Dynamic First Electronic Hyperpolarizability $\beta(-\omega_\sigma; \omega_1, \omega_2)$ of Periodic Systems. Theory, Validation, and Application to Multi-Layer MoS₂. *J. Chem. Phys.* **2015**, *143*, 244102, DOI: 10.1063/1.4937770.
- (42) Rérat, M.; Maschio, L.; Kirtman, B.; Civalleri, B.; Dovesi, R. Computation of Second Harmonic Generation for Crystalline Urea and KDP. An ab Initio Approach through the Coupled Perturbed Hartree-Fock/Kohn-Sham Scheme. *J. Chem. Theory Comput.* **2016**, *12*, 107–113, DOI: 10.1021/acs.jctc.5b00791.
- (43) Zhang, Y.; Champagne, B. Theoretical Insight into the Second-Order NLO Response of the Bis{4-[2-(4-pyridyl)ethenyl]benzoato}-zinc(II) Metal–Organic Framework. *J. Phys. Chem. C* **2012**, *116*, 21973–21981, DOI: 10.1021/jp307283m.
- (44) Seidler, T.; Stadnicka, K.; Champagne, B. Evaluation of the Linear and Second-Order NLO Properties of Molecular Crystals within the Local Field Theory: Electron Correlation Effects, Choice of XC Functional, ZPVA Contributions, and Impact of the Geometry in the Case of 2-Methyl-4-nitroaniline. *J. Chem. Theory Comput.* **2014**, *10*, 2114–2124.
- (45) Seidler, T.; Champagne, B. Second-Order Nonlinear Optical Susceptibilities of Metal–Organic Frameworks Using a Combined Local Field Theory/Charge Embedding Electrostatic Scheme. *J. Phys. Chem. C* **2016**, *120*, 6741–6749, DOI: 10.1021/acs.jpcc.6b00217.
- (46) Fang, Z.; Lin, J.; Liu, R.; Liu, P.; Li, Y.; Huang, X.; Ding, K.; Ning, L.; Zhang, Y. Computational Design of Inorganic Nonlinear Optical Crystals Based on a Genetic Algorithm. *CrystEngComm* **2014**, *16*, 10569–10580, DOI: 10.1039/C4CE01606H.
- (47) Ni, B.; Sun, W.; Kang, J.; Zhang, Y. Understanding the Linear and Second-Order Nonlinear Optical Properties of UiO-66-Derived Metal–Organic Frameworks: A Comprehensive DFT Study. *J. Phys. Chem. C* **2020**, *124*, 11595–11608, DOI: 10.1021/acs.jpcc.0c01580.

- (48) Castet, F.; Bogdan, E.; Plaquet, A.; Ducasse, L.; Champagne, B.; Rodriguez, V. Reference Molecules for Nonlinear Optics: A Joint Experimental and Theoretical Investigation. *J. Chem. Phys.* **2012**, *136*, 024506, DOI: 10.1063/1.3675848.
- (49) Brasselet, S.; Zyss, J. Multipolar Molecules and Multipolar Fields: Probing and Controlling the Tensorial Nature of Nonlinear Molecular Media. *J. Opt. Soc. Am. B* **1998**, *15*, 257, DOI: 10.1364/JOSAB.15.000257.
- (50) Rodriguez, V.; Grondin, J.; Adamietz, F.; Danten, Y. Local Structure in Ionic Liquids Investigated by Hyper-Rayleigh Scattering. *J. Phys. Chem. B* **2010**, *114*, 15057–15065, DOI: 10.1021/jp107165k.
- (51) Tuer, A.; Krouglov, S.; Cisek, R.; Tokarz, D.; Barzda, V. Three-Dimensional Visualization of the First Hyperpolarizability Tensor. *J. Comput. Chem.* **2011**, *32*, 1128, DOI: 10.1002/jcc.21694.
- (52) Liégeois, V.; UNamur DrawMol, 2018.
- (53) Zutterman, F.; Louant, O.; Mercier, G.; Leyssens, T.; Champagne, B. Predicting Keto–Enol Equilibrium from Combining UV/Visible Absorption Spectroscopy with Quantum Chemical Calculations of Vibronic Structures for Many Excited States. A Case Study on Salicylideneanilines. *J. Phys. Chem. A* **2018**, *122*, 5370–5374, DOI: 10.1021/acs.jpca.8b03389.
- (54) Barboza, C. A.; Sobolewski, A. L. An Ab Initio Study on the Photophysics of Tris(Salicylideneaniline). *Phys. Chem. Chem. Phys.* **2018**, *20*, 25164–25168, DOI: 10.1039/C8CP04416C.
- (55) Halbout, J.-M.; Blit, S.; Donaldson, W.; Chung Tang Efficient Phase-Matched Second-Harmonic Generation and Sum-Frequency Mixing in Urea. *IEEE J. Quantum Electron.* **1979**, *15*, 1176–1180, DOI: 10.1109/JQE.1979.1069900.
- (56) Morita, R.; Kondo, T.; Kaneda, Y.; Sugihashi, A.; Ogasawara, N.; Umegaki, S.; Ito, R. Dispersion of Second-Order Nonlinear Optical Coefficient d_{11} of 2-Methyl-4-Nitroaniline (MNA). *Jpn. J. Appl. Phys.* **1988**, *27*, L1131–L1133, DOI: 10.1143/JJAP.27.L1131.
- (57) Bogdan, E.; Plaquet, A.; Antonov, L.; Rodriguez, V.; Ducasse, L.; Champagne, B.; Castet, F. Solvent Effects on the Second-Order Nonlinear Optical Responses in the Keto-Enol Equilibrium of a 2-Hydroxy-1-naphthaldehyde Derivative. *J. Phys. Chem. C* **2010**, *114*, 12760–12768, DOI: 10.1021/jp103556c.
- (58) Guillaume, M.; Champagne, B.; Markova, N.; Enchev, V.; Castet, F. Ab Initio Investigation on the Second-Order Nonlinear Optical Responses in Keto-Enol Equilibria of Salicylideneanilines. *J. Phys. Chem. A* **2007**, *111*, 9914–9923, DOI: 10.1021/jp074567e.

MOLECULAR SWITCHES: ASSESSING THEIR THERMODYNAMICAL EQUILIBRIA IN SOLUTION USING HIGH-LEVEL QUANTUM CHEMISTRY METHODS

To Be Published

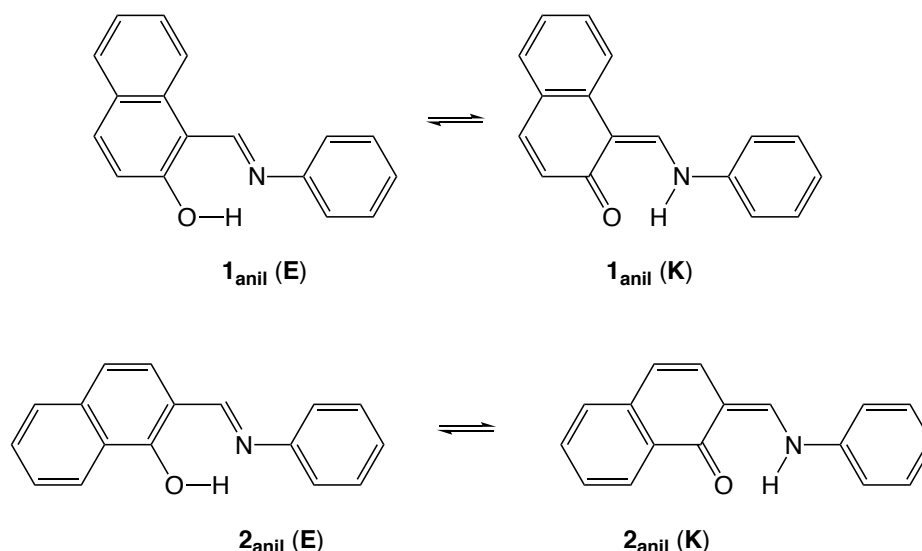
J.Q. performed all the TURBOMOLE calculations and contributed to the writing of this Chapter that will become a Section in a future publication.

9.1 Introduction

Molecular switches constitute a class of compounds that can undergo reversible transformations between their different forms accompanied by a modification of their properties.^{1–3} Well-known examples are photochromic, thermochromic, acidochromic, solvatochromic, electrochromic, and piezochromic compounds where (at least one of) the transformations is triggered by light irradiation, by a change of temperature, of pH, or of solvent, as well as by the application of a redox potential or of pressure, respectively. There remains a strong interest in knowing and subsequently controlling the differences of energy between the states of molecular switches.^{4–7} Still, to determine experimentally these equilibria and their associated free enthalpies of transformation, ΔG^\ominus , the different forms should be present in detectable amounts. Assuming that the detection is possible if there are at least 5 %, 1 %, or 0.2 % of the minority form, its absence means that, at 298.15 K, its free enthalpy is at least 1.7 kcal mol^{–1}, 2.7 kcal mol^{–1}, or 3.7 kcal mol^{–1} higher than that of the majority form. Experimentally, chemometrics⁸ has been employed for several switches so that the equilibrium constants have been determined from chemometrics analysis of their UV/visible absorption spectra⁹ as well as NMR spectra.¹⁰ Alternatives include the use of quantum chemistry methods as a tool *per se*, like in this Chapter, or in combination with experimental data. Indeed, on the one hand, quantum chemistry (QC) methods can provide nowadays accurate thermodynamical properties (enthalpies, free enthalpies).¹¹ On the other hand, quantum chemistry calculations of spectral signatures can be combined with experimental data. This was the case of a recent study of our group where the UV/vis absorption spectra of N-salicylideneanilines have been simulated upon taking account of the lowest-energy excited states and of their vibronic structures and compared to experiment.⁷ In practice, the spectra of the different tautomers of N-salicylideneanilines have been mixed in different ratios until best fitting the experimental spectra. In that study, the calculated ΔG^\ominus of transformation were in good agreement with the results from chemometrics but their agreement with Møller-Plesset second-order perturbation theory (MP2) or with density functional theory (DFT) employing selected exchange-correlation functionals was rather poor. This contradiction between the performance of these two approaches (simulated spectra *versus* by QC ΔG^\ominus calculations) was one of the incentives for the current investigation, which aims at using high-level QC methods.

To tackle this issue, two families of molecular switches are considered, N-salicylideneanilines (or anils) and spiropyrans. In the first, the molecular switches are characterized by a enol-imine/keto-enamine (E/K) tautomerism (Scheme 9.1) and the two selected compounds are the same as those of the recent work quoted above.⁷ As shown in Scheme 9.1, the equilibrium occurs between the *cis*-enol and *cis*-keto forms. The *trans*-keto form, which can be accessed by photoexcitation is not discussed here because it is of much higher energy, owing

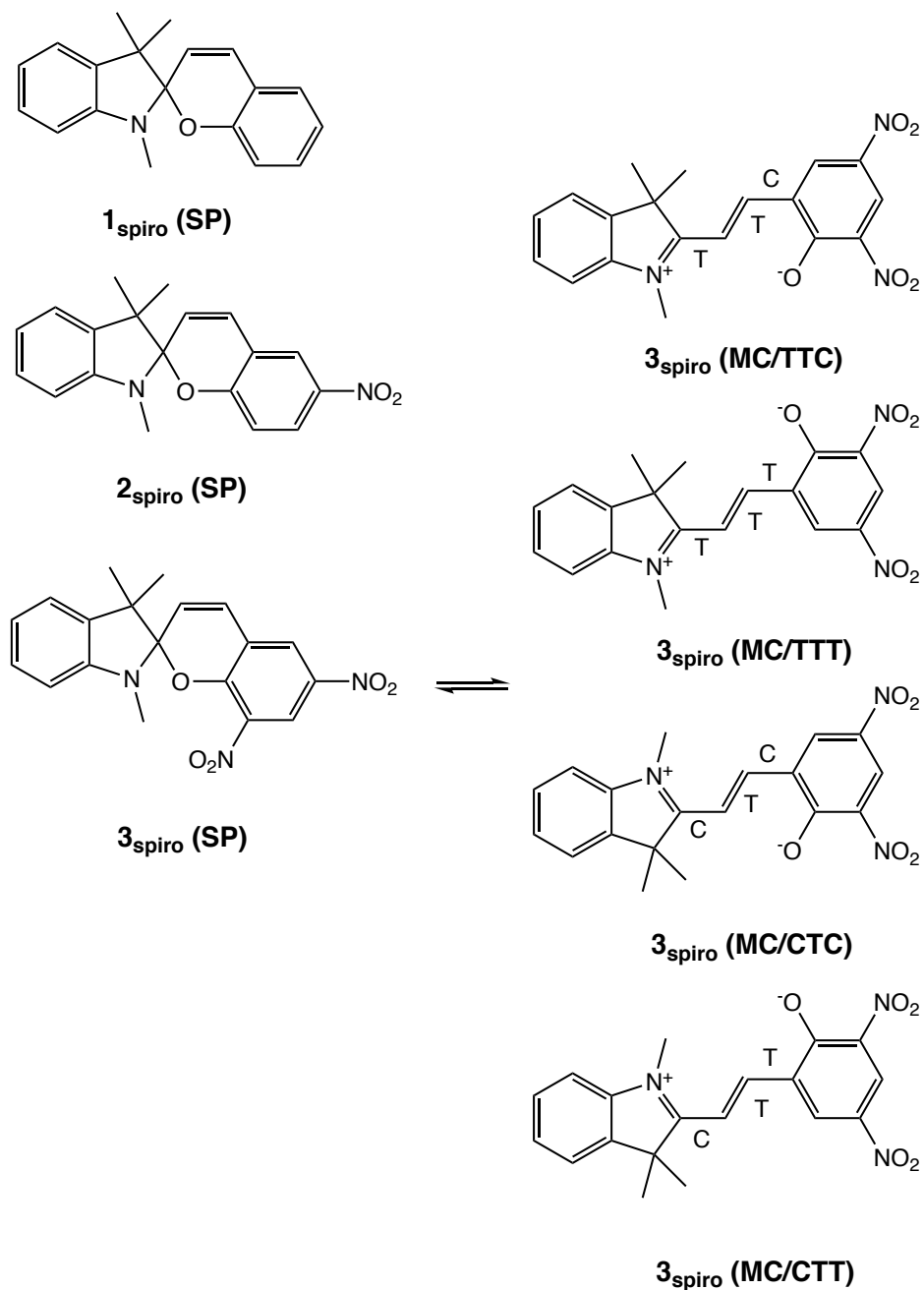
to the absence of stabilizing H-bond (or any other mean to stabilize this form, like crystal packing).¹²



Scheme 9.1: Enol-keto equilibria of the 1_{anil} and 2_{anil} compounds.

The second family concerns molecules that switch between a spiropyran (SP) and a merocyanine (MC) form (Scheme 9.2). Three compounds were selected owing to the available experimental data as well as to the interest they attracted in other QC investigations. In addition to the $\text{SP} \rightleftharpoons \text{MC}$ equilibrium, for the MC forms, different conformers can co-exist. *Cis* and *trans* conformations can indeed be defined for each of the three bonds between the two aromatic moieties of the MC form, leading in principle to $2^3 = 8$ conformers. Yet, for stability reasons, in solution, the inner one should adopt a *trans* conformation, leaving only 4 conformers to study (TTC for *trans trans cis*, TTT, CTC, and CTT, Scheme 9.2).

The choice of N-salicylideneanilines and spiropyranes can be found in the availability of experimental data but also in our recent works on their chromisms^{13–16} and nonlinear optical properties.¹⁷ The first objective of this Chapter is therefore to assess how accurately quantum chemistry calculations can predict the relative stability of the different states of these molecular switches. Following recent investigations,^{11,18} this is performed using a combination of highly-correlated wavefunction methods. A future objective — not discussed here — will be to see how computationally less-demanding techniques can perform. Among these, DFT with typical exchange-correlation (XC) functionals and MP2 calculations. Table 9.1 gathers the experimental data that are used for comparisons.



Scheme 9.2: SP-MC equilibria of the **1_{spiro}**, **2_{spiro}**, and **3_{spiro}** compounds as well as the key conformers of the MC form of **3_{spiro}**.

Table 9.1: ΔG^\ominus (kcal mol⁻¹) of the E \rightleftharpoons K and SP \rightleftharpoons MC equilibria as determined with different experimental techniques and comparisons with selected results from the literature

Experiment		Other methods
1_{anil}	UV/visible absorption (acetonitrile)	0.34 ^a , 0.30 ^b
2_{anil}	UV/visible absorption (acetonitrile)	-0.13 ^c , -0.34 ^b
1_{spiro}	Photochemical ring opening (n-pentane)	>5 TTT and TTC ^e
	UV/visible absorption (propanol)	5.9 ^f
	UV/visible absorption (C ₂ Cl ₄)	>5 ^g
2_{spiro}	¹ H NMR (DMSO)	2.6 ^f
	UV/visible absorption (C ₂ Cl ₄)	>5 ^g
	UV/visible absorption (acetonitrile)	4.57 ^h
3_{spiro}	¹ H NMR (DMF)	-2.3 ^f

^a Ref. [9]

^b Ref. [19]

^c Ref. [20]

^d UV/vis absorption spectra combined with QC calculations, from Ref. [7]

^e Ref. [21]

^f Ref. [22]

^g Ref. [23]

^h Ref. [24]

9.2 Theoretical and Computational Aspects

High-level energy values were obtained using a composite approach. First full geometry optimizations were performed at the MP2 level of approximation with the 6-311+G(d,p) basis set. These calculations were performed for isolated species (infinitely diluted gas phase) or for solvated species. In the latter case, the effects of the solvent were described using the integral equation formalism of the polarizable continuum model (IEF-PCM).²⁵ For all compounds the solvent is acetonitrile but for the spiropyran-merocyanine derivatives heptane, tetrachloroethylene, and dimethylformamide was also used. These calculations provide the geometry for further energy calculations as well as the thermal corrections to evaluate the free enthalpies, $\Delta G_{T=0\text{ K} \rightarrow 298\text{ K}}$. They were performed using the Gaussian16 package.²⁶

For the N-salicylideneaniline derivatives, RI-CCSD(T) energies (and energies of reaction) were evaluated using the def2-TZVPP basis set. RI-CCSD(T) employs the resolution of the identity²⁷ in coupled cluster calculations including the singles, doubles, and perturbative triples. These are the highest-level calculations we could perform and provide the so-called $E_{\text{CCSD(T)}}$ values. Then, basis set corrections were estimated by calculating the RI-MP2 energies using the def2-QZVPP and def2-TZVPP basis sets:

$$E_{\text{correction}} = E_{\text{QZVPP}} - E_{\text{TZVPP}}. \quad (9.1)$$

Solvent contributions,

$$E_{\text{solvation}} = E_{\text{solute-PTED}} - E_{\text{isolated}} \quad (9.2)$$

were evaluated using the COSMO model²⁸ in combination with the perturbation theory on energy and density (PTED) scheme²⁹ at the RI-MP2 level of approximation with the def2-QZVPP basis set. In the PTED approach the polarizable environment is self-consistently equilibrated with the correlated MP2 density, leading for an improved description of solvent effects. Adding these two corrections to the initial value provide the best estimate for the total electronic energy (so, at 0 K) in solution:

$$E_{T=0\text{ K}} = E_{\text{CCSD(T)}} + E_{\text{correction}} + E_{\text{solvation}} \quad (9.3)$$

These calculations were carried out using the Turbomole program³⁰ and the Ahlrichs and coworkers' basis sets.³¹⁻³⁴ Finally, the thermal contributions ($E_{\text{thermal}} = \Delta G_{T=0\text{ K} \rightarrow 298\text{ K}}$) previously evaluated at the IEF-PCM/MP2/6-311+G(d,p) were added to get the Gibbs enthalpies at 298.15 K:

$$G_{T=298.15\text{ K}} = E_{T=0\text{ K}} + \Delta G_{T=0\text{ K} \rightarrow 298\text{ K}}. \quad (9.4)$$

For the two largest spiropyran-merocyanine derivatives, sufficient computer resources were not available to evaluate the RI-CCSD(T)/def2-TZVPP. Instead,

PNO-RI-CCSD(T)/def2-QZVPP were performed to get the so-called ECCSD(T) values.³⁵ Subsequently, the $E_{\text{correction}}$ quantity was evaluated as the difference between the PNO-RI-MP2 and RI-MP2 values, as obtained with the def2-QZVPP basis set:

$$E_{\text{correction}} = E_{\text{RI-MP2}} - E_{\text{PNO-RI-MP2}}. \quad (9.5)$$

This equation replaces therefore Eq. 9.1 for these spiropyran-merocyanine derivatives.

9.3 Results and Discussions

Table 9.2 reports the calculated values and their decomposition, as described in Section 9.2. For both anils, the predicted $\Delta G_{T=298\text{ K}}$ values are in good agreement with the experimental results, especially because the transformation equilibrium constants are close to 1 (or $\Delta G_{T=298\text{ K}}$ close to zero). In particular, the calculations correctly predict that, in acetonitrile, the keto form is the most stable for **1_{anil}** while it is the enol one for **2_{anil}**. In such a case, all contributions to $\Delta G_{T=298\text{ K}}$ are important, with a substantial relative stabilization of the keto form due to solvation effects and a smaller one attributed to the thermal corrections. On the other hand, the basis set corrections ($\Delta E_{\text{correction}}$) are small and similar for both anil derivatives. Note that these results contrast by their accuracy with those that were reported by using the MP2 method or selected DFT XC functionals.⁷

In the case of **1_{spiro}** the $\Delta G_{T=298\text{ K}}$ value (which are ΔG^\ominus values) for the most stable conformer (TTC) amounts to 7.6 kcal mol⁻¹, 12.7 kcal mol⁻¹, and 13.0 kcal mol⁻¹ in acetonitrile, heptane, and tetrachloroethylene, respectively. This difference results mostly from the stronger effect (−9 versus −2 kcal mol⁻¹) of the polar solvent in stabilizing the zwitterionic open form. It is also noteworthy that the thermal effects are larger than in the case of the anil derivatives, as expected since the number of bonds is reduced (C–O cleavage), leading to an increase of entropy. This $\Delta G_{T=298\text{ K}}$ value of 7.6 kcal mol⁻¹ is in close agreement with the experimental one determined in propanol.²² For the other solvents, the comparison is hampered by the small concentration in MC forms. Still, the dominance of TTC and TTT forms is also observed. The presence of a nitro function on the benzopyran (**2_{spiro}**) stabilizes the merocyanine form by about 3.5 kcal mol⁻¹ and another stabilization by 4.5 kcal mol⁻¹ is achieved with the presence of a second nitro function (**3_{spiro}**). These data refer to the most stable conformer (again TTC) and acetonitrile as solvent. Like for **1_{spiro}**, for both nitro-substituted species, the solvation contribution is important for acetonitrile (above 10 kcal mol⁻¹) while the thermal corrections remain of the order of −4 kcal mol⁻¹. All in all, the predicted $\Delta G_{T=298\text{ K}}$ value of **2_{spiro}** in acetonitrile (TTC conformer) amounts to 4.1 kcal mol⁻¹ in comparison to an experimental value of 4.6 kcal mol⁻¹.²⁴ Qualitatively the agreement is also good when the solvent is tetrachloroethylene, still the $\Delta G_{T=298\text{ K}}$ value is much

larger ($10.9 \text{ kcal mol}^{-1}$) and the experimental determination is extremely difficult ($\Delta G_{T=298 \text{ K}} > 5 \text{ kcal mol}^{-1}$). Among the three compounds, **3_{spiro}** is the only one for which the MC form is the most stable. The calculations predict a small $\Delta G_{T=298 \text{ K}}$ of $-0.3 \text{ kcal mol}^{-1}$ whereas ^1H NMR determination in DMF gives a value substantially more negative, $-2.3 \text{ kcal mol}^{-1}$.²² The origin of this difference might be double, *i.e.* i) the ^1H NMR technique that has been employed experimentally since for anils it was observed to lead to quite different results in comparison to UV/vis absorption¹⁰ or ii) the remaining limitations of the QC method, which does not account for explicit solute-solvent interactions.

Table 9.2: ΔE and $\Delta G_{T=298\text{ K}}$ (kcal mol⁻¹) of reactions for the enol to keto ($\Delta E = E_K - E_E$) and spiropyran to merocyanine ($\Delta E = E_{MC} - E_{SP}$) transformations and its components (see the text for their definition) as evaluated with the composite method. Except when noted otherwise, the solvent is acetonitrile. In the case of **1_{spiro}**/C₂Cl₄, **2_{spiro}**/C₂Cl₄, and **3_{spiro}**/DMF, the geometry optimizations and thermal corrections were carried out in acetonitrile.

		$\Delta E_{\text{CCSD(T)}}$	$\Delta E_{\text{correction}}$	$\Delta E_{\text{solvation}}$	$\Delta E_{T=0\text{ K}}$	E_{thermal}	$\Delta G_{T=298\text{ K}}$
1_{anil}		3.53	-0.25	-2.59	0.69	-0.45	0.24
2_{anil}		2.83	-0.19	-2.48	0.16	-0.36	-0.20
1_{spiro}	TTC	21.40	-0.83	-8.96	11.61	-4.04	7.57
	TTT	22.23	-0.30	-9.81	12.12	-4.66	7.46
	CTC	24.34	-0.88	-9.74	13.72	-3.77	9.95
	CTT	24.21	-0.87	-9.31	14.03	-4.26	9.77
1_{spiro} heptane	TTC	19.79	-0.67	-2.04	17.08	-4.38	12.70
	TTT	20.67	-0.76	-2.11	17.80	-4.89	12.91
	CTC	22.39	-0.73	-2.05	19.61	-3.84	15.77
	CTT	22.31	-0.72	-2.06	19.53	-4.17	15.36
1_{spiro} C₂Cl₄	TTC	21.40	-0.82	-3.21	17.37	-4.38	12.99
	TTC	19.65	-0.61	-10.94	8.10	-4.01	4.09
2_{spiro}	TTT	21.70	-0.84	-11.85	9.01	-4.32	4.69
	CTC	23.04	-0.63	-12.35	10.06	-3.39	6.67
	CTT	24.78	-0.87	-13.13	10.78	-3.60	7.18
2_{spiro} C₂Cl₄	TTC	19.65	-0.61	-4.09	14.95	-4.01	10.94
3_{spiro}	TTC	17.49	-0.04	-13.41	4.04	-4.30	-0.26
3_{spiro} DMF	TTC	17.49	-0.03	-13.45	4.01	-4.30	-0.29

9.4 Conclusions and Outlook

In this Chapter we have demonstrated that high-level quantum chemistry calculations can provide accurate ΔG^\ominus of transformation for representative molecular switches like N-salicylideneanilines and spiropyrans, that solvent and thermal effects can influence the sign of ΔG^\ominus and should therefore be taken into account. Still, improvements of this scheme are still possible, e.g. by accounting for explicit solvation. Following a recent paper, one of the next step consists in challenging these thermodynamical data with those of theoretical spectroscopy, combining the simulated UV/vis absorption spectra of the different species and comparing them to experiment.⁷

Bibliography

- (1) De Silva, A. P.; Vance, T. P.; West, M. E. S.; Wright, G. D. Bright Molecules with Sense, Logic, Numeracy and Utility. *Org. Biomol. Chem.* **2008**, *6*, 2468, DOI: 10.1039/b802963f.
- (2) *Molecular Switches*; Feringa, B. L., Browne, W. R., Eds.; Wiley-VCH Verlag GmbH & Co. KGaA: Weinheim, Germany, 2011, DOI: 10.1002/9783527634408.
- (3) Andréasson, J.; Pischel, U. Molecules with a Sense of Logic: A Progress Report. *Chem. Soc. Rev.* **2015**, *44*, 1053–1069, DOI: 10.1039/C4CS00342J.
- (4) Amos, R. D.; Kobayashi, R. Ab Initio Investigation of the Structures and Energies of Spiropyran and Merocyanine Isomers. *Mol. Phys.* **2015**, *113*, 1674–1681, DOI: 10.1080/00268976.2014.1003987.
- (5) Brügger, O.; Reichenbach, T.; Sommer, M.; Walter, M. Substituent Correlations Characterized by Hammett Constants in the Spiropyran–Merocyanine Transition. *J. Phys. Chem. A* **2017**, *121*, 2683–2687, DOI: 10.1021/acs.jpca.7b01248.
- (6) Saritas, K.; Grossman, J. C. Accurate Isomerization Enthalpy and Investigation of the Errors in Density Functional Theory for Dihydroazulene/Vinylheptafulvene Photochromism Using Diffusion Monte Carlo. *J. Phys. Chem. C* **2017**, *121*, 26677–26685, DOI: 10.1021/acs.jpcc.7b09437.
- (7) Zutterman, F.; Louant, O.; Mercier, G.; Leyssens, T.; Champagne, B. Predicting Keto–Enol Equilibrium from Combining UV/Visible Absorption Spectroscopy with Quantum Chemical Calculations of Vibronic Structures for Many Excited States. A Case Study on Salicylideneanilines. *J. Phys. Chem. A* **2018**, *122*, 5370–5374, DOI: 10.1021/acs.jpca.8b03389.

- (8) Antonov, L.; Nedeltcheva, D. Resolution of Overlapping UV–Vis Absorption Bands and Quantitative Analysis. *Chem. Soc. Rev.* **2000**, *29*, 217–227, DOI: 10.1039/a900007k.
- (9) Antonov, L.; Fabian, W. M. F.; Nedeltcheva, D.; Kamounah, F. S. Tautomerism of 2-Hydroxynaphthaldehyde Schiff Bases. *J. Chem. Soc. Perkin Trans. 2* **2000**, 1173–1179, DOI: 10.1039/b000798f.
- (10) Nedeltcheva, D.; Antonov, L.; Lycka, A.; Damyanova, B.; Popov, S. Chemometric Models For Quantitative Analysis of Tautomeric Schiff Bases and Azo Dyes. *Curr. Org. Chem.* **2009**, *13*, 217–240, DOI: 10.2174/138527209787314832.
- (11) Paulechka, E.; Kazakov, A. Efficient DLPNO–CCSD(T)-Based Estimation of Formation Enthalpies for C-, H-, O-, and N-Containing Closed-Shell Compounds Validated Against Critically Evaluated Experimental Data. *J. Phys. Chem. A* **2017**, *121*, 4379–4387, DOI: 10.1021/acs.jpca.7b03195.
- (12) Hadjoudis, E.; Mavridis, I. M. Photochromism and Thermochromism of Schiff Bases in the Solid State: Structural Aspects. *Chem. Soc. Rev.* **2004**, *33*, 579–588.
- (13) Carletta, A.; Buol, X.; Leyssens, T.; Champagne, B.; Wouters, J. Polymorphic and Isomorphic Cocrystals of a N-Salicylidene-3-aminopyridine with Dicarboxylic Acids: Tuning of Solid-State Photo- and Thermochromism. *J. Phys. Chem. C* **2016**, *120*, 10001–10008.
- (14) Quertinmont, J.; Carletta, A.; Tumanov, N. A.; Leyssens, T.; Wouters, J.; Champagne, B. Assessing density functional theory approaches for predicting the structure and relative energy of salicylideneaniline molecular switches in the solid state. *J. Phys. Chem. C* **2017**, *121*, 6898–6908, DOI: 10.1021/acs.jpcc.7b00580.
- (15) Seiler, V. K.; Robeyns, K.; Tumanov, N.; Cinčić, D.; Wouters, J.; Champagne, B.; Leyssens, T. A Coloring Tool for Spiropyrans: Solid State Metal–Organic Complexation Versus Salification. *CrystEngComm* **2019**, *21*, 4925–4933, DOI: 10.1039/C9CE00805E.
- (16) Quertinmont, J.; Leyssens, T.; Wouters, J.; Champagne, B. Periodic DFT Study of the Effects of Co-Crystallization on a N-Salicylideneaniline Molecular Switch. *ChemPhysChem* **2019**, *20*, 2434–2442, DOI: 10.1002/cphc.201900463.
- (17) Castet, F.; Champagne, B. In *Tautomerism*; Wiley-VCH Verlag GmbH & Co. KGaA: Weinheim, Germany, 2016, pp 175–202, DOI: 10.1002/9783527695713.ch8.

- (18) Ali, S. T.; Antonov, L.; Fabian, W. M. F. Phenol–Quinone Tautomerism in (Arylazo)naphthols and the Analogous Schiff Bases: Benchmark Calculations. *J. Phys. Chem. A* **2014**, *118*, 778–789, DOI: 10.1021/jp411502u.
- (19) Antonov, L. Tautomerism in Azo and Azomethyne Dyes: When and If Theory Meets Experiment. *Molecules* **2019**, *24*, 2252, DOI: 10.3390/molecules24122252.
- (20) Fabian, W. M. F.; Antonov, L.; Nedeltcheva, D.; Kamounah, F. S.; Taylor, P. J. Tautomerism in Hydroxynaphthaldehyde Anils and Azo Analogues: a Combined Experimental and Computational Study. *J. Phys. Chem. A* **2004**, *108*, 7603–7612, DOI: 10.1021/jp048035z.
- (21) Ernsting, N. P.; Arthen-Engeland, T. Photochemical Ring-Opening Reaction of Indolinespiropyrans Studied by Subpicosecond Transient Absorption. *J. Phys. Chem.* **1991**, *95*, 5502–5509, DOI: 10.1021/j100167a027.
- (22) Kießwetter, R.; Pustet, N.; Brandl, F.; Mannschreck, A. 1',3',3'-Trimethyl-6-nitrospiro[2H-1-benzopyran-2,2'-indoline]: Its Thermal Enantiomerization and the Equilibration with its Merocyanine. *Tetrahedron: Asymmetry* **1999**, *10*, 4677–4687, DOI: 10.1016/S0957-4166(99)00538-8.
- (23) Holm, A.-K.; Mohammed, O. F.; Rini, M.; Mukhtar, E.; Nibbering, E. T. J.; Fidler, H. Sequential Merocyanine Product Isomerization Following Femtosecond UV Excitation of a Spiropyran. *J. Phys. Chem. A* **2005**, *109*, 8962–8968, DOI: 10.1021/jp053543.
- (24) Piard, J. Influence of the Solvent on the Thermal Back Reaction of One Spiropyran. *J. Chem. Educ.* **2014**, *91*, 2105–2111, DOI: 10.1021/ed4005003.
- (25) Tomasi, J.; Mennucci, B.; Cammi, R. Quantum Mechanical Continuum Solvation Models. *Chem. Rev.* **2005**, *105*, 2999–3094, DOI: 10.1021/cr9904009.
- (26) Frisch, M. J. et al. Gaussian~16 Revision B.01, Gaussian Inc. Wallingford CT, 2016.
- (27) Feyereisen, M.; Fitzgerald, G.; Komornicki, A. Use of Approximate Integrals in Ab Initio Theory. An Application in MP2 Energy Calculations. *Chem. Phys. Lett.* **1993**, *208*, 359–363, DOI: 10.1016/0009-2614(93)87156-W.
- (28) Klamt, A.; Schüürmann, G. COSMO: A New Approach to Dielectric Screening in Solvents with Explicit Expressions for the Screening Energy and its Gradient. *J. Chem. Soc. Perkin Trans. 2* **1993**, 799–805, DOI: 10.1039/P29930000799.

- (29) Cammi, R.; Mennucci, B.; Tomasi, J. Second-Order Møller-Plesset Analytical Derivatives for the Polarizable Continuum Model Using the Relaxed Density Approach. *J. Phys. Chem. A* **1999**, *103*, 9100–9108, DOI: 10.1021/jp991564w.
- (30) TURBOMOLE V7.2 2017, a development of University of Karlsruhe and Forschungszentrum Karlsruhe GmbH, 1989-2007, TURBOMOLE GmbH, since 2007; available from <http://www.turbomole.com>.
- (31) Schäfer, A.; Horn, H.; Ahlrichs, R. Fully Optimized Contracted Gaussian Basis Sets for Atoms Li to Kr. *J. Chem. Phys.* **1992**, *97*, 2571–2577, DOI: 10.1063/1.463096.
- (32) Weigend, F.; Häser, M.; Patzelt, H.; Ahlrichs, R. RI-MP2: Optimized Auxiliary Basis Sets and Demonstration of Efficiency. *Chem. Phys. Lett.* **1998**, *294*, 143–152, DOI: 10.1016/S0009-2614(98)00862-8.
- (33) Weigend, F.; Ahlrichs, R. Balanced Basis Sets of Split Valence, Triple Zeta Valence and Quadruple Zeta Valence Quality for H to Rn: Design and Assessment of Accuracy. *Phys. Chem. Chem. Phys.* **2005**, *7*, 3297, DOI: 10.1039/b508541a.
- (34) Rappoport, D.; Furche, F. Property-Optimized Gaussian Basis Sets for Molecular Response Calculations. *J. Chem. Phys.* **2010**, *133*, 134105, DOI: 10.1063/1.3484283.
- (35) Schmitz, G.; Hättig, C. Accuracy of Explicitly Correlated Local PNO-CCSD(T). *J. Chem. Theory Comput.* **2017**, *13*, 2623–2633, DOI: 10.1021/acs.jctc.7b00180.

ASSESSING THE STRUCTURE OF OCTASTATE MOLECULAR SWITCHES USING ^1H NMR DENSITY FUNCTIONAL THEORY CALCULATIONS

JOURNAL OF PHYSICAL CHEMISTRY C, 2018, 122, 1800–1808

Slim Hadj-Mohamed,^{†,‡,⊥} Jean Quertinmont,^{‡,⊥} Stéphanie Delbaere,[§] Lionel Sanguinet,^{||} & Benoît Champagne[‡]

[†] *Laboratory of Natural Substances, Faculty of Sciences, University of Sfax, 3038 Sfax, Tunisia.*

[‡] *Laboratory of Theoretical Chemistry, Theoretical and Structural Physical Chemistry Unit, University of Namur, 61 rue de Bruxelles, B-5000 Namur, Belgium.*

[§] *LASIR, Université de Lille, CNRS UMR 8516, F-59000 Lille, France.*

^{||} *MOLTECH-Anjou, Université d'Angers, CNRS-UMR 6200, F-49045 Angers, France*

[⊥] *S.H.M. and J.Q. contributed equally.*

J.Q. performed all geometry optimizations and contributed to the analyses of all results and to the redaction of the article.

Abstract

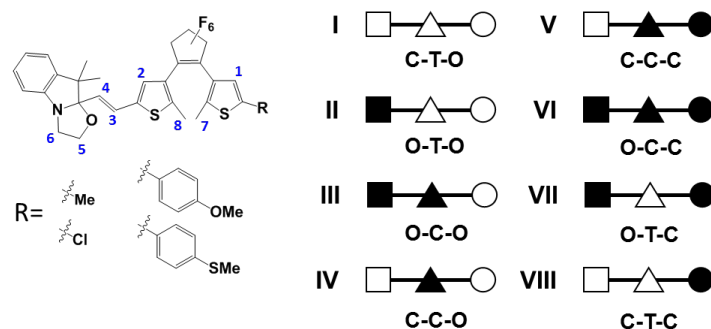
Density functional theory calculations are used to reveal the relationships between the structures, energies, and NMR signatures of an octastate molecular switch composed of a dithienylethene (DTE) unit covalently linked to an indolino[2,1-b]oxazolidine (BOX) moiety through an ethylenic junction. Both the DTE and BOX moieties can adopt open or closed forms. The ethylenic junction can be *Z* or *E* but the latter has been confirmed to be, by far, more stable than the former for all BOX/DTE combinations. In addition, when the DTE is open, the two thienyl units can fold to form parallel conformers, by opposition to the antiparallel or unfolded conformers. Usually parallel conformers present a higher energy than the antiparallel ones but in the case of compound **2** having a bulky substituent ($R = p\text{Ph-SMe}$) on the terminal thienyl group, the enthalpy of one conformer is very closed ($1\text{--}2\text{ kJ mol}^{-1}$) to that of the most stable antiparallel one, making photocyclization less efficient. These conformational differences and the presence of parallel DTE forms have been substantiated by analyzing experimental ^1H NMR chemical shifts at the light of their calculated values. These ^1H NMR chemical shifts calculations led to the following statements: i) going from state **I** (DTE open, BOX closed) to state **II** (both DTE and BOX are open) the H_8 proton of compound **1** ($R = \text{Me}$) is deshielded by $\sim 0.15\text{ ppm}$, ii) the deshielding of H_8 proton of compound **2** is larger and attains 0.41 ppm whereas H_7 is more shielded by 0.11 ppm , iii) then, going from compound **1** to compound **2** leads to deshielding of both H_7 and H_8 protons. As consequence, the difference of photochromism gating efficiency between compounds **1**, **2** and **3** ($R = p\text{Ph-OMe}$) can be attributed to the stabilization of parallel conformer due to an establishment of an intramolecular interaction with BOX opening.

10.1 Introduction

The combination at a molecular level of several switchable units in order to elaborate multiresponsive molecular systems continue to raise a strong interest due to their promising application in many fields such as logic gates or high-density optical memories to name a few.^{1,2} Indeed, the combination of n two-states switches shapes a multi-switch system that can exhibit up to 2^n various metastable states. Numerous molecular systems combining different types of switch moieties have been reported^{3–6} with a particular interest for photo- and redox-active materials.^{7–9} In this context, numerous systems incorporating a diarylethene (DAE) unit, undoubtedly the most studied photoswitch family,^{10–20} associated with a redox probe, with a photochromic unit, and even with a pH sensitive moiety were reported.^{21–23} However, this association could conduct to a strong modification of the switching abilities of the DAE moiety and lead in the most interesting cases to a complete control of the photochromism behavior on demand. Indeed, the material addressability and nondestructive readout capacity by light is one of the major challenges to overcome in the design of efficient memory devices at the molecular scale. Concerning the DAE based systems, the control of the photochromism is generally obtained either by a strong modification of the electronic properties of the molecular system or due to geometric considerations. Concerning these last ones, it should be mentioned that systems based on DAE unit can exist in both parallel and antiparallel conformations. Parallel conformers have the methyl group of both thiophenes pointing toward the same direction while they point in opposite directions for the antiparallel ones and only the latter can photocyclize according to the Woodward–Hoffmann rules.

In this context, the elaboration of a biphotochrome molecular switch composed of a dithienylethene (DTE) unit covalently linked to an indolino[2,1-b]oxazolidine (BOX) moiety through an ethylenic junction has demonstrated complementary features (Scheme 10.1). Besides the 8 (2^3) reachable states thanks to the open and closed forms of both DTE and BOX units and the Z/E isomerization of the ethylenic junction, results have demonstrated that the photochromism of the DTE core is largely influenced by the status of the BOX unit.²⁴ In fact, the photocyclization of the DTE is largely diminished when the oxazolidine ring is open (from state **II** to **VII**). More important, the efficiency of this photochemical process quenching is largely influenced by the nature of the second substituent borne by the DTE core. In fact, phenyl groups substituted by a donating group [$R = p\text{Ph-SMe}$ (**2**), $p\text{Ph-OMe}$ (**3**)] increase the photocyclization quenching (less than 1 % of cyclized form is observed) in comparison to more classical DTE substituent ($R = \text{Cl}$ or Me (**1**) with respectively 4 and 10 %).

To the best of our knowledge, the influence of the BOX opening on the reduction of the DTE photocyclization capacity was already apprehended using



Scheme 10.1: Schematic representation of the eight possible metastable states of BOX-DTE hybrids resulting from the combination of the open/closed (O/C) form of the BOX (■/□) and DTE (○/●) units linked together by an ethylenic bridge in a *trans/cis* (T/C, △/▲) conformation.

theoretical tools such as time-dependent density functional theory (TDDFT) but without geometrical consideration.²⁵ To fill this gap, conformers distribution between parallel and antiparallel ones have to be determined for all different states of the different DTE/BOX hybrids. In such purpose, the differences of chemical shift of proton NMR (especially those of the methyl groups) can generally be used but this requires NMR chemical shift calculations for both conformers.²⁶ In this context, *ab initio* NMR chemical shift calculations constitute a useful tool for interpreting and assigning NMR spectra of complex molecules.^{27–29} The development of accurate *ab initio* methods including electron correlation, solvent, ro-vibrational, relativistic, and temperature effects has led to predict quantitatively the nuclear magnetic shielding tensors. In parallel, density functional theory (DFT) methods with ad hoc exchange-correlation functionals, which can be employed to systems containing hundreds of atoms and more,³⁰ are very accurate, or at least, their errors are systematic and can easily be corrected, for instance, by using linear scaling procedures,^{31–36} opening the way to applications to a broad range of compounds of increasing complexity. In addition, errors with respect to high-level *ab initio* methods are generally small and less than 0.2 ppm for ¹H.^{33,35} These first principles NMR investigations have contributed to determine the structures as well as the conformations and configurations of complex systems, including supramolecular host-guest compounds,³⁷ elatenyne,³⁸ strychnine,³⁹ heparin trisaccharide,⁴⁰ *Z/E* isomers of alkyl phenyl ketone phenylhydrazones,⁴¹ poly(vinyl chloride) oligomers bearing unsaturated and branched defects.⁴² They have also played a key role in the assignment or reassignment of the stereostructure of organic and natural products.^{43–45} On the other hand, to our knowledge, such a combined theoretical-experimental approach was not yet applied to molecular switches.

Concerning the studied BOX/DTE hybrids, the opening/closure of the oxazolidine ring induces a strong modification of the ¹H NMR spectrum facilitating

the complete identification and quantification of generated species.²⁴ The strong variation of the acceptor ability of BOX during its opening leads to an important deshielding of the different nuclei chemical shifts occulting a potential effect of conformational change on it. As consequence, the increase of the chemical shifts of methyl protons (nuclei 7, Scheme 10.1) of the thienyl group bearing the R substituent with the BOX opening is up to now the only element suggesting a variation of the parallel and antiparallel conformers ratio. Unfortunately, the latter being strongly correlated to the nature of the substituent R, the simple analysis of the NMR spectrum is not accurate enough to determine the influence of R on the parallel and antiparallel conformers ratio, and then, on the photochromism gating.

In order to fill this gap, we have carried out a comparative theoretical study on different BOX/DTE hybrids where the second substituent borne by the DTE is respectively a Me (**1**), (Cl), and *p*Ph-SMe (**2**), *p*Ph-OMe (**3**) group. After their confrontation to experimental results, our objective is to determine, using DFT, in the same time the electronic and conformational influence of the BOX status on the DTE photocyclization process. This paper is organized as follows. The next Section summarizes the key computational aspects. Section 10.3 presents and discusses the results before conclusions are drawn in Section 10.4.

10.2 Computational Methods

The geometries of the 8 states were optimized using DFT with the M06 XC functional⁴⁶ and the 6-311G(d) basis set. For each state, the potential energy surface has been widely probed to locate the minima, characterized by real vibrational frequencies. Only the conformers within a 12 kJ mol⁻¹ range from the most stable one are considered further (at T = 298.15 K, if their energies differ by 12 kJ mol⁻¹ the corresponding populations are in the 99:1 ratio). Their standard enthalpy (H[⊖]), entropy (S[⊖]), and Gibbs enthalpy (G[⊖]) were then evaluated for T = 298.15 K and P = 1 atm. A scaling factor of 0.97 was used for all vibrational frequencies. Then, the isotropic shielding constants were evaluated using the B3LYP XC functional and the 6-311+G(2d,p) basis set in combination with the GIAO method.⁴⁷ This approach was already employed and its performance substantiated in Ref. [48]. Then the chemical shifts were evaluated as $\delta = \sigma_{\text{ref}} - \sigma$, where σ_{ref} is the shielding constant of ¹H of tetramethylsilane (TMS) as reference compound. Based on the Gibbs enthalpies, Maxwell-Boltzmann averaging of the chemical shifts was carried out for the conformers within the 12 kJ mol⁻¹ range. Solvent (acetonitrile) effects were taken into account by using the IEFPCM approach⁴⁹ for the geometry optimizations, the evaluation of the thermodynamic state functions, and the calculations of the isotropic shielding constants of all compounds and states. All calculations were performed using the Gaussian 09 program package.⁵⁰ An ultrafine integration

Table 10.1: M06/6-311G(d) relative enthalpies (ΔH^\ominus) and Gibbs free energies (ΔG^\ominus) for the most stable conformers of the 8 states of compound **1**. Differences of enthalpies [$\Delta\Delta H^\ominus = \Delta H^\ominus(\text{trans}) - \Delta H^\ominus(\text{cis})$] and Gibbs free energies ($\Delta\Delta G^\ominus$) for each pair of *cis-trans* isomer are also provided together with the corresponding *cis* population calculated using Maxwell-Boltzmann distribution. Solvent effects were taken into account using the IEFPCM scheme (solvent = acetonitrile).

State	ΔG^\ominus [kJ mol ⁻¹]	$\Delta\Delta G^\ominus$ [kJ mol ⁻¹]	%(<i>cis</i>)	ΔH^\ominus [kJ mol ⁻¹]	$\Delta\Delta H^\ominus$ [kJ mol ⁻¹]	%(<i>cis</i>)
c-c-o	15.9			12.3		
c-t-o	0.0	-15.9	0.17 %	0.0	-12.3	0.69 %
c-c-c	51.1			43.0		
c-t-c	35.9	-16.3	0.14 %	28.1	-14.9	0.25 %
o-c-c	210.3			205.7		
o-t-c	184.9	-25.4	0.004 %	186.8	-18.9	0.05 %
o-c-o	170.6			167.3		
o-t-o	146.8	-23.8	0.007 %	159.4	-7.9	3.94 %

grid has been employed for all calculations.

10.3 Results and Discussion

10.3.1 Geometrical Optimization of the Different Metastable States

As mentioned above, the BOX-DTE hybrids are known to exhibit eight different metastable states depending on the status of the three different switchable units. However, the existence of an equilibrium between several conformers as long as the DTE unit is in its open form should be considered to rationalize the photochromic behavior of these compounds. This leads to a potentially large number of conformers. In order to select the most stable ones, for compound **1**, we have first compared the *cis* and *trans* isomers by performing geometry optimizations. At this stage, the enthalpies and Gibbs free energies were calculated only for the most stable conformer of each state. They are reported in Table 10.1 together with the *cis-trans* relative values and the *cis* population, as computed with the Maxwell-Boltzmann distribution. In agreement with experimental results from Szaloki et al.,⁵¹ the *trans* conformers are more stable than the *cis* ones. The populations of the latter range from 0.004 to 0.17 % according to the Gibbs free energies and from 0.05 to 4 % when using the enthalpies. From now on, we only consider the *trans* isomers.

In order to confirm the mechanism responsible for the gated DTE photocy-

clization of these biphotochromes, the optimized structures of the **I** and **II** states of compounds **1** and **2** were analyzed in details and their enthalpies are compared in Table 10.2 with representative geometrical parameters. For each compound and state, eight low-energy conformers, labelled from a to h, were obtained on the basis of the 12 kJ mol⁻¹ range. The two dihedral angles between the hexafluorocyclopentene ring and the thiophenes, φ_1 and φ_2 , schematically shown in Table 10.2, allow distinguishing between four antiparallel conformers, where φ_1 and φ_2 are of the same sign and vary both between 35 and 55° (conformers a to d), and four parallel conformers where φ_1 and φ_2 have opposite signs and vary between 40-70° and 115-145° (conformers e to h). The distance (R_{CC}) between the thiophene carbons involved in the photocyclization allows also this distinction because for antiparallel conformers $R_{CC} \sim 3.5$ Å while for the parallel ones, R_{CC} is larger than 4.1 Å.

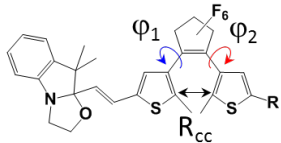
In the case of compound **1** ($R = \text{Me}$), the most stable conformers are unfolded/antiparallel, irrespective of the open(**I**)/closed(**II**) state of the BOX. Indeed, the difference of enthalpy between the most stable parallel and antiparallel conformers are 6.6 and 7.3 kJ mol⁻¹ for state **I** and state **II**, respectively. The situation is different for compound **2** ($R = p\text{Ph-SMe}$). When BOX is closed, the most stable folded conformer (Figure 10.1) presents an enthalpy similar ($\Delta H^\ominus \leq 1.8$ kJ mol⁻¹) to those of the four unfolded conformers. Then, when BOX is open, the second most stable conformer ($\Delta H^\ominus \leq 1.3$ kJ mol⁻¹) is folded, owing to stabilizing intra-molecular interactions between the aromatic substituent and the hydroxyl function (Figure 10.1). Additional calculations on compound **3** ($R = p\text{Ph-OMe}$, not reported here) highlight similar effects associated with stabilizing intra-molecular interactions. In a subsequent step, the relative populations of the folded and unfolded conformers were calculated using the electronic energy as well as the enthalpy, and the Gibbs enthalpy (Table 10.3).

The percentage of folded conformers evaluated from the electronic energy and the enthalpy are in agreement, highlighting the increased stability of the folded conformers in compound **2** with respect to **1**. On the other hand, when including entropy contributions these effects are strongly damped and the percentage of folded conformers goes down to 4 % for the **o-t-o** form of compound **2**. This originates from the decrease of entropy of the folded conformers because the intra-molecular interactions reduce the flexibility of the molecule. Still, we consider that these entropy effects are probably slightly overestimated because the IEFPCM calculations do not account for the solvent molecules reorganization upon folding/unfolding.

10.3.2 ¹H NMR Chemical Shifts of Biphotochrome **1** in its Eight States

Subsequently, the ¹H NMR chemical shifts of the molecule **1** for each of its eight states were calculated at the B3LYP/6-311+G(2d,p)//M06/6-311G(d) level. The averaged ¹H NMR chemical shifts are reported in Table 10.4 together

Table 10.2: IEFPCM(solvent = acetonitrile)/M06/6-311G(d) relative enthalpies (ΔH^\ominus , kJ mol^{-1}) and representative geometrical parameters (φ_1 and φ_2 in degrees and R_{CC} in Å) of the 8 most stable conformers of states I and II of compounds 1 and 2.

								
State I	R = Me				R = <i>p</i> Ph-SMe			
	φ_1	φ_2	R_{CC}	ΔH^\ominus	φ_1	φ_2	R_{CC}	ΔH^\ominus
Conf. a	-38.4	-53.8	3.512	0.6	-38.5	-53.6	3.526	0.3
Conf. b	54.5	38.0	3.522	0.0	54.7	39.3	3.518	0.3
Conf. c	54.0	38.0	3.518	0.1	54.4	39.2	3.520	0.0
Conf. d	-38.4	-53.8	3.513	0.2	-39.0	-53.8	3.525	0.6
Conf. e	-40.5	115.8	4.129	9.3	-44.3	120.7	4.119	8.3
Conf. f	54.6	-140.6	4.258	6.6	70.2	-143.5	4.165	1.8
Conf. g	54.3	-140.5	4.255	6.7	60.3	-143.8	4.236	4.2
Conf. h	-40.2	115.8	4.129	9.0	-115.0	40.7	4.121	8.5

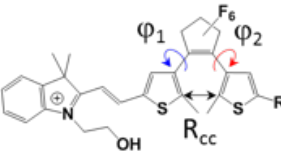
								
State II	R = Me				R = <i>p</i> Ph-SMe			
	φ_1	φ_2	R_{CC}	ΔH^\ominus	φ_1	φ_2	R_{CC}	ΔH^\ominus
Conf. a	55.1	39.1	3.533	0.0	57.2	39.8	3.544	0.0
Conf. b	-39.3	-54.2	3.529	1.3	-40.3	-55.8	3.528	1.4
Conf. c	55.7	38.7	3.542	5.5	55.7	40.1	3.532	5.8
Conf. d	-40.1	-54.7	3.532	6.5	-40.5	-55.2	3.533	6.6
Conf. e	138.8	-55.3	4.241	7.3	137.3	-54.5	4.237	7.3
Conf. f	-42.1	116.6	4.133	9.1	-42.3	116.6	4.130	9.2
Conf. g	139.9	-56.9	4.232	11.8	143.7	-68.8	4.184	1.3
Conf. h	-42.1	116.8	4.136	14.9	-41.7	116.0	4.126	14.8

Table 10.3: Percentage of folded/unfolded conformers for compounds **1** and **2** in their *c-t-o* (I) and *o-t-o* (II) states as determined from different thermodynamic state functions evaluated at the M06/6-311G(d) level using the IEFPCM scheme (solvent = acetonitrile) and a scaling factor of 0.97 for the vibrational frequencies.

	Electronic Energy	H^\ominus	G^\ominus
Compound 1, R = Me			
(I) <i>c-t-o</i>	5.0/95.0	4.8/95.2	11.0/89.0
(II) <i>o-t-o</i>	4.9/95.1	4.8/95.2	7.7/92.3
Compound 2, R = <i>p</i> Ph-SMe			
(I) <i>c-t-o</i>	20.6/79.4	17.2/82.8	5.0/95.0
(II) <i>o-t-o</i>	30.5/69.5	27.8/72.2	4.1/96.9

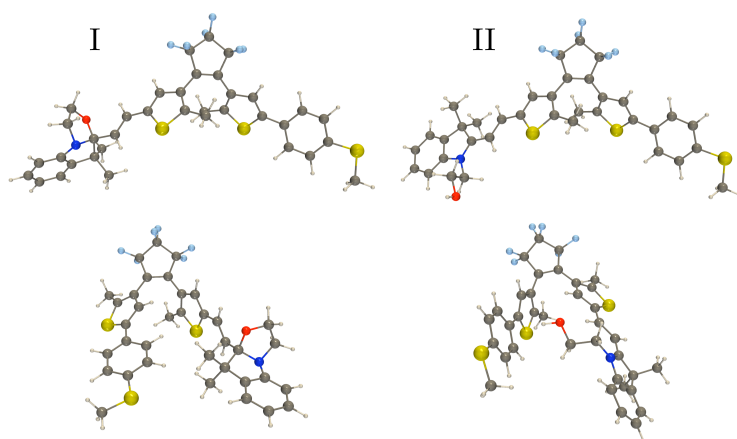


Figure 10.1: Sketch of representative folded (parallel, bottom) and unfolded (antiparallel, top) conformers of **2(I)** and **2(II)** as determined from M06/6-311G(d) geometry optimization using the IEFPCM scheme (solvent = acetonitrile).

with the experimental values from Ref. [51]. According to their position and spectral range, they are discussed in four different groups: aromatic (1 and 2), vinylic (3 and 4), aliphatic (5 and 6), and methyl ones (7 and 8). In a first step, the reliability of the computational procedure is confirmed by only considering the states where the DTE is closed. Indeed, Woodward–Hoffmann rules conduct to only one conformer, contrary to the states where DTE is open where both parallel or antiparallel (*vide infra*) conformers have to be considered.

DFT calculations reproduce, for all states, the δ ordering of protons H_1 and H_2 , *i.e.* H_2 is logically more deshielded than H_1 [due to the positive mesomeric effect of the methyl substituent] and this phenomenon is exalted when the BOX is open. The average calculated difference [$\delta(H_2) - \delta(H_1)$] amounts to 0.39 ppm for all states with the closed BOX, which is in good agreement with the experimental average value of 0.33 ppm. The BOX opening conducts to an increase of this difference (0.82 ppm), which is again well reproduced by theoretical calculation (0.77 ppm). These δ differences are mostly unchanged upon closing the DTE moiety. Opening the BOX enables the resonance between the iminium function and the DTE, mostly in the inner thiophene ring, which results in the deshielding of H_2 whereas H_1 is almost not impacted. This is supported by the amplitudes and variations of the Mulliken charges of the corresponding CH groups evaluated at the M06/6-311G(d) level. For CH_1 , the charge amounts to $-0.17/-0.18 e$ for forms **I-II** and **VII-VIII** whereas for CH_2 , the negative charge is reduced to $-0.10 e$ ($-0.10 e$) for **II (VII)** in comparison to $-0.13 e$ ($-0.16 e$) for **I (VIII)**. Then, closing the DTE shifts to higher fields both protons (by 0.6 to 1.3 ppm according to the calculations and 0.5 to 0.9 ppm to experiments) as a result of destroying the aromaticity of both thiophene rings. Whatever the status of the BOX and the DTE, the expected decrease of conjugation along the ethylenic bridge *trans*-to-*cis* isomerization is also well reproduced by the calculation. We can notice its negligible impact on the H_1 chemical shift (less than 0.1 ppm for both calculated and experimental data). On the other hand, in both the experiment and the calculations the *trans*-to-*cis* isomerization induces shielding or deshielding of H_2 by up to 0.6 ppm.

Concerning vinylic 1H , calculated and experimental results both show that H_4 is more shielded than H_3 , with differences ranging between 0.7 and 1.8 ppm. Opening the BOX enhances the deshielding of both protons (by as much as 1.5 ppm) whereas closing the DTE ring has a smaller effect, *i.e.* δ variations are smaller than 0.4 ppm. The *cis-trans* isomerization increases the δ values, by 0.2 to 0.9 ppm, as a function of the state of the BOX and DTE moieties. For the latter, the deshielding is stronger on H_3 provided BOX is open, which is attributed to the acceptor (iminium) π -conjugation effects. Considering the 2-Th-CH=CHMe model compound where $\delta(H_3)$ decreases by 0.26 ppm and $\delta(H_4)$ increases by 0.19 ppm upon *cis* to *trans* conversion enables to disentangle the effects of *cis-trans* isomerization from those of donor/acceptor charge transfer effects and to show that the latter are dominant. Globally, the calculations reproduce the experimental values as well as the variations upon closing/opening

the BOX and DTE units and upon *cis-trans* isomerization.

Concerning H₅ and H₆, the closed status of the oxazolidine ring prevents from assigning their chemical shifts where four different nuclei should be considered. Once BOX open, one observes that the H₆ protons are more deshielded than the H₅ ones, both experimentally and in the DFT calculations. Moreover, opening/closing the DTE has a small impact on these protons whereas the *cis-trans* isomerization presents smaller and less systematic effects.

The calculated and experimental chemical shifts of H₇ and H₈ are systematically smaller when the DTE moiety is open than when closed, due to the loss of thiophene aromaticity in the closed form and due to the change on the hybridization of quaternary carbons upon cyclization ($sp^3 \rightarrow sp^2$). Then, the difference between $\delta(H_7)$ and $\delta(H_8)$ is generally very small (for either calculations or experiment; forms **I**, **III**, **IV**, **VI**, **VIII**), of the order of 0.1 ppm or smaller, demonstrating similar chemical environment for these methyl protons.

For the three couples H₁-H₂, H₃-H₄, and H₇-H₈, least-squared linear regressions have been performed to quantify the agreement between the experimental and calculated chemical shifts (Figure 10.2), showing R² values of 0.95 or slightly larger for H₁ to H₄ and of 0.89 for H₇ and H₈. As mentioned above, the signal complexity and impossible assignment of H₅ and H₆ protons when BOX is closed render similar regression for this couple irrelevant. For H₁-H₄ the slopes of the linear regressions are smaller than 1.0 (by 14 and 9 % for H₁-H₂ and H₃-H₄, respectively), demonstrating that calculated δ variations are slightly overestimated with respect to experiment. On the other hand, the slope is clearly smaller than unity for H₇-H₈.

Table 10.4: B3LYP/6-311+G(2d,p)//M06/6-311G(d) average ^1H NMR chemical shifts (ppm) of the 8 states of the BOX-DTE biphotochrome **1** in comparison to the experimental values of Ref. [51] recorded at RT, except for **VI** at 243 K. Solvent effects were taken into account using the IEFPCM scheme (solvent = acetonitrile).

	States	H ₁	H ₂	H ₃	H ₄	H ₅	H ₆	H ₇	H ₈
exp	c-t-o (I)	6.81	7.12	6.92	6.08	[3.38–3.80]	[3.38–3.80]	1.91	1.92
calc		7.00	7.49	7.07	6.37	[3.42–3.91]	[3.42–3.94]	1.82	1.74
exp	o-t-o (II)	6.83	7.96	8.39	7.27	4.02	4.65	1.92	2.06
calc		7.16	8.10	8.73	7.16	4.23	4.45	1.80	2.03
exp	o-c-o (III)	6.77	7.37	7.47	6.47	3.90	4.43	1.87	1.86
calc		7.11	7.67	7.84	6.46	4.13	4.46	1.75	1.77
exp	c-c-o (IV)	6.79	7.21	6.71	5.50	[3.30–3.77]	[3.30–3.77]	1.83	1.83
calc		7.00	7.58	6.99	5.63	[3.20–3.89]	[3.33–3.93]	1.75	1.80
exp	c-c-c (V)	6.10	6.40	6.54	5.80	[3.30–3.77]	[3.30–3.77]	2.10	2.03
calc		6.18	6.29	6.73	6.01	[3.30–3.87]	[3.36–3.83]	2.25	1.96
exp	o-c-c (VI)	6.20	6.88	7.41	6.71	[3.90–4.60]	[3.90–4.60]	2.12	2.13
calc		6.38	7.12	7.69	6.68	4.19	4.35	2.16	2.27
exp	o-t-c (VII)	6.31	7.18	8.22	6.86	4.02	4.60	2.19	2.18
calc		6.41	7.23	8.39	6.60	4.05	4.36	2.39	2.20
exp	c-t-c (VIII)	6.16	6.46	6.97	6.04	[3.30–3.80]	[3.30–3.80]	2.08	2.07
calc		6.26	6.64	6.76	6.01	[3.52–3.90]	[3.42–3.93]	2.24	2.22

10.3.3 Conformational Effects on the NMR Signatures of the c-t-o (I) and o-t-o (II) States of Compounds 1 and 2

Having assessed the reliability of the ^1H NMR chemical shifts calculations, the question is now to investigate whether the presence of folded conformers in the state I *versus* the state II would be visible on the NMR signatures; *i.e.* whether the two categories of conformers have distinct chemical shifts. Since the experimental structural characterizations are based on the Me ^1H , the chemical shifts of H_7 and H_8 were evaluated for the eight conformers of compounds 1 and 2 in states I and II. They can be found in Table 10.5 with their weighted averages as a function of the relative electronic energies, enthalpies, and Gibbs free energies (highlighting thermal and entropic effects) as well as the experimental values.^{24,51}

Concerning the methyl protons of both compounds under state I, the antiparallel (parallel) conformers are characterized by H_7 having a chemical shift smaller (higher) than 2.0 ppm and by H_8 being always below the same 2.0 ppm limit, with the exception of conformer h of 2 for which the H_7 and H_8 behaviors are reversed. Under state I, the most deshielded shifts are observed for H_7 in the parallel conformers at around 2.4 and 2.7 ppm for compounds 1 and 2, respectively. Then, considering compound 1 under state II, the same H_7 behavior is observed, but the H_8 protons are overall more deshielded than in state I, especially in the case of the parallel conformers where their chemical shifts now exceed 2.1 ppm. Finally, for state II of compound 1 and 2, there is no systematic behavior among H_7 or H_8 , but, the antiparallel conformers are characterized by one of its proton being around 1.9 ppm and the second one around 2.0 ppm while in the parallel conformers they are less shielded (about 2 and 2.8 ppm). In general, folding the thiophene rings on each other deshields the methyl protons as a result of the anisotropic effect.

For compound 1, the averages calculated for both states show almost no variation among each other, *i.e.* whether they are calculated from the electronic energies, enthalpies or Gibbs free energies. Thus, going from state I to state II, the chemical shift of H_7 is hardly changed whereas it increases by 0.24 ppm for H_8 . These averages are also a good agreement with the previously discussed results obtained for the most stable conformer (Section 10.3.1, Table 10.4). For compound 2, the averages based on the electronic energy and the enthalpy are consistent, showing a significant decrease (with respect to compound 1) of the shielding for H_7 in state I (0.15 ppm) and for H_8 in state II (0.25 ppm) due to a larger contribution of the parallel conformers (see Section 10.3.1, Table 10.3). As a matter of fact, H_7 gets more shielded (~ 0.11 ppm) and H_8 gets more deshielded (~ 0.42 ppm) when going from state I to state II. The averages based on the Gibbs free energy do not show this behavior (or it is reduced in amplitude), most probably because the entropic effects are overestimated.

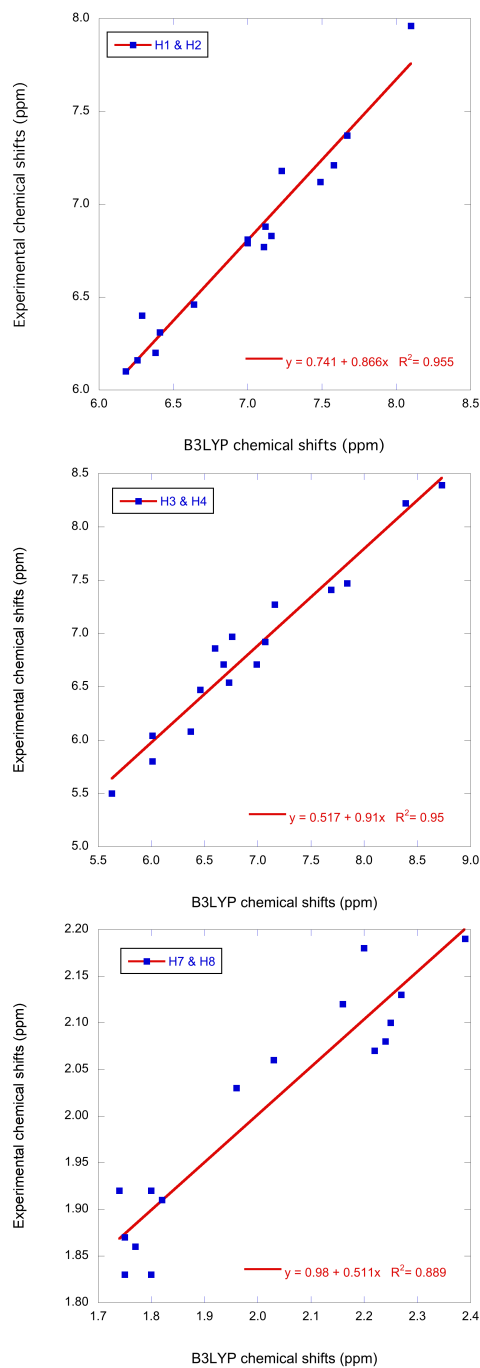


Figure 10.2: Experimental versus B3LYP ^1H chemical shifts for the $\text{H}_1\text{-H}_4$ and $\text{H}_7\text{-H}_8$ protons of the 8 states of the BOX-DTE **1** switch.

Table 10.5: B3LYP/6-311+G(2d,p)//M06/6-311G(d) ^1H NMR chemical shifts (ppm) of compounds **1** and **2** in their *c-t-o* (I) and *o-t-o* (II) states. In addition to the values for the eight most stable conformers, Maxwell-Boltzmann averages are given using the total electronic energy, the enthalpy, and the Gibbs enthalpy differences as well as the experimental values of Ref. [24] and [51]. Conformers a-d (e-h) are unfolded (folded). Solvent effects were taken into account using the IEFPCM scheme (solvent = acetonitrile).

Conf.	H ₇	H ₈	H ₇	H ₈
Compound 1				
	<i>c-t-o</i> (I)		<i>o-t-o</i> (II)	
a	1.85	1.77	1.79	2.03
b	1.81	1.76	1.85	1.91
c	1.81	1.78	1.84	1.98
d	1.85	1.76	1.84	1.86
e	2.37	1.86	2.61	2.88
f	2.39	1.74	2.27	2.17
g	2.41	1.78	2.56	2.86
h	2.36	1.90	2.29	2.13
Av. (ΔE_{elec})	1.86	1.77	1.85	2.01
Av. (ΔH^{\ominus})	1.86	1.77	1.85	2.01
Av. (ΔG^{\ominus})	1.89	1.77	1.87	2.01
Experimental	1.91	1.92	1.92	2.06
Compound 2				
	<i>c-t-o</i> (I)		<i>o-t-o</i> (II)	
a	1.84	1.80	1.87	2.05
b	1.87	1.81	1.88	2.01
c	1.86	1.81	1.86	1.98
d	1.88	1.83	2.00	1.92
e	2.73	1.87	1.96	2.97
f	2.71	1.88	2.72	2.11
g	2.76	1.96	1.86	2.86
h	1.94	2.74	2.71	2.04
Av. (ΔE_{elec})	2.03	1.84	1.89	2.27
Av. (ΔH^{\ominus})	2.00	1.83	1.89	2.25
Av. (ΔG^{\ominus})	1.88	1.84	1.88	2.07
Experimental	2.03	1.99	2.04	2.13

10.4 Conclusions

Density functional theory has been used to investigate the relationships between the structures, energies, and NMR signatures of an octastate molecular switch, that is composed of a dithienylethene (DTE) unit covalently linked to an indolino[2,1-b]oxazolidine (BOX) moiety through an ethylenic junction. Both the DTE and BOX moieties can adopt open or closed forms while the ethylenic junction can be *Z* or *E*. In a first part, the *E* conformer has been confirmed to be, by far, more stable than the *Z* one for all BOX/DTE combinations. Then, when the DTE is open, the two thienyl units can fold to form parallel conformers, by opposition to the antiparallel or unfolded conformers. Parallel conformers present a higher energy than the antiparallel ones. Still, in the case of compound **2** having a bulky substituent ($R = p\text{Ph-SMe}$) on the terminal thienyl group, the enthalpy of one conformer is very closed ($1\text{--}2\text{ kJ mol}^{-1}$) to that of the most stable antiparallel one, making photocyclization less efficient. Less favorable intermolecular interactions are present in compound **1** ($R = \text{Me}$) than in compound **2** so that the enthalpy of the parallel conformers of **1** is higher by $6\text{--}7\text{ kJ mol}^{-1}$ than that of the antiparallel ones. In a second part, ^1H NMR chemical shifts calculations have been carried out on the different parallel and antiparallel conformers of compounds **1** and **2** when DTE is open to highlight the presence of parallel DTE forms. The reliability of these calculations was substantiated by a preliminary comparison between the calculated and experimental ^1H NMR chemical shifts of the 8 states of compound **1** providing least-squares linear regressions with R^2 values larger than ~ 0.90 . The analysis of the calculated ^1H NMR chemical shifts shows that, in agreement with the experimental data, i) going from state I to state II, the H_8 proton of compound **1** is deshielded by $\sim 0.15\text{ ppm}$, ii) the deshielding of H_8 proton of compound **2** is larger and attains 0.41 ppm whereas H_7 is more shielded by 0.11 ppm , iii) then, going from compound **1** to compound **2** leads to deshielding of both H_7 and H_8 protons. As consequence, we can now assume that the difference of photochromism gating efficiency between compounds **1**, **2** and **3** results mainly from the stabilization of parallel conformer due to an establishment of an intramolecular interaction with BOX opening in addition to previously mentioned electronic effect.

Acknowledgments

This work, carried out within the MORIARTY project, has benefited from financial support from Wallonie-Bruxelles International (WBI), from the Fund for Scientific Research (F.R.S.-FNRS), from the French Ministry of Foreign and European Affairs, and from the Ministry of Higher Education and Research in the frame of the Hubert Curien partnerships. S.H.M. thanks the Fonds Spécial de Recherche of UNamur for his Ph.D. grant while J.Q. thanks the "Actions de Recherche Concertées" (ARC) of the Direction générale de l'Enseignement non

Obligatoire et de la Recherche Scientifique of the French Community of Belgium, under convention No. 15/20-068, for his Ph.D. grant. This work was also supported by funds from the Francqui Foundation. SD and LS thank ANR SIMI 7 for financial support (Grant no: 2011 BS08 007 02). The calculations were performed on the computers of the Consortium des Équipements de Calcul Intensif, including those of the Technological Platform of High-Performance Computing, for which we gratefully acknowledge the financial support of the FNRS-FRFC (Conventions No. 2.4.617.07.F and 2.5020.11) and of the University of Namur.

Bibliography

- (1) Andréasson, J.; Pischel, U. Smart Molecules at Work-Mimicking Advanced Logic Operations. *Chem. Soc. Rev.* **2010**, *39*, 174–188, DOI: 10.1039/B820280J.
- (2) Andréasson, J.; Pischel, U. Molecules with a Sense of Logic: A Progress Report. *Chem. Soc. Rev.* **2015**, *44*, 1053–1069, DOI: 10.1039/C4CS00342J.
- (3) Irie, M.; Fukaminato, T.; Matsuda, K.; Kobatake, S. Photochromism of Diarylethene Molecules and Crystals: Memories, Switches, and Actuators. *Chem. Rev.* **2014**, *114*, 12174–12277, DOI: 10.1021/cr500249p.
- (4) De Silva, A. P.; Vance, T. P.; Wannalerse, B.; West, M. E. S. In *Molecular Switches*; Wiley-VCH Verlag GmbH & Co. KGaA: Weinheim, Germany, 2011, pp 669–696, DOI: 10.1002/9783527634408.ch18.
- (5) Minkin, V. I. In *Molecular Switches*; Wiley-VCH Verlag GmbH & Co. KGaA: Weinheim, Germany, 2011, pp 37–80, DOI: 10.1002/9783527634408.ch2.
- (6) *Molecular Switches*; Feringa, B. L., Browne, W. R., Eds.; Wiley-VCH Verlag GmbH & Co. KGaA: Weinheim, Germany, 2011, DOI: 10.1002/9783527634408.
- (7) Oms, O.; Hakouk, K.; Dessapt, R.; Deniard, P.; Jobic, S.; Dolbecq, A.; Palacin, T.; Nadjo, L.; Keita, B.; Marrot, J.; Mialane, P. Photo- and Electrochromic Properties of Covalently Connected Symmetrical and Unsymmetrical Spiropyran–Polyoxometalate Dyads. *Chem. Commun.* **2012**, *48*, 12103, DOI: 10.1039/c2cc35376h.
- (8) Browne, W. R.; Pollard, M. M.; de Lange, B.; Meetsma, A.; Feringa, B. L. Reversible Three-State Switching of Luminescence: A New Twist to Electro- and Photochromic Behavior. *J. Am. Chem. Soc.* **2006**, *128*, 12412–12413, DOI: 10.1021/ja064423y.

- (9) Ivashenko, O.; Logtenberg, H.; Areephong, J.; Coleman, A. C.; Wesenhagen, P. V.; Geertsema, E. M.; Heureux, N.; Feringa, B. L.; Rudolf, P.; Browne, W. R. Remarkable Stability of High Energy Conformers in Self-Assembled Monolayers of a Bistable Electro- and Photoswitchable Overcrowded Alkene. *J. Phys. Chem. C* **2011**, *115*, 22965–22975, DOI: 10.1021/jp206889y.
- (10) Harvey, E. C.; Feringa, B. L.; Vos, J. G.; Browne, W. R.; Pryce, M. T. Transition Metal Functionalized Photo- and Redox-Switchable Diarylethene Based Molecular Switches. *Coord. Chem. Rev.* **2015**, *282-283*, 77–86, DOI: 10.1016/j.ccr.2014.06.008.
- (11) Bondu, F.; Quertinmont, J.; Rodriguez, V.; Pozzo, J.-L.; Plaquet, A.; Champagne, B.; Castet, F. Second-Order Nonlinear Optical Properties of a Dithienylethene-Indolinoxazolidine Hybrid: a Joint Experimental and Theoretical Investigation. *Chem. Eur. J.* **2015**, *21*, 18749–18757.
- (12) Szalóki, G.; Pozzo, J.-L. Synthesis of Symmetrical and Nonsymmetrical Bisthiencylcyclopentenes. *Chem. - A Eur. J.* **2013**, *19*, 11124–11132, DOI: 10.1002/chem.201301645.
- (13) Fukaminato, T. Single-Molecule Fluorescence Photoswitching: Design and Synthesis of Photoswitchable Fluorescent Molecules. *J. Photochem. Photobiol. C Photochem. Rev.* **2011**, *12*, 177–208, DOI: 10.1016/j.jphotochemrev.2011.08.006.
- (14) Bertarelli, C.; Bianco, A.; Castagna, R.; Pariani, G. Photochromism into Optics: Opportunities to Develop Light-Triggered Optical Elements. *J. Photochem. Photobiol. C Photochem. Rev.* **2011**, *12*, 106–125, DOI: 10.1016/j.jphotochemrev.2011.05.003.
- (15) Tsujioka, T.; Irie, M. Electrical Functions of Photochromic Molecules. *J. Photochem. Photobiol. C Photochem. Rev.* **2010**, *11*, 1–14, DOI: 10.1016/j.jphotochemrev.2010.02.001.
- (16) Irie, M. Photochromism of Diarylethene Single Molecules and Single Crystals. *Photochem. Photobiol. Sci.* **2010**, *9*, 1535, DOI: 10.1039/c0pp00251h.
- (17) Yun, C.; You, J.; Kim, J.; Huh, J.; Kim, E. Photochromic Fluorescence Switching from Diarylethenes and its Applications. *J. Photochem. Photobiol. C Photochem. Rev.* **2009**, *10*, 111–129, DOI: 10.1016/j.jphotochemrev.2009.05.002.
- (18) Wigglesworth, T. J.; Myles, A. J.; Branda, N. R. High-Content Photochromic Polymers Based on Dithienylethenes. *European J. Org. Chem.* **2005**, *2005*, 1233–1238, DOI: 10.1002/ejoc.200400623.
- (19) Tian, H.; Yang, S. Recent Progresses on Diarylethene Based Photochromic Switches. *Chem. Soc. Rev.* **2004**, *33*, 85, DOI: 10.1039/b302356g.

- (20) Matsuda, K.; Irie, M. Diarylethene as a Photoswitching Unit. *J. Photochem. Photobiol. C Photochem. Rev.* **2004**, *5*, 169–182, DOI: 10.1016/j.jphotochemrev.2004.07.003.
- (21) Gust, D.; Andréasson, J.; Pischel, U.; Moore, T. A.; Moore, A. L. Data and Signal Processing Using Photochromic Molecules. *Chem. Commun.* **2012**, *48*, 1947–1957, DOI: 10.1039/C1CC15329C.
- (22) Irie, M. Diarylethenes for Memories and Switches. *Chem. Rev.* **2000**, *100*, 1685–1716, DOI: 10.1021/cr980069d.
- (23) Tomasulo, M.; Sortino, S.; Raymo, F. M. A Fast and Stable Photochromic Switch Based on the Opening and Closing of an Oxazine Ring. *Org. Lett.* **2005**, *7*, 1109–1112, DOI: 10.1021/o1050045a.
- (24) Sanguinet, L.; Delbaere, S.; Berthet, J.; Szalóki, G.; Jardel, D.; Pozzo, J.-L. Dithienylethene-Based Gated Ambichromic Dyads. *Adv. Opt. Mater.* **2016**, *4*, 1358–1362, DOI: 10.1002/adom.201600233.
- (25) Jacquemin, D.; Perpète, E. A.; Maurel, F.; Perrier, A. Photochromic Properties of a Dithienylethene–Indolinoxazolidine Switch: A Theoretical Investigation. *Comput. Theor. Chem.* **2011**, *963*, 63–70, DOI: 10.1016/j.comptc.2010.09.009.
- (26) Nakamura, S.; Yokojima, S.; Uchida, K.; Tsujioka, T.; Goldberg, A.; Murakami, A.; Shinoda, K.; Mikami, M.; Kobayashi, T.; Kobatake, S.; Matsuda, K.; Irie, M. Theoretical Investigation on Photochromic Diarylethene: A Short Review. *J. Photochem. Photobiol. A Chem.* **2008**, *200*, 10–18, DOI: 10.1016/j.jphotochem.2008.05.005.
- (27) Helgaker, T.; Jaszuński, M.; Ruud, K. Ab Initio Methods for the Calculation of NMR Shielding and Indirect Spin-Spin Coupling Constants. *Chem. Rev.* **1999**, *99*, 293–352, DOI: 10.1021/cr960017t.
- (28) *Calculation of NMR and EPR Parameters*; Kaupp, M., Bühl, M., Malkin, V., Eds.; Wiley-VCH: 2004.
- (29) Bifulco, G.; Dambruoso, P.; Gomez-Paloma, L.; Riccio, R. Determination of Relative Configuration in Organic Compounds by NMR Spectroscopy and Computational Methods. *Chem. Rev.* **2007**, *107*, 3744–3779, DOI: 10.1021/cr030733c.
- (30) Ochsenfeld, C.; Kussmann, J.; Koziol, F. Ab Initio NMR Spectra for Molecular Systems with a Thousand and More Atoms: A Linear-Scaling Method. *Angew. Chemie Int. Ed.* **2004**, *43*, 4485–4489, DOI: 10.1002/anie.200460336.
- (31) Chesnut, D. B. In 2007, pp 245–297, DOI: 10.1002/9780470125854.ch5.

- (32) Rablem, P.; Pearlman, S.; Finkbiner, J. A Comparison of Density Functional Methods for the Estimation of Proton Chemical Shifts with Chemical Accuracy. *J. Phys. Chem. A* **1999**, *103*, 7357–7363.
- (33) D’Antuono, P.; Botek, E.; Champagne, B.; Spassova, M.; Denkova, P. Theoretical Investigation on ^1H and ^{13}C NMR Chemical Shifts of Small Alkanes and Chloroalkanes. *J. Chem. Phys.* **2006**, *125*, 144309, DOI: 10.1063/1.2353830.
- (34) Laskowski, R.; Blaha, P.; Tran, F. Assessment of DFT Functionals with NMR Chemical Shifts. *Phys. Rev. B* **2013**, *87*, 195130, DOI: 10.1103/PhysRevB.87.195130.
- (35) Flaig, D.; Maurer, M.; Hanni, M.; Braunger, K.; Kick, L.; Thubauville, M.; Ochsenfeld, C. Benchmarking Hydrogen and Carbon NMR Chemical Shifts at HF, DFT, and MP2 Levels. *J. Chem. Theor. Comput.* **2014**, *10*, 572–578.
- (36) Toomsalu, E.; Burk, P. Critical Test of some Computational Methods for Prediction of NMR ^1H and ^{13}C Chemical Shifts. *J. Mol. Model.* **2015**, *21*, 244, DOI: 10.1007/s00894-015-2787-x.
- (37) Mugridge, J. S.; Bergman, R. G.; Raymond, K. N. ^1H NMR Chemical Shift Calculations as a Probe of Supramolecular Host–Guest Geometry. *J. Am. Chem. Soc.* **2011**, *133*, 11205–11212, DOI: 10.1021/ja202254x.
- (38) Dyson, B. S.; Burton, J. W.; Sohn, T.-i.; Kim, B.; Bae, H.; Kim, D. Total Synthesis and Structure Confirmation of Elatenyne: Success of Computational Methods for NMR Prediction with Highly Flexible Diastereomers. *J. Am. Chem. Soc.* **2012**, *134*, 11781–11790, DOI: 10.1021/ja304554e.
- (39) Kutateladze, A. G.; Mukhina, O. A. Relativistic Force Field: Parametric Computations of Proton–Proton Coupling Constants in ^1H NMR Spectra. *J. Org. Chem.* **2014**, *79*, 8397–8406, DOI: 10.1021/jo501781b.
- (40) Hricovíni, M.; Driguez, P.-A.; Malkina, O. L. NMR and DFT Analysis of Trisaccharide from Heparin Repeating Sequence. *J. Phys. Chem. B* **2014**, *118*, 11931–11942, DOI: 10.1021/jp508045n.
- (41) Trabelsi, M.; Salem, M.; Champagne, B. Investigation of the Configuration of Alkyl Phenyl Ketone Phenylhydrazones from Ab Initio ^1H NMR Chemical Shifts. *Org. Biomol. Chem.* **2003**, *1*, 3839, DOI: 10.1039/b307528a.
- (42) D’Antuono, P.; Botek, E.; Champagne, B.; Wieme, J.; Reyniers, M.-F.; Marin, G. B.; Adriaenssens, P. J.; Gelan, J. M. A Joined Theoretical–Experimental Investigation on the ^1H and ^{13}C NMR Signatures of Defects in Poly(Vinyl Chloride). *J. Phys. Chem. B* **2008**, *112*, 14804–14818, DOI: 10.1021/jp805676q.

- (43) Smith, S.; Goodman, J. Assigning the Stereochemistry of Pairs of Diastereoisomers Using GIAO NMR Shift Calculation. *J. Org. Chem.* **2009**, *74*, 4597–4607.
- (44) Kleinpeter, E.; Lämmermann, A.; Kühn, H. Synthesis and NMR Spectra of the *Syn* and *Anti* Isomers of Substituted Cyclobutanes—Evidence for Steric and Spatial Hyperconjugative Interactions. *Tetrahedron* **2011**, *67*, 2596–2604, DOI: 10.1016/j.tet.2011.02.012.
- (45) Bartlett, M. J.; Northcote, P. T.; Lein, M.; Harvey, J. E. ^{13}C NMR Analysis of 3,6-Dihydro-2H-pyrans: Assignment of Remote Stereochemistry Using Axial Shielding Effects. *J. Org. Chem.* **2014**, *79*, 5521–5532, DOI: 10.1021/jo500678k.
- (46) Zhao, Y.; Truhlar, D. G. The M06 Suite of Density Functionals for Main Group Thermochemistry, Thermochemical Kinetics, Noncovalent Interactions, Excited States, and Transition Elements: Two New Functionals and Systematic Testing of Four M06-Class Functionals and 12 Other Function. *Theor. Chem. Acc.* **2008**, *120*, 215, DOI: 10.1007/s00214-007-0310-x.
- (47) Cheeseman, J. R.; Trucks, G. W.; Keith, T. A.; Frisch, M. J. A Comparison of Models for Calculating Nuclear Magnetic Resonance Shielding Tensors. *J. Chem. Phys.* **1996**, *104*, 5497–5509, DOI: 10.1063/1.471789.
- (48) Diliën, H.; Marin, L.; Botek, E.; Champagne, B.; Lemaire, V.; Beljonne, D.; Lazzaroni, R.; Cleij, T. J.; Maes, W.; Lutsen, L.; Vanderzande, D.; Adriaenssens, P. J. Fingerprints for Structural Defects in Poly(thienylene vinylene) (PTV): A Joint Theoretical–Experimental NMR Study on Model Molecules. *J. Phys. Chem. B* **2011**, *115*, 12040–12050, DOI: 10.1021/jp206663v.
- (49) Tomasi, J.; Mennucci, B.; Cammi, R. Quantum Mechanical Continuum Solvation Models. *Chem. Rev.* **2005**, *105*, 2999–3094, DOI: 10.1021/cr9904009.
- (50) Frisch, M. J. et al. Gaussian 09 Revision A.01, Gaussian Inc. Wallingford CT 2009.
- (51) Szalóki, G.; Sevez, G.; Berthet, J.; Pozzo, J.-I.; Delbaere, S. A Simple Molecule-Based Octastate Switch. *J. Am. Chem. Soc.* **2014**, *136*, 13510–13513, DOI: 10.1021/ja506320j.

MULTI-STATE NONLINEAR OPTICAL SWITCHES: A QUANTUM CHEMICAL INVESTIGATION OF COMPOUNDS BEARING TWO IDENTICAL MULTI-ADDRESSABLE BENZAZOLO-OXAZOLIDINE UNITS

To Be Submitted

Jean Quertinmont[†], Julien Stiennon[†], Pierre Beaujean[†], Youssef Aidibi[§],
Philippe Leriche[§], Vincent Rodriguez[‡], Lionel Sanguinet[§], & Benoît
Champagne[†]

[†] *Unité de Chimie Physique Théorique et Structurale, Chemistry Department, University of Namur, 61 rue de Bruxelles, B-5000 Namur, Belgium*

[‡] *Institut des Sciences Moléculaires (ISM, UMR CNRS 5255), Université de Bordeaux, 351 cours de la Libération, 33405 Talence, France*

[§] *MOLTECH-Anjou, Université d'Angers, CNRS-UMR 6200, F-49045 Angers, France*

J.Q. contributed to the supervision of the Master work of J. Stiennon. He took part in the analysis of the results and to the writing of the article.

Abstract

Molecular switches are chemical compounds displaying the possibility of reversible transformations between their different forms accompanied by a modification of their properties. Among these molecules, BenzazoloOXazolidines (BOX's) have the particularity of being multi-addressable (by light, pH variations, and redox variations). The modification of their structure from a closed to an open form results in a drastic modification of their linear and nonlinear. In this paper, molecules containing two BOX units (DiBOX) connected by different π -conjugated linkers are targeted and studied by adopting a multidisciplinary approach that combines synthesis, UV/vis absorption and hyper-Rayleigh scattering measurements, together with quantum chemical calculations carried out at the DFT level. The latter are employed to unravel their structural, linear and nonlinear optical, and thermodynamical properties, in order to help in the interpretation of the experimental data as well as to provide design guidelines. More precisely, this study focuses on three derivatives exhibiting two BOX switches connected by different π -conjugated linkers: i) a bithiophene moiety (Bt), ii) a bis-3,4-ethylenedioxythiophene unit (BtO), and iii) a triad composed of the EDOT-thiophene-EDOT sequence (TtO). As a matter of fact, these systems can adopt three states (CF-CF, POF-POF and CF-POF) depending on the Closed (CF) or Protonated Open form (POF) of each BOX unit. Indeed, despite a chemical equivalence, the stepwise commutation of such systems under the addition of chemical acid or oxidant was experimentally evidenced for two of them (DiBOX-Bt and DiBOX-TtO). By performing DFT calculations, it was possible to rationalize this behavior as a function of the nature of the linker and to show that the first opening leads to the formation of a push-pull π -conjugated segment, built from the π -donating linker and the indoleninium acceptor, exhibiting a huge increase of β and a bathochromic shift with respect to the fully closed form. At opposite, the second BOX opening induces only a slight bathochromic shift but also a reduction of their β values conferring the nice and uncommon abilities to modulate their linear and nonlinear properties over three discrete levels. This smaller β results from the formation of POF-POF states with a pull-push-pull character, which from the symmetry viewpoint is detrimental to β . Moreover, if the nature of the aromatic moieties of the π -linker prevents the formation of non-centrosymmetric V-shape structures, the β values can even be negligible. Among these results, those on DiBOX-Bt are in agreement with experimental data obtained by HRS measurements and further shed light and their structure-property relationships. The variations of the β values have been unraveled by resorting to the two-state approximation, which demonstrates the key role of the change of dipole moment between the ground state and the first excited state that determines the UV-visible absorption spectra. Moreover, though the BOX's are chemically equivalent, calculations support, for the three DiBOX derivatives, the possibility to control their level of opening when trig-

gered by the addition of acid or oxidant, in agreement with experimental data on DiBOX-Bt and DiBOX-TtO.

11.1 Introduction

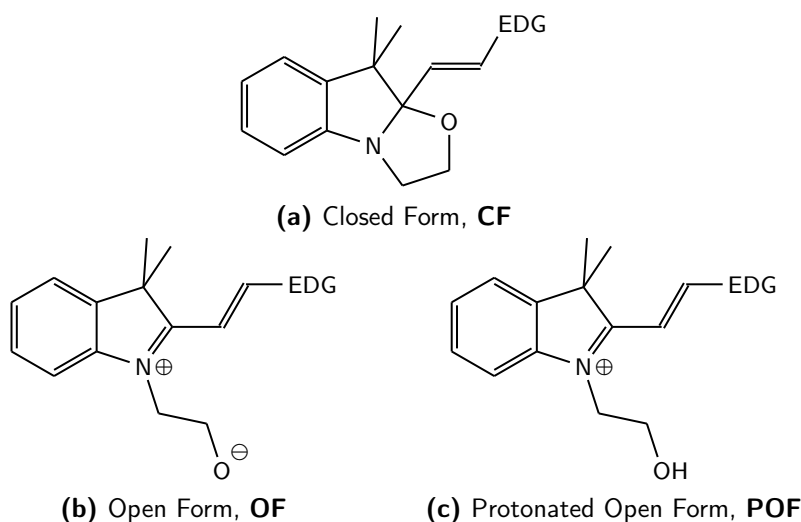
Molecular switches constitute a class of compounds that can undergo, under an external stimulation, reversible transformations between at least two metastable states.¹⁻⁴ Due to a change of structure, this switching results in a variation of the molecular properties where the modification of the absorption spectrum, and therefore the color, is certainly one of the most noticeable phenomenon. These color changing systems are generally classified as a function of the nature of the stimulation. Halochromism (also referenced as acidochromism)⁵ defining a color change with the pH is certainly the most widespread with applications such as pH indicators. Nevertheless, many other chromisms phenomena have been reported so far: thermochromism (temperature), photochromism (light irradiation), electrochromism (electrical potential), solvatochromism (solute-solvent interactions), and piezochromism (pressure) to name a few.⁶

These molecular property changes go beyond the absorption spectrum. They can also encompass motion,⁷ change of emission (fluorescence, phosphorescence)⁸ like in fluorescent proteins, variation of the nonlinear optical responses,⁹⁻¹¹ and modifications of the reactivity.

Since the last decades, we and others are interested in the modulation of the quadratic hyperpolarizabilities where molecular systems based on Benzazolo-OXazolidines switchable unit (abbreviated BOX's) have demonstrated remarkable abilities.^{12,13} Under stimulation, the oxazolidine ring opening leads to the formation of an indoleninium unit, which acts as strong electron withdrawing group (EWG). Combined with an electron-donating group (EDG) through a π -conjugated bridge, the open form of BOX's behaves as a push-pull system providing a drastic enhancement of the first hyperpolarizability (β) and leading to observed high β contrasts between the closed and open forms (Scheme 11.1). Systems incorporating a BOX unit can switch between two discrete levels, generally referenced as ON and OFF states. Their efficiency (the β contrast) can be maximized by appropriately selecting the EDG and the substituents on the EWG.¹⁴

Interestingly, the opening of the oxazolidine ring can be induced by using different kinds of stimulation conferring to BOX's some photo-, electro-, and acido-chromic properties.¹⁵ If the protonation leads directly to the formation of the positively-charged Protonated Open Form (POF), UV light irradiation leads to the formation of the meta-stable zwitterionic Open Form (OF) through cleavage of the C-O bond. In protic media, this later is able to capture a proton and readily converted in POF form. Noticeably, for a given BOX, both open forms (OF and POF) do not display any difference in their UV/Vis absorption spectra, leading to the conclusion that the state of protonation on the O atom negligibly affects the electronic properties of the molecule. From another point of view, the first excitation energy is not affected by the protonation of the open BOX.^{16,17} As consequence, regeneration of the Closed Form (CF) is generally obtained by

treatment with a base or, more rarely, by irradiation with visible light. Aside from photochromism and acidochromism, the BOX's electrochemical properties were investigated more lately.¹⁸ Additionally to direct oxidation, the oxazolidine ring opening under an electrochemical potential can be obtained by an electro-mediated process when the BOX unit is associated to a bithiophene moiety as EDG. The latter is known to form stable radical cation and enhances the electrochemical properties of the BOX.^{14,19} In that case, the assumed mechanism for the opening by oxidation is the following: i) the oxidation occurs on the bithiophene, leading to the formation of a radical-cation species, ii) the radical is delocalized to the BOX, before iii) the homolytic cleavage of the C-O bond occurs, and then, iv) the POF is formed.¹⁵



Scheme 11.1: A BOX in its three different forms: CF, OF, and POF. EDG stands for an aromatic fragment with electron donating character, which could bear different types of substituents.

To modulate a molecular property over more than two discrete levels, one strategy consists of building units that can switch between more than two states, like dinitrobenzylpyridine²⁰ and oxazines.²¹ In another approach leading to the formation of multi-state molecular switches several switching units are combined. So, a system combining n different two-state molecular switches displays 2^n different forms, each one possessing its own properties. An illustration is given by the system built from the following three different units: a BOX, a diarylethene, and an alkene linker (which can display two conformations: *cis* and *trans*), leading to an octa-state molecular switch.^{22–25} However, in that case, the different reactions of switching can be in competition and may lead to difficulties in controlling one or more forms of the molecular switch, especially if the reactions of photoisomerization are achieved in similar conditions. This is particularly true when the different molecular switches are chemically close to each other.

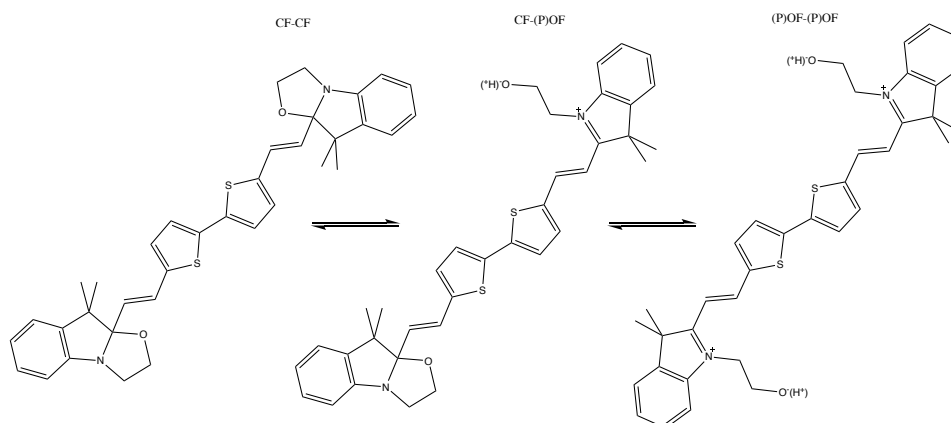
Nevertheless, we have recently demonstrated that a stepwise opening selectivity between two identical BOX units is reachable when they are grafted on a same π -conjugated core.^{26,27} If such systems did not obey to the classical "2ⁿ states" rule, they are able to commute between three different states (CF-CF, POF-CF, and POF-POF) (Scheme 11.2). As we assessed in this work, from one state to the others, the successive openings of the oxazolidine rings must induce drastic changes in the molecular electronic structures, leading to the first compounds possessing two identical BOX units able to modulate their NLO properties over three discrete levels.

Within this context, molecular switches containing two identical BOX units (referenced as DiBOX's) rise several questions: i) since the different BOX's are chemically equivalent, is it possible to control the level of opening of these molecules?, ii) does the chemical nature of the linker affect the selectivity of the successive openings?, and iii) how does the level of opening of the switch modulate the linear and nonlinear optical properties of these systems? These questions are addressed here by considering three DiBOX's, which differ by the linker connecting the BOX units. The linker of the first compound is composed of a Bithiophene (Bt), the second one contains two 3,4-EthyleneDiOxyThiophene (EDOT) units (BtO), and the last one is composed of an EDOT-thiophene-EDOT sequence (called TtO) (Scheme 11.3). In this way, comparison between DiBOX-Bt and DiBOX-BtO enables to study the impact of a stronger donating π -linker (BtO) while the comparisons between these and TtO tackles the effects of the linker length and π -electron delocalization. These questions are addressed by adopting a multidisciplinary approach that combines synthesis, experimental characterizations, and quantum chemical calculations. The synthesis of DiBOX-Bt has already been reported together with the control of its successive openings and their impact on the linear optical properties.²⁶ Here, we target the synthesis of the two other compounds, the characterization of their linear and nonlinear optical properties for the different opening states, while we present a detailed quantum chemical investigation of their structural, electronic, and optical properties. The latter are performed at the density functional theory (DFT) and time-dependent DFT (TDDFT) levels of approximation.

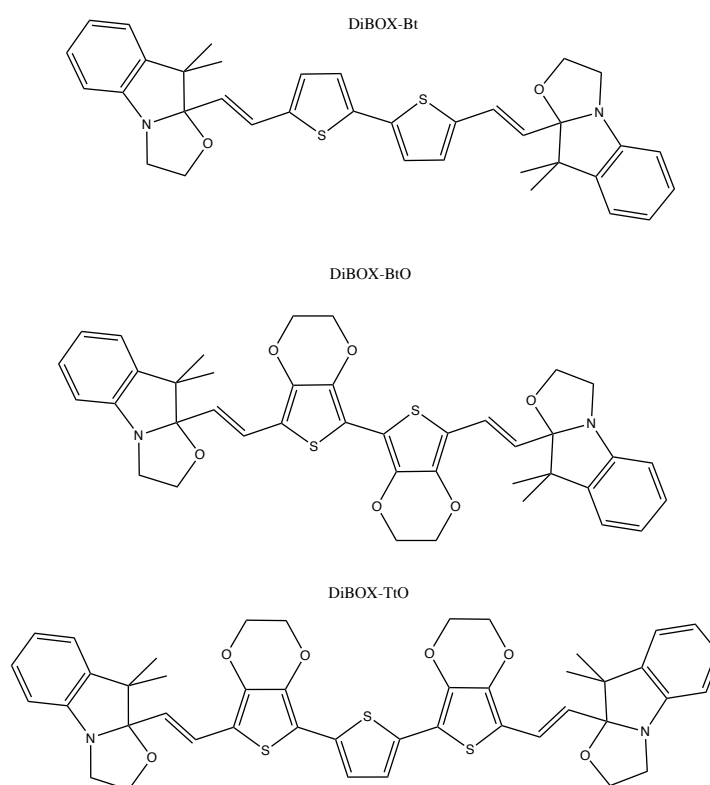
11.2 Theoretical and Computational Aspects

11.2.1 Synthesis

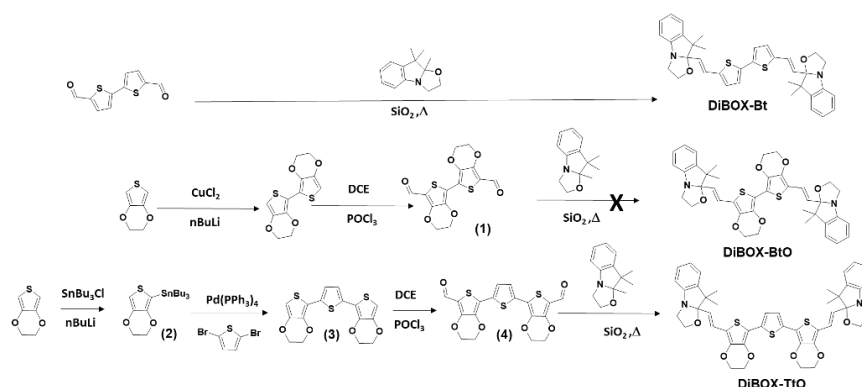
The preparation of DiBOX compounds has already been reported in the literature. The corner stone of most of them is the condensation of an aromatic core bearing two carbonyl functions with trimethylindolino-oxazolidine derivatives. If many experimental conditions have been described to perform such condensation (protic/aprotic solvent, with and without acid/base catalysis, ...) recent solvent-free methodology using silica powder²⁸ have demonstrated high efficiency and allowing the preparation of DiBOX-Bt in good yield.²⁶



Scheme 11.2: The different levels of opening of DiBOX-Bt, a molecular switch combining two BOX units, linked together by a bithiophene (Bt) bridge.



Scheme 11.3: Structure of the three DiBOX's in their fully closed form.



Scheme 11.4: Preparation of three DiBOX derivatives by solvent-free silica mediated condensation between trimethyl indolino[2,1-b]oxazolidine and three bis-aldehyde aromatics prepared by Vilsmeier-Haack reaction according to reported procedures.

In order to prepare DiBOX-BtO we have synthesized 5,5'-dicarbaldehyde-2,2'-bis-EDOT (**1**) according to already-reported procedures,²⁹ but the replacement of thiophene by EDOT moieties comes with a drop of the solubility of the corresponding bis-aldehyde. Due to this lack of stability, it was impossible to carry out its condensation with 2,3,3-trimethylindolino[2,1,b]oxazolidine in classical conditions. Unfortunately, all our attempts to circumvent this problem by changing either the experimental condition or our synthetic strategy to prepare DiBOX-BtO have been up to now unsuccessful. Starting from this, a thiophene was introduced between both EDOT units in order to improve the solubility. A Stille coupling performed on 2,5-dibromothiophene³⁰ followed by a classical Vilsmeier-Haack reaction allowed to prepare 2,5-di(5'-carbaldehyde-EDOT)thiophene (**3**). Exhibiting a better solubility than **2**, its condensation with 2,3,3-trimethylindolino[2,1,b]oxazolidine leading to DiBOX-TtO did not raise any particular problem. Noticeably, it should be mentioned that the higher donor ability of this π -conjugated core, compared to bithiophene, impacts the reaction efficiency as the time of the reaction has to be increased of up to 7 hours in order to reach similar yield. All syntheses are resumed below in Scheme 11.4. More details are provided in SI.

11.2.2 UV/vis Absorption and hyper-Rayleigh Scattering Measurements

UV/visible absorption spectra were acquired with a Varian Cary 50 single beam spectrometer with a 0.1 s integration time every 1 nm. Solvent used is commercially available spectroscopic grade acetonitrile without further purification. Quartz cuvettes were used with a 1 cm optical path.

The first hyperpolarizabilities were determined by using a homemade set up. An OPG picosecond laser source (signal: 720-1000 nm, idler: 1150-2200 nm)

is used as probing source to adjust the incident energy (ω) to tune the SHS (2ω). A block power, constituted of a half-wave plate and a polarizer, is placed after the source in order to control the incident intensity and deliver linear vertical polarization. This fundamental relative intensity is precisely determined via the measurement of the scattered light intensity by the half-wave plate routed through an optical fiber to a photodiode connected at an oscilloscope. More important, the polarization of the incident beam can be continuously controlled (P, S, left/right circular polarization and all intermediate elliptic polarizations) thanks to the juxtaposition of a half-wave plate and a rotatable quarter-wave plate. This tunability of the incident beam polarization allows to probe different beta tensor components. The scattered light is collected at 90° and analyzed by a spectrograph using CCD detector.

The β_{HRS} of each form of DiBOX-Bt was investigated in acetonitrile solution (varying between 0.25 and 1.0×10^{-4} M) by using the solvent as internal reference.³¹ The CF-POF and POF-POF species were obtained by stimulating the CF-CF one by adding respectively 1 and 2 eq. of chemical oxidant (NOSbF_6). Figure F.3 gathers all results and shows the variations of the incoherent scattered light at optical frequency 2ω as a function of the concentration of the chromophore but also of the incident power. Then, Figure F.4 gives the polarization curves. In the case of DiBOX-TtO, the β_{HRS} measurements were not successful due to too strong two-photon-induced fluorescence.

11.2.3 Theoretical and Computational Aspects

The geometries of all compounds were fully optimized at the DFT level with the M06 XC functional,³² the 6-311G(d) basis set, and by accounting for solvent effects using the integral equation formalism of the polarizable continuum model (IEF-PCM) (the solvent is acetonitrile).³³ Real vibrational frequencies demonstrate the optimized geometries are minima on the potential energy hyper-surface. Since the DiBOX compounds are mostly composed of cyclic units and conjugated segments, the numbers of stable conformers in solution are rather small and the search of those conformers possessing a non-negligible weight within the Maxwell-Boltzmann (MB) statistics can be carried out in a systematic manner. This was done i) by defining the key torsion angles to distinguish the main conformations (Scheme F.1), ii) by performing rigid scans to locate the extrema of the potential energy hyper-surface, iii) by combining the minima of the rigid scans to preselect conformations, and iv) then by performing full geometry optimizations. Finally, only those conformers within an energy window of 12.5 kJ mol^{-1} were kept to calculate the MB populations, on the basis of the Gibbs free energies, ΔG^\ominus at 298.15 K. These results are presented in SI. This approach is efficient to locate the key conformations because the torsion angles are far enough from each other and, in first approximation, their impact on the total energy is considered as independent from each other, leading to a quasi-additive behavior. Note that, contrary to Ref. [23], the *cis-trans* isomerizations

are not considered here. Indeed, as observed in calculations not detailed here, the fraction of the *cis* form is negligible, so that only the *trans* alkene forms are taken into account.

The vertical excitation energies (ΔE_{ge}) and the transition dipole moments (μ_{ge}) were calculated for at least the 10 lowest-energy excited states at the TDDFT level using the M06-2X XC functional,³² and accounting for solvent effects using the IEF-PCM scheme. The μ_{ge} quantities were used to calculate the oscillator strengths ($f_{ge} = 2/3 \Delta E_{ge} \Delta \mu_{ge}^2$) and then employed to plot the UV/vis absorption spectra (each transition was associated with a Gaussian function, centered on ΔE_{ge} , of intensity proportional to f_{ge} , and of full width at half maximum of 0.3 eV). The differences of dipole moment between the ground and key excited states, $\Delta \mu_{ge} = \mu_e - \mu_g$, were then evaluated. The calculations of all these excited state-related properties, including μ_e , employ the nonequilibrium solvation approach since electronic excitation processes are very fast with respect to the solvent reorganization.³⁴ Nonequilibrium solvation TDDFT calculations were performed to evaluate the difference of electronic density between the ground and excited states, $\Delta \rho(\vec{r}) = \rho_e(\vec{r}) - \rho_g(\vec{r})$. Following the procedure described by Le Bahers et al.,³⁵ the barycenters of the positive [$\Delta \rho^+(\vec{r})$] and negative [$\Delta \rho^-(\vec{r})$] electronic density variations were evaluated. The distance between these barycenters defines the charge-transfer distance (d_{CT}) while their integration over the whole space gives the amount of charge transferred (q_{CT}). The product of these two quantities gives $\Delta \mu_{ge} = q_{CT} \times d_{CT}$.

The β tensor components were calculated using the TDDFT method^{36,37} with the M06-2X XC functional, the 6-311+G(d) basis set, and the IEFPCM scheme to account for solvent effects. Both static and dynamic (for incident wavelengths of 1907, 1300, and 1064 nm) responses were evaluated. In this work, in parallel to the experimental data, we concentrated on the second harmonic generation (SHG) phenomenon, $\beta(-2\omega; \omega, \omega)$, and more precisely on the hyper-Rayleigh scattering (HRS) first hyperpolarizabilities, $\beta_{HRS}(-2\omega; \omega, \omega)$, and their decompositions.³⁸ For an experimental set-up where the incident light is non-polarized and the vertically polarized (along the *Z* axis of the laboratory frame) signal scattered at 90° with respect to the propagation direction (*Y* axis) is detected, the HRS intensity is proportional to the square of $\beta_{HRS}(-2\omega; \omega, \omega)$, which depends on two ensemble averages ($\langle \beta_{ZZZ}^2 \rangle$ and $\langle \beta_{ZXX}^2 \rangle$) over the molecular orientations:

$$\beta_{HRS}(-2\omega; \omega, \omega) = \sqrt{\langle \beta_{ZZZ}^2 \rangle + \langle \beta_{ZXX}^2 \rangle} = \sqrt{\langle \beta_{ZZZ}^2 \rangle} \left(1 + \frac{1}{DR} \right) \quad (11.1)$$

The depolarization ratio DR, which reflects the chromophore shape, is the ratio between the scattered intensities obtained when the incident light is vertically ($\langle \beta_{ZZZ}^2 \rangle$) and horizontally ($\langle \beta_{ZXX}^2 \rangle$) polarized, respectively. The relationships between these averages (in the laboratory frame) and the molecular tensor components (in the molecular frame) are available from previous papers.^{31,39}[41,49]

In the case of a push-pull π -conjugated system, the β tensor is often dominated by a single diagonal tensor component (namely β_{zzz} so that $DR = 5$ and $\beta_{HRS} = \sqrt{6/35}\beta_{zzz}$). The static β_{HRS} responses were also analyzed in terms of the β irreducible spherical representations,^{40,41} namely $|\beta_{J=1}|$, the dipolar contribution, and $|\beta_{J=3}|$, the octupolar one:

$$\beta_{HRS}(-2\omega; \omega, \omega) = \sqrt{\frac{10}{45} |\beta_{J=1}|^2 + \frac{10}{105} |\beta_{J=3}|^2} = |\beta_{J=1}| \sqrt{\frac{2}{3} \left(\frac{1}{3} + \frac{1}{7} \rho^2 \right)} \quad (11.2)$$

where $\rho = |\beta_{J=3}| / |\beta_{J=1}|$ is the nonlinear anisotropy factor, describing the relative importance of the octupolar contribution with respect to the dipolar one. Note that ρ and DR are related:

$$DR = 9 \left(\frac{1 + \frac{2}{7} \rho^2}{1 + \frac{12}{7} \rho^2} \right) \quad (11.3)$$

For purely dipolar responses, $DR = 9$ and $\rho = 0$ whereas for octupolar ones, $DR = 1.5$ and $\rho = \infty$. For one-dimensional (1D) NLO-phore with a unique dominant diagonal β tensor component, $DR = 5$ and $\rho = 0.82$.

To visualize the β tensor, the unit sphere representation (USR), initially proposed for the first hyperpolarizability tensor,⁴² was adopted. It consists i) in computing an effective induced dipole moment (either static or dynamic like the current SHG responses):

$$\vec{\mu}_{ind} = \vec{\beta} : \vec{E}^2(\theta, \phi) \quad (11.4)$$

where the tensor nature of β has been evidenced and $\vec{E}^2(\theta, \phi)$ is a unit vector of electric field, of which the polarization direction is defined in spherical coordinates by the θ and ϕ angles and ii) by representing all the induced dipole moment vectors on a sphere centered on the center of mass of the compound. This enables highlighting the directions where the second-order polarization is the strongest (it corresponds to the largest induced dipoles), its orientation (the acceptor-donor direction), and subsequently showing how much the β response is dipolar/octupolar. These USR were plotted using the Drawmol package.⁴³

As noted, a different XC functional was used for calculating the linear and nonlinear optical properties (M06-2X, 54 % HF exchange) than the structural and thermodynamic data (M06, 27 % HF exchange). This is consistent with previous studies on related compounds,¹⁴ which show that a larger amount of exact Hartree-Fock (HF) exchange is needed to calculate the optical properties.⁴⁴⁻⁴⁸ All (TD)DFT calculations were carried out using the Gaussian16 package.⁴⁹

11.3 Results and Discussion

The DiBOX-Bt and DiBOX-TtO compounds have been prepared following the procedure described in the Methods Section with complements given in the Sup-

porting Information, while DiBOX-BtO could not be prepared owing to stability issues.

11.3.1 Geometrical Structures

For each DiBOX and each of their three states, Supporting Information provide a summary of the key geometrical parameters (torsion angles and bond length alternations (BLA's)) of the most stable conformers, their relative Gibbs free enthalpies (ΔG^\ominus) and their populations with Maxwell-Boltzmann (MB) approach (Scheme F.1, Tables F.1-F.9). The three DiBOX's share several structural features in common. For all forms, the most stable conformation of the π -conjugated linkers tends to be the one where all torsion angles are close to 180° (θ_2 to θ_4 for DiBOX-Bt and DiBOX-BtO and θ_2 to θ_5 : DiBOX-TtO). When the BOX units are in CF, the torsion angles between the BOX and the vinylene bridge (θ_1 as well as θ_5 or θ_6 for the three compounds) adopt two conformations: 1,3-OH interaction ($\sim -115^\circ$) and 1,3-NH interaction ($\sim 115^\circ$). For CF-CF, the θ_1 - $\theta_5 \sim -115^\circ$ conformation (1,3-OH) leads to the most stable conformers, while for CF-POF the conformation with θ_1 at $\sim 115^\circ$ (1,3-NH) leads to the most stable ones. The opening of the BOX units induces an enhancement of the planarity of the system. As a consequence, the torsion angles between the BOX and the vinylene bridge tend to adopt a value around 0° . More important, changing this value from $\sim 0^\circ$ to $\sim 150^\circ$ leads to a drastic increase of ΔG^\ominus , by about 10 kJ mol^{-1} .

To better describe the π -conjugated segments, instead of one, two types of BLA's were considered: a "global" BLA, taken from one BOX to the other one (noted *BLA*) and "local" BLA's, measured individually on each vinylene bridge (Scheme F.1) and denoted *BLA'* and *BLA''*. For CF-POF, the two local BLA's are noted *BLA'* when associated with the vinylene on the CF while *BLA''* with the POF side. The global BLA values decrease upon the successive openings (Table 11.1):

$$BLA[\text{POF-POF}] < BLA[\text{CF-POF}] < BLA[\text{CF-CF}]$$

while for the local *BLA'* and *BLA''* the following trend is observed:

$$BLA''[\text{CF-POF}] < BLA''[\text{POF-POF}] \ll BLA'[\text{CF-CF}] < BLA''[\text{CF-POF}]$$

Two trends are evidenced. First, the presence of indoleninium moieties, which corresponds to the transformation of a sp^3 C atom into a sp^2 one, increases the general π -electron delocalization (expressed by a smaller BLA's). Therefore, a decrease of the excitation energies is expected to come alongside the successive openings. In parallel, opening a BOX strongly reduces the local BLA values ($BLA'' \ll BLA'$) due to the better π -electron delocalization. Noticeably, this transformation of only one BOX unit has an impact on the electron delocalization of both vinylene bridges, as evidenced by a slight increase of the *BLA'*

between CF-CF and CF-POF forms. Surprisingly, the second BOX opening has antagonistic effects because smaller global BLA values are associated with larger BLA'' for state POF-POF than CF-POF. These results seem to indicate that the indoleninium-linker delocalization is the strongest when only one BOX is open.

As observed with the status of the BOX unit, BLA' values are less affected by the nature of the linker, since all BLA' range between 0.132 Å to 0.139 Å. On the other hand, the BLA'' values depend on the nature of the linker: the BLA'' becomes smaller when the thiophenes are substituted by EDOT. This is due to the ether functions of the EDOT, which enhance the delocalization between the linker and the indoleninium(s) by strengthening the donor character of the linker.^{50,51} For the DiBOX's in POF-POF, the length of the linker has an additional effect on the BLA'' , it is smaller for DiBOX-TtO than DiBOX-BtO (0.026 Å vs 0.035 Å). This BLA analysis — as well as the differences between the global and local BLA's — find its roots in the way the successive CF openings impact the C–C bond lengths from one BOX to the other (Figure F.1). The presence of indoleninium moieties in the π -conjugated system results in a better delocalization, leading to a decrease of BLA. When induced by a single BOX in POF, this delocalization attenuates after one aromatic ring. This delocalization is the strongest for the DiBOX's in CF-POF, with a stronger weight of the quinoïdal form. This effect is then further enhanced by the substitution of a thiophene by an EDOT, as illustrated by the variation of BLA'' .

Table 11.1: BLA's values (in Å) for the DiBOX's in their different forms as evaluated from geometry optimizations at the M06/6-311G(d)/IEF-PCM (acetonitrile) level of approximation. These values are averaged over the MB distributions, using the data from Tables F.1-F.9.

		DiBOX-Bt	DiBOX-BtO	DiBOX-TtO
CF-CF	BLA^a	0.081	0.079	0.072
	BLA'	0.136	0.133	0.133
CF-POF	BLA	0.048	0.041	0.042
	BLA'	0.139	0.136	0.135
	BLA''	0.032	0.013	0.015
POF-POF	BLA	0.032	0.026	0.024
	BLA''	0.049	0.035	0.026

^a all BLA values being negative, their absolute values are reported.

11.3.2 UV/Visible Absorption Spectra and Related Properties

The experimental UV/vis absorption spectra of DiBOX-Bt and DiBOX-TtO were recorded along a titration with NOSbF_6 as chemical oxidant (See Methods Section for more details). Figures 11.1 and 11.2 show that the switching abilities of the DiBOX are not affected by the nature of the π -conjugated linker. As already reported for DiBOX-Bt, a stepwise transformation of DiBOX-TtO is observed under electrochemical stimulation leading successively to the CF-POF, then POF-POF form from the CF-CF form. In both cases, the first BOX opening induces a huge bathochromic shift of the absorption maxima wavelength [151 and 218 nm (corresponding to 0.94 and 0.98 eV) for DiBOX-Bt and DiBOX-TtO, respectively, Table 11.2]. At the opposite, the second BOX opening induces only a moderate variation of the absorption maxima wavelength [17 and 20 nm (0.07 and 0.06 eV) for DiBOX-Bt and DiBOX-TtO, respectively]. This stepwise switching under external stimulation is translated by an irregular evolution of the UV/vis spectra along the titration with acid or oxidant aliquots. Such as presented for electrochemical stimulation (Figures 11.1 and 11.2), below one equivalent two isosbestic points are noticed in each case (321/427 and 368/476 nm for DiBOX-Bt and DiBOX-TtO, respectively). When the stimulation is pushed further, an enhancement of the coloration is observed and, more important, this increment did not allow maintaining the observation of the previous isosbestic points which are replaced by new ones (326 and 358/464 nm for DiBOX-Bt and DiBOX-TtO, respectively).

Turning now to the QC calculations, using the populations given in SI, the weighted averages of the excitation energies were evaluated at the M06-2X/6-311+G(d)/IEF-PCM (acetonitrile) level of approximation. The oscillator strengths were calculated with the objective of simulating the UV/Vis absorption spectra (Table 11.1). The charge-transfer character of the first dominant excitation are also listed. These quantities are indeed often useful to interpret the dominant diagonal (in the following expression, along the z axis) first hyperpolarizability tensor components within the two-state approximation⁵²

$$\beta_{zzz} = 9 \frac{f_{ge} \Delta\mu_{ge}}{\Delta E_{ge}^3} \quad (11.1)$$

As a matter of fact, large β responses can be achieved by 1) a low ΔE_{ge} , 2) a strong absorbance (large oscillator strength, f_{ge}), and, 3) a large variation of the dipole moment ($\Delta\mu_{ge}$) between the ground and that excited state.

The low-excitation energy peak in the UV/Vis spectra is attributed to a $S_0 \rightarrow S_1$ excitation since the contributions of the other excitation bands are negligible. We can notice a good agreement between the experimental maximum wavelengths of absorption and the calculated vertical excitation wavelengths of this first transition (Table 11.2, Figures 11.1 and 11.2). This substantiates the selection of the M06-2X XC functional for the investigation of the linear optical properties of these systems as a function of the nature of the π -conjugated linker.

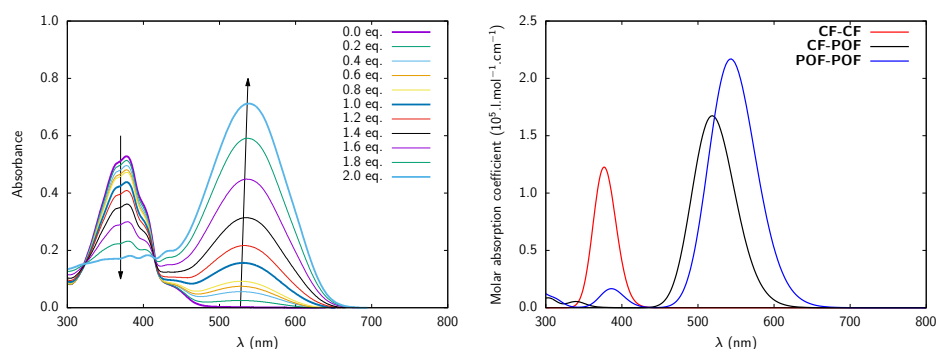


Figure 11.1: Experimental (left) and simulated (right) UV/vis absorption spectra of DiBOX-Bt. The experimental ones are obtained in acetonitrile (0.086 M) along a titration with NOSbF₆ as chemical oxidant. The simulated spectra are given for three different forms (red: CF-CF, black: CF-POF and blue: POF-POF) using the weighted average results as calculated at the M06-2X/6-311+G(d)/IEF-PCM (acetonitrile) level of theory.

Numerical simulations confirm that the global evolution of the linear optical properties as a function of the level of opening are not affected by the nature of the linker. In each case, a bathochromic shift accompanies the successive openings (Figures 11.1 and 11.2). This shift is more important for the first opening (0.74-0.90 eV) than for the second (0.11-0.23 eV). As expected, the value of ΔE_{ge} is strongly influenced by the nature of the linker. By increasing the electron donor character of the π -conjugated linker (*vide supra*), it seems possible to reduce ΔE_{ge} and, as consequence, generates higher dominant diagonal first hyperpolarizability tensor components. As consequence, the substitution of thiophene(s) by EDOT(s) moieties and the enhancement of the linker length results in the smallest ΔE_{ge} values for DiBOX-TtO whatever the considered form.

Second key parameter in order to reach larger β responses, the evolution of the oscillator strength of the DiBOX's is mainly affected by the successive BOX openings but also by the nature of the π -conjugated linker. Indeed, f_{ge} increases by about the same amount (~ 0.40 - 0.60) after each oxazolidine ring opening. For a given form, the absorbance does not vary much between DiBOX-Bt and DiBOX-BtO. On the contrary, the length of the linker affects the oscillator strength: DiBOX-TtO possesses the largest f_{ge} values (~ 0.30 higher than DiBOX-Bt and -BtO).

Achieving large β responses requires a large variation of the dipole moment ($\Delta\mu_{ge}$) between the ground and excited states. This third parameter can be expressed as the product of the charge-transfer associated with the (first) excitation, q_{CT} , by its distance d_{CT} . Concerning q_{CT} the following trend is observed for the three molecules:

$$q_{CT}[\text{CF-CF}] < q_{CT}[\text{POF-POF}] < q_{CT}[\text{CF-POF}]$$

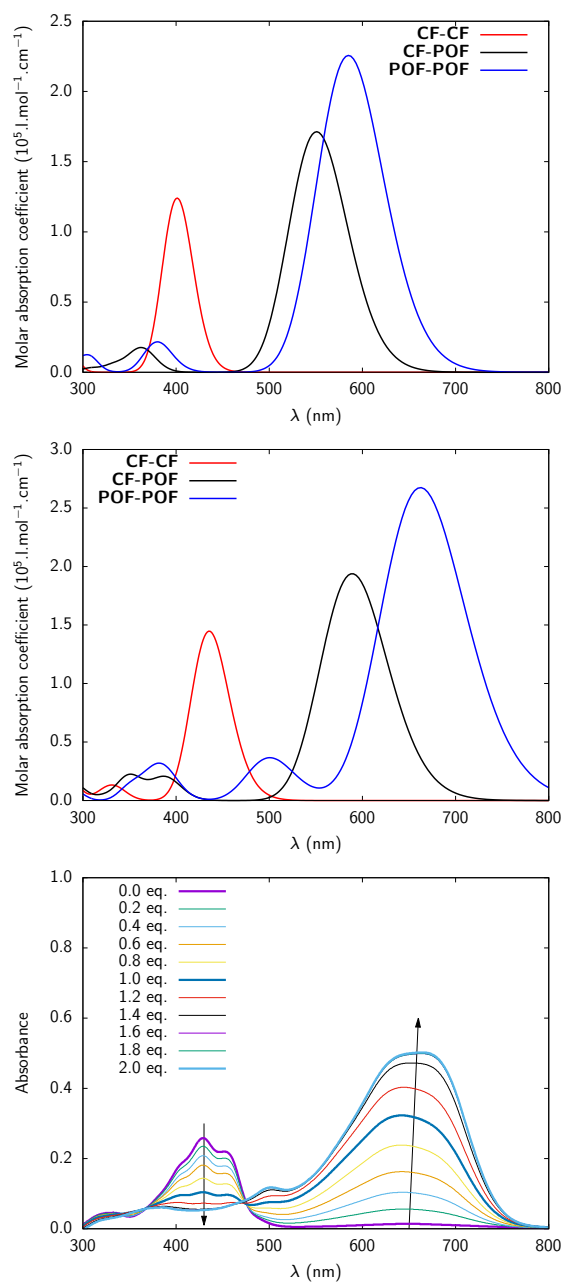


Figure 11.2: Simulated (top) UV/vis absorption spectra of DiBOX-BtO and comparison between the simulated (middle) and experimental (bottom) UV/vis absorption spectra of DiBOX-TtO. The simulated spectra are given for three different forms (red: CF-CF, black: CF-POF and blue: POF-POF) using the weighted average results as calculated at the M06-2X/6-311+G(d)/IEF-PCM (acetonitrile) level of theory. The experimental ones are obtained in acetonitrile (0.06 M) along a titration with NOSbF₆ as chemical oxidant.

Table 11.2: Experimental (maximum absorption) wavelengths (λ_{exp} , nm), computed (vertical) excitation wavelengths (λ_{ge} , nm), excitation energies (ΔE_{ge} , eV), oscillator strengths (f_{ge}), amounts of charge transfer (q_{CT} , e), distances of charge transfer (d_{CT} , Å), and variations of dipole moment ($\Delta\mu_{ge}$, D) associated with the $S_0 \rightarrow S_1$ excitation of the three DiBOX's in their different forms, as evaluated at the M06-2X/6-311+G(d)/IEF-PCM (acetonitrile) level of approximation. The averages are weighted using the populations of conformers at 298.15 K.

		λ_{exp}	λ_{ge}	ΔE_{ge}	f_{ge}	q_{CT}	d_{CT}	$\Delta\mu_{ge}$
DiBOX-Bt	CF-CF	375 ^a	377	3.29	1.39	0.395	0.090	0.176
	CF-POF	530 ^a	519	2.39	1.87	0.550	3.287	8.697
	POF-POF	545 ^a	543	2.28	2.43	0.494	0.182	0.433
DiBOX-BtO	CF-CF		401	3.09	1.38	0.384	0.022	0.040
	CF-POF		551	2.25	1.91	0.498	2.546	6.098
	POF-POF		585	2.12	2.55	0.490	0.020	0.046
DiBOX-TtO	CF-CF	428	437	2.84	1.70	0.410	0.425	0.840
	CF-POF	646	589	2.10	2.16	0.601	4.137	11.945
	POF-POF	666	662	1.87	2.98	0.563	0.222	0.600

^a From Ref. [26]

$q_{CT}[\text{CF-CF}]$ and $q_{CT}[\text{CF-POF}]$ do not vary much between the different compounds, between 0.38 e and 0.41 e, and between 0.49 e and 0.56 e, respectively. Obviously, the $q_{CT}[\text{CF-POF}]$ values depend on the nature of the linker and follows the evolution of electron donor ability of the π -conjugated linker (DiBOX-BtO: 0.49, DiBOX-Bt: 0.55 e, and DiBOX-TtO: 0.60 e). Concerning the distance of charge transfer, its evolution is specific to the degree of opening and it depends on the nature of the linker. For DiBOX-Bt, one observes:

$$d_{CT}[\text{CF-CF}] < d_{CT}[\text{POF-POF}] \ll d_{CT}[\text{CF-POF}]$$

while for DiBOX-BtO:

$$d_{CT}[\text{POF-POF}] \sim d_{CT}[\text{CF-CF}] \ll d_{CT}[\text{CF-POF}]$$

and DiBOX-TtO:

$$d_{CT}[\text{POF-POF}] < d_{CT}[\text{CF-CF}] \ll d_{CT}[\text{CF-POF}].$$

For the three compounds, the CF-POF form displays a large d_{CT} , owing to its push-pull π -conjugated character and the CT character of the lowest-energy excitation. Since $\Delta\mu_{ge}$ is the product of q_{CT} by d_{CT} , and since d_{CT} is more affected by the level of opening than q_{CT} , the variations of $\Delta\mu_{ge}$ follow those of d_{CT} . The variations of the amplitude of charge transfer between the different

DiBOX and the different forms can be rationalized in terms of the topology of the molecular orbitals implied in the first excitation (Figure 11.3). For all structures, the first excitation corresponds mostly to a HOMO to LUMO electronic transition. Both frontier orbitals are quite delocalized over the π -conjugated system. For the CF-CF form, these orbitals are distributed symmetrically on the linker. For the other symmetric form (POF-POF), their distributions extend towards the indoleninium groups, in particular for the HOMO. Finally, for the CF-POF form, the distributions are a mixed of those of the symmetric forms. Subsequently, the variations of electron density also spread over the molecule (Figure 11.4), with alternant positive and negative regions but globally, the electronic charge goes from the linker to the oxazolidine, especially when it is open.

Note that for DiBOX's in CF-CF and POF-POF, d_{CT} depends on the conformation of the linker. Indeed, the conformation affects the symmetry of the molecule and modulates the amplitude of d_{CT} . This is particularly true for DiBOX-Bt, where the bithiophene linker can adopt both *syn* and *anti* conformations. The *anti* conformation corresponds to a centrosymmetric structure, resulting in a $\Delta\mu_{ge}$ close to zero. On the other hand, the *syn* conformation leads to a structure displaying a C_{2v} -like symmetry. As a result, switching from the *anti* to the *syn* conformation of the bithiophene (θ_3 : $180^\circ \rightarrow 0^\circ$) results in an increase of the amplitude of $\Delta\mu_{ge}$ (Tables F.10 and F.12). This effect is further enhanced by the $0^\circ \rightarrow 180^\circ$ switching of the θ_2 - θ_4 torsion angles. It corresponds to a $\Delta\mu_{ge}$ increase from 0.056 D to 0.451 D for CF-CF and from 0.002 D to 1.379 D for POF-POF. Furthermore, the change of conformation of DiBOX-Bt from *anti* to *syn* in CF-CF and POF-POF is associated with a reduction of the intensity of the $S_0 \rightarrow S_1$ absorption. For CF-CF, the f_{ge} value associated with the $S_0 \rightarrow S_1$ excitation decreases from ~ 1.35 – 1.45 to ~ 1.15 – 1.20 , while f_{ge} of $S_0 \rightarrow S_2$ is ~ 0.30 – 0.40 when the bithiophene adopts a *syn* conformation. For POF-POF, the θ_2 - θ_4 torsion angles impact also f_{ge} of the two first excitations. For the second excitation, conformer 6 (θ_2 and θ_4 : *s-cis*) has $f_{ge} = 0.12$, conformer 4 (θ_2 : *s-trans* and θ_4 : *s-cis*) has $f_{ge} = 0.39$ and conformer 2 (θ_2 and θ_4 : *s-trans*) has $f_{ge} = 0.77$. For the form with the largest oscillator strength associated with the second excitation (POF-POF-2), this excitation was further analyzed. ΔE_{ge} is larger than the first excitation (3.22 eV vs 2.28 eV), the oscillator strength is relatively weak (0.77 vs 2.42), still its $\Delta\mu_{ge}$ is relatively high for this considered conformer (0.62 D), but its contribution to the SOS expression of β is expected to be small since this conformer only represents 18.5 % of the total population at 298.15 K (*vide infra*).

For DiBOX-BtO, the two EDOT units adopt an *anti* conformation due to the repulsion between these units, resulting in a small $\Delta\mu_{ge}$, especially for CF-CF (between 0.04 and 0.05 D) and POF-POF (between 0.03 and 0.12 D) (Tables F.13 and F.14). Since the linker of DiBOX-TtO possesses three thiophene-based units, it cannot display a centrosymmetric structure. The CF-CF and POF-POF forms correspond to V-shaped NLO-phores, with C_2 symmetry. The displacement of the electron cloud occurring along the first excitation is a displacement from

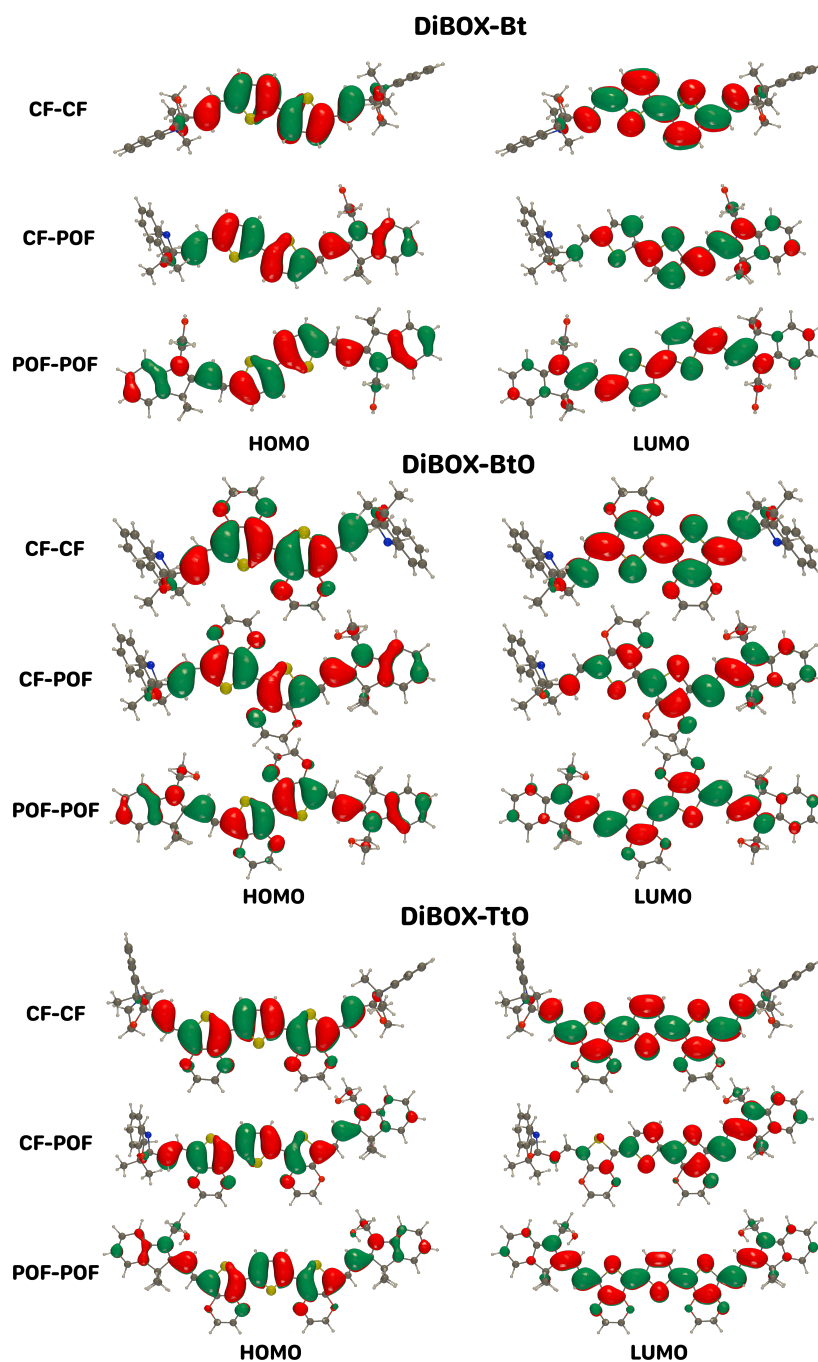


Figure 11.3: HOMO and LUMO of DiBOX's (in their most stable conformations), which mostly determine the first excitation of these compounds as evaluated at the M06-2X/6-311+G(d)/IEF-PCM (acetonitrile) level of theory. Green = negative, Red = positive, isovalue = 0.02 a.u..

the center of the linker to the BOX moieties. The amplitude of d_{CT} (and $\Delta\mu_{ge}$) can be enhanced by constraining the linker, e.g. switching from *anti* to *syn* conformation between the thiophene-based units (θ_3 - θ_4 : $180^\circ \rightarrow 0^\circ$). Indeed, for CF-CF and POF-POF $\Delta\mu_{ge}$ varies between 0.37 D and 1.58 D, and between 0.54 D and 1.47 D, as a function of the conformation of the linker (Tables F.16 and F.18). In the next paragraph, we present the first hyperpolarizability values for the different compounds in each of their three states and we see that these can be rationalized, to a given extent, by using the linear optical responses.

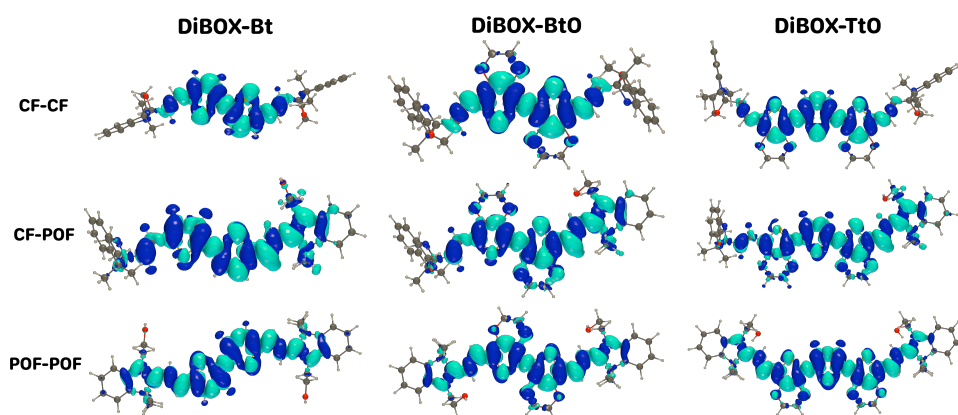


Figure 11.4: Variation of electron density associated with the first excitation for the three DiBOX's (in their most stable conformations) as evaluated at the M06-2X/6-311+G(d)/IEF-PCM (acetonitrile) level of approximation. Cyan: positive, Blue: negative, isovalue: 0.0004 a.u..

11.3.3 Nonlinear Optical Properties

The key second-order NLO properties of the DiBOX compounds, evaluated at TDDFT/M06-2X/6-311+G(d)/IEF-PCM (acetonitrile) level of approximation, are listed in Table 11.3. For all three DiBOX derivatives, to act as efficient NLO switches, the three different states should present very distinct β_{HRS} . For a large range of wavelengths, calculations reveal that the smallest β_{HRS} values are achieved with the fully closed forms where the EWG potential of the BOX is not expressed. The first BOX opening, leading to CF-POF from CF-CF induces a substantial increase of β_{HRS} , at least by a factor of 30 but often by two orders of magnitude. In this form exhibiting the largest $\Delta\mu_{ge}$, the second smallest $\Delta\mu_{ge}$ (yet close to the smallest one), and the smallest local BLA's, all systems present logically the largest β_{HRS} value. In this state, the systems present a dipolar character whatever the nature of the π -conjugated linker and a depolarization ratio (DR) close to 5 [DR = 4.79 (DiBOX-Bt), 4.67 (DiBOX-BtO), and 4.84 (DiBOX-TtO)].

As expected, the second BOX opening leading to POF-POF from CF-POF

generates a β_{HRS} decreases. As explained above, due to the (partial) centrosymmetry, the EWG characters of the indoleninium groups cancel each other, which prevent the systems to exhibit large β_{HRS} responses. This is especially the case of DiBOX-BtO where the *syn* form of the bis-EDOT linker has a vanishingly small MB weight (*vide infra*), resulting in a contrast ratio around 0.01 for the CF-POF to POF-POF transition (at $\lambda = 1300$ nm). On the other hand, in DiBOX-Bt V-shape structures are more stable (steric interactions between the thiophene groups are smaller than between the EDOT's) and in DiBOX-TtO V-shape structures are naturally present owing to the EDOT-Th-EDOT structure of linker, conducting to observe smaller contrast ratios, 0.14 and 0.12, respectively (again at $\lambda = 1300$ nm). The comparison of the β_{HRS} contrasts of the three DiBOX's is summarized in Figure 11.5.

While the CF-POF species present a strong dipolar character ($|\beta_{J=1}|$ larger than $|\beta_{J=3}|$ and $\rho < 1$) in all cases, the dipolar/octupolar character of the other forms (CF-CF and POF-POF) depends on the nature of the linker. For DiBOX-Bt, for which the linker can be centrosymmetric or not (in the latter case, when the bithiophene adopts a *syn* conformation, the molecule can adopt a C_{2v} -like symmetry), the DR amounts to 3.54 and 3.74 for CF-CF and POF-POF, respectively. These values correspond to a slight predominance of the octupolar character ($\rho \sim 1.2$). In both cases, this is due to the fact that some of the contributing conformers have a V-shape structure (DR around 3) while others have a 1-D NLOphore character (DR close to 5). As it was discussed in the sub-section 11.3.2, the change of conformation of the bithiophene from *anti* to *syn* results in an increase of $\Delta\mu_{ge}$. Since within the two-state approximation, β is directly proportional to $\Delta\mu_{ge}$, the β response of DiBOX-Bt increases upon the *anti* to *syn* switching, as illustrated in Figure 11.6 for the POF-POF using the unit sphere representation.⁴²

When the bithiophene is replaced by a bis-EDOT moiety as π -conjugated linker, the *syn* conformation is impeded due to steric hindrance between the two EDOT units. As consequence, POF-POF of DiBOX-BtO exhibits a very small β response but we can also notice a significantly smaller DR than in DiBOX-Bt (2.26 versus 3.76), "translating" an enhancement of the octupolar character of the system. An antagonist effect is observed on CF-CF state, though the β responses are small. Under this state, bis-EDOT exhibits a more pronounced dipolar character translated by a DR closer to 5 than DiBOX-Bt (3.74). This is explained by the existence for CF-CF state of non-centrosymmetric conformers with non-negligible MB weights.

Lastly, the CF-CF and POF-POF states of DiBOX-TtO have ρ values equal to 0.92 and 1.83, respectively. These values are similar than their analogs of DiBOX-BtO (0.82 and 2.20), but not necessarily for the same reasons. Indeed, many conformers contribute to the MB population of the CF-CF state and larger β_{HRS} responses are associated with DR values close to 5, *i.e.* typical of 1-D NLOphores (Conformers 5, 6, 12, 14, and 15, Table F.25). Then, for the fully open species, the octupolar character is always dominant ($1.8 < \rho < 2.1$) no

Table 11.3: β_{HRS} (10^3 a.u., static and dynamic fields at $\lambda = 1907$ nm, 1300 nm, and 1064 nm) as well as static β_{ZZZ} , β_{ZXX} , $|\beta_{J=1}|$, $|\beta_{J=3}|$ 10^3 a.u., DR, and ρ for the DiBOX's in their different forms as evaluated at the TDDFT/M06-2X/6-311+G(d)/IEF-PCM (acetonitrile) level of theory. These are averaged values calculated using the Boltzmann's populations at 298.15 K. The last column reports experimental data at 1300 nm.

		β_{HRS}				Exp.
		∞	1907 nm	1300 nm	1064 nm	1300 nm
DiBOX-Bt	CF-CF	0.4	0.3	0.4	0.5	4.1
	CF-POF	36.2	33.7	77.9	739.0	88.3
	POF-POF	9.5	6.6	11.0	41.5	47.3
DiBOX-BtO	CF-CF	1.3	1.2	1.7	2.6	
	CF-POF	37.4	33.4	95.9	466.0	
	POF-POF	0.4	0.3	1.3	1.6	
DiBOX-TtO	CF-CF	2.1	1.8	2.7	5.1	
	CF-POF	80.6	87.6	392.0	416.0	
	POF-POF	9.0	8.9	48.4	40.5	

		β_{ZZZ}	β_{ZXX}	DR	$ \beta_{J=1} $	$ \beta_{J=3} $	ρ
DiBOX-Bt	CF-CF	0.4	0.2	3.74	0.7	0.8	1.19
	CF-POF	32.9	15.0	4.79	66.5	57.4	0.86
	POF-POF	8.4	4.3	3.76	15.7	18.3	1.16
DiBOX-BtO	CF-CF	1.2	0.5	4.98	2.5	2.0	0.82
	CF-POF	34.0	15.7	4.67	68.5	61.2	0.89
	POF-POF	0.3	0.2	2.26	0.4	1.0	2.28
DiBOX-TtO	CF-CF	1.9	0.9	4.51	3.8	3.5	0.93
	CF-POF	73.4	33.4	4.84	150.0	127.0	0.85
	POF-POF	7.6	4.7	2.58	12.2	22.3	1.82

matter whether both θ_3 and θ_4 correspond to a anti conformation ($\sim 180^\circ$) or only one. Therefore, for DiBOX-Bt with the bithiophene in syn conformation and DiBOX-TtO with trans conformations of the thiophene-EDOT units, the POF-POF state corresponds to V-shaped (or Λ -shaped) A-D-A (attractor-donor-attractor) NLO-phores, with larger β responses than in DiBOX-BtO. In order to enhance the β responses of the POF-POF form, several strategies can be foreseen to constrain the conformation of the linker so that the EWG's draw a V-shape form. This can be achieved by using rigid linkers or, like in the present study,

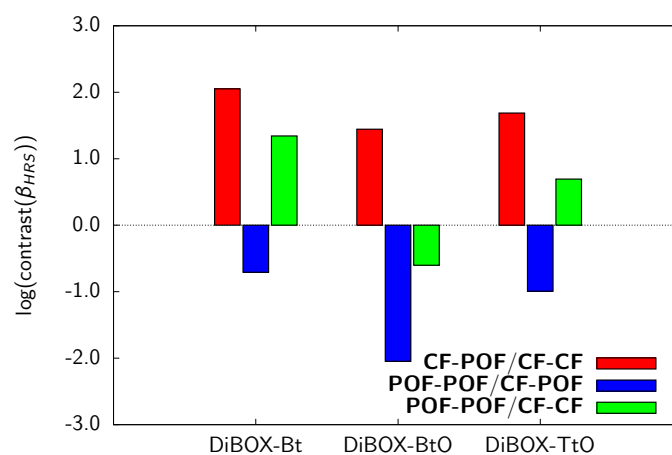


Figure 11.5: Effect of the linker on the β_{HRS} contrasts for an incident wavelength of 1907 nm, as calculated at the TDDFT/M06-2X/6-311+G(d)/IEF-PCM (acetonitrile) level of approximation.

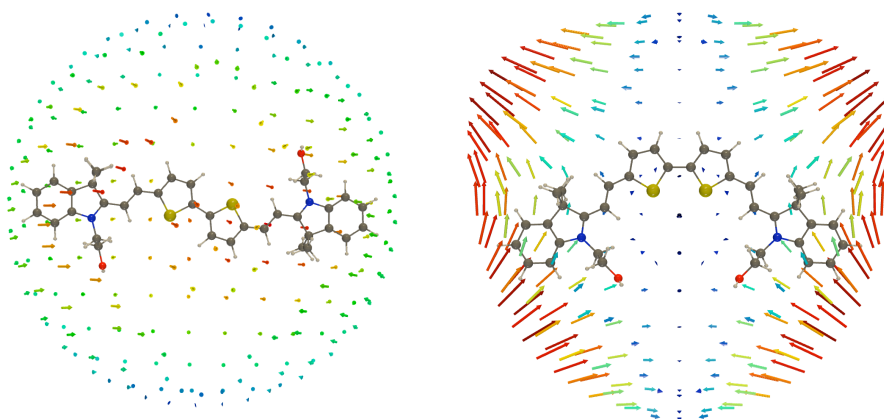


Figure 11.6: Progressive increase of the static β response of DiBOX-Bt in POOF-POF upon the C_i -like $\rightarrow C_{2v}$ -like change of symmetry. Left, conformer 1 ($\beta_{\text{HRS}} < 0.1 \times 10^3$ a.u.) and right: conformer 2 ($\beta_{\text{HRS}} < 13 \times 10^3$ a.u., DR = 2.31). A USR factor of 1×10^{-4} (5) Å a.u.⁻¹ was used for conformers 2 (1).

by combining an odd number of aromatic units adopting an *anti* conformation (DiBOX-TtO) or an even number of aromatic units allowing *syn* conformation (DiBOX-Bt).

The DiBOX-BT results were confronted to experimental data at 1300 nm (Table 11.3). For CF-POF the computational and the experimental procedures give responses of the same order of magnitude (78×10^3 a.u. versus 88×10^3 a.u., respectively). On the other hand, the computations underestimate strongly the

responses of the CF-CF and POF-POF. This leads to a general overestimation of the β_{HRS} contrasts. Nevertheless, as illustrated in Figure 11.7, the experimental trends are reproduced. Yet, as discussed in the Methods Section, measurements were only made for DiBOX-Bt because we did not succeed in synthesizing DiBOX-BtO while HRS measurements on DiBOX-TtO were hampered by huge two-photon fluorescence.

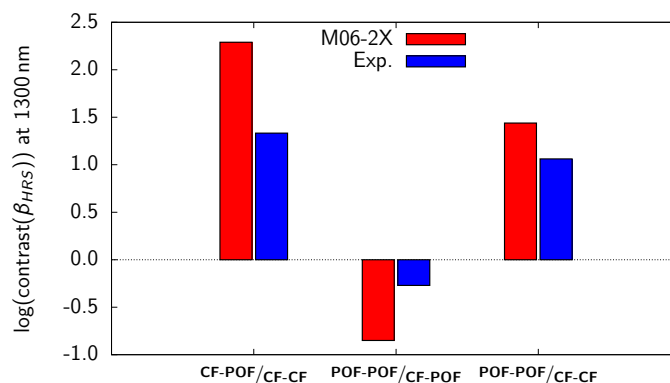


Figure 11.7: Contrasts of the β_{HRS} responses for the individual opening reactions of DiBOX-Bt as well as for the whole switching from the fully closed to the fully open forms, as represented by their $\log(\text{contrast}(\beta_{\text{HRS}}))$ at 1300 nm. The experimental results are compared to the calculations enacted at the TDDFT/M06-2X/6-311+G(d)/IEF-PCM (acetonitrile) level of theory.

11.4 Further Discussions, Conclusions, and Outlook

By adopting a multidisciplinary approach that combines synthesis, UV/vis absorption and hyper-Rayleigh scattering measurements, together with quantum chemical calculations performed at the DFT level it has been shown that DiBOX derivatives possessing two identical BOX units are efficient NLO switches. Since each BOX can be either closed or open, these systems can adopt three different states (CF-CF, CF-POF, and POF-POF). In these compounds, the acceptor character of the BOX units is unleashed when it opens to form an indoleninium unit, so that low excitation energies are obtained for the CF-POF and POF-POF states. Then, since non-centrosymmetry is required to achieve non-zero first hyperpolarizability, only the non-symmetric CF-POF state is expected to exhibit a substantial β response. Indeed, calculations show that the $\beta(\text{CF-POF})/\beta(\text{CF-CF})$ contrast is larger than 10, corresponding to the opening of the first BOX, while $\beta(\text{POF-POF})/\beta(\text{CF-POF})$ is smaller than 1/3 for the opening of the second. Still, these contrasts depend on the nature of the linker, which controls the extent of the π -electron delocalization but also the symmetry of the system. In particular, better contrasts are achieved when centro-symmetry can be

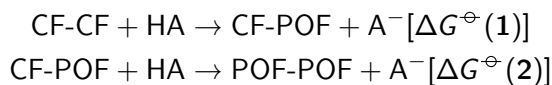
enforced for the fully open and fully closed states; in other words when these two states have zero or negligible first hyperpolarizabilities. From the DFT analysis, it is shown that such centro-symmetry can be enforced when the linker between the BOX's contains two EDOT units (in the case of the DiBOX-BtO compound) because they can adopt a *anti* centro-symmetric conformation while the *syn* conformation is prevented due to steric hindrance. On the other hand, when the central part of the linker is replaced by a bithiophene (DiBOX-Bt compound), there is a non-zero population of the *syn* conformation. Similarly, when the linker is an EDOT-thiophene-EDOT sequence, a V-shape conformation is the most stable, leading to β responses that are not negligible — though still smaller — with respect to those of the corresponding CF-POF state.

Calculations have further evidenced that the largest β_{HRS} responses (in the CF-POF state) are achieved with the largest linker, EDOT-thiophene-EDOT, owing to better push-pull π -delocalization effects, as shown by the largest $\Delta\mu_{ge}$ among the three DiBOX's (Table 11.2). Taking advantage of the two-state approximation (TSA)⁵² where $\beta \propto f_{ge}\Delta\mu_{ge}/\Delta E_{ge}^3$ one can derive the following relationship, assuming a dominant 1-D character for the static first hyperpolarizability:

$$\beta_{HRS} = \sqrt{\frac{6}{35}}\beta_{zzz} = 3.73 \frac{f_{ge}\Delta\mu_{ge}}{\Delta E_{ge}^3} \quad (11.1)$$

Then, using the MB averages of Table 11.2, the corresponding TSA β_{HRS} values of the CF-POF state of DiBOX-Bt, DiBOX-BtO, and DiBOX-TtO amount to 35×10^3 , 30×10^3 , and to 82×10^3 a.u., respectively. These values match nicely the full values given in Table 11.3.

To complement the experimental investigations of the successive switching steps, that can operate by the addition of acid or of oxidant, and therefore to analyze the control of the level of opening of these molecules, the Gibbs free energies were calculated for the following reactions (298.15 K in acetonitrile; the most stable conformer of each state was considered)



where HA is an acid and A^- its conjugate base. Besides the irreversibility of the reactions [$\Delta G^\ominus(1)$ and/or $(2) < 0$], in particular we concentrated on their difference, [$\Delta\Delta G^\ominus = \Delta G^\ominus(2) - \Delta G^\ominus(1)$], because a negative value would mean that the second opening is easier than the first one and therefore that the level of opening cannot be controlled, which would be in contradiction with experiment. For DiBOX-Bt, using the M06 XC functional, the 6-311G(d) basis set and IEFPCM, positive $\Delta G^\ominus(1)$ values of 61 and 31 kJ mol⁻¹ were calculated when HA is acetic acid and formic acid, demonstrating these are poor acids to trigger the transformation, respectively. On the other hand, with HClO₄ $\Delta G^\ominus(1)$ amounts to -81 kJ mol⁻¹ and to -15 kJ mol⁻¹ for trifluoroacetic acid (TFA), the acid that is often employed experimentally. We

then considered only TFA as acid and found that the opening reaction is facilitated in the case of DiBOX-BtO [$\Delta G^\ominus(1) = -59 \text{ kJ mol}^{-1}$] and DiBOX-TtO [$\Delta G^\ominus(1) = -50 \text{ kJ mol}^{-1}$]. Finally, calculations were performed, for DiBOX-Bt, at the ω B97X-D/6-311+G(d)/IEFPCM level and it was found that the second opening is less favorable [$\Delta G^\ominus(2) = -10 \text{ kJ mol}^{-1}$] than the first [$\Delta G^\ominus(1) = -24 \text{ kJ mol}^{-1}$] so that $\Delta\Delta G^\ominus(1) = 14 \text{ kJ mol}^{-1}$.

The opening by oxidation was then investigated (also by considering the most stable conformers). It consists of four steps (Scheme F.2): i) the oxidation of the CF to form a radical cation, ii) the C–O bond breaking (homolytic cleavage), iii) the reduction of the product, and iv) its protonation to obtain the POF. The rate determining step is the first one (Table F.28) so that the potential of oxidation versus the Fc/Fc⁺ electrode (ferrocene/ferrocenium system) was evaluated. In the case of DiBOX-Bt, M06/6-311G(d)/IEFPCM calculations predict that the oxidation potential amounts to 0.34 V for the CF-CF state while for CF-POF it amounts to 0.71 V. This larger value is attributed to the fact that it is more difficult to extract an electron from CF-POF, which bears a positive charge. In the case of DiBOX-BtO, the successive redox potentials versus the Fc/Fc⁺ electrode amount to -0.12 V and 0.39 V , evidencing the role of the better electron donating bis-EDOT with respect to bithiophene. These redox potentials further decrease in the case of the EDOT-thiophene-EDOT linker with values of -0.18 eV and 0.18 eV , highlighting now the role of a larger π -conjugated linker. Therefore, owing to the fact that the redox potentials are larger for the second opening and that they are sufficiently different (differences of 0.51 V for DiBOX-BtO, 0.37 V for DiBOX-Bt, and 0.36 V for DiBOX-TtO), the calculations also demonstrate that the level of opening can also be controlled by redox reactions. These results also evidence that this computational protocol can be employed to other, not yet synthesized, compounds in the process of designing new multi-state switches with a control of its successive transformations. The analysis of the spin density distribution of the oxidized species (Figure F.2) and the related atomic spin densities (Table F.29) demonstrates it is delocalized over the π -linker with large values on the vinyl C atom adjacent to the BOX (named CBOX, Scheme F.3). This atom is directly involved in the cleavage step and its larger atomic spin density in CF-POF^{•+} than CF-CF^{•+} accounts for the fact that the cleavage is less endergonic for the second opening than the first (Table F.28). Calculations further show that these C_{BOX} spin densities are similar for DiBOX-BtO but smaller for DiBOX-TtO, where the spin density is delocalized over three rings rather than two.

The general good agreement between the calculations on DiBOX-Bt and experiment demonstrates that the same approach can be used to study other multi-state multi-addressable BOX derivatives and therefore to help selecting the best ones for the synthesis. Current directions of investigation encompass the study of i) DiBOX with asymmetric linkers and ii) TriBOX and TetraBOX derivatives with symmetric or asymmetric linkers in order to improve the control of the switching process as well as to maximize the linear and nonlinear optical prop-

erty contrasts. Different functionalization patterns can also be investigated.⁵³ Among these, the use of linkers able to chelate transition metals would open the field considerably.^{54–56} Though it does not affect the design strategy, from the methodological and computational viewpoint, it is important to explain why the predicted β_{HRS} values of the CF-CF and POF-POF states of DiBOX-Bt are underestimated with respect to experiment. This could require using sequential Molecular Dynamics then Quantum Chemistry approaches like done recently for ion pairs and chromophores embedded in lipid bilayers.^{57,58}

Acknowledgments

J.Q. thanks the "Actions de Recherche Concertées" (ARC) de la Direction générale de l'Enseignement non obligatoire et de la Recherche scientifique - Direction de la Recherche scientifique - Communauté française de Belgique, under convention No. 15/20-068 for his PhD grant. This work, carried out within the MORIARTY project, has benefited from financial support from Wallonie-Bruxelles International (WBI), from the Fund for Scientific Research (F.R.S.-FNRS), from the French Ministry of Foreign and European Affairs, and from the Ministry of Higher Education and Research in the frame of the Hubert Curien partnerships. The calculations were performed on the computers of the Consortium des Équipements de Calcul Intensif (CÉCI, <http://www.cec-hpc.be>) and particularly those of the Technological Platform of High-Performance Computing, for which the authors gratefully acknowledge the financial support of the FNRS-FRFC, of the Walloon Region, and of the University of Namur (Conventions No. 2.5020.11, GEQ U.G006.15, 1610468, and RW/GEQ2016), as well as on zenobe, the Tier-1 facility of the Walloon Region (Convention 1117545).

Bibliography

- (1) Bissell, R. A.; Córdova, E.; Kaifer, A. E.; Stoddart, J. F. A chemically and electrochemically switchable molecular shuttle. *Nature* **1994**, *369*, 133–137, DOI: 10.1038/369133a0.
- (2) De Silva, A. P.; Vance, T. P.; West, M. E. S.; Wright, G. D. Bright Molecules with Sense, Logic, Numeracy and Utility. *Org. Biomol. Chem.* **2008**, *6*, 2468, DOI: 10.1039/b802963f.
- (3) *Molecular Switches*; Feringa, B. L., Browne, W. R., Eds.; Wiley-VCH Verlag GmbH & Co. KGaA: Weinheim, Germany, 2011, DOI: 10.1002/9783527634408.
- (4) Andréasson, J.; Pischel, U. Molecules with a Sense of Logic: A Progress Report. *Chem. Soc. Rev.* **2015**, *44*, 1053–1069, DOI: 10.1039/C4CS00342J.

- (5) Muller, P. Glossary of terms used in physical organic chemistry (IUPAC Recommendations 1994). *Pure Appl. Chem.* **1994**, *66*, 1077–1184, DOI: 10.1351/pac199466051077.
- (6) Bamfield, P. In *Chromic Phenom.* Royal Society of Chemistry: Cambridge, 2010; Chapter 1, pp 9–140, DOI: 10.1039/9781849731034-00009.
- (7) Kassem, S.; van Leeuwen, T.; Lubbe, A. S.; Wilson, M. R.; Feringa, B. L.; Leigh, D. A. Artificial molecular motors. *Chem. Soc. Rev.* **2017**, *46*, 2592–2621, DOI: 10.1039/C7CS00245A.
- (8) McConnell, A. J.; Wood, C. S.; Neelakandan, P. P.; Nitschke, J. R. Stimuli-Responsive Metal–Ligand Assemblies. *Chem. Rev.* **2015**, *115*, 7729–7793, DOI: 10.1021/cr500632f.
- (9) Coe, B. J. Molecular Materials Possessing Switchable Quadratic Nonlinear Optical Properties. *Chem. - A Eur. J.* **1999**, *5*, 2464–2471, DOI: 10.1002/(SICI)1521-3765(19990903)5:9<2464::AID-CHEM2464>3.0.CO;2-L.
- (10) Delaire, J. A.; Nakatani, K. Linear and Nonlinear Optical Properties of Photochromic Molecules and Materials. *Chem. Rev.* **2000**, *100*, 1817–1846, DOI: 10.1021/cr980078m.
- (11) Castet, F.; Rodriguez, V.; Pozzo, J.-L.; Ducasse, L.; Plaquet, A.; Champagne, B. Design and Characterization of Molecular Nonlinear Optical Switches. *Acc. Chem. Res.* **2013**, *46*, 2656–2665, DOI: 10.1021/ar4000955.
- (12) Mançois, F.; Sanguinet, L.; Pozzo, J. L.; Guillaume, M.; Champagne, B.; Rodriguez, V.; Adamietz, F.; Ducasse, L.; Castet, F. Acido-triggered nonlinear optical switches: Benzazolo-oxazolidines. *J. Phys. Chem. B* **2007**, *111*, 9795–9802, DOI: 10.1021/jp073386.
- (13) Mançois, F.; Pozzo, J.-L.; Pan, J.; Adamietz, F.; Rodriguez, V.; Ducasse, L.; Castet, F.; Plaquet, A.; Champagne, B. Two-Way Molecular Switches with Large Nonlinear Optical Contrast. *Chem. Eur. J.* **2009**, *15*, 2560, DOI: 10.1002/chem.200801967.
- (14) Pielak, K.; Bondu, F.; Sanguinet, L.; Rodriguez, V.; Champagne, B.; Castet, F. Second-Order Nonlinear Optical Properties of Multiaddressable Indolinooxazolidine Derivatives: Joint Computational and Hyper-Rayleigh Scattering Investigations. *J. Phys. Chem. C* **2017**, *121*, 1851–1860, DOI: 10.1021/acs.jpcc.6b11082.
- (15) Szalóki, G.; Sanguinet, L. In *Photon-Working Switch*. Springer Japan: Tokyo, 2017, pp 69–91, DOI: 10.1007/978-4-431-56544-4_3.

- (16) Sanguinet, L.; Pozzo, J.-L.; Rodriguez, V.; Adamietz, F.; Castet, F.; Ducasse, L.; Champagne, B. Acido- and Phototriggered NLO Properties Enhancement. *J. Phys. Chem. B* **2005**, *109*, 11139–11150, DOI: 10.1021/jp0442450.
- (17) Bondu, F.; Hadji, R.; Szalóki, G.; Alévêque, O.; Sanguinet, L.; Pozzo, J.-L.; Cavagnat, D.; Buffeteau, T.; Rodriguez, V. Huge Electro-/Photo-/Acidoinduced Second-Order Nonlinear Contrasts From Multiaddressable Indolinoxazolodine. *J. Phys. Chem. B* **2015**, *119*, 6758–6765, DOI: 10.1021/acs.jpcc.5b03070.
- (18) Hadji, R.; Szalóki, G.; Alévêque, O.; Levillain, E.; Sanguinet, L. The Stepwise oxidation of Indolino[2,1-b]oxazolidine Derivatives. *J. Electroanal. Chem.* **2015**, *749*, 1–9, DOI: 10.1016/j.jelechem.2015.04.032.
- (19) Szalóki, G.; Alévêque, O.; Pozzo, J.-L.; Hadji, R.; Levillain, E.; Sanguinet, L. Indolinoxazolodine: A Versatile Switchable Unit. *J. Phys. Chem. B* **2015**, *119*, 307–315, DOI: 10.1021/jp511825f.
- (20) Houbrechts, S.; Clays, K.; Persoons, A.; Pikramenou, Z.; Lehn, J.-M. Hyper-Rayleigh scattering investigation of nitrobenzyl pyridine model compounds for optical modulation of the hyperpolarisability. *Chem. Phys. Lett.* **1996**, *258*, 485–489, DOI: 10.1016/0009-2614(96)00676-8.
- (21) Beaujean, P.; Bondu, F.; Plaquet, A.; Garcia-Amorós, J.; Cusido, J.; Raymo, F. M.; Castet, F.; Rodriguez, V.; Champagne, B. Oxazines: a New Class of Second-Order Nonlinear Optical Switches. *J. Am. Chem. Soc.* **2016**, *138*, 5052–5062.
- (22) Sevez, G.; Gan, J.; Delbaere, S.; Vermeersch, G.; Sanguinet, L.; Levillain, E.; Pozzo, J.-L. Photochromic Performance of a Dithienylethene-Indolinoxazolodine Hybrid. *Photochem. Photobiol. Sci.* **2010**, *9*, 131.
- (23) Szalóki, G.; Sevez, G.; Berthet, J.; Pozzo, J.-L.; Delbaere, S. A Simple Molecule-Based Octastate Switch. *J. Am. Chem. Soc.* **2014**, *136*, 13510–13513, DOI: 10.1021/ja506320j.
- (24) Bondu, F.; Quertinmont, J.; Rodriguez, V.; Pozzo, J.-L.; Plaquet, A.; Champagne, B.; Castet, F. Second-Order Nonlinear Optical Properties of a Dithienylethene-Indolinoxazolodine Hybrid: a Joint Experimental and Theoretical Investigation. *Chem. Eur. J.* **2015**, *21*, 18749–18757.
- (25) Sanguinet, L.; Berthet, J.; Szalóki, G.; Alévêque, O.; Pozzo, J.-L.; Delbaere, S. 13 metastable states arising from a simple multifunctional unimolecular system. *Dye. Pigment.* **2017**, *137*, 490–498, DOI: 10.1016/j.dyepig.2016.10.027.
- (26) Aidibi, Y.; Guerrin, C.; Alévêque, O.; Leriche, P.; Delbaere, S.; Sanguinet, L. BT-2-BOX: An Assembly toward Multimodal and Multilevel Molecular System Simple as a Breeze. *J. Phys. Chem. C* **2019**, *123*, 11823–11832, DOI: 10.1021/acs.jpcc.9b00546.

- (27) Guerrin, C.; Aidibi, Y.; Sanguinet, L.; Leriche, P.; Aloise, S.; Orio, M.; Delbaere, S. When Light and Acid Play Tic-Tac-Toe with a Nine-State Molecular Switch. *J. Am. Chem. Soc.* **2019**, *141*, 19151–19160, DOI: 10.1021/jacs.9b11048.
- (28) Szalóki, G.; Sanguinet, L. Silica-Mediated Synthesis of Indolinoxazolidine-Based Molecular Switches. *J. Org. Chem.* **2015**, *80*, 3949–3956, DOI: 10.1021/acs.joc.5b00282.
- (29) Leriche, P.; Turbiez, M.; Monroche, V.; Frère, P.; Blanchard, P.; Skabara, P. J.; Roncali, J. Strong π -electron donors based on a self-rigidified 2,2'-bi(3,4-ethylenedioxy)thiophene-tetrathiafulvalene hybrid π -conjugated system. *Tetrahedron Lett.* **2003**, *44*, 649–652, DOI: 10.1016/S0040-4039(02)02702-8.
- (30) Imae, I.; Sagawa, H.; Mashima, T.; Komaguchi, K.; Ooyama, Y.; Harima, Y. Synthesis of Soluble Polythiophene Partially Containing 3,4-Ethylenedioxythiophene and 3-Hexylthiophene by Polycondensation. *Open J. Polym. Chem.* **2014**, *04*, 83–93, DOI: 10.4236/ojpchem.2014.43010.
- (31) Castet, F.; Bogdan, E.; Plaquet, A.; Ducasse, L.; Champagne, B.; Rodriguez, V. Reference Molecules for Nonlinear Optics: A Joint Experimental and Theoretical Investigation. *J. Chem. Phys.* **2012**, *136*, 024506, DOI: 10.1063/1.3675848.
- (32) Zhao, Y.; Truhlar, D. G. The M06 Suite of Density Functionals for Main Group Thermochemistry, Thermochemical Kinetics, Noncovalent Interactions, Excited States, and Transition Elements: Two New Functionals and Systematic Testing of Four M06-Class Functionals and 12 Other Function. *Theor. Chem. Acc.* **2008**, *120*, 215, DOI: 10.1007/s00214-007-0310-x.
- (33) Tomasi, J.; Mennucci, B.; Cammi, R. Quantum Mechanical Continuum Solvation Models. *Chem. Rev.* **2005**, *105*, 2999–3094, DOI: 10.1021/cr9904009.
- (34) Scalmani, G.; Frisch, M. J.; Mennucci, B.; Tomasi, J.; Cammi, R.; Barone, V. Geometries and Properties of Excited States in the Gas Phase and in Solution: Theory and Application of a Time-Dependent Density Functional Theory Polarizable Continuum Model. *J. Chem. Phys.* **2006**, *124*, 094107, DOI: 10.1063/1.2173258.
- (35) Le Bahers, T.; Adamo, C.; Ciofini, I. A Qualitative Index of Spatial Extent in Charge-Transfer Excitations. *J. Chem. Theory Comput.* **2011**, *7*, 2498–2506, DOI: 10.1021/ct200308m.
- (36) Van Gisbergen, S. J. A.; Snijders, J. G.; Baerends, E. J. Calculating Frequency-Dependent Hyperpolarizabilities using Time-Dependent Density Functional Theory. *J. Chem. Phys.* **1998**, *109*, 10644–10656, DOI: 10.1063/1.477762.

- (37) Helgaker, T.; Coriani, S.; Jørgensen, P.; Kristensen, K.; Olsen, J.; Ruud, K. Recent Advances in Wave Function-Based Methods of Molecular-Property Calculations. *Chem. Rev.* **2012**, *112*, 543–631, DOI: 10.1021/cr2002239.
- (38) Verbiest, T.; Clays, K.; Rodriguez, V., *Second-Order Nonlinear Optical Characterization Techniques: An Introduction*; CRC Press: New York, 2009.
- (39) Bersohn, R.; Pao, Y.-H.; Frisch, H. L. Double-Quantum Light Scattering by Molecules. *J. Chem. Phys.* **1966**, *45*, 3184, DOI: 10.1063/1.1728092.
- (40) Brasselet, S.; Zyss, J. Multipolar Molecules and Multipolar Fields: Probing and Controlling the Tensorial Nature of Nonlinear Molecular Media. *J. Opt. Soc. Am. B* **1998**, *15*, 257, DOI: 10.1364/JOSAB.15.000257.
- (41) Rodriguez, V.; Grondin, J.; Adamietz, F.; Danten, Y. Local Structure in Ionic Liquids Investigated by Hyper-Rayleigh Scattering. *J. Phys. Chem. B* **2010**, *114*, 15057–15065, DOI: 10.1021/jp107165k.
- (42) Tuer, A.; Krouglov, S.; Cisek, R.; Tokarz, D.; Barzda, V. Three-Dimensional Visualization of the First Hyperpolarizability Tensor. *J. Comput. Chem.* **2011**, *32*, 1128, DOI: 10.1002/jcc.21694.
- (43) Liégeois, V.; UNamur DrawMol, 2018.
- (44) De Wergifosse, M.; Champagne, B. Electron Correlation Effects on the First Hyperpolarizability of Push–Pull π -Conjugated Systems. *J. Chem. Phys.* **2011**, *134*, 074113, DOI: 10.1063/1.3549814.
- (45) Johnson, L. E.; Dalton, L. R.; Robinson, B. H. Optimizing Calculations of Electronic Excitations and Relative Hyperpolarizabilities of Electrooptic Chromophores. *Acc. Chem. Res.* **2014**, *47*, 3258–3265, DOI: 10.1021/ar5000727.
- (46) Garrett, K.; Sosa Vazquez, X.; Egri, S. B.; Wilmer, J.; Johnson, L. E.; Robinson, B. H.; Isborn, C. M. Optimum Exchange for Calculation of Excitation Energies and Hyperpolarizabilities of Organic Electro-optic Chromophores. *J. Chem. Theory Comput.* **2014**, *10*, 3821–3831, DOI: 10.1021/ct500528z.
- (47) Champagne, B.; Beaujean, P.; de Wergifosse, M.; Cardenuto, M. H.; Liégeois, V.; Castet, F. In *Front. Quantum Chem.* Springer Singapore: Singapore, 2018, pp 117–138, DOI: 10.1007/978-981-10-5651-2_6.
- (48) Lescos, L.; Sitkiewicz, S. P.; Beaujean, P.; Blanchard-Desce, M.; Champagne, B.; Matito, E.; Castet, F. Performance of DFT Functionals for Calculating the Second-Order Nonlinear Optical Properties of Dipolar Merocyanines. *Phys. Chem. Chem. Phys.* **2020**, *22*, 16579–16594, DOI: 10.1039/D0CP02992K.

- (49) Frisch, M. J. et al. Gaussian~16 Revision B.01, Gaussian Inc. Wallingford CT, 2016.
- (50) Blanchard, P.; Cravino, A.; Levillain, E. In *Handb. Thiophene-Based Mater.* Perepichka, I. F., Perepichka, D. F., Eds.; John Wiley & Sons, Ltd: Chichester, UK, 2009; Chapter 9, pp 419–453, DOI: 10.1002/9780470745533.ch9.
- (51) Chevallier, F.; Charlot, M.; Mongin, F.; Champagne, B.; Franz, E.; Clays, K.; Blanchard-Desce, M. Synthetic, Optical and Theoretical Study of Alternating Ethylenedioxythiophene-Pyridine Oligomers: Evolution from Planar Conjugated to Helicoidal Structure towards a Chiral Configuration. *ChemPhysChem* **2016**, *17*, 4090–4101, DOI: 10.1002/cphc.201601057.
- (52) Oudar, J. L.; Chemla, D. S. Hyperpolarizabilities of the Nitroanilines and their Relations to the Excited State Dipole Moment. *J. Chem. Phys.* **1977**, *66*, 2664, DOI: 10.1063/1.434213.
- (53) Bureš, F. Fundamental Aspects of Property Tuning in Push–Pull Molecules. *RSC Adv.* **2014**, *4*, 58826–58851, DOI: 10.1039/C4RA11264D.
- (54) Yam, V. W.-W.; Ko, C.-C.; Zhu, N. Photochromic and Luminescence Switching Properties of a Versatile Diarylethene-Containing 1,10-Phenanthroline Ligand and Its Rhenium(I) Complex. *J. Am. Chem. Soc.* **2004**, *126*, 12734–12735, DOI: 10.1021/ja047446q.
- (55) Guerchais, V.; Ordroneau, L.; Le Bozec, H. Recent Developments in the Field of Metal Complexes Containing Photochromic Ligands: Modulation of Linear and Nonlinear Optical Properties. *Coord. Chem. Rev.* **2010**, *254*, 2533–2545, DOI: 10.1016/j.ccr.2010.01.013.
- (56) Pielak, K.; Bondu, F.; Sanguinet, L.; Rodriguez, V.; Castet, F.; Champagne, B. Acido-Triggered Switching of the Second-Order Nonlinear Optical Properties of a Ferrocenyl-Containing Indolino-Oxazolidine Derivative. *Dye. Pigment.* **2019**, *160*, 641–646, DOI: 10.1016/j.dyepig.2018.07.007.
- (57) Pielak, K.; Tonnelé, C.; Sanguinet, L.; Cariati, E.; Righetto, S.; Muccioli, L.; Castet, F.; Champagne, B. Dynamical Behavior and Second Harmonic Generation Responses in Acido-Triggered Molecular Switches. *J. Phys. Chem. C* **2018**, *122*, 26160–26168, DOI: 10.1021/acs.jpcc.8b08697.
- (58) Bouquiaux, C.; Tonnelé, C.; Castet, F.; Champagne, B. Second-Order Nonlinear Optical Properties of an Amphiphilic Dye Embedded in a Lipid Bilayer. A Combined Molecular Dynamics–Quantum Chemistry Study. *J. Phys. Chem. B* **2020**, *124*, 2101–2109, DOI: 10.1021/acs.jpcc.9b10988.

SUMMARY, CONCLUSIONS, AND PERSPECTIVES

In my PhD thesis I have used quantum chemistry methods to study molecular switches both in solution and in the crystalline state. A large part has been dedicated to a crystalline N-salicylideneaniline (anil) switch that can tautomerize between an enol (E) and a keto (K) form, see Chapters 3 to 7. These are contributions of a larger research project: the ARC CONTRAST, that aims at using co-crystallization to improve thermo- and photo-chromism in crystals. My contribution to the ARC project was to use quantum chemistry to study co-crystals and their properties in order to enhance our understanding of a rather subtle field: co-crystallization. Owing to the strong relationship between the geometry of a molecule and its properties, Chapters 3 and 4 focus on the selection of reliable approaches to optimize both the molecular geometry and the unit cell parameters of three anils. The method chosen is periodic boundary conditions (PBC) density functional theory (DFT) as implemented in the CRYSTAL14 package. There exist many other programs that allow PBC DFT calculations, but CRYSTAL uses periodic Gaussian-type orbitals (GTOs) that are particularly appropriate for systems with localized wave functions such as molecules (molecular crystals), by opposition to metals or semiconductors. Then, since DFT is used, the issue turns out to be the choice of exchange-correlation functional (XCF). A broad selection of XCFs was used and showed that the hybrid versions of the PBEsol XCF and ω B97X provide results in agreement with single-crystal X-ray diffraction data for the molecular geometries, unit cell parameters, as well as the relative stabilities of the E and K forms (Chapter 3). Furthermore, the addition of empirical dispersion corrections was shown to be detrimental for those functionals while somewhat improving the results of other commonly used functionals such as PBE0 and B3LYP (Chapter 4).

These two chapters paved the way to the next chapter, focusing on co-crystals (Chapter 5), where several co-crystals of an anil switch (namely, PYV3) are investigated. Two types of co-crystals have been obtained by our collaborators within the ARC CONTRAST: hydrogen bond (H-bond) co-crystals (with coformers such as succinic acid, SA) and halogen bond (X-bond) co-crystals (with coformers such as 1,4-diiodotetrafluorobenzene). The inclusion of coform-

ers in the unit cell has very significant effects, most noticeably on the E/K equilibrium. Indeed, for all co-crystals except one, the more stable enol form is even more favored. This was linked to the stabilization of the enol form while the effects on the keto form are smaller. The observed (de)stabilizations are related to changes in the geometry of PYV3 in the co-crystals compared to the pure PYV3 crystal. Those geometrical changes are subtle and are not systematic, *i.e.* all H-bond co-crystals do not display the same changes. On the other hand, in the case of the co-crystal with sulfonyldiphenol (SDP), the keto form is the most stable of the two forms, just like observed experimentally. Overall, this study shows the essential role of quantum chemistry in deciphering the impact of co-crystallization. Indeed, whatever method (X-ray or neutron diffraction) is used to resolve the molecular structures they are bound by the laws of thermodynamics, which means that even at low or ultra-low temperatures, crystalline switches are probably not in a pure form, *e.g.* for anils, there might always be some keto molecules in the mainly enol crystal. In that respect, computational chemistry has a full control of which form of the switch is being studied. This study also calls for enlarging the set of crystals and co-crystals (not only anils, but also other families of switches) to investigate, in a multidisciplinary frame, the relationships between molecular and crystal structures.

Thanks to these prerequisite structural investigations, properties of the crystals with pure enol or keto forms have been predicted. First, NMR isotropic magnetic shielding constants have been calculated to support solid state magic angle spinning NMR experiments in view of determining the E/K ratio. This is the topic of Chapter 6 where elaborating a multi-scale method, the isotropic shieldings of the pure enol and keto forms of the PYV3 crystal and of two of its co-crystals (with the dihydroxybiphenyl, DHBP, and SDP coformers) are computed. This multi-scale method relies firstly on the optimization of the crystal structure and the calculation of the atomic charges using PBC DFT (with the PBEsol0 XCF and the 6-31G(d,p) basis set) and, secondly, on the evaluation of the isotropic shielding constants of selected clusters in an embedding of point-charges fitted to reproduce the crystal field potential. This embedding has been generated by the Ewald program while the shielding tensors are calculated with a well-established method: B3LYP/6-311+G(2d,p) with the gauge-independent atomic orbital method.

A strength of quantum chemistry methods is their ability to decompose a phenomenon. This is illustrated in the last chapter contribution to the ARC CONTRAST dealing with the effects of co-crystallization on the optical properties of PYV3 (Chapter 7). To do so, the same multi-scale strategy as for calculating the NMR isotropic shieldings has been followed to compute the excitation energies and oscillator strengths of PYV3 and its co-crystals. While the established geometry optimization method has been used, the optical properties have been computed with the coupled cluster approximate doubles (CC2) model in combination with the resolution of the identity approximation and the def2-TZVPD basis set. Moreover, the performance of this method has been challenged and

substantiated in a few cases by the coupled cluster singles and doubles (CCSD) method and larger basis sets. Using these calculations, co-crystallization is shown to have two types of effects on the UV/Vis absorption spectra: *indirect* effects coming from the changes of geometry and *direct* effects originating from the polarizations created either by the presence of the neighboring conformer(s) or by the crystal field. The former show that modifications of the π -conjugation (which relates to specific torsion angles between the two aromatic parts of the chromophore) leads to decreasing or increasing of the excitation energies. The latter effects are antagonistic. Indeed, while adding the coformer in the quantum chemical calculations leads to a decrease of the excitation energies, the inclusion of the crystal field increases them. Note that the coformer only polarizes the chromophore since the natural transition orbitals of the excited states (the set of orbitals that best characterize the electronic transitions of an excited state) are all found to be located on the anil.

As shown by these studies and particularly by Chapter 7 focusing on the UV/vis absorption spectra, the effects of co-crystallization are complex, which makes it an amazing and promising tool to modify the properties of crystals. In particular, molecular switches are prime systems to apply co-crystallization techniques, as the various forms of the switch can be affected in different manners by the coformers, thus adding a new dimension for tuning crystals properties. On the topic of the anils, there remain many properties to study, such as the kinetics of the enol to keto transformation (thermochromism) or the excited states dynamics (photochromism). Indeed, during the ARC CONTRAST, it was showed that the co-crystal of PYV3 with SA is photochromic while the pure PYV3 crystal is not. The same multi-scale model could therefore be applied to study the excited states and finding out which parameter or which driving force enables the photoswitching in the co-crystal with SA.

These investigations on anil crystals and co-crystals have stimulated a study on covalent organic frameworks (COFs), multi-state switches. These are built from stacked 2D layers of tris(N-salicylideneaniline) units linked together by various aromatic units, forming hexagonal channels. Besides structural and energy aspects of the successive switching of keto functions into enol functions (in this case the keto forms are more stable than the enol ones), this study has focused on their linear and nonlinear optical (NLO) properties by adopting PBC approaches to evaluate both the structural and optical properties. Calculations demonstrate that these COFs exhibit promising second-order NLO responses ($\chi^{(2)}$, the second-order NLO susceptibility) and that these NLO responses can be modulated as a function of the successive enol/keto tautomerisms, leading to efficient solid-state second-order NLO switches. They further highlight the key role of symmetry, *i.e.* of the distribution of enol and keto functions in the unit cell, on the $\chi^{(2)}$ values as well as on their dipolar/octupolar character. This proof-of-concept calls for further investigations on a broader variety of COFs, combining stronger electron donor and acceptor units. Moreover, hopefully, this work will motivate both the synthesis of new anil-based COFs and the measurement of

their linear and nonlinear optical properties.

The three last Chapters of my PhD thesis take place "in solution". First, the equilibrium constants of two families of molecular switches, spiropyrans and anils, are characterized using a composite scheme of various post Hartree-Fock methods, namely second-order Møller-Plesset (MP2), coupled cluster singles, doubles, and perturbative triples (CCSD(T)), combined with efficient approximations such as the resolution of the identity and pair of natural orbitals. These calculations, which also account for the effects of the solvent using the polarizable continuum model, provide accurate ΔG^\ominus of transformation for representative molecular switches, evidencing that solvent and thermal effects can influence the sign of ΔG^\ominus and should therefore be taken into account. A future challenge for theoretical chemistry is therefore to develop the necessary tools to extend such high-level calculations to crystals and co-crystals.

Molecular-based approaches have also been used to study two types of multi-state molecular switches. The first one is composed of three *different* switching units, a benzazolo-oxazolidine (BOX) and a dithienylethene (DTE) linked by an ethylene group, thus achieving $2^3 = 8$ states. The chemical shifts of the various conformations of the 8 states have been computed in order to interpret experimental data, highlighting the presence of rather unexpected structures, *i.e.* folded conformers that make photocyclization less efficient. Then, switches composed of two *identical* BOX units linked by three different thiophene-containing linkers have been investigated using (time-dependent) DFT. These systems can adopt three states where either i) both BOX units are closed (CF-CF), or ii) one of these is open and protonated (CF-POF), or iii) both are open and protonated (POF-POF). Calculations show that the first opening leads to the formation of a push-pull π -conjugated segment, built from the π -donating linker and the indoleninium acceptor, exhibiting a huge increase of the first hyperpolarizability β and a bathochromic shift with respect to the fully closed form. Then, upon opening the second BOX, the bathochromic shift is much reduced and β drops considerably because of symmetry reasons. The role of the linker on the molecular geometry and symmetry, and subsequently on the β amplitude has been unraveled. Moreover, though the BOXs are chemically equivalent, calculations support, for the three derivatives, the possibility to control their level of opening when triggered by pH variation or by application of a redox potential.

Although these three *molecular* chapters deal with different compounds and properties, they confirm the key role of molecular geometries, including their shape and symmetry. While in the solid state, the molecular degrees of freedom are mostly frozen, in solution, they are free to move and adopt different conformations. Over times, quantum chemistry codes and super-computers have evolved and improved to the point where the study of any property should require first probing of the conformational space. The next steps will eventually be micro-solvation and then quantum dynamics, which will provide more accurate descriptions of the interactions with solvent molecules and thus better reflect reality.

CHAPTER A

ASSESSING DENSITY FUNCTIONAL
THEORY APPROACHES FOR
PREDICTING THE STRUCTURE
AND RELATIVE ENERGY OF
SALICYLIDENEANILINE MOLECULAR
SWITCHES IN THE SOLID STATE.
SUPPORTING INFORMATION.

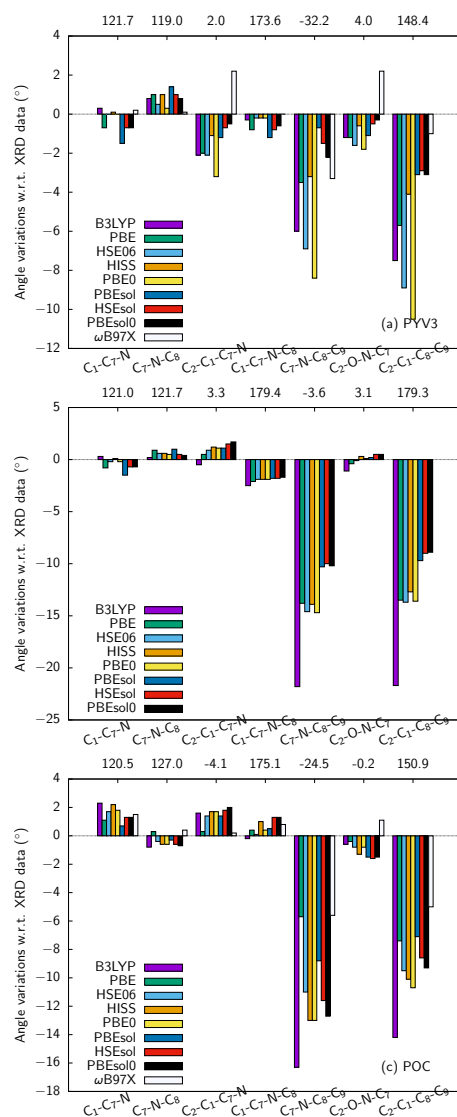


Figure A.1: Deviations of key angles optimized with different XC functionals with respect to XRD data. The XRD values are given on the top of each figure, $\Delta = a(\text{DFT}) - a(\text{XRD})$. The 6-31G(d,p) basis set and full optimization scheme (F-OPT) were employed for all calculations.

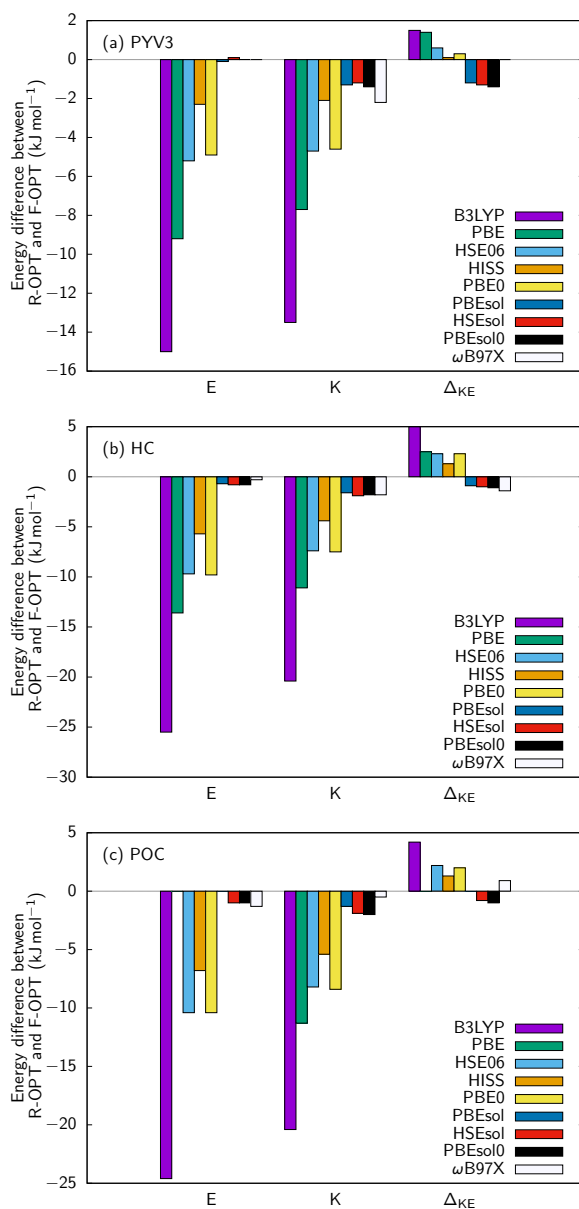


Figure A.2: Energy difference between the restricted (R-OPT) and full (F-OPT) optimization schemes [$\Delta X = \text{F-OPT}/X - \text{R-OPT}/X$, where X is the energy of the enol or keto forms, or the K – E energy difference]. The 6-31G(d,p) basis set was employed for all calculations.

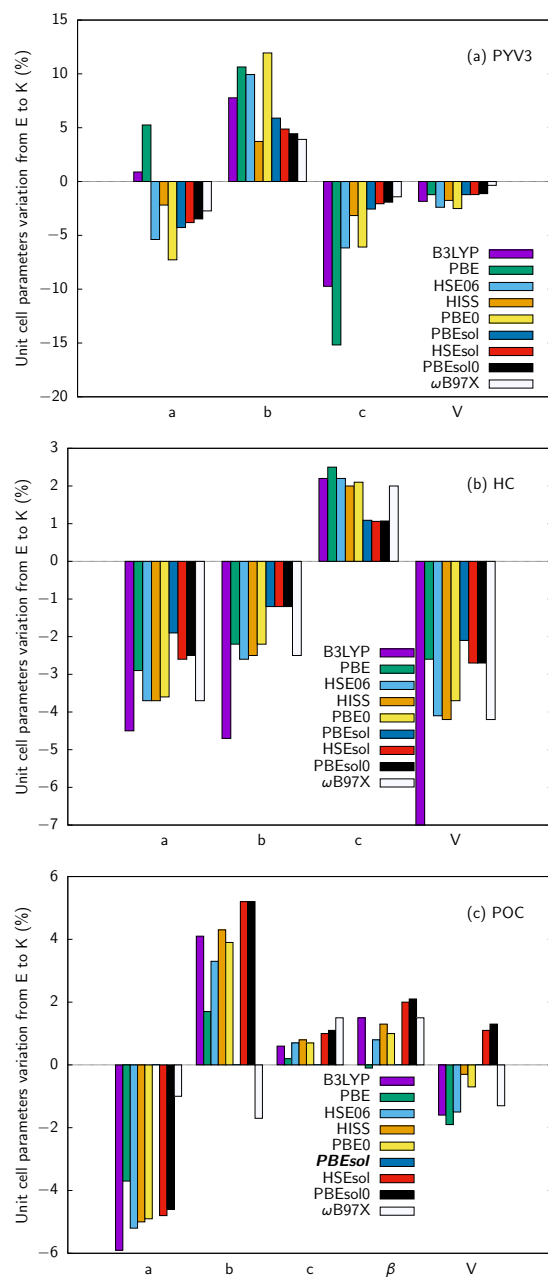


Figure A.3: Variation of the unit cell parameters for the E→K reaction, $\Delta = X(K) - X(E)$ where X is a unit cell parameter, as optimized with different XC functionals after full geometry optimization with the 6-31G(d,p) basis set.

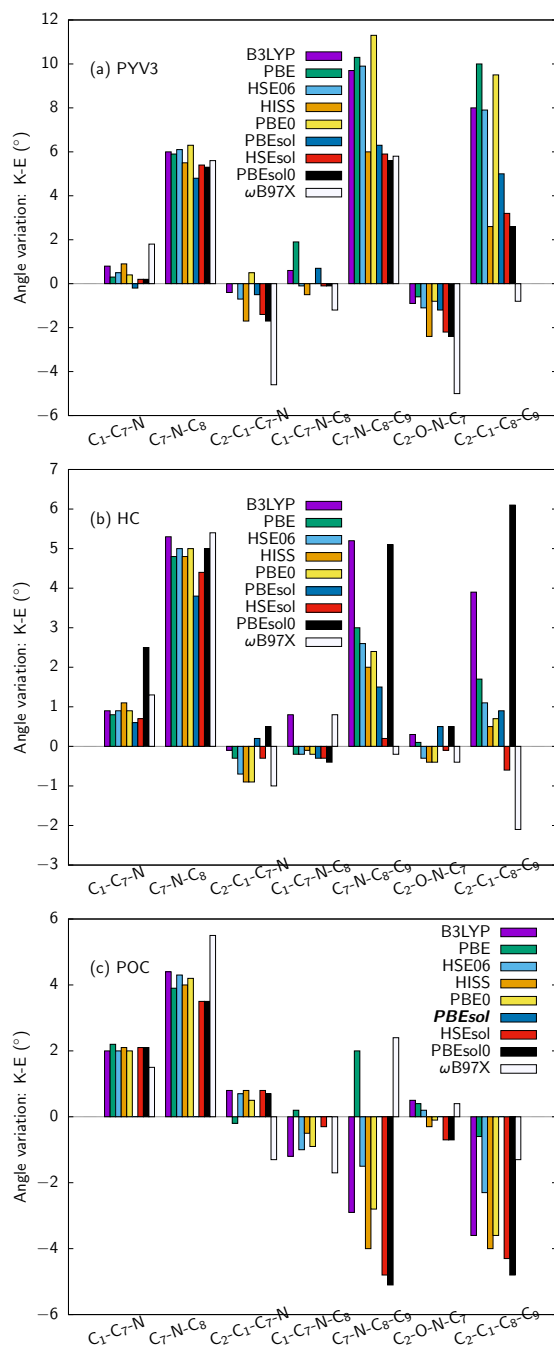


Figure A.4: Variation of the angles for the E→K reaction, $\Delta = a(K) - a(E)$, as optimized with different XC functionals after full geometry optimization with the 6-31G(d,p) basis set.

PERIODIC DFT STUDY OF THE
EFFECTS OF
CO-CRYSTALLIZATION ON A
N-SALICYLIDENEANILINE
MOLECULAR SWITCH.
SUPPORTING INFORMATION.

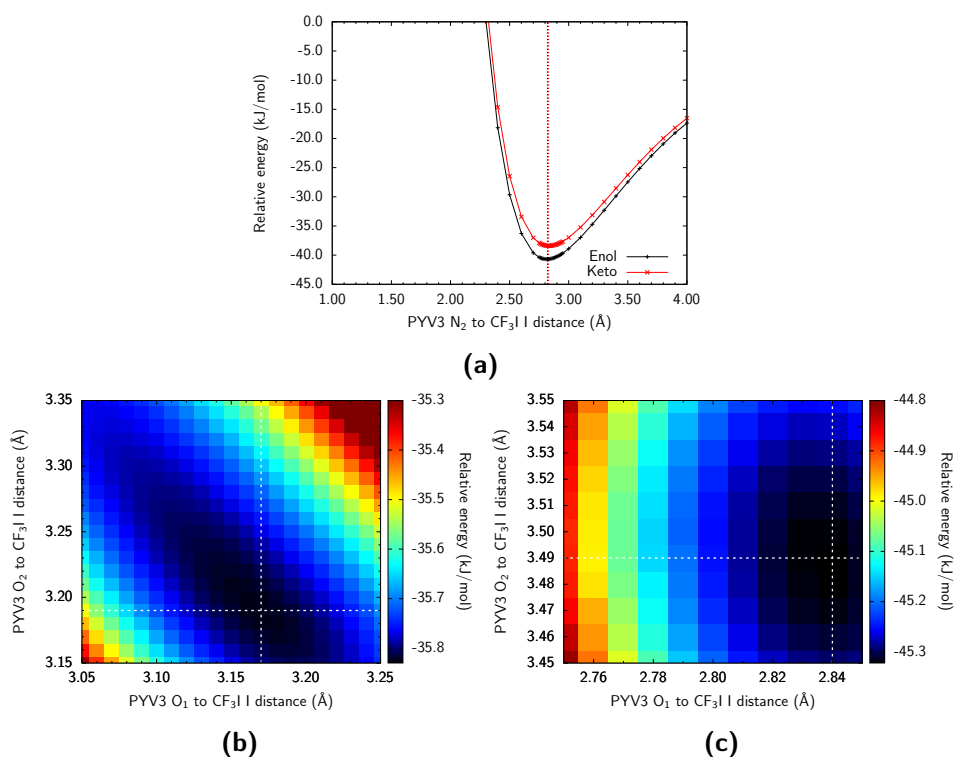


Figure B.1: Potential energy scans for the PYV3[PYV3]...ICF₃ complex using a CF₃I molecule as a probe, computed at MP2/aug-cc-pVDZ level of approximation. (a) N₂...ICF₃ potential energy scans, for the enol, the minimum is at (2.82 Å, -40.7 kJ mol⁻¹) while for the keto, at (2.83 Å, -38.4 kJ mol⁻¹); (b) O₁...ICF₃ and O₂...ICF₃ 2D potential energy scans for the enol form, minimum at (3.17 Å, 3.19 Å, -35.8 kJ mol⁻¹) and (c) for the keto form, minimum at (2.84 Å, 3.49 Å, -45.3 kJ mol⁻¹).

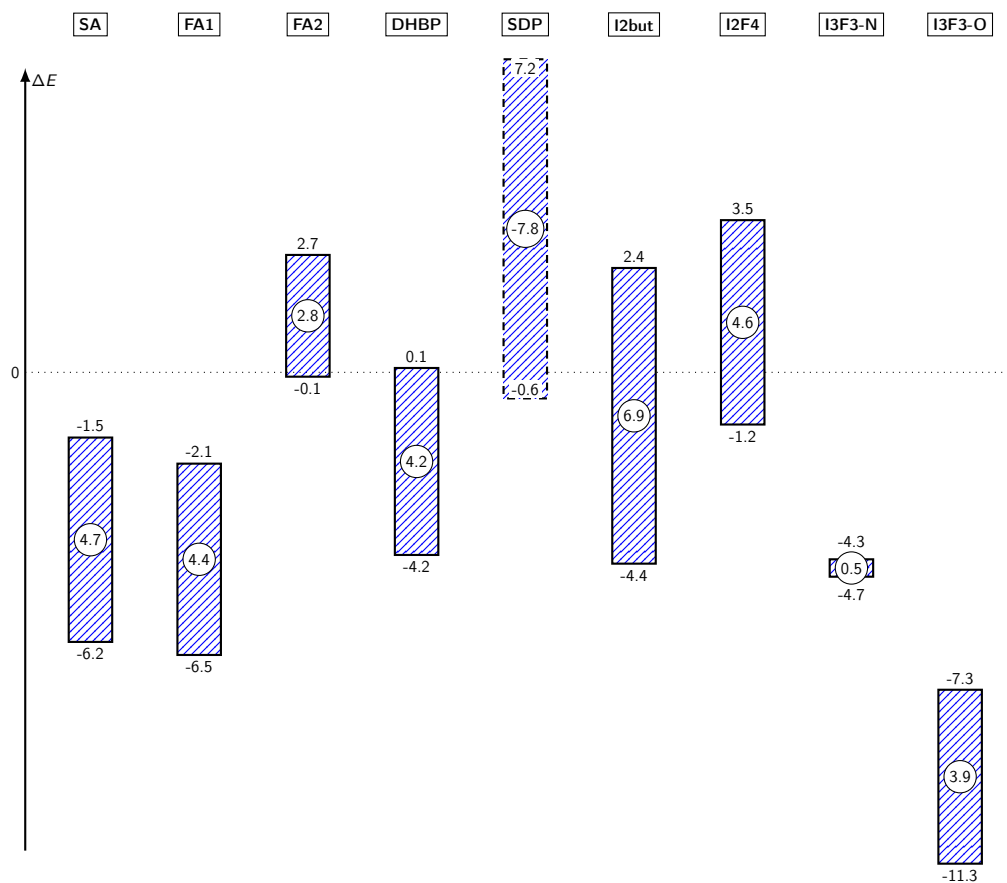


Figure B.2: Relative energies of PYV3[co-crystal] with respect to PYV3[PYV3] for the enol form, $\Delta E_E^{\text{relax}}$ (below the box), and the keto one, $\Delta E_K^{\text{relax}}$ (above the box), while $\Delta\Delta E_{EK}^{\text{relax}}$ is displayed inside the box. Boxes with negative $\Delta\Delta E_{EK}^{\text{relax}}$ have dashed borders and the positions of the enol and keto values are reversed (below the top bar for E and above the bottom bar for K). All values are in kJ mol⁻¹.

Table B.1: Mulliken charges and their variations with respect to PYV3 calculated at the PBC/PBEsol0/6-31G(d,p)/I(LANL2DZ) level of approximation (in atomic units). Largest values are highlighted in bold.

	Enol									
	PYV3	SA	FA1	FA2	DHBP	SDP	I2but	I2F4	I3F3-N	I3F3-O
H	0.40	−0.00	−0.00	0.00	0.00	0.11	0.00	0.01	−0.01	0.01
O ₁	−0.59	0.02	0.03	0.02	0.01	−0.15	0.02	0.01	0.03	0.02
C _O	0.27	−0.00	−0.00	−0.01	−0.00	0.03	−0.01	−0.01	−0.00	−0.01
C _{Nβ}	−0.04	−0.02	−0.02	−0.02	0.01	0.04	−0.00	−0.01	0.02	−0.01
C _{Nα}	0.16	−0.02	−0.02	−0.03	−0.02	−0.05	−0.02	−0.01	0.00	−0.00
N ₁	−0.60	0.00	0.01	−0.01	−0.00	−0.03	−0.01	−0.01	0.03	0.00
C _{Nγ}	0.22	−0.04	−0.04	−0.03	−0.02	0.01	−0.02	−0.00	−0.04	−0.01
O ₂	−0.52	0.01	0.01	0.01	0.01	0.01	0.01	0.01	0.01	0.01
N ₂	−0.41	−0.16	−0.16	−0.14	−0.12	−0.13	−0.06	−0.06	−0.06	−0.05
Continued on next page										

Table B.1 – continued from previous page

	Keto									
	PYV3	SA	FA1	FA2	DHBP	SDP	I2but	I2F4	I3F3-N	I3F3-O
H	0.38	0.00	0.00	0.02	0.01	0.09	0.01	0.01	0.01	0.01
O ₁	−0.63	0.03	0.03	0.01	0.01	−0.05	0.01	0.01	0.01	0.04
C _O	0.34	0.01	0.01	−0.00	0.01	0.03	0.00	0.00	0.00	0.01
C _{Nβ}	−0.08	−0.04	−0.04	−0.02	−0.01	0.04	−0.01	−0.02	−0.02	−0.01
C _{Nα}	0.13	−0.01	−0.01	0.01	−0.02	−0.05	−0.01	−0.00	−0.00	−0.00
N ₁	−0.59	−0.02	−0.02	−0.04	−0.02	−0.12	−0.03	−0.03	−0.01	−0.01
C _{Nγ}	0.25	−0.05	−0.04	−0.02	−0.02	0.03	−0.00	−0.00	0.02	−0.02
O ₂	−0.51	0.00	0.00	0.01	0.00	0.01	0.00	0.00	0.00	0.01
N ₂	−0.42	−0.15	−0.15	−0.14	−0.12	−0.11	−0.05	−0.05	−0.05	−0.05

Table B.2: Comparison between the Mulliken and Hirshfeld charges for the enol and keto forms of PYV3 as well as for the keto/enol differences calculated at the PBC/PBEsol0/6-31G(d,p)/I(LANL2DZ) level of approximation (in atomic units).

	Enol		Keto		K-E	
	Mull.	Hirsh.	Mull.	Hirsh.	Mull.	Hirsh.
H	0.40	0.34	0.38	0.30	-0.02	-0.04
O ₁	-0.59	-0.47	-0.63	-0.49	-0.04	-0.02
C _O	0.27	0.30	0.34	0.38	0.07	0.08
C _{Nβ}	-0.04	-0.21	-0.08	-0.27	-0.04	-0.07
C _{Nα}	0.16	0.24	0.13	0.27	-0.03	0.02
N ₁	-0.60	-0.37	-0.59	-0.35	0.01	0.02
C _{Nγ}	0.22	0.22	0.25	0.22	0.03	0.01
O ₂	-0.52	-0.16	-0.51	-0.15	0.01	0.01
N ₂	-0.41	-0.28	-0.42	-0.27	-0.01	0.01

INVESTIGATION OF THE
EVOLUTION OF ISOTROPIC
MAGNETIC SHIELDINGS ALONG
THE ENOL-KETO TAUTOMERISM
OF A *N*-SALICYLIDENE-3-
AMINOPYRIDINE DERIVATIVE AND
TWO OF ITS CO-CRYSTALS IN
THE SOLID STATE. SUPPORTING
INFORMATION

Table C.1: Parameters used in the Ewald program.

Crystal	Zone 1 composition (Number of atoms)	Number of charges in zone 2 (diameter of zone 2)	Unit cell composition	Supercell "zones 1 + 2 + 3" dimensions	Total number of atoms ^a
PYV3	PYV3 (29)	4971 (44 Å)	4 PYV3	16x10x4	74240
PYV3 DHBP	PYV3 + DHBP (53)	9947 (56 Å)	4 PYV3 + 2 DHBP	12x4x8	62976
PYV3 SDP	PYV3 + 2 SDP (83)	9917 (58 Å)	4 PYV3 + 4 SDP	8x12x4	86016

^a The total number of atoms corresponds to the sum of the numbers of atoms in zones 1, 2, and 3, in other words, the sum of the number of point charges in zones 2 and 3 and the number of atoms in the QC zone 1.

Table C.2: PYV3 atomic charges (a.u.) for the enol tautomer obtained at different levels of approximation for the PBC/PBEsol0/6-31G(d,p) geometry, their variations with respect to the scrf-ESPd embedding (in parentheses), mean signed errors (MSE), and mean absolute errors (MAE).

	Mulliken ^a	i-ESPd ^b	ESPd ^c	scr-ESPd ^d
N ₁	−0.60 (−0.08)	−0.51 (0.02)	−0.59 (−0.07)	−0.52
N ₂	−0.41 (0.34)	−0.63 (0.12)	−0.75 (0.002)	−0.75
O ₁	−0.59 (0.11)	−0.62 (0.09)	−0.72 (−0.02)	−0.70
O ₂	−0.52 (−0.22)	−0.23 (0.08)	−0.33 (−0.03)	−0.30
C ₁	0.27 (−0.10)	0.32 (−0.06)	0.42 (0.05)	0.37
C ₂	0.31 (0.05)	0.25 (−0.004)	0.25 (−0.01)	0.26
C ₃	−0.15 (0.10)	−0.23 (0.03)	−0.25 (0.01)	−0.26
C ₄	−0.18 (0.03)	−0.20 (0.01)	−0.21 (−0.001)	−0.21
C ₅	−0.15 (0.06)	−0.21 (−0.01)	−0.15 (0.05)	−0.20
C ₆	−0.04 (0.21)	−0.14 (0.11)	−0.35 (−0.09)	−0.25
C ₇	0.16 (−0.27)	0.30 (−0.12)	0.49 (0.07)	0.42
C ₈	0.22 (0.23)	0.04 (0.05)	0.01 (0.03)	−0.02
C ₉	−0.11 (−0.31)	0.13 (−0.08)	0.16 (−0.04)	0.20
C ₁₀	−0.18 (0.41)	−0.50 (0.09)	−0.61 (−0.02)	−0.59
C ₁₁	0.01 (−0.44)	0.41 (−0.05)	0.48 (0.02)	0.46
C ₁₂	0.04 (−0.37)	0.35 (−0.06)	0.40 (−0.01)	0.41
C ₁₃	−0.22 (−0.09)	−0.10 (0.03)	−0.09 (0.04)	−0.13

Continued on next page

Table C.2 – Continued from previous page

	Mulliken ^a	i-ESPd ^b	ESPd ^c	scr-ESPd ^d
H ₁	0.40 (−0.08)	0.46 (−0.01)	0.49 (0.01)	0.48
H ₃	0.15 (−0.05)	0.16 (−0.04)	0.18 (−0.02)	0.20
H ₄	0.14 (−0.02)	0.15 (−0.01)	0.16 (0.01)	0.16
H ₅	0.14 (−0.03)	0.15 (−0.03)	0.17 (−0.003)	0.17
H ₇	0.19 (0.13)	0.03 (−0.01)	0.05 (−0.01)	0.06
H ₉	0.16 (0.05)	0.09 (−0.02)	0.13 (0.02)	0.11
H ₁₀	0.18 (−0.07)	0.19 (−0.06)	0.27 (0.02)	0.25
H ₁₁	0.15 (0.12)	0.04 (0.01)	0.03 (−0.001)	0.03
H ₁₂	0.15 (0.11)	0.05 (0.01)	0.04 (0.01)	0.04
H ₁₃	0.16 (0.05)	0.08 (−0.03)	0.10 (−0.01)	0.11
MSE	−0.0040	0.0020	0.0004	
MAE	0.15	0.05	0.02	

^a Ewald embedding evaluated using the PBC/PBEsol0/6-31G(d,p) Mulliken charges

^b B3LYP/6-311+G(2d,p) ESPd charges of the isolated molecule

^c Ewald embedding evaluated using the B3LYP/6-311+G(2d,p) ESPd charges obtained using a zero-order embedding described by PBC/PBEsol0/6-31G(d,p) Mulliken charges

^d Ewald self-consistent reaction field embedding using the B3LYP/6-311+G(2d,p) ESPd charges of the QC region

Table C.3: PYV3 atomic charges (a.u.) for the keto tautomer obtained at different level of approximation for the PBC/PBEsol0/6-31G(d,p) geometry, their variations with respect to scrf-ESPd (in parentheses), mean signed errors (MSE), and mean absolute errors (MAE).^a

	Mulliken	i-ESPd	ESPd	scr-ESPd
N ₁	−0.59 (−0.25)	−0.46 (−0.12)	−0.37 (−0.04)	−0.33
N ₂	−0.42 (0.37)	−0.60 (0.18)	−0.77 (0.01)	−0.79
O ₁	−0.63 (0.11)	−0.64 (0.10)	−0.74 (−0.01)	−0.74
O ₂	−0.51 (−0.17)	−0.26 (0.08)	−0.38 (−0.04)	−0.34
C ₁	0.34 (−0.14)	0.46 (−0.02)	0.53 (0.04)	0.48
C ₂	0.28 (0.09)	0.19 (0.003)	0.19 (0.001)	0.18
C ₃	−0.16 (0.02)	−0.18 (−0.01)	−0.16 (0.01)	−0.17
C ₄	−0.21 (0.04)	−0.21 (0.03)	−0.24 (0.01)	−0.24
C ₅	−0.12 (0.10)	−0.23 (−0.01)	−0.20 (0.02)	−0.22
C ₆	−0.08 (0.15)	−0.17 (0.06)	−0.29 (−0.06)	−0.23
C ₇	0.13 (−0.13)	0.22 (−0.04)	0.31 (0.06)	0.26
C ₈	0.25 (0.39)	0.02 (0.16)	−0.10 (0.03)	−0.14
C ₉	−0.11 (−0.31)	0.10 (−0.09)	0.14 (−0.06)	0.19
C ₁₀	−0.19 (0.36)	−0.46 (0.08)	−0.55 (−0.004)	−0.55
C ₁₁	0.02 (−0.47)	0.39 (−0.10)	0.50 (0.01)	0.48
C ₁₂	0.03 (−0.42)	0.33 (−0.13)	0.43 (−0.02)	0.45
C ₁₃	−0.22 (−0.16)	−0.01 (0.05)	−0.01 (0.05)	−0.06
H ₁	0.38 (−0.02)	0.43 (0.04)	0.38 (−0.02)	0.40
H ₃	0.15 (−0.02)	0.14 (−0.03)	0.16 (−0.02)	0.17
H ₄	0.14 (−0.02)	0.14 (−0.01)	0.16 (0.001)	0.16
H ₅	0.13 (−0.03)	0.14 (−0.02)	0.17 (0.003)	0.16
H ₇	0.21 (0.06)	0.09 (−0.06)	0.13 (−0.02)	0.15
H ₉	0.19 (0.07)	0.10 (−0.01)	0.14 (0.03)	0.12
H ₁₀	0.19 (−0.06)	0.19 (−0.06)	0.27 (0.02)	0.25
H ₁₁	0.16 (0.13)	0.04 (0.02)	0.02 (−0.01)	0.03
H ₁₂	0.16 (0.11)	0.06 (0.01)	0.06 (0.01)	0.05
H ₁₃	0.16 (0.07)	0.06 (−0.03)	0.08 (−0.01)	0.09
MSE	−0.0051	0.0022	0.0006	
MAE	0.16	0.06	0.02	

^a for the acronyms of the embedding charges see the caption of Table C.2

Table C.4: PYV3 atomic charges (a.u.) for the PYV3 DHBP co-crystal obtained at different levels of approximation for the PBC/PBEsol0/6-31G(d,p) geometry, their variations with respect to scrf-ESPd (in parentheses), mean signed errors (MSE), and mean absolute errors (MAE).^a

	Enol		
	Mulliken	ESPd	scrf-ESPd
N ₁	−0.60 (−0.06)	−0.54 (−0.004)	−0.54
N ₂	−0.53 (−0.31)	−0.20 (0.02)	−0.22
O ₁	−0.58 (0.08)	−0.69 (−0.03)	−0.66
O ₂	−0.51 (−0.22)	−0.30 (−0.01)	−0.29
C ₁	0.27 (0.02)	0.22 (−0.03)	0.25
C ₂	0.31 (0.03)	0.29 (0.01)	0.27
C ₃	−0.18 (0.11)	−0.29 (−0.001)	−0.29
C ₄	−0.17 (−0.04)	−0.14 (−0.01)	−0.13
C ₅	−0.18 (0.18)	−0.37 (−0.01)	−0.36
C ₆	−0.03 (−0.02)	0.06 (0.06)	−0.00
C ₇	0.13 (−0.10)	0.20 (−0.03)	0.23
C ₈	0.20 (−0.18)	0.43 (0.06)	0.38
C ₉	−0.09 (0.06)	−0.15 (−0.01)	−0.15
C ₁₀	−0.19 (0.07)	−0.31 (−0.06)	−0.25
C ₁₁	0.06 (0.01)	0.11 (0.06)	0.05
C ₁₂	0.10 (0.15)	−0.12 (−0.07)	−0.05
C ₁₃	−0.20 (−0.11)	−0.08 (0.01)	−0.09
H ₁	0.40 (−0.06)	0.50 (0.04)	0.46
H ₃	0.16 (−0.05)	0.19 (−0.02)	0.21
H ₄	0.16 (−0.01)	0.17 (0.004)	0.16
H ₅	0.18 (−0.04)	0.25 (0.03)	0.21
H ₇	0.19 (0.11)	0.04 (−0.03)	0.08
H ₉	0.17 (−0.01)	0.20 (0.03)	0.18
H ₁₀	0.17 (−0.02)	0.19 (−0.002)	0.19
H ₁₁	0.18 (0.05)	0.13 (0.001)	0.13
H ₁₂	0.17 (0.06)	0.10 (−0.01)	0.11
H ₁₃	0.15 (0.06)	0.09 (−0.006)	0.09
MSE	−0.0098	−0.0002	
MAE	0.08	0.02	
Continued on next page			

Table C.4 – Continued from previous page

	Keto		
	Mulliken	ESPd	scrf-ESPd
N ₁	−0.61 (−0.13)	−0.56 (−0.09)	−0.47
N ₂	−0.54 (−0.33)	−0.16 (0.04)	−0.20
O ₁	−0.62 (0.10)	−0.74 (−0.03)	−0.72
O ₂	−0.51 (−0.16)	−0.36 (−0.01)	−0.35
C ₁	0.35 (−0.04)	0.40 (0.01)	0.39
C ₂	0.27 (0.05)	0.20 (−0.02)	0.23
C ₃	−0.19 (0.06)	−0.22 (0.03)	−0.25
C ₄	−0.17 (−0.02)	−0.18 (−0.02)	−0.15
C ₅	−0.15 (0.19)	−0.34 (0.01)	−0.35
C ₆	−0.08 (−0.02)	−0.08 (−0.02)	−0.06
C ₇	0.11 (−0.07)	0.24 (0.06)	0.18
C ₈	0.23 (−0.07)	0.41 (0.12)	0.30
C ₉	−0.08 (0.03)	−0.17 (−0.05)	−0.12
C ₁₀	−0.19 (0.03)	−0.24 (−0.02)	−0.22
C ₁₁	0.07 (0.06)	0.02 (0.02)	0.00
C ₁₂	0.10 (0.14)	−0.14 (−0.09)	−0.04
C ₁₃	−0.20 (−0.18)	0.01 (0.03)	−0.02
H ₁	0.38 (−0.07)	0.49 (0.04)	0.45
H ₃	0.16 (−0.04)	0.17 (−0.02)	0.19
H ₄	0.15 (−0.02)	0.18 (0.01)	0.17
H ₅	0.16 (−0.04)	0.22 (0.03)	0.20
H ₇	0.23 (0.07)	0.11 (−0.04)	0.15
H ₉	0.18 (0.01)	0.20 (0.03)	0.17
H ₁₀	0.17 (−0.02)	0.19 (−0.01)	0.20
H ₁₁	0.18 (0.04)	0.15 (0.003)	0.15
H ₁₂	0.18 (0.05)	0.13 (0.005)	0.13
H ₁₃	0.15 (0.07)	0.07 (−0.01)	0.08
MSE	−0.0110	0.0001	
MAE	0.08	0.03	

^a for the acronyms of the embedding charges see the caption of Table C.2

Table C.5: PYV3 atomic charges (a.u.) for the PYV3 SDP co-crystal obtained at different levels of approximation for the PBC/PBEsol0/6-31G(d,p) geometry, their variations with respect to scrf-ESPd (in parentheses), mean signed errors (MSE), and mean absolute errors (MAE).^a

	Enol		
	Mulliken	ESPd	scrfl-ESPd
N ₁	−0.63 (−0.19)	−0.44 (−0.0004)	−0.44
N ₂	−0.54 (−0.28)	−0.13 (0.12)	−0.26
O ₁	−0.73 (−0.09)	−0.71 (−0.07)	−0.64
O ₂	−0.51 (−0.39)	−0.16 (−0.04)	−0.12
C ₁	0.30 (−0.07)	0.41 (0.04)	0.38
C ₂	0.34 (0.22)	0.13 (0.02)	0.11
C ₃	−0.26 (−0.06)	−0.21 (−0.01)	−0.20
C ₄	−0.23 (−0.02)	−0.17 (0.03)	−0.20
C ₅	−0.22 (0.01)	−0.28 (−0.05)	−0.23
C ₆	0.00 (0.12)	−0.08 (0.04)	−0.12
C ₇	0.10 (−0.12)	0.21 (−0.02)	0.23
C ₈	0.23 (−0.01)	0.34 (0.11)	0.24
C ₉	−0.12 (−0.15)	−0.10 (−0.12)	0.02
C ₁₀	−0.22 (0.04)	−0.18 (0.07)	−0.25
C ₁₁	−0.01 (−0.06)	−0.03 (−0.08)	0.05
C ₁₂	0.02 (0.06)	−0.16 (−0.13)	−0.04
C ₁₃	−0.35 (−0.07)	−0.27 (0.01)	−0.28
H ₁	0.51 (0.10)	0.38 (−0.02)	0.41
H ₃	0.21 (0.05)	0.16 (−0.001)	0.17
H ₄	0.21 (0.04)	0.16 (−0.01)	0.17
H ₅	0.20 (0.01)	0.23 (0.03)	0.19
H ₇	0.22 (0.14)	0.10 (0.02)	0.08
H ₉	0.23 (0.12)	0.13 (0.01)	0.11
H ₁₀	0.21 (0.04)	0.17 (−0.002)	0.17
H ₁₁	0.25 (0.11)	0.16 (0.01)	0.14
H ₁₂	0.22 (0.04)	0.20 (0.03)	0.17
H ₁₃	0.21 (0.07)	0.14 (0.0002)	0.14
MSE	−0.013	−0.001	
MAE	0.10	0.04	
Continued on next page			

Table C.5 – Continued from previous page

	Keto		
	Mulliken	ESPd	scrf-ESPd
N ₁	−0.71 (−0.29)	−0.36 (0.06)	−0.42
N ₂	−0.53 (−0.31)	−0.09 (0.14)	−0.22
O ₁	−0.67 (0.11)	−0.80 (−0.02)	−0.79
O ₂	−0.50 (−0.38)	−0.17 (−0.05)	−0.12
C ₁	0.37 (−0.25)	0.59 (−0.04)	0.62
C ₂	0.30 (0.30)	0.04 (0.04)	0.01
C ₃	−0.26 (−0.13)	−0.14 (−0.01)	−0.13
C ₄	−0.25 (0.01)	−0.23 (0.03)	−0.26
C ₅	−0.20 (0.03)	−0.29 (−0.07)	−0.22
C ₆	−0.04 (0.19)	−0.12 (0.11)	−0.23
C ₇	0.08 (−0.16)	0.18 (−0.06)	0.24
C ₈	0.28 (0.03)	0.33 (0.07)	0.25
C ₉	−0.14 (−0.11)	−0.14 (−0.11)	−0.03
C ₁₀	−0.22 (0.02)	−0.17 (0.07)	−0.24
C ₁₁	−0.00 (−0.07)	−0.02 (−0.08)	0.06
C ₁₂	0.02 (0.11)	−0.22 (−0.13)	−0.09
C ₁₃	−0.35 (−0.07)	−0.26 (0.02)	−0.28
H ₁	0.46 (0.05)	0.36 (−0.05)	0.41
H ₃	0.21 (0.06)	0.15 (−0.004)	0.15
H ₄	0.21 (0.03)	0.17 (−0.01)	0.18
H ₅	0.20 (0.005)	0.23 (0.04)	0.20
H ₇	0.25 (0.13)	0.12 (−0.00001)	0.12
H ₉	0.25 (0.09)	0.16 (0.01)	0.16
H ₁₀	0.22 (0.04)	0.17 (−0.003)	0.18
H ₁₁	0.26 (0.11)	0.16 (0.02)	0.15
H ₁₂	0.23 (0.04)	0.23 (0.04)	0.19
H ₁₃	0.21 (0.07)	0.13 (−0.003)	0.14
MSE	−0.0127	0.0001	
MAE	0.12	0.05	

^a for the acronyms of the embedding charges see the caption of Table C.2

Table C.6: PYV3 isotropic NMR shieldings (in ppm) as obtained at the B3LYP/6-311+G(2d,p)//PBC/PBEsol0/6-31G(d,p) level of approximation with different embedding schemes in comparison to the isolated molecule results.^a

	Enol			
	Isolated	Mulliken	ESPd	scrf-ESPd
N ₁	−39.66	−37.70	−39.26	−39.26
N ₂	−98.51	−84.34	−82.90	−81.96
O ₁	169.86	189.31	188.78	186.89
O ₂	233.14	243.11	244.68	242.47
C ₁	21.05	24.29	23.86	23.56
C ₂	27.67	29.47	29.60	29.15
C ₃	64.98	63.55	62.85	63.01
C ₄	61.76	60.49	61.47	61.75
C ₅	55.90	52.66	52.67	53.30
C ₆	59.49	58.79	58.90	58.95
C ₇	12.39	7.58	7.58	7.66
C ₈	32.97	32.02	31.37	31.23
C ₉	55.10	50.88	50.09	50.03
C ₁₀	54.90	52.81	53.38	53.35
C ₁₁	29.49	29.89	31.01	31.00
C ₁₂	29.45	30.80	30.48	30.67
C ₁₃	125.82	126.17	126.45	126.37
H ₁	16.14	15.99	15.97	15.98
H ₃	24.74	24.38	24.23	24.22
H ₄	24.91	24.65	24.77	24.79
H ₅	24.77	24.21	24.29	24.34
H ₇	22.93	22.45	22.41	22.42
H ₉	24.36	23.84	23.90	23.91
H ₁₀	24.41	23.49	23.80	23.81
H ₁₁	23.05	23.11	23.18	23.20
H ₁₂	22.82	22.94	22.96	22.97
H ₁₃	27.91	27.62	27.64	27.65
MSE	−1.10	0.04	0.10	
MAE	2.67	0.57	0.28	
Continued on next page				

Table C.6 – Continued from previous page

	Keto			
	Isolated	Mulliken	ESPd	scrf-ESPd
N ₁	90.17	81.55	79.63	80.02
N ₂	−101.51	−83.87	−81.63	−79.90
O ₁	−73.88	−7.07	−7.62	−12.39
O ₂	224.05	236.62	237.77	236.01
C ₁	2.42	4.83	5.06	4.88
C ₂	22.85	24.84	25.07	24.74
C ₃	66.98	63.16	63.00	63.22
C ₄	64.28	65.59	66.30	66.41
C ₅	56.21	52.54	52.16	52.68
C ₆	62.21	62.20	62.46	62.52
C ₇	23.71	17.19	16.52	16.64
C ₈	42.31	41.28	40.37	40.19
C ₉	54.71	50.33	49.89	49.68
C ₁₀	54.12	50.73	51.32	51.25
C ₁₁	30.10	29.81	30.43	30.54
C ₁₂	33.19	35.00	34.86	34.96
C ₁₃	126.21	126.77	127.04	127.03
H ₁	14.09	14.23	14.21	14.19
H ₃	25.08	24.57	24.47	24.47
H ₄	25.35	25.21	25.26	25.27
H ₅	25.13	24.66	24.67	24.72
H ₇	23.72	22.92	22.78	22.80
H ₉	24.24	23.47	23.50	23.51
H ₁₀	24.34	23.21	23.50	23.51
H ₁₁	23.05	23.11	23.14	23.17
H ₁₂	22.91	22.97	23.02	23.03
H ₁₃	28.00	27.68	27.70	27.71
MSE	−2.47	0.10	0.15	
MAE	5.32	0.65	0.41	

^a for the acronyms of the embedding charges see the caption of Table C.2

Table C.7: PYV3 enol to keto isotropic NMR shielding variations, $\Delta\sigma_{\text{EK}}$, (in ppm) as obtained at the B3LYP/6-311+G(2d,p)//PBC/PBEsol0/6-31G(d,p) level of approximation with different embedding schemes in comparison to the isolated molecule results.^a

	Isolated	Mulliken	ESPd	scrf-ESPd
N ₁	129.82	119.25	118.89	119.28
N ₂	−3.01	0.48	1.28	2.06
O ₁	−243.74	−196.38	−196.40	−199.28
O ₂	−9.10	−6.49	−6.91	−6.46
C ₁	−18.64	−19.46	−18.79	−18.68
C ₂	−4.81	−4.63	−4.53	−4.41
C ₃	2.00	−0.39	0.16	0.22
C ₄	2.52	5.10	4.82	4.66
C ₅	0.31	−0.11	−0.51	−0.62
C ₆	2.72	3.41	3.55	3.56
C ₇	11.31	9.61	8.94	8.99
C ₈	9.33	9.26	9.00	8.97
C ₉	−0.40	−0.55	−0.20	−0.35
C ₁₀	−0.78	−2.07	−2.06	−2.10
C ₁₁	0.61	−0.08	−0.57	−0.46
C ₁₂	3.74	4.19	4.37	4.29
C ₁₃	0.40	0.59	0.59	0.65
H ₁	−2.05	−1.75	−1.76	−1.79
H ₃	0.35	0.19	0.24	0.24
H ₄	0.44	0.55	0.49	0.48
H ₅	0.37	0.45	0.38	0.38
H ₇	0.79	0.47	0.37	0.37
H ₉	−0.13	−0.36	−0.40	−0.40
H ₁₀	−0.08	−0.28	−0.30	−0.30
H ₁₁	0.00	−0.00	−0.04	−0.03
H ₁₂	0.09	0.03	0.06	0.06
H ₁₃	0.09	0.06	0.06	0.06
MSE	−1.38	0.06	0.05	
MAE	2.82	0.35	0.21	

^a for the acronyms of the embedding charges see the caption of Table C.2

Table C.8: PYV3 isotropic NMR shieldings (in ppm) for the PYV3 DHBP co-crystal as obtained at the B3LYP/6-311+G(2d,p)//PBC/PBEsol0/6-31G(d,p) level of approximation with different embedding schemes in comparison to the isolated molecule results.^a

	Enol			
	Isolated	Mulliken	ESPd	scrf-ESPd
N ₁	−34.71	−37.58	−33.03	−34.70
N ₂	−68.31	−60.55	−57.52	−56.76
O ₁	170.06	190.60	187.15	186.26
O ₂	231.24	245.65	241.25	240.00
C ₁	21.46	24.90	24.23	24.21
C ₂	28.00	31.10	29.83	29.66
C ₃	64.32	63.84	62.06	62.38
C ₄	61.01	58.58	58.41	58.60
C ₅	55.75	52.14	54.30	54.62
C ₆	59.47	58.21	59.05	59.04
C ₇	11.44	8.32	7.95	8.41
C ₈	31.53	31.36	30.70	30.61
C ₉	53.27	52.15	51.08	50.95
C ₁₀	53.12	52.81	52.11	52.25
C ₁₁	32.27	30.58	32.40	32.31
C ₁₂	32.85	33.57	33.21	33.31
C ₁₃	126.93	127.19	126.66	126.73
H ₁	16.63	16.45	16.56	16.53
H ₃	24.69	24.39	24.11	24.13
H ₄	24.81	24.30	24.41	24.40
H ₅	24.74	23.81	24.13	24.19
H ₇	22.85	22.47	22.49	22.52
H ₉	24.05	23.85	23.70	23.73
H ₁₀	24.25	24.09	23.81	23.87
H ₁₁	23.03	22.79	22.95	22.92
H ₁₂	22.56	22.66	22.71	22.70
H ₁₃	27.92	27.77	27.72	27.73
MSE	−0.94	0.18	0.07	
MAE	2.14	1.11	0.26	
Continued on next page				

Table C.8 – Continued from previous page

	Keto			
	Isolated	Mulliken	ESPd	scrf-ESPd
N ₁	94.39	85.02	86.68	86.95
N ₂	−71.76	−63.40	−59.65	−58.71
O ₁	−78.58	−9.47	−17.94	−19.52
O ₂	222.95	243.41	239.71	238.40
C ₁	1.96	4.88	4.37	4.23
C ₂	22.95	27.01	26.33	25.76
C ₃	66.04	62.82	63.42	62.59
C ₄	63.58	62.35	62.20	62.02
C ₅	56.29	52.05	52.74	54.29
C ₆	61.51	61.18	61.29	61.56
C ₇	23.64	16.58	17.19	17.53
C ₈	39.75	39.45	39.01	38.80
C ₉	51.83	49.79	48.91	48.68
C ₁₀	52.78	52.79	51.73	51.89
C ₁₁	32.76	31.48	32.38	32.71
C ₁₂	36.83	36.61	36.84	36.84
C ₁₃	126.73	127.44	127.00	127.00
H ₁	13.74	13.85	13.84	13.84
H ₃	25.02	24.54	24.38	24.34
H ₄	25.26	24.74	24.75	24.80
H ₅	25.19	24.31	24.54	24.62
H ₇	23.63	22.70	22.78	22.81
H ₉	23.97	23.65	23.55	23.56
H ₁₀	24.28	24.02	23.76	23.80
H ₁₁	23.03	22.78	22.86	22.90
H ₁₂	22.58	22.59	22.65	22.64
H ₁₃	28.01	27.78	27.75	27.75
MSE	−2.36	0.33	0.04	
MAE	4.54	1.24	0.34	

^a for the acronyms of the embedding charges see the caption of Table C.2

Table C.9: PYV3 enol to keto isotropic NMR shielding variations, $\Delta\sigma_{EK}$, (in ppm) for the PYV3 DHBP co-crystal as obtained at the B3LYP/6-311+G(2d,p)//PBC/PBEsol0/6-31G(d,p) level of approximation with different embedding schemes in comparison to the isolated molecule results.^a

	Isolated	Mulliken	ESPd	scrf-ESPd
N ₁	129.10	122.60	119.71	121.65
N ₂	−3.45	−2.85	−2.12	−1.95
O ₁	−248.64	−200.07	−205.09	−205.77
O ₂	−8.30	−2.24	−1.53	−1.60
C ₁	−19.51	−20.03	−19.86	−19.98
C ₂	−5.06	−4.09	−3.50	−3.90
C ₃	1.73	−1.02	1.36	0.21
C ₄	2.57	3.77	3.79	3.42
C ₅	0.54	−0.08	−1.56	−0.33
C ₆	2.04	2.97	2.24	2.52
C ₇	12.20	8.26	9.24	9.12
C ₈	8.23	8.09	8.31	8.18
C ₉	−1.44	−2.36	−2.16	−2.27
C ₁₀	−0.34	−0.02	−0.38	−0.36
C ₁₁	0.48	0.90	−0.01	0.40
C ₁₂	3.98	3.04	3.63	3.53
C ₁₃	−0.20	0.24	0.34	0.27
H ₁	−2.89	−2.60	−2.71	−2.69
H ₃	0.34	0.15	0.27	0.21
H ₄	0.44	0.44	0.34	0.41
H ₅	0.45	0.50	0.40	0.43
H ₇	0.78	0.22	0.29	0.29
H ₉	−0.07	−0.19	−0.14	−0.17
H ₁₀	0.03	−0.07	−0.05	−0.07
H ₁₁	0.01	−0.00	−0.08	−0.03
H ₁₂	0.03	−0.07	−0.06	−0.06
H ₁₃	0.09	0.01	0.03	0.02
MSE	−1.42	0.15	−0.03	
MAE	2.60	0.50	0.28	

^a for the acronyms of the embedding charges see the caption of Table C.2

Table C.10: PYV3 isotropic NMR shieldings (in ppm) for the PYV3 SDP co-crystal as obtained at the B3LYP/6-311+G(2d,p)//PBC/PBEsol0/6-31G(d,p) level of approximation with different embedding schemes in comparison to the isolated molecule results.^a

	Enol			
	Isolated	Mulliken	ESPd	scrf-ESPd
N ₁	−27.61	−25.79	−29.60	−29.91
N ₂	−66.36	−56.55	−55.42	−54.73
O ₁	179.01	187.86	188.68	186.11
O ₂	231.70	238.26	237.92	235.96
C ₁	24.64	25.98	26.77	26.07
C ₂	28.68	29.94	29.90	29.53
C ₃	64.59	64.28	64.00	64.44
C ₄	58.46	58.51	57.66	58.53
C ₅	55.11	52.14	52.98	53.31
C ₆	60.95	60.12	60.62	60.56
C ₇	18.47	14.66	16.42	16.63
C ₈	36.91	36.69	37.11	36.84
C ₉	40.65	38.16	36.64	36.45
C ₁₀	52.52	52.57	52.61	52.78
C ₁₁	31.05	32.42	31.29	31.67
C ₁₂	44.91	42.54	43.76	43.84
C ₁₃	127.28	127.07	126.95	126.92
H ₁	14.25	14.04	14.02	14.04
H ₃	24.58	24.44	24.34	24.41
H ₄	24.74	24.61	24.42	24.51
H ₅	24.75	24.13	24.37	24.39
H ₇	22.27	22.08	22.18	22.20
H ₉	23.45	23.21	23.15	23.12
H ₁₀	23.98	23.78	23.87	23.93
H ₁₁	23.03	22.82	22.70	22.74
H ₁₂	22.40	22.21	22.32	22.34
H ₁₃	27.89	27.78	27.74	27.77
MSE	−0.45	0.13	0.11	
MAE	1.49	0.72	0.37	
Continued on next page				

Table C.10 – Continued from previous page

	Keto			
	Isolated	Mulliken	ESPd	scrf-ESPd
N ₁	89.58	83.30	80.79	80.57
N ₂	−70.42	−60.26	−59.64	−58.53
O ₁	−18.89	16.49	18.93	13.14
O ₂	222.82	230.91	230.22	228.26
C ₁	5.01	6.59	7.39	6.99
C ₂	24.05	25.54	25.23	24.94
C ₃	64.40	64.02	63.60	64.47
C ₄	60.83	63.62	62.73	63.71
C ₅	54.90	51.11	52.49	52.54
C ₆	63.79	63.71	64.83	64.68
C ₇	28.52	23.07	23.53	23.70
C ₈	42.95	43.42	44.00	43.70
C ₉	48.44	44.93	43.23	42.90
C ₁₀	52.12	52.10	52.35	52.51
C ₁₁	31.96	32.21	31.05	31.39
C ₁₂	46.23	43.52	44.11	44.17
C ₁₃	127.24	127.22	127.01	127.04
H ₁	25.13	16.52	16.48	16.45
H ₃	23.28	24.74	24.61	24.70
H ₄	24.89	25.16	24.96	25.05
H ₅	25.16	24.44	24.68	24.68
H ₇	23.66	22.86	22.92	22.95
H ₉	23.97	23.29	23.22	23.19
H ₁₀	23.05	23.70	23.77	23.83
H ₁₁	22.61	22.76	22.64	22.68
H ₁₂	28.10	22.24	22.32	22.35
H ₁₃	24.13	27.87	27.82	27.85
MSE	−0.83	0.19	0.20	
MAE	3.86	0.76	0.51	

^a for the acronyms of the embedding charges see the caption of Table C.2

Table C.11: PYV3 enol to keto isotropic NMR shielding variations, $\Delta\sigma_{EK}$, (in ppm) for the PYV3 SDP co-crystal as obtained at the B3LYP/6-311+G(2d,p)//PBC/PBEsol0/6-31G(d,p) level of approximation with different embedding schemes in comparison to the isolated molecule results.^a

	Isolated	Mulliken	ESPd	scrf-ESPd
N ₁	117.19	109.09	110.39	110.49
N ₂	−4.06	−3.71	−4.22	−3.80
O ₁	−197.90	−171.37	−169.75	−172.97
O ₂	−8.88	−7.35	−7.70	−7.70
C ₁	−19.63	−19.39	−19.38	−19.08
C ₂	−4.63	−4.39	−4.66	−4.58
C ₃	−0.19	−0.26	−0.41	0.02
C ₄	2.37	5.11	5.07	5.18
C ₅	−0.21	−1.02	−0.49	−0.77
C ₆	2.84	3.59	4.21	4.11
C ₇	10.04	8.41	7.11	7.07
C ₈	6.05	6.74	6.89	6.86
C ₉	7.78	6.77	6.59	6.46
C ₁₀	−0.40	−0.47	−0.25	−0.28
C ₁₁	0.91	−0.21	−0.24	−0.28
C ₁₂	1.31	0.99	0.35	0.34
C ₁₃	−0.04	0.16	0.06	0.11
H ₁	10.88	2.48	2.45	2.41
H ₃	−1.30	0.30	0.27	0.30
H ₄	0.16	0.55	0.53	0.53
H ₅	0.41	0.31	0.32	0.29
H ₇	1.39	0.78	0.74	0.76
H ₉	0.52	0.07	0.06	0.06
H ₁₀	−0.93	−0.09	−0.10	−0.09
H ₁₁	−0.42	−0.05	−0.06	−0.06
H ₁₂	5.70	0.03	0.00	0.01
H ₁₃	−3.76	0.09	0.08	0.08
MSE	−0.38	0.06	0.09	
MAE	2.54	0.30	0.20	

^a for the acronyms of the embedding charges see the caption of Table C.2

Table C.12: Enol and keto isotropic NMR shielding (in ppm) for PYV3, PYV3 DHBP and PYV3 SDP co-crystals as well as, in parentheses, their variations induced by the co-crystallization, $\Delta\sigma_{\text{co-crystal}} = \sigma_{\text{co-crystal}} - \sigma_{\text{PYV3}}$, (in ppm) as obtained at the B3LYP/6-311+G(2d,p)//PBC/PBEsol0/6-31G(d,p) level of approximation with the scrf-ESPd embedding scheme and the variation with respect to PYV3.^a

	Enol		
	PYV3	PYV3 DHBP	PYV3 SDP
N ₁	−39.26	−34.70 (4.56)	−29.91 (9.35)
N ₂	−81.96	−56.76 (25.19)	−54.73 (27.23)
O ₁	186.89	186.26 (−0.64)	186.11 (−0.78)
O ₂	242.47	240.00 (−2.47)	235.96 (−6.51)
C ₁	23.56	24.21 (0.65)	26.07 (2.51)
C ₂	29.15	29.66 (0.51)	29.53 (0.37)
C ₃	63.01	62.38 (−0.63)	64.44 (1.44)
C ₄	61.75	58.60 (−3.15)	58.53 (−3.22)
C ₅	53.30	54.62 (1.32)	53.31 (0.01)
C ₆	58.95	59.04 (0.09)	60.56 (1.61)
C ₇	7.66	8.41 (0.75)	16.63 (8.97)
C ₈	31.23	30.61 (−0.62)	36.84 (5.61)
C ₉	50.03	50.95 (0.92)	36.45 (−13.58)
C ₁₀	53.35	52.25 (−1.10)	52.78 (−0.57)
C ₁₁	31.00	32.31 (1.31)	31.67 (0.67)
C ₁₂	30.67	33.31 (2.64)	43.84 (13.17)
C ₁₃	126.37	126.73 (0.35)	126.93 (0.56)
H ₁	15.98	16.53 (0.55)	14.04 (−1.94)
H ₃	24.22	24.13 (−0.10)	24.41 (0.19)
H ₄	24.79	24.40 (−0.39)	24.51 (−0.27)
H ₅	24.34	24.19 (−0.15)	24.39 (0.05)
H ₇	22.42	22.52 (0.10)	22.20 (−0.23)
H ₉	23.91	23.73 (−0.18)	23.12 (−0.79)
H ₁₀	23.81	23.87 (0.06)	23.93 (0.12)
H ₁₁	23.20	22.92 (−0.27)	22.74 (−0.45)
H ₁₂	22.97	22.70 (−0.28)	22.34 (−0.63)
H ₁₃	27.65	27.73 (0.08)	27.77 (0.12)
Continued on next page			

Table C.12 – Continued from previous page

	Keto		
	PYV3	PYV3 DHBP	PYV3 SDP
N ₁	80.02	86.95 (6.93)	80.58 (0.55)
N ₂	-79.90	-58.71 (21.19)	-58.53 (21.37)
O ₁	-12.39	-19.52 (-7.13)	13.14 (25.53)
O ₂	236.01	238.40 (2.38)	228.26 (-7.75)
C ₁	4.88	4.23 (-0.65)	6.99 (2.11)
C ₂	24.74	25.76 (1.02)	24.94 (0.20)
C ₃	63.22	62.59 (-0.63)	64.47 (1.24)
C ₄	66.41	62.02 (-4.39)	63.71 (-2.70)
C ₅	52.68	54.29 (1.61)	52.54 (-0.14)
C ₆	62.52	61.56 (-0.96)	64.68 (2.16)
C ₇	16.64	17.53 (0.89)	23.70 (7.06)
C ₈	40.19	38.80 (-1.40)	43.70 (3.51)
C ₉	49.68	48.68 (-1.00)	42.91 (-6.77)
C ₁₀	51.25	51.89 (0.64)	52.51 (1.26)
C ₁₁	30.54	32.71 (2.17)	31.39 (0.85)
C ₁₂	34.96	36.84 (1.88)	44.17 (9.21)
C ₁₃	127.03	127.00 (-0.03)	127.04 (0.01)
H ₁	14.19	13.84 (-0.35)	16.45 (2.26)
H ₃	24.47	24.34 (-0.13)	24.70 (0.24)
H ₄	25.27	24.80 (-0.47)	25.05 (-0.22)
H ₅	24.72	24.62 (-0.10)	24.68 (-0.04)
H ₇	22.80	22.81 (0.02)	22.95 (0.15)
H ₉	23.51	23.56 (0.05)	23.19 (-0.32)
H ₁₀	23.51	23.80 (0.29)	23.83 (0.33)
H ₁₁	23.17	22.90 (-0.28)	22.69 (-0.49)
H ₁₂	23.03	22.64 (-0.39)	22.35 (-0.68)
H ₁₃	27.71	27.75 (0.04)	27.85 (0.14)

^a for the acronyms of the embedding charges see the caption of Table C.2

Table C.13: PYV3 enol to keto isotropic NMR shielding variations, $\Delta\sigma_{\text{EK}}$, (in ppm) for PYV3, PYV3 DHBP and PYV3 SDP co-crystals as well as in parentheses, their variations induced by the co-crystallization, $\Delta\sigma_{\text{EK,co-crystal}} = \Delta\sigma_{\text{EK,co-crystal}} - \Delta\sigma_{\text{EK,PYV3}}$ (in ppm) as obtained at the B3LYP/6-311+G(2d,p)//PBC/PBEsol0/6-31G(d,p) level of approximation with the scrf-ESPD embedding scheme and the variation with respect to PYV3.^a

	PYV3	PYV3 DHBP	PYV3 SDP
N ₁	119.28	121.65 (2.37)	110.49 (−8.79)
N ₂	2.06	−1.95 (−4.01)	−3.80 (−5.85)
O ₁	−199.28	−205.77 (−6.49)	−172.97 (26.31)
O ₂	−6.46	−1.61 (4.85)	−7.70 (−1.24)
C ₁	−18.68	−19.98 (−1.30)	−19.08 (−0.40)
C ₂	−4.41	−3.90 (0.51)	−4.59 (−0.17)
C ₃	0.22	0.21 (−0.01)	0.02 (−0.19)
C ₄	4.66	3.42 (−1.24)	5.18 (0.52)
C ₅	−0.62	−0.33 (0.28)	−0.77 (−0.15)
C ₆	3.57	2.52 (−1.05)	4.11 (0.55)
C ₇	8.99	9.12 (0.14)	7.07 (−1.92)
C ₈	8.97	8.18 (−0.78)	6.87 (−2.10)
C ₉	−0.35	−2.27 (−1.92)	6.46 (6.81)
C ₁₀	−2.10	−0.37 (1.73)	−0.28 (1.82)
C ₁₁	−0.46	0.40 (0.86)	−0.28 (0.18)
C ₁₂	4.29	3.53 (−0.76)	0.34 (−3.96)
C ₁₃	0.65	0.27 (−0.38)	0.11 (−0.54)
H ₁	−1.79	−2.69 (−0.91)	2.41 (4.20)
H ₃	0.24	0.21 (−0.03)	0.30 (0.05)
H ₄	0.49	0.41 (−0.08)	0.53 (0.05)
H ₅	0.38	0.43 (0.05)	0.29 (−0.09)
H ₇	0.37	0.29 (−0.08)	0.76 (0.38)
H ₉	−0.40	−0.17 (0.24)	0.06 (0.47)
H ₁₀	−0.30	−0.07 (0.23)	−0.10 (0.21)
H ₁₁	−0.03	−0.03 (−0.00)	−0.06 (−0.03)
H ₁₂	0.06	−0.06 (−0.12)	0.01 (−0.05)
H ₁₃	0.06	0.02 (−0.04)	0.08 (0.02)

^a for the acronyms of the embedding charges see the caption of Table C.2

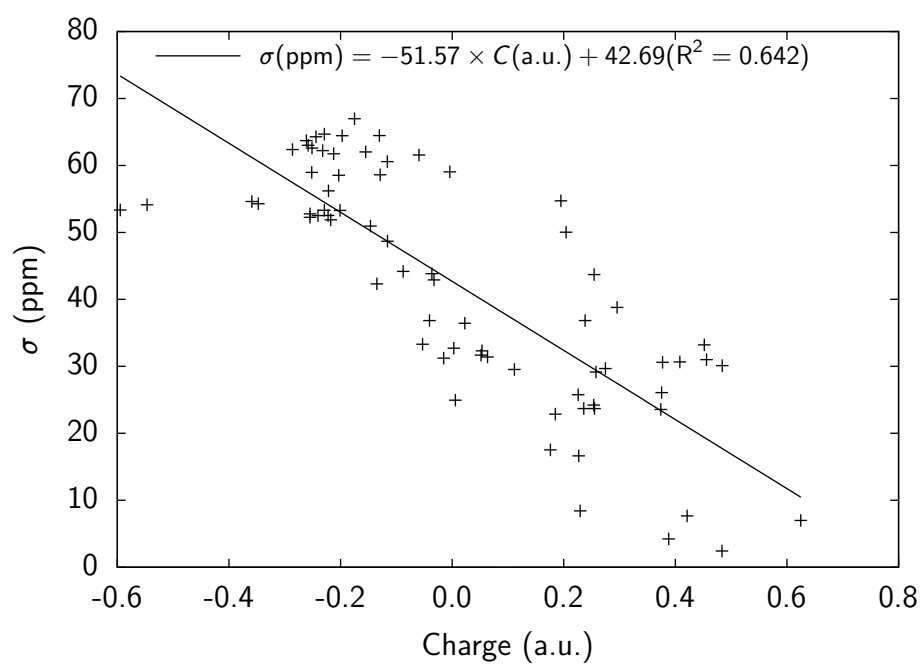


Figure C.1: Relationship between the NMR shielding constants of the aromatic C atoms and their scrf-ESPd charges. All quantities were calculated at the B3LYP/6-311+G(2d,p)//PBC/PBEsol0/6-31G(d,p) level of approximation with the scrf-ESPd embedding scheme.

UNRAVELING THE EFFECTS OF
CO-CRYSTALLIZATION ON THE
UV/VIS ABSORPTION SPECTRA
OF A N-SALICYLIDENEANILINE. A
COMPUTATIONAL RI-CC2
INVESTIGATION. SUPPORTING
INFORMATION

Table D.1: Parameters used in the Ewald program.

Crystal	Zone 1 composition (Number of atoms)	Number of charges in zone 2 (diameter of zone 2)	Unit cell composition	Supercell "zones 1 + 2 + 3" dimensions	Total number of atoms ^a
PYV3	PYV3 (29)	4971 (44 Å)	4 PYV3	16x10x4	74240
PYV3 SA	PYV3 + SA (43)	9957 (56 Å)	4 PYV3 + 2 SA	20x4x10	115200
PYV3 FA1	PYV3 + FA (41)	9959 (56 Å)	4 PYV3 + 2 FA	20x4x10	112000

^a The total number of atoms corresponds to the sum of the numbers of atoms in zones 1, 2, and 3, in other words, the sum of the number of point charges in zones 2 and 3 and the number of atoms in the QC zone 1.

Table D.2: Ahlrichs basis sets and their contracted compositions for the atoms in PYV3-I2but.

Basis Set	Composition
def2-SVP	C, N, O, F 3s 2p 1d I 4s 4p 2d H 2s 1p
def2-SVPD	C, N 4s 2p 2d O, F 4s 3p 2d I 5s 5p 3d H 2s 2p
def2-TZVP	C, N, O, F 5s 3p 2d 1f I 6s 5p 3d 2f H 3s 1p
def2-TZVPP	C, N, O, F, I def2-TZVP H 3s 2p 1d
def2-TZVPD	C, N 6s 3p 3d 1f O, F 6s 4p 3d 1f I 7s 6p 4d 2f H 3s 2p
def2-TZVPPD	C, N, O, F, I def2-TZVPD H 3s 3p 1d
def2-QZVP	C, N, O, F 7s 4p 3d 2f 1g I 7s 6p 4d 4f 1g H 4s 3p 2d 1f

Table D.3: Contributions of the T_1 and T_2 clusters to the RI-CC2 and RI-CCSD excited states of the enol and keto forms of the isolated PYV3[PYV3] molecule (in %), as calculated with the def2-TZVPD basis set.

State	Enol			
	RI-CC2		RI-CCSD	
	T_1	T_2	T_1	T_2
1	87.1	12.9	92.2	7.8
2	89.0	11.0	93.0	7.0
3	87.6	12.4	92.9	7.1
4	87.6	12.4	91.6	8.4
5	88.8	11.2	92.9	7.1

State	Keto			
	RI-CC2		RI-CCSD	
	T_1	T_2	T_1	T_2
1	87.4	12.6	91.8	8.2
2	85.5	14.5	92.3	7.7
3	87.6	12.4	92.4	7.6
4	86.6	13.5	91.8	8.2
5	89.3	10.8	94.5	5.6

Table D.4: RI-CC2/def2-TZVPD wavelengths of excitation, λ in nm, and oscillator strengths, f , for the enol forms of isolated PYV3 (PYV3[PYV3]) and its co-crystals (PYV3[PYV3·XXX]). For PYV3, the absolute values are given while for the co-crystals, the absolute variations and relative variations are given for the wavelengths and oscillator strengths, respectively.

Crystal	2 nd absorption band			
	2 nd excitation		3 rd excitation	
	λ	f	λ	f
PYV3[PYV3]	293	0.466	273	0.144
PYV3[SA]	−3	+10 %	+3	−75 %
PYV3[FA1]	−2	+11 %	+4	−73 %
PYV3[FA2]	+2	−24 %	+2	+13 %
PYV3[DHBP]	−1	+8 %	+4	−45 %
PYV3[SDP]	−2	+54 %		—
PYV3[I2but]	+8	−75 %	+9	+301 %
PYV3[I2F4]	+11	−72 %	+10	+287 %
PYV3-N[I3F3]	−4	−89 %	0	+356 %
PYV3-O[I3F3]	−11	−75 %	−8	+267 %

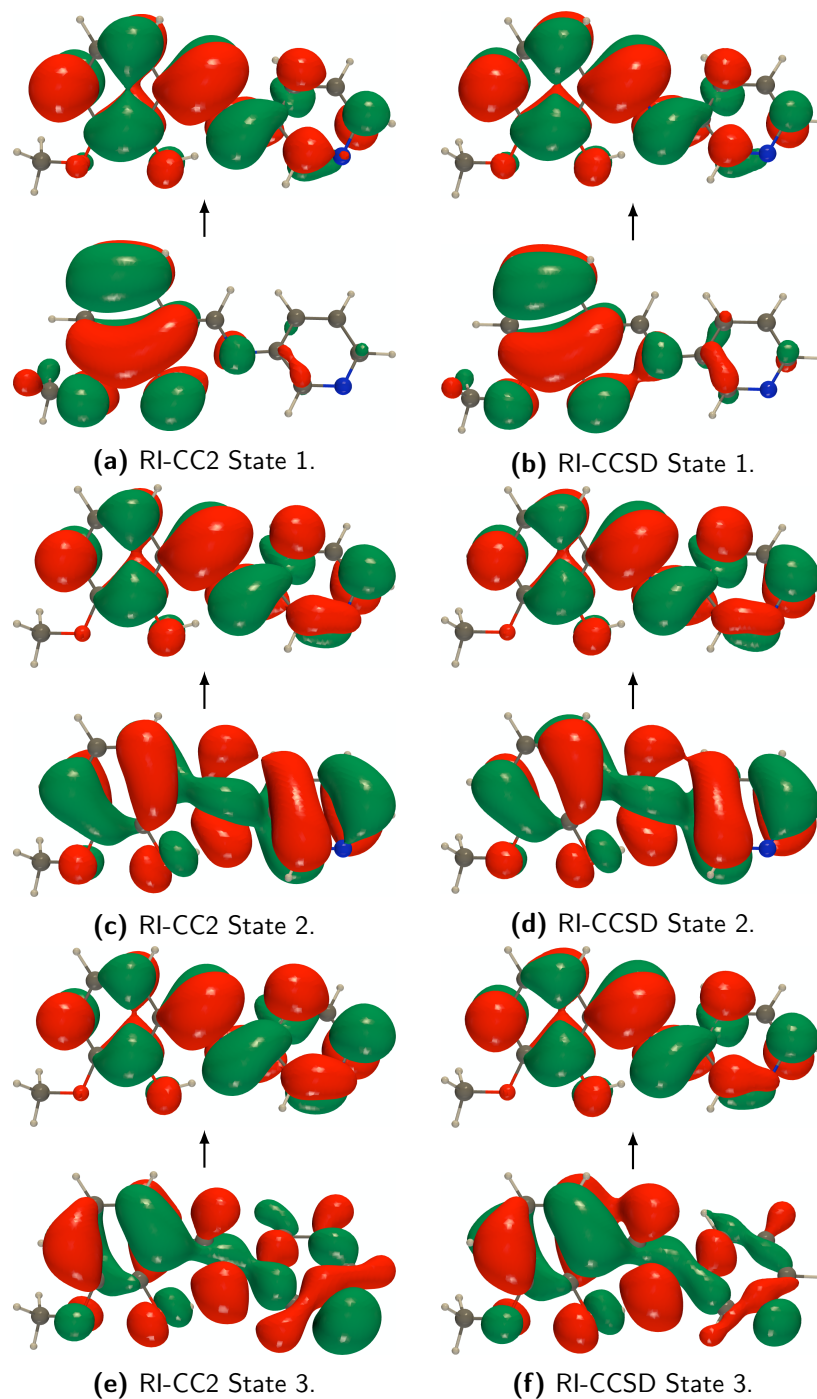


Figure D.1: def2-TZVPD NTOs (holes below the arrows and particles above them) of the isolated PYV3[PYV3] enol form (isovalue of 0.02 a.u.).

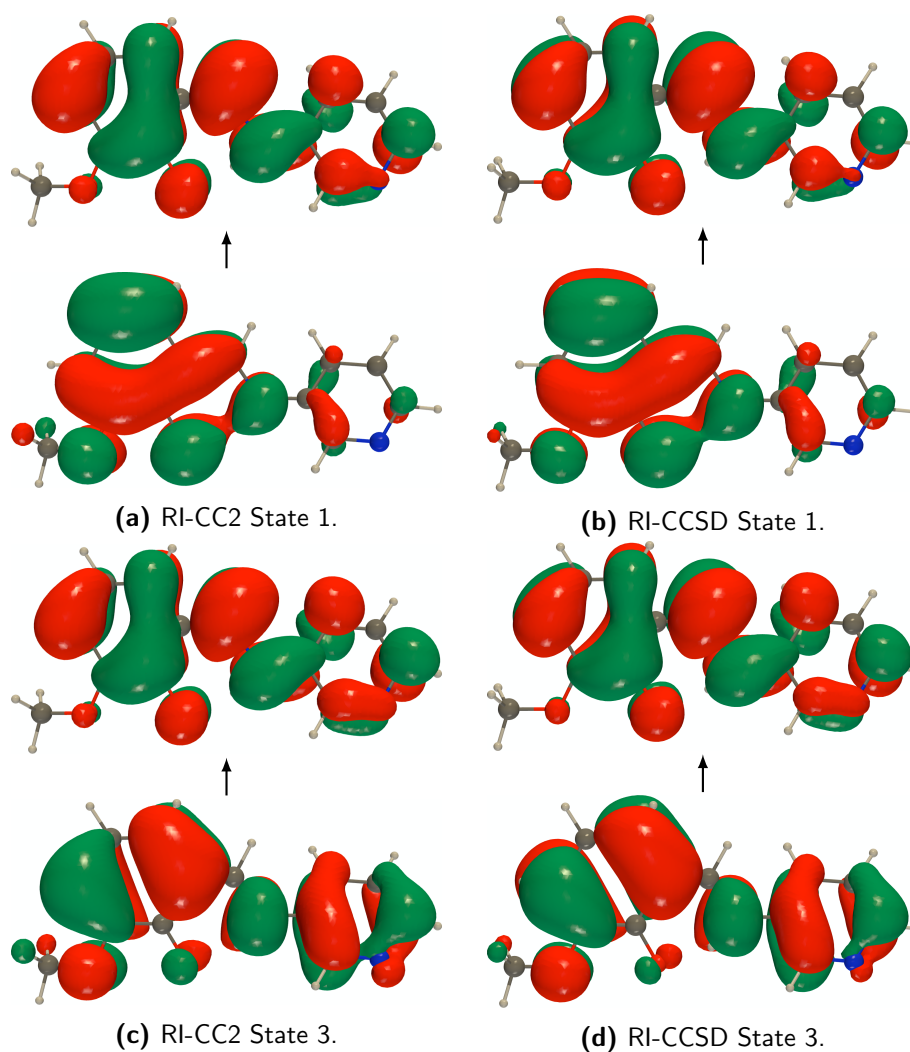


Figure D.2: def2-TZVPD NTOs (holes below the arrows and particles above them) of the isolated PYV3[PYV3] keto form (isovalue of 0.02 a.u.).

Table D.5: RI-CC2/def2-TZVPD wavelengths of excitation, λ in nm, and oscillator strengths, f , for the keto forms of isolated PYV3 (PYV3[PYV3]) and its co-crystals (PYV3[PYV3·XXX]). For PYV3, the absolute values are given while for the co-crystals, the absolute variations and relative variations are given for the wavelengths and oscillator strengths, respectively.

	2 nd absorption band	
	3 rd excitation	
	λ	f
PYV3[PYV3]	304	0.476
PYV3[PYV3·SA]	−3	−3 %
PYV3[PYV3·FA1]	−2	−2 %
PYV3[PYV3·FA2]	0	0 %
PYV3[PYV3·DHBP]	0	0 %
PYV3[PYV3·SDP]	+6	+4 %
PYV3[PYV3·I2but]	+4	+1 %
PYV3[PYV3·I2F4]	+3	+1 %
PYV3-N[PYV3·I3F3]	0	+1 %
PYV3-O[PYV3·I3F3]	−11	−3 %

Table D.6: RI-CC2/def2-TZVPD wavelengths of excitation, λ in nm, and oscillator strengths, f , for the enol forms of isolated PYV3 (PYV3[PYV3]) and the heteromers of its co-crystals (PYV3+XXX[PYV3·XXX]). For PYV3, the absolute values are given while for the co-crystals, the absolute variations and relative variations are given for the wavelengths and oscillator strengths, respectively.

Crystal	2 nd absorption band			
	2 nd excitation		3 rd excitation	
	λ	f	λ	f
PYV3[PYV3]	293	0.466	273	0.144
PYV3+SA[PYV3·SA]	−3	+30 %	−6	−8 %
PYV3+FA[PYV3·FA1] ^a	−2	+33 %	−6	−12 %

^a The oscillator strength of actual 3rd excited state is null, here the data is given for the 4th one.

Table D.7: RI-CC2/def2-TZVPD wavelengths of excitation, λ in nm, and oscillator strengths, f , for the keto forms of isolated PYV3 (PYV3[PYV3]) and the heteromers of its co-crystals (PYV3+XXX[PYV3·XXX]). For PYV3, the absolute values are given while for the co-crystals, the absolute variations and relative variations are given for the wavelengths and oscillator strengths, respectively.

Crystal	2 nd absorption band	
	3 rd excitation	
	λ	f
PYV3[PYV3]	304	0.476
PYV3+SA[PYV3·SA]	0	0 %
PYV3+FA[PYV3·FA1]	0	0 %

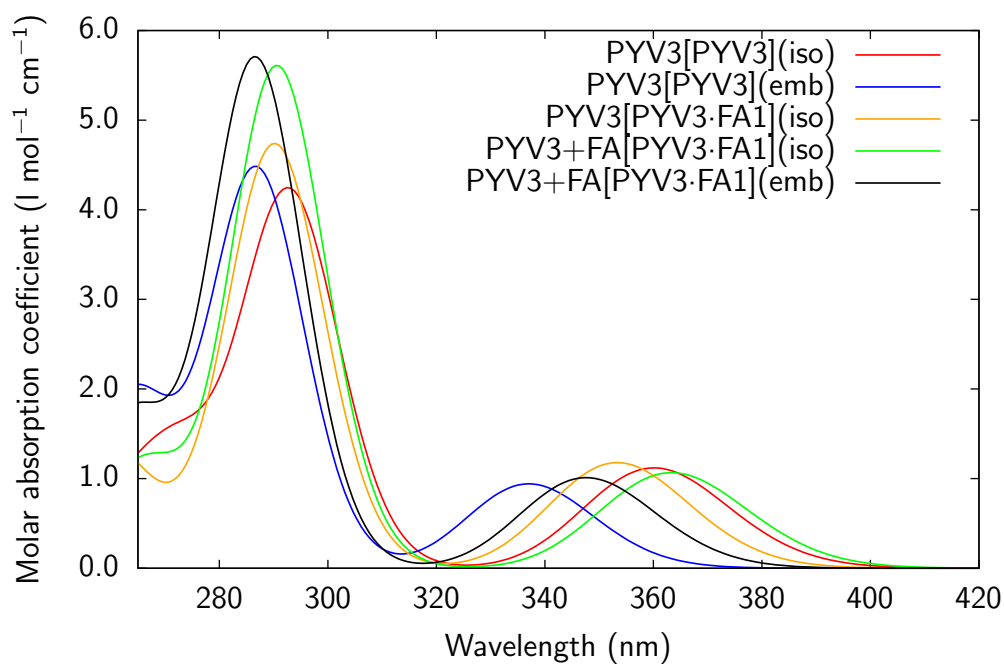
Table D.8: RI-CC2/def2-TZVPD wavelengths of excitation (λ in nm) and oscillator strengths (f) for the enol forms of the isolated and embedded PYV3 (PYV3[PYV3]) and the embedded heteromers of its co-crystals (PYV3+XXX[PYV3·XXX]). For PYV3, the absolute values are given while for the co-crystals, the absolute variations and relative variations are given for the wavelengths and oscillator strengths, respectively.

Crystal		2 nd absorption band			
		2 nd excitation		3 rd excitation	
		λ	f	λ	f
PYV3[PYV3]	(iso)	293	0.466	273	0.144
PYV3[PYV3]	(emb)	287	0.495	264	0.214
PYV3+SA[PYV3·SA]	(emb)	−1	+26 %	0	−22 %
PYV3+FA[PYV3·FA1]	(emb)	0	+27 %	0	−22 %

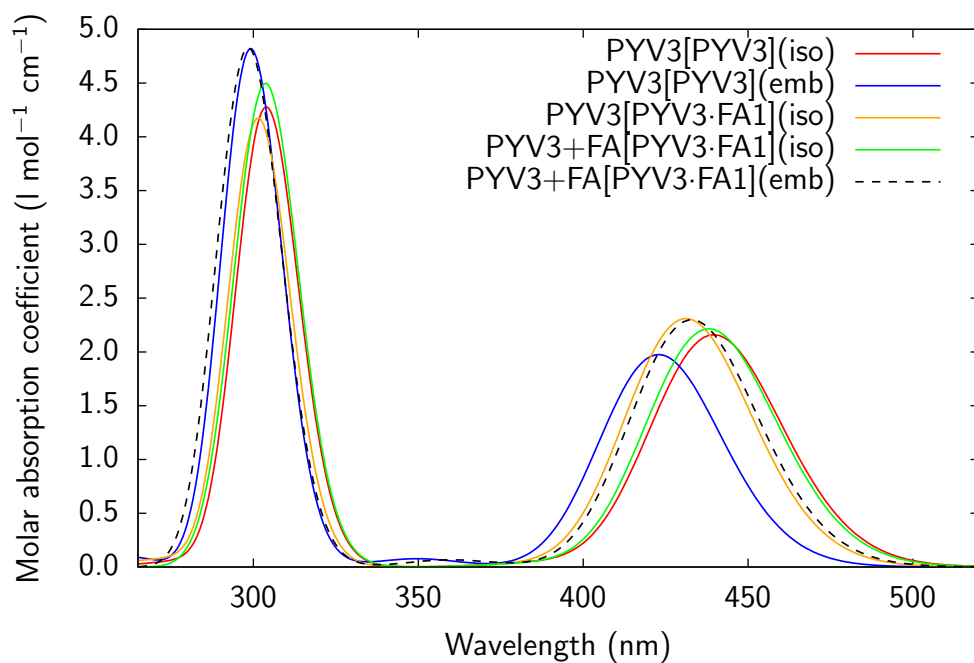
The oscillator strength of actual 3rd excited state is null, here the data is given for the 4th one.

Table D.9: RI-CC2/def2-TZVPD wavelengths of excitation (λ , in nm) and oscillator strength (f) for the keto forms of the isolated and embedded monomer of PYV3 (PYV3[PYV3]) and the variations for the embedded heteromers of co-crystals (PYV3+XXX[PYV3·XXX], w.r.t. the embedded PYV3).

Crystal		2 nd absorption band			
		3 rd excitation		4 th excitation	
		λ	f	λ	f
PYV3[PYV3]	(iso)	304	0.476	—	—
PYV3[PYV3]	(emb)	299	0.536	—	—
PYV3+SA[PYV3·SA]	(emb)	+1	−33 %	−6	−61 %
PYV3+FA[PYV3·FA1]	(emb)	+2	−38 %	−5	−54 %



(a) Enol.



(b) Keto.

Figure D.3: RI-CC2/def2-TZVPD UV/Vis absorption spectra of all models considered for PYV3 and PYV3·FA1.

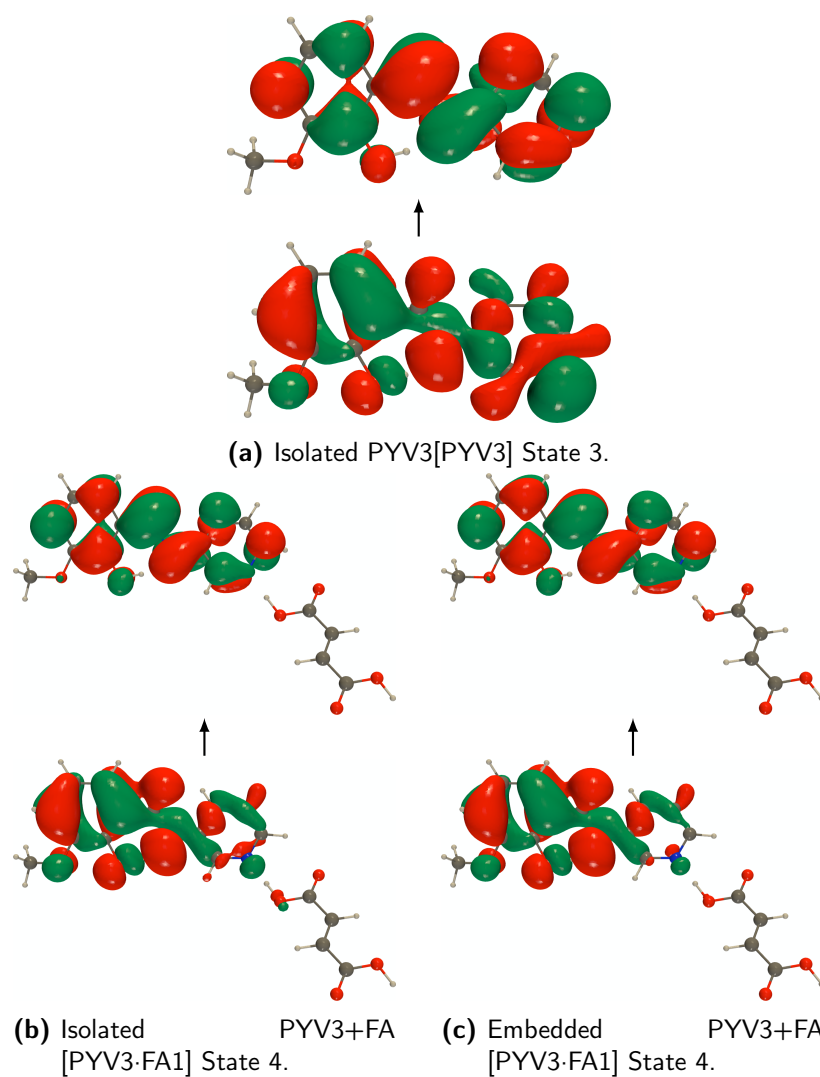


Figure D.4: RI-CC2/def2-TZVPD NTOs (holes below the arrows and particles above them) of the 3rd excited state of the isolated PYV3[PYV3] enol form and of the 4th excited state of the isolated and embedded PYV3+FA[PYV3·FA1] (isovalue of 0.02 a.u.).

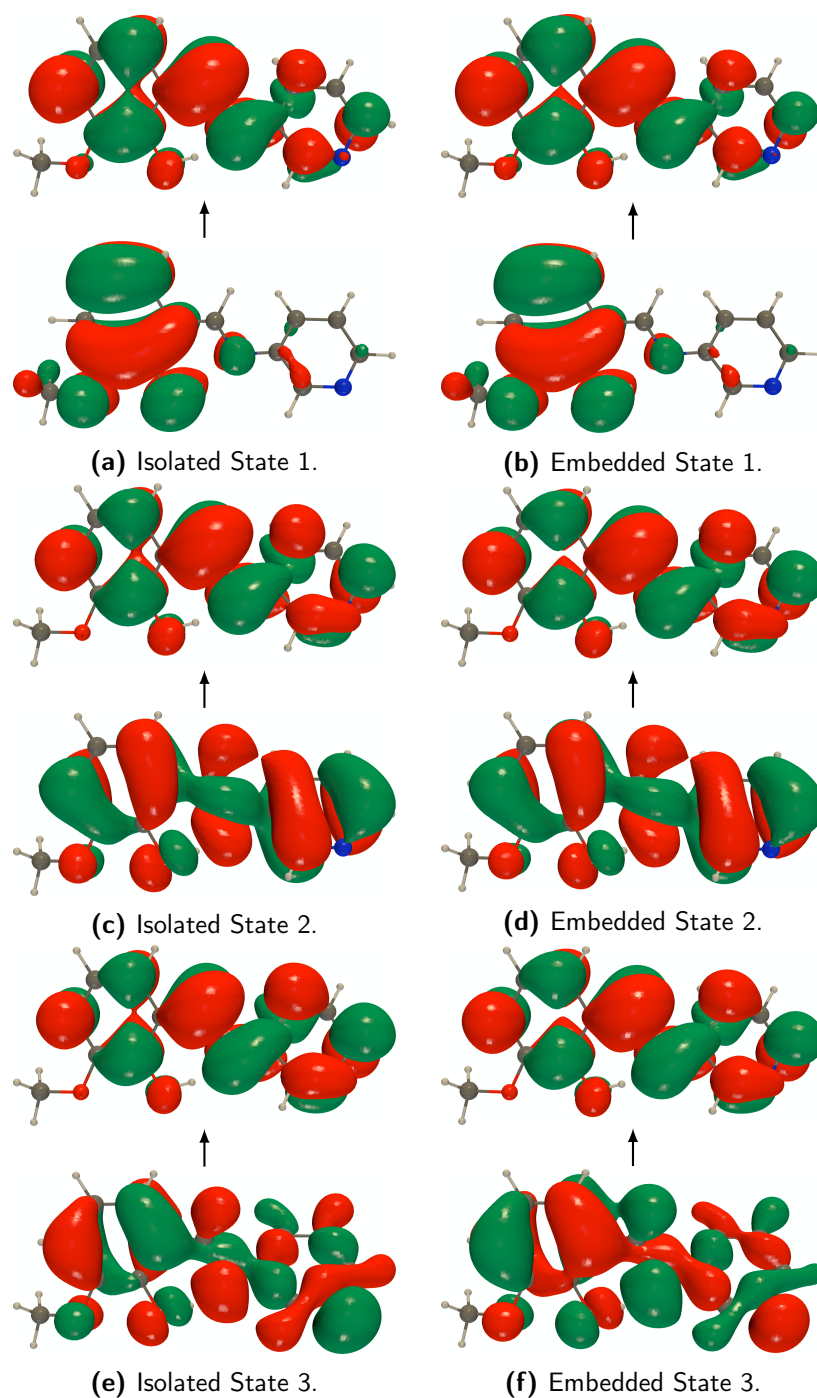


Figure D.5: RI-CC2/def2-TZVPD NTOs (holes below the arrows and particles above them) of the isolated and embedded PYV3[PYV3] enol form (isovalue of 0.02 a.u.).

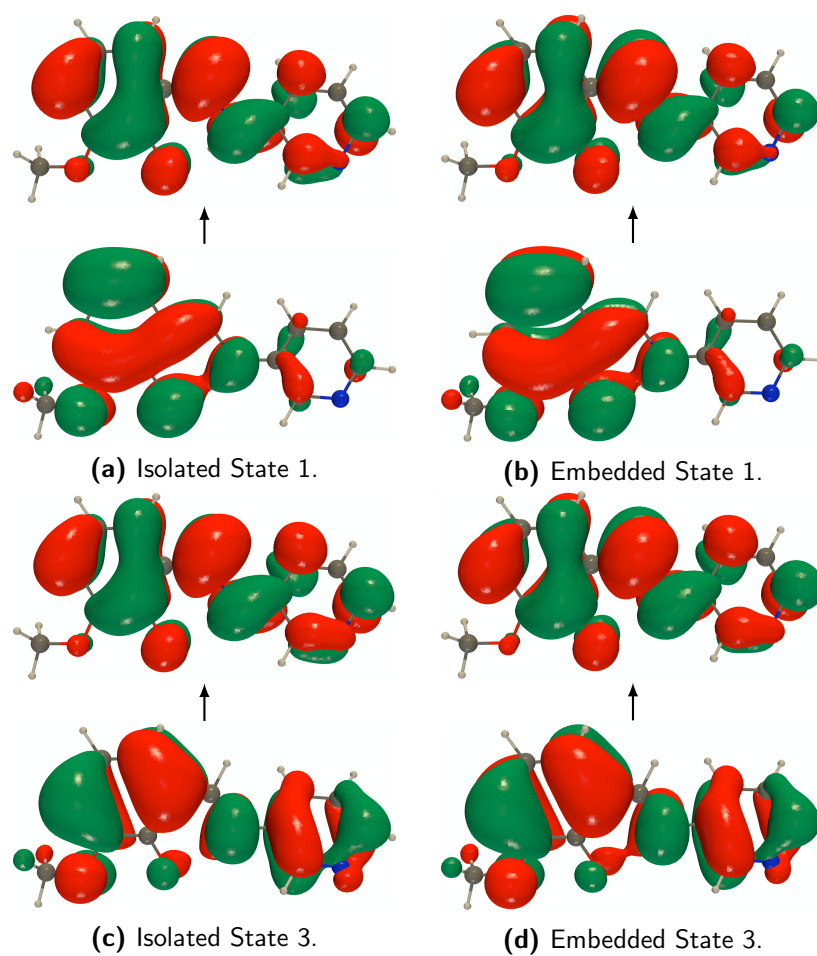


Figure D.6: RI-CC2/def2-TZVPD NTOs (holes below the arrows and particles above them) of the isolated and embedded PYV3[PYV3] keto form (isovalue of 0.02 a.u.).

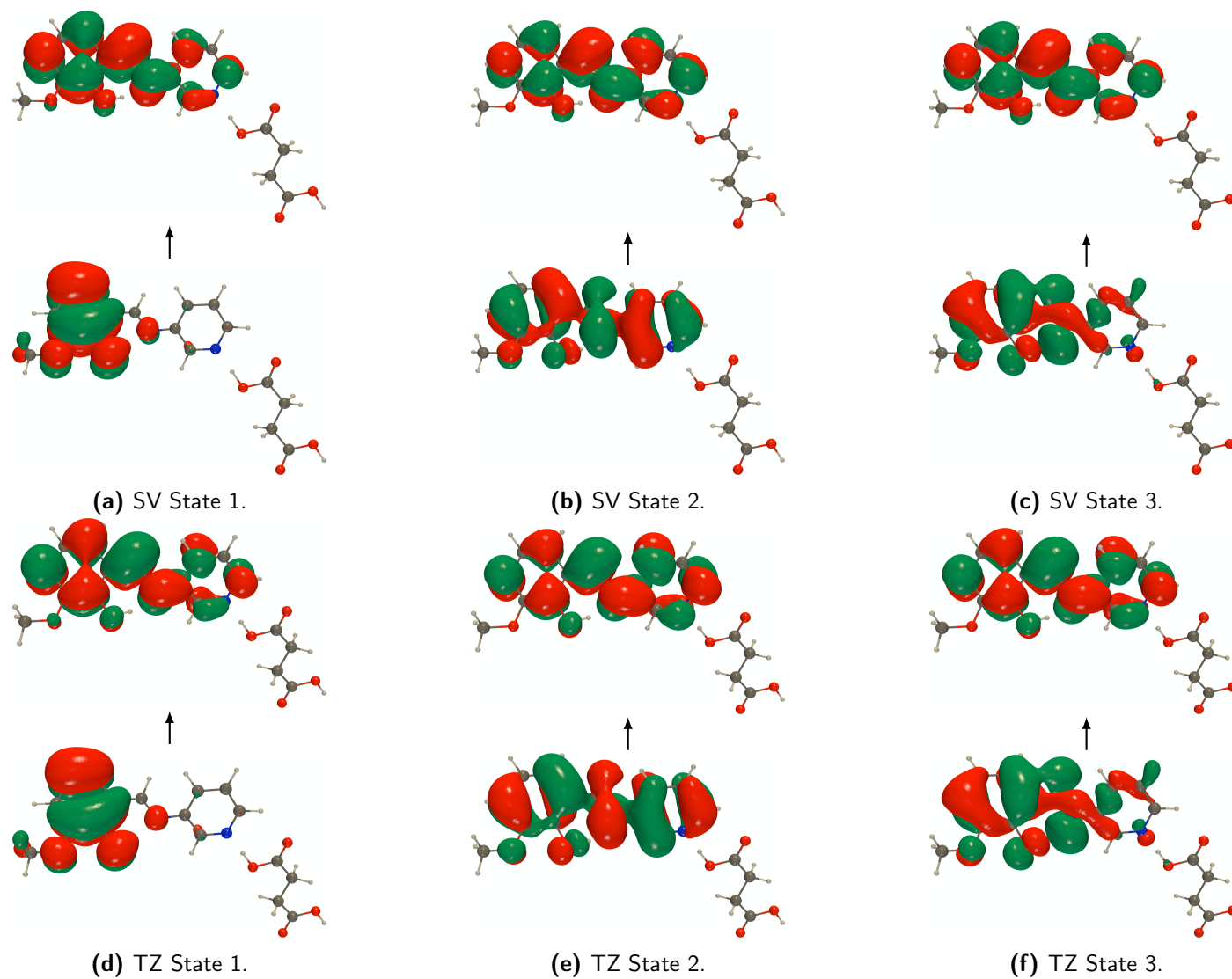


Figure D.7: RI-CC2 def2-SVPD (SV) and def2-TZVPD (TZ) NTOs (holes below the arrows and particles above them) of the embedded PYV3+SA[PYV3·SA] enol form (isovalue of 0.02 a.u.).

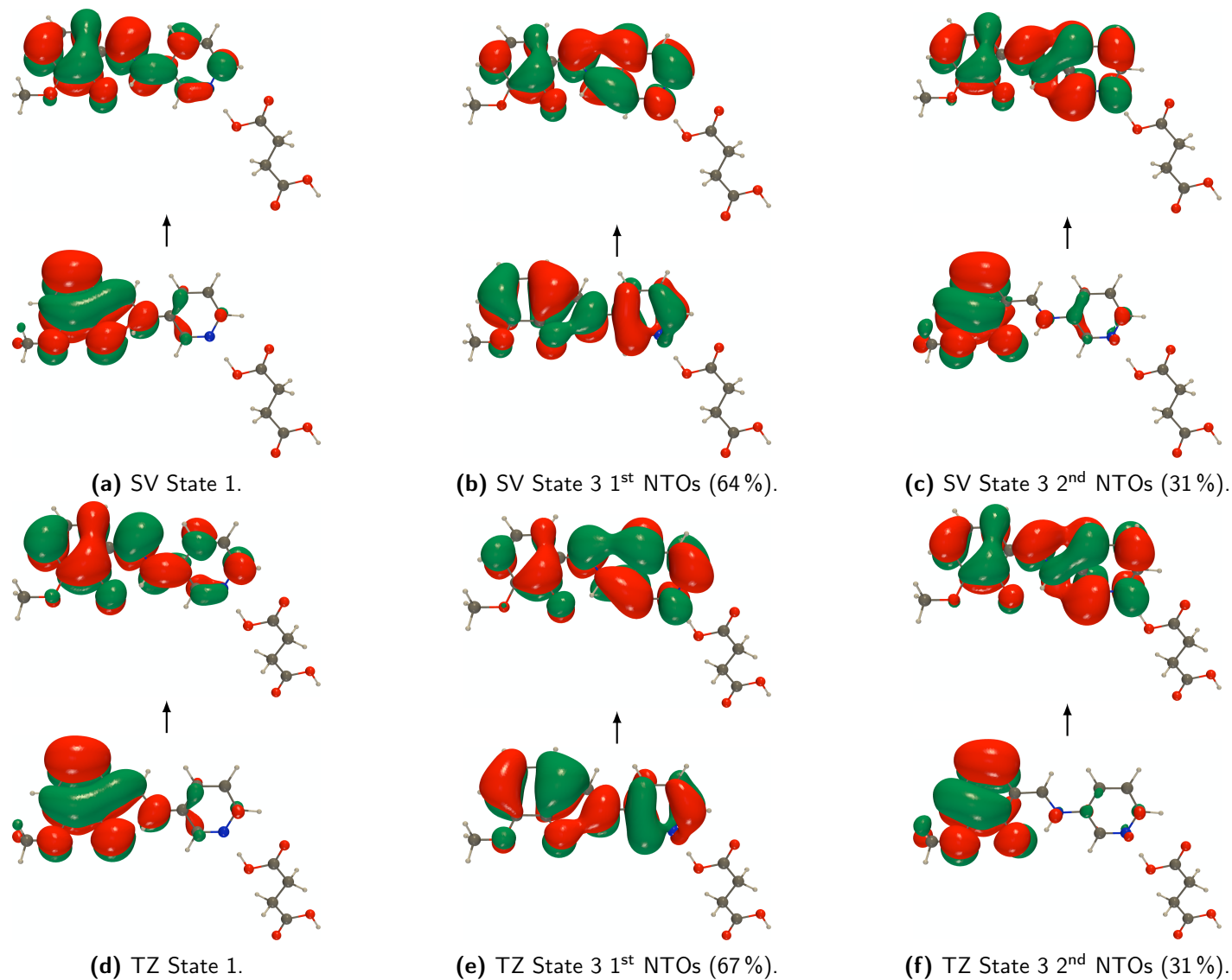


Figure D.8: RI-CC2 def2-SVPD (SV) and def2-TZVPD (TZ) NTOs (holes below the arrows and particles above them) of the embedded PYV3+SA[PYV3·SA] keto form (isovalue of 0.02 a.u.).

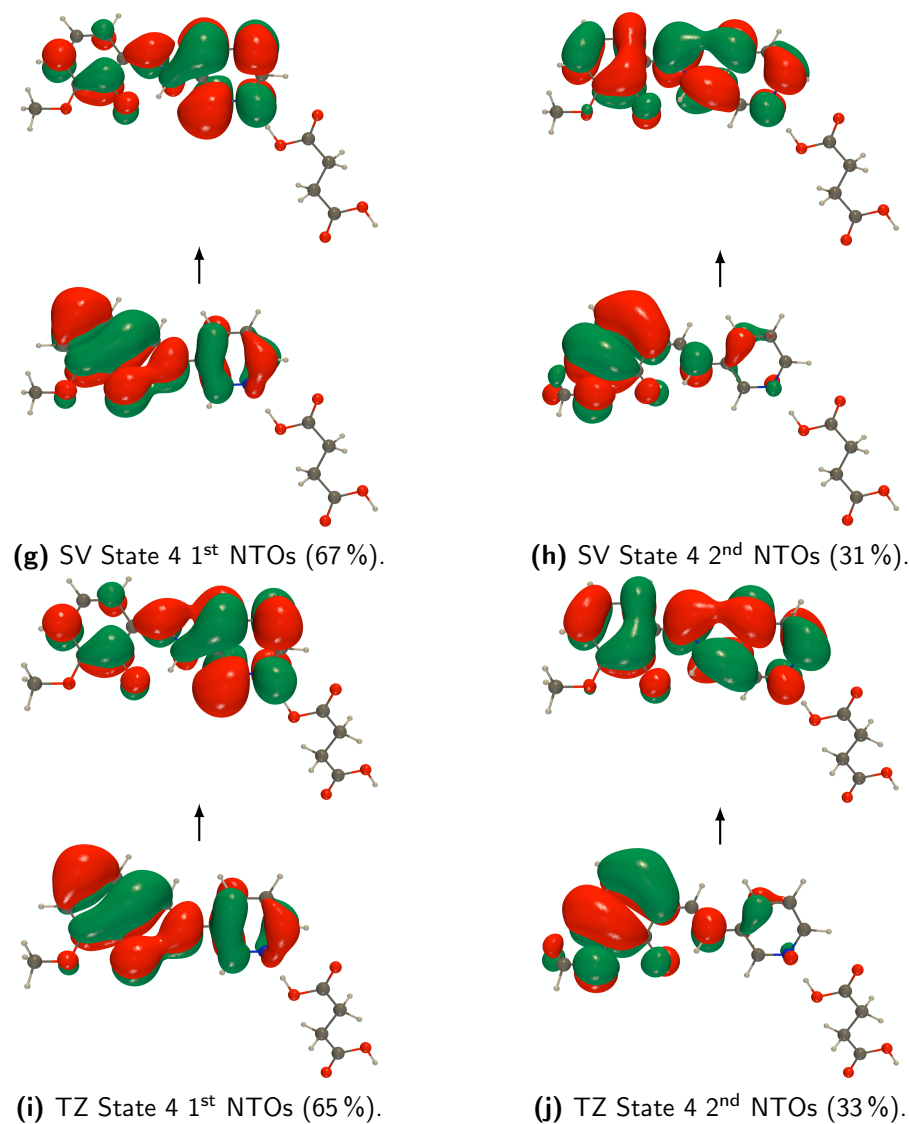
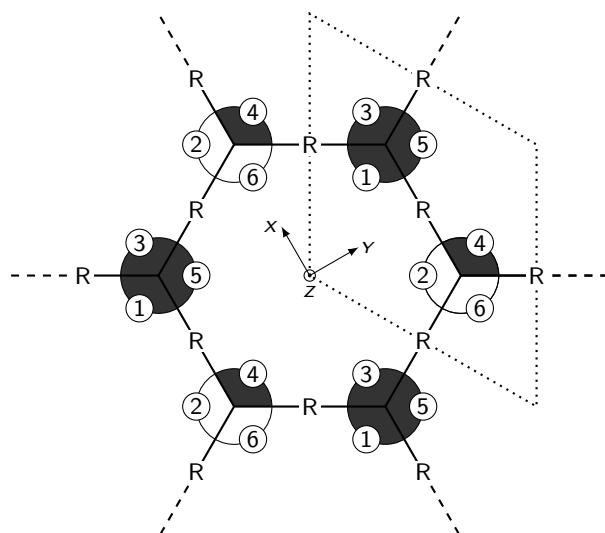


Figure D.8: RI-CC2 def2-SVPD (SV) and def2-TZVPD (TZ) NTOs (holes below the arrows and particles above them) of the embedded PYV3+SA[PYV3·SA] keto form (isovalue of 0.02 a.u., continued).

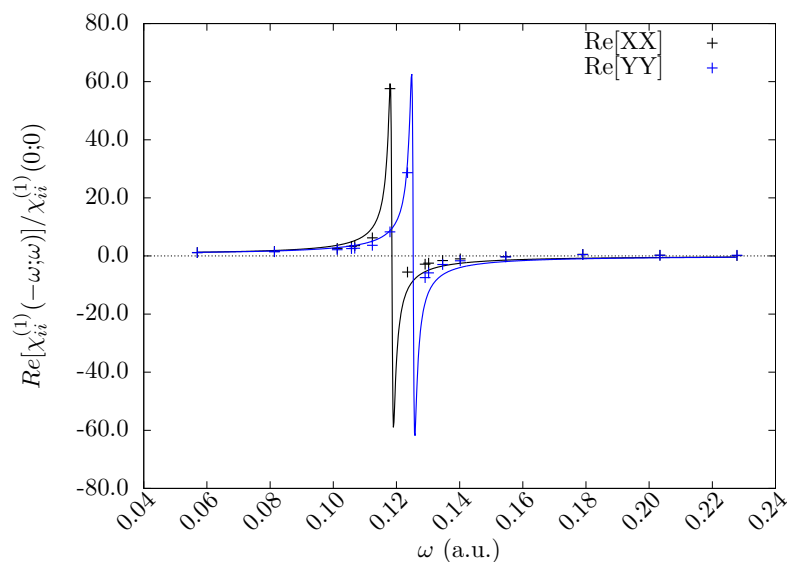
SALICYLIDENEANILINE-BASED
COFs: A NEW FAMILY OF
MULTI-STATE SECOND-ORDER
NONLINEAR OPTICAL SWITCHES.
SUPPORTING INFORMATION



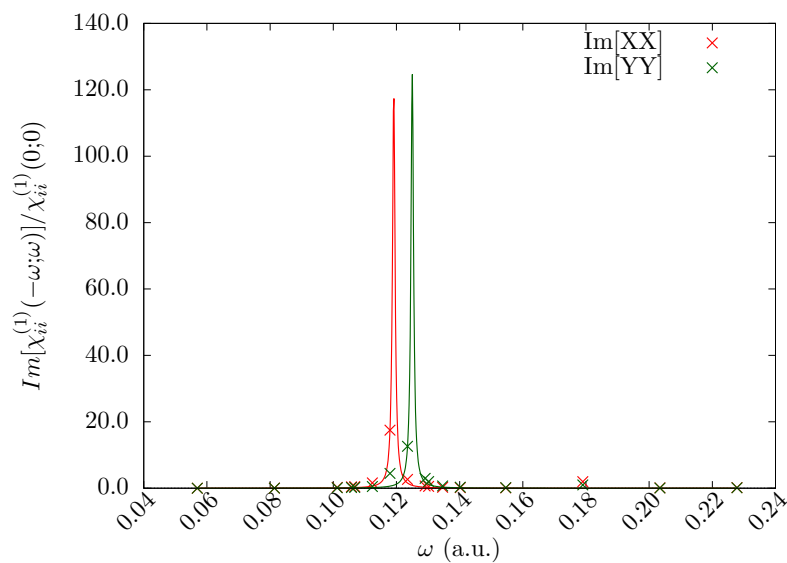
Scheme E.1: Schematic representation of the 2K4E/1-3-4-5 isomer of a model COF, primitive unit cell, and numbering code for distinguishing the tautomers in the Cartesian space. The full spaces denote E forms while empty spaces K forms.

Table E.1: Schematic representations and space groups of the different tautomers (centro-symmetric or not) and list of independent non-zero components of their static $\chi^{(1)}$ and $\chi^{(2)}$ tensors. Components identical by Kleinmann symmetry are not specified (e.g. $\chi_{XXY}^{(2)} = \chi_{XYX}^{(2)} = \chi_{YXX}^{(2)}$).

Tautomer		Space group (centro-symmetry)	$\chi^{(1)}$ tensor components	$\chi^{(2)}$ tensor components
6K0E		P6/m (✓)	$XX(=YY), ZZ$	—
5K1E		P11m (✗)	XX, XY, YY, ZZ	$XXX, XXY, XYY, XZZ, YYY, YZZ$
4K2E	1-2	P11m (✗)	XX, XY, YY, ZZ	$XXX, XXY, XYY, XZZ, YYY, YZZ$
	1-3	P11m (✗)	XX, XY, YY, ZZ	$XXX, XXY, XYY, XZZ, YYY, YZZ$
	1-4	P112/m (✓)	XX, XY, YY, ZZ	—
3K3E	1-2-3	P11m (✗)	XX, XY, YY, ZZ	$XXX, XXY, XYY, XZZ, YYY, YZZ$
	1-3-4	P11m (✗)	XX, XY, YY, ZZ	$XXX, XXY, XYY, XZZ, YYY, YZZ$
	1-3-5	$P\bar{6}$ (✗)	$XX(=YY), ZZ$	$XXX = -XYY, YYY = -XXY$
	1-4-5	P11m (✗)	XX, XY, YY, ZZ	$XXX, XXY, XYY, XZZ, YYY, YZZ$
2K4E	1-2-3-4	P11m (✗)	XX, XY, YY, ZZ	$XXX, XXY, XYY, XZZ, YYY, YZZ$
	1-2-4-5	P112/m (✓)	XX, XY, YY, ZZ	—
	1-3-4-5	P11m (✗)	XX, XY, YY, ZZ	$XXX, XXY, XYY, XZZ, YYY, YZZ$
1K5E		P11m (✗)	XX, XY, YY, ZZ	$XXX, XXY, XYY, XZZ, YYY, YZZ$
0K6E		P6/m (✓)	$XX(=YY), ZZ$	—

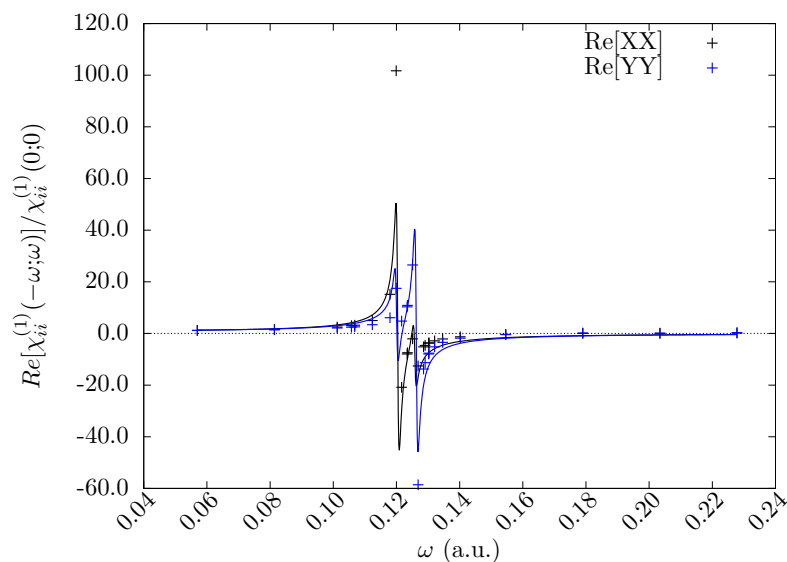


(a) Excitation energies: 0.119 a.u. (3.23 eV) and 0.125 a.u. (3.41 eV)

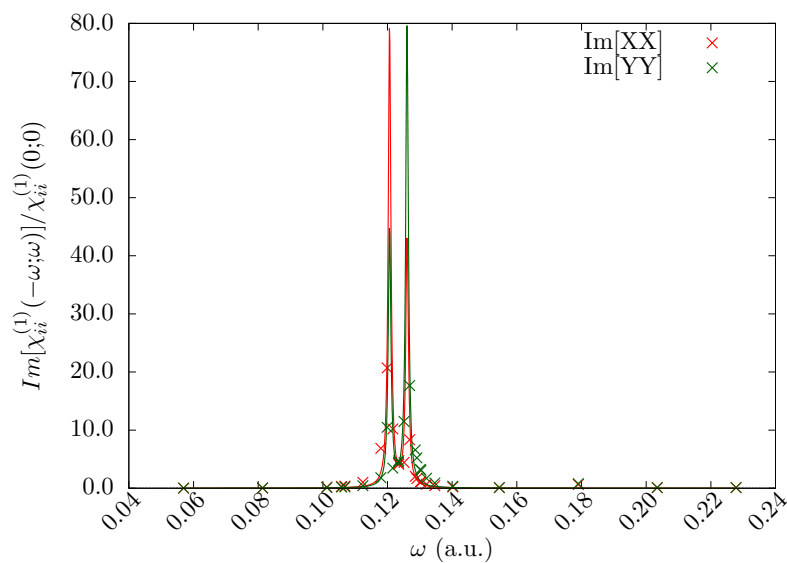


(b) Excitation energies: 0.119 a.u. (3.23 eV) and 0.125 a.u. (3.41 eV)

Figure E.1: Frequency dispersions of $\chi^{(1)}$ of the 4K2E/1-2 tautomer of COF 1 as evaluated at the PBC/ ω B97X/6-31G(d,p) level of approximation, its fitting curves, and the corresponding excitation energies. Top/bottom graphs give the real/imaginary component of the frequency dispersion.



(a) Excitation energies: 0.121 a.u. (3.30 eV) and 0.127 a.u. (3.45 eV)



(b) Excitation energies: 0.121 a.u. (3.30 eV) and 0.127 a.u. (3.45 eV)

Figure E.2: Frequency dispersions of $\chi^{(1)}$ of the 5K1E tautomer of COF 1 as evaluated at the PBC/ ω B97X/6-31G(d,p) level of approximation, its fitting curves, and the corresponding excitation energies. Top/bottom graphs give the real/imaginary component of the frequency dispersion.

Table E.2: Linear optical properties of the different tautomers of COF 1: average refractive index in the XY plane, $n_{XY} = (n_X + n_Y)/2$, refractive index along Z, n_Z , birefringence, $\delta = (n_{XY} - n_Z)$, and acute angle between the optical axes, $2V$ (degrees). All values were evaluated at the PBC/ ω B97X/6-31G(d,p) level of approximation for $\omega = 0$.

Tautomer	n_{XY}	n_Z	δ	2V	
6K0E	1.479	1.110	0.369	—	
5K1E	1.486	1.111	0.375	24.6	
4K2E	1-2	1.494	1.112	0.382	25.1
	1-3	1.489	1.112	0.378	23.2
	1-4	1.492	1.112	0.380	33.9
3K3E	1-2-3	1.499	1.113	0.386	19.1
	1-3-4	1.496	1.113	0.383	29.4
	1-3-5	1.481	1.112	0.369	—
	1-4-5	1.495	1.112	0.383	31.8
2K4E	1-2-3-4	1.501	1.113	0.388	23.7
	1-3-4-5	1.497	1.113	0.384	32.7
	1-2-4-5	1.488	1.113	0.375	24.1
1K5E	1.490	1.113	0.377	23.1	
0K6E	1.481	1.114	0.367	—	

Table E.3: $\chi_{XXX}^{(2)}$ ($= 2d_{11}$) tensor components (pm V^{-1}) for the tautomers of COF 1-5 as evaluated at the PBC/ ω B97X/6-31G(d,p) level of approximation.

Tautomer		1	2	3	4	5
5K1E		3.50	3.57	2.04	1.98	1.09
4K2E	1-2	9.77	10.16	5.58	6.01	3.90
	1-3	7.32	7.46	4.44	4.11	2.18
3K3E	1-2-3	14.75	15.13	8.19	7.49	5.15
	1-3-4	−6.75	−7.06	−3.62	−3.18	−2.84
	1-3-5	0.83	0.76	0.47	0.59	0.40
	1-4-5	4.19	4.21	2.50	2.27	1.14
2K4E	1-2-4-5	11.77	12.07	6.25	5.63	4.12
	1-3-4-5	−2.82	−2.94	−1.51	−1.38	−1.57
1K5E		3.88	4.05	1.96	1.75	1.24

Table E.4: $\chi_{XY}^{(2)}$ ($= 2d_{12}$) tensor components (pm V^{-1}) for the tautomers of COF 1-5 as evaluated at the PBC/ ω B97X/6-31G(d,p) level of approximation.

Tautomer		1	2	3	4	5
5K1E		1.34	1.43	0.81	0.64	0.80
4K2E	1-2	2.94	3.07	1.73	1.58	1.24
	1-3	2.76	2.85	1.63	1.30	1.59
3K3E	1-2-3	4.85	4.95	2.74	2.37	2.14
	1-3-4	-1.72	-1.84	-1.01	-0.99	-0.45
	1-3-5	-0.84	-0.76	-0.49	-0.60	-0.40
	1-4-5	1.29	1.28	0.78	0.62	0.77
2K4E	1-2-4-5	3.58	3.67	1.98	1.79	1.31
	1-3-4-5	-2.30	-2.33	-1.29	-1.26	-0.41
1K5E		-0.24	-0.18	-0.18	-0.18	0.10

Table E.5: $\chi_{XY}^{(2)}$ ($= 2d_{31}$) tensor components (pm V^{-1}) for the tautomers of COF 1-5 as evaluated at the PBC/ ω B97X/6-31G(d,p) level of approximation.

Tautomer		1	2	3	4	5
5K1E		-1.36	-1.35	-0.84	-0.71	-0.72
4K2E	1-2	-0.72	-0.83	-0.52	-0.43	-0.44
	1-3	0.58	0.72	0.40	0.44	0.03
3K3E	1-2-3	1.63	1.66	0.79	0.76	0.40
	1-3-4	-1.27	-1.15	-0.79	-0.71	-0.41
	1-3-5	0.71	0.90	0.29	0.28	0.26
	1-4-5	2.13	2.28	1.28	1.18	0.83
2K4E	1-2-4-5	3.87	3.79	2.17	1.95	1.30
	1-3-4-5	2.27	2.45	1.13	1.04	0.98
1K5E		3.17	3.25	1.74	1.60	1.29

Table E.6: $\chi_{YYY}^{(2)}$ ($= 2d_{22}$) tensor components (pm V^{-1}) for the tautomers of COF 1-5 as evaluated at the PBC/ ω B97X/6-31G(d,p) level of approximation.

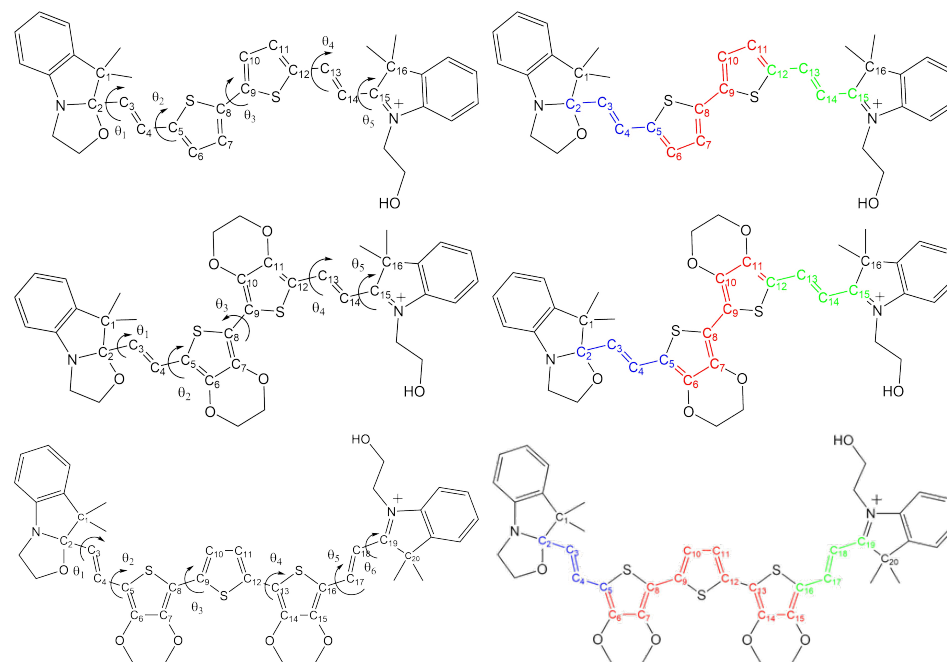
Tautomer		1	2	3	4	5
5K1E		−3.65	−3.96	−2.27	−2.00	−1.60
4K2E	1-2	−2.86	−3.10	−1.80	−1.44	−1.49
	1-3	1.33	1.04	1.00	1.10	0.66
3K3E	1-2-3	2.82	2.62	1.80	1.71	0.96
	1-3-4	−3.12	−3.15	−1.95	−1.90	−0.83
	1-3-5	−0.72	−0.90	−0.31	−0.28	−0.26
	1-4-5	5.00	5.10	3.33	2.99	2.29
2K4E	1-2-4-5	9.51	9.54	5.71	5.34	3.39
	1-3-4-5	3.33	3.43	2.03	1.78	1.44
1K5E		7.01	7.10	4.13	3.86	2.45

Table E.7: Volume (\AA^3) of the primitive unit cells of the tautomers of COFs 1-5 as evaluated from full geometry optimization at the PBC/ ω B97X/6-31G(d,p) level of approximation.

Tautomer		1	2	3	4	5
6K0E		1622.7	1674.8	3559.7	3740.6	2997.9
5K1E		1617.7	1668.3	3550.3	3730.4	2980.2
4K2E	1-2	1612.1	1662.5	3542.3	3719.8	2971.7
	1-3	1611.6	1663.0	3543.1	3722.1	2971.2
	1-4	1609.3	1661.6	3541.6	3717.5	2971.5
3K3E	1-2-3	1603.3	1657.3	3536.2	3713.0	2963.0
	1-3-4	1602.7	1656.4	3535.4	3711.5	2961.3
	1-3-5	1605.3	1659.5	3537.7	3716.6	2966.0
	1-4-5	1605.8	1657.3	3533.7	3712.9	2961.5
2K4E	1-2-3-4	1600.2	1651.3	3525.8	3703.5	2953.8
	1-3-4-5	1599.0	1650.5	3527.3	3710.0	2952.1
	1-2-4-5	1599.1	1653.4	3527.7	3706.0	2957.9
1K5E		1596.2	1648.0	3520.6	3699.5	2949.4
0K6E		1591.7	1644.6	3517.0	3693.5	2944.5

MULTI-STATE
MULTI-ADDRESSABLE NONLINEAR
OPTICAL SWITCHES: A
QUANTUM CHEMICAL
INVESTIGATION OF COMPOUNDS
POSSESSING TWO IDENTICAL
BENZAZOLOOXAZOLIDINE UNITS.
SUPPORTING INFORMATION

F.1 Optimized Geometries and Maxwell-Boltzmann Distribution



Scheme F.1: Left) Definition of the torsion angles used to define the conformation of the different forms of DiBOX-Bt θ_1 : $[C_1-C_2-C_3-C_4]$, θ_2 : $[C_3-C_4-C_5-C_6]$, θ_3 : $[C_7-C_8-C_9-C_{10}]$, θ_4 : $[C_{11}-C_{12}-C_{13}-C_{14}]$ and θ_5 : $[C_{13}-C_{14}-C_{15}-C_{16}]$, DiBOX-BtO θ_1 : $[C_1-C_2-C_3-C_4]$, θ_2 : $[C_3-C_4-C_5-C_6]$, θ_3 : $[C_7-C_8-C_9-C_{10}]$, θ_4 : $[C_{11}-C_{12}-C_{13}-C_{14}]$ and θ_5 : $[C_{13}-C_{14}-C_{15}-C_{16}]$ and DiBOX-TtO θ_1 : $[C_1-C_2-C_3-C_4]$, θ_2 : $[C_3-C_4-C_5-C_6]$, θ_3 : $[C_7-C_8-C_9-C_{10}]$, θ_4 : $[C_{11}-C_{12}-C_{13}-C_{14}]$, θ_5 : $[C_{15}-C_{16}-C_{17}-C_{18}]$ and θ_6 : $[C_{17}-C_{18}-C_{19}-C_{20}]$. Right) Definition of the segments considered for evaluating the BLA's: the global BLA (BLA , red + blue + green) and the local BLA's (BLA' , in blue, and BLA'' , in green).

F.1.1 DiBOX-Bt

Table F.1 lists all the conformers retained for further analysis and illustrates how the change of conformation around a torsion angle impact the Gibbs free enthalpy of DiBOX-Bt in CF-CF. g is degeneracy factor associated with the symmetry of the conformers. It is used to calculate the Boltzmann's populations. The conformation of the bithiophene is the one with the most important impact on the stability of a conformer, with an increase of $6-9 \text{ kJ mol}^{-1}$ between CF-CF-1 and CF-CF-5,8,9. The $s\text{-trans} \rightarrow s\text{-cis}$ changes for the conformation around θ_2 is accompanied by an increase of ΔG^\ominus of $\sim 4-7 \text{ kJ mol}^{-1}$. For θ_1 and θ_5 ,

the 1,3–OH \rightarrow 1,3–NH interaction tends to be accompanied by an increase of energy, even if, for a given conformation of the linker, the evolution of energy with the successive 1,3–OH \rightarrow 1,3–NH conversion is not constant. Concerning the BLA's: the global BLA (BLA) amounts $(0.080 \pm 0.001) \text{ \AA}$ while BLA' attains $(0.136 \pm 0.001) \text{ \AA}$.

Table F.1: Values of the torsion angles (in $^\circ$), degeneracy factors (g), Gibbs free energies (ΔG^\ominus , kJ mol^{-1}), weights in the final Boltzmann's population (in %), and BLA's (local, BLA' , and global, BLA , in \AA) for the different conformers of DiBOX-Bt in its CF-CF form, as determined by geometry optimization at the M06/6-311G(d)/IEF-PCM (acetonitrile) level of theory.

Conf.	g	θ_1	θ_2	θ_3	θ_4	θ_5	ΔG^\ominus	%	BLA^a	BLA'
1	1	–112	–179	167	180	–112	0.0	48.5	0.081	0.135
2	2	–112	180	165	–6	–113	4.9	13.3	0.081	0.136
3	1	106	180	–165	180	106	4.7	7.4	0.081	0.135
4	2	–113	180	165	179	106	6.2	8.1	0.081	0.135
5	2	–113	180	–21	–179	106	6.3	7.8	0.081	0.135
6	2	–114	–6	164	–179	106	6.9	6.1	0.081	0.137
7	2	–113	179	164	–2	106	7.4	5.0	0.081	0.137
8	1	–110	–177	–15	–177	–110	7.8	2.1	0.080	0.135
9	1	106	–179	–21	–179	106	9.7	1.0	0.081	0.135
10	2	106	6	167	–178	106	11.8	0.8	0.081	0.137

^a all BLA values being negative, their absolute values are reported.

In the situation of DiBOX-Bt in CF-POF (Table F.2) the 1,3–NH interaction ($\theta_1 \sim 115^\circ$) tends to form more stable conformers than the 1,3–OH interaction ($\theta_1 \sim -115^\circ$), with a difference of ΔG^\ominus of about $2\text{--}3 \text{ kJ mol}^{-1}$. Concerning the conformation of the bithiophene, switching from the anti-parallel conformation ($\theta_3 \sim 180^\circ$) to the parallel one ($\theta_3 \sim 0^\circ$) is accompanied by a variation of $\sim 5 \text{ kJ mol}^{-1}$. The conformations around the θ_2 and θ_4 torsion angles have similar impact on the energy, with an increase of $3\text{--}5 \text{ kJ mol}^{-1}$ when a given conformer switches from the *s-trans* to *s-cis* conformations. The conformers with $\theta_1 \sim \pm 140^\circ$ are not presented since their Gibbs free enthalpies were superior to the energetic criterion, and therefore they are not retained. Concerning the BLA's, BLA' is largely superior to BLA'' ($\sim 0.140 \text{ \AA}$ vs $\sim 0.030 \text{ \AA}$), indicating that the π -electrons delocalization between the BOX in its POF and the bithiophene has a strong impact on the structure of the vinylene. The global BLA is about 0.050 \AA .

For POF-POF, the most stable conformer presents a bithiophene unit in anti conformation ($\theta_3 \sim 180^\circ$), the thiophenes and vinylenes in *s-trans* conformation (θ_2 and $\theta_4 \sim 180^\circ$), while the torsion angles between the BOX's and vinylenes are close to 0° . The results are summarized in Table F.3. As explained for DiBOX-

Table F.2: Values of the torsion angles (in $^{\circ}$), Gibbs free energies (ΔG^{\ominus} , kJ mol $^{-1}$), weights in the final Boltzmann's population (in %) and BLA's (global, BLA , and local, BLA' on CF side and BLA'' , on POF side, in \AA) for the different conformers of DiBOX-Bt in its CF-POF form, as determined by geometry optimization at the M06/6-311G(d)/IEF-PCM (acetonitrile) level of theory.

Conf.	θ_1	θ_2	θ_3	θ_4	θ_5	ΔG^{\ominus}	%	BLA^a	BLA'	BLA''
1	113	-180	-177	-179	-1	0.0	58.5	0.048	0.139	0.033
2	-117	-180	180	180	-2	2.3	22.8	0.047	0.139	0.032
3	114	179	-2	-179	-1	5.1	7.6	0.046	0.139	0.031
4	114	179	177	0	-2	6.3	4.6	0.048	0.139	0.035
5	-116	179	3	180	-2	7.0	3.4	0.046	0.138	0.030
6	-116	180	177	0	-2	7.3	3.1	0.047	0.139	0.034

^a all BLA values being negative, their absolute values are reported.

Bt in CF-POF, the increase of energy when θ_1 and/or θ_5 switches from $\sim 0^{\circ}$ to $\sim \pm 140^{\circ}$ was too important (~ 14 kJ mol $^{-1}$), so that all the retained conformers have θ_1 and θ_5 close to 0° . For θ_3 , switching from the *anti* to *syn* conformation is accompanied by an increase of ~ 3 -4 kJ mol $^{-1}$ while for θ_2 and θ_4 , changing a *s-trans* conformation to a *s-cis* conformation is accompanied by an augmentation of ~ 4 -5 kJ mol $^{-1}$. For this form the global BLA is close to ~ 0.030 \AA while the local BLA' tends to 0.050 \AA .

Table F.3: Values of the torsion angles (in $^{\circ}$), degeneracy factors (g), Gibbs free energies (ΔG^{\ominus} , kJ mol $^{-1}$), weights in the final Boltzmann's population (in %), and BLA's (local, BLA'' and global, BLA , in \AA) for the different conformers of DiBOX-Bt in its POF-POF form, as determined by optimization at the M06/6-311G(d)/IEF-PCM (acetonitrile) level of theory.

Conf.	g	θ_1	θ_2	θ_3	θ_4	θ_5	ΔG^{\ominus}	%	BLA^a	BLA''
1	1	2	-179	180	179	-2	0.0	52.8	0.032	0.049
2	1	1	179	6	180	-2	2.6	18.5	0.032	0.048
3	2	2	1	-180	180	-2	4.5	17.4	0.032	0.049
4	2	-2	-180	-2	-1	1	6.7	7.1	0.031	0.049
5	2	0	-2	177	-1	-3	9.1	2.7	0.031	0.050
6	2	-1	1	10	-1	2	10.5	1.5	0.030	0.049

^a all BLA values being negative, their absolute values are reported.

F.1.2 DiBOX-BtO

Only two conformers were retained in the final population of DiBOX-BtO in CF-CF form (Table F.4). These two conformers differ only by the value of the torsion between a BOX and a vinylene. All the other optimized conformers have too high energy to be considered in the final population. The global BLA has a value of about 0.080 Å while the local BLA's amounts to 0.130 Å.

Table F.4: Values of the torsion angles (in °), degeneracy factors (g), Gibbs free energies (ΔG^\ominus , kJ mol⁻¹), weights in the final Boltzmann's population (in %), and BLA's (local, BLA' , and global, BLA , in Å) for the different conformers of DiBOX-BtO in its CF-CF form, as determined by geometry optimization at the M06/6-311G(d)/IEF-PCM (acetonitrile) level of theory.

Conf.	g	θ_1	θ_2	θ_3	θ_4	θ_5	ΔG^\ominus	%	BLA^a	BLA'
1	2	108	179	179	179	116	0.0	99.7	0.079	0.133
2	1	114	-180	-180	179	-113	12.5	0.3	0.080	0.134

^a all BLA values being negative, their absolute values are reported.

The most stable conformer of DiBOX-BtO in CF-POF displays a 1,3-NH interaction ($\theta_1 \sim 115^\circ$), θ_2 , θ_3 , and θ_4 torsion angles at 180° and a θ_5 value close to 0° (Table F.5). Switching from $\theta_1 \sim 115^\circ$ to $\theta_1 \sim -115^\circ$ leads to an energy increase by 2.5 kJ mol⁻¹. The change of conformation around the vinylene-EDOT torsion angle has a more important impact on the energy: switching from a *s-trans* (180°) to a *s-cis* conformation (0°) leads to a ΔG^\ominus increase of ~ 5 -6 kJ mol⁻¹. The global BLA is close to 0.040 Å. Then, BLA' attains 0.135 Å (CF side), while BLA'' (POF side) is one order of magnitude smaller.

Table F.5: Values of the torsion angles (in °), Gibbs free energies (ΔG^\ominus , kJ mol⁻¹), weights in the final Boltzmann's population (in %) and BLA's (global, BLA , and local, BLA' on CF side and BLA'' , on POF side, in Å) for the different conformers of DiBOX-BtO in its CF-POF form, as determined by geometry optimization at the M06/6-311G(d)/IEF-PCM (acetonitrile) level of theory.

Conf.	θ_1	θ_2	θ_3	θ_4	θ_5	ΔG^\ominus	%	BLA^a	BLA'	BLA''
1	114	179	-180	-180	-5	0.0	63.8	0.042	0.136	0.013
2	-116	178	180	-180	-4	2.5	23.0	0.041	0.135	0.012
3	112	14	179	180	-5	5.8	6.2	0.040	0.135	0.012
4	-116	2	-180	-180	-4	5.9	5.9	0.039	0.134	0.011
5	-116	177	180	-1	-7	10.2	1.1	0.042	0.136	0.015

^a all BLA values being negative, their absolute values are reported.

For DiBOX-BtO in POF-POF, the most stable conformers have torsion an-

gles between the vinylene and BOX about 0° , while the EDOT's and vinylenes adopt a *s-trans* conformation (Table F.6). At the first *s-trans* \rightarrow *s-cis* conversion (conformer 1 to conformer 3), ΔG^\ominus increases by 7.2 kJ mol^{-1} whereas the second *s-trans* \rightarrow *s-cis* conversion (conformer 3 to conformer 2) decreases ΔG^\ominus by 3.2 kJ mol^{-1} because of cooperative effects. The global BLA of DiBOX-BtO is 0.027 \AA while BLA'' is 0.035 \AA .

Table F.6: Values of the torsion angles (in $^\circ$), degeneracy factors (g), Gibbs free energies (ΔG^\ominus , kJ mol^{-1}), weights in the final Boltzmann's population (in %), and BLA's (local, BLA'' and global, BLA , in \AA) for the different conformers of DiBOX-BtO in its POF-POF form, as determined by optimization at the M06/6-311G(d)/IEF-PCM (acetonitrile) level of theory.

Conf.	g	θ_1	θ_2	θ_3	θ_4	θ_5	ΔG^\ominus	%	BLA^a	BLA''
1	1	6	-179	-179	-179	-4	0.0	63.5	0.027	0.035
2	2	6	4	180	1	-6	4.0	25.8	0.026	0.036
3	2	5	4	-179	-179	-3	7.2	7.0	0.026	0.036
4	2	5	-180	-180	176	156	8.8	3.7	0.027	0.036

^a all BLA values being negative, their absolute values are reported.

F.1.3 DiBOX-TtO

The most stable conformation of CF-CF form has its torsion angle between vinylene and BOX with 1,3-OH interaction (θ_1 and $\theta_6 \sim -115^\circ$), the vinylene and EDOT in *s-trans* conformation (θ_2 and $\theta_5 \sim 180^\circ$), and the EDOT-thiophene in anti conformation (θ_3 and $\theta_4 \sim 180^\circ$) (Table F.7). For all these angles, switching from one conformation to another is accompanied by a small increase of the energy (about $\sim 1\text{-}2 \text{ kJ mol}^{-1}$). For this form, the global BLA (BLA) is 0.072 \AA for all the conformers while BLA' does not vary much, with $\sim 0.132 \text{ \AA}$.

As shown in Table F.8, for CF-POF, the changes of conformation do not have a big impact on the energy of the compound (except for θ_6 for which the *s-cis* conformation is by far the most stable). The conformers are usually more stable when θ_3 is at 180° . BLA amounts to about 0.040 \AA , BLA' to 0.135 \AA while BLA'' is much smaller with a value of 0.015 \AA .

Three conformers with non-negligible weight are found for POF-POF (Table F.9). The most stable one has its two torsion angles between the BOX and vinylene at about 0° and all the other torsion angles at 180° . Switching the conformation of θ_3 from *s-trans* to *s-cis* is accompanied by an increase of ΔG^\ominus of 8.6 kJ mol^{-1} , then changing the conformation of θ_1 from 0° to 160° results in an increase of 3.1 kJ mol^{-1} . BLA is about 0.025 \AA while BLA' is 0.026 \AA .

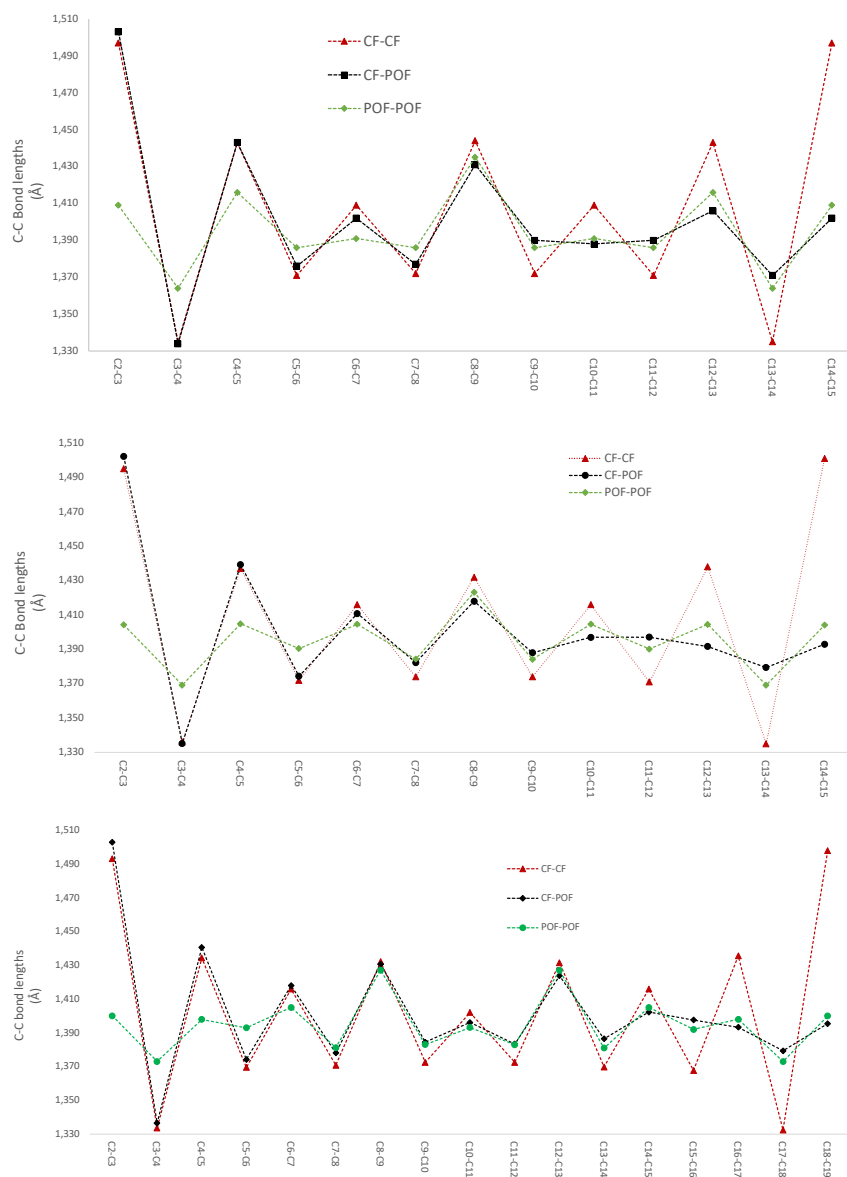


Figure F.1: C–C bond lengths (in Å) of the linker for the different forms of DiBOX's [(top) DiBOX-Bt, (Middle) DiBOX-BtO, and (Bottom) DiBOX-TtO]. These values are averaged over the Maxwell-Boltzmann's distribution at the M06/6-311G(d)/IEF-PCM (acetonitrile) level of approximation.

Table F.7: Values of the torsion angles (in $^{\circ}$), degeneracy factors (g), Gibbs free energies (ΔG^{\ominus} , kJ mol^{-1}), weights in the final Boltzmann's population (in %), and BLA's (local, BLA' , and global, BLA , in \AA) for the different conformers of DiBOX-TtO in its CF-CF form, as determined by geometry optimization at the M06/6-311G(d)/IEF-PCM (acetonitrile) level of theory.

Conf.	g	θ_1	θ_2	θ_3	θ_4	θ_5	θ_6	ΔG^{\ominus}	%	BLA^a	BLA'
1	1	-111	179	-180	180	-178	115	0.0	13.3	0.072	0.133
2	2	-111	179	13	-178	-177	116	1.3	15.9	0.072	0.133
3	2	116	-178	-180	180	-180	106	1.4	15.1	0.072	0.133
4	2	106	179	7	179	-179	115	1.4	15.3	0.072	0.133
5	2	108	180	12	-8	-177	116	2.3	10.3	0.072	0.133
6	2	-112	177	10	180	0	117	2.3	10.4	0.071	0.132
7	2	115	-178	179	-179	2	-113	4.0	5.3	0.072	0.133
8	2	106	7	-179	-179	-177	115	4.0	5.3	0.072	0.133
9	2	-113	-14	-177	12	177	-113	5.4	3.0	0.072	0.132
10	1	116	-1	180	180	1	-114	5.5	1.4	0.072	0.133
11	2	-114	0	-180	-180	-178	116	6.5	1.9	0.072	0.133
12	1	-112	179	11	-10	-178	116	7.7	0.6	0.072	0.133
13	2	115	-178	179	12	6	106	7.9	1.1	0.072	0.133
14	1	-114	-178	-10	9	179	108	8.7	0.4	0.072	0.133
15	2	116	-1	180	8	179	108	9.9	0.5	0.071	0.133

^a all BLA values being negative, their absolute values are reported.

F.2 UV/vis Absorption Spectra and Related Quantities

This SI Section provides the linear optical properties of the different compounds and their conformers before calculating their Maxwell-Boltzmann's averages. These quantities are the characteristics of the main low-energy excited states: the excitation energies (ΔE) and corresponding wavelengths (λ), the oscillator strengths (f), the changes of dipole moment amplitude ($\Delta\mu_{ge}$) accompanying the first excitation, and their analysis in terms of amplitudes (q_{CT}) and distances (d_{CT}) of charge transfer. A brief discussion on the results is also provided.

F.2.1 DiBOX-Bt

The weak $\Delta\mu_{ge}$ amplitude for conformers with the bithiophene in *anti* conformation can be explained by the topology of the HOMO and LUMO, which are located on the linker (Table F.10). So, when the bithiophene adopts a quasi-centrosymmetric conformation, d_{CT} and $\Delta\mu_{ge}$ tends toward zero (conformers 1 and 3) but if the bithiophene presents a *syn* conformation, $\Delta\mu_{ge}$ is not negligible (particularly conformer 9). Then, despite their weaker absorbance at ~ 380 nm, the conformers with *syn* thiophenes display a stronger absorbance at the second

Table F.8: Values of the torsion angles (in $^{\circ}$), Gibbs free energies (ΔG^{\ominus} , kJ mol^{-1}), weights in the final Boltzmann's population (in %) and BLA's (global, BLA , and local, BLA' on CF side and BLA'' , on POF side, in \AA) for the different conformers of DiBOX-TtO in its CF-POF form, as determined by geometry optimization at the M06/6-311G(d)/IEF-PCM (acetonitrile) level of theory.

Conf.	θ_1	θ_2	θ_3	θ_4	θ_5	θ_6	ΔG^{\ominus}	%	BLA^a	BLA'	BLA''
1	112	14	-180	179	-179	4	0.0	23.0	0.041	0.135	0.015
2	-116	179	-178	-180	-179	5	0.1	21.7	0.042	0.136	0.015
3	114	180	-178	-179	-179	4	0.6	17.9	0.042	0.135	0.016
4	-116	-2	8	180	-179	5	1.8	11.4	0.041	0.135	0.015
5	114	179	-180	3	-179	5	2.7	7.9	0.041	0.135	0.015
6	-116	178	5	2	-179	5	4.2	4.2	0.041	0.135	0.015
7	113	178	2	178	-180	4	4.5	3.7	0.042	0.135	0.016
8	-116	0	-180	179	-179	4	4.9	3.2	0.041	0.135	0.014
9	-116	179	-178	4	-179	5	5.3	2.7	0.041	0.136	0.014
10	111	14	3	179	-179	4	5.5	2.5	0.042	0.135	0.016
11	-116	177	8	179	-179	4	7.4	1.2	0.042	0.135	0.016
12	-116	1	-179	4	-179	5	8.8	0.7	0.040	0.135	0.013

^a all BLA values being negative, their absolute values are reported.

excitation (at ~ 275 nm) with a f_{ge} at ~ 0.30 - 0.40 (conformer 5, 8, and 9), while the other conformers have oscillator strengths close to zero.

DiBOX-Bt in CF-POF has its first band of absorption located in the visible light region, on an average of 518 nm (2.38 eV) (Table F.11). Since this form cannot display centro-symmetric conformation d_{CT} and $\Delta\mu_{ge}$ remain similar among the different conformers. In the visible domain, the first excitation is the only one with $f_{ge} > 0.5$. It is mainly due to a HOMO-LUMO electronic transition. This form displays f_{ge} between 1.59 and 1.96. The amount of charge transfer is close to $0.55 e$ with a distance varying between ~ 3.0 and 3.5 \AA . $\Delta\mu_{ge}$ has an average of 8.7 D. The variation of dipole moment upon excitation to the first excited state is consistent with the molecular structure. Indeed, the electron density moves from the linker to the indolinium moiety resulting in large $\Delta\mu_{ge}$. As a matter of fact, CF-POF is expected to display a high β response.

For DiBOX-Bt in POF-POF, the first excitation energy has an average value of 2.28 eV, corresponding to 543 nm (Table F.12). Again, this excitation is mainly due to HOMO \rightarrow LUMO electronic transition ($\sim 90\%$) with contribution of the HOMO-1 \rightarrow LUMO+1 transition ($\sim 5\%$). The oscillator strength of this first excitation varies among the different conformers (between 1.90 and 2.77) and it tends to be smaller when the bithiophene adopts a parallel conformation. Then, like for CF-CF, the conformation of the linker affects d_{CT} and $\Delta\mu_{ge}$ while q_{CT} is not affected. When the linker adopts a centrosymmetric conformation, the

Table F.9: Values of the torsion angles (in $^{\circ}$), degeneracy factors (g), Gibbs free energies (ΔG^{\ominus} , kJ mol^{-1}), weights in the final Boltzmann's population (in %), and BLA's (local, BLA'' and global, BLA , in \AA) for the different conformers of DiBOX-TtO in its POF-POF form, as determined by optimization at the M06/6-311G(d)/IEF-PCM (acetonitrile) level of theory.

Conf.	g	θ_1	θ_2	θ_3	θ_4	θ_5	θ_6	ΔG^{\ominus}	%	BLA^a	BLA''
1	1	-3	180	179	-180	-180	4	0.0	92.5	0.024	0.026
2	2	4	-179	1	178	179	-4	8.6	5.8	0.024	0.026
3	2	-160	-175	4	178	179	-5	11.7	1.7	0.025	0.026

^a all BLA values being negative, their absolute values are reported.

resulting $\Delta\mu_{ge}$ tends to zero, but the non-centrosymmetric conformers with the thiophenes in *syn* conformation (2, 4, and 6) display the largest $\Delta\mu_{ge}$. The switching from the *anti* to the *syn* conformation of the bithiophene leads to the apparition of a second band of absorption at $\sim 380\text{-}390\text{ nm}$.

Table F.10: Excitation energies (ΔE_{ge} , in eV), corresponding wavelengths (λ_{ge} , in nm), oscillator strengths (f_{ge}) associated with the $S_0 \rightarrow S_1$ and $S_0 \rightarrow S_2$ excitations, amounts of charge transfer (q_{CT} , in e), distances of charge transfer (d_{CT} , Å) and variations of dipole moments ($\Delta\mu_{ge}$, in D) associated with the $S_0 \rightarrow S_1$ excitation, for DiBOX-Bt in CF-CF evaluated at the M06-2X/6-311+G(d)/IEF-PCM (acetonitrile) level of theory. The averaged values are calculated using the Boltzmann's distributions weights at 298.15 K.

Conf.	%	$S_0 \rightarrow S_1$						$S_0 \rightarrow S_2$		
		λ_{ge}	ΔE_{ge}	f_{ge}	q_{CT}	d_{CT}	$\Delta\mu_{ge}$	λ_{ge}	ΔE_{ge}	f_{ge}
1	48.5	378	3.28	1.39	0.392	0.030	0.056	275	4.51	0.00
2	13.3	373	3.32	1.46	0.391	0.151	0.284	278	4.47	0.04
3	7.4	379	3.28	1.38	0.395	0.037	0.070	276	4.50	0.00
4	8.1	377	3.28	1.38	0.394	0.081	0.153	275	4.50	0.01
5	7.8	373	3.32	1.19	0.395	0.219	0.415	274	4.53	0.27
6	6.1	374	3.32	1.46	0.392	0.095	0.179	278	4.46	0.03
7	5.0	373	3.32	1.44	0.392	0.240	0.451	278	4.45	0.03
8	2.1	378	3.28	1.16	0.391	0.187	0.350	273	4.54	0.31
9	1.0	387	3.20	1.23	0.605	0.639	1.856	282	4.40	0.38
10	0.8	376	3.30	1.44	0.392	0.161	0.303	279	4.45	0.02
Av.		377	3.29	1.39	0.395	0.090	0.176	276	4.50	0.04

Table F.11: Excitation energies (ΔE_{ge} , in eV), corresponding wavelengths (λ_{ge} , in nm), oscillator strengths (f_{ge}), amounts of charge transfer (q_{CT} , in e), distances of charge transfer (d_{CT} , in Å), and variations of dipole moment ($\Delta\mu_{ge}$, in D) associated with the $S_0 \rightarrow S_1$ excitation of DiBOX-Bt in CF-POF at the M06-2X/6-311+G(d)/IEF-PCM (acetonitrile) level of theory. The averaged values are calculated using the Boltzmann's distributions weights at 298.15 K.

Conf.	%	λ_{ge}	ΔE_{ge}	f_{ge}	q_{CT}	d_{CT}	$\Delta\mu_{ge}$
1	58.5	517	2.40	1.89	0.549	3.255	8.589
2	22.8	521	2.38	1.90	0.557	3.430	9.172
3	7.6	520	2.38	1.68	0.537	2.982	7.684
4	4.6	521	2.38	1.96	0.552	3.460	9.166
5	3.4	525	2.36	1.59	0.545	3.101	8.116
6	3.1	525	2.36	1.94	0.560	3.591	9.661
Av.		519	2.39	1.87	0.550	3.287	8.697

Table F.12: Excitation energies (ΔE_{ge} , in eV), corresponding wavelengths (λ_{ge} , in nm), oscillator strength (f_{ge}) associated with the $S_0 \rightarrow S_1$ and $S_0 \rightarrow S_2$ excitations, amounts of charge transfer (q_{CT} , in e), distances of charge transfer (d_{CT} , Å) and variations of dipole moments ($\Delta\mu_{ge}$ in D) associated with the $S_0 \rightarrow S_1$ excitation, for DiBOX-Bt in POF-POF at the M06-2X/6-311+G(d)/IEF-PCM (acetonitrile) level of theory. The averaged values are calculated using the Boltzmann's distributions weights.

Conf.	%	$S_0 \rightarrow S_1$						$S_0 \rightarrow S_2$					
		λ_{ge}	ΔE_{ge}	f_{ge}	q_{CT}	d_{CT}	$\Delta\mu_{ge}$	λ_{ge}	ΔE_{ge}	f_{ge}	q_{CT}	d_{CT}	$\Delta\mu_{ge}$
1	52.8	541	2.29	2.54	0.492	0.001	0.002	388	3.19	0.00	0.424	0.305	0.621
2	18.5	548	2.26	1.90	0.494	0.581	1.379	385	3.22	0.77			
3	17.4	543	2.28	2.59	0.496	0.154	0.367	391	3.17	0.08			
4	7.1	550	2.26	2.33	0.496	0.557	1.327	388	3.19	0.39			
5	2.7	544	2.28	2.77	0.498	0.008	0.019	395	3.14	0.00			
6	1.5	548	2.26	2.68	0.497	0.507	1.209	392	3.17	0.12			
Av.		543	2.28	2.43	0.494	0.182	0.433	388	3.19	0.19			

F.2.2 DiBOX-BtO

DiBOX-BtO in its CF-CF form displays its first low-energy absorption in the visible, at an average wavelength of 399 nm (3.11 eV) (Table F.13). This excitation is mainly composed of the HOMO - LUMO electronic transition, with both MO's located on the EDOT's. The average oscillator strength is 1.37. The amount of charge-transfer attains ~ 0.38 e. Like for DiBOX-Bt, d_{CT} depends on the structure: breaking the centrosymmetry (conformer 2 \rightarrow conformer 1) leads to an increase of d_{CT} from 0.022 to 0.445 Å.

Table F.13: Excitation energies (ΔE_{ge} , in eV), corresponding wavelengths (λ_{ge} , in nm), oscillator strength (f_{ge}), amounts of charge transfer (q_{CT} , in e), distances of charge transfer (d_{CT}) and variations of dipole moment ($\Delta\mu_{ge}$ in D) associated with the $S_0 \rightarrow S_1$ excitation, for DiBOX-BtO in CF-CF at the M06-2X/6-311+G(d)/IEF-PCM (acetonitrile) level of theory. The averages are weighted using the population of conformers at 298.15 K.

Conf.	%	λ_{ge}	ΔE_{ge}	f_{ge}	q_{CT}	d_{CT}	$\Delta\mu_{ge}$
1	99.7	401	3.09	1.38	0.384	0.022	0.040
2	0.3	399	3.11	1.37	0.385	0.028	0.051
Av.		401	3.09	1.38	0.384	0.022	0.040

As shown in Table F.14, DiBOX-BtO in its CF-POF form has its first excitation energy at 2.25 eV (551 nm), an associated oscillator strength of 1.91, and it corresponds mainly to a HOMO - LUMO electronic transition, but, contrary to the CF-CF form, this transition accounts for a charge transfer from the EDOT's to the open BOX (the indolinium function). $q_{CT} \sim 0.50$ e, while d_{CT} goes from 2.5 to 2.9 Å, as a function of the conformation.

For POF-POF, the first excitation energy is even smaller (2.11 eV or 587 nm) (Table F.15). The oscillator strength attains 2.51. Since only the anti-parallel conformation has a non-negligible Maxwell-Boltzmann's weight, and since for these systems, the HOMO and LUMO are centrosymmetric, d_{CT} is close to zero so is also $\Delta\mu_{ge}$.

F.2.3 DiBOX-TtO

The conformers with the most important contribution in the final population of CF-CF absorbs at a wavelength between 424 and 438 nm (2.92-2.83 eV) with an oscillator strength between 1.34 and 2.01. d_{CT} is a function of the conformation of the linker, varying between 0.189 and 0.797 Å (Table F.16). The largest d_{CT} are obtained for a "bent" linker, where $\theta_2-\theta_3-\theta_4-\theta_5 \sim 0^\circ$. The charge transfer associated with the first excitation amounts to ~ 0.41 e.

For CF-POF, the four most abundant conformers absorb between 587 and 592 nm (2.11 and 2.09 eV) (Table F.17). Due to its push-pull character, the

Table F.14: Excitation energies (ΔE_{ge} , in eV), corresponding wavelengths (λ_{ge} , in nm), oscillator strength (f_{ge}), amounts of charge transfer (q_{CT} , in e), distances of charge transfer (d_{CT}) and variations of dipole moment ($\Delta\mu_{ge}$ in D) associated with the $S_0 \rightarrow S_1$ excitation, for DiBOX-BtO in CF-POF at the M06-2X/6-311+G(d)/IEF-PCM (acetonitrile) level of theory. The averages are weighted using the population of conformers at 298.15 K.

Conf.	%	λ_{ge}	ΔE_{ge}	f_{ge}	q_{CT}	d_{CT}	$\Delta\mu_{ge}$
1	63.8	550	2.25	1.90	0.497	2.513	6.005
2	23.0	554	2.24	1.91	0.500	2.599	6.253
3	6.2	548	2.26	1.91	0.497	2.518	6.010
4	5.9	551	2.25	1.96	0.501	2.656	6.394
5	1.1	544	2.28	2.06	0.515	2.910	7.193
Av.		551	2.25	1.91	0.498	2.546	6.098

Table F.15: Excitation energies (ΔE_{ge} , in eV), corresponding wavelengths (λ_{ge} , in nm), oscillator strength (f_{ge}), amounts of charge transfer (q_{CT} , in e), distances of charge transfer (d_{CT}) and variations of dipole moment ($\Delta\mu_{ge}$ in D) associated with the $S_0 \rightarrow S_1$ excitation, for DiBOX-BtO in POF-POF at the M06-2X/6-311+G(d)/IEF-PCM (acetonitrile) level of theory. The averages are weighted using the population of conformers at 298.15 K.

Conf.	%	λ_{ge}	ΔE_{ge}	f_{ge}	q_{CT}	d_{CT}	$\Delta\mu_{ge}$
1	63.5	590	2.10	2.45	0.488	0.014	0.032
2	25.8	575	2.16	2.81	0.495	0.026	0.062
3	7.0	583	2.13	2.57	0.492	0.029	0.068
4	3.7	585	2.12	2.43	0.491	0.051	0.120
Av.		585	2.12	2.55	0.490	0.020	0.046

conformation of the molecule does not have a strong impact on d_{CT} , which varies between 3.8 and 4.3 Å, with a q_{CT} of ~ 0.60 e.

POF-POF has only one representative conformer, with a weight superior to 90 %. It absorbs at 615 nm and has an associated f_{ge} of 2.84 (Table F.18). The d_{CT} is a function of the conformation of the linker with a variation between 0.19 and 0.53 Å. The amount of charge-transfer is ~ 0.52 e. This value increases when the "bending" of the linker increases.

F.3 Nonlinear Optical Properties

In this section, the main characteristics associated with the first hyperpolarizability are reported: the static and dynamic (wavelengths of 1907 nm, 1300 nm, and

Table F.16: Excitation energies (ΔE_{ge} , in eV), corresponding wavelengths (λ_{ge} , in nm), oscillator strength (f_{ge}), amounts of charge transfer (q_{CT} , in e), distances of charge transfer (d_{CT}) and variations of dipole moment ($\Delta\mu_{ge}$ in D) associated with the $S_0 \rightarrow S_1$ excitation, for DiBOX-TtO in CF-CF at the M06-2X/6-311+G(d)/IEF-PCM (acetonitrile) level of theory. The weighted averages are obtained by using the population of conformers at 298.15 K.

Conf.	%	λ_{ge}	ΔE_{ge}	f_{ge}	q_{CT}	d_{CT}	$\Delta\mu_{ge}$
1	13.3	435	2.85	1.75	0.409	0.486	0.954
2	15.9	435	2.85	1.65	0.409	0.317	0.623
3	15.1	436	2.84	1.76	0.408	0.419	0.820
4	15.3	438	2.83	1.67	0.408	0.283	0.555
5	10.3	457	2.71	1.44	0.431	0.600	1.243
6	10.4	432	2.87	1.70	0.412	0.744	1.471
7	5.3	430	2.89	1.87	0.403	0.189	0.365
8	5.3	430	2.88	1.84	0.402	0.237	0.459
9	3.0	429	2.89	1.66	0.408	0.542	1.063
10	1.4	424	2.92	2.01	0.403	0.486	0.942
11	1.9	432	2.87	1.83	0.404	0.222	0.431
12	0.6	438	2.83	1.34	0.409	0.570	1.121
13	1.1	431	2.88	1.79	0.406	0.315	0.614
14	0.4	438	2.83	1.44	0.407	0.543	1.060
15	0.5	433	2.86	1.72	0.413	0.797	1.579
Av.		437	2.84	1.70	0.410	0.425	0.840

1064 nm) β_{HRS} responses and their depolarization ratios (DR), the dipolar and octupolar component of the first hyperpolarizability ($|\beta_{J=1}|$ and $|\beta_{J=3}|$) and their corresponding anisotropic ratio (ρ) for all conformers and all forms of the three DiBOX's, as well as their averages calculated using Maxwell-Boltzmann's distribution of the conformers.

F.3.1 DiBOX-Bt

The distribution of β_{HRS} values among the different conformers of the CF-CF form illustrates the need to account for their whole population (Table F.19). As expected the conformers with the weakest responses display a nearly centrosymmetric structure (bithiophene in anti conformation, $\theta_2 = \theta_4$ and $\theta_1 = \theta_5$). On the other hand, the largest responses are obtained for conformers displaying a "V-like" structure (bithiophene in syn conformation, conformers 5, 8, and 9). As a consequence, DiBOX-Bt displays also a wide variety of dipolar vs. octupolar character, with $0.62 \leq \rho \leq 7.02$ ($5.99 \geq DR \geq 1.59$).

Since DiBOX-Bt in CF-POF is asymmetric, most its properties are "homoge-

Table F.17: Excitation energies (ΔE_{ge} , in eV), corresponding wavelengths (λ_{ge} , in nm), oscillator strength (f_{ge}), amounts of charge transfer (q_{CT} , in e), distances of charge transfer (d_{CT}) and variations of dipole moment ($\Delta\mu_{ge}$ in D) associated with the $S_0 \rightarrow S_1$ excitation, for DiBOX-TtO in CF-POF at the M06-2X/6-311+G(d)/IEF-PCM (acetonitrile) level of theory. The weighted averages are obtained by using the population of conformers at 298.15 K.

Conf.	%	λ_{ge}	ΔE_{ge}	f_{ge}	q_{CT}	d_{CT}	$\Delta\mu_{ge}$
1	23.0	588	2.11	2.23	0.601	4.174	12.053
2	21.7	590	2.10	2.16	0.603	4.187	12.127
3	17.9	587	2.11	2.16	0.598	4.125	11.857
4	11.4	591	2.10	2.26	0.611	4.331	12.708
5	7.9	588	2.11	1.99	0.587	3.835	10.815
6	4.2	594	2.09	1.69	0.597	3.766	10.801
7	3.7	589	2.11	2.17	0.600	4.127	11.885
8	3.2	590	2.10	2.28	0.609	4.296	12.557
9	2.7	591	2.10	1.99	0.593	3.923	11.170
10	2.5	588	2.11	2.22	0.603	4.215	12.215
11	1.2	591	2.10	2.13	0.606	4.185	12.176
12	0.7	592	2.09	1.97	0.598	3.948	11.348
Av.		589	2.10	2.16	0.601	4.137	11.945

nous" among the different conformers (Table F.20). Conformer 3 displays the smallest β_{HRS} while conformer 6 possesses the largest one. The particularly large responses at 1064 nm originate from resonance effects: the second harmonic of the incident light has a wavelength of 532 nm (2.33 eV), close to the first excitation energy, located at 518 nm (2.38 eV). This NLO-phore displays a strong 1-D character with $0.82 \leq \rho \leq 0.87$ ($4.96 \geq DR \geq 4.80$), and a predominance of the β_{zzz} component, where z is in the bithiophene to indolinium direction, the one of the charge-transfer associated with the first excitation.

Like CF-CF, the β_{HRS} responses of POF-POF strongly depend on the conformation and it varies between 0.0 and 90.4×10^3 a.u. in the static case (Table F.21). The vanishing response of conformer 1 results from its perfect centrosymmetric structure. To display an important β_{HRS} response, DiBOX-Bt in POF-POF requires the bithiophene to be in syn conformation (conformers 2, 4, and 6). Concerning the dipolar/octupolar character, the conformers with non-zero β have a dominant octupolar character (ρ between 1.93 and 2.55). Conformer 5, with $DR \sim 4.76$ displays a typical 1D-donor-acceptor character. So, DiBOX-Bt in POF-POF achieves a large β response provided it is V-shape.

Table F.18: Excitation energies (ΔE_{ge} , in eV), corresponding wavelengths (λ_{ge} , in nm), oscillator strength (f_{ge}), amounts of charge transfer (q_{CT} , in e), distances of charge transfer (d_{CT}) and variations of dipole moment ($\Delta\mu_{ge}$ in D) associated with the $S_0 \rightarrow S_1$ excitation, for DiBOX-TtO in POF-POF at the M06-2X/6-311+G(d)/IEF-PCM (acetonitrile) level of theory. The weighted averages are obtained by using the population of conformers at 298.15 K.

Conf.	%	λ_{ge}	ΔE_{ge}	f_{ge}	q_{CT}	d_{CT}	$\Delta\mu_{ge}$
1	92.5	662	1.87	2.98	0.563	0.201	0.544
2	5.8	664	1.87	2.90	0.561	0.459	1.237
3	1.7	659	1.88	2.92	0.564	0.545	1.474
Av.		662	1.87	2.98	0.563	0.222	0.600

Table F.19: Static ($\lambda = \infty$) and dynamic ($\lambda = 1907, 1300$, and 1064 nm) β_{HRS} (a.u.) as well as static β_{ZZZ} , β_{ZXX} , $|\beta_{J=1}|$, $|\beta_{J=3}|$ (a.u.), DR and ρ of the conformers of DiBOX-Bt in CF-CF as calculated at the TDDFT/M06-2X/6-311+G(d)/IEF-PCM (acetonitrile) level of theory. The averages were obtained using the Boltzmann's populations at 298.15 K.

Conf.	%	β_{HRS}				Static quantities					
		∞	1907 nm	1300 nm	1064 nm	β_{ZZZ}	β_{ZXX}	DR	$ \beta_{J=1} $	$ \beta_{J=3} $	ρ
1	48.5	150	73	74	79	117	93	1.59	68	474	7.02
2	13.3	694	627	802	1065	637	275	5.39	1327	976	0.74
3	7.4	229	182	188	188	205	103	3.98	396	431	1.09
4	8.1	324	273	323	397	288	149	3.74	547	639	1.17
5	7.8	1050	768	924	1142	929	489	3.62	1741	2121	1.22
6	6.1	690	599	752	978	628	286	4.82	1276	1093	0.86
7	5.0	847	771	1000	1351	778	334	5.42	1621	1184	0.73
8	2.1	1206	880	1048	1281	1081	534	4.11	2110	2209	1.05
9	1.0	922	666	819	1036	798	462	2.98	1378	2121	1.54
10	0.8	745	686	885	1189	690	282	5.99	1464	914	0.62
Av.		414	319	386	487	365	191	3.54	645	807	1.25

Table F.20: Static ($\lambda = \infty$) and dynamic ($\lambda = 1907, 1300$, and 1064 nm) β_{HRS} (10^3 a.u.) as well as static β_{ZZZ} , β_{ZXX} , $|\beta_{J=1}|$, $|\beta_{J=3}|$ (10^3 a.u.), DR and ρ of the conformers of DiBOX-Bt in CF-POF as calculated at the TDDFT/M06-2X/6-311+G(d)/IEF-PCM (acetonitrile) level of theory. The averages were obtained using the Boltzmann's populations at 298.15 K.

Conf.	%	β_{HRS}				Static quantities					
		∞	1907 nm	1300 nm	1064 nm	β_{ZZZ}	β_{ZXX}	DR	$ \beta_{J=1} $	$ \beta_{J=3} $	ρ
1	58.5	35.2	32.8	74.9	591	32.0	14.7	4.77	64.9	56.4	0.87
2	22.8	38.3	36.1	84.9	930	34.9	15.9	4.80	70.8	61.0	0.86
3	7.6	31.6	28.1	64.4	628	28.7	13.1	4.81	58.3	50.1	0.86
4	4.6	37.8	35.5	84.4	896	34.4	15.7	4.81	69.8	60.0	0.86
5	3.4	33.0	29.0	68.1	1082	30.1	13.5	4.96	61.6	50.8	0.82
6	3.1	40.5	38.3	93.5	1627	36.9	16.8	4.85	75.1	63.9	0.85
Av.		35.9	33.4	77.1	734	32.6	14.9	4.79	66.2	57.2	0.86

Table F.21: Static ($\lambda = \infty$) and dynamic ($\lambda = 1907, 1300$, and 1064 nm) β_{HRS} (10^3 a.u.) as well as static β_{ZZZ} , β_{ZXX} , $|\beta_{J=1}|$, $|\beta_{J=3}|$ (10^3 a.u.), DR and ρ of the conformers of DiBOX-Bt in POF-POF as calculated at the TDDFT/M06-2X/6-311+G(d)/IEF-PCM (acetonitrile) level of theory. The averages were obtained using the Boltzmann's populations at 298.15 K.

Conf.	%	β_{HRS}				Static quantities					
		∞	1907 nm	1300 nm	1064 nm	β_{ZZZ}	β_{ZXX}	DR	$ \beta_{J=1} $	$ \beta_{J=3} $	ρ
1	52.8	<0.1	<0.1	<0.1	<0.1	<0.1	<0.1	—	<0.1	<0.1	—
2	18.5	13.0	10.1	22.3	97.7	10.9	7.2	2.31	15.8	34.7	2.19
3	17.4	1.8	1.4	3.6	40.2	1.5	1.0	2.12	2.0	5.0	2.55
4	7.1	94.0	62.1	84.2	170.3	85.5	39.1	4.79	173.5	149.9	0.86
5	2.7	0.2	0.2	0.5	3.1	0.2	0.1	2.16	0.3	0.6	2.46
6	1.5	14.0	11.0	24.6	114.5	11.8	7.4	2.51	18.4	35.5	1.93
Av.		9.6	6.7	11.1	39.0	8.5	4.4	3.74	15.8	18.5	1.17

F.3.2 DiBOX-BtO

The minor centrosymmetric conformer (CF-CF-2) has a negligible response while it is much larger for the major one, CF-CF-1 (1320 vs. 40 a.u. in the static limit) (Table F.22). Conformer 2 displays a strong octupolar character ($DR = 1.95$, $\rho = 3.02$), whereas breaking its symmetry leads to an enhancement of the dipolar character, and a 1-D like response ($DR = 4.98$, $\rho = 0.82$).

Owing to the strong push-pull character of CF-POF DiBOX-BtO, the conformation impacts hardly the character and the amplitude of β_{HRS} (Table F.23). This form has a dipolar character, close to a typical 1D donor- π -acceptor systems with an average DR of 4.67.

The β_{HRS} response of POF-POF DiBOX-BtO varies between 200 and 1570 a.u. ($\lambda = \infty$) and appears to follow the amplitude of $\Delta\mu_{ge}$ (Table F.23). It displays a predominant octupolar character (ρ is between 1.44 and 2.57).

Table F.22: Static ($\lambda = \infty$) and dynamic ($\lambda = 1907, 1300$, and 1064 nm) β_{HRS} (a.u.) as well as static β_{ZZZ} , β_{ZXX} , $|\beta_{J=1}|$, $|\beta_{J=3}|$ (a.u.), DR and ρ of the conformers of DiBOX-BtO in CF-CF as calculated at the TDDFT/M06-2X/6-311+G(d)/IEF-PCM (acetonitrile) level of theory. The averages were obtained using the Boltzmann's populations at 298.15 K.

Conf.	%	β_{HRS}				Static quantities					
		∞	1907 nm	1300 nm	1064 nm	β_{ZZZ}	β_{ZXX}	DR	$ \beta_{J=1} $	$ \beta_{J=3} $	ρ
1	99.7	1320	1222	1707	2588	1205	540	4.98	2468	2024	0.82
2	0.3	39	22	27	38	31	22	1.95	37	112	3.01
Av.		1316	1218	1701	2579	1201	538	4.98	2460	2018	0.82

Table F.23: Static ($\lambda = \infty$) and dynamic ($\lambda = 1907, 1300$, and 1064 nm) β_{HRS} (10^3 a.u.) as well as static β_{ZZZ} , β_{ZXX} , $|\beta_{J=1}|$, $|\beta_{J=3}|$ (10^3 a.u.), DR and ρ of the conformers of DiBOX-BtO in CF-POF as calculated at the TDDFT/M06-2X/6-311+G(d)/IEF-PCM (acetonitrile) level of theory. The averages were obtained using the Boltzmann's populations at 298.15 K.

Conf.	%	β_{HRS}				Static quantities					
		∞	1907 nm	1300 nm	1064 nm	β_{ZZZ}	β_{ZXX}	DR	$ \beta_{J=1} $	$ \beta_{J=3} $	ρ
1	63.8	36.4	32.4	89.6	434.0	33.0	15.3	4.65	66.5	59.6	0.90
2	23.0	38.9	34.9	99.4	388.5	35.3	16.3	4.70	71.4	63.2	0.89
3	6.2	38.0	33.3	89.4	502.0	34.4	16.0	4.64	69.3	62.5	0.90
4	5.9	41.8	37.6	103.6	470.2	38.0	17.6	4.65	76.5	68.7	0.90
5	1.1	41.6	37.1	100.8	807.7	37.9	17.1	4.94	77.5	64.4	0.83
Av.		37.4	33.4	92.8	433.8	34.0	15.7	4.67	68.5	61.2	0.89

Table F.24: Static ($\lambda = \infty$) and dynamic ($\lambda = 1907, 1300$, and 1064 nm) β_{HRS} (a.u.) as well as static β_{ZZZ} , β_{ZXX} , $|\beta_{J=1}|$, $|\beta_{J=3}|$ (a.u.), DR and ρ of the conformers of DiBOX-BtO in POF-POF as calculated at the TDDFT/M06-2X/6-311+G(d)/IEF-PCM (acetonitrile) level of theory. The averages were obtained using the Boltzmann's populations at 298.15 K.

Conf.	%	β_{HRS}				Static quantities					
		∞	1907 nm	1300 nm	1064 nm	β_{ZZZ}	β_{ZXX}	DR	$ \beta_{J=1} $	$ \beta_{J=3} $	ρ
1	63.5	289	269	1003	1027	238	164	2.11	313	806	2.57
2	25.8	202	223	973	1958	176	99	3.14	311	449	1.44
3	7.0	717	577	2209	3619	596	399	2.23	835	1943	2.33
4	3.7	1575	1623	5429	5369	1332	840	2.51	2071	4003	1.93
Av.		344	329	1243	1609	287	189	2.31	414	911	2.20

F.3.3 DiBOX-TtO

Like for the other CF-CF structures, the β_{HRS} responses are small and strongly depend on the conformation (Table F.25). Conformers 5, 6, 9, 12, 14, and 15 are bent, they display the largest $\Delta\mu_{ge}$ (Table F.16) and β_{HRS} values, and DR close to 5. On the opposite, the conformers with an octupolar character (conformers 11 and 13) are the ones with the smallest responses.

As for the CF-POF species, β_{HRS} does not vary much between the different conformers (Table F.26). These behave as typical 1-D π -conjugated systems, with DR between 4.82 and 5.01, respectively.

For POF-POF, the major conformer (>92% of the population) displays a β_{HRS} value about twice smaller than the other two conformers (Table F.27). This originates from the conformation of the linker, which is less "bent", and it is related to the smaller $\Delta\mu_{ge}$ (Table F.18). The β of all conformers is dominantly octupolar.

Table F.25: Static ($\lambda = \infty$) and dynamic ($\lambda = 1907, 1300$, and 1064 nm) β_{HRS} (10^3 a.u.) as well as static β_{ZZZ} , β_{ZXX} , $|\beta_{J=1}|$, $|\beta_{J=3}|$ (10^3 a.u.), DR and ρ of the conformers of DiBOX-TtO in CF-CF as calculated at the TDDFT/M06-2X/6-311+G(d)/IEF-PCM (acetonitrile) level of theory. The averages were obtained using the Boltzmann's populations at 298.15 K.

Conf.	%	β_{HRS}				Static quantities					
		∞	1907 nm	1300 nm	1064 nm	β_{ZZZ}	β_{ZXX}	DR	$ \beta_{J=1} $	$ \beta_{J=3} $	ρ
1	13.3	2.2	1.9	2.8	5.0	2.0	0.8	6.31	4.3	2.5	0.57
2	15.9	1.9	1.7	2.6	4.6	1.6	0.9	3.12	2.9	4.2	1.45
3	15.1	1.9	1.6	2.5	4.4	1.8	0.7	6.07	3.8	2.3	0.61
4	15.3	1.9	1.7	2.6	4.5	1.6	0.9	2.89	2.7	4.3	1.60
5	10.3	3.4	2.6	3.6	5.9	3.1	1.4	5.20	6.4	5.0	0.77
6	10.4	3.1	2.9	4.6	8.3	2.8	1.3	4.62	5.6	5.1	0.91
7	5.3	1.2	0.7	0.9	1.1	1.1	0.5	6.13	2.4	1.4	0.60
8	5.3	1.3	0.9	1.0	1.5	1.2	0.5	7.11	2.7	1.2	0.44
9	3.0	2.1	2.0	3.1	5.6	1.9	1.0	3.89	3.7	4.1	1.12
10	1.4	1.6	1.6	2.5	4.4	1.4	0.7	4.30	2.8	2.8	0.99
11	1.9	1.2	0.9	1.2	1.8	1.0	0.7	1.79	0.9	3.6	3.84
12	0.6	3.3	2.4	3.3	5.3	3.0	1.3	5.30	6.2	4.7	0.75
13	1.1	1.1	0.8	1.1	1.9	0.9	0.7	1.78	0.9	3.3	3.85
14	0.4	3.2	2.4	3.3	5.3	2.8	1.4	4.25	5.7	5.7	1.01
15	0.5	3.4	3.3	5.1	9.3	3.0	1.4	4.59	6.1	5.5	0.91
Av.		2.1	1.8	2.7	4.7	1.9	0.9	4.56	3.8	3.5	0.92

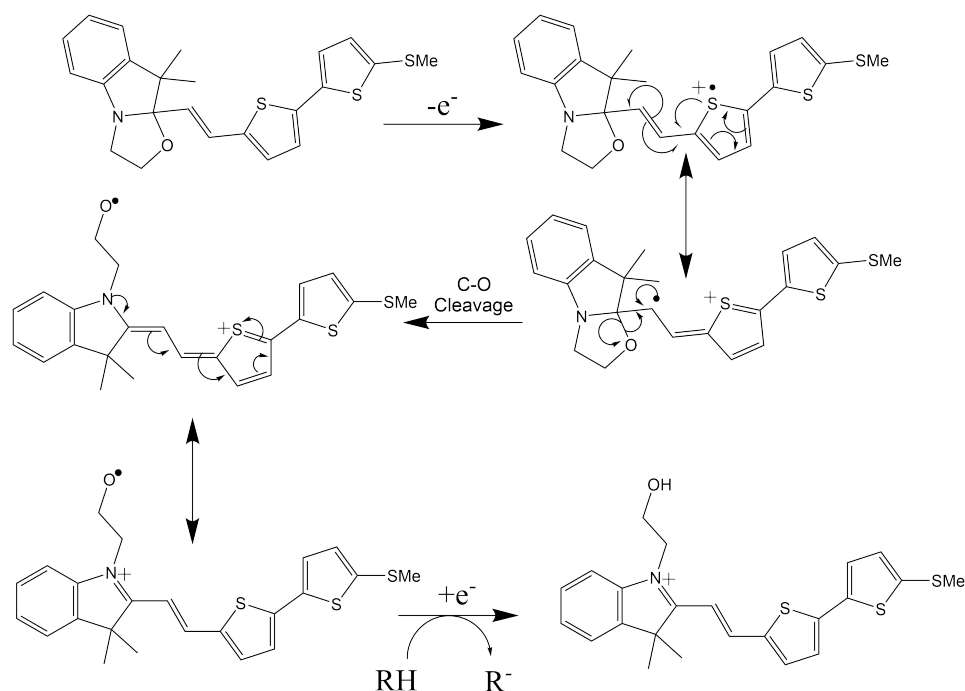
Table F.26: Static ($\lambda = \infty$) and dynamic ($\lambda = 1907, 1300$, and 1064 nm) β_{HRS} (10^3 a.u.) as well as static β_{ZZZ} , β_{ZXX} , $|\beta_{J=1}|$, $|\beta_{J=3}|$ (10^3 a.u.), DR and ρ of the conformers of DiBOX-TtO in CF-POF as calculated at the TDDFT/M06-2X/6-311+G(d)/IEF-PCM (acetonitrile) level of theory. The averages were obtained using the Boltzmann's populations at 298.15 K.

Conf.	%	β_{HRS}				Static quantities					
		∞	1907 nm	1300 nm	1064 nm	β_{ZZZ}	β_{ZXX}	DR	$ \beta_{J=1} $	$ \beta_{J=3} $	ρ
1	23.0	83.6	90.6	397	437	76.1	34.6	4.83	155	132	0.86
2	21.7	81.9	88.9	407	414	74.6	33.9	4.85	152	129	0.85
3	17.9	78.4	85.3	372	427	71.3	32.5	4.82	145	124	0.86
4	11.4	87.7	98.1	453	456	79.9	36.3	4.85	163	138	0.85
5	7.9	70.5	74.9	323	351	64.1	29.2	4.83	130	112	0.86
6	4.2	66.4	67.6	314	278	60.6	27.1	5.02	124	101	0.81
7	3.7	77.0	84.1	379	415	70.1	31.8	4.84	143	122	0.85
8	3.2	88.9	98.5	450	455	80.9	36.8	4.83	165	141	0.86
9	2.7	74.1	80.0	364	350	67.4	30.7	4.83	137	117	0.86
10	2.5	82.7	89.8	397	441	75.3	34.2	4.85	153	130	0.85
11	1.2	79.1	85.6	397	407	72.1	32.6	4.90	147	124	0.84
12	0.7	77.7	83.3	381	348	70.8	32.0	4.89	144	122	0.84
Av.		80.6	87.5	392	415	73.4	33.3	4.84	149	127	0.85

Table F.27: Static ($\lambda = \infty$) and dynamic ($\lambda = 1907, 1300$, and 1064 nm) β_{HRS} (10^3 a.u.) as well as static β_{ZZZ} , β_{ZXX} , $|\beta_{J=1}|$, $|\beta_{J=3}|$ (10^3 a.u.), DR and ρ of the conformers of DiBOX-TtO in POF-POF as calculated at the TDDFT/M06-2X/6-311+G(d)/IEF-PCM (acetonitrile) level of theory. The averages were obtained using the Boltzmann's populations at 298.15 K.

Conf.	%	β_{HRS}				Static quantities					
		∞	1907 nm	1300 nm	1064 nm	β_{ZZZ}	β_{ZXX}	DR	$ \beta_{J=1} $	$ \beta_{J=3} $	ρ
1	92.5	8.2	8.3	44.8	40.3	7.0	4.3	2.65	11.3	20.2	1.79
2	5.8	18.9	16.8	94.1	42.7	15.9	10.3	2.40	23.8	49.3	2.07
3	1.7	19.4	17.7	93.9	47.3	16.4	10.3	2.53	25.6	49.1	1.92
Av.		9.0	9.0	48.5	40.6	7.6	4.7	2.61	12.2	22.3	1.83

F.4 Redox Reactions



Scheme F.2: Proposed mechanism of the opening reaction of BOX's by a redox process from Ref. [1].

Table F.28: ΔG^\ominus (kJ mol⁻¹) of the different steps (Scheme F.2) involved in the reactions of opening of DiBOX-Bt by oxidation as calculated at the M06/6-311G(d)/IEF-PCM (acetonitrile) level of theory.

		CF-CF	CF-POF
Oxidation	ΔG_O^\ominus	515.1	552.9
CO cleavage	ΔG_B^\ominus	86.9	33.6
Reduction	ΔG_R^\ominus	-441.8	-455.7
Protonation	ΔG_P^\ominus	-823.6	-806.9

F.5 Synthesis

F.5.1 DiBOX-Bt

The DiBOX-Bt was prepared according to the reported procedure of Ref. [2]. A mixture of 2,2'-bithiophene-5,5'-dicarbaldehyde (0.3 g, 1.35 mmol) and cor-

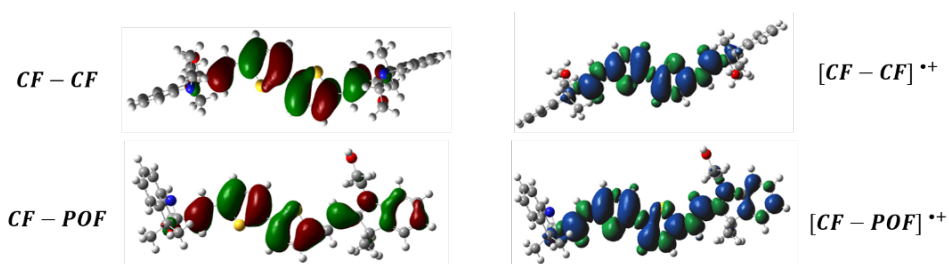
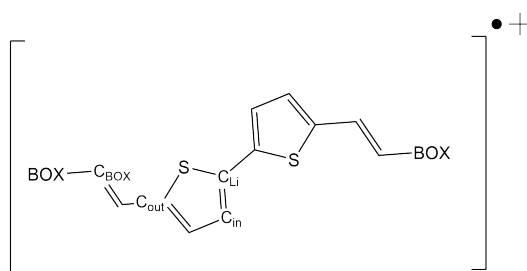


Figure F.2: HOMO of **CF-CF** (top) and **CF-POF** (bottom) (left, green = positive, red= negative, isovalue= 0.02 a.u.) and spin density of the corresponding oxidized form (right, blue= negative, green= positive, isovalue= 0.0004 a.u.) at the M06/6-311G(d)/IEF-PCM (acetonitrile) level of theory.



Scheme F.3: Labelling of the atoms for the analysis of the spin density of the radical cation species.

Table F.29: Spin density (a.u.) on selected C atoms of the CF-CF and CF-POF radical cations of DiBOX-Bt as evaluated using the Mulliken population analysis at the M06/6-311G(d)/IEF-PCM (acetonitrile) level of theory. See Scheme F.3 for the atom labelling.

	[CF–CF] ^{+•}	[CF–POF] ^{+•}	
		CF side	POF side
C _{BOX}	0.23	0.27	0.16
C _{out}	0.23	0.22	0.20
C _{in}	0.12	0.06	0.15
C _{Li}	0.09	0.18	−0.02

responding 2,3,3-trimethylindolino[2,1,b]oxazolidine (0.55 g, 2.7 mmol) was dissolved in little amount of acetonitrile (ACN). Technical grade silica (1.35 g) was put in suspension, and the solvent was removed under reduced pressure. The resulting reaction mixture was heated under stirring at 100 °C during 10 min. After cool down to room temperature, the crude material was directly purified by flash chromatography (dichloromethane/methanol, 98/2). Product was isolated as a yellow solid (496 mg, 62 %).

mp: 70-173 °C. ¹H NMR (300 MHz, CDCl₃): δ (ppm) 7.17 (td, J = 7.7, 1.3 Hz, 1H), 7.09 (d, J = 7.4 Hz, 1H), 7.05 (d, J = 3.7 Hz, 1H), 6.98-6.91 (m, 3H), 6.80 (d, J = 7.7 Hz, 1H), 6.11 (d, J = 15.6 Hz, 1H), 3.83-3.42 (m, 4H), 1.45 (s, 3H), 1.18 (s, 3H).

F.5.2 DiBOX-TtO

Tributyl(2,3-dihydrothieno[3,4-b][1,4]dioxin-5-yl)stannane (2)³

Under argon atmosphere, EDOT (2 g, 14 mmol) was dissolved in dry THF (40 mL) and cooled to −78 °C. To this solution n-BuLi (1.6 M in hexane 8.75 mL, 14 mmol) was added dropwise. The resulting mixture was stirred for 15 min at −78 °C, then 100 min at room temperature. The solution was cooled again to −78 °C and a solution of tributyltin chloride (4.94 mL, 18.2 mmol) in dry THF (20 mL) was added dropwise over a period of 20 min. The mixture was allowed to warm to room temperature and stirred at this temperature for another 19 hours. The reaction mixture was poured into cold water and the aqueous layer was extracted with Et₂O three times. The combined organic phases were dried over MgSO₄ and filtered over celite. The solvent and the residual starting material were removed under reduced pressure to afford yellow oil (6 g, 98 %). The compound was used without further purification.

¹H NMR (300 MHz, CDCl₃): δ (ppm) 6.58 (s, 1H), 4.16 (s, 4H), 0.86-1.64 (m, 27H).

2,5-bis(2,3-dihydrothieno[3,4-b][1,4]dioxin-5-yl)thiophene (3)³

The synthesis of 2,5-bis(2,3-dihydrothieno[3,4-b][1,4]dioxin-5-yl)thiophene was done following the procedure described in Ref. [3] with modifications. A mixture of 2, 5-dibromothiophene (1 g, 4.1 mmol), EDOT derivative (3.96 g, 9.1 mmol) and 7 % of Pd(PPh₃)₄ was dissolved in 30 mL of DMF. The mixture was refluxed overnight, then poured into sat. aq. NH₄Cl and extracted with DCM and the organic phase was washed with water. After being dried over anhydrous Na₂SO₄, the solvent was evaporated and the residue was purified by flash column chromatography on silica gel using a mixture of hexane/ethyl acetate (3/2) to afford a yellow solid (1.3 g, 86 %).

¹H NMR (300 MHz, CDCl₃): δ (ppm) 7.12 (s, 1H), 6.21(s, 1H), 4.24-4.35(m, 4H).

7,7'-(thiophene-2,5-diyl)bis(2,3-dihydrothieno[3,4-b][1,4]dioxine-5-carbaldehyde) (4)

To a solution of 2,5-bis(2,3-dihydrothieno[3,4-b][1,4]dioxin-5-yl)thiophene (3) (0.5 g, 1.37 mmol) and anhydrous DMF (0.22 mL, 2.88 mmol) in anhydrous 1,2-dichloroethane (30 mL) at 0 °C, POCl₃ (0.27 mL, 2.88 mmol) was added dropwise. The mixture was then refluxed for 18 hours under argon atmosphere. After being cooled to room temperature, the mixture was slowly poured into an aqueous solution of sodium acetate and then stirred for 2 hours. The obtained precipitate was filtered and the solid was washed by ethanol to afford pure compound as an orange solid (500 mg, 87 %).

¹H NMR (300 MHz, DMSO): δ (ppm) 9.85 (s, 1H), 7.50 (s, 1H), 4.52 (s, 4H). IR ν (cm⁻¹): 2923, 2852, 1727, 1636, 1450, 1122, 955. No ¹³C NMR due to very low solubility.

DiBOX-TtO

A mixture of 4 (100 mg, 0.238 mmol) and corresponding inolinoxazolidine (106 mg, 0.524 mmol) was dissolved in little amount of DCM. 0.8 g of technical grade silica were put in suspension and the solvent was removed under reduced pressure. The resulting reaction mixture was heated under stirring at 100 °C during 7 hours. After cool down to room temperature, the crude material was removed from silica by washing first with DCM followed by methanol. Solvent was slowly removed under reduced pressure until a precipitate was obtained. The precipitate was filtered and the solid was purified by flash column chromatography on silica gel using a mixture of CHCl₃/MeOH (9/1) to afford a yellow solid (120 mg, 63 %).

¹H NMR (300 MHz, CDCl₃): δ (ppm) 7.16 (t, J = 7.1 Hz, 1H), 7.13 (s, 1H), 7.07 (d, J = 6.2 Hz, 1H), 6.92 (dd, J = 15.5, 9.3 Hz, 2H), 6.79 (d, J = 7.7 Hz, 1H), 6.03 (d, J = 15.7 Hz, 1H), 4.42-4.26 (m, 4H), 3.84-3.42 (m, 4H), 1.43 (s, 3H), 1.16 (s, 3H). ¹³C NMR (75 MHz, CDCl₃): δ (ppm) 150.6, 139.8, 139.5, 137.6,

133.3, 127.6, 123.6, 123.2, 122.4, 121.7, 121.4, 113, 112.1, 110.8, 109.9, 65.2, 64.7, 63.6, 50.3, 48, 28.5, 20.3. HRMS (FAB+): m/z calcd. for $C_{44}H_{42}N_2O_6S_3$: 790.2205 $[M+H]^+$; found: 791.2279. Anal. Calc. (%) for $C_{44}H_{42}N_2O_6S_3$: C 66.81, H 5.35, S 12.16, N 3.54; found: C 66.62, H 5.46, S 12.29, N 3.63.

F.6 HRS Measurements

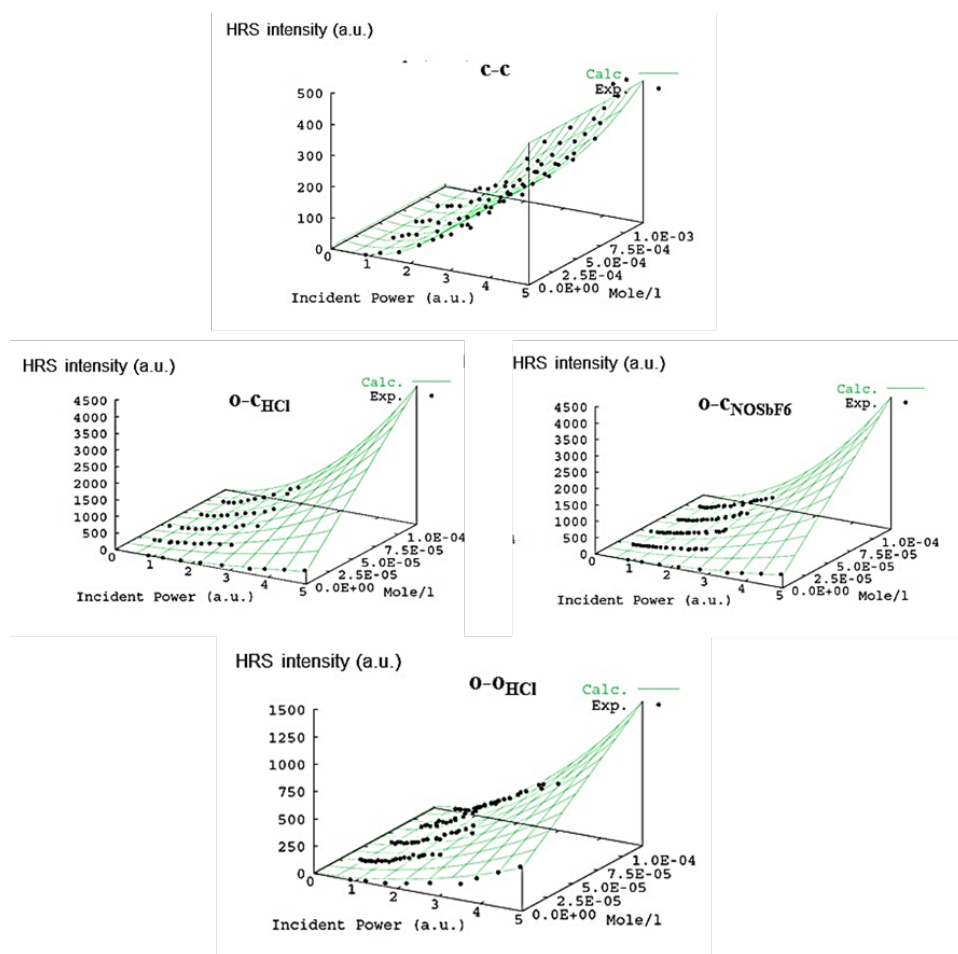


Figure F.3: HRS responses of the CF-CF (c-c) (top), POF-CF (o-c_{HCl} and o-c_{NOSbF₆}) by pH and NOSbF₆ (middle), and POF-POF (o-o_{HCl}) by pH (bottom) forms of DiBOX-Bt in acetonitrile solution.

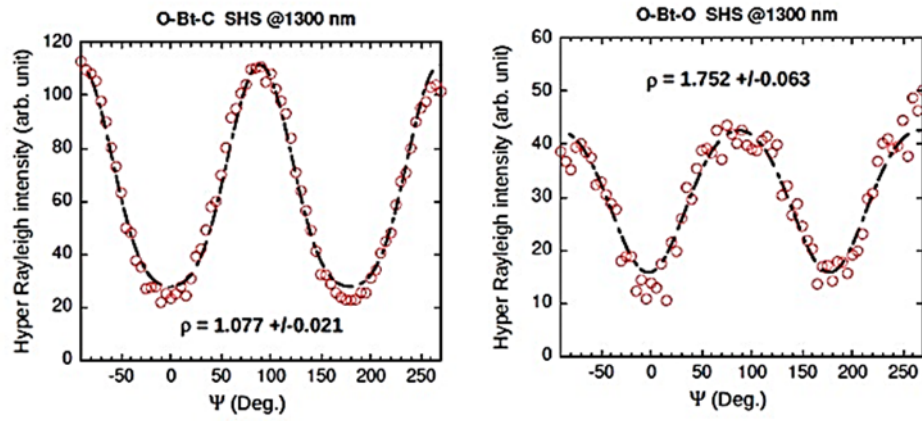


Figure F.4: Extracted plot of the polarization curve of DiBOX-Bt in its POFCF (left) and POFCF (right) forms.

Bibliography

- (1) Szalóki, G.; Sanguinet, L. In *Photon-Working Switch*. Springer Japan: Tokyo, 2017, pp 69–91, DOI: 10.1007/978-4-431-56544-4_3.
- (2) Aidibi, Y.; Guerrin, C.; Alévêque, O.; Leriche, P.; Delbaere, S.; Sanguinet, L. BT-2-BOX: An Assembly toward Multimodal and Multilevel Molecular System Simple as a Breeze. *J. Phys. Chem. C* **2019**, *123*, 11823–11832, DOI: 10.1021/acs.jpcc.9b00546.
- (3) Sevez, G.; Gan, J.; Delbaere, S.; Vermeersch, G.; Sanguinet, L.; Levillain, E.; Pozzo, J.-L. Photochromic Performance of a Dithienylethene-Indolinooxazolidine Hybrid. *Photochem. Photobiol. Sci.* **2010**, *9*, 131.